FLOW FIELD ANALYSIS OF SOME MIXING AND CONVEYING SCREW ELEMENT REGIONS, WITHIN A CLOSELY INTERMESHING, CO-ROTATING TWIN-SCREW EXTRUDER

VOLUME 1

DAVID PAUL BRUCE

Doctor of Philosophy

THE UNIVERSITY OF ASTON IN BIRMINGHAM

March 1997

THESIS SUMMARY

Grafting of antioxidants and other modifiers onto polymers by reactive extrusion, has been performed successfully by the Polymer Processing and Performance Group at Aston University. Traditionally the optimum conditions for the grafting process have been established within a Brabender internal mixer. Transfer of this batch process to a continuous processor, such as an extruder, has, typically, been empirical. To have more confidence in the success of direct transfer of the process requires knowledge of, and comparison between, residence times, mixing intensities, shear rates and flow regimes in the internal mixer and in the continuous processor. The continuous processor chosen for the current work is the closely intermeshing, co-rotating twin-screw extruder (CICo-TSE). CICo-TSEs contain screw elements that convey material with a self-wiping action and are widely used for polymer compounding and blending. Of the different mixing modules contained within the CICo-TSE, the trilobal elements, which impose intensive mixing, and the mixing discs, which impose extensive mixing, are of importance when establishing the intensity of mixing. In this thesis, the flow patterns within the various regions of the single-flighted conveying screw elements and within both the trilobal element and mixing disc zones of a Betol BTS40 CICo-TSE, have been modelled using the computational fluid dynamics package Polyflow. A major obstacle encountered when solving the flow problem within all of these sets of elements, arises from both the complex geometry and the time-dependant flow boundaries as the elements rotate about their fixed axes. Simulation of the time dependant boundaries was overcome by selecting a number of sequential 2D and 3D geometries, used to represent partial mixing cycles. The flow fields were simulated using the ideal rheological properties of polypropylene and characterised in terms of velocity vectors, shear stresses generated and a parameter known as the mixing efficiency. The majority of the large 3D simulations were performed on the Cray J90 supercomputer situated at the Rutherford-Appleton laboratories, with pre- and post-processing operations achieved via a Silicon Graphics Indy workstation. A mechanical model was constructed consisting of various CICo-TSE elements rotating within a transparent outer barrel. A technique has been developed using coloured viscous clays whereby the flow patterns and mixing characteristics within the CICo-TSE may be visualised. In order to test and verify the simulated predictions, the patterns observed within the mechanical model were compared with the flow patterns predicted by the computational model. The flow patterns within the single-flighted conveying screw elements in particular, showed good agreement between the experimental and simulated results.

Keywords: Twin-screw extruder, Reactive extrusion, Polyflow, Mixing discs, Trilobal elements

DEDICATION

The author would like to dedicate this thesis to Karen Tinker, without whose patience and understanding, this work would not have been possible.

ACKNOWLEDGEMENTS

The author would like to acknowledge the support of Polyflow S.A., Betol Machinery Ltd. and also the use of the supercomputing services from the Rutherford-Appleton Laboratory. The invaluable support of Drs M P Wilson, S Generalis and S Al-Malaika are gratefully acknowledged. Finally Mr R Evans for his assistance on the construction of the CICo-TSE mechanical model.

LIST OF CONTENTS

VOLUME 1

LIST OF FIGURES

LIST OF TABLES

Table 8-9: 3D Results Table for the Simulation of Flow Within the Trilobal Element Mixing Zone (II).

LIST OF GRAPHS

LIST OF APPENDICES

Appendices T1-T5:

Macro-Vertices Assigned to Each of the Set 1, 2D Mixing Disc Meshes.

Appendix U: Macro-Element Numbering Schemes Assigned to Each of the Set 1, 2D Mixing Disc Meshes.

Appendix V: Macro-Element Construction Details for Each of the Set 1, 2D Mixing Disc Meshes.

Appendix W: Boundary Numbering Scheme Used for Each of the Set 1, 2D Mixing Disc Meshes.

Appendix X: Macro-Vertex Numbering Scheme Assigned to Meshes Pertaining to Set 2 Representations of the 2D Mixing Discs.

Appendices Y1-Y2:

Macro-Vertices Assigned to Each of the Set 2, 2D Mixing Disc Meshes.

Appendix Z: Macro-Element Numbering Schemes Assigned to Each of the Set 2, 2D Mixing Disc Meshes.

Appendix AA: Macro-Element Construction Details for Each of the Set 2, 2D Mixing Disc Meshes.

Appendix AB: Boundary Numbering Scheme Used for Each of the Set 2, 2D Mixing Disc Meshes.

Appendix AC: Macro-Vertex Numbering Scheme Assigned to Meshes Pertaining to Set 1 Representations of the 2D Trilobal Elements.

Appendices AD1-AD6:

Macro-Vertices Assigned to Each of the Set 1, 2D Trilobal Element Meshes.

Appendix AE: Macro-Element Numbering Schemes Assigned to Each of the Set 1, 2D Trilobal Element Meshes.

Appendix AF: Macro-Element Construction Details for Each of the Set 1, 2D Trilobal Element Meshes.

Appendix AG: Boundary Numbering Scheme Used for Each of the Set 1, 2D Trilobal Element Meshes.

Appendix AH: Macro-Vertex Numbering Scheme Assigned to the Mesh Pertaining to the Set 2 Representation of the 2D Trilobal Elements.

Appendix AI: Macro-Vertices Assigned to the 2D Trilobal Element Mesh Pertaining to Set 2.

Appendix AJ: Macro-Element Numbering Scheme Assigned to the 2D Trilobal Element Mesh Pertaining to Set 2.

Appendix AK: Macro-Element Construction Details for the 2D Trilobal Element Mesh Pertaining to Set 2.

Appendix AL: Boundary Numbering Scheme Used for Each of the Set 2, 2D Trilobal Element Meshes.

Appendix AM: 3D Parameters Table for the Single-Flighted, Conveying Screw Elements.

Appendix AN: 3D Parameters Table for the Staggered Mixing Disc Zone.

Appendix AO: 3D Parameters Table for the Trilobal Element Mixing Zone.

(41 Appendices).

1 INTRODUCTION

The traditional approach to the design and scale-up of equipment for the processing of viscous materials is typically empirical. Whilst empiricism has intrinsic value, it may be time-consuming, expensive and is unlikely to lead to the optimum design for a particular duty. Thus it would be of significant value to the designer to be able to predict the characteristics of flow within a proposed configuration before committing the design to pilot tests or production. With the aid of increasingly sophisticated CFD packages, competent researchers can now address important industrial flow problems, such as the simulation of complex fluid rheology within the closely intermeshing, co-rotating twin screw extruder (CICo-TSE). The work described in this thesis, helps to establish procedures for identifying ideal configurations for optimum mixing and shear levels for a particular extrusion process, within the following CICo-TSE sections;

- Single-flighted conveying screw elements.
- Staggered mixing disc zone.
- Trilobal element mixing zone.

1.1 Processing Viscous Materials

In a viable commercial process involving the mixing of feed components to produce a highly viscous end-product, a compromise needs to be met between the degree of mixing and the processing costs. To identify the position of this compromise, knowledge of both the fluid flow patterns and mixing mechanisms are needed together with an ability to evaluate the degree of mixing achieved. One important process that combines mixing and reaction of viscous material components within a single vessel, is Reactive Extrusion (REX). REX may be achieved in either batch or continuous operation. The process is particularly suited to the modification of bulk polymers such as polypropylene (PP) or polyethylene (PE) to produce high value-added speciality materials. REX is the subject of significant commercial interest and activity [1-3] in both the polymer and food industry. Optimisation of the design of REX processes is not easily achieved empirically. Many processing parameters have a marked effect on the levels of mixing achieved and these effects need to be fully understood for successful design. Better understanding of the rheological and mechanistic behaviour of the processes involved is therefore required in order to have more confidence in the prediction of a particular process performance.

Within the Chemical Engineering and Applied Chemistry (CEAC) Department at Aston University, UK, the Polymer Processing and Performance Group (PPPG) have performed successful grafting of antioxidants and other modifiers onto bulk polymers using REX [4-6].

These grafting reactions have initially been carried out within an internal mixer and the process then transferred to a continuous mixer, specifically the BTS30 CICo-TSE, manufactured by Betol Machinery Ltd. [7]. Improvements in the amount of modifier grafted have been achieved empirically. This approach can be time consuming and the transfer, particularly to large scale equipment, is not easy. For the process transfer from a batch to continuous mixer for instance, the role of process parameters such as processing temperature, rotational speed of the elements and the state of the components (liquid, powder or pellet form for example) all need to be fully appreciated.

1.2 The Batch Process

The Banbury mixer, which was developed in 1916 by Fernley Banbury [8-9] is widely used within industry for high intensity mixing processes, particularly in the processing of rubber compounds. The mixer consists of a figure-of-eight chamber containing two spiral lobed rotors, one contained in each half chamber; there are small clearances between these rotor tips and the chamber wall and this is shown schematically in Figure 1-1. Other types of internal mixer based on the Banbury have been developed with differing rotor designs, each specifically constructed to exhibit different types of mixing. The PPPG at Aston use an internal mixer known as the Brabender Plasti-corder [9] in their research work and this type of mixer is a variable torque rheometer, which possesses lobed rotors of the design shown in Figures 1-2 and 1-3. This type of rotor design imposes lower shear levels on the material matrix than the Banbury does and is thus more suited for processing plastic composites. In the typical internal mixer design, the feed material and additives are loaded, using a hydraulic ram, into the heated internal mixer chamber via a vertical chute. Mixing of material is achieved by the counter-rotation of the two rotors, each rotating at a different speed. The constituents are mixed for a set time period and after this, the product is removed. The torque exerted by the rotors is monitored and mixing is said to be complete once this torque reading remains steady. In the typical empirical approach, improvements in the desired products of the end-product may be achieved by either modifying the quantities of the initial constituents or by changing the process parameters such as processing temperature, rotor speed or residence time.

1.3 The Continuous Process

The continuous process for processing high viscosity media is the screw extrusion process. Material is processed as it is conveyed by the screws along a heated barrel. The individual constituents are mixed by selectively imposing different mixing mechanisms at different stages along the flow path. The viscous end-product is shaped after processing by extrusion,

Figure 1-1:

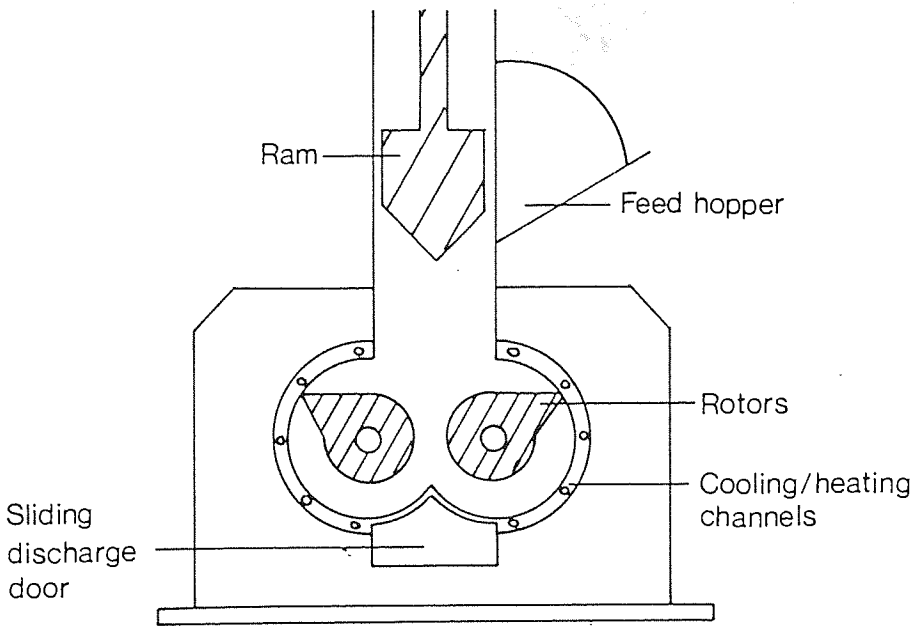

Banbury mixer – diagrammatic.

Figure 1-2: Brabender Plasti-corder Internal Mixer, Utilised by the PPPG at Aston.

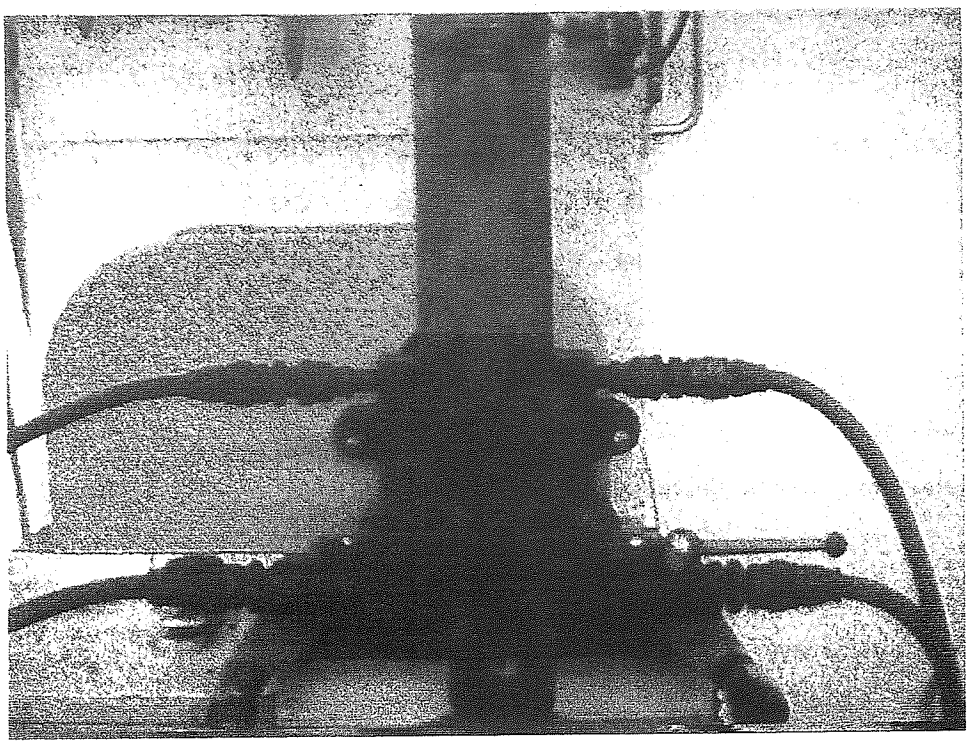

Figure 1-3: Close-up of the Processing Chamber of the Brabender Plasti-corder Internal Mixer.

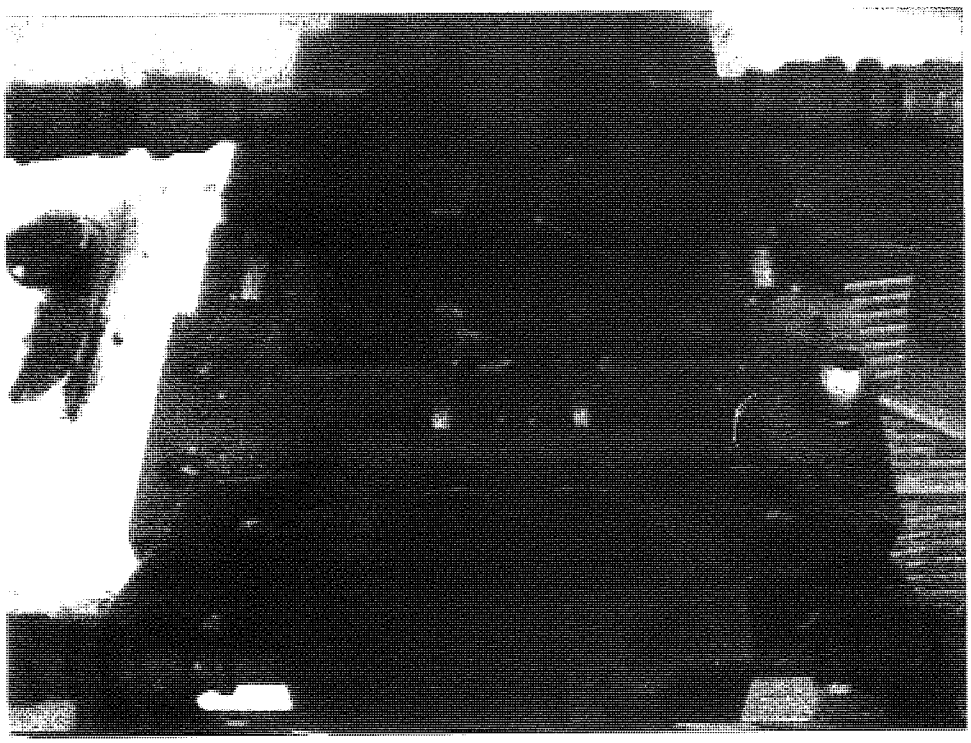

which is the forcing of material under pressure through a shaped die.

The workhorse of the polymer processing industry, as well as other industries such as the food industry, is the single screw extruder (SSE). Figure 1-4 shows a diagram of a typical extrusion screw together with the appropriate nomenclature used to describe its features. The SSE imposes compression and decompression on the material by changing the area for flow by varying either or both the root diameters of the screw and the screw pitch; the screw outside diameter remains unchanged. Figure 1-5 shows illustrations of typical SSE screw shaft configurations used in industry for various processing applications. Much research has been published on the SSE and its processing mechanisms are suggested to be very well understood [10 and references therein].

The SSE has limitations and cannot be claimed to process all materials successfully. For heat sensitive polymers such as unplasticised polyvinylchloride (uPVC), the SSE is deemed unsuitable as the high shear generated degrades the polymer significantly. To overcome these limitations other extruder designs, notably the twin screw extruder (TSE), have grown in industrial use over approximately the past 30 years as the machinery of choice for processes for which the SSE is regarded as unsuitable. The TSE differs from the SSE in exhibiting a self-wiping mechanism, which has the great advantage of eliminating stagnant zones.

1.4 Processing Using a TSE

The TSE [11-14] is more sophisticated in design than both the internal mixer and SSE and its processing mechanisms are complex and not as well understood [15-16 and references therein]. This is partly due to the TSEs more complicated geometry and the fact that the wider use of multiple screw extruders in industry is a more recent development. A typical TSE consists of two parallel screw shafts each carrying modular screw and mixing elements. The whole is enclosed by the modular, figure-of-eight sections of the outer barrel, as shown in Figures 1-6 and 1-7. Figure 1-8 shows an example of a Werner and Pfleiderer CICo-TSE machine [17], illustrating the position of the CICo-TSE elemental train within the machinery as a whole. Figures 1-9 and 1-10 illustrate typical TSE sections, representing the outer and inner machinery details respectively. The TSE screw shafts are both driven at the same rotational speed. The nature of the machine assembly means that more sophisticated parameter regulation can be utilised within the TSE. For example, the following may be achieved;

- A temperature profile can be programmed along the outer barrel of a TSE.
- The feed rate of both the feed polymer and additives may be varied independently.
- The positions of the TSE elements and feed additive ports may be changed to influence the

Figure 1-4:

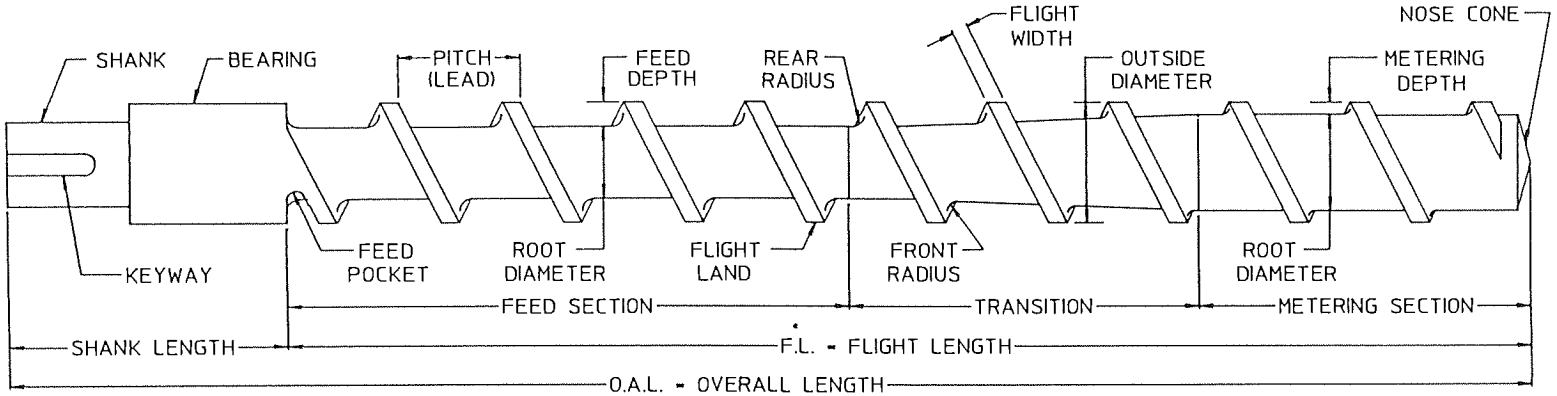

Nomenclature: Extrusion Screw

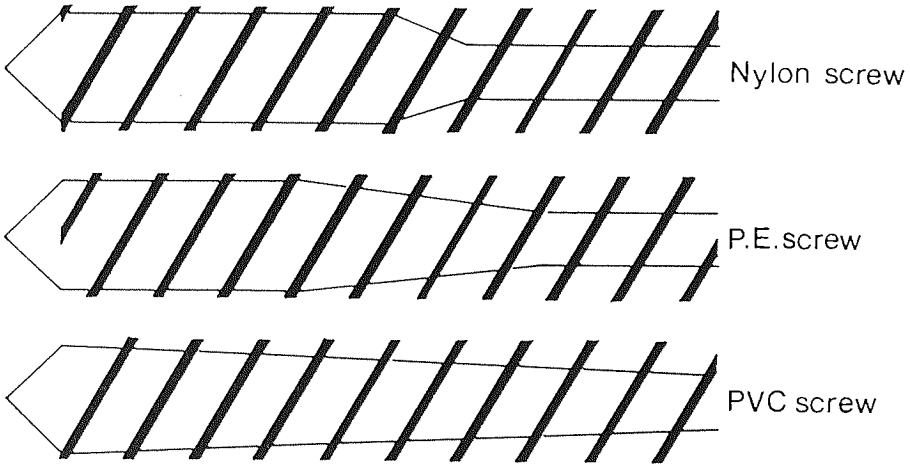

Figure 1-5:
Variations in screw design.

Figure 1-6:
Modular TSE Outer Barrel Casings.

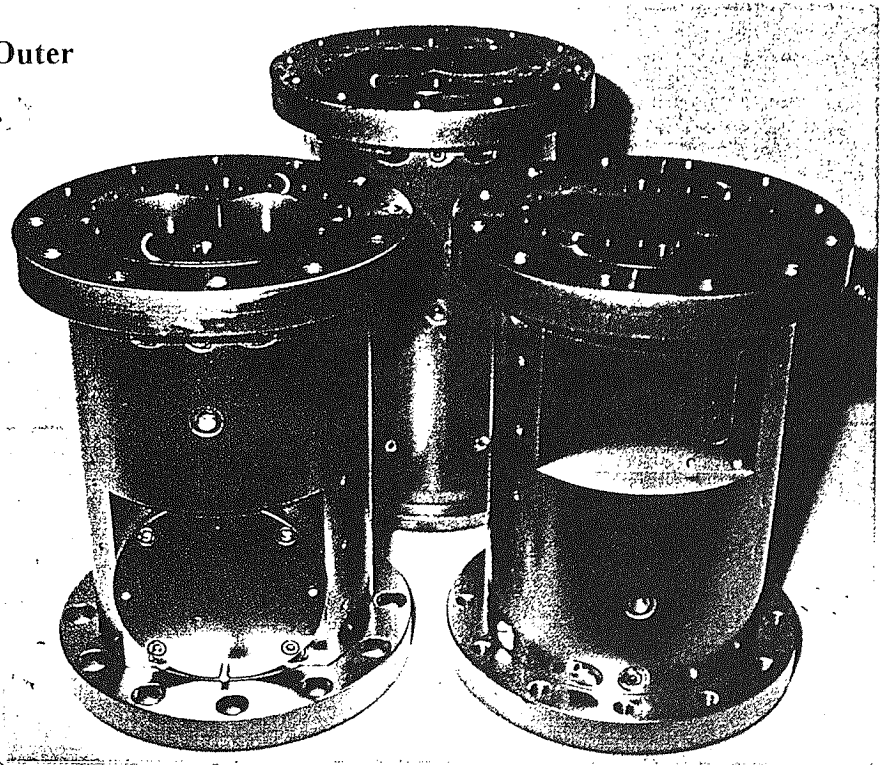

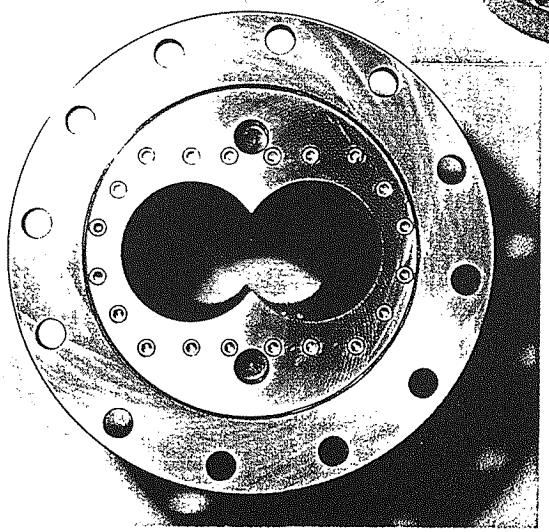

Figure 1-7:
Close-up of the X-Y Cross-Sectional Plane for a TSE Outer Barrel Casing.

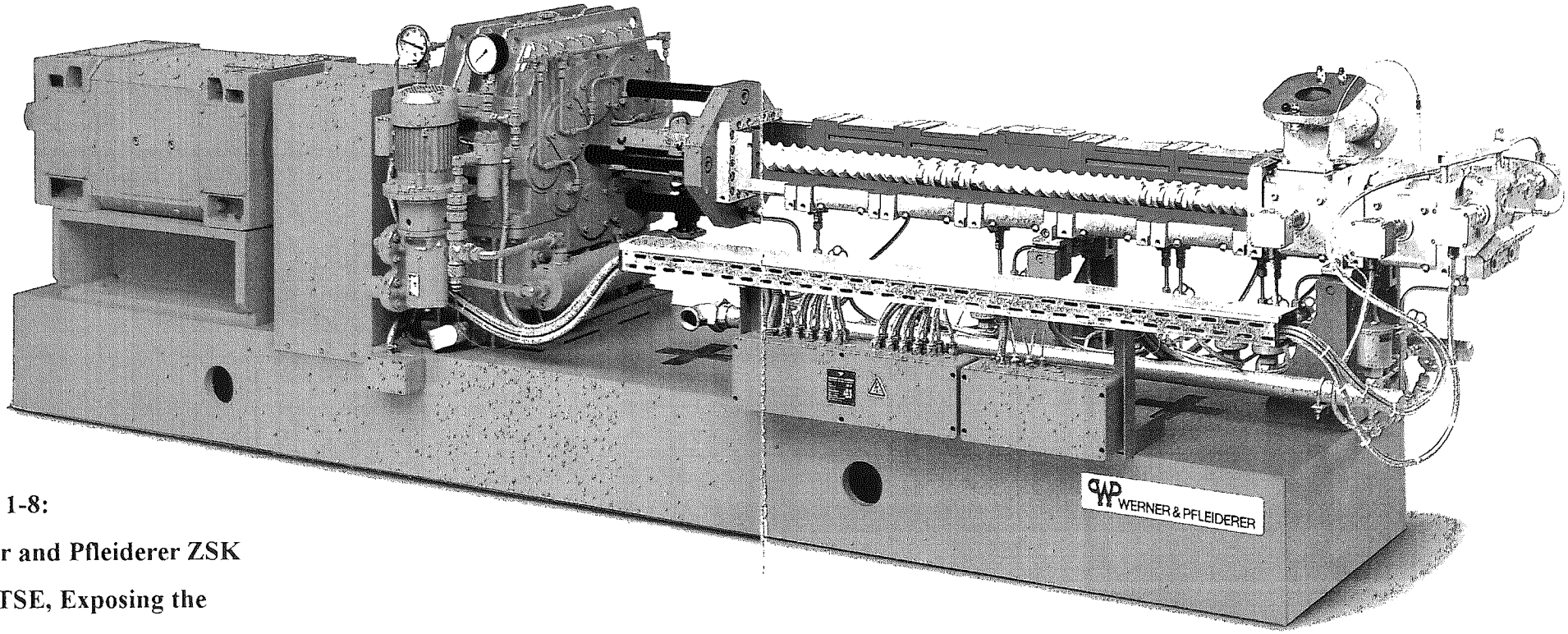

Figure 1-8:
Werner and Pfleiderer ZSK CICo-TSE, Exposing the Position of the Screw Train Within the Machinery.

Figure 1-9:
Schematic Diagrams of the Outer Casing of the Betol BTS40 CICo-TSE.

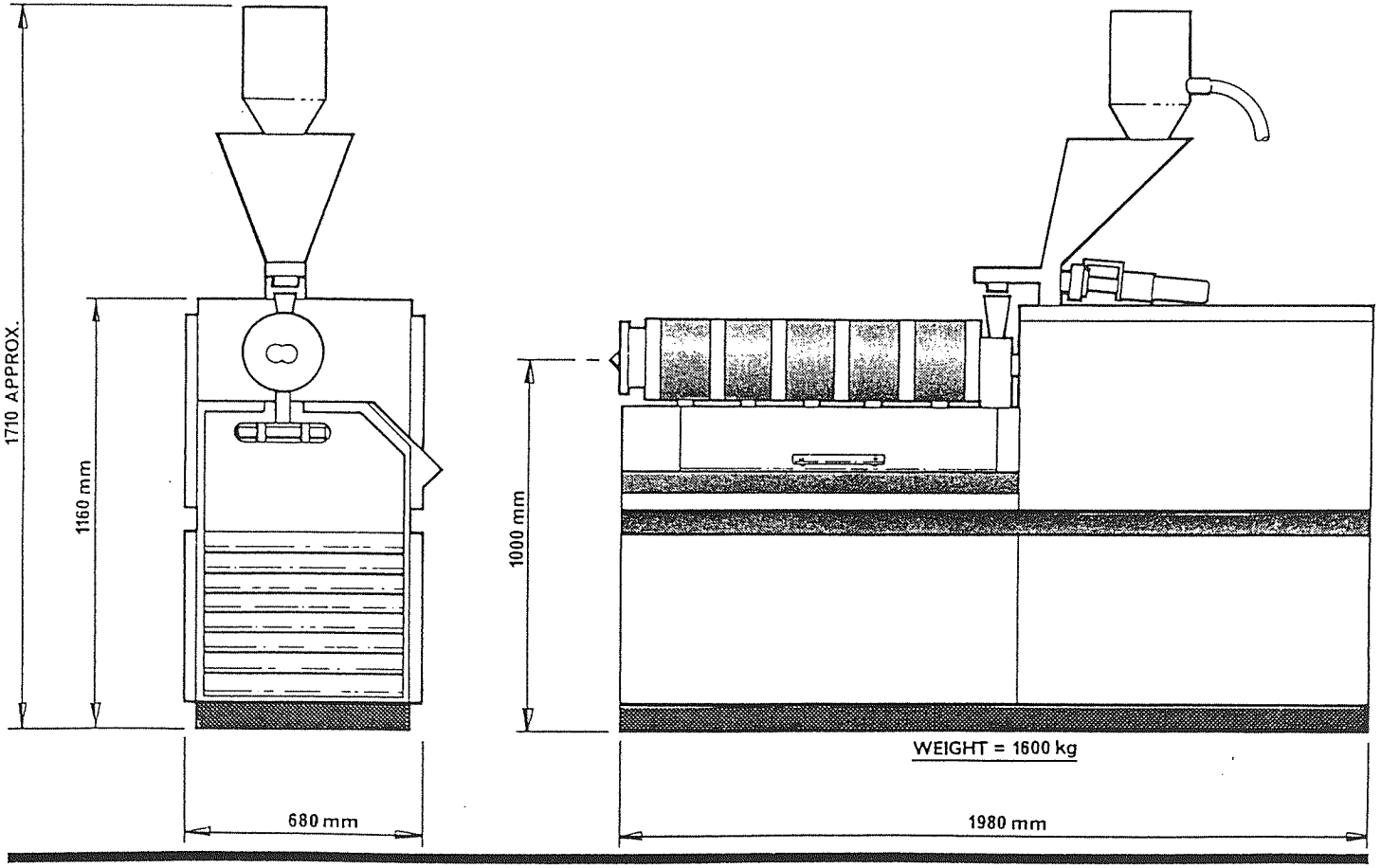

Figure 1-10:
Schematic Diagrams of the Inner Component of the Betol BTS40 $ClCo_6$-TSE.

mixing process.

The principle of operation of the TSE continuous process may be represented by the following steps;

- Feed material is melted and conveyed via the feed screws into a compression screw section.
- Compressed material is then highly mixed using a set of mixing elements.
- Mixed material is decompressed to release any volatiles
- The compression, mixing and decompression steps may be repeated several times using different types of mixing element as required.
- Processed end-product is metered and extruded under pressure through a shaped die.

The above steps may be modified and repeated many times to introduce and mix a number of different additives at each of the different process stages. Thus, different TSE configurations may consist of any number of discrete mixing element zones and different arrangements of compression or decompression sections may be exploited. Figures 1-11 and 1-12 show typical TSE configurations indicating positions were these zones may be located. The character of the end-product and the cost of processing are affected by the intensity and duration of mixing. It is clearly advantageous to ensure that polymeric material is well mixed before further additives are introduced or before the end-product is extruded. If a multi-component polymeric product is extruded without being well mixed, then its likelihood of service failure will be higher than that of a well-mixed product. As with the different types of internal mixer, residence time plays a major role in the mixing process of a TSE. It is clearly wasteful of energy to continue to mix material which is adequately mixed. Moreover, any stored excess thermal energy will need to be removed from the polymeric end-product and will only add to the processing costs.

The increase in flexibility that is gained by using two screw shafts in parallel allows a number of different types of TSE mixing process, each exhibiting a different mixing mechanism. The list of TSE machinery options and elements that are available to the polymer engineer are listed as follows [18];

- TSE machinery can either rotate the screw shafts in a co-rotating or counter-rotating manner An example of each type of screw profile is shown in Figures 1-13 and 1-14 respectively.
- The screw shafts contain screw elements that may be either closely intermeshing, partially

Figure 1-11:

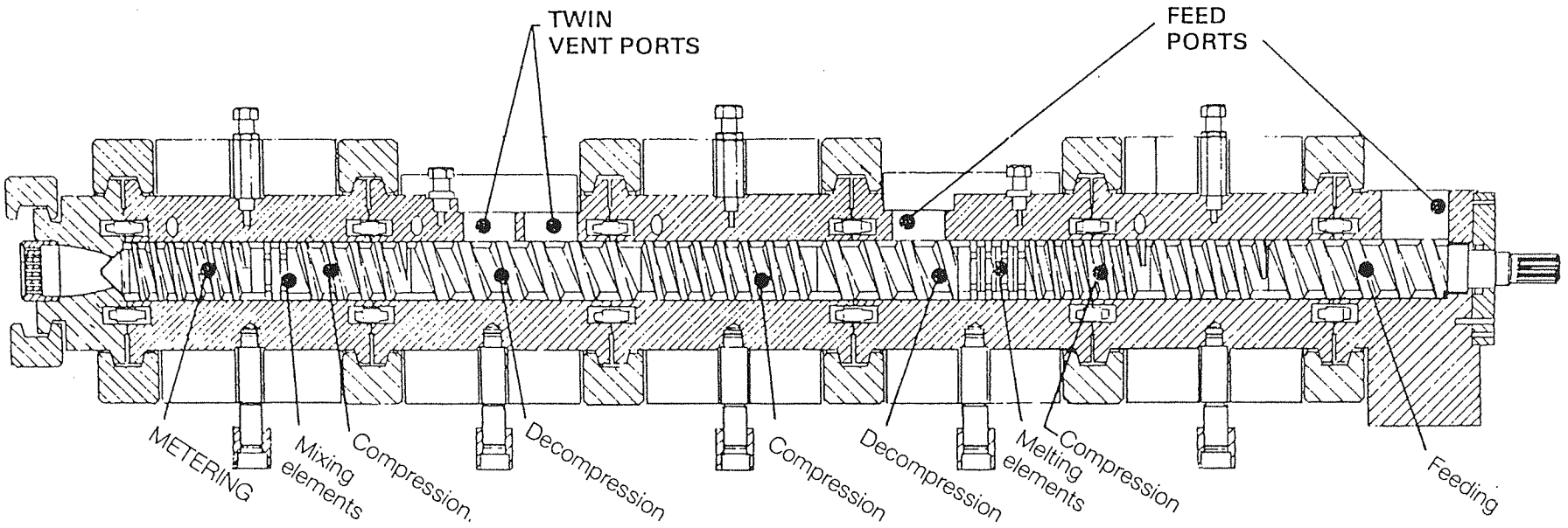

Typical screw and barrel configuration for the compounding of highly filled thermoplastics.

Figure 1-12:

Schematic Diagrams of Further CICo-TSE Screw Train Arrangements.

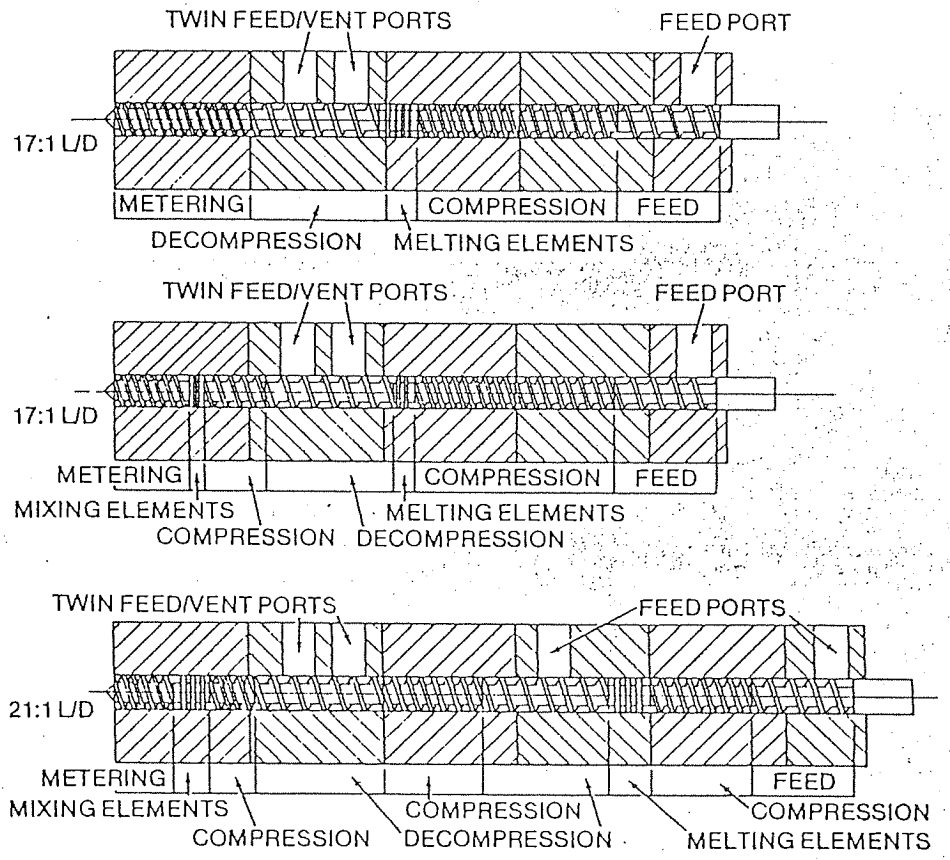

. Schematic diagrams of screw and barrel assemblies for various compounding applications.

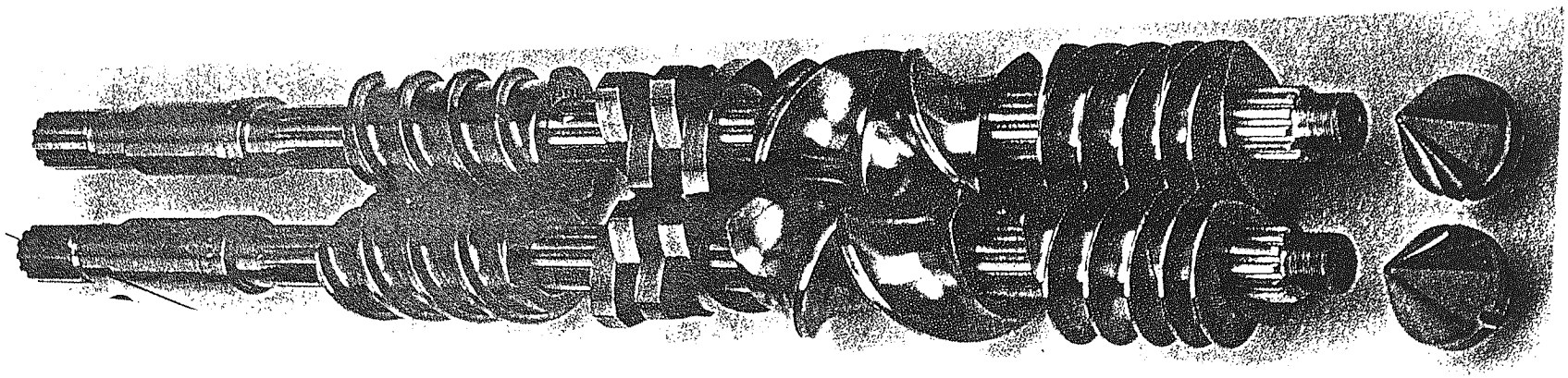

Figure 1-13:

Example of the Modular Elements and Screw Shafts Used Within a Typical CICo-TSE Screw Train Arrangement.

47

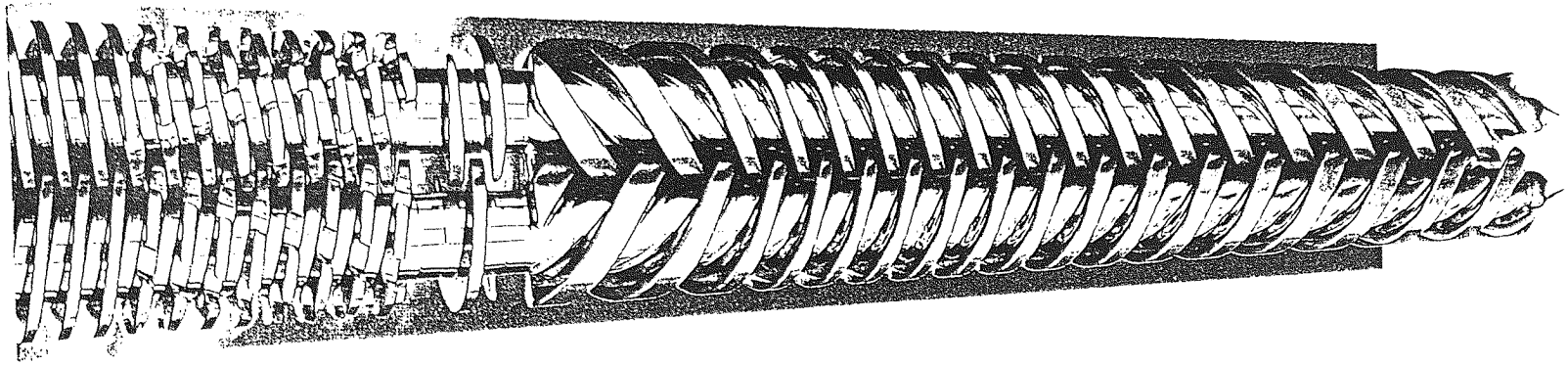

Figure 1-14:

Example of How the Conical Modular Elements Used Within a Typical Counter-Rotating TSE Screw Train Arrangement Intermesh.

intermeshing or non-intermeshing as shown both in the table of Figure 1-15 and the cross sections of Figure 1-16.

- These screw elements may be either single-, double-or triple-flighted in design. Diagrams illustrating these different screw types and 2D cross sections are given in Figure 1-17.
- The mixing elements contained within a TSE may impose either intensive or extensive mixing mechanisms on the material matrix. In addition, pairs of elements on opposing screw shafts may be configured in one of two ways;

1. Mixing elements may be arranged in the same plane, so as not to intermesh,

or,

2. mixing elements may be staggered down the barrel in an intermeshing fashion.

It is apparent from the preceding list that there are many different configurations of TSE machinery that may be utilised. TSE screw elements are very different in design from those of the SSE. Both types of extruder convey, compress and decompress material, but this compression and decompression is achieved within TSE screw elements by varying the screw pitch. The screw inner shaft diameter, which may vary for the SSE screw shaft, does not vary for any TSE screw element. The exception to this rule is that counter-rotating Co-TSEs may be conical, as shown in Figure 1-18.

The role of the mixing elements are vitally important in the successful mixing process. A wide variety of mixing elements and configurations may be utilised. In order to better describe the mixing process, two basic types of mixing mechanisms need to be clearly defined, so that an appreciation of the distinct differences between the action of each mixing element type may be gained [9].

1.4.1 Intensive mixing

Otherwise known as dispersive mixing. Involves the intimate dispersion of one phase into the bulk material matrix. Usually the result of good dispersive mixing is an irreversible mechanical break-up of the elements of the dispersed phase. Dispersive mixing, involving viscous materials, requires high shear forces to bring about this change.

1.4.2 Extensive mixing

Otherwise known as distributive mixing. Involves the spatial distribution of components without the changing of their physical size. In theory, the stirring together of components to bring about distributive mixing implies that the individual components may be separated back to their original unmixed condition.

Figure 1-15:
Schematic Diagram of the Possible TSE Arrangements, Describing How Screw Element Pairs Would Configure.

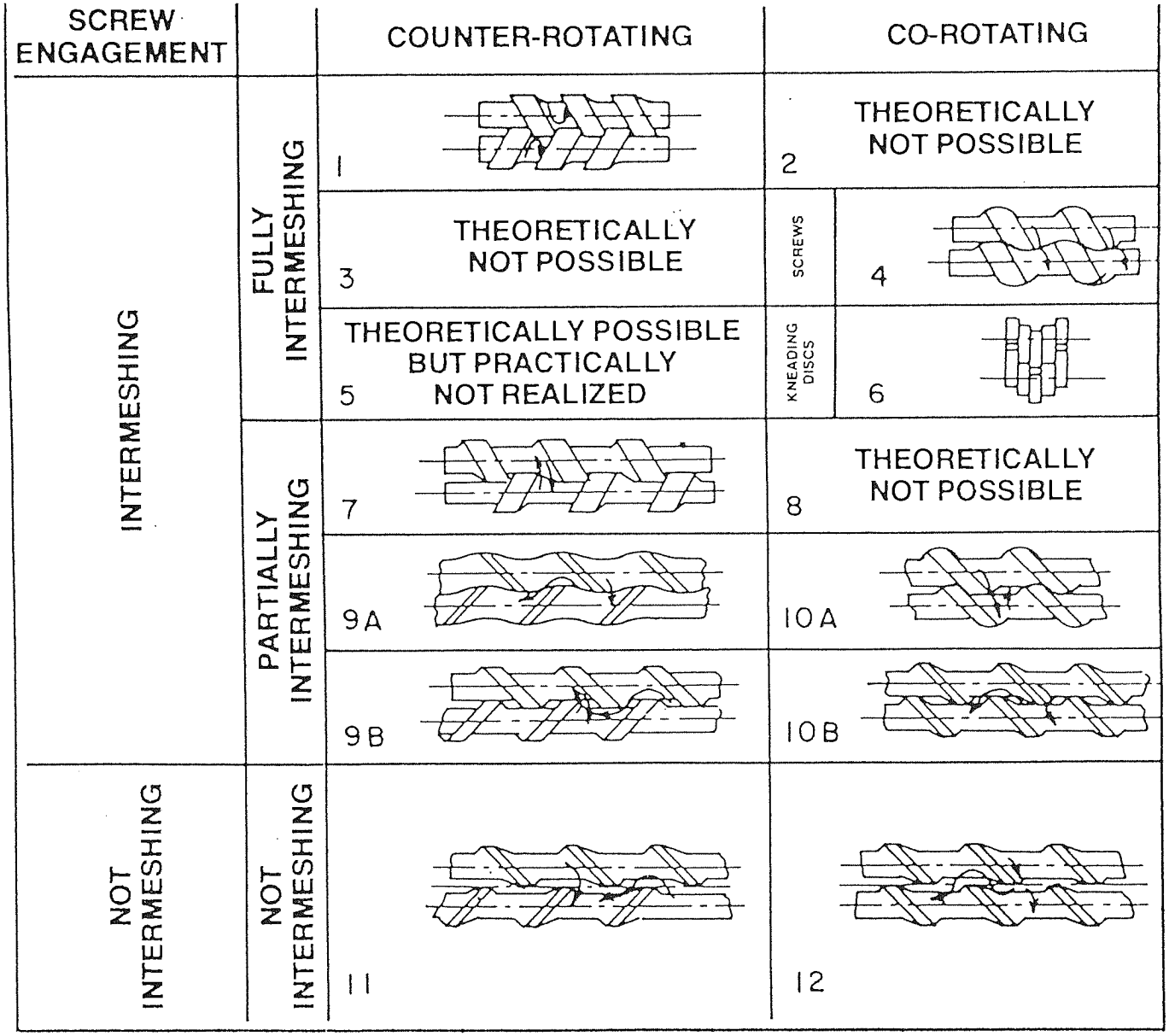

Figure 1-16:

Schematic Diagrams Describing the Intermeshing of Screw Elements for the Different TSE Arrangements.

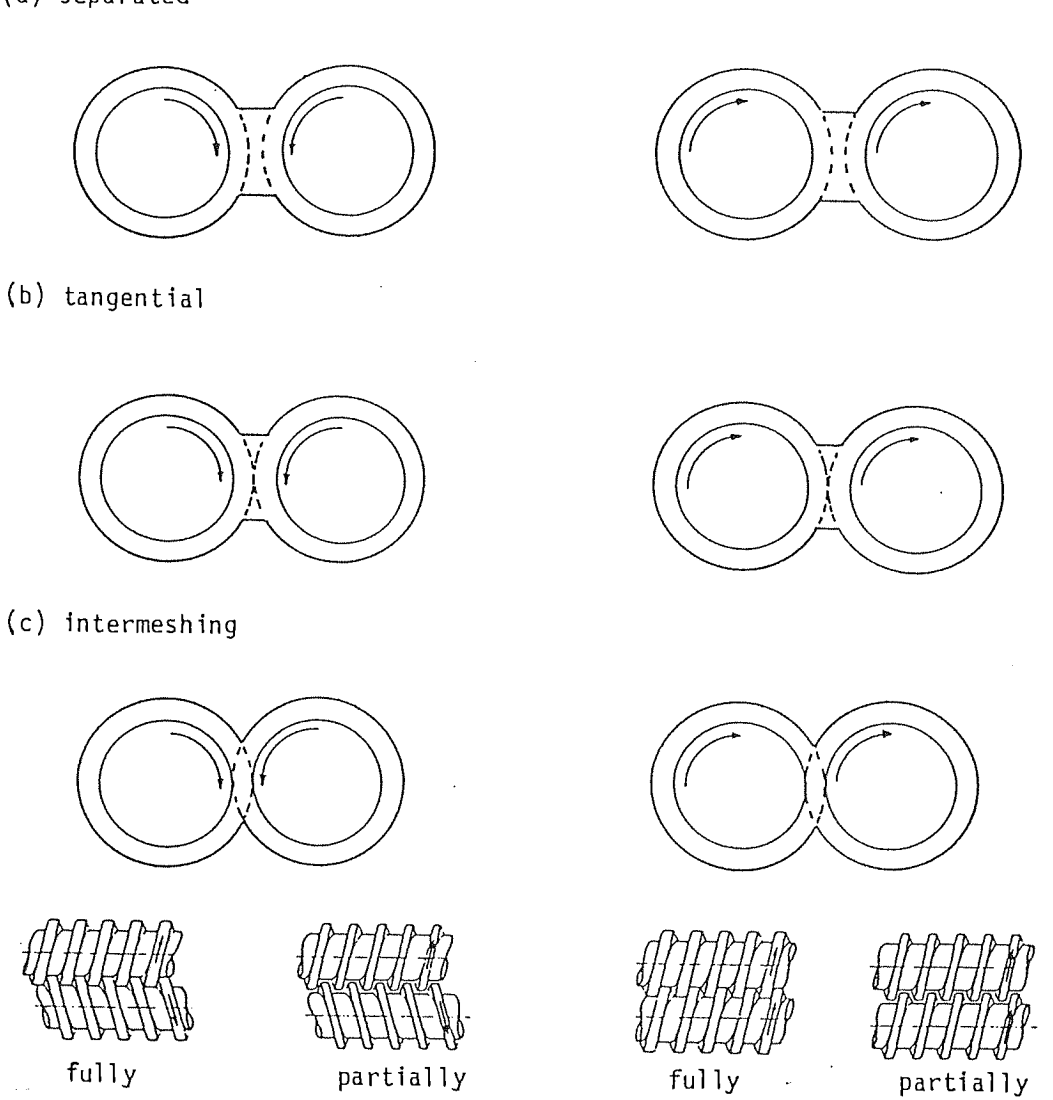

Classes of contact between screws in twin screw extruders (a) separated, (b) tangential, and (c) intermeshing.

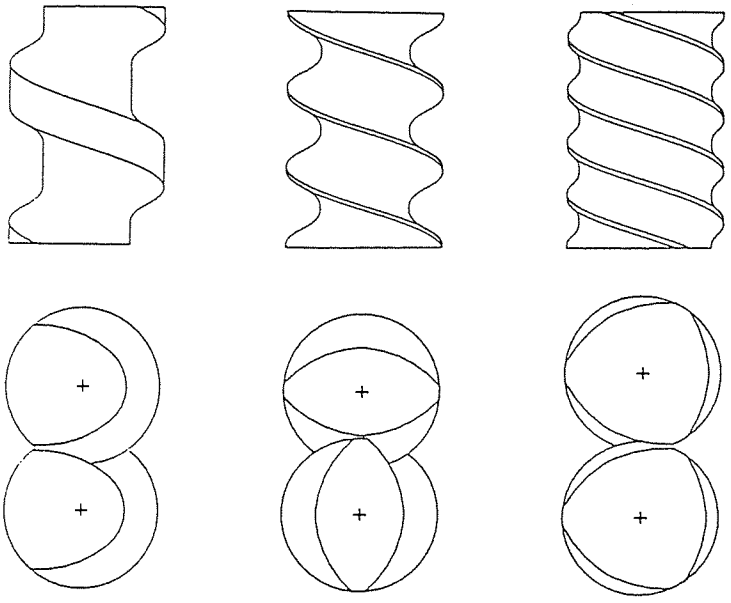

Single, double, and triple lobe intermeshing co-rotating twin screws

Figure 1-17:

Schematic Diagrams Showing Both the Screw Profiles and X-Y Cross-Sectional Planes of the Single-, Double- and Triple-Flighted, CICo-TSE Conveying Screw Elements.

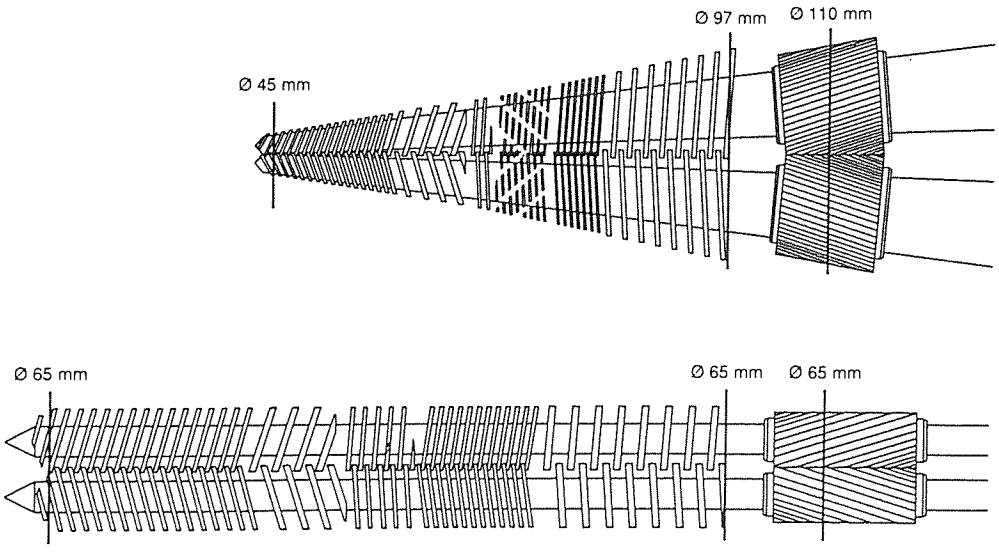

Figure 1-18:

Schematic Diagrams Contrasting the Difference Between the Conical and Normal Counter-Rotating, TSE Screw Train Arrangements.

Schematic examples of the routes taken for both dispersive and distributive mixing mechanisms are shown diagrammatically in Figure 1-19.

1.5 The Betol BTS type of CICo-TSE

The Betol BTS range of CICo-TSE machinery, contains single-flighted conveying screw elements, that convey material with a self-wiping action and several different sets of mixing elements. The Betol BTS30 CICo-TSE owned by the PPPG at Aston is shown in Figure 1-20. The different types of mixing elements used within the BTS range are listed as follows;

- Mixing discs, exhibiting predominantly extensive mixing mechanisms.
- Trilobal elements, exhibiting intensive mixing mechanisms.
- Bilobal elements (not considered in this study).

Each set of mixing elements can be used either mutually exclusively or in combination within a particular CICo-TSE configuration. There are many other different types of mixing element that may be utilised and the most popular and most widely examined set of mixing element used within the polymer processing industry, are the kneading blocks patented by Erdmenger in 1950's [19] and developed commercially by Werner and Pfleiderer [20]. Diagrams showing the different types of mixing elements available to the polymer processing engineer when using CICo-TSEs are shown in Figures 1-21 to 1-23 for the kneading blocks and Figure 1-24 for the Betol BTS range of mixing elements.

The Betol BTS range of CICo-TSEs are designed such that each of the modular outer metal barrel sections can be heated independently and can be removed to allow polymeric samples to be taken in-situ. This sampling procedure is carried out after processing the polymeric samples having set the desired temperature profile. The screw rotation is stopped and, whilst the modular barrel sections are maintained at high temperature, the sections are removed one at a time. The screw shafts are then exposed and samples may be taken. Once sampling has been completed, the barrel sections are replaced whilst still hot. This procedure is complex and may take a team of trained personnel several hours to perform successfully. In order to avoid this demand on limited manpower and expertise, other ways of investigating mixing mechanisms within the CICo-TSE have been sought and successfully developed.

1.6 Visualisation and Prediction of flow parameters

The ability to represent fluid flow in terms of velocity vectors, pressure profiles and shear stresses generated and to predict values for these various fluid flow parameters, is of invaluable assistance to the polymer engineer investigating mixing behaviour of viscous

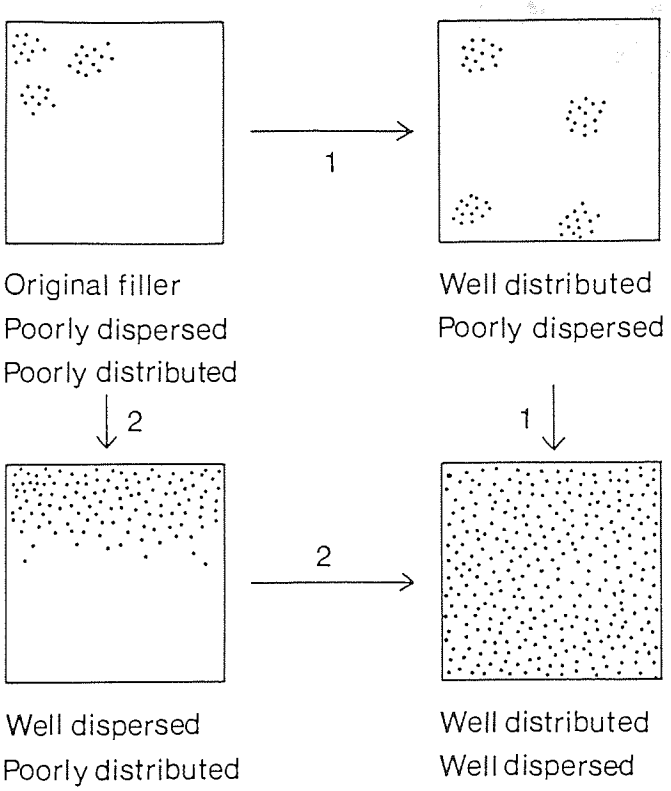

Routes to mixing.

Figure 1-19:

Schematic Diagram Illustrating the Different Dispersive and Distributive Routes to Mixing.

Figure 1-20:
Betol BTS30 CICo-TSE Utilised by the PPPG at Aston.

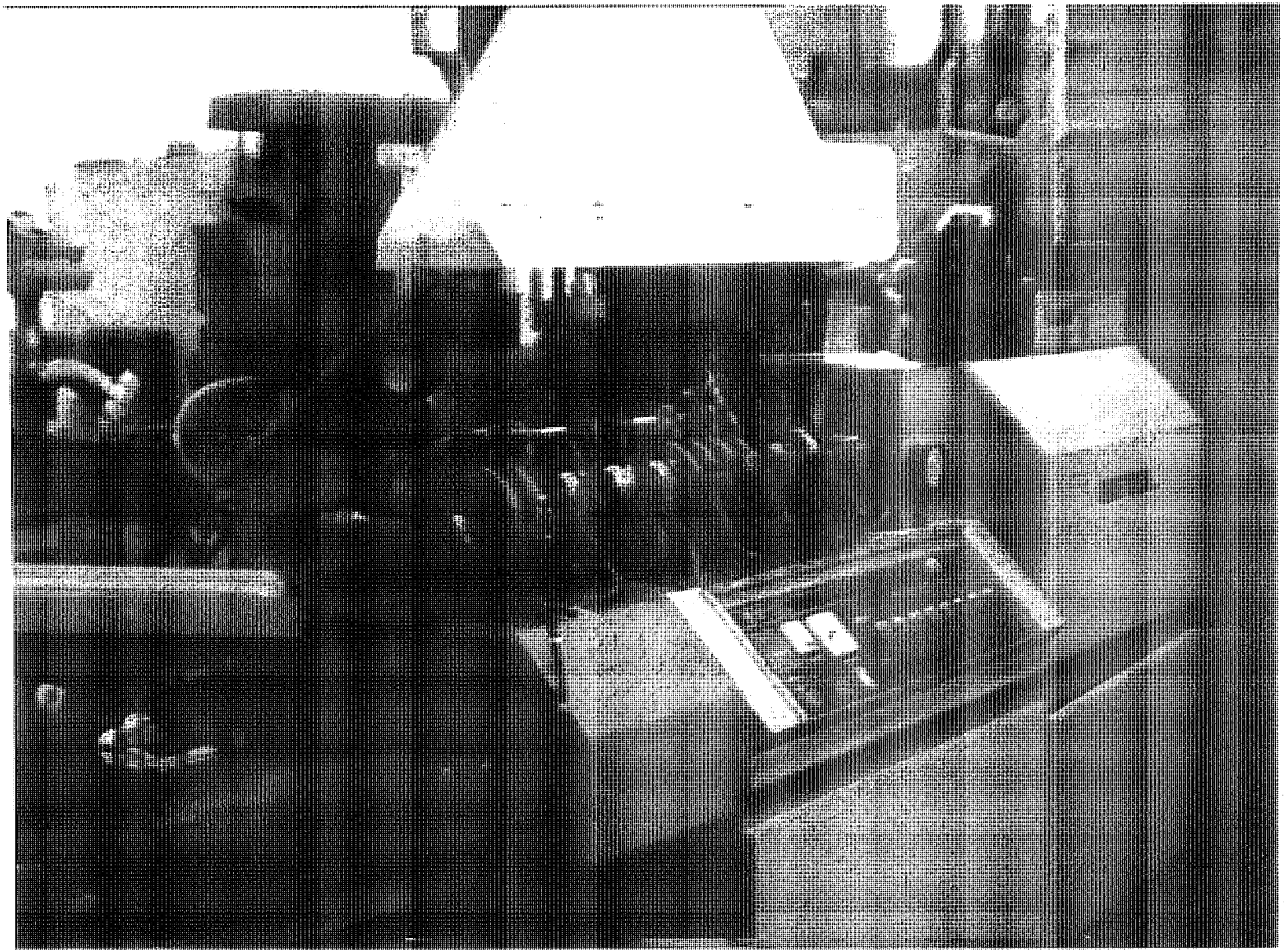

54

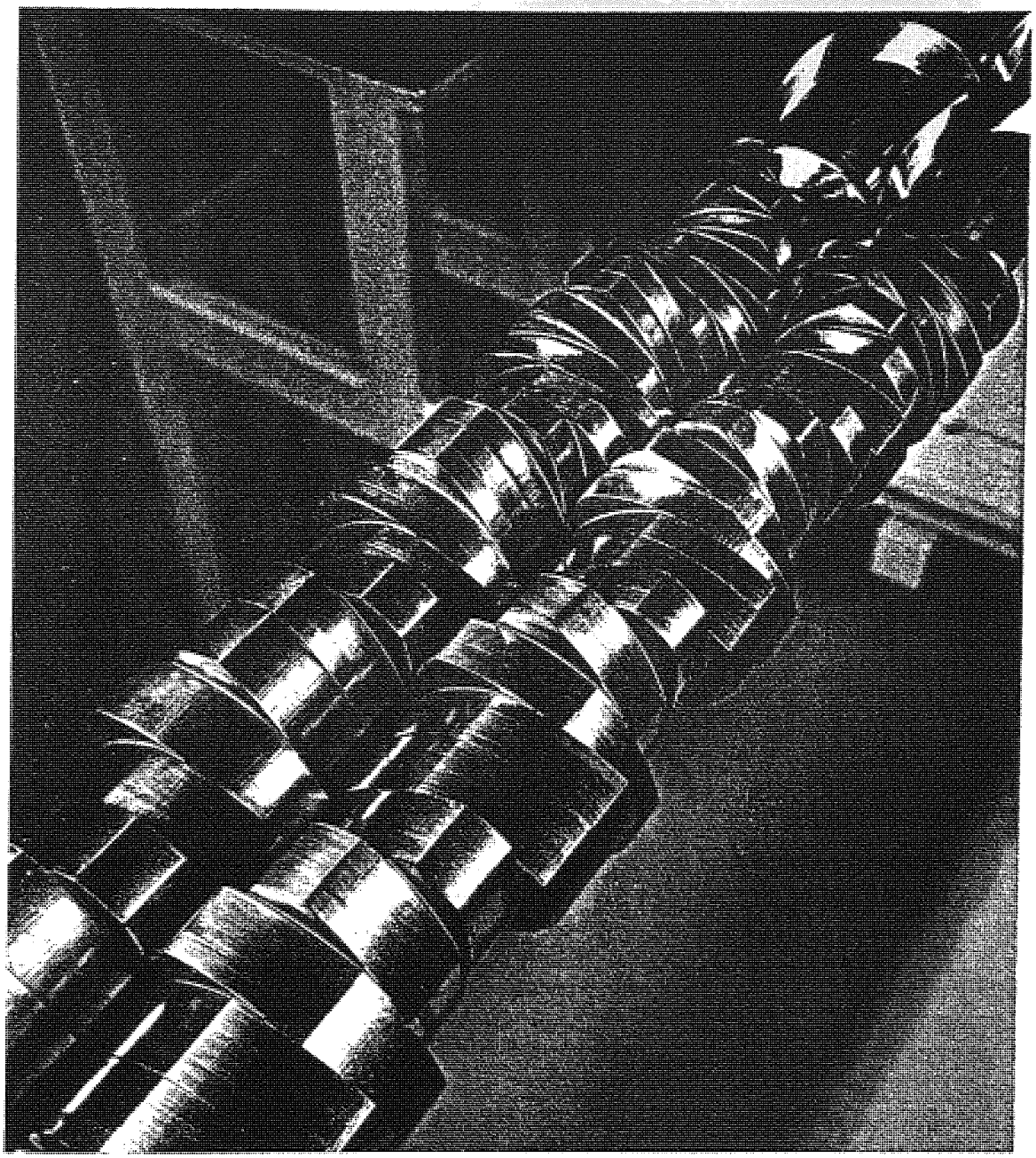

Figure 1-21:

Example of a Complex Kneading Block Arrangement.

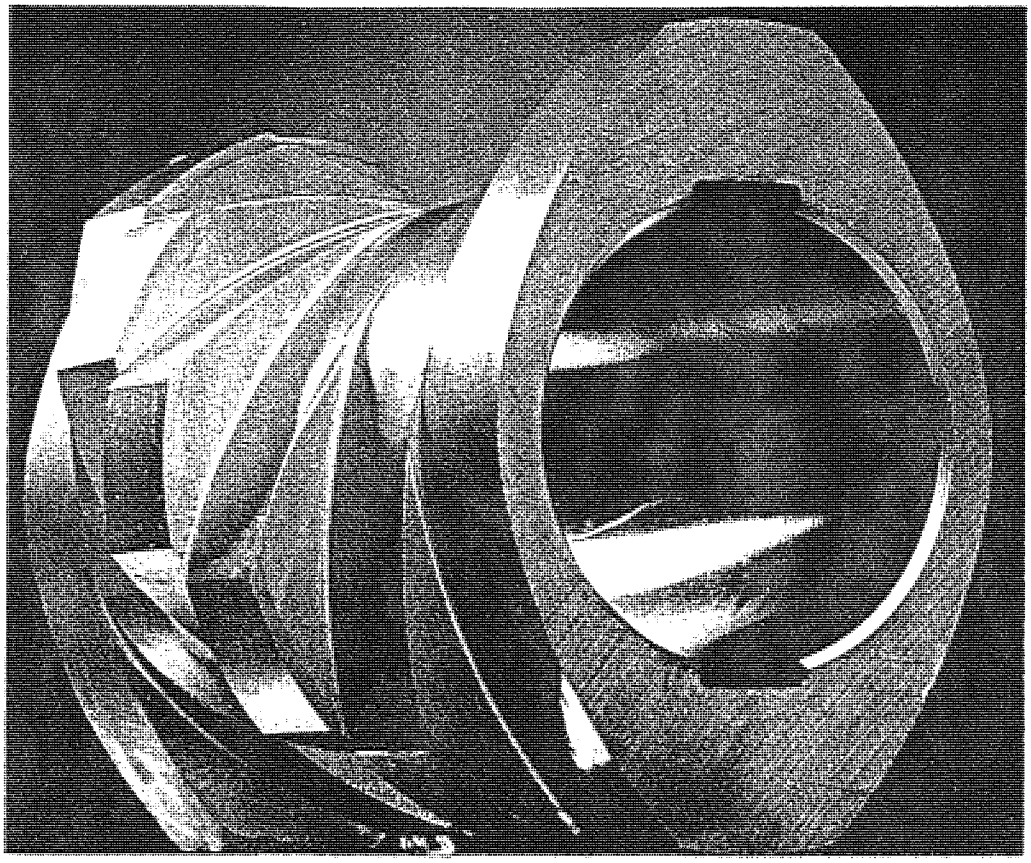

Figure 1-22:

Modular Kneading Block.

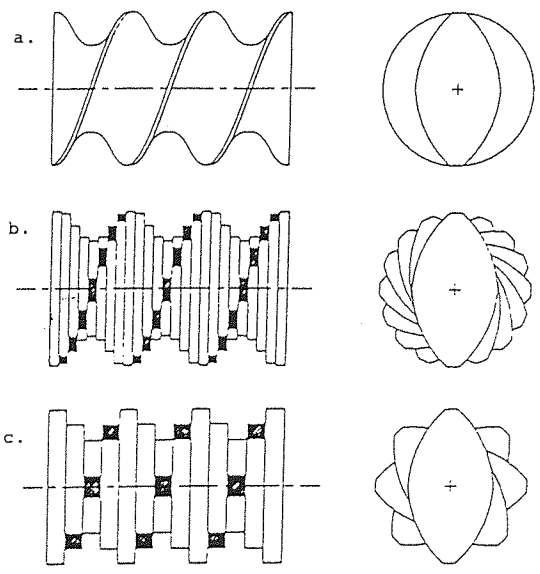

Arrangement of kneading paddles with screw-like characteristics:
a = square pitch bilobe screw b = same pitch with D/16 thick paddles at 22.5° offset
c = same pitch with D/8 thick paddles at 45° offset

Figure 1-23:

Schematic Diagrams Describing Different Kneading Block Arrangements.

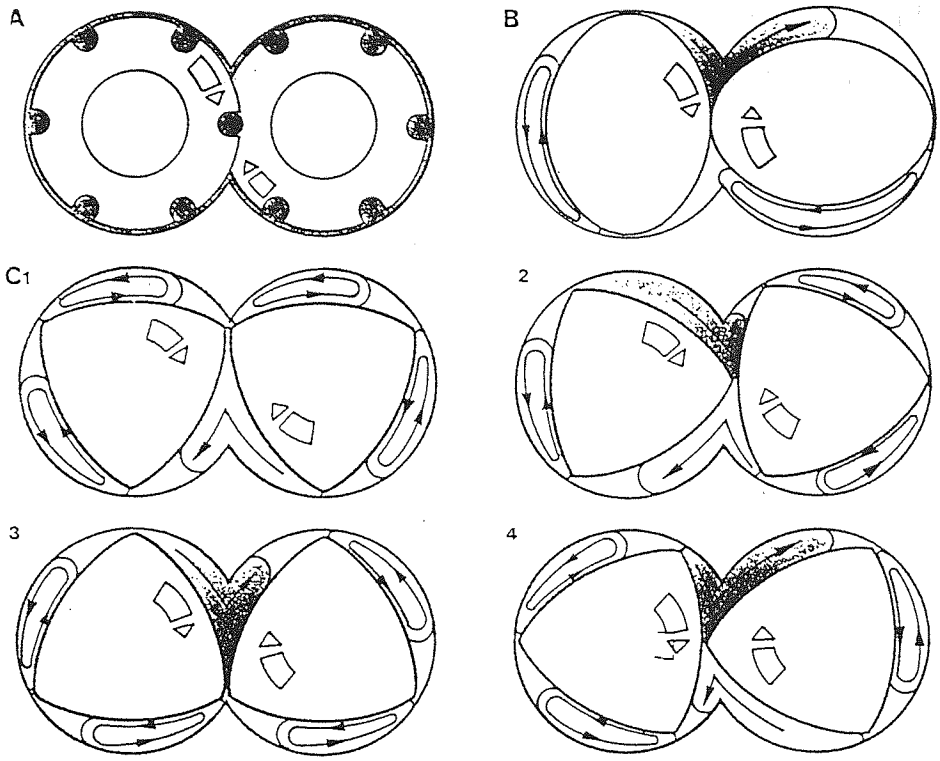

Figure 1-24:

X-Y Cross-Sectional Planes Describing the Shearing Action of the Mixing Discs, Bilobal Elements and Trilobal Elements.

fluids. Prediction of fluid flow behaviour may be achieved by the use of computational fluid dynamics (CFD) programs and this has been an area of much recent activity (discussed in Chapters 2 to 4). The highly non-linear equations that govern some of the properties of, for instance, non-Newtonian or viscoelastic liquids, are impossible to solve analytically and thus realistic solutions can only be achieved by the application of numerical techniques on very fast and powerful computers. The advent of both more powerful and cheaper computers and the development of new computational techniques such as parallel processing, has allowed the solution of the fundamental equations of flow governing more realistic fluids in complex domains such as those found within a CICo-TSE.

Visualisation of the actual mixing of viscous materials undergoing processing within a CICo-TSE, would be very advantageous. Commercially made CICo-TSE machinery, especially laboratory scale CICo-TSE machinery used for the small scale development of novel products such as the Betol BTS30, are designed such that both the modular element configuration can be altered and that the outer barrel housings may be removed for in-situ sampling. Some workers have directly fitted transparent outer barrels to their CICo-TSE machinery and have developed techniques whereby these transparent barrel sections have been heated (discussed in Chapter 5). For the current research however, restriction of both funds and equipment prohibited the encasing of the PPPGs BTS30 CICo-TSE within a heated transparent outer barrel. Instead a model was assembled which was both more economical to construct and easier to use. Using a set of 40 mm screw shafts from a BTS40 CICo-TSE, loaned from Betol Machinery Ltd., a mechanical model encased by removable transparent barrel housing sections was constructed.

1.7 Dual Track Research: Comparison of Computational and Experimental Models

Many CFD packages contain in built computational validation of the goodness of any calculations performed. Results generated by CFD however must be comparable with real life data before any acceptance may be assumed. This is extremely important for new areas of research where CFD techniques are being applied, such as the investigation of the flow fields generated by the different sections of a CICo-TSE. Commercial CFD packages gain credence by publishing simulation results from various fluid flow situations, with comparisons of results from real life scenarios. At the time of publication however, no CFD package has any built-in comparator of CFD simulations with real-life flow situations.

The ideas and results presented in this thesis and other similar work, are intended to lead eventually to a greater understanding of the mechanics of processing viscous materials using a CICo-TSE. An ability to predict with confidence the values of a wide range of physical properties of end-products from a CICo-TSE processing, is a major goal of this research. The

use of CFD will greatly assist in the attainment of this goal but the application of CFD has its limitations. Polyflow, the CFD package used within this research, [21] is a finite element CFD code designed specifically to predict the flow of rheologically complex materials in such processing applications as SSE and die swell. Being a commercial package, Polyflow has been designed to be used in a generalised way and there are many applications for which Polyflow may be utilised. It must be noted however that even though these applications are wide ranging, Polyflow is still a specialised CFD package and not a generalised one and this is explained further in Chapter 2. Because Polyflow has not been designed specifically for the simulation of in-situ processing within the CICo-TSE, its use for this application has been adaptive and developmental.

1.8 The Research Problem Defined

The research presented within this thesis has been performed in order to assist in the work being carried out by the PPPG at Aston and also the wider scientific community. This work involves the development of formulations of novel, speciality materials initially within an internal mixer, with the process then being transferred to the Betol BTS30 CICo-TSE. The application of CFD in the simulation of viscous fluid flow within such complex processing geometries as the CICo-TSE is a recent development. Numerical simulations of CICo-TSE sections were first published in 1987 by Szydlowski *et al* [22]. To compare directly the real life processing of viscous material within a complete CICo-TSE machine configuration with a full simulation of this process generated using CFD, is not yet possible. The present state of CFD technology means that only certain parts of the real life process may be simulated and that these simulations can only be realistically performed separately on each CICo-TSE section under investigation. The advantages in design that makes the CICo-TSE such a useful processing device, perversely hinder its simulation due to the following reasons;

- The four types of TSE machinery described in Section 1.4 are all complex in design and may contain many different types of mixing zone. Each separate TSE type and mixing zone is designed to perform different mixing tasks and hence any CFD investigation would have to be performed separately on each. For example, CFD work performed on the mixing discs produces flow fields that are totally different from those exhibited by the trilobal elements and so extrapolation of results from one type of mixing section to the other is meaningless. CFD simulations for a screw element of a particular pitch may be extrapolated to other screw elements of different pitches, assuming that these screw elements are of the same flight type. Clearly, CICo-TSE flow fields will be different from those generated by counter-rotating TSEs.

- TSEs are designed to accommodate multi-component, reacting species. Thus ideally the CFD simulation would have to cope with the mixing of several reacting species that are rheologically diverse, such as the introduction of a low viscosity liquid into the bulk polymer matrix. This would also introduce slip between the material matrix and any incident surfaces (i.e. the outer barrel walls and TSE element surfaces). Slip values would vary at different points along the barrel, due to the reactions taking place within the material matrix and because of the removal of unwanted volatiles via the decompression vents.
- The viscous polymeric material being processed will almost certainly be non-Newtonian and possibly viscoelastic in behaviour.
- TSEs possess modular heated outer barrel casings that are capable of producing temperature gradients along the barrel, from the feed to the die end. Hence the viscous material matrix contained between the TSE elements and the outer barrel wall will possess a temperature profile which is wholly dependent on the outer barrel temperature gradient. Moreover, the rotation and displacement of this viscous material through the different CICo-TSE sections, will produce differing degrees of viscous heating within the material matrix. These localised viscous heating values would need quantification in conjunction with the temperature gradient generated by heat conduction.

Some of the problems specified in the preceding paragraphs, may be solved using either Polyflow or other CFD packages. Certainly Polyflow is capable of simulating viscoelastic fluid flow, but simulating all of the previous problems together in one simulation is not yet possible with current CFD software. It was decided that one of the most important priorities to performing this research was the development and critical evaluation of both the CFD solution schemes and experimental methods used in the solving of the flow fields generated within the CICo-TSE. Taking into account all of the previous complexities the following limitations were set for the research programme;

- All CFD simulations were to be performed using the geometric data of the Betol BTS40 closely intermeshing, CICo-TSE.
- CFD simulations were performed assuming isothermal flow conditions and experimentation using the mechanical CICo-TSE model was performed at room temperature.
- Only single-flighted conveying screw elements of differing pitch and mixing elements of the mixing disc and trilobal element type, were to be investigated.
- Multi-reacting species were not to be considered. However two non-reacting, viscous fluids

separated by a movable interface and contained within the single-flighted conveying screw elements, would be examined.

- Slip within all three CICo-TSE element types would be investigated, but only as 2D cross sections.
- CFD simulation of fluid flow were to be performed using the ideal rheology of PP. The rheological data of PP to be simulated is that of a generalised-Newtonian type, described by a power law model.
- Investigations were to be performed separately within each CICo-TSE section. The only way in which the pre-and proceeding elements next to the zone of investigation may be taken into account, would be in the assignment of a large arbitrary pressure profile at the inlet of the zone under investigation (i.e. representing a preceding compression section) and the assignment of a zero pressure profile at the outlet of the zone (i.e. representing the proceeding decompression section).

Thus, the structure of this thesis is four parts, described as follows;

CFD Part:

Chapter 2 of this thesis describes a review of the current state of CFD technology, Chapter 3 describes the CFD program Polyflow, whilst Chapter 4 discusses the possible CFD approaches to solving the flow field analysis problem within typical CICo-TSE sections.

Process Machinery:

Chapter 5 describes both the mechanical model and a review of previous experimental work using TSEs in the investigation of visualisation of the processing of viscous materials.

Results Section:

CFD and experimental results are reported together. Chapter 6 describes the single-flighted conveying screw elements, Chapter 7 deals with the mixing discs and Chapter 8 with the trilobal elements.

Conclusions:

Chapter 9 discusses the summary and conclusions drawn from this research and also recommendations for future research work, as a result of realised and possible improvements in CFD technology.

1.9 Summary

This thesis examines the simulation and visualisation of the flow of viscous polymeric materials through the various regions of the Betol BTS type of CICo-TSE. Prediction of viscous fluid flow parameters is achieved using the CFD program Polyflow. Visualisation of viscous flow will be demonstrated using a mechanical model having a transparent outer barrel. Results from the CFD predictions are compared with those obtained from the mechanical model to critically assess the CFD methods applied and to validate any assumptions made. The long term aim of this research program is to assist in the work being carried out by the PPPG at Aston using the laboratory scale Betol BTS30 CICo-TSE and the scientific community in general, to help identify ideal configurations for optimum mixing and shear levels within the CICo-TSE.

2 COMPUTATIONAL FLUID DYNAMICS (CFD): AN OVERVIEW

CFD is the computer based numerical solution of fluid flow equations and the simulation of patterns of flow and related phenomena. The prediction of characteristics of flow is of interest to a very wide range of real life situations, such as in the production of many consumer commodities, the environment and within living organisms. During the past 10-15 years, a great deal of work has been performed using CFD to demonstrate to the industrial and scientific communities, the high levels of confidence the results of CFD packages may produce. CFD has been used to simulate the initiation and propagation of real life disasters, such as the King's Cross tube station fire and the severe gales that Britain endured in 1988. CFD packages may also be used as a predictive tool in the design of flow environments where knowledge and control of the properties of the fluid(s) of interest are crucial.

CFD simulation software has been available commercially since the early 1980's and spectacular growth in both the capabilities and applications of CFD began in earnest in the late 1980's and has continued. Both the capabilities of commercial CFD packages and improvements in the computer hardware technology needed to run the software, are still at a high rate of development. A review of the standing of CFD technology in 1994 was undertaken by Bruce [23]. Due to the developments in CFD, some of the information contained within that report has now been superseded. Thus this chapter will provide both a brief survey of the components that make up a typical CFD package and an update on the current state of commercial CFD technology.

2.1 Background

The last two decades has seen the arrival of very powerful, sophisticated and affordable workstation computers, which have allowed fundamental mathematical modelling techniques, such as the finite element and difference methods, to be applied to problems of engineering importance. Solutions to engineering problems such as stress analysis or fluid flow within or around complex geometries, are now solvable and direct comparisons with real life situations may be realised. It is also possible to impose heat transfer between two or more fluids, mass transfer, chemical reactions, turbulence and free surface phenomena on the basic fluid flow equations. The success with which CFD may simulate this wide range of flow phenomena, however, is variable. For example, it may be argued that the modelling of free surfaces cannot be fully attained due to the inherent unpredictability of the flow domain. Despite these limitations, widespread recognition of the usefulness of CFD in many engineering disciplines is beginning to be accepted, as CFD packages may be used as predictive tools in the development of a wide variety of products and industrial processes. By utilising CFD, potential gains in reduced personnel, time taken and costs incurred during experimentation,

may be realised. However, the operation and application of CFD have and continue to require expertise, because of their complexity. The interpretation of CFD results similarly require significant expertise.

Concentration, Heat and Momentum Ltd., (CHAM) founded in 1969 by Professor D.B. Spalding at Imperial College, London, was the first company in the world to release a general purpose CFD program commercially. Their package, released in 1981 and called Phoenics-81, was the first of many CFD packages developed within the University community. Other companies originating with an academic background included Fluent Europe Ltd. (from Sheffield University, however, their corporate headquarters are located in Lebanon, NH, USA), Polyflow S.A. (from University of Louvain, Belgium) and CAPPA-D (McMaster University, Canada). CFD development though has not been the exclusive reserve of academia. Large industrial companies such as Nuclear Electric and AEA Technology have developed their own CFD software for in-house problem solving and these too have then been made commercially available, as the CFD programs FEAT and CFX4 respectively.

Most CFD packages contain three core program parts, these being the pre-processor part for the generation of computational meshes, the interface/solver program for specifying and solving the flow problem and the post-processor part, utilised in the visualisation of simulation results generated. Many CFD companies supply unified CFD codes that come as a complete package, but alternatively there are many companies who will supply either a stand alone pre-processor, a CFD solver program or a post-processor package only. Currently the trend seems to be that a CFD company supplying a unified CFD package will also supply alternative pre- and/or post-processor software, developed by other companies, to complement and enhance their own CFD software. Shown below is the total number of commercial CFD companies world-wide as of 1994 [24];

Package	Number of Companies
Pre-processor	13
Flow solver	19
Post-processor	22
Complete CFD package	18

Obviously with such a wide range of CFD companies and products to choose from, care must be exercised when choosing the CFD package for a given fluid flow application. Some companies market their CFD packages for very specific flow problems. For example Flowmerics Ltd. produce two CFD codes, Flotherm used in the prediction of air flow and heat

transfer around electronic components and Flovent used for predicting ventilation within buildings. Other companies have developed general purpose CFD packages, such as Star-CD and Phoenics, to be used for a wider range of fluid flow applications. Each of the three core parts of a unified CFD package will be briefly described in the following sections.

2.2 Pre-processor

The computational mesh used to represent the flow domain of the problem under investigation must be specified and generated by the user. As advanced as some pre-processor software packages are, it is still not yet possible to request a particular mesh design from say, a mesh library facility. Thus for any new flow problem under investigation, mesh design will need to be begun from scratch. All types of computational mesh will contain a series of topologically connected cells, called elements or domains, and these elements will possess point positions in space called nodal points. The fundamental flow equations are then solved on each nodal point of each element contained within the specified mesh. There are fundamentally two types of mesh construction possible and each type contains elements that are either structured (having a well-defined topology) or unstructured (the grid points connected in an irregular manner) in arrangement. These two element designs may briefly be described as follows;

- Structured mesh:

  A structured mesh is the simplest mesh construction possible and contains finite elements that are well ordered. The topologically connected elements contained, may be of any regular shape, the most common being the 8-noded hexahedron for 3D problems and the 4-noded quadrilateral for 2D.

- Unstructured mesh

  Creating an unstructured mesh is achieved by the (automatically performed) refinement of a structured mesh, whereby the regular 4-noded 2D quadrilateral is split into a series of triangular structures. This procedure is performed in order to generate a mesh with a better distribution of nodal points in space, in relation to the domain being modelled. Examples of a structured and an unstructured element, are given in Figures 2-1 and 2-2 respectively.

The use of unstructured meshes for CFD is a very recent development and the very first commercial CFD package to contain an unstructured pre-processor was Rampant, released in 1992 and developed by Fluent Inc. Unstructured meshes allow more complex geometries to be modelled more accurately, because of the refinement of nodal point positions. An example

Figure 2-1:

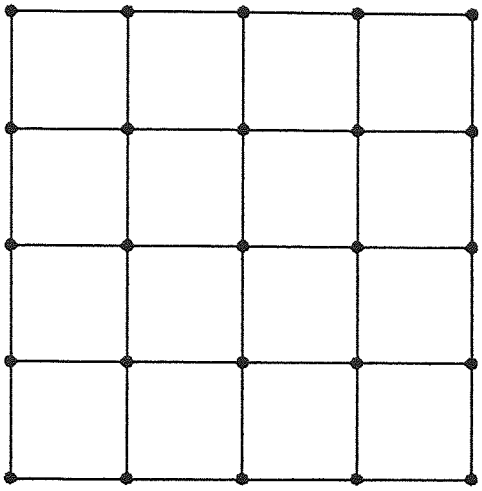

Structured Finite Element Grid

Figure 2-2:

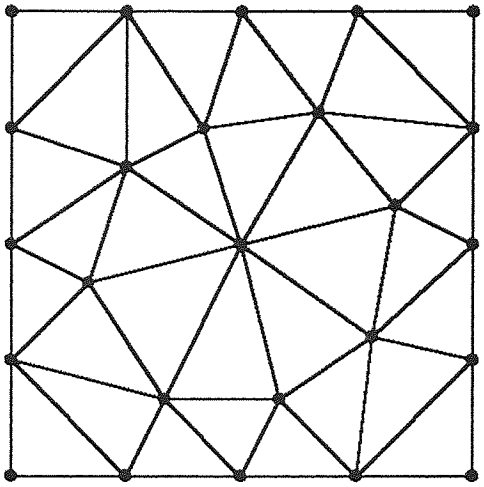

Unstructured Finite Element Grid

Figure 2-3:

Example of the Application of a Complex Unstructured Finite Element Grid.

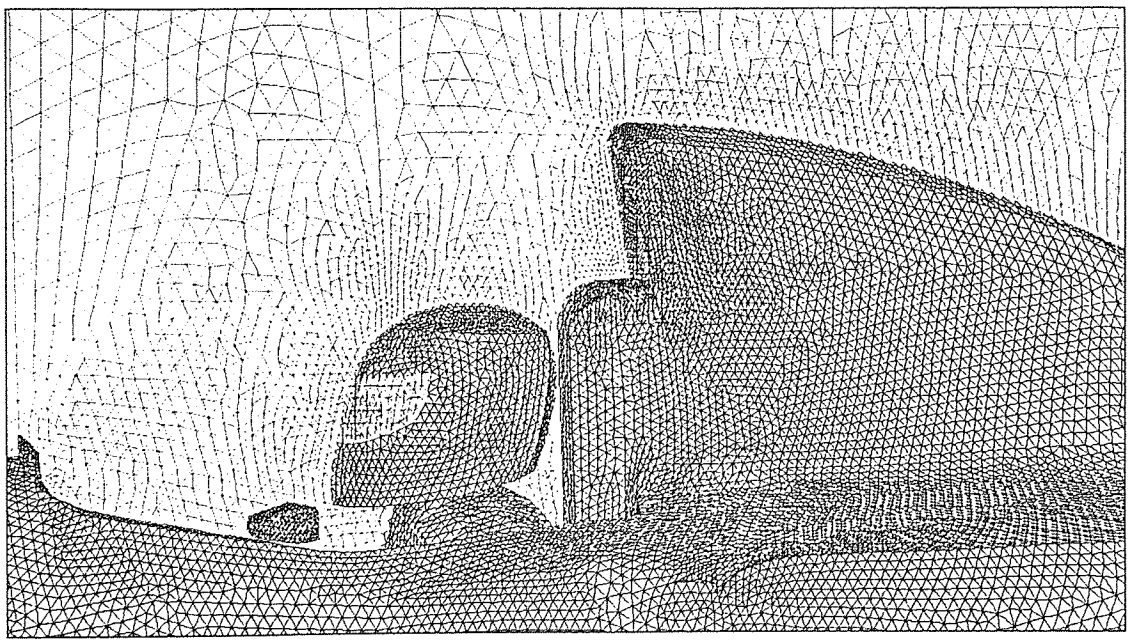

GeoMesh 3.D Provides much Easier Tri-Surface Mesh Generation, more Diagnostic Tools and Faster Display Performance

of a difficult meshing geometry whereby the creation of an unstructured mesh is essential, is shown in Figure 2-3 (mesh generated using the package Fluent). The process of converting a structured mesh to an unstructured mesh, results in the merging of some nodal point positions within the domain, generating a mesh containing fewer nodes on which the calculations are to be performed. However, the computational solution for using an unstructured mesh is not necessarily any faster due to this reduction of nodal points. Both the memory requirements and the time taken to obtain a solution, are the same whether a structured or unstructured mesh is used for the flow domain calculation. The major advantages of using an unstructured mesh facility for very complicated flow domain problems, are as follows;

- The generation of an unstructured mesh is much faster than the generation of a complex structured multi-block mesh. An unstructured mesh needs only the definition of the surface geometry and surface distribution, with the interior volume mesh being generated automatically.
- Automatic mesh generation algorithms may be utilised within the particular CFD solver, such that the solution for an unstructured mesh is adaptive. This means that the unstructured mesh will be refined or coarsened during the solver calculation, based on certain criteria such as the gradient of a defined quantity or an error estimate.

Unstructured pre-processor packages are used in the generation of meshes for very complex flow domain problems and these meshes are, more often than not, conceived using a computer aided design (CAD) package. It would clearly be most advantageous to be able to import a 3D structure directly from a CAD package into the pre-processor. Many unstructured pre-processor packages in fact do possess a CAD/CAE interface so that files saved from within a CAD package that uses the IGES format facility, may be directly imported into the pre-processor for unstructured mesh generation.

The quality of any results generated from a CFD simulation, depend directly upon the quality of the computational mesh used. Thus, a large proportion of the total time spent on a CFD problem is concerned with the construction of the computational mesh or meshes on which the calculations are to be performed. Much care and attention needs to be taken when creating these meshes, if the CFD simulation results are to be interpreted with any degree of confidence. When performing a simulation from scratch it is almost certain that any initial mesh used for the fluid flow prediction will need subsequent changes or enhancements to improve the simulation results generated. With all CFD packages the desired number of nodal points to be used within the mesh generated, is still found by trial and error; too few nodes and the flow calculations generated might be inaccurate and not give enough information,

whilst too many nodes would generate a problem taking an unnecessarily long time to execute. The desired aim is to find the optimum number of nodal points within the mesh, needed to perform the calculations, such that the problem solved is mesh independent. The convention for verifying the quality of results generated by a particular computational mesh and its subsequent optimisation to ensure a mesh independent solution, is discussed in Chapter 4.

2.3 Interface and Solver program

Fluid properties, boundary conditions and starting problem parameters, such as initial fluid temperatures, must be specified for the flow problem being solved. These flow problem specifications are generated within an interface program that is linked directly to the CFD solver. The solver program solves the fundamental equations for the conservation of mass, momentum, energy and chemical species at each nodal point within the mesh, for the fluid problem specified. There are several numerical techniques that may be employed for obtaining a predictive solution. The most popular techniques include the finite element, finite difference and finite volume methods. Different CFD packages employ different techniques, dependant upon the application. For viscous flow situations, such as polymeric or molten metal flow, the finite element method is generally used, whereas for turbulent flow cases the finite volume or differences methods are the preferred techniques.

An initial guess is usually needed to start the solution process since the procedure is an iterative one. The equations are then used to find a better approximation for each solution found. These iterations are continued until the residuals, which are the measures of calculated errors, are sufficiently small. These residuals are used to check whether the solution is converging (residual values decreasing after each iteration) or diverging (residuals increasing). If the solution diverges then the problem is not being solved in the real world and is thus imaginary. A diverging solution may be due to a number of different circumstances. A poorly specified mesh may be the cause. For example, the mesh may contain a small number of nodes in an area where a large fluid parameter gradient is being experienced, such as for conduction at a heated boundary wall. The most common cause of divergence though, is the inadequate treatment of non-linearity's within the problem specified. Non-linearity plays an important role within common real life flow situations such as in non-isothermal behaviour, viscoelastic flows or free surface problems. It is these types of flow problem, especially within very complex flow domains, for which solution is highly desirable. Non-linearity arises because the properties to be calculated involve terms that are complex products of other variables. For example, in non-isothermal flow problems, convection generates terms that are products of both the velocity components and temperature gradients. The way to solve a

non-linear problem is to start at a linear solution, for example by assigning a zero value for one or more of the variables involved and then gradually introduce non-linearity into the problem, using the previous solution each time as a starting point. This approach is explained further using the schematic diagrams shown in Figure 2-4.

The general types of flow phenomena for which most commercially available CFD packages are applicable, are listed in the following paragraphs. Typically commercial CFD packages do not claim competence in all of the following capabilities. The modelling of both turbulence and viscoelasticity are the extremes of fluid flow behaviour which may be modelled and it is very difficult for the same CFD package to model both areas successfully. Some packages do provide both facilities for example, FIDAP, Star-CD and other general purpose CFD packages possess both turbulence and non-Newtonian models. However, for simulating a wide variety of highly viscous flow behaviour, such as die swell and inverse extrusion, the choice is between Polyflow, Nekton or Polycad, because these CFD packages have been specifically designed for that purpose. This is due to the fact that a CFD package designed specifically for complex viscous flow of non-Newtonian or viscoelastic fluids, has no need of the ability to model turbulence, a phenomenon that a highly viscous fluid does not exhibit. Typically the market leaders in CFD produce several CFD packages covering the full spectrum of fluid flow behaviour. Fluent Inc. for instance offer Fluent, their general purpose CFD package possessing a wide variety of turbulence modelling, Nekton, their finite element package designed for viscous fluid flow and Rampant, which has been designed for flow within complex domains as found in the automotive and aerospace industries.

<u>CFD package - desired capabilities</u>

- Steady/unsteady state:

  Problems in 2D, axisymmetric and 3D geometries.

- Transient state:

  Time marching schemes for changing physical properties over time, such as that found at a two fluid interface.

- Incompressible/slightly compressible/fully compressible:

  Problems involving the subsonic, transonic and supersonic flow speeds.

- Buoyancy:

  Flow in accelerating reference frames, swirling flows and buoyancy driven flows.

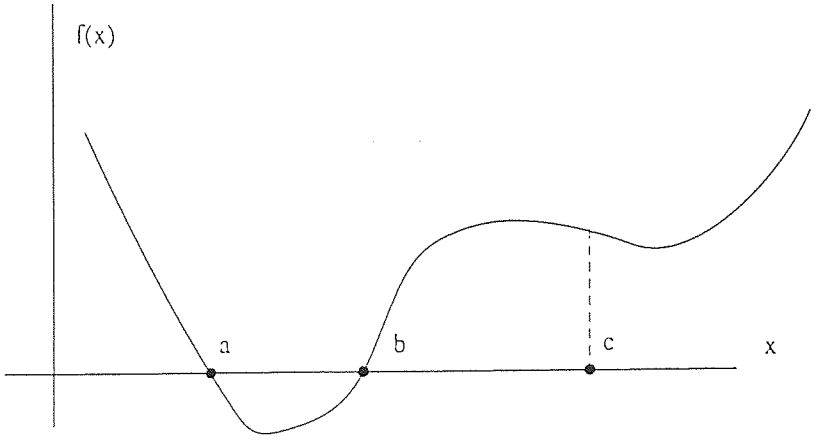

Non linear problem : f(x) = 0.

There are two solutions : x = a and x = b. It will be hard to find x=a if one starts from x = c.

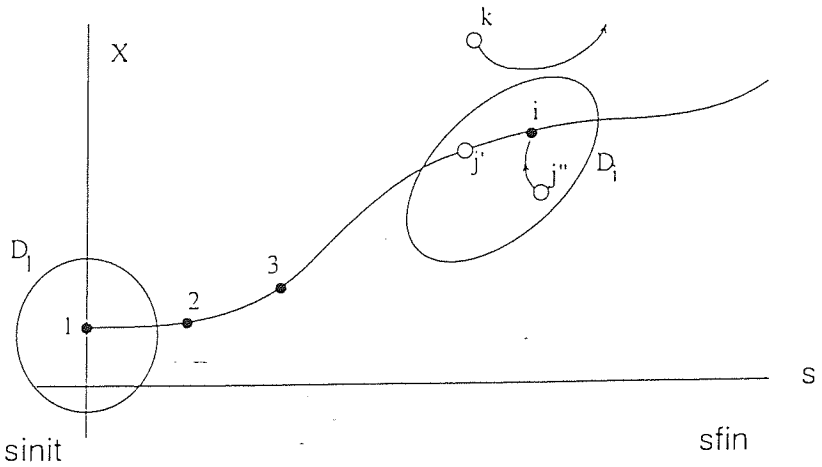

The disc of convergence and the evolution path.

Figure 2-4:

Non-Linear Problems: Solution Technique and Disc of Convergence.

- Dispersed multiphase flows:

  Problems involving multiphase systems containing particles, bubbles or droplets (either inert, evaporating, reacting or combusting) within the continuous phase. Particle tracking may be calculated using a Lagrangian statistical scheme.

- Newtonian/non-Newtonian/viscoelastic fluids:

  Problems involving Newtonian fluids possessing a constant viscosity, may be simulated quite readily. Non-Newtonian fluids may be predicted using the different shear dependent viscosity models such as Carreau, Bingham, Cross, Herschel-Bulkley or power law. Viscoelastic fluids exhibiting complex rheologies may be simulated for viscoelastic behaviour of the differential or integral type (see Chapter 3).

- Turbulence modelling:

  Turbulence models may be incorporated into the different CFD packages and a wide variety of models are available. The standard k-ε turbulence model is the most popular model utilised and others may include the full Reynolds stress model (RSM), renormalisation-group theory (RNG) k-ε model and the two layer model for flow close to a wall region.

- Mass transfer/Chemical reaction:

  Problems may be modelled for mixing and/or reacting of a number of gaseous/liquid species present within the fluid matrix. Reacting species are predicted using sophisticated chemical kinetics models for such cases as combustion, vapour deposition processes, NO_x formation and reactive processing.

- Flow with distributed resistances:

  Cases were the flow is resisted such as through porous media, heat exchangers, chemical reactors, filters or grills, may be simulated.

- Different forms of heat transfer:

  Problems may involve the modelling for the mechanisms of convection, conduction and radiation.

2.3.1 User Defined Subroutines

Most CFD packages include a facility within the interface/solver program, whereby the users may define their own solver subroutines. This enables an advanced user to define

non-standard information, written as a FORTRAN subroutine, within the solver. To use this facility to the full, the user needs to have a much greater knowledge of the way in which the solver has been written and also a competence in the use of FORTRAN.

2.4 Post-processor

All post calculation and simulation facilities are handled by the post-processor part of the CFD package. Viewing of the flow patterns generated for different orientations of the geometry specified, may be performed either on-screen or in printed form. The flow fields calculated by the solver may be represented physically in a number of different ways and the manner in which the calculated fluid properties may be perceived, is dependent on whether the fluid property is a scalar or vector quantity. The visualisation of the different fluid properties is also dependent on whether the problem solved was in 2D or 3D. This is because the fluid property to be represented will be either within a volume, such as particle tracking, or within a surface area, such as on a 3D boundary or 2D cross sectional cut. The different formats for representing a fluid property are given as follows;

- Vector arrows

  This type of representation possesses both an orientation and magnitude and is thus used for vector quantities such as fluid point velocities. Relative magnitude may be represented either by the length or thickness of the vector arrow and optionally graduated by use of a colour scale.

- Scalar contours

  For scalar parameters calculated for the fluid under investigation, there are many ways of representation. The simplest is to display the value of the quantity of interest at single points within the domain. Line contour plots at a specified number of discrete intervals may also be chosen or alternatively, a solid continuous contour plot may be applied.

- Graphical plots

  Knowledge of the relationship for a fluid parameter as a function of some distance within the flow domain and/or, in addition, the values of a parameter on the surface of a boundary, would be of value. The post-processor plots a parameter, such as pressure, velocity magnitude or shear rate along nodal points on a specified line in space. This line is assigned by specifying the line extremities, the positions of which always originate at a boundary. The graphical plot drawn is the relationship between the fluid parameter on one axis and the distance along the line in space, on the remaining axis.

- Animation

  Some post-processors possess an animation facility to track and display the history of particle loci within the flow domain.

2.5 Choice of CFD package - Finite element package Polyflow

Early CFD developmental work concentrated on using the finite difference technique for solving the governing equations of fluid flow. The reason for using finite difference techniques in the early days, was due to the fact that their implementation was relatively easy. The finite difference technique is currently not in-vogue and it is the finite element method that has achieved the most recent attention as a vehicle for improving the capabilities of CFD [25]. Finite element techniques are more difficult to implement, but are very versatile and they are the current method of choice for simulating viscous fluid flow. Developments have also been made in the employment of finite volume techniques and spectral element methods for the simulation of complex fluid flow behaviour. The successful application of a particular technique is intrinsically linked to the type of mesh being used. As there is so much research currently being performed in the area of mesh generation then it is fair to say that different techniques, other than the finite element technique, may in the future become preferred for the simulation of viscous flow.

In 1993 when the search for a suitable CFD package was first considered for this work, it was decided that a CFD package employing the finite element method was to be chosen, because of its versatility and state of the art development. This decision narrowed the choice of suitable packages to approximately eight. To narrow the possibilities further it was decided that only packages designed for simulating viscous flow would be considered [26]. This then narrowed the possible choice to the following four packages (it must be noted that other packages may have been just as suitable, but where unknown to the author at that time);

- Polyflow
- Nekton
- FIDAP
- Polycad

From the preceding list, Polycad was rejected because of its (then) high licence costs (approximately $20,000 for a perpetual licence). Each of the remaining three packages were of comparable capability but Polyflow was chosen because of its well-developed viscoelastic modelling capabilities. Whilst these capabilities were not used within this particular work program, future examination of viscoelastic behaviour within the CICo-TSE models presented

here would be highly advantageous.

2.6 Discussion

Although CFD provides an insight into many flow problems, some of its limitations must be appreciated. Each simulation depends upon a model supplied by a user and the results therefore can only be as accurate as that model. As explained previously, assigning the appropriate mesh is an integral part of the successive solution of the flow problem. Despite the fact that some CFD codes are highly advanced, the generation of a mesh containing the optimum number of points needed to execute the problem effectively remains a trial and error process, successful application of which is learnt from experience. Obviously very complex phenomena cannot be simulated accurately using a very coarse mesh, but on the other hand, use of an extremely fine grid containing too many nodal points, is wasteful of computer time. The generation of meshes, however, has significantly developed from the first structured Cartesian grids and the introduction of unstructured meshes has enabled very complex geometries to be modelled more easily, quickly and successfully than before.

User-friendliness is another important attribute of any CFD package. Obviously this is very subjective and depends on personal preference, but most CFD companies realise that the commercial success of their product, depends on making it more attractive to potential customers. Some packages have a text based interface, whereas others have a graphical user interface (GUI) which greatly eases the process of data input to the various program parts. The GUI development has been aimed at the new CFD user, as in utilising this facility, it is easier to execute CFD operations within each program part. GUI is discussed in further detail in Chapter 3.

2.7 Conclusion

During the last decade CFD has advanced significantly from the user-unfriendly codes first released in the early to mid 1980's, to the sophisticated, easier to use packages that are now commercially available for an ever expanding range of applications. An increasing number of CFD packages possess the ability to perform calculations on unstructured meshes, thus allowing solution of much more complex flow domains. A brief description of the three main parts of a typical CFD package are presented in this section and, although the specific solution technique, mesh structures and flow application area may vary significantly between the different commercial CFD codes, the theory behind and description of the method of operation are essentially similar for them all.

3 OVERVIEW OF THE CFD PROGRAM POLYFLOW

3.1 Introduction

Polyflow is a finite element based CFD package used for the simulation of rheologically complicated fluid flow environments as found in processing applications such as extrusion or blow moulding. A number of distinct programs, each performing a different task in a mutually interactive manner, forms the complete Polyflow package. Supplied with the Polyflow package is a comprehensive set of user manuals describing all theoretical details and operational procedures needed for the successful execution of Polyflow. More than twenty manuals accompany Polyflow [27-45] and it is not considered appropriate to reproduce them here. Instead this thesis will only survey the details specific to how Polyflow was used within the context of this research investigation. For example, descriptions of the detailed theoretical discussion of blow moulding and film casting or the finer points of using the pre- and post-processors, are omitted. However, some practicable aspects of the use of Polyflow not contained within these manuals, such as any deficiencies with the software that have been encountered during use, are discussed.

Commercial CFD software may be classified as belonging to one of the following three categories;

- Pre-processor software
- Interface and solver(s)
- Post-processor software

Figure 3-1 lists the names (including relevant version numbers) and functions of all the different programs contained within the complete Polyflow package, up to and including version 3.4.6.1. Figures 3-2 and 3-3 present and describe all the input and output files generated by each of these different programs, whilst Figure 3-4 graphically depicts the complete computational arrangement of both the hardware and software used during this research. At the time of writing this thesis, the CEAC department had acquired the recently released Polyflow version 3.5 package. This new version contains additional modules that are of direct interest to the research being investigated in this thesis, and, therefore these modules will be discussed in Chapter 9. Each of the separate programs contained within the complete Polyflow package, with the latest relevant version number of that program, is described in the following sections.

3.2 Pre-processor software

3.2.1 Polymesh 2D and 3D (versions 1.2.0 and 0.0.0 respectively)

Figure 3-1:

AN OVERVIEW OF PROGRAM ORGANISATION OF POLYFLOW

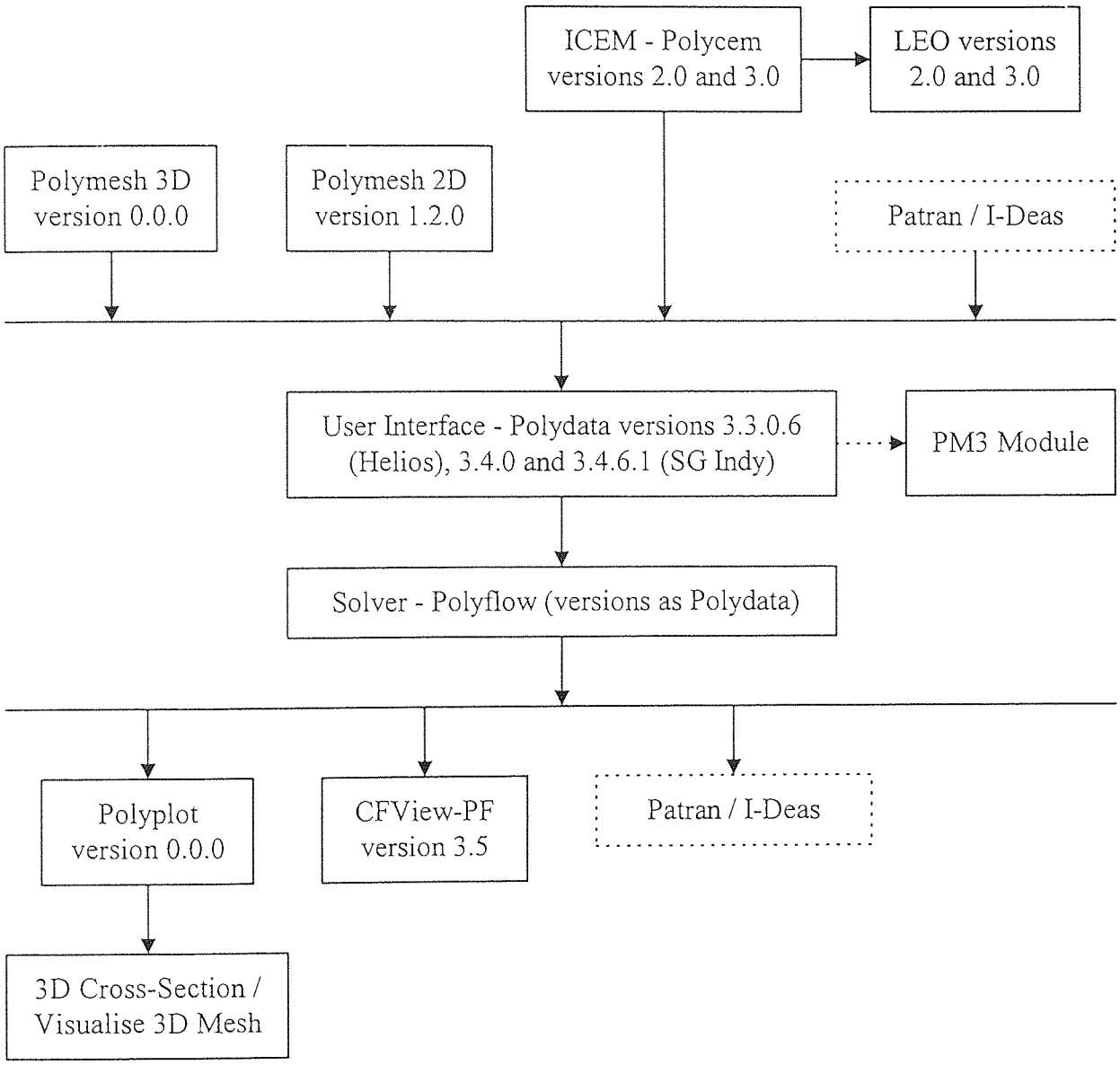

Figure 3-2:

AN OVERVIEW OF THE VARIOUS POLYFLOW PROGRAM FILES

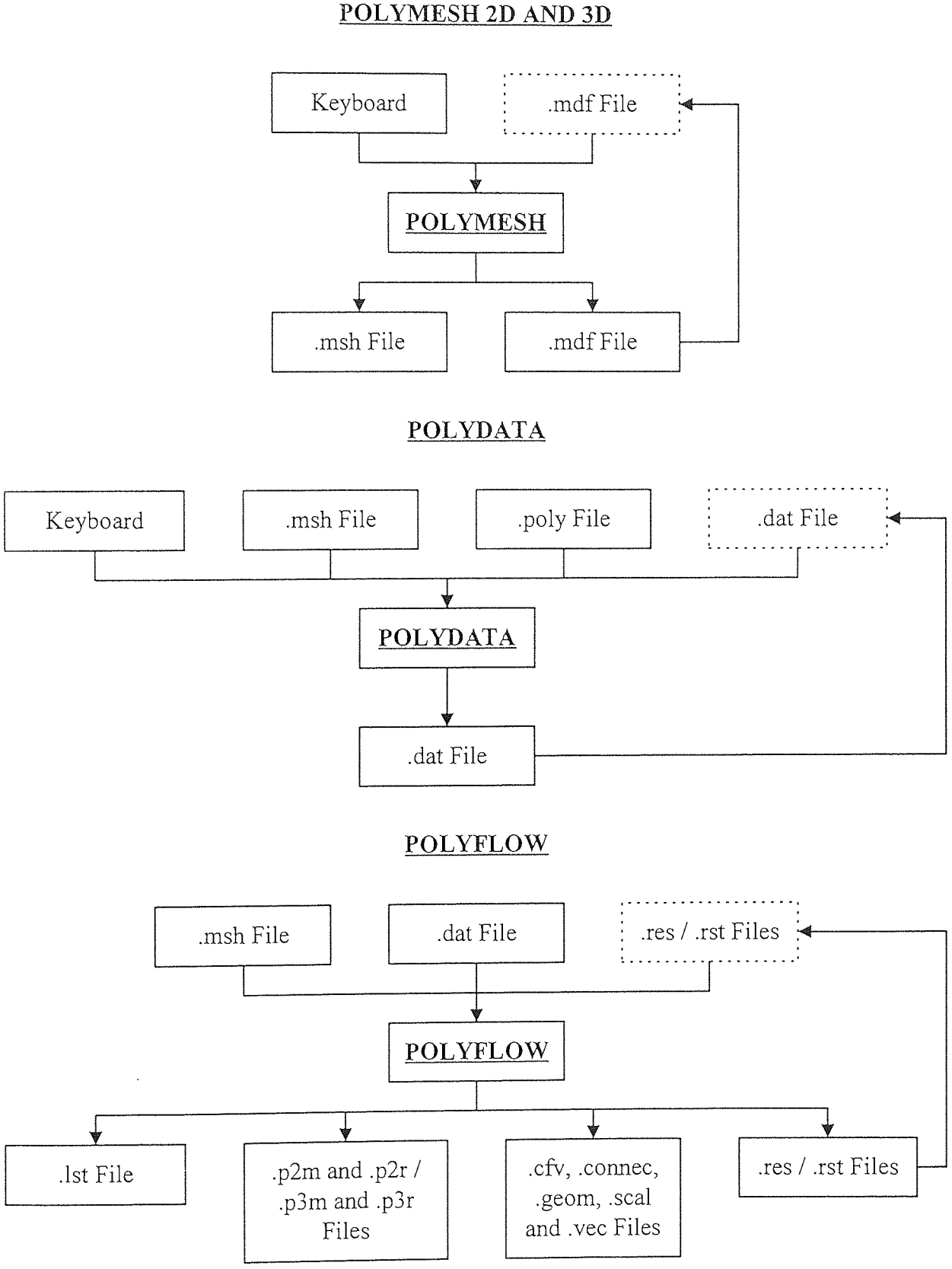

Figure 3-2: (Cont.)

AN OVERVIEW OF THE VARIOUS POLYFLOW PROGRAM FILES

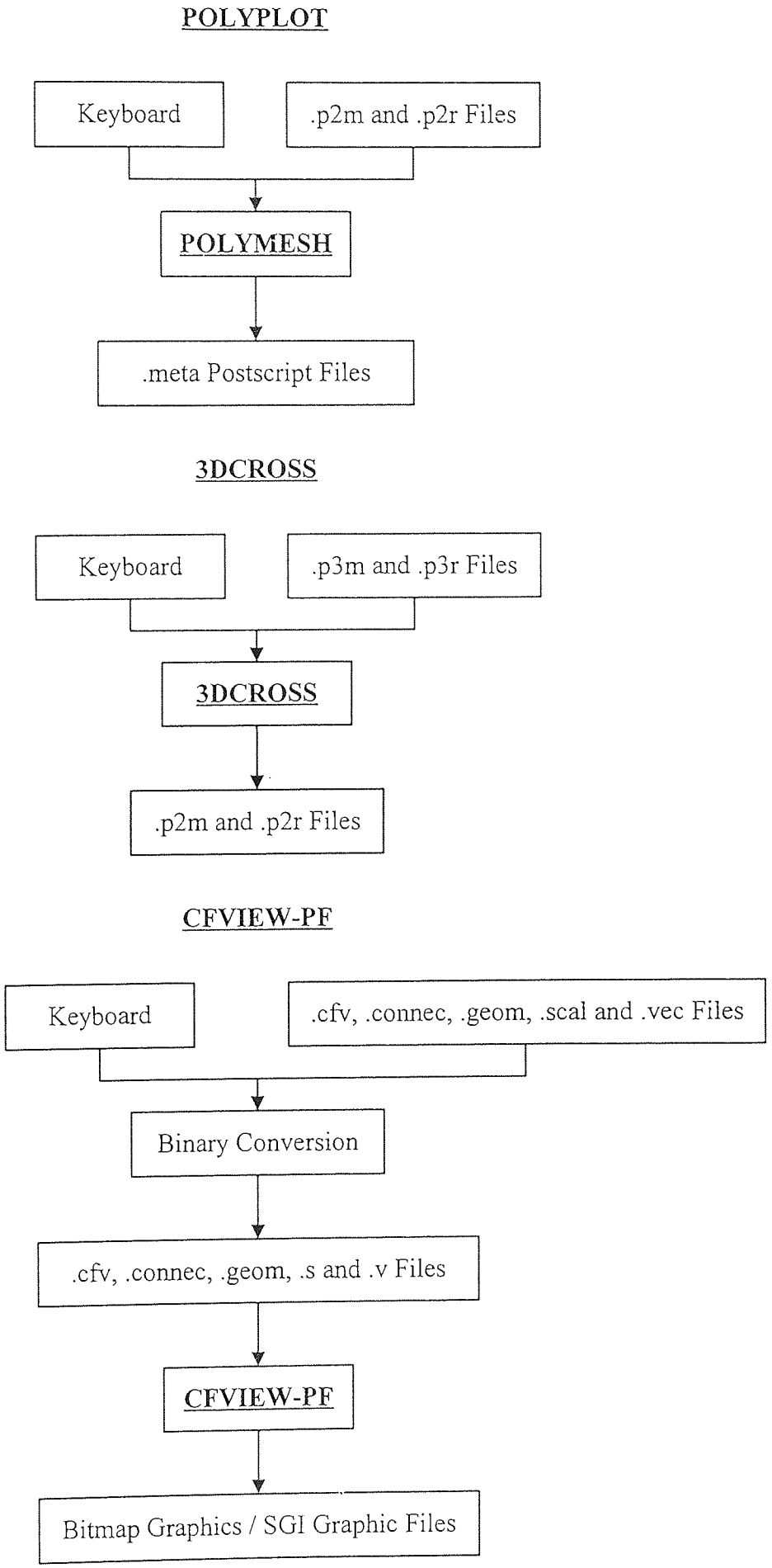

Figure 3-3:

Names and Descriptions of all Files Created by the Various Polyflow Modules

Polymesh

- Mesh Data File (.mdf) (example of contents shown in Appendix A)
  - Polymesh input file (optional)
  - Polymesh output file
- Mesh File (.msh) (example of contents shown in Appendix B)
  - Polymesh output file

ICEM Polycem

- Polycem mesh file (.poly)
  - Polycem output file

Polydata

- Mesh File (.msh)
  - Polydata input file
- Polycem mesh file (.poly)
  - Polydata input file - must be converted to Mesh File (.msh).
- Data File (.dat) (example of contents shown in Appendix C)
  - Polydata input file (optional)
  - Polydata output file

Polyflow

- Mesh File (.msh)
  - Polyflow input file
- Data File (.dat)
  - Polyflow input file
- Result File (.res) (example of contents shown in Appendix E)
  - Polyflow input file (optional)
  - Polyflow output file
- Restart File (.rst)
  - Polyflow input file (optional)
  - Polyflow output file (optional)

Figure 3-3: (Cont.)

- Listing File (.lst) (example of contents shown in Appendix D)
  - Polyflow output file (optional - file can be written to screen instead)

Polyplot and 3DCross

- Polyplot and 3DCross Files (.p2m, .p2r, .p3m and .p3r)
  - Polyflow output files (optional)

CFView-PF

- CFView-PF Files (.cfv, .connec, .geom, .scal and .vec)
  - Polyflow output files (optional)

Figure 3-4:

FLOW DIAGRAM DESCRIBING THE COMPUTER NETWORKING USED DURING THIS RESEARCH

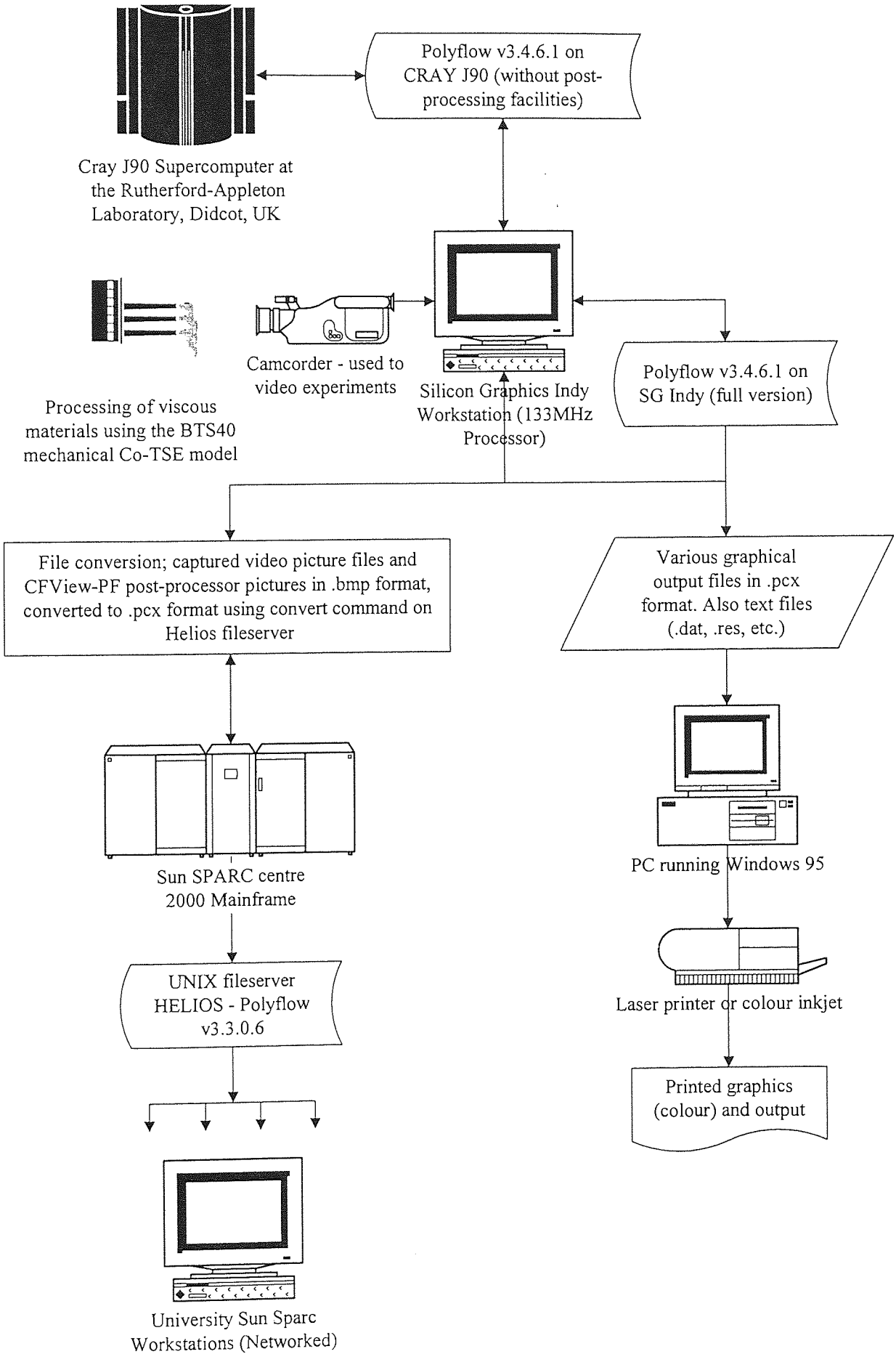

Polymesh 2D and 3D are the original pre-processor programs with which Polyflow was first developed. Both programs are still supplied with new versions of the complete Polyflow package, however, upgrading and development of these two pre-processor programs has ceased and their useful employment has all but been replaced by the pre-processor package ICEM-Polycem (see Section 3.2.2 - Overview of the advanced pre-processor ICEM-Polycem). ICEM-Polycem has been optionally supplied with the Polyflow package from versions 3.4 and onwards. Supplied by Control Data Systems Inc. [46] ICEM-Polycem is an advanced pre-processor package, specially developed to make use of its graphical user interface (GUI) facilities. GUI is the facility by which functions seen on-screen may be directly manipulated by the use of either a mouse or by keyboard. The use of GUI is of paramount importance to the construction of complex 3D meshes because GUI enables the direct visualisation of the mesh whilst under construction. This approach means that any changes or corrections that are needed whilst the mesh is being constructed may be seen immediately. Both Polymesh 2D and 3D are totally manipulated via the keyboard and so the advantages of using GUI cannot be realised when using either Polymesh 2D or 3D.

The full procedure for using both Polymesh 2D and 3D for the construction of a computational mesh is given in Figure 3-5 and may be summarised in the following paragraphs.

3.2.1.1 Assignment of macro-vertices

The positions of all macro-vertices contained within the computational domain (X and Y co-ordinates in 2D and X, Y and Z co-ordinates in 3D) are entered. Each macro-vertex must be numbered in sequence.

3.2.1.2 Construction of macro-elements

Macro-elements are constructed by selecting, in sequence, macro-vertices in an anti-clockwise direction from a series of either -

- Three or four macro-vertices in Polymesh 2D to form triangles or squares respectively.
- Six or eight macro-vertices in Polymesh 3D to form tetrahedrons or hexahedrons respectively.

Each topologically connected edge of a macro-element is called a macro-segment (i.e. the line connecting two macro-vertices). A macro-segment may be assigned as being either straight or circular in nature as shown in Figure 3-6.

In Polymesh 2D, for a circular macro-segment, its radius and arc orientation must be

Figure 3-5: **MESH GENERATION - PROCEDURE USING POLYMESH 2D**

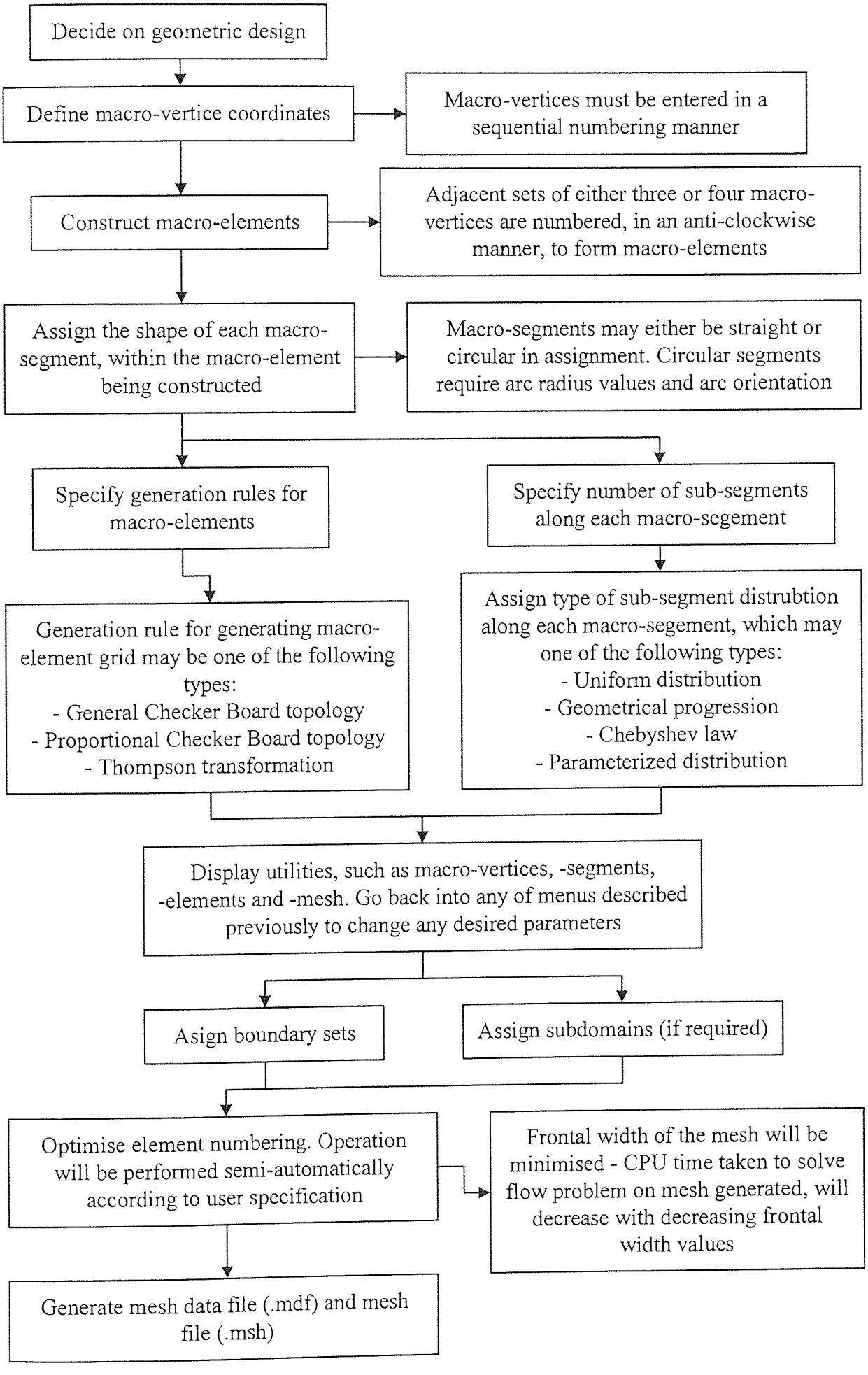

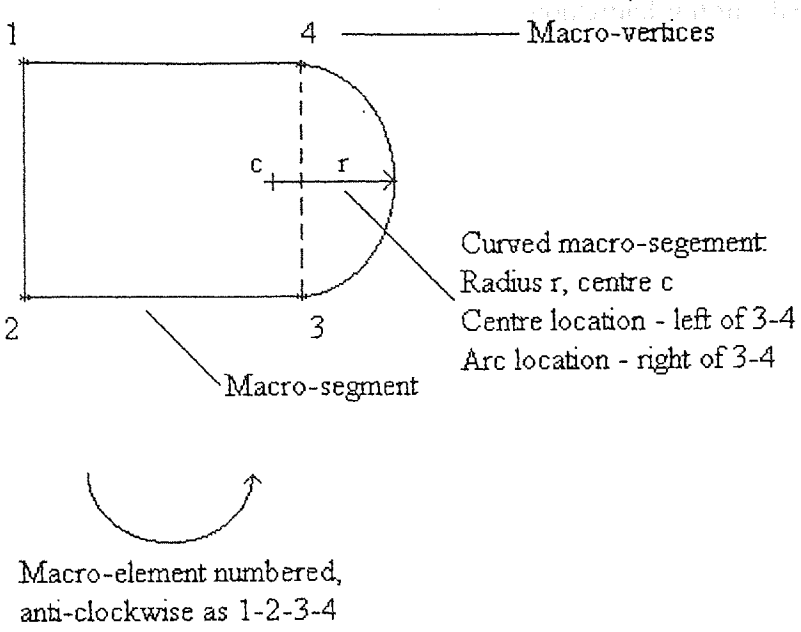

Figure 3-6:
Full Description of a Quadrilateral Macro-Element Generated Within Polymesh 2D.

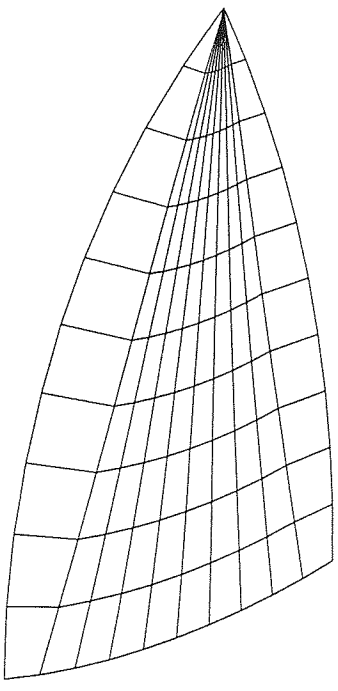

Figure 3-7:
Triangular Finite Element, Possessing Curved Edges and Meshed Via the Fan Topology Rule.

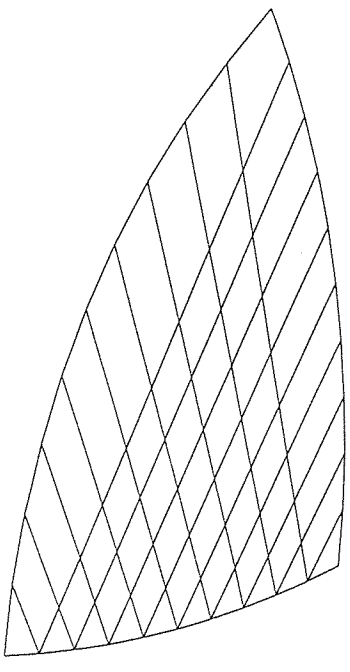

Figure 3-8:
Triangular Finite Element, Possessing Curved Edges and Meshed Via the Checkerboard for Triangles Rule.

specified. In Polymesh 3D a different procedure is used as any 3D arcs contained within the computational flow domain cannot be specified by its arc radius only. Instead a point along the arc, for example its mid-point, is specified by assigning its x, y and z co-ordinates. For even moderately simple 3D structures, this task is extremely time-consuming and the likelihood of wrongly assigning a 3D curve mid-point, especially without the aid of GUI, is very probable.

3.2.1.3 Finite element generation

Once all macro-elements have been constructed, they are divided into finite elements. The method by which each macro-element is divided, is set by the assignment of one of the following finite element generation rules;

2D triangles and 3D tetrahedrons:

- Fan topology for triangles and tetrahedrons (example shown in Figure 3-7).
- Checkerboard for triangles (example shown in Figure 3-8).
- Proportional checkerboard for tetrahedrons.
- Fan-pyramids for tetrahedrons.

2D rectangles and 3D hexahedrons:

- General checkerboard for rectangles and hexahedrons - used if all macro-segments are straight.
- Proportional checkerboard for rectangles and hexahedrons - used if 1 or 2 macro-segments are curved (examples shown in Figures 3-9 to 3-10).
- Thompson transformation for rectangles - used for macro-elements containing 3 or more macro-segments (example shown in Figure 3-11).

If a macro-element contains circular macro-segments then to create a curved mesh, either the proportional checkerboard rule or the Thompson transformation (available in Polymesh 2D only) should be used. Both Polymesh 2D and 3D does not handle the difficulties associated with using triangular macro-elements containing curved macro-segments. No matter which rule is used, the mesh created within a triangular macro-element will be constructed using straight directors only (as shown in Figures 3-7 to 3-8).

3.2.1.4 Sub-segment distribution

The number of sub-segments and the distribution of these segments along each macro-segment must be specified (the default value is one sub-segment, which corresponds to

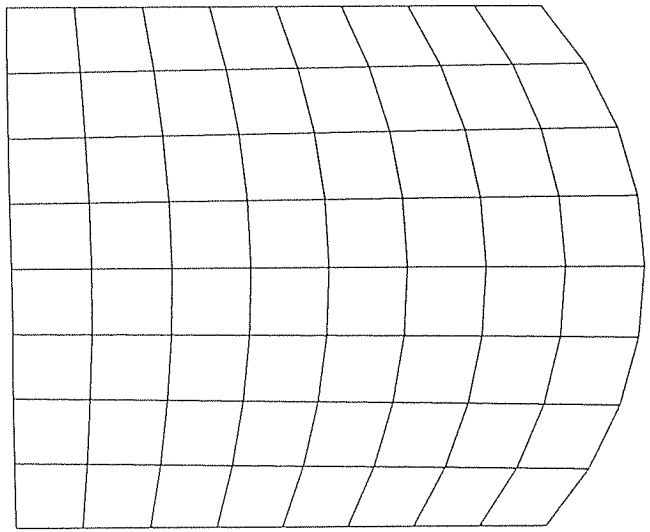

Figure 3-9:
Quadrilateral Finite Element, Meshed Using the Proportional Checkerboard Rule (I).

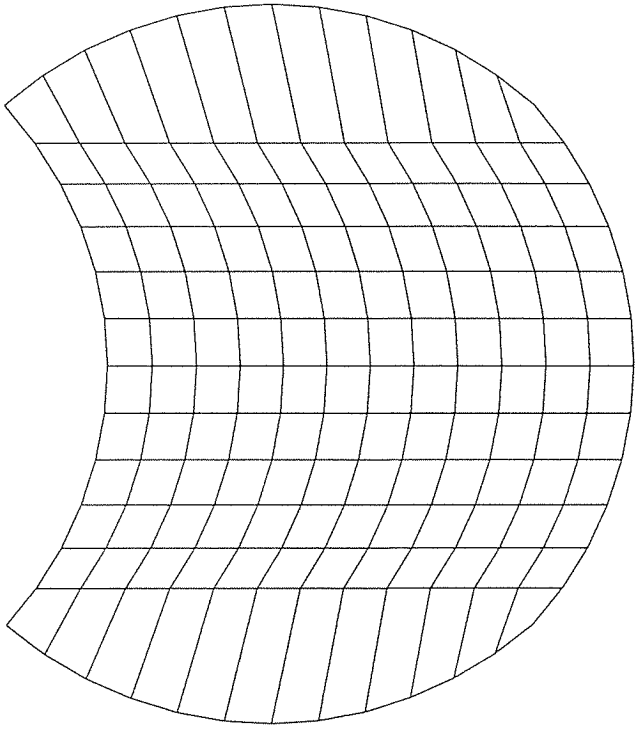

Figure 3-10:
Quadrilateral Finite Element, Meshed Using the Proportional Checkerboard Rule (II).

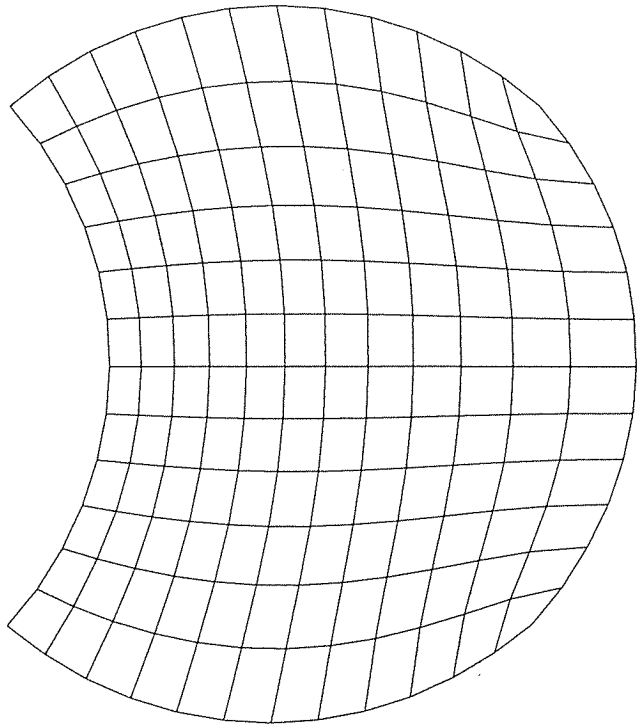

Figure 3-11:
Quadrilateral Finite Element, Meshed Using the Thompson Transformation Rule.

possessing no distribution). Both Polymesh 2D and 3D contain a built-in verification law called the Graph of Constraints law. Any number of sub-segments may be specified, but the Graph of Constraints law checks that the same number of sub-segments are specified for opposing macro-segments contained within the same macro-element. This law also verifies that macro-segments shared between connecting macro-elements must also have the same number of sub-segments. Both of these previous constraints are illustrated in Figure 3-12.

The nodal distribution laws by which the sub-segments are distributed along a macro-segment are described as follows;

- Uniformly spaced distribution of elements along a macro-segment (as shown in Figure 3-13).
- Geometric progression of elements weighted towards a specified macro-vertex of a macro-segment.
- Chebyshev distribution of elements applied either towards a specified macro-vertex or towards both macro-vertices of a macro-segment (examples shown in Figures 3-13 and 3-14 respectively).
- Parametrised distribution of elements.

3.2.1.5 Assignment of boundaries and sub-domains

The outer boundaries of the computational flow domain must be fully defined in order for the problem to be completely solved on the mesh representing that flow domain. If all or part of the boundary is undefined then this will generate a discontinuity in the solver calculation, leading to an incomplete solution. Both Polymesh 2D and 3D contain built-in checks to ensure that all the boundaries describing or contained within the computational flow domain are completely specified. This is achieved by treating the assignment of the collection of boundaries as a series of closed loops, starting and ending at the same points. For example, Figure 3-15 shows a 2D problem requiring the assignment of two boundaries. Polymesh 2D or 3D will need to be told that boundary 1 starts and ends at macro-vertex 1 and that macro-vertices 2, 3 and 4 are also contained within this boundary. The assignment of boundary 1 then is the walk from macro-vertex 1 to 2 to 3 to 4 and back to 1 (i.e. 1-2-3-4-1). Each boundary must be specified such that the fluid domain is always on the left hand side as one progresses along the boundary walk. Thus for boundary 2, starting and ending at macro-vertex 5, the boundary walk specified must be 5-8-7-6-5.

If the problem involves more than one fluid, for example a two fluids heat conduction problem or two fluids separated by an interface, then sub-domains must be specified by assigning (initial) locations of these fluids within the flow domain. The program default is that

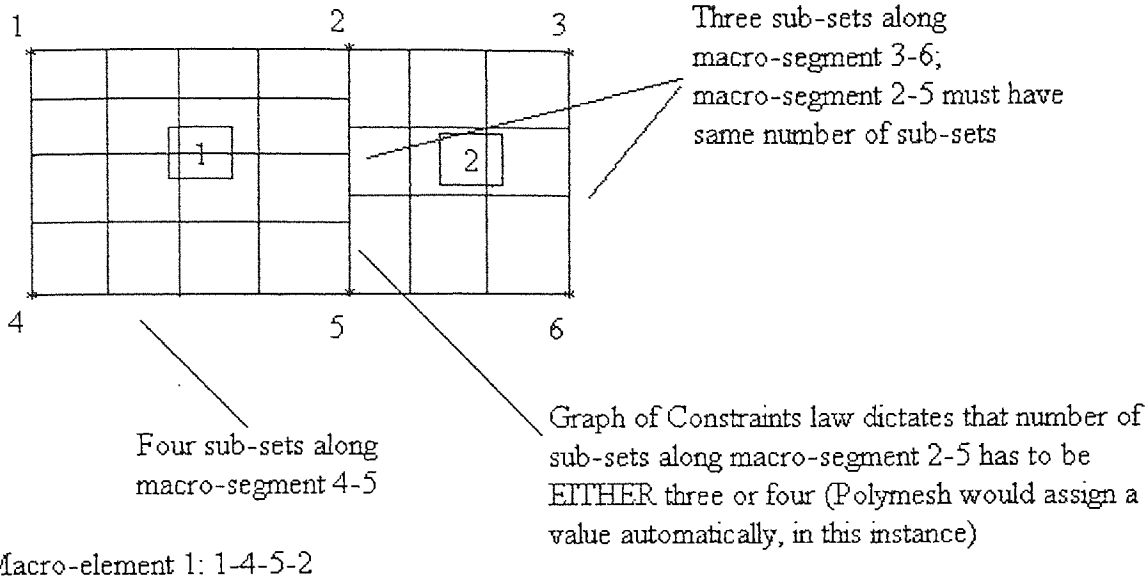

Macro-element 1: 1-4-5-2

Macro-element 2: 2-5-6-3

Figure 3-12:

Example of the Graph of Constraints Law.

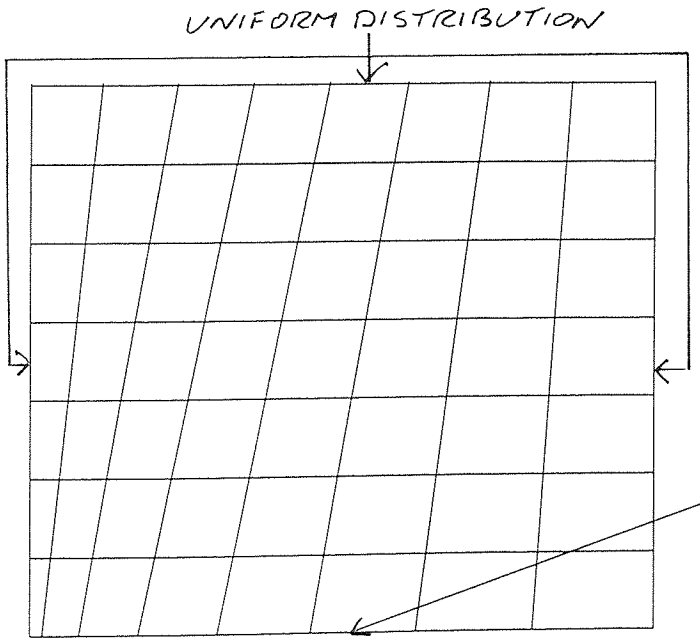

Figure 3-13:

Finite Element Mesh, Where a Chebyshev Distribution of Elements has been Applied (I).

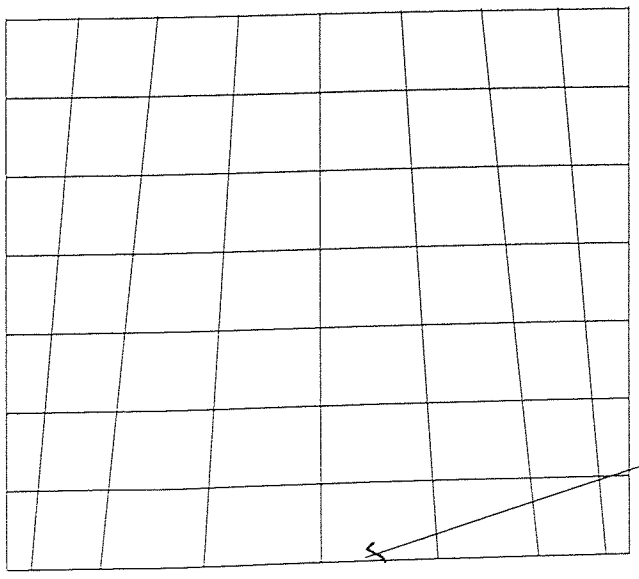

Figure 3-14:

Finite Element Mesh, Where a Chebyshev Distribution of Elements has been Applied (II).

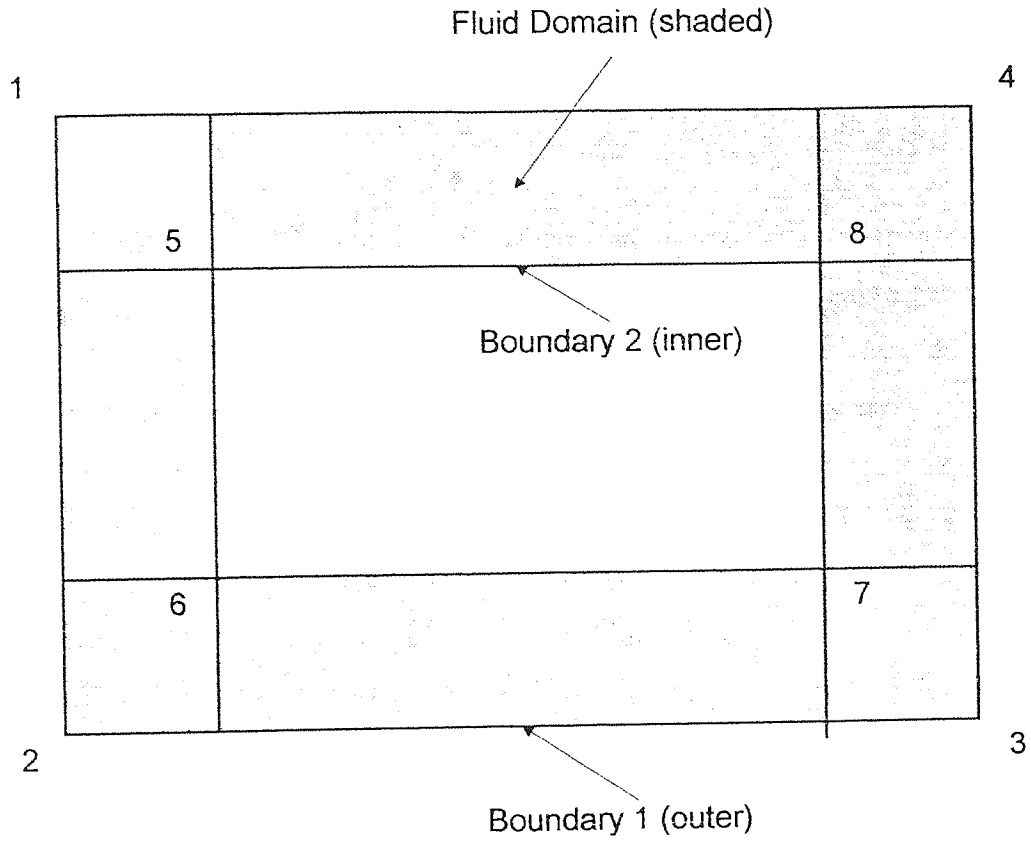

Figure 3-15:

2D Domain Requiring the Assignment of Two Boundary Conditions.

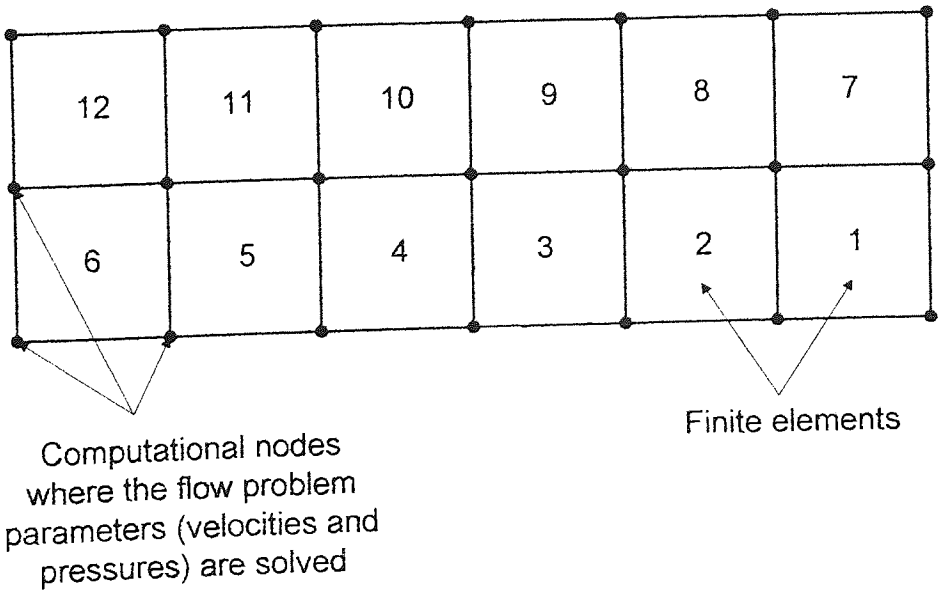

Figure 3-16:

Finite Element Numbering Scheme (I).

all macro-elements belong to the same sub-domain. To specify more than one sub-domain, Polymesh 2D and 3D must be instructed as to the assignment of which macro-element belongs to which sub-domain.

3.2.1.6 Optimisation and the creation of files

After mesh generation, the relevant files are created and saved. This process involves the optional optimisation of the mesh, in order to influence the CPU time taken to solve the flow problem on it. Polymesh 2D and 3D both possess optimisation numbering techniques that can be performed either semi-automatically or manually. The full procedures and explanation of how CPU optimisation may be achieved is not of direct interest within the context of this thesis. However, the explanation as to why a mesh will need to be optimised is described as follows.

Figure 3-16 shows a simple mesh that has been numbered in terms of the finite elements it contains. The four corners of each finite element are the positions where the flow problem, in terms of velocities and pressures generated, is to be solved and these positions are called the nodal points (other solution techniques may also be employed, such as solving the problem at eight nodal positions per finite element). Polyflow solves each finite element in a set numerical order, solving first finite element 1, then element 2 and *ad infinitum*. As may be seen from Figure 3-16, most of these finite elements possess shared nodal points, so once the problem has been solved on the four nodal points of finite element 1, then for finite element 2 only two remaining nodal points need to be solved. Thus the more finite elements that exist within a mesh that possess shared nodal points, the shorter will be the time taken to solve the computational problem as a whole. This may be further illustrated in Figures 3-17 to 3-19. All of these meshes contain the same number of finite elements, however it is obvious from the previous explanation that the CPU time taken to solve the problem shown in Figure 3-17, will be much greater than the problem shown in Figure 3-18. Furthermore, the numbering of elements shown in Figure 3-19, would produce a solution more quickly than solving the problem using the mesh numbering of Figure 3-18.

Polyflow classes the different numbering arrangements of finite elements in terms of frontal widths and an important value in the calculation of required CPU time for the solution of the flow problem on each mesh, is the maximum frontal width (MFW) value. The MFW of the mesh shown in Figure 3-17 is 12 finite elements, whereas for Figures 3-18 and 3-19, the MFW values are 4 and 3 respectively. It is found that the CPU time taken to solve the flow problem on any mesh is directly proportional to its MFW value. Thus obtaining the lowest value of MFW for any mesh is always advantageous, in terms of the required CPU time taken to solve the flow problem specified.

Figure 3-17:

Finite Element Numbering Scheme (II).

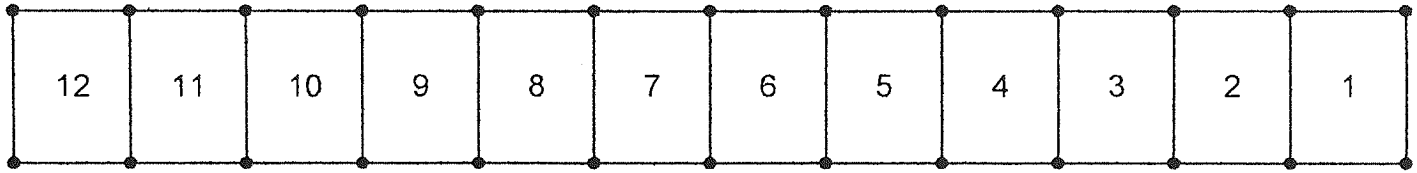

Total number of nodal points to be solved: 26

Figure 3-18:

Finite Element Numbering Scheme (III).

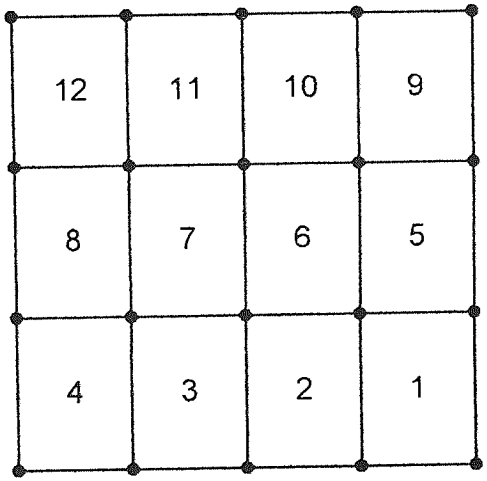

Total number of nodal points to be solved: 20

Figure 3-19:

Finite Element Numbering Scheme (IV).

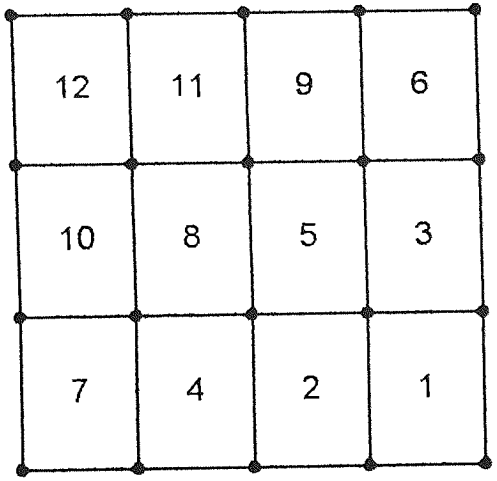

Total number of nodal points to be solved: 20

Both Polymesh 2D and 3D generate the following files;

- A file containing all details defining the mesh problem (.mdf),
- A file containing all nodal co-ordinates of the mesh to be used as an input for Polydata (.msh).

In summary the positive and negative attributes of both Polymesh 2D and 3D are given below.

Positive attributes

- Both Polymesh 2D and 3D are simple to use.
- For both programs, a wide range of mesh designs may be constructed.

Negative attributes

- Complex 3D meshes are not possible to construct using Polymesh 3D.
- A template from Polymesh 2D cannot be used as a template for Polymesh 3D, as there is no inter-program compatibility.
- For Polymesh 3D, a maximum number of thirty 3D elements may be used in the construction of a mesh (see Figure 3-20).

3.2.2 Overview of the advanced pre-processor ICEM-Polycem (version 3.0)

Control Data Systems Inc. produce a wide range of sophisticated pre-processor software, originally designed for the application of solving engineering problems in both the automotive and aerospace industries. This range of software, called the ICEM range, has been used in the past by both NASA, in the design of the space shuttle, and by Lamborghini for car design. There has been a recent trend for CFD companies, such as Fluent, to integrate certain software, such as the ICEM modules, into their own CFD software package. Thus, rather than develop and improve their own pre-processor software at considerable expense, CFD companies may now lease and thus benefit from advanced pre-processor facilities, as developed by other software companies. In 1995, Polyflow S.A. took the decision to complement its pre-processor software - Polymesh 2D and 3D - with the ICEM module Powermesh. Small modifications were made to this module for its use as a pre-processor for Polyflow and as a result the applied package is now known as ICEM-Polycem. Fluent have also performed the same operation using the same pre-processor, such that their modification of the ICEM-Powermesh module, used as a pre-processor for Fluent, is now known as GeoMesh.

Figure 3-20:
Example of a 3D Mixing Disc Mesh, Constructed Using Polymesh 3D and Containing the Maximum Number of Macro-Elements Available Within that Program.

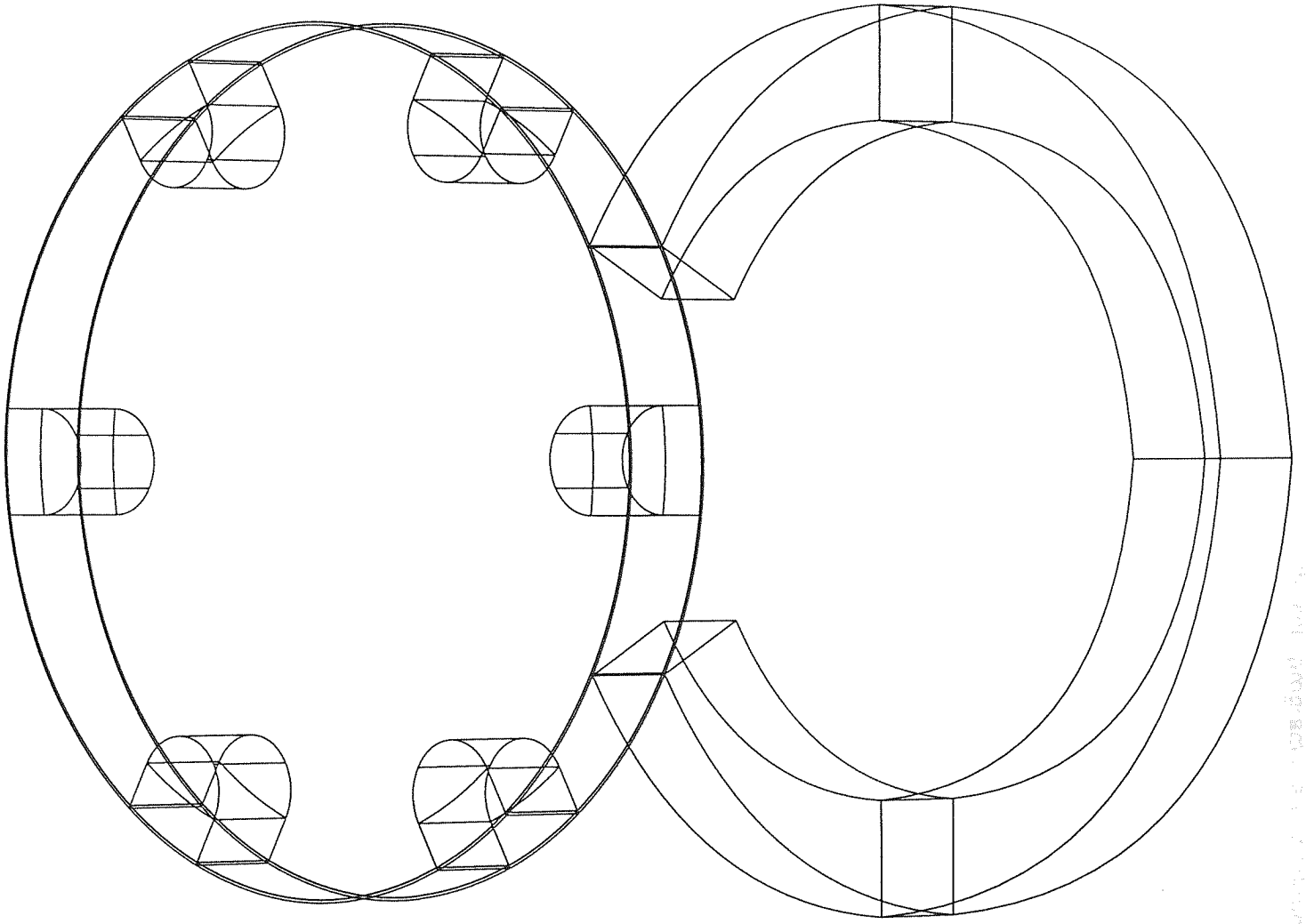

The ICEM-Polycem module contains a number of different programs all working interactively. A full list of the components - in order of (optional) use - which form the ICEM-Polycem module are as follows;

- ICEM-Powermesh manager - handles all project data and applications.
- ICEM-DDN - CAD package used to generate wireframe geometry templates to be imported into ICEM-Powermesh P-Cube.
- ICEM-Powermesh input.
- ICEM-Powermesh P-Cube - multi-block modeller and mesh grid generator.
- ICEM-Powermesh output - generates input mesh files to be used by the CFD solver such as Polyflow.
- ICEM-Powermesh LEO grid visualiser - utilised for the visualisation of structured and unstructured grids.
- ICEM IGES translator - allows the input and export of IGES geometry files. IGES files may be generated either by other CAD packages or by other CFD programs such as Pheonics.

Figure 3-21 shows a flow diagram of how the ICEM-Polycem components interact. The components of ICEM-Polycem that will need to be described in detail are DDN, P-Cube and LEO, each executed via their respective GUI facilities.

3.2.2.1 ICEM DDN

DDN is a fully integrated, multi-functional computer aided design (CAD) package used within the ICEM-Polycem module to create wireframe models and ruled surfaces. These CAD templates are copied to the P-Cube module, where they are then used to create solid models (i.e. the mesh for the volumetric fluid domain). DDN is an extremely powerful package with many advanced features and it possesses the capability of creating very complex engineering designs by the integrated use of both curve and surface tools. The important facilities contained within the DDN module, which are essential to creating a wireframe template structure for use within P-Cube, are listed as follows;

- Wireframe construction is achieved using a combination of points, lines, arcs, 2D surfaces and 3D volumes. Advanced CAD facilities such as the creation of a fillet at a corner, the ability to cut and paste desired sections or to create an ellipse, also exist.
- The ability to perform any operation on the wireframe construction such as copy, rotate, translate and mirror is possible.

Figure 3-21: Schematic Diagram Showing the Different Modules Constituting the Pre-Processor ICEM POLYCEM

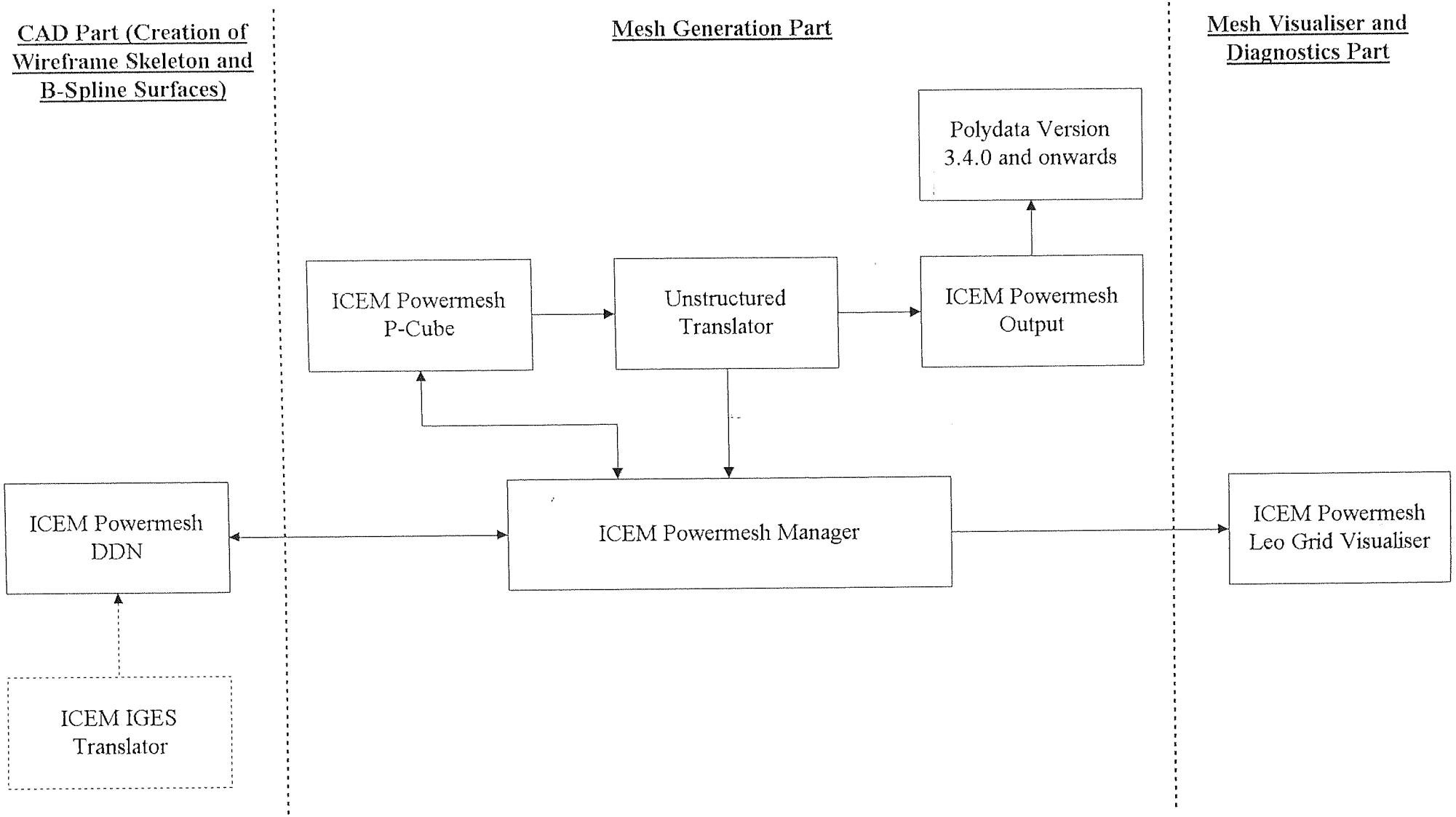

- Ruled surfaces for all non-planar faces can be created and then converted to B-Spline surfaces. This serves the purpose of fully mapping the contour points, for any 3D surface. All ruled surfaces created will need to be converted to B-Spline surfaces for recognition within P-Cube.

All of the capabilities for DDN and its full operation are well documented within the manuals and replication here would serve no purpose. However the schematic procedure for creating a full 3D wireframe model, containing non-planar surfaces may be summarised as follows.

- A fully developed 2D cross section, in the X-Y plane only, is constructed.
- This 2D cross section is selected and then copied and translated along the Z-direction to create a 3D structure.
- Ruled surfaces are created on all non-planar surfaces and the surface contours are mapped by converting all ruled surfaces to B-Spline surfaces.

3.2.2.2 ICEM Powermesh P-Cube

ICEM-Polycem version 2.1, the first version of the pre-processor software used within this research, contained a version of the P-Cube module that had limits imposed on the size of mesh that potentially could be constructed. As stated previously, Polymesh 3D is constrained by the fact that a maximum of 30 macro-elements may be used in the construction of its 3D meshes. The P-Cube program within ICEM-Polycem version 2.1 is constrained by the fact that a maximum of 170 domains (domains being the equivalent to the a macro-element used within Polymesh 3D) and 1500 boundary conditions may be used during mesh construction. The latest version of ICEM-Polycem, version 3.0, acquired in April 1996, is capable of producing meshes with a maximum of 300 domains and 2500 boundary conditions. As may be seen in the mixing disc results section of Chapter 7, the meshes needed for the simulation of one full pair of mixing discs, with each disc being separated by a small gap, contain approximately 280 domains per mesh.

Many of the principles described in the Polymesh 2D and 3D section are applicable to the operation of P-Cube. The major difference is the way in which the two packages generate a structure.

- Polymesh 2D and 3D both rely on the manual input, by way of the keyboard, of all the co-ordinates contained within the flow domain.
- P-Cube, by utilising its GUI facilities, generates meshes by "snapping" block structures

onto the CAD wireframe skeleton generated within DDN.

Again the complete description of P-Cube is contained within the user manuals and is far too involved to be replicated here. Instead a summary of the procedures used in the construction of a 3D mesh using P-Cube is given below.

3.2.2.2.1 Face and block generation

The complete CAD skeleton generated within DDN may be copied to P-Cube via the menu option in the ICEM-Powermesh manager. Once P-Cube is entered, the CAD skeleton will appear and this is then used as a mesh building block template. Figure 3-22 shows an example for a CICo-TSE structure, of how the DDN skeleton will look once it has been imported into P-Cube, with the red outlines representing the CAD skeleton, the white crosses representing the CAD points and the green lines showing the surfaces that are B-Spline. Figure 3-23 schematically illustrates that the building, or dismantling of blocks, may be achieved at any block constituent level. For example, a block may be constructed by snapping on eight vertices at various positions on the CAD skeleton, then by selecting pairs of these vertices in turn, twelve edges may be created and so on until the complete block is created. Alternatively, a block may be created automatically using a one key command. This block, when created, will be of a free position and so the user will need to anchor the block location, by snapping one of its corners to the CAD skeleton. Unfortunately the one key command will create a completely square block and so the remaining seven corner vertex positions will need to be manually assigned also.

As previously described, much freedom has been given to the creation of blocks within P-Cube, however one very important rule must be observed. The components making up each block and also the collection of blocks within the flow domain, must all be topologically connected and no duplication of any component, such as vertices or edges, is allowed. If this rule is not obeyed, then a mesh will be created that is not topologically correct and consequently insoluble within Polyflow. Thus to ensure that this rule will be obeyed when creating a complete mesh from scratch within P-Cube, a block generation strategy has been formulated and its procedure is summarised as follows;

- A block is created by starting the structure at the face level. One face in the formation of the block is created via a one-key command and initially its position will be free. The four vertices of this initially square, free positioned face are snapped onto desired sites upon the CAD skeleton.
- Any curved edges required within the face, are created using the curved edge option.

Figure 3-22:
Example of a DDN Skeleton, Imported into P-Cube for a Typical 3D CICo-TSE Structure.

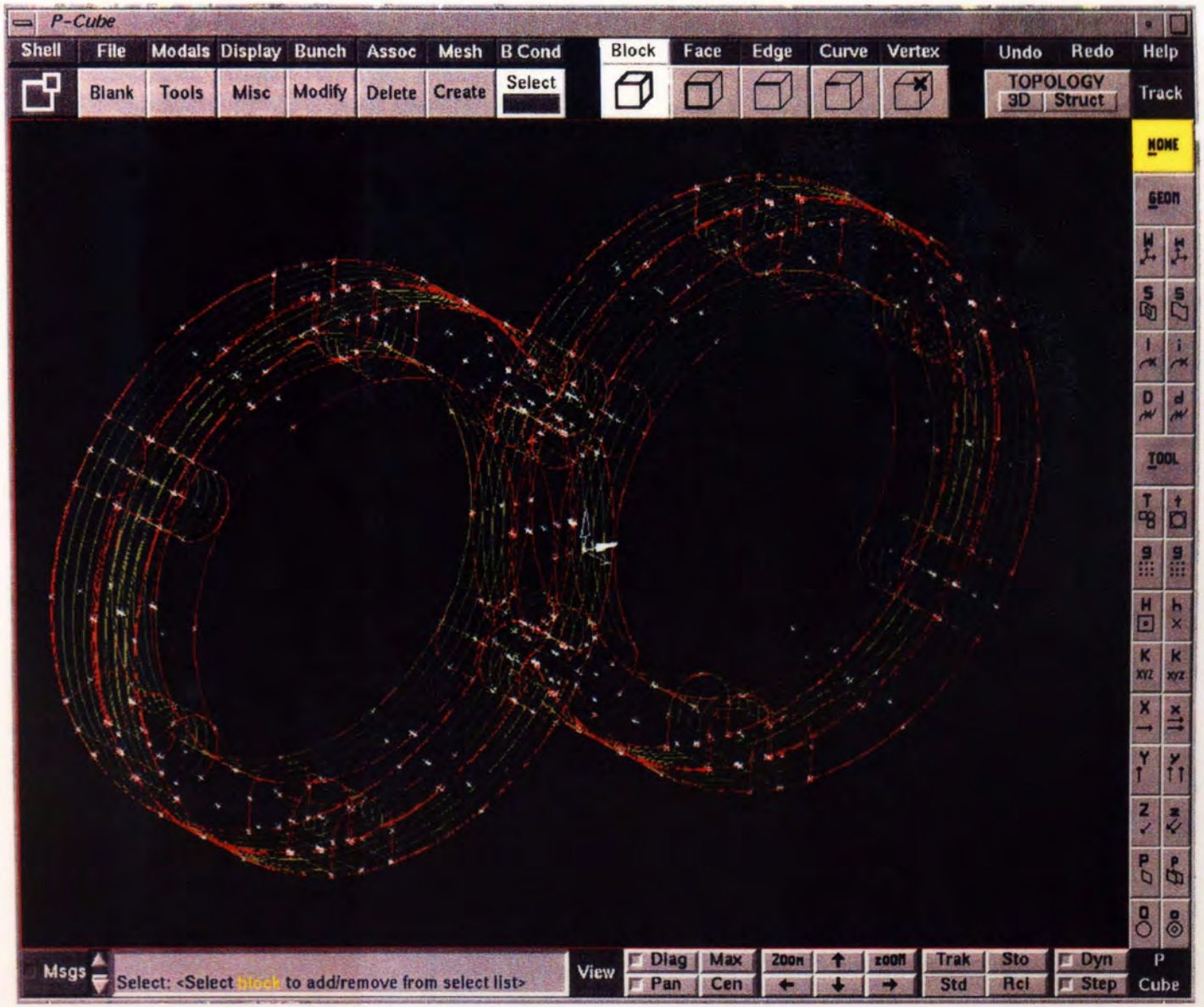

Figure 3-23:

Description of P-Cube Block Creation Strategies.

Several possibilities are given :

- Directly generating blocks. In this case, faces, edges and vertices are implicitly defined.
- Building the blocks hierarchically, that is, generating vertices, then edges based on vertices, then faces based on edges and finally blocks based on faces.
- Combination of both previous possibilities.

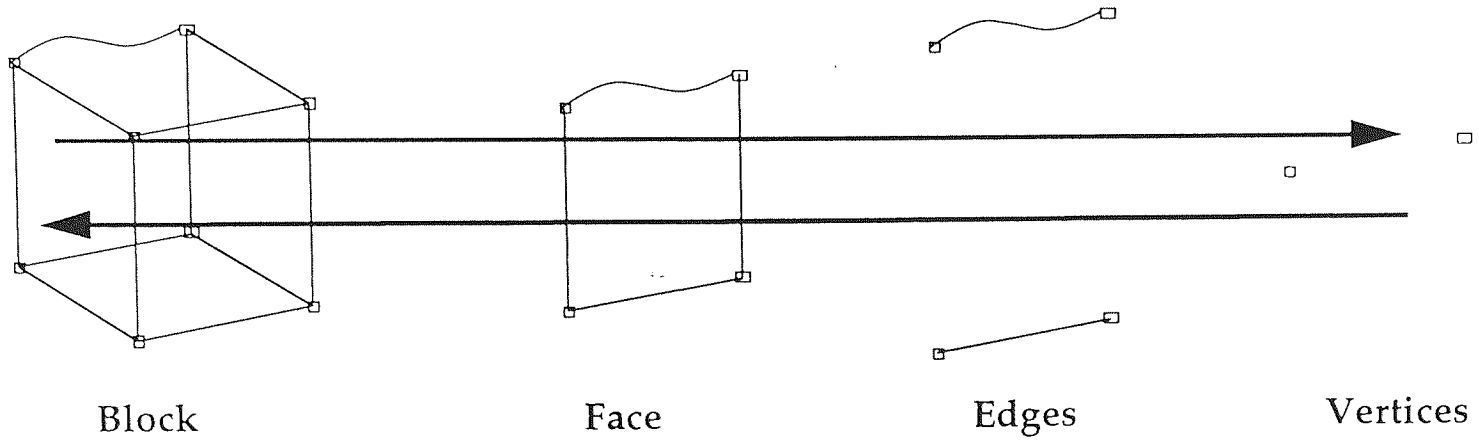

Utilising the GUI facility, the user selects an initially straight edge. An arc is created by specifying points along the curved CAD skeleton outline, to which the curved edge within the face is to be snapped. This curved edge will arc through each identified point on the CAD skeleton. The greater the number of points specified along the CAD skeleton, the greater the accuracy of the arc to be generated. For an arc possessing a small angle, of the order of 5-10°, usually only one point will be needed. However for angles up to 180°, 6-8 points will be needed to generate an arc of an acceptable quality.

- The next face to be created must be topologically connected to the first. To ensure this, the shared edge possessed by both faces is first selected (this will automatically select the two shared vertices also). The second face is then created and one of its edges will be automatically assigned as the shared edge. The positions of the remaining two vertices from the second face are then snapped onto the CAD skeleton.
- All the remaining faces within the same plane, usually the X-Y plane, are created (remembering to select all shared edges first, before creating the relevant faces).
- The blocks are then created automatically by the following process. By first selecting any vertex, an edge is created in the direction for which the blocks will need to be created (usually the Z-direction). This edge, called the leading edge, is then selected.
- All the faces contained within the same plane are selected one by one. Once selected the "create block" option is chosen and all blocks to be composed from the faces selected, are created automatically in the direction of the leading edge. All edges contained within the blocks created in the leading edge direction, will be both of the same length and orientation to the leading edge. The faces created at the ends of these edges and contained also within the blocks created, will mirror those faces that were initially selected.
- These blocks created will be constrained and they cannot be worked upon until the constraint is broken. This is a simple procedure whereby all the blocks are selected and the automatic "break constraints" option is applied. Once completed the positions of the vertices, etc., may be modified if desired.

A summary of the above procedure is schematically represented in Figure 3-24. The latter three paragraphs from the above procedure may be repeated several times in order to create as many series of blocks as required at each subsequent X-Y plane.

3.2.2.2.2 Edge bunching (number and distribution of nodal points)

The number and distribution of nodal points along all edges, is obtained by performing the semi-automated edge bunching procedure, by way of the GUI facility, within P-Cube. The "set bunching" option is accessed and initially P-Cube will automatically check the structure

Figure 3-24:

Procedure for Creating 3D Blocks in ICEM P-Cube

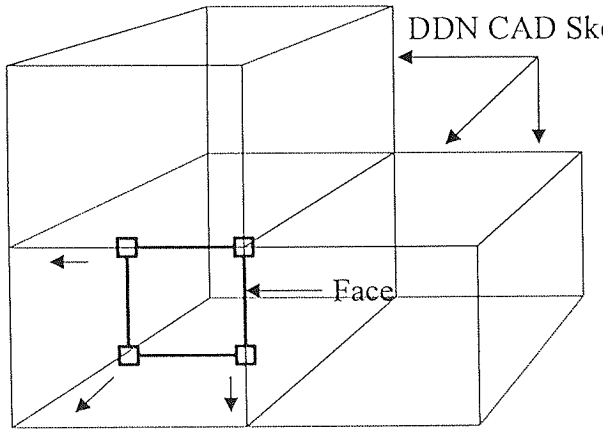

1. Create face and position 1st vertex. Snap 1st vertex, position each of the remaining vertices snapping these also one at a time.

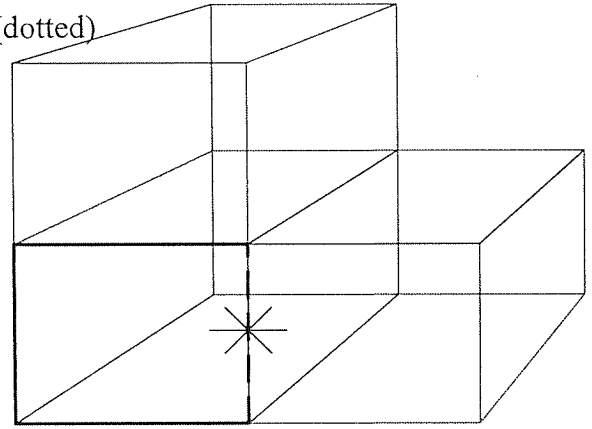

2. Select shared edge

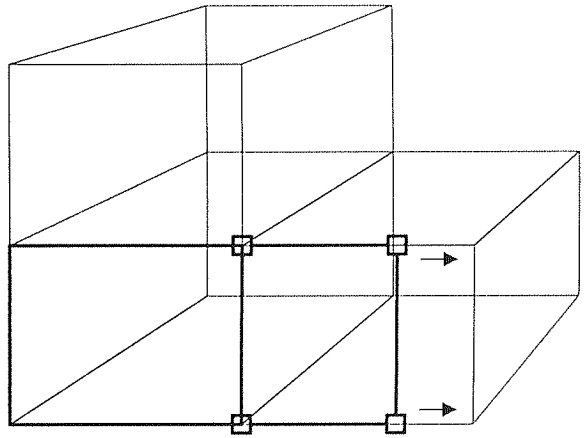

3. Create 2nd face, which will be automatically bolted onto the shared edge. Position and snap the two remaining vertices.

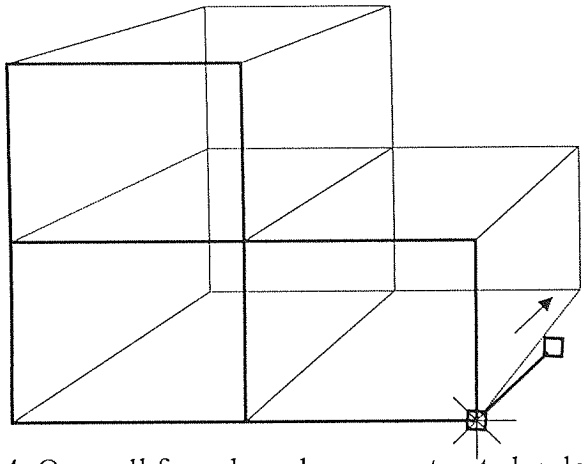

4. Once all faces have been constructed, select any vertex and create leading edge. Position and snap remaining vertex.

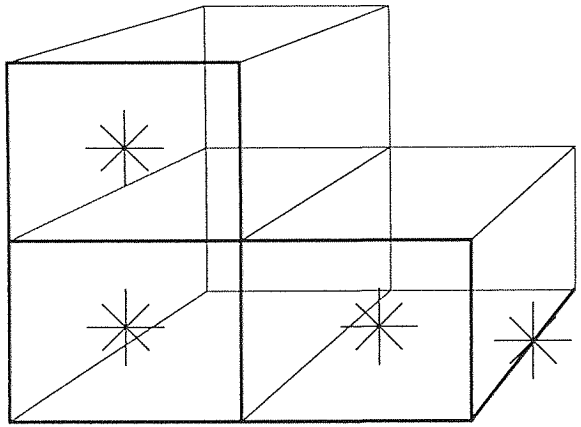

5. Select all faces in the same plane, select leading edge and then create all blocks automatically.

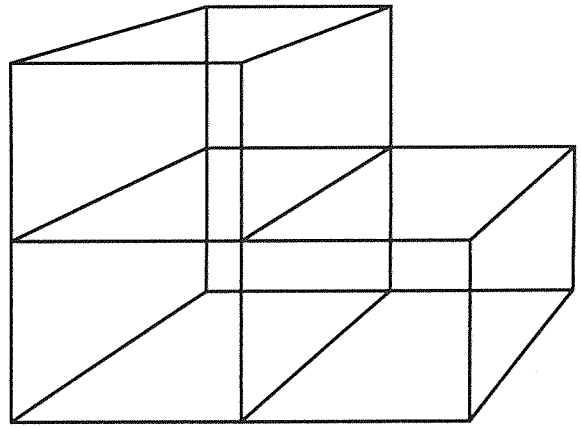

6. Select all blocks and break constraints. Repeat steps 5 and 6 to create further blocks in the leading edge direction.

for the quality of its topology. Once the verification has been completed, P-Cube will assign edges as to whether they are Masters or Slaves. Figure 3-25 shows an example for a CICo-TSE structure, of the assignment of both Masters, shown as yellow lines and Slave edges, shown as red lines. The Masters are the edges to which the desired number of points along an edge, are allowed to be assigned. Assigned for each Master will be a series of Slave edges, which are unique to that Master edge only. Thus the number of divisions contained along the Master edge, will automatically be assigned along all corresponding Slave edges. If the number of divisions along a Slave edge needs to be subsequently changed, then this may only be achieved by changing the number of points along its assigned Master edge.

The distribution of points along an edge, may be independently assigned for both Master and Slave edges. P-Cube possesses many sophisticated distribution laws and their pre-application along an edge, may be previewed via the GUI. There is little point in listing all distribution laws available within P-Cube, but it may be taken for granted that any distribution (linear, exponential, weighted towards any defined position(s) along the edge, etc.) of any number of points along an edge, may be specified. This is not the case when using Polymesh 2D or 3D as both possess very limited nodal distribution laws.

3.2.2.2.3 Patch sub-face association

The fluid boundaries, such as the inlet, outlet and walls, are the physical limits to which the flow domain may be defined. These boundaries in 3D will be a series of surfaces and if they are of a uniform, non-curved type, then all points on that surface may be easily found. However if the boundary is curved, then before the structure may be imported into P-Cube, all curved CAD faces pertaining to that boundary must have been converted to B-Spline surfaces previously within DDN (as described in Section 3.2.2.1 - ICEM-DDN). Before P-Cube can utilise the B-Spline information assigned within DDN, P-Cube must be informed as to which faces belong to which curved boundaries. This process is called the face-surface family association.

Figure 3-26 shows a diagram of a mesh for which the face-surface family association has not been performed. The curved surfaces of the two inner boundaries indicated, should be perfectly circular. If P-Cube does not know of the face-surface family association at these two boundaries, then the exact positions of the nodal points on the two curved surfaces will not be known. As a consequence, for the example shown in Figure 3-26, P-Cube will place these boundary nodal points at irregular positions.

The procedure for performing face-surface family association on a structure containing curved boundaries, may be described as follows;

Figure 3-25:
Example of the P-Cube, Master and Slave Assignments for a Typical 3D CICo-TSE Structure.

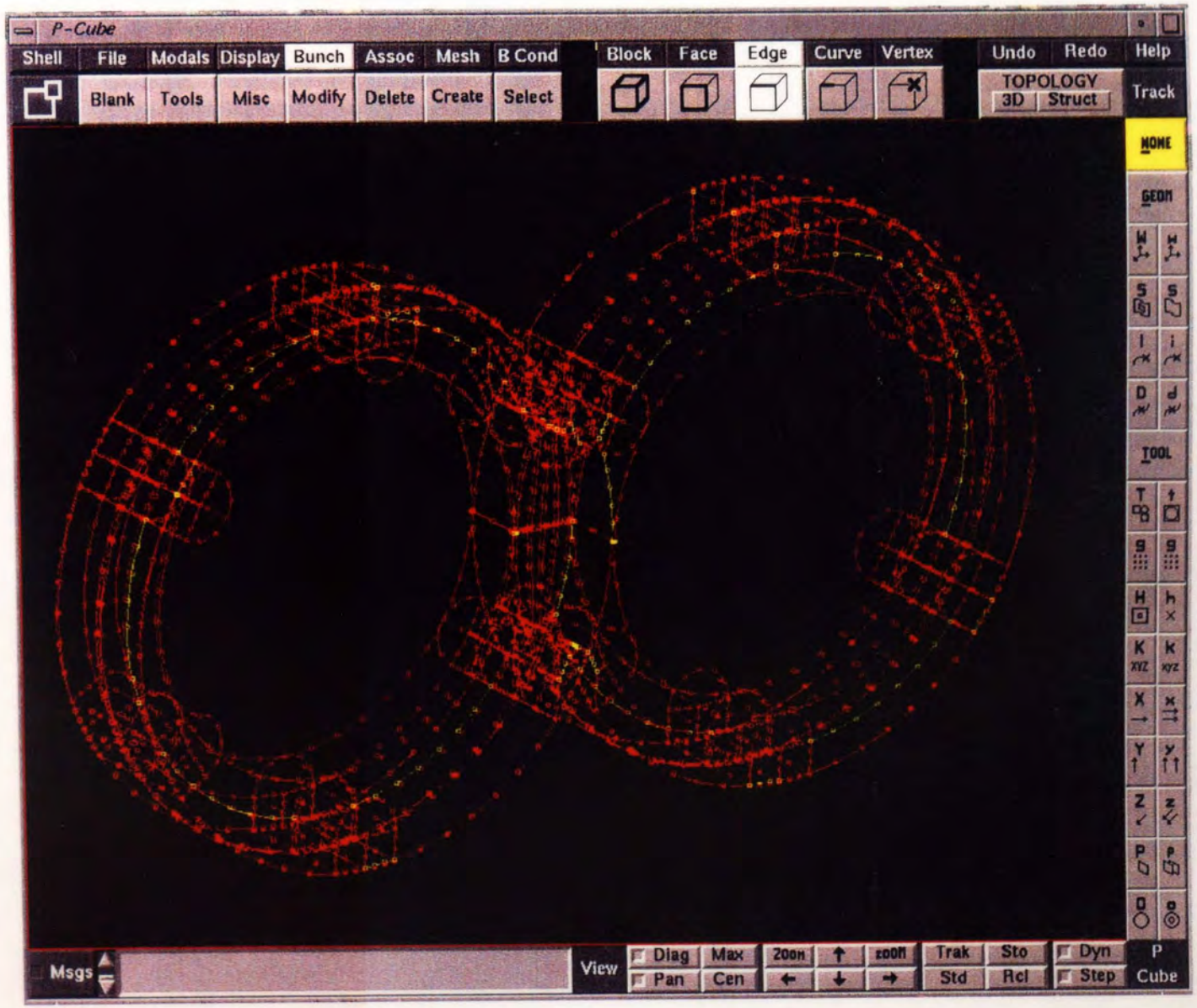

Figure 3-26:
Irregular Mesh Construction (Obtained by the Omission of Face-Surface Association Assignment).

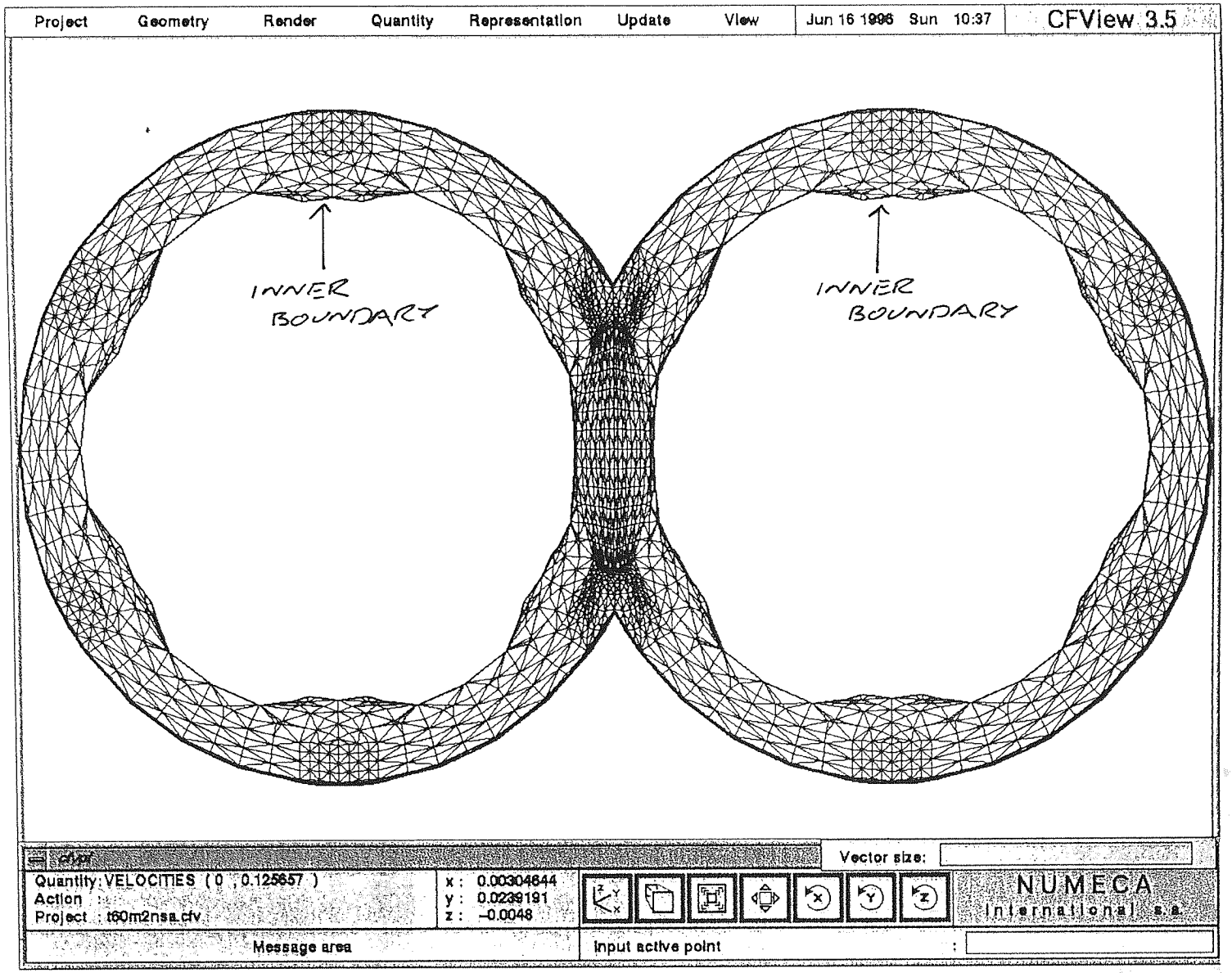

- Groups of B-Spline surfaces are characterised into families. These families are grouped arbitrarily at the discretion of the user. For example, the mesh shown in Figure 3-26 would need three sets of surface families to be assigned. One family would be the grouping of all B-Spline surfaces contained on the outer figure-of-eight shaped boundary. The remaining two families would each be composed from the B-Spline surfaces contained within each of the two inner circular boundaries.
- Once all the B-Spline surface families are characterised, then all faces contained within each surface family must be assigned. If a singular face from a particular surface family is missing, then the assignment of nodal points on that curved face only, will not be known.

Figure 3-27 illustrates the assignment of the face-surface family association for a CICo-TSE structure, which are shown in blue. One of the three surface families assigned for this structure (the right CICo-TSE element) is represented by the green lines, with the associated faces for that surface family shown as white outlines. The B-Spline surface lines of the other two surface families assigned (the left CICo-TSE element and the figure-of-eight outer barrel) are represented by the light grey lines.

3.2.2.2.4 Assignment of boundaries and sub-domains

The assignment of boundaries and sub-domains within P-Cube is a straightforward procedure, however it can be very time consuming for large meshes. The convention used within P-Cube is as follows;

- Boundaries are assigned on faces.
- Sub-domains are assigned within blocks.

Thus a face lying on a boundary is selected and the user assigns its physical representation and chronological boundary number. For a one-domain problem, all blocks will be assigned to the same sub-domain automatically. P-Cube assigns boundaries as physical representations such as inlet, outlet and wall boundaries and similarly sub-domains may be either assigned as being porous or free-surface domains (the full list of possible representations is given within the ICEM-Polycem manuals). Once the mesh is imported into Polydata, boundary and sub-domain information is only partly recognised. As a consequence, the physical representation of each boundary and sub-domain imported is not transferred and this information must be reassigned from within Polydata (see Section 3.3.1.4 - Definition of boundary conditions). The correct number and chronological order of boundaries, faces contained and their differentiation, is all that Polydata will require from the mesh generated

Figure 3-27:
Example of the P-Cube, Face-Surface Association for a Typical 3D CICo-TSE Structure.

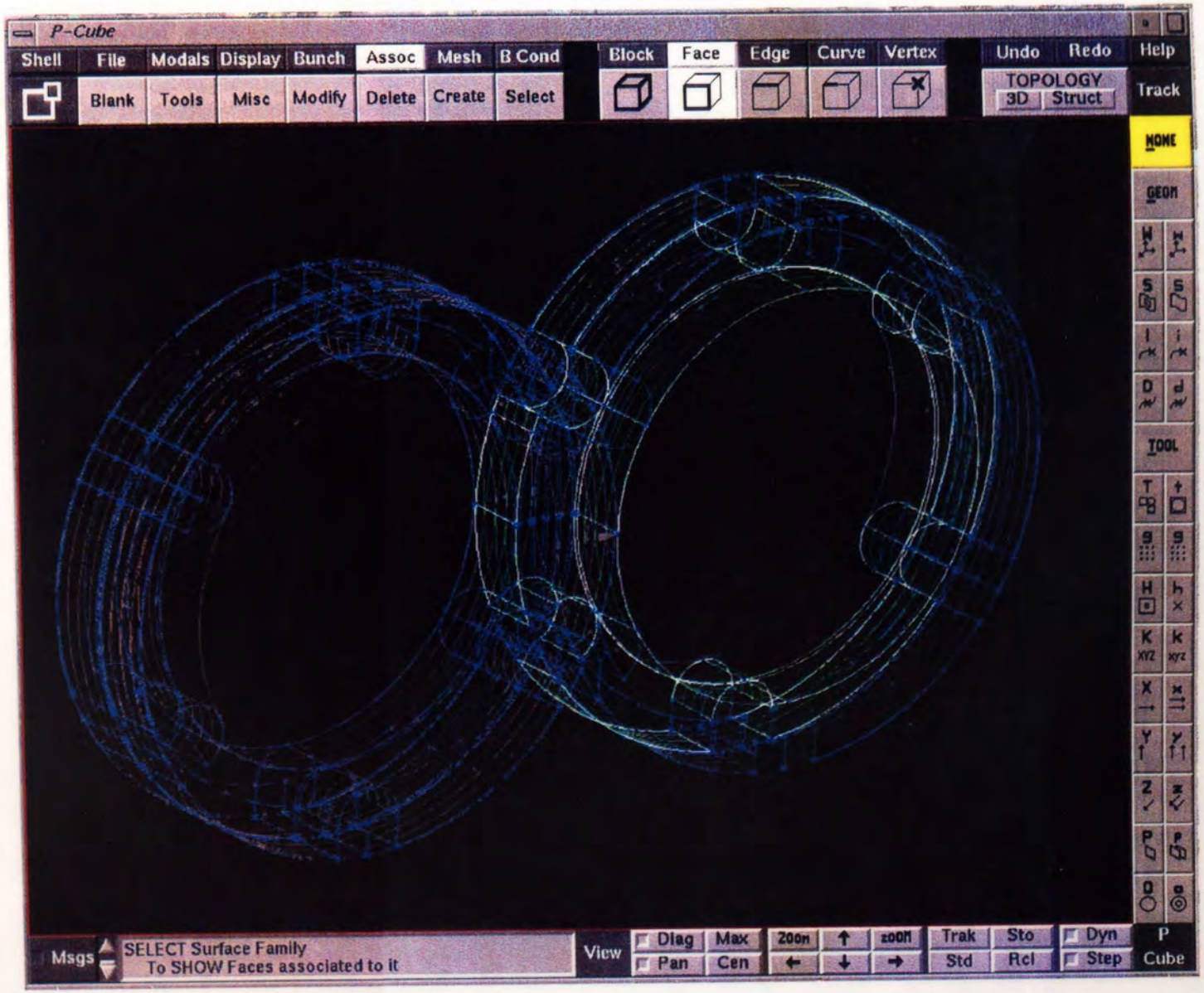

within P-Cube. Hence the physical characterisation of boundaries and sub-domains within P-Cube is for the user's information only.

The block generation strategy outlined in Section 3.2.2.2.1 - Face and block generation, describes how by creating a series of faces and a leading edge, blocks may be generated. This procedure promotes the vertex, edge and face constituents to their higher hierarchies of edges, faces and blocks respectively. Problems in assigning boundaries will arise though if the full structural topology is either not complete or incorrect before block transformation is undertaken. This may be illustrated by the diagram shown in Figure 3-28, which shows an example of two faces that have a shared, but duplicated edge. This edge duplication will arise if Face 2 is created and then attached to Face 1, without the prior selection of the shared edge within this process. As a consequence, when the block conversion process is executed, these two overlaid edges will be converted to two overlaid faces. P-Cube will not be able to differentiate between these two overlaid faces and when it comes to assignment of boundaries or sub-domains, one of two situations may arise;

- If the user specifies the boundary on just one of these faces, then when the mesh is imported into Polydata, an error message will be given stating that there are undefined boundaries.
- Alternatively, if the user specifies the same boundary assignment on both of these two shared faces, then problems will arise when the flow calculation is performed.

The duplication of edges is, in the Author's opinion, the most common cause of error when using P-Cube, especially for the new user. There is an in-built diagnostics facility for checking the topology of the mesh under construction, however, it is not sophisticated enough to solve every topological error that the user could possibly create. For the example shown in Figure 3-28, P-Cube will fix the topology once the file has been saved, such that when the user re-enters P-Cube, the two overlaid edges will be "fixed" and the full topology restored. However for meshes with more severe topological faults, P-Cube's ability to rectify the topology is limited. The Author's approach when confronted with a structure that has an incorrect topology that is not easily rectified, is to start the P-Cube structure again from scratch, taking care not to repeat the duplication of topological parameters. The checking of a mesh structure at every stage of its construction, is thus considered to be essential.

Figure 3-29 shows the assignment of five boundary sets, for a CICo-TSE structure represented by the blue outline. The red and light blue arrows seen within the structure, represent the assignment of faces as being either inlet or outlet boundaries. The three remaining sets of boundaries for this particular structure, are the wall boundaries and these are

Figure 3-28:

Diagram Illustrating the Problems Encounted With the Block Transformation Procedure, if Duplicate Edges are Present

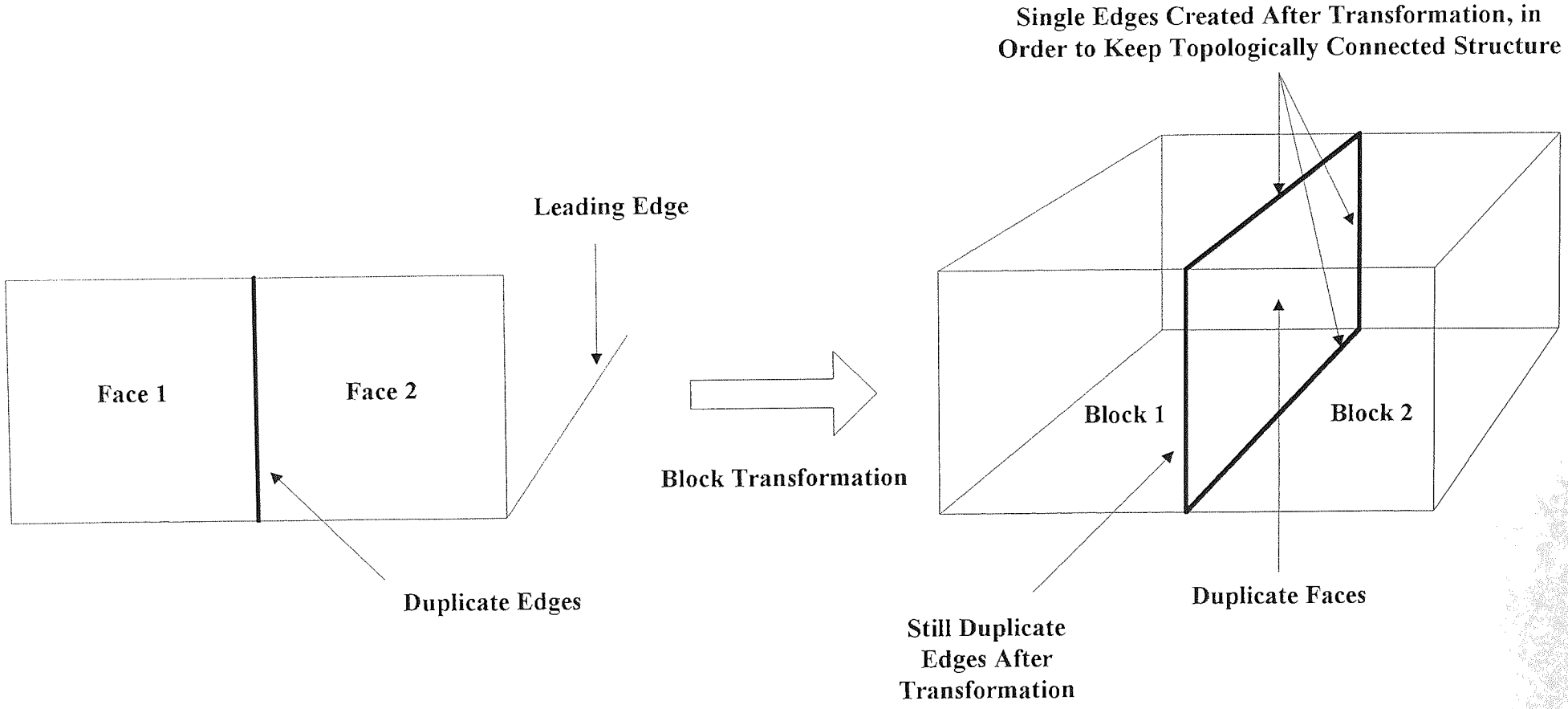

Figure 3-29:
Example of the P-Cube Assignment of Boundaries on Faces for a Typical 3D CICo-TSE Structure.

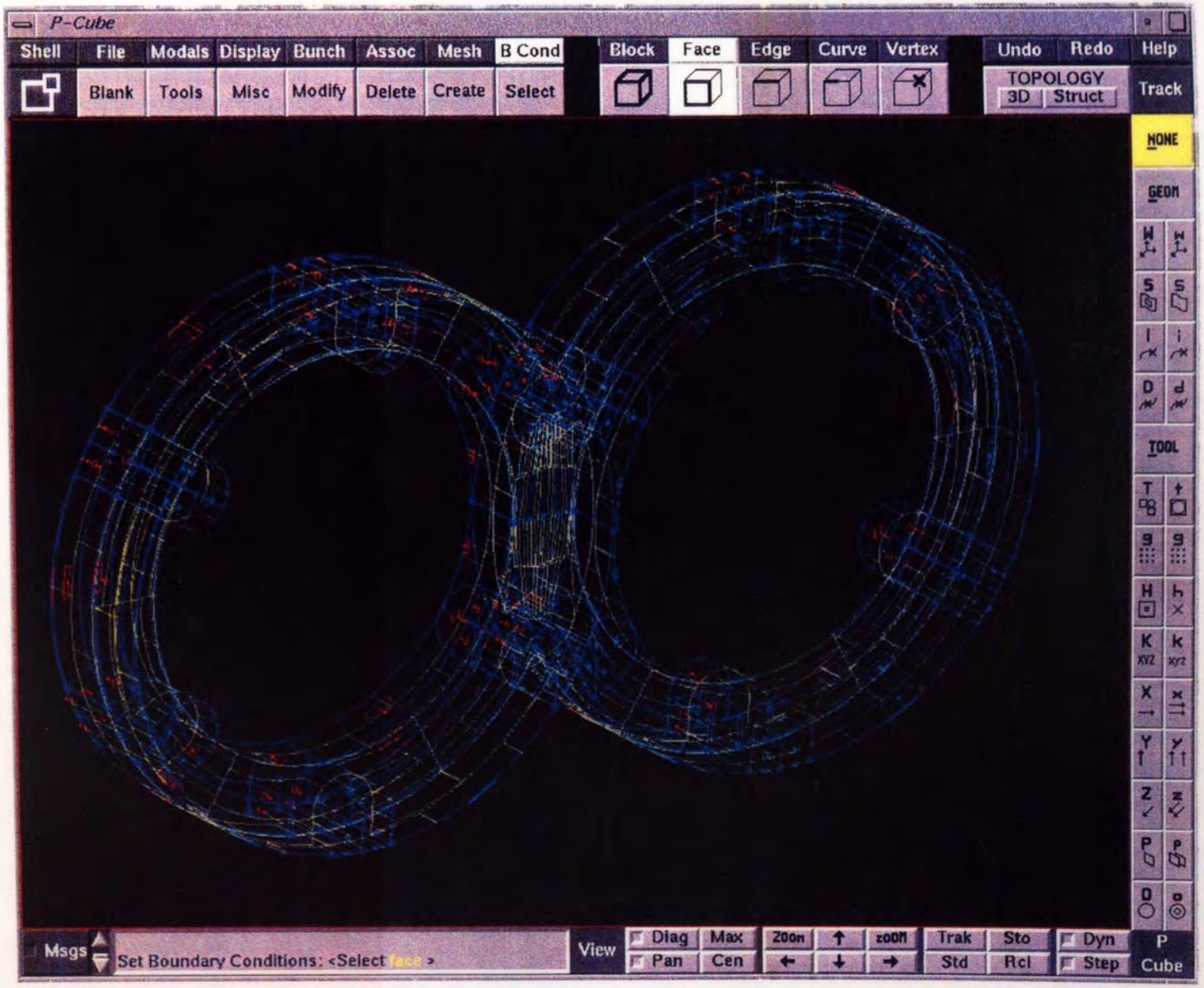

shown as light green lines, arranged as a series of brick patterns. These three wall boundaries have been assigned to faces belonging to both the left and right CICo-TSE elements and to the outer barrel wall respectively.

3.2.2.2.5 Generation of computational grid

Once the structure has been fully assembled, the "create mesh" option is executed. This procedure involves the conversion of blocks into domains and the splitting up of these domains into finite elements. P-Cube, during its mesh generation procedure, will check all properties such as topology structure and boundary assignments and any faults found will be reported. At this stage the mesh created will be of the structured type. Once P-Cube has finished generating the structured mesh, the user will be prompted to save the mesh information and then exit to the ICEM-Powermesh manager module.

3.2.2.2.6 Conversion to unstructured grid

The structured mesh is converted to an unstructured mesh using the automatic transfer process, which is accessed from one of the menus contained within the ICEM-Powermesh manager module. The process is achieved by selecting all structured domains and then converting them automatically to unstructured domains. Finally the user may generate the output mesh file for Polydata (of the .poly type) by using the "write input" option.

3.2.2.3 ICEM Powermesh LEO grid visualiser (versions 2.0 and 3.0)

The user is able to inspect the quality of the mesh structure generated by P-Cube and perform several diagnostic checks, using the grid visualiser module ICEM-LEO. As can be seen from the P-Cube examples shown within this chapter (Figures 3-22, 3-25, 3-27 and 3-29), P-Cube displays the structure on screen as a transparent wireframe model at all stages. These transparent representations are very useful for mesh construction, as every part of the structure may be seen at all times. In addition, if the mesh gets too complicated to be manipulated with ease, then P-Cube possesses the ability to "hide" selected parts of it. However, if a mistake needs to be rectified within the mesh structure, or particular structural properties need to be investigated, such as boundaries on faces, then this ability to see all parts of the structure at once, especially when working on large complex structures, is actually a hindrance for the user. More importantly, P-Cube does not possess the ability to show user-selected parts of the structure only, such as the exclusive display of the boundary details on a single face or the number of nodes along a particular edge.

ICEM-LEO has been specifically designed for mesh visualisation and it achieves that goal by virtue of its solid block modeller capabilities. The user is able to selectively pinpoint and

visualise with ease, desired points, areas or volumes within the mesh and to represent faces and domains as solid areas or volumes. On screen these solid representations may be seen with ease, because they are automatically portrayed using different colours. It must be noted though that when ICEM-LEO is used as a fault finder tool, then the correction of that fault within the mesh may only be achieved by re-accessing P-Cube.

The mesh of interest is imported into LEO by selecting the following mesh properties;

- Structured and unstructured domains.
- Topological and boundary files.

ICEM-LEO may be accessed using just one of each of the options from the above two selections. As will be seen in Chapters 7 and 8, some of the meshes generated within P-Cube were too big for ICEM-LEO to process. Consequently for those examples, it was only possible to import their topological files. This unfortunately meant that the boundary details on faces could not be viewed.

By default, the structured mesh is the one first seen, but the user is able to transfer between both mesh types. Properties of the mesh, such as boundaries assigned on faces, may be represented either as a wireframe structure, as a series of nodal points along its constituent edges, or as a solid entity. Each vertex, edge, face and domain created within P-Cube is numbered and the assignment of numbering may be easily viewed by way of the many menus. ICEM-LEO's most usefully employment in the Author's opinion, is as a convenient way of ensuring that all faces belonging to each boundary has been assigned within P-Cube. By utilising the solid block modeller within ICEM-LEO, faces on a boundary that are not assigned will contrast with those that have been assigned. Only assigned boundary faces will be shown as solid colours. Examples of using ICEM-LEO to show the faces contained within boundaries for the structures under investigation in this work, are shown in Chapters 6-8.

ICEM-LEO, in addition, has many useful diagnostic subroutines such as the Determinant and Jacobian (the full list of diagnostics is given within the user manuals). These diagnostics will perform calculations on the mesh to determine the goodness of certain qualities. For example, the measure of deviation from the perfect quadrilateral or triangular structure may be calculated for all finite elements contained within the mesh.

3.3 Interface and solver software

3.3.1 Interface program: Polydata (version 3.4.6.1)

Polydata is the interface part of the package, used for specifying the flow problem needing to be solved within Polyflow. The chronological procedure for creating the flow problem on

the mesh generated from either Polymesh 2D/3D or ICEM-Polycem is summarised in Figures 3-30 to 3-32. The summaries given in Figures 3-30 to 3-32 have had several procedures omitted, such as the description of using Polydata in the simulation of bubble growth, due to the fact that they are not directly applicable to this work. A summary of the full capabilities of Polyflow will be given in the remaining sections, but only the capabilities of interest within this work will be detailed further.

3.3.1.1 Define the global parameters of a task

The type of solution scheme needed to solve the flow problem specified is called the task and this task will contain sub-tasks for solving different parts of the problem, such as the heat conduction part, the isothermal flow problem or one of many post-processor calculations. Many different sub-tasks may be assigned within a task. One global parameter for a task may be selected from the following four options.

3.3.1.1.1 Steady state problem

The problem is solved directly using the fluid properties specified and these parameters are assumed to be unchanging with time. Highly non-linear problems would almost certainly be insoluble using a steady state solution scheme.

3.3.1.1.2 Evolution scheme

Highly non-linear problems are best solved by using an evolution scheme. The evolution scheme is the creation of a step by step procedure for solving the flow problem. This step by step solution of the problem is achieved by varying, at each stage, the value of the fluid parameter(s) causing non-linearity. The solution of the full non-linear problem specified, is only possible by solving the derived linear problem first. Once an initial easy linear solution is found, then non-linearity may be progressively introduced into the problem by a series of steps. The problem is solved at each incremental step, using the previous solution as initial conditions at each stage. For example, a problem involving a large increase of flow rate, requiring the quantification of viscous heating generated, will be highly non-linear. A solution to this problem will be unattainable using the steady state method. Solving this problem by using an evolution scheme would first involve generating an initial solution using the starting value of fluid flow rate and assuming isothermal conditions. Having found this initial solution, the flow rate is increased by values pre-specified by the user. The step incrementation of flow rate may be achieved by using a function, such as a linear, exponential or ramp function. The steps are solved at each stage, until the full non-linear solution is obtained. If the problem starts to diverge, then non-linearity is most probably being

Figure 3-30: **Schematic Diagram Illustrating the Recommended Chronological Order for Creating a Data File Within Polydata**

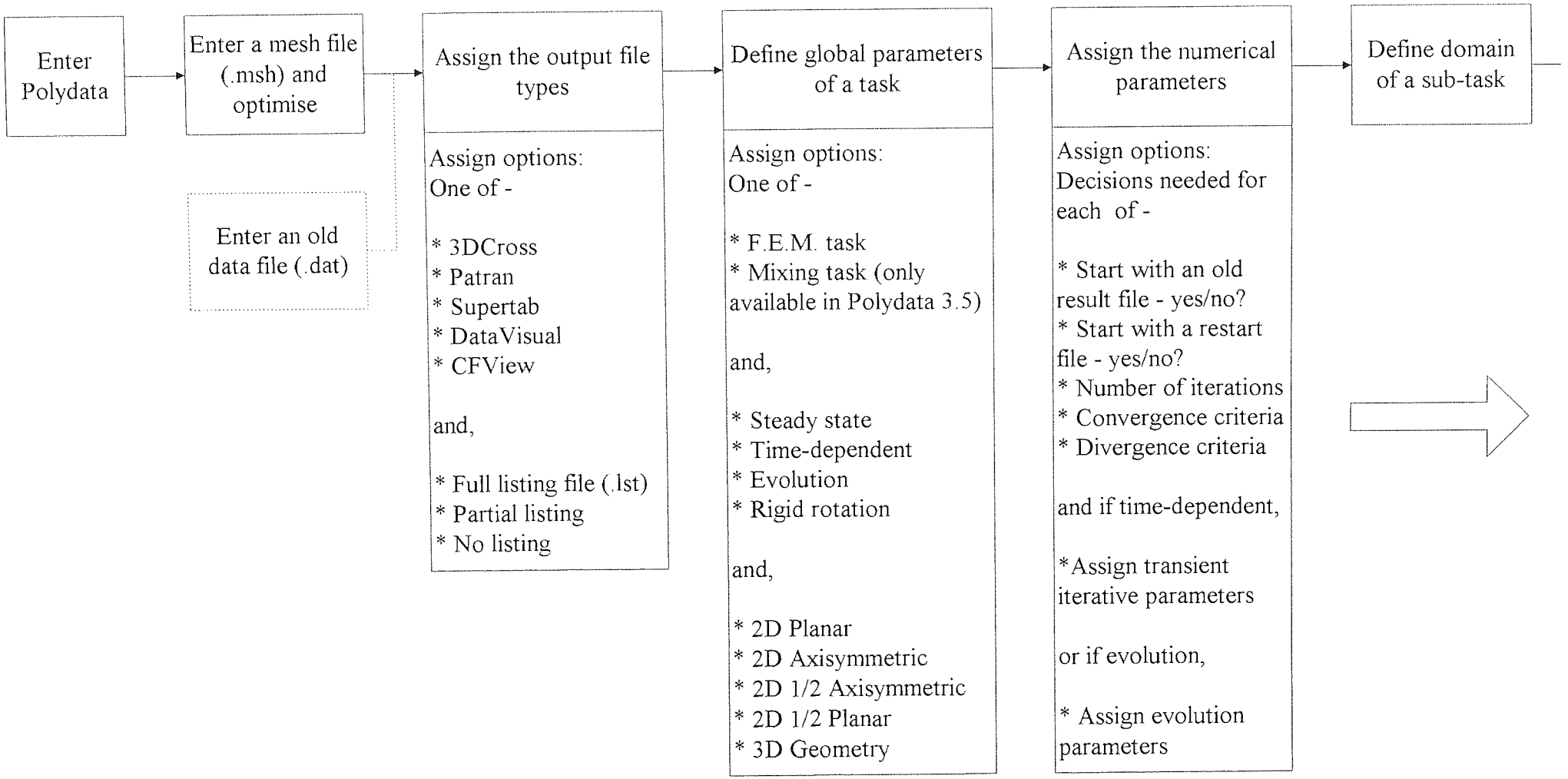

Figure 3-30: (Cont.) **Schematic Diagram Illustrating the Recommended Chronological Order for Creating a Data File Within Polydata (Cont.)**

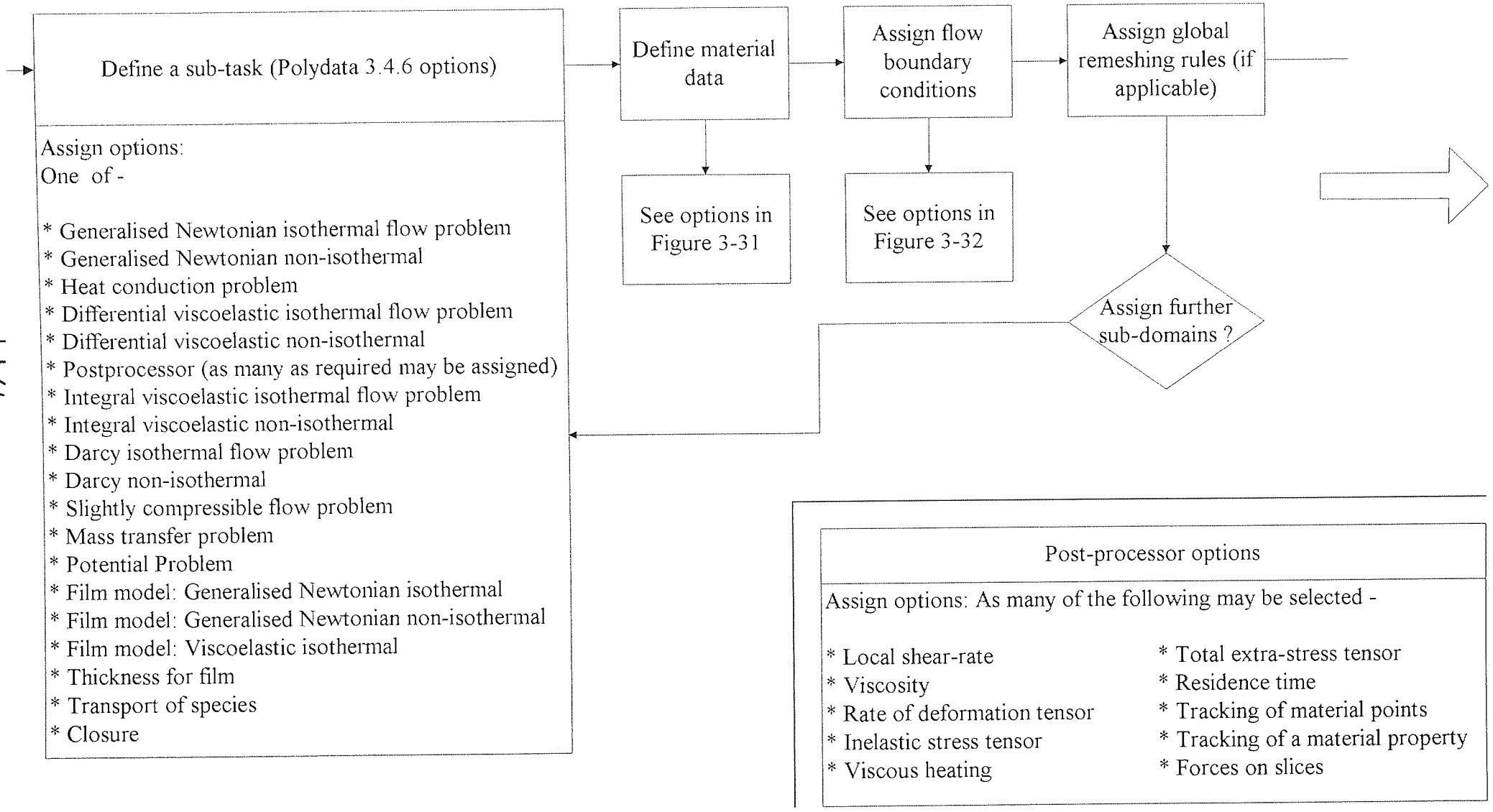

Figure 3-30: (Cont.) **Schematic Diagram Illustrating the Recommended Chronological Order for Creating a Data File Within Polydata (Cont.)**

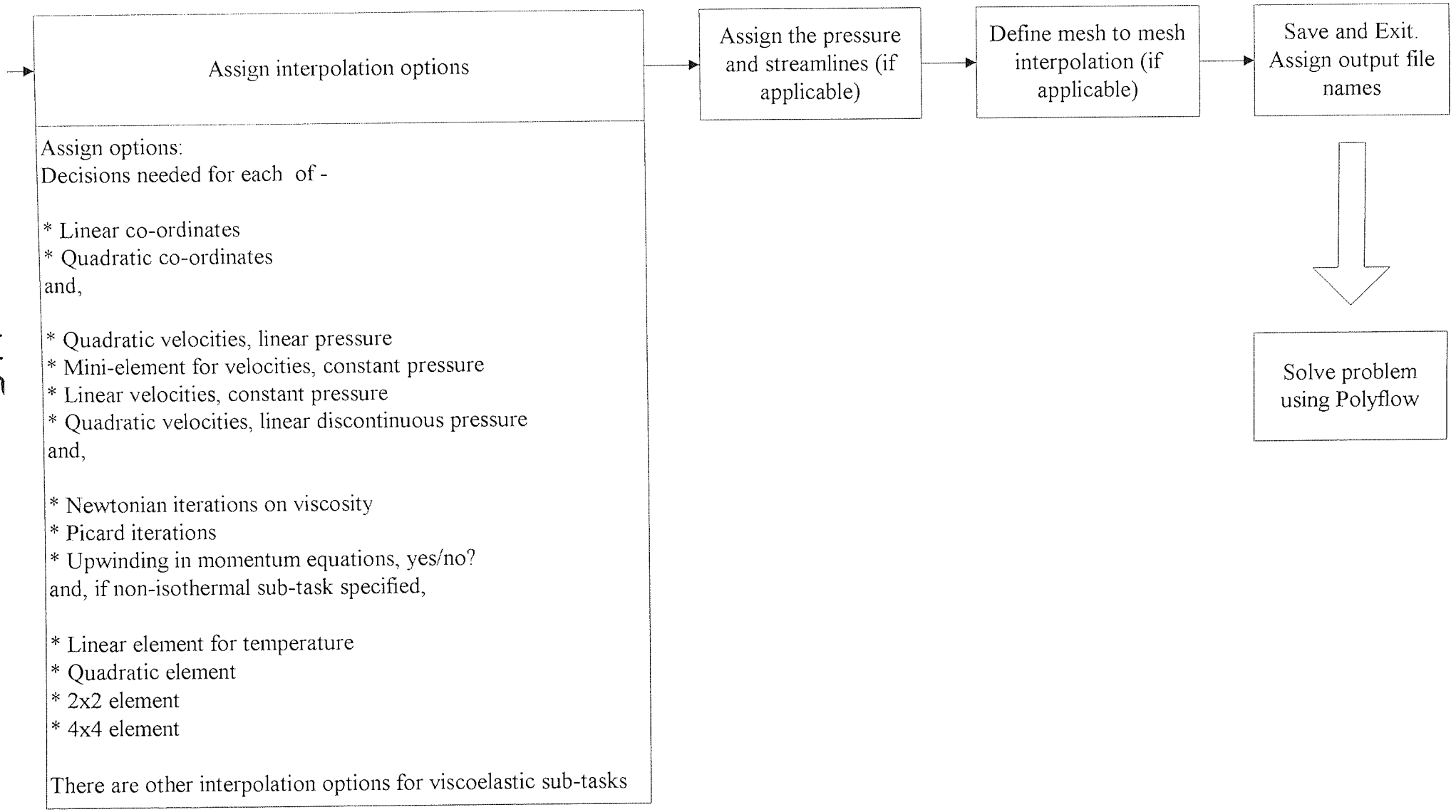

Figure 3-31:

Options for Assigning the Material Data Within Polydata

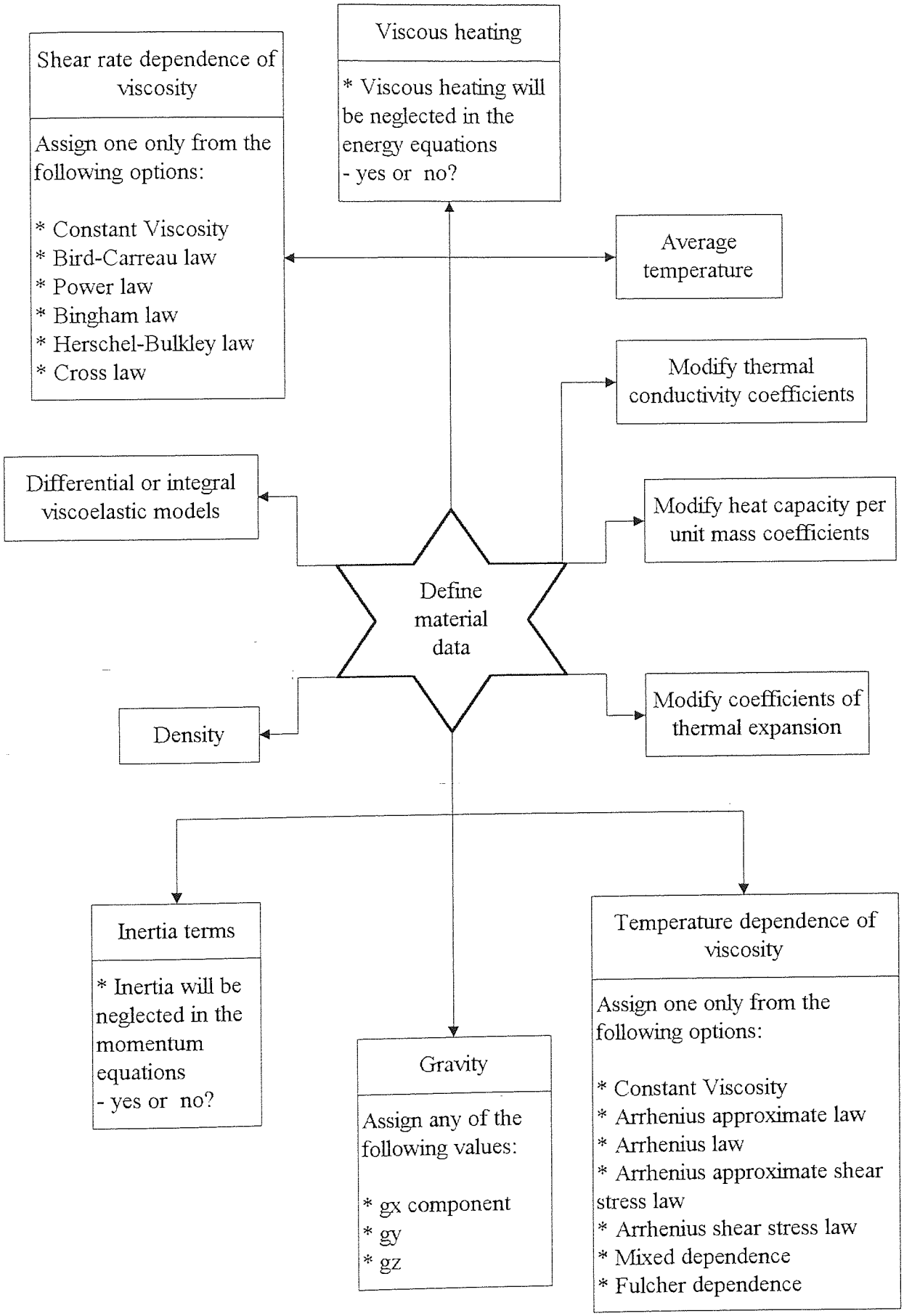

Figure 3-32:

Options for Assigning the Flow Boundary Conditions Within Polydata

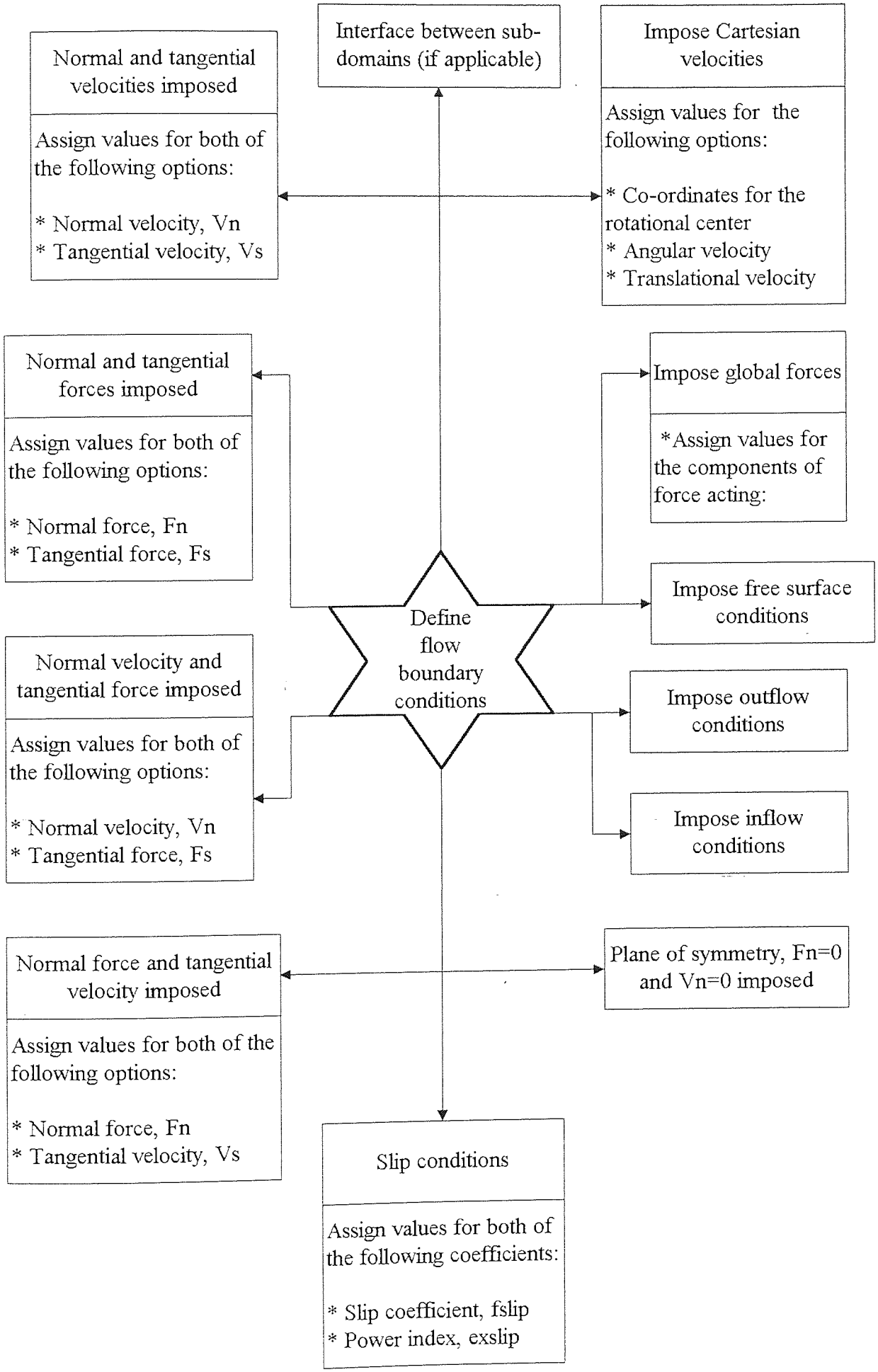

introduced into the scheme too quickly. There are facilities within Polydata to take automatic corrective action if this happens. However, if the problem fails to converge at all, then other evolution schemes may need to be considered.

3.3.1.1.3 Time-dependent problem

A time-dependence problem involves one or more time derivatives in the governing equations of flow. The time dependence scheme is very similar to the evolution scheme, with the material properties and/or boundaries depending on an incrementation of time. The crucial difference between the two techniques is that time-dependent solutions are controlled not only by the convergence criteria, but also by the accuracy of the time-integration method being used. The different methods used to integrate the equations containing time derivatives, are given as follows;

- Crank-Nicolson.
- Galerkin.
- Implicit Euler.

Each method has a different degree of precision. The precision used in the Implicit Euler technique is Δt, whereas the precision obtainable using the Crank-Nicolson technique is Δt^2. A more detailed discussion for the use of the different time-dependent schemes will be given for the channel flow results of the single-flighted, CICo-TSE conveying screw element section in Chapter 6.

3.3.1.1.4 Rigid rotation

Rigid rotation is a simple procedure for solving rotational problems involving symmetry, such as that shown in Figure 3-33, which illustrates the rotation of fluid within a cylindrical vessel using a fixed rotating agitator. Due to the symmetry, the problem is solved by keeping the agitator stationary and rotating the outer vessel instead. The flow field obtained is thus taken from the perspective of an observer positioned centrally on the agitator. The rigid rotation problem assumes steady state conditions, with no time derivatives.

3.3.1.2 Definition of a sub-task

Once a task has been assigned for the flow problem as a whole, then the designation of sub-tasks within this task may be chosen. All the different sub-tasks contained within Polydata version 3.4.6 are given as follows. This list of sub-tasks constitutes most of what may be classified as Polyflow's solver capabilities, so as a consequence, each sub-task will be

Figure 3-33:

Structure Suitable for the Rigid Rotation Problem.

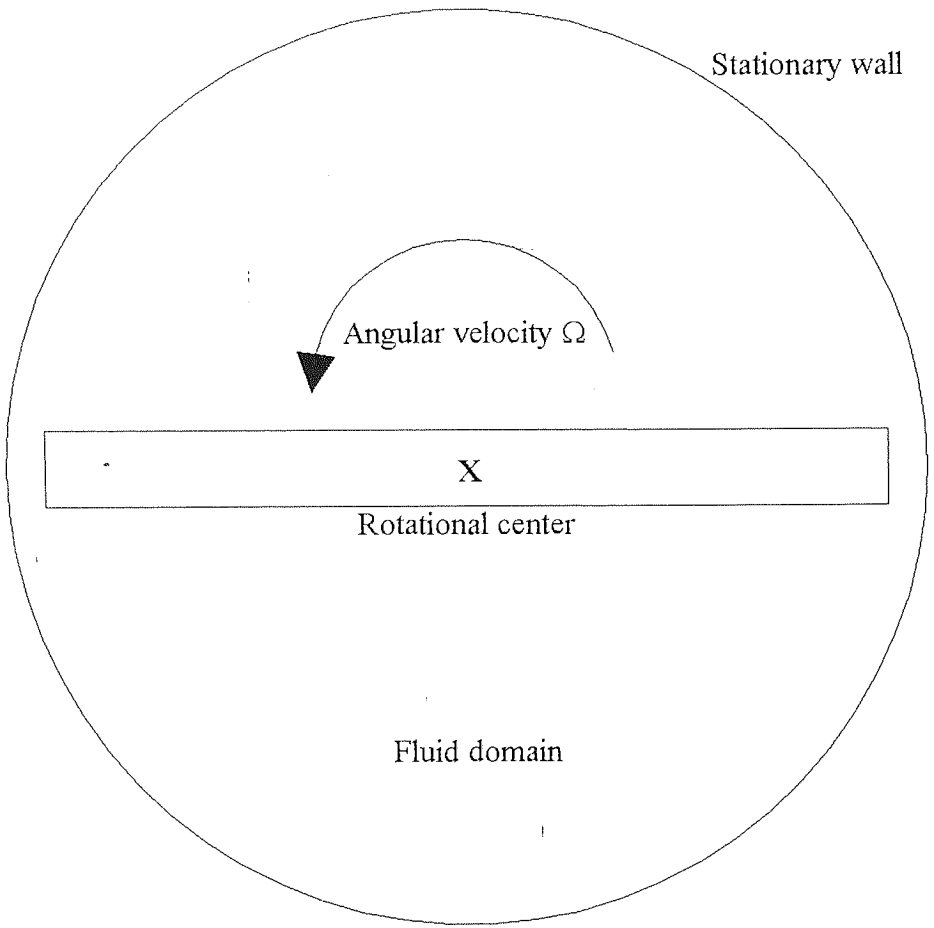

Due to the symmetry of the construction, rigid rotation solves the problem by keeping the central agitator stationary and rotating the outer boundary instead.
i.e. the resulting fluid motion seen would be that as observed from a viewer at the rotational center

explained further within the description of the Polyflow sections;

- Generalised Newtonian isothermal flow problem (see Section 3.3.2.1 - Generalised Newtonian flow problems).
- Generalised Newtonian non-isothermal (see Section 3.3.2.1).
- Heat conduction problem (see Section 3.3.2.1).
- Differential viscoelastic isothermal flow problem (see Section 3.3.2.2- Viscoelastic problems of the differential and integral type).
- Differential viscoelastic non-isothermal (see Section 3.3.2.2).
- Integral viscoelastic isothermal flow problem (see Section 3.3.2.2).
- Integral viscoelastic non-isothermal (see Section 3.3.2.2).
- Postprocessor (as many as required may be assigned - see Section 3.3.2.4 - Post-processing sub-tasks).
- Darcy isothermal flow problem (see Section 3.3.2.5 - Darcy flow problem).
- Darcy non-isothermal (see Section 3.3.2.5).
- Slightly compressible flow problem.
- Mass transfer problem (see Section 3.3.2.6 - Gas flow and mass transfer).
- Potential Problem.
- Film model: Generalised Newtonian isothermal (see Section 3.3.2.7 - Film casting).
- Film model: Generalised Newtonian non-isothermal (see Section 3.3.2.7).
- Film model: Viscoelastic isothermal (see Section 3.3.2.7).
- Thickness for film (see Section 3.3.2.7).
- Transport of species.
- Closure.

3.3.1.3 Definition of material properties and temperature dependence

The different types of material rheology that may be assigned within Polydata, are listed as follows. Again the important rheological models will be explained in further detail within the Polyflow description sections.

- Shear rate dependence of viscosity model for fluid (see Section 3.3.2.1 - Generalised Newtonian flow problems).
- Differential viscoelastic model (see Section 3.3.2.2 - Viscoelastic problems of the differential and integral type).
- Integral viscoelastic model (see Section 3.3.2.2).
- Density (default 0).

- Inertia terms (option: to be or not to be included into momentum equations).
- Gravity (default is 0 for all components).

Components of gravity may be specified, such that a volumetric force may be taken into account in the momentum equation.

$$g = gx + gy + gz \tag{3-1}$$

If the problem is non-isothermal, then Polydata allows the user to specify the following options thermal properties of a fluid;

- Temperature dependence of viscosity model for fluid (see Section 3.3.2.1 - Generalised Newtonian flow problems).
- Coefficient of thermal expansion - Boussinesq's approximation (default 0).

$$\rho_T = \rho_\beta(1 - \beta(T-T_o) \tag{3-2}$$

- Thermal conductivity (default is 0 for all components).

  Used to modify the value of k(T) in the energy equation

$$k(T) = a + bT + cT^2 + dT^3 \tag{3-3}$$

- Heat capacity per unit mass (default is 0 for all components).

  Used to modify the value of Cp(T) in the energy equation

$$Cp(T) = a + bT + cT^2 + dT^3 \tag{3-4}$$

- Viscous heating (option: to be or not to be included into energy equations).
- Average temperature value (initial temperature calculation point - default 0).
- Heat source per unit volume.

3.3.1.4 Definition of boundary conditions

For each boundary specified within either Polymesh 2D/3D or ICEM-Polycem, the information specified, as to the type of boundary assigned, is lost once the mesh file is imported into Polydata. For each discrete boundary specified within the pre-processor, its physical assignment must be chosen from one of the following list (the default assignment for each boundary present is that $v_n = v_s = 0$);

- Interface conditions.
- Normal and tangential velocities imposed, v_n and v_s (for 3D flows, $v_s = 0$).
- Normal and tangential forces imposed, f_n and f_s (for 3D flows, $f_s = 0$).
- Normal velocity and tangential force imposed, v_n and f_s (for 3D flows, $f_s = 0$).
- Normal force and tangential velocities imposed, f_n and v_s (for 3D flows, $v_s = 0$).
- Slip conditions.

  For slip on a boundary, f_s and v_n are specified such that

$$v_n = 0 \tag{3-5}$$

and,

$$f_s = -F_{slip}\, v_s\, |v_s|^{Exslip} \tag{3-6}$$

To specify a slip force (which will act against the direction of fluid velocity), values of F_{slip} and Ex_{slip} may be specified ($Ex_{slip} < 0$ will make the problem non-linear). If $f_s = 0$, then at the boundary there will be no opposition to fluid velocity, thus full slip ($v_s = v_s$). A non-slip boundary would result for an infinitely large value of f_s, such that $v_s = 0$.

- Plane of symmetry, $f_n = v_n = 0$.
- Inlet - a volumetric or mass flow rate may be specified.
- Outlet.

  A pressure value within the domain may be specified for the problem, depending on the choice from the following outlet conditions.

  - zero normal force imposed at inlet, such that $f_n = v_n = 0$. This choice of condition includes a pressure term.
  - zero normal derivative on velocity imposed. This condition excludes a pressure term such that at a point within the domain, the pressure value may be specified.

- Free surface (see Section 3.3.2.3 - Interface and free surface problems).
- Global force imposed.
- Cartesian velocities imposed, v_x, v_y and v_z.

A rotating boundary may be specified in terms of either Cartesian or cylindrical co-ordinates. This rotating boundary is expressed in terms of its rotational (co-ordinate centre and angular velocity) and translational components.

If the problem is a non-isothermal problem, then the temperature of each boundary may be assigned in addition.

3.3.1.5 Interpolation

The interpolation menu within Polydata allows the user to specify different properties for the quadratic or triangular finite elements contained within the mesh. For example, certain non-isothermal problems may need a greater assignment of computational nodes per finite element than an isothermal problem would on the same mesh. The different options within the menu are as follows;

- Linear co-ordinates.
- Quadratic co-ordinates.

Isothermal options.

- Linear velocities, constant pressure.
- Mini-element for velocities, constant pressure (recommended for all 3D flows).
- Quadratic velocities, linear pressure.
- Quadratic velocities, linear discontinuous pressure.

The last two options allow the most number of nodes that may be assigned, but these options are expensive in terms of CPU time. Examples of how a quadrilateral finite element would be represented by the above options, is given in Figure 3-34.

- Newtonian iterations on viscosity.
- Picard iterations on viscosity.

A Newtonian iteration scheme would take typically 4 to 5 iterations to converge on a well-defined problem (for a convergence criteria of $1x10^{-3}$). The same problem using a Picard scheme would take in excess of 20 iterations to converge. The reason why a Picard scheme is preferable for some problems though, especially those with a low value of power law index, is because the disc of convergence for a Newtonian scheme is quite small.

- Upwinding in momentum equations, yes or no?

Temperature options.

- Linear element for temperature
- Quadratic element for temperature
- 2x2 element for temperature

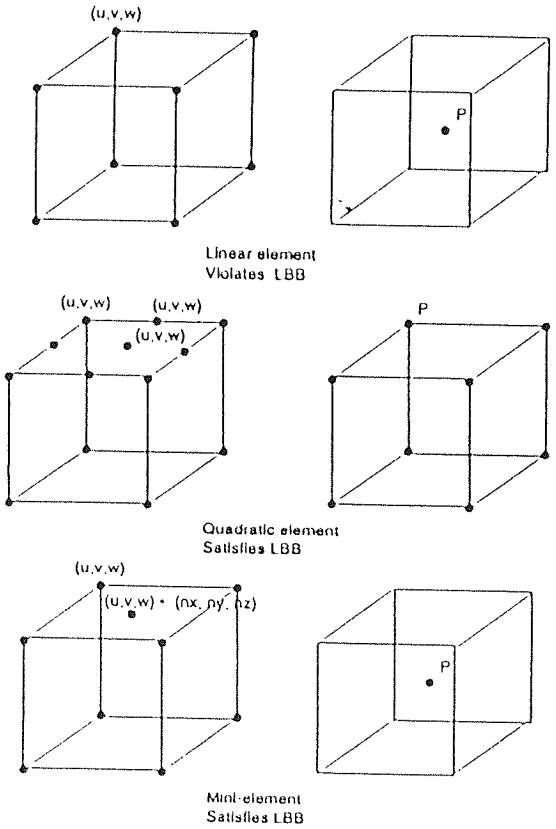

Figure 3-34:

Examples of the Quadrilateral Finite Elements Assigned for the Different Interpolation Options.

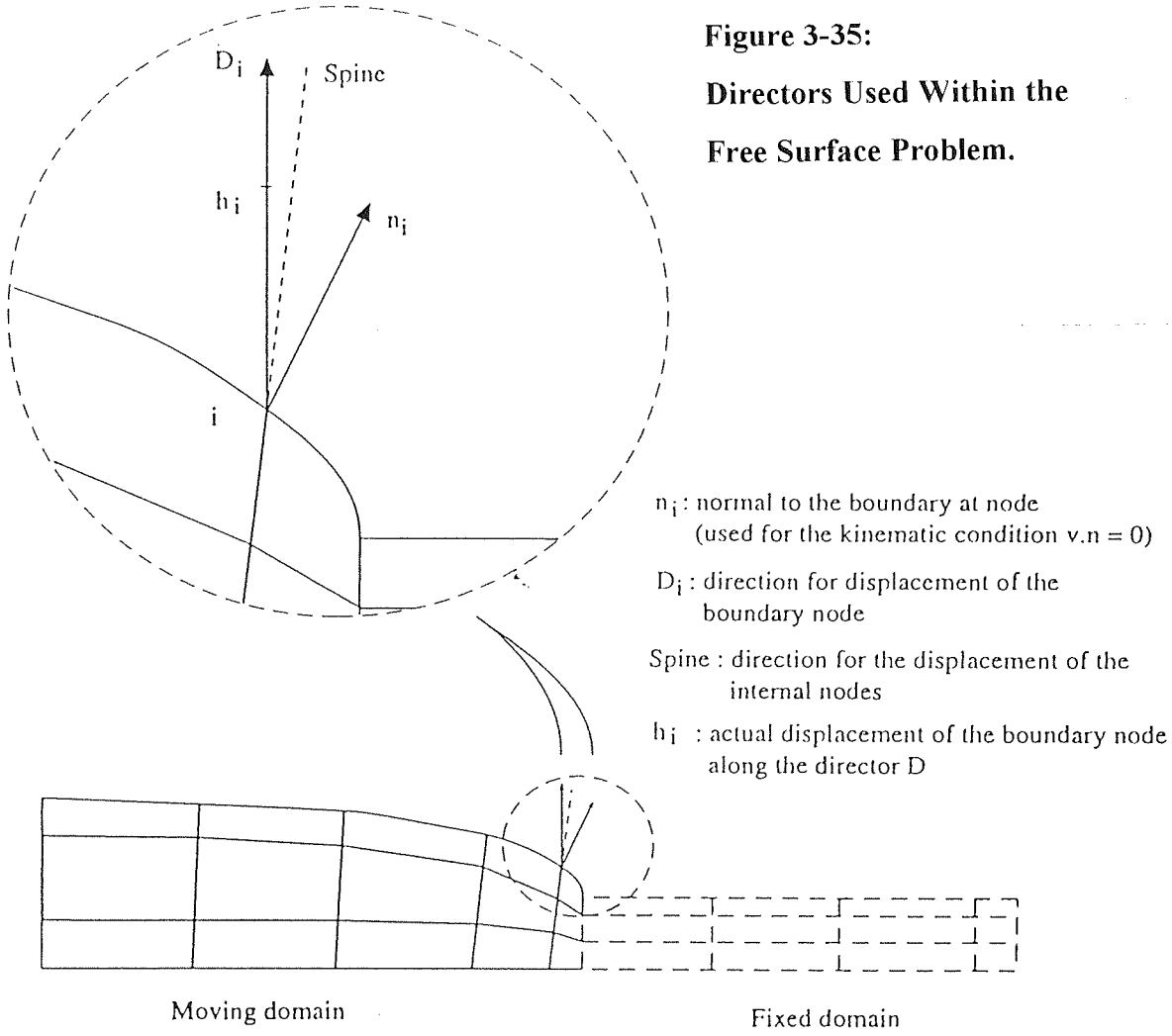

Figure 3-35:

Directors Used Within the Free Surface Problem.

n_i : normal to the boundary at node (used for the kinematic condition v.n = 0)

D_i : direction for displacement of the boundary node

Spine : direction for the displacement of the internal nodes

h_i : actual displacement of the boundary node along the director D

Free surface: direction of displacement (D), spine, and normal direction (n).

- 4x4 element for temperature

A parameter called the Peclet number needs to be taken into account when solving non-isothermal problems and the Peclet number is defined as follows.

$$Pe = \frac{\rho C_p V L}{k} \qquad (3\text{-}7)$$

The assignment of interpolation option for non-isothermal flows depends upon the value of Pe within the simulation. For example, the linear or quadratic element would be option of choice for a low value of Pe, whereas for moderate or high values of Pe, a 2x2 or 4x4 element will need to be considered.

Viscoelastic options.

- 4x4 SU elements for stresses
- 4x4 SUPG element for stresses
- EVSS for stresses
- EVSS SU for stresses
- EVSS SUPG for stresses

The choice of interpolation for a viscoelastic material from the above options, is dependent on whether the material under investigation is of the differential or integral type and whether the problem involves temperature or not.

3.3.1.6 Mesh to mesh interpolation

Mesh to mesh interpolation (MMI) is a procedure whereby results from a mesh, may be interpolated to a different mesh, for use as initial conditions. Unfortunately, this procedure is not suited to non-symmetrical rotating boundary problems, such as the simulation of flow within the CICo-TSE or internal mixer, because the geometries involved are too complex. The preparation and execution of MMI in Polyflow version 3.4.6.1 is totally manual and as such is very long winded to warrant sensible use on problems involving more than two geometries. It would be far more advantageous to use new techniques, such as the automatic sliding mesh facility (discussed in Chapter 4) for interpolation of results between different meshes.

3.3.2 Solver program: Polyflow (version 3.4.6.1)

Polyflow executes the data file (.dat) problem generated by Polydata, on the mesh file (.msh) generated by the pre-processor. Polyflow uses the finite element method (FEM) for discretising the continuous problem posed by the governing flow equations. Different finite

element solution techniques will be needed for the different flow problems posed. For example, an isothermal problem will involve the momentum equation in its reduced form (constant density) and the exclusion of the energy equation (constant temperature). For a non-isothermal problem however, the energy equation will need to be taken into account and so a different integration scheme will be needed to solve the flow problem fully. This is also true for problems involving time derivatives and viscoelastic flows. The different capabilities of Polyflow and the equations used for solving the different types of flow problem, are given in the following sections.

3.3.2.1 Generalised Newtonian flow problems

If Ω denotes the flow domain, then to solve the flow for both the isothermal and non-isothermal generalised Newtonian flow problems, the following governing equations are solved simultaneously over Ω.

- Full momentum equation.

$$\nabla.[-p + \mathbf{T}] + \rho_o[1 - \beta(T - T_o)]\mathbf{f} = \rho_o \frac{Dv}{Dt} \tag{3-8}$$

where,

$$\frac{Dv}{Dt} = \frac{\partial v}{\partial t} + \mathbf{v}.\nabla\mathbf{v} \tag{3-9}$$

and in rectangular co-ordinates,

$$\nabla = \delta_i \frac{\partial}{\partial x_i} + \delta_j \frac{\partial}{\partial y_j} + \delta_k \frac{\partial}{\partial z_k} \tag{3-10}$$

For isothermal conditions, where the density is constant, Equation (3-8) reduces to

$$\nabla.[-p + \mathbf{T}] + \rho\mathbf{f} = \rho \frac{Dv}{Dt} \tag{3-11}$$

and for steady state conditions (no time derivatives), Equation (3-11) reduces to

$$\nabla.[-p + \mathbf{T}] + \rho \mathbf{f} = \rho \mathbf{v}.\nabla \mathbf{v} \qquad (3\text{-}12)$$

- Incompressibility equation

$$\nabla.\mathbf{v} = 0 \qquad (3\text{-}13)$$

- Energy equation (for non-isothermal flow problems)

$$\rho C(T)\frac{DT}{Dt} = \mathbf{T}:\nabla \mathbf{v} + r + \nabla.(k(T)\nabla T) \qquad (3\text{-}14)$$

which reduces to the following equation for heat conduction (i.e. where the viscous heating term involving fluid motion is omitted).

$$\rho C(T)\frac{\partial T}{\partial t} = r + \nabla.(k(T)\nabla T) \qquad (3\text{-}15)$$

The $(k(T)\nabla T)$ term in Equation (3-15) is given by the heat flux $\mathbf{q}$

$$\mathbf{q} = -k(T)\nabla T \qquad (3\text{-}16)$$

and for problems where temperature is variable upon a boundary, the heat flux may be calculated as the sum of the constant flux, the convective flux and the radiative flux.

$$q = q_c + \text{alpha}*[T - T_{\text{alpha}}] + \sigma[(T + T_o)^4 - (T_\sigma + T_o)^4] \qquad (3\text{-}17)$$

For a generalised Newtonian fluid, the inelastic stress tensor $\mathbf{T}$ is given by the following equation;

$$\mathbf{T} = 2\eta(\dot{\gamma}, T)\mathbf{d} \qquad (3\text{-}18)$$

which reduces to the following equation for isothermal conditions;

$$\mathbf{T} = 2\eta(\dot{\gamma})\mathbf{d} \qquad (3\text{-}19)$$

For Newtonian fluids possessing a constant viscosity, Equation (3-18) may be represented by just the following the equation;

$$\mathbf{T} = 2\eta\mathbf{d} \tag{3-20}$$

The local shear rate $\dot{\gamma}$, is given by the following equation;

$$\dot{\gamma} = \sqrt{2 \text{ tr } \mathbf{d}^2} \tag{3-21}$$

The rate of deformation tensor **d**, is given by;

$$\mathbf{d} = \tfrac{1}{2} (\nabla\mathbf{v} + \nabla\mathbf{v}^T) \tag{3-22}$$

such that in 2D, one of the components would be represented by the following equation;

$$\mathbf{d}_{ij} = \frac{1}{2}\left(\frac{\partial v_i}{\partial x_j} + \frac{\partial v_j}{\partial x_i}\right) \tag{3-23}$$

where i and j are directional vectors ($\nabla\mathbf{v}^T$ is thus the transpose of the vector).

The shear rate and temperature dependence of the viscosity possessed by Generalised Newtonian fluids, may be described using one of a variety of models solvable within Polyflow. If we represent $\eta(\dot{\gamma},T) \equiv F(\dot{\gamma})H(T)$, then Polyflow will solve for the following $F(\dot{\gamma})$ and H(T) viscosity models;

- Shear-rate dependence of viscosity models.

Newtonian $\qquad F(\dot{\gamma}) = \text{constant}$ (3-24)

Power law: $\qquad F(\dot{\gamma}) = K\dot{\gamma}^{n-1}$ (3-25)

Bird-Carreau, Bingham, Herschel-Bulkley and Cross models also exist within Polyflow and the shear rate dependency on viscosity equations are given within the manuals.

- Temperature dependence of viscosity models.

No temperature dependence: $\qquad H(T) = 1$ (3-26)

Approximate Arrehenius: $H(T) = \exp[-\alpha(T - T_\alpha)]$ (3-27)

Arrehenius: $$H(T) = \exp\left[\alpha\frac{1}{T} - \frac{1}{T_\alpha}\right]$$ (3-28)

Polyflow will also solve for a number of other temperature dependent viscosity models, which again are contained within the user manuals.

3.3.2.2 Viscoelastic problems of the differential and integral type

Polyflow possesses many models to describe viscoelasticity of both the differential and integral type. To describe the viscoelasticity for a viscous material, an extra stress term is added to the stress tensor equation, such that

$$\mathbf{T} = \mathbf{T}_1 + \mathbf{T}_2$$ (3-29)

The extra stress tensor $\mathbf{T}$ is thus decomposed into the viscoelastic contribution $\mathbf{T}_1$, and the purely viscous term $\mathbf{T}_2$. The purely viscous is described by the equation

$$\mathbf{T}_2 = 2\eta_2\mathbf{d}$$ (3-30)

where η_2 may be a function of $\dot{\gamma}$ and T. The viscoelastic component $\mathbf{T}_1$ may be described by a number of different models. The difference between the integral component and the differential component is the scheme by which they are calculated. Differential viscoelastic fluid models solve the stresses, velocity and pressure variables simultaneously in what is termed as a coupled scheme. With integral models, by knowing the initial velocity or temperature fields, the viscoelastic stress tensor $\mathbf{T}_1$ is first solved. The momentum and incompressibility equations are then subsequently updated and this is performed iteratively. This type of solver method is known as an uncoupled solution scheme.

The viscoelastic stress tensor $\mathbf{T}_1$, is of the following general form for the differential viscoelastic fluid;

$$\mathbf{A}(\mathbf{T}_1, \lambda_1).\mathbf{T}_1 + \lambda_1(\dot{\gamma}, T)\frac{\delta\mathbf{T}_1}{\delta t} = 2\eta_1(\dot{\gamma}, T)\mathbf{d}$$ (3-31)

where $\mathbf{A}$ represents the model-dependent tensor function. The different differential viscoelastic models that Polyflow possesses, that may represent the $\mathbf{A}$ term in the above

equation, are as follows;

- Upper-convected Maxwell
- Oldroyd-B
- White-Metzner
- Phan Thien-Tanner
- Giesekus

For the viscoelastic fluid of the integral type, the viscoelastic stress tensor $\mathbf{T}_1$, is of the following general form;

$$\mathbf{T}_1(t) = \int_{-\infty}^{t} M(t-t')\mathbf{S}_t(t')dt' \qquad (3\text{-}32)$$

where M(t-t') represents the different integral memory models. The different integral models that Polyflow possesses, representing the M(t-t') term in the above equation, are listed as follows;

- Lodge-Maxwell
- Doi-Edwards
- K.B.K.Z

3.3.2.3 Interface and free surface problems (co-extrusion and die swell)

For a significant number of commercial viscous processing problems, the following situations may arise;

- Viscous fluid will come into contact with other viscous fluid(s), which may be of different rheology (co-extrusion process).
- A viscous fluid will possess free surfaces (die swell problem).

The final positions of either the fluid interfaces or free surface boundaries are *a priori* unknown and both of these problem types are solvable within Polyflow. They are solved by calculating a change in the structural property of the mesh representing the flow domain. This mesh may either possess a deforming interface between two (or more) viscous fluids, or the mesh as a whole may be deformed to accommodate the expanded flow domain of the viscous material swell. Co-extrusion of viscous material through a die will involve both of these

calculations being performed on the same mesh. These deformations of interface and mesh domain, introduces new degrees of freedom that are absent for fixed domain problems. In Polyflow, the displacement of nodal points within a deforming mesh is described in terms of spines and directors. The assignment of directors and spines within a typical die swell problem is shown in Figure 3-35. The different techniques for recalculating the new positions of nodal points within a mesh, so as to accommodate a movable interface or deforming mesh, are called the remeshing rules and those contained within Polyflow version 3.4.6 may be listed as follows;

- Method of spines

  Most basic remeshing technique and used for 2D problems only. The remeshing technique itself acts in only 1D and so is suitable for 2D die swell or 2D deforming interface problems.

- Eulidean distance remeshing (or the method of planes)

  Similar to the method of spines technique except that it may be used for 3D problems. The remeshing technique is only applicable in 2D and not in the direction of flow. The Eulidean distance remeshing technique however cannot handle large deformations.

- Thompson transformation

  Able to cope with complex deformations in both 2D and 3D and is not constrained. The Thompson transformation rule is quite complex to execute and can be quite expensive in terms of CPU time and memory requirements.

- Optimesh (minimum remeshing rule)

  This technique is the most accurate remeshing rule for extrusion and may be performed for 2D and 3D deformations. It is similar to the Thompson transformation in the that it is expensive in terms of CPU time, however it is far more robust. The technique works by relocating nodes within a mesh, so as to minimise the energy of deformation for that mesh.

- Thin shell remeshing

  Used for blow molding and thermoforming simulations.

For an interface between two fluids or for a free surface model, surface tension effects will have to be taken into account. The equation used to calculate the surface tension force, normal to the interface or free surface is given as follows;

$$f_n = -\frac{\sigma_s}{R} \qquad (3\text{-}33)$$

3.3.2.4 Post-processing sub-tasks

Once the main flow problem is solved for in terms of velocities and pressures profiles generated, then Polyflow, if requested, may calculate the following fluid flow properties;

- Local shear-rate
- Viscosity
- Rate of deformation tensor
- Inelastic stress tensor
- Viscous heating
- Total extra-stress tensor
- Residence time
- Tracking of material points
- Tracking of a material property
- Forces on slices

3.3.2.5 Darcy flow problem

The flow of a fluid through porous media, such as a sieve, is given by the following equation;

$$v = -\frac{1}{\eta}\mathbf{K}.\nabla p \qquad (3\text{-}34)$$

Polyflow allows the user to enter the Cartesian components of K.

3.3.2.6 Gas flow and mass transfer

The typical application of gas flow and mass transfer for which Polyflow may investigate, is in the simulation of flow within a chemical vapour deposition (CVD) reactor.

3.3.2.7 Film casting

Polyflow possesses the ability to simulate film casting or film stretching problems. For solving these problems, the assumption that the sheet is perfectly flat (no curvature) is made. In addition because the film thickness in relation to the sheet size is so small, the film casting model used within Polyflow is 2D only.

3.3.2.8 Glass furnace (bubbling) and electrical heating

Polyflow possesses many capabilities for the simulation of molten glass flow, with the incorporation of electrical heating if required. Due to the fact that glass is semi-transparent, internal radiation must be taken into account and the model used in 3D to modify the apparent conductivity of molten glass is the Roseland approximation. In addition, bubbling may be taken into account by describing globally, the action of these bubbles by modifying the momentum equation.

3.4 Post-processor software

3.4.1 Polyplot and 3Dcross (no version numbers)

Polyplot and 3Dcross are the original post-processor software programs with which the complete Polyflow package was first designed. As with Polymesh 2D and 3D, Polyplot and 3Dcross have been superseded by post-processor software designed by other companies, which in Polyflow S.A.'s case is the post-processor CFView-PF, as supplied by Numeca International S.A. [47].

Polyplot and 3Dcross are very basic post-processor programs, both of which possessing certain limitations. Similar to Polymesh 2D and 3D, Polyplot and 3Dcross are very simple to use. Polyplot is capable of viewing 2D structures only, whereas 3Dcross is a utility program used for generating 2D cross sections from 3D results. Once the desired 2D cross sections are generated using 3Dcross, they are viewed directly using Polyplot.

Polyplot requires two file types to operate (these are generated by specification via the relevant option in the Output menu within Polydata). These two file types are described as follows;

- .p2m files, which contain all mesh information on which the results are to be overlaid.
- .p2r files, which contain all results information.

Polyplot classifies its post-processing operations into different levels, a brief description of which is as follows;

- Contour lines

  Allows the user to draw lines, or block colour contours, to represent constant values for any variable calculated.

- Cross sectional and partial boundary curve

  Either a line between two points or a line along a boundary may be specified and an X-Y

profile of desired properties along the line chosen may be drawn.

- Vector plots

  Velocity vector plots may be represented, however their depiction may only be attained in black and white only.

- Particle history section

  This option allows the user to plot the pathline for a particle and thus calculate residence times. The pathline plotted will be "static" and pathlines are used to illustrate the path history taken. Polyplot has no facility for animating in real time, particle migration.

The major drawback for using Polyplot is the fact that any 2D cross-sections taken within a 3D domain are viewed as individual entities, instead of in-situ representations within the 3D flow domain as a whole (i.e. the rest of the 3D domain is not seen). This presents clear problems in appreciation of results when attempting to relate the 2D cross section to the rest of the flow domain, especially if the 3D domain is complex. In addition there are other drawbacks to using Polyplot, which are listed as follows;

- There is a lack of control for specifying colour contour plots. Colour contours are calculated automatically by Polyplot and these contours may be displayed containing either 13, 26 or 52 parameter intervals. These intervals will automatically be graded between the highest and lowest parameter values found within the .p2r file. In addition there is no control as to the specification of a cut-off value (such as specifying all values below a specific parameter value, for instance). If a results file has been generated containing localised areas of high parameter values, such as certain shear rate plots, then these small localised areas within the 2D domain will possess extremely large parameter gradients. If the bulk of the domain possesses parameter values that are significantly smaller than the values being experienced within these small localised areas, then the limitations of specifying only 13, 26 or 52 equally incremented solid contours, means that the bulk of the domain will be represented by just one single colour. Significant changes within the bulk of the domain, if they are much lower than the high localised parameter values, cannot be properly represented using Polyplot.
- Polyplot, due to bugs within the software, will sometimes display incorrect information as shown in Figure 3-36. There is no explanation for this other than being caused by bugs within the software. This is quite usual for any computer software as once found, corrections to the source can be made so as to ensure that the reported software fault is

Figure 3-36:

Example of a Polyplot Software Bug.

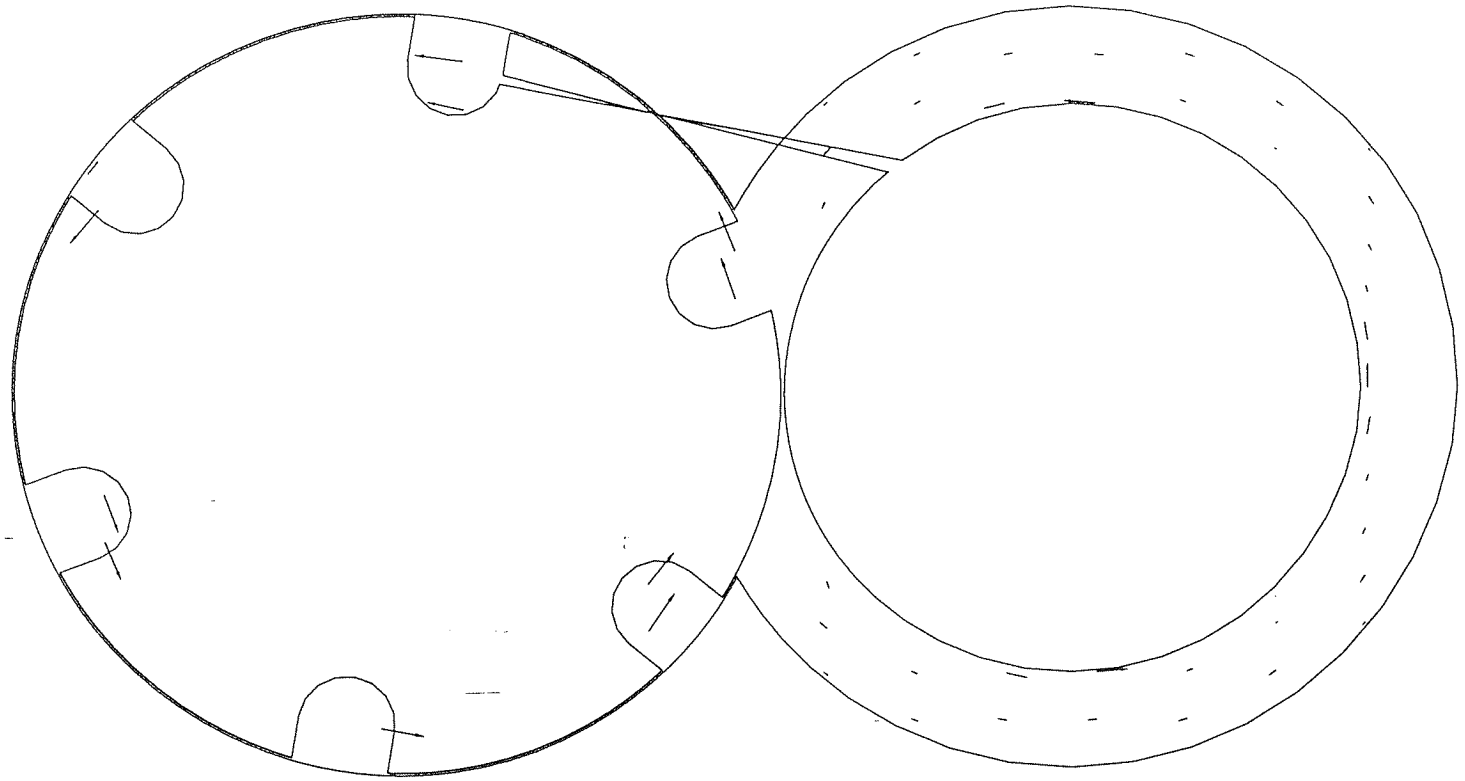

rectified. However, Polyflow S.A. no longer develop Polyplot, so these software faults will remain.

3.4.2 Overview of the post-processor CFView-PF (version 3.5)

CFView-PF is a powerful Object-Orientated post-processor, for viewing and manipulating results from unstructured finite element meshes. Many of the principles described in Section 3.4.1 - Polyplot and 3Dcross, such as the representation of velocities by vector arrows and the quantification of flow parameters by the use of contour plots, are still relevant when using CFView-PF. All operating procedures for the use of CFView-PF are given in the User's Manual [45]. As a consequence, there is very little to be gained by replicating these procedures of operation within this thesis. Instead a general description of CFView-PF will be given, including discussions as to certain differences between CFView-PF and Polyplot and 3Dcross.

For 2D flow problems, Polyplot may be used to view results directly and, as previously stated, all manipulations of results (such as magnification of a specific area within the flow domain) are performed via the keyboard. CFView-PF uses files in binary format, so any results generated from within Polyflow must first be converted, using automatic subroutines, before they may be viewed within CFView-PF. CFView-PF also views 2D results directly, however the important advantage of using CFView-PF rather than Polyplot, is the fact that manipulation of any parameter, such as orientation or magnification, is performed via the mouse. Important as this may be, it does not however totally render Polyplot redundant for the visualisation of 2D results. It is only when viewing results from 3D simulations that the dramatic difference between Polyplot and CFView-PF is fully realised. Polyplot does not view 3D results directly. Instead 2D cross sections are generated via 3Dcross and then these cross sections are viewed using Polyplot. Due to the reasons detailed in Section 3.4.1, for complex 3D domains this procedure is very inconvenient. CFView-PF works by a completely different concept. The 3D domain, in its entirety, is viewed directly using CFView-PF and all operations are performed via the concept of volume, surfaces, fields and view manipulations. Each of these four basic CFView-PF concepts are thus described as follows;

- Volume

  The 3D mesh is the computational volume wherein the flow problem specified by the User has been solved. This computational volume is obviously an object which may be manipulated within CFView-PF. Viewing, for example, all velocity vectors contained within the volume, would be nonsense as there would be too much information on display. Furthermore, this amount of information would thus be difficult to comprehend when

viewed on a flat 2D computer screen. Instead the User may, with ease, take 2D cross sections, plot particle paths through the domain or generate, between two specified points, Cartesian plots within the computational volume. The advantage of using CFView-PF in this way is the fact that any cross sections taken, may be viewed within the context of the remaining 3D flow domain. This has the obvious advantage of permitting the User to visualise the exact position(s) within the computational domain for which any cross section(s), for example, have been generated. This type of concept cannot be executed using Polyplot or 3Dcross.

- Surfaces

  The 2D cross sections referred to within the Volume description are called surfaces. In addition, the boundaries containing the 3D computational domain, such as the inlet, outlet or walls, are also referred to as surfaces within CFView-PF. These surfaces are geometrical objects used as supports for the display of flow variables calculated within the flow problem and they may be planar or curve-linear in shape.

- Fields

  All flow parameters calculated within the flow problem are called fields. These fields are either scalar, such as local shear rates or viscosity values, or they are vector fields, such as velocity profiles. CFView-PF will represent these fields as either isolines, contour shadings or, if appropriate, vectors and the support for the representation of these field variables are the generated surfaces within the computational volume.

- View

  CFView-PF possesses multi-functional viewer facilities. The User has the option to view the same computational flow domain either singly or as a multi-viewed domain representation, whereby different perspectives of the same volume may be viewed on-screen together. In addition, many different flow domains may be shown on screen in unison. CFView-PF also possesses the benefit of being able to represent Cartesian plot(s) on screen, alongside the flow domain from which the path of the plot(s) have been taken. The ease by which the manipulation of views may be performed interactively using the mouse, makes CFView-PF an extremely powerful tool for advanced post-processing.

Within this thesis, all post-processing results shown have been generated using CFView-PF and the exact nature of all post-processor representations will be described at the appropriate times. This, however, is with the exception of results for the time-dependant,

deforming interface problem, obtained for the 2D Y-Z cross section representing the single-flighted conveying screw elements, given in Chapter 6, which have been generated using Polyplot.

4 CFD APPROACH TO THE SIMULATION OF VISCOUS FLOW WITHIN THE VARIOUS ELEMENTS OF THE BETOL BTS40 CICo-TSE

4.1 Background

The governing equations of flow, as stated in Chapter 3, may be represented in different forms depending upon the flow problem to be solved. The solution of the flow problem for an incompressible, generalised Newtonian fluid (ignoring inertia terms and assuming low Reynolds number) necessitate solution of the following governing equations of flow.

- Momentum equation (steady state case, constant density):

$$-\nabla p + \nabla . \mathbf{T} + \rho \mathbf{f} = \rho \mathbf{v} . \nabla \mathbf{v} \tag{4-1}$$

where,

$$\rho \mathbf{v} . \nabla \mathbf{v} = 0 \tag{4-2}$$

for Reynolds number $R_e <<< 1$.

- Incompressibility equation:

$$\nabla . \mathbf{v} = 0 \tag{4-3}$$

- Generalised Newtonian rheology equation (isothermal conditions):

$$\mathbf{T} = 2\eta(\dot{\gamma})\mathbf{d} \tag{4-4}$$

For the CICo-TSE flow problem considered here, these are the appropriate forms of the equations which have been utilised. Substitution of Equation (4-4) into Equation (4-1) leads to the classical Navier-Stokes equations. These equations of flow, even when significantly simplified, may be solved analytically for only a very limited number of real life flow problems (for example, where $F(\dot{\gamma})$ is a constant and the fluid is flowing within a very simple flow domain geometry). When these governing equations of flow are modified for the solution of complicated flow problems, such as non-Newtonian or viscoelastic flows in non-isothermal environments, then these governing equations of flow become highly

non-linear and insoluble directly. Thus for the great majority of "real life" flow problems encountered, only approximate solutions using suitable numerical methods may be obtained. There are many numerical methods used for obtaining approximate solutions to the governing equations of flow and some of these were listed in Chapter 2. For this particular work, only the finite element method (FEM) will be used and it is this method which is described in the following section.

4.2 FEM solution technique

Let us consider a 2D fluid domain Ω, over which we wish to solve the flow problem. Within the limits of the flow problem (i.e. within the fluid boundaries) the problem is meshed and finite elements are created containing a finite number of nodal points. For a given function, F(x,y), representing properties such as velocity, pressure, shear rate, etc., approximate solutions are needed within each of the finite elements of the problem. The finite element approximation F^a of the function F, is defined by a polynomial interpolation within each finite element, based on the value of F at each nodal point. To illustrate this statement, consider a finite element within the flow domain Ω, contained in the ζ-ψ plane represented by the domain Ω_e, possessing four nodal points as shown in Figure 4-1. On this four noded finite element, we associate with its four numbered vertices, four shape functions, defined as follows;

$$\phi_1 = \frac{(1+\zeta)(1+\psi)}{4}, \phi_2 = \frac{(1-\zeta)(1+\psi)}{4}, \phi_3 = \frac{(1-\zeta)(1-\psi)}{4}, \phi_4 = \frac{(1+\zeta)(1-\psi)}{4} \quad (4\text{-}5 - 4\text{-}8)$$

As may be seen from Figure 4-1, the sign conventions of these four shape functions are easily verified by inspection. A one-to-one correspondence between the parent element in domain Ω and the finite element in domain Ω_e may be established.

$$x(\zeta,\psi) = \sum_{i=1}^{4} x_i \phi_i(\zeta,\psi) \quad (4\text{-}9)$$

$$y(\zeta,\psi) = \sum_{i=1}^{4} y_i \phi_i(\zeta,\psi) \quad (4\text{-}10)$$

By bi-linear interpolation, we may define an approximation F^a over the whole domain Ω for all nodal points i, to give the following generalised expression;

Figure 4-1:

Mapping of a Quadrilateral Finite Element to the Parent Domain.

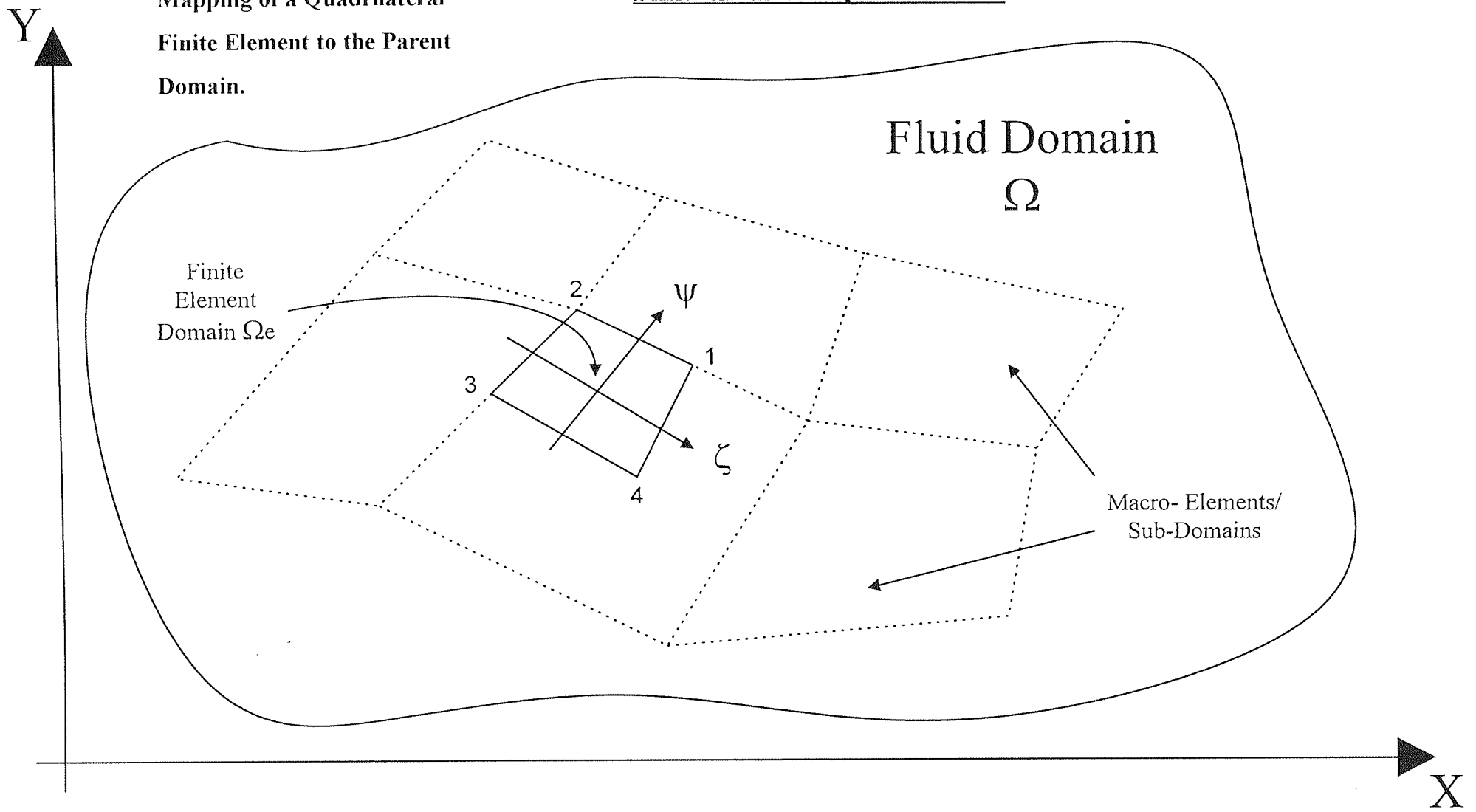

$$F^a(\mathbf{x}) = \sum_{i=1}^{N} F^i \phi_i(\mathbf{x}) \qquad (\mathbf{x}) \in \Omega \qquad (4\text{-}11)$$

The term N represents the number of nodal points within the mesh. In Equations (4-9) and (4-10), for the quadrilateral element domain Ω_e, $N = 4$ and for triangular domains, $N = 3$. Equation (4-11) can also be modified to incorporate a time-dependent function F(x,t). For a stationary mesh, the generalised form is represented as

$$F^a(\mathbf{x}, t) = \sum_{i=i}^{N} F^i(t) \phi_i(\mathbf{x}) \qquad (4\text{-}12)$$

and for a moving mesh it is thus;

$$F^a(\mathbf{x}, t) = \sum_{i=1}^{N} F^i(t) \phi_i(\mathbf{x}, \mathbf{x}_m(t)) \qquad (4\text{-}13)$$

The finite element shape functions (such as those represented in Equations (4-5) - (4-8)) are known at the outset, whilst the time-dependent nodal values of the approximated fields, e.g. velocity and pressure fields represented in their general form by Equations (4-11) - (4-13), must be determined. Discretisation is used to transform the original continuous problem (the governing partial differential equations) into a discrete problem (a finite number of ordinary equations for the nodal values). The various discretisation treatments needed to deal with the energy equation and the different types of viscous fluid (generalised Newtonian and viscoelastic) is well reported elsewhere [29, 48-50] and will not be reproduced here. The CFD package Polyflow solves the discretisation problem in its most general form (steady state conditions in a fully coupled manner), by using either a Picard or Newton iteration scheme. In addition, Polyflow possesses many further iterative schemes for solving decoupled, evolutive or time-dependent problems.

4.3 Solving the flow problem within the CICo-TSE model

There are a number of obstacles that need to be overcome when attempting to solve, computationally, the flow field problem within the different sets of modular elements contained within a particular CICo-TSE arrangement. These obstacles may be described as follows:

- CICo-TSE elements are of a complex geometry due to the intermesh of two modular

elements on opposing screw shafts, within the figure-of-eight barrel. As the elements rotate about their fixed axes, the figure-of-eight shape of the outer barrel dictates that any geometry frozen in time, will nearly always be of a non-symmetrical nature; this is an unfortunate hindrance to the computational solution and is absent from the SSE flow problem.

- Different CICo-TSE elements may be manipulated and arranged so as to exhibit different mixing mechanisms; this is essential for the selective and effective mixing of a wide variety of viscous, non-viscous or particulate components present within any intrinsic REX process. As a consequence of this, CICo-TSE elements come in a wide variety of complex designs to give the desired mixing mechanisms. As is discussed in Chapter 7, the 3D computational flow simulation of one full pair of mixing discs, due to the discs complex geometry, has, at the time of writing, only recently become soluble, though the capabilities of both Polyflow and computer hardware are constantly being improved. Investigating modifications in the design of the mixing discs or investigating other more complex CICo-TSE elements, may however, be constrained by the state of computational hardware and software capabilities at the time when the research is to be performed.
- Time-dependent flow boundaries exhibited as the CICo-TSE elements rotate about their fixed axes give rise to a very considerable problem. However by definition, processing within a CICo-TSE is of a steady state nature - it is essential that the melt properties of the end-product are the same at the beginning (after machine optimisation) as at the end time of any processing run. So by this definition, for viscous materials possessing no inertia, a snap shot of the process at a set position along the barrel, will be the same at all times during the process. Transient time-dependent boundaries do matter however, when certain fluid properties change with time though, for example, viscous heating of the melt. Steady state methods using sequential snap shot geometries can very accurately predict the flow of fluid within a CICo-TSE. In addition, instantaneous viscous heating values through a particular 3D CICo-TSE element's mixing cycle may also be predicted and this may be achieved for different rotational screw speeds. However, it is not possible to predict viscous heating accumulation for increasing screw speed over a specified time interval, for the same CICo-TSE element's mixing cycle.
- The imposition of high deformations and stresses through the different parts of the CICo-TSE can prove difficult if the flow parameter gradients are large. CICo-TSE machinery contain elements that possess regions where small clearances between each element and between the outer barrel wall exist. Any material within these regions will be subjected to disproportionately high levels of shear, compared to material contained within the rest of the flow domain. This high shear of material through small clearances is the

very method by which the trilobal elements successfully mix material by the mechanism of dispersion. However, solving this problem computationally can be subject to error if these high shear gradients are not considered carefully.

To overcome the problem of time-dependent flow boundaries as the CICo-TSE elements rotate about their fixed axes, incremental sequential geometries may be selected to represent parts of the process. To simulate polymer processing operations with laminar flow of highly viscous materials, the overall effect caused by rotation can be reasonably deduced from the results obtained separately for successive sequential geometries; this method assumes that inertia effects are ignored and that the Reynolds number is very small (10^{-3}). Viscous melts such as molten plastics, tend to possess low thermal conductivity values which consequently generate high Peclet numbers (given by Equation 3-7). However, the transient thermal flow fields within a CICo-TSE for a viscous fluid of low Reynolds number, is dominated by convection mechanisms [51]. As a consequence, the representation of non-isothermal viscous flow by incremental sequential geometries (i.e. conduction solutions) would not be an acceptable representation of the flow physics. Thus isothermal conditions only are considered within this thesis, so as to neglect the complex nature of the viscous heating problem. The pseudo steady-state/isothermal model is readily soluble because the mathematical problem has been greatly simplified by ignoring both time and temperature effects. The advantage of using this approach is that it may be applied to quite complicated 3D geometries that closely represent the fluid domain over which the flow problem needs to be solved. Careful optimisation of the distribution of nodal points over areas where large fluid parameter gradients are expected, for example, between the trilobal tips and the outer barrel where the flow domain is restricted, must be performed in order to minimise any possible errors in the flow calculation. This, however, may only effectively be achieved for 2D simulations, as increasing nodal points in 3D domains may be too expensive in terms of CPU times needed to solve the flow problem.

One of the first workers to publish CFD work on the simulation of flow within the screw elements of a CICo-TSE were Kaylon *et al.* in 1988 [52]. Their work, which was a combined experimental and computational approach, was for the investigation of flow of a power law fluid inside the double-flighted, conveying screw element sections of a CICo-TSE. The approach they utilised was to represent bulk fluid mixing by tracking a moving interface between two fluids contained within the screw flight volume. CICo-TSE conveying screw elements possess two important flow domains. The first domain is that representing channel flow, whilst the second represents the nip region. This nip region of a CICo-TSE conveying screw element section, is the location where the two screw elements from opposing screw

shafts intermesh and it is this intermesh of screw flights that forces the melt to re-orientate, when travelling from one screw element to the next. Kaylon *et al.* considered the flow of viscous fluid through each of these regions separately by representing each as a 2D cross section. The results from their simulations closely match those of their experimental trials.

The first workers to publish results on the simulation of flow through a specific TSE mixing zone - the kneading disc region of a CICo-TSE - taking into account the intermeshing region, were Szydlowski and White in 1988 [53]. Their approach was to simulate the flow of a non-Newtonian fluid, represented by a power law viscosity model using the Tadmor *et al.* flow analysis network (FAN) method [54] as a numerical solution. Essentially they treated the flow domain as being unwrapped, such that the outer barrel rotates relative to the kneading discs. The pseudo steady-state/isothermal technique described previously within this section and executed via the finite element method (FEM), is the most commonly used numerical technique in commercially available CFD packages, such as Polyflow. The application of the FEM is superior to the FAN method since it does not require the unwrapping of the flow domain and is not restricted to a lubrication approximation of the flow [51]. The pseudo steady-state/isothermal FEM approach has been successfully employed by Manas-Zloczower *et al.* on a number of occasions for simulating fluid flow within a wide variety of processing applications. The Banbury Mixer has been studied on numerous occasions by these workers, firstly by Cheng and Manas-Zloczower in 2D [8], Wong and Manas-Zloczower in 2D, considering a partially filled Banbury mixer [55] and by Yang and Manas-Zloczower in a 3D Banbury mixer [56]. Yang and Manas-Zloczower in 1991-92 [57-58] used the FEM package FIDAP on a CRAY Y-MP supercomputer to simulate the flow of a power law fluid through the kneading disc region of a CICo-TSE and the problems solved in their study, were for meshes containing up to approximately 20,000 nodal points. It is this pseudo steady-state/isothermal FEM approach that is utilised so far for our work at Aston and is thus detailed within this thesis. Some of our work at Aston using this method has already been published and these are for the simulation of the single-flighted conveying screw element sections and the trilobal element and mixing disc zones of the Betol BTS40 CICo-TSE respectively [59-68]. The problems solved in the study for Bruce *et al.* [67] were for meshes containing up to approximately 7,000 nodal points, with each flow problem taking up to 15 CRAY CPU hours to solve to suitable convergence criteria. As well as assuming isothermal, incompressible, steady state flow conditions, all these previous publications have assigned non-slip flow conditions for all fluid domain boundaries. In reality there will be some degree of slip between the fluid in contact with both the CICo-TSE elements and the outer barrel wall. Harries and Bruce [66] extended the non-slip model on 2D mixing zone geometries, to include differing values of slipping force between the viscous material and the outer barrel

wall; the possible effects on mixing behaviour were thus observed. All work given in our publications will be fully described in both this chapter and in Chapters 6-8. Other processing devices simulated using the pseudo steady-state/isothermal method include the flow field analysis of an intermeshing counter-rotating twin screw extruder [69-71] and of a cavity transfer mixer (CTM), published by Wang and Manas-Zloczower [72].

One of the simulation parameters that successive workers have progressively increased, is the size of the mesh on which the flow problem has been solved. Cheng and Manas-Zloczower [8] in 1989 solved eighteen different geometries containing between 420 to 476 nodal points per mesh, whereas for Wang and Manas-Zloczower [72] in 1994, the problem was solved for one mesh containing 25,551 nodal points. The increase of both complexity of mesh design and the number of mesh points that can be solved by commercial CFD programs, has increased significantly.

An interesting observation from many of the Manas-Zloczower *et al.* publications [72] is that for each of their simulation studies undertaken, all the average values for the flow field characteristics remain almost unchanged when going from one geometry to another. Thus the conclusion drawn from their publications is that it is possible to use the flow simulation results obtained for one single geometry only, for any process optimisation study. Unfortunately nothing is stated about process devices which exhibit periodic behaviour such as the trilobal elements, which are discussed in Chapter 8, so it is hoped that further research published by these workers may clarify this aspect.

Other workers have used the pseudo steady-state/isothermal method to solve the flow field problem for the kneading block region within a CICo-TSE. Kaylon *et al.* [73-74] have employed the 3D FEM, Van der Wal *et al.* [75] have used a modified FEM called the Penalty method described by Cuvelier *et al.* [76], whereas Kiani [51, 77] has utilised the CFD finite element program Nekton [78], which employs the spectral element method (SEM). Furthermore, it was Kiani *et al.* [51] who solved the transient thermal field problem for the Erdmenger disc rotating in an eccentric orbit. They achieved this by using a sliding or deforming grid to overcome the time dependent flow boundaries. However, simulation of the Erdmenger disc is greatly simplified by the fact that its geometry is symmetrical; this is not the case for a typical CICo-TSE configuration. One very important omission in many of the publications that utilise CFD, including those by Manas-Zloczower *et al.* and by Kiani *et al.*, is the lack of reporting any precision of results in terms of whether optimisation studies were carried out for number of nodal points used or for the number of iterations performed and convergence criteria employed. All work reported within this thesis will thus report all CFD precisions employed.

4.4 Description of the CICo-TSE geometries investigated within this research

4.4.1 General description of geometries

Simulations described in this thesis were performed on meshes representing the exact dimensions, including the clearances between the element tips and the barrel housing, for the following CICo-TSE element configurations pertaining to the Betol BTS40 CICo-TSE;

- Single-flighted conveying screw elements:
  2D Y-Z profile, used to represent screw channel flow ($\Delta X(time)$).
  3D half profile, used to represent nip region flow.

- Mixing disc and trilobal element mixing zones:
  2D X-Y profiles ($\Delta Z = 0$ as elements rotate).
  3D mixing zone profiles, containing differing numbers of element pairs.

All 2D meshes used within this research were constructed using the pre-processor Polymesh, whilst all 3D meshes were created using the advanced pre-processor, ICEM-Polycem. Every 2D mesh needed for this work had already been constructed using Polymesh before ICEM-Polycem had been purchased. As stated in Chapter 3, in the Author's opinion it is preferable to use ICEM-Polycem rather than Polymesh for the construction of all meshes. However, it was decided that little would be gained by repeating the 2D mesh constructions afresh using ICEM-Polycem.

For all 2D X-Y profiles representing the two mixing zones, the origin is taken to be the exact central point within the figure-of-eight outer barrel structure, as illustrated in Figure 4-2. The X-axis lies within the horizontal plane with positive X-values viewed to the right of the origin and negative values to the left. The Y-axis lies within the vertical plane with positive Y-values viewed above the origin and negative values below. All 2D Y-Z profiles used to represent screw channel flow possess a different origin position, which is shown in Figure 4-3. These profiles have been constructed and will be viewed such that the die end always lies to the right hand side of the 2D screw channel representation. For the 2D X-Y mixing zone representations only, the simulation results contained within this thesis are viewed looking from the feed end, down towards the die end.

For all 3D profiles representing the two mixing zones (i.e. those excluding the representation of the 3D single-flighted conveying screw element sections) the origin is determined at the same position within the X-Y plane as was defined in the 2D X-Y profiles, with its axial position lying within the inlet plane as shown in Figure 4-4. The Z-direction in 3D is taken to be the translational line that goes from the feed (inlet) to the die (outlet) end. In

Figure 4-2: **2D X-Y Simulations - Sign Convention**

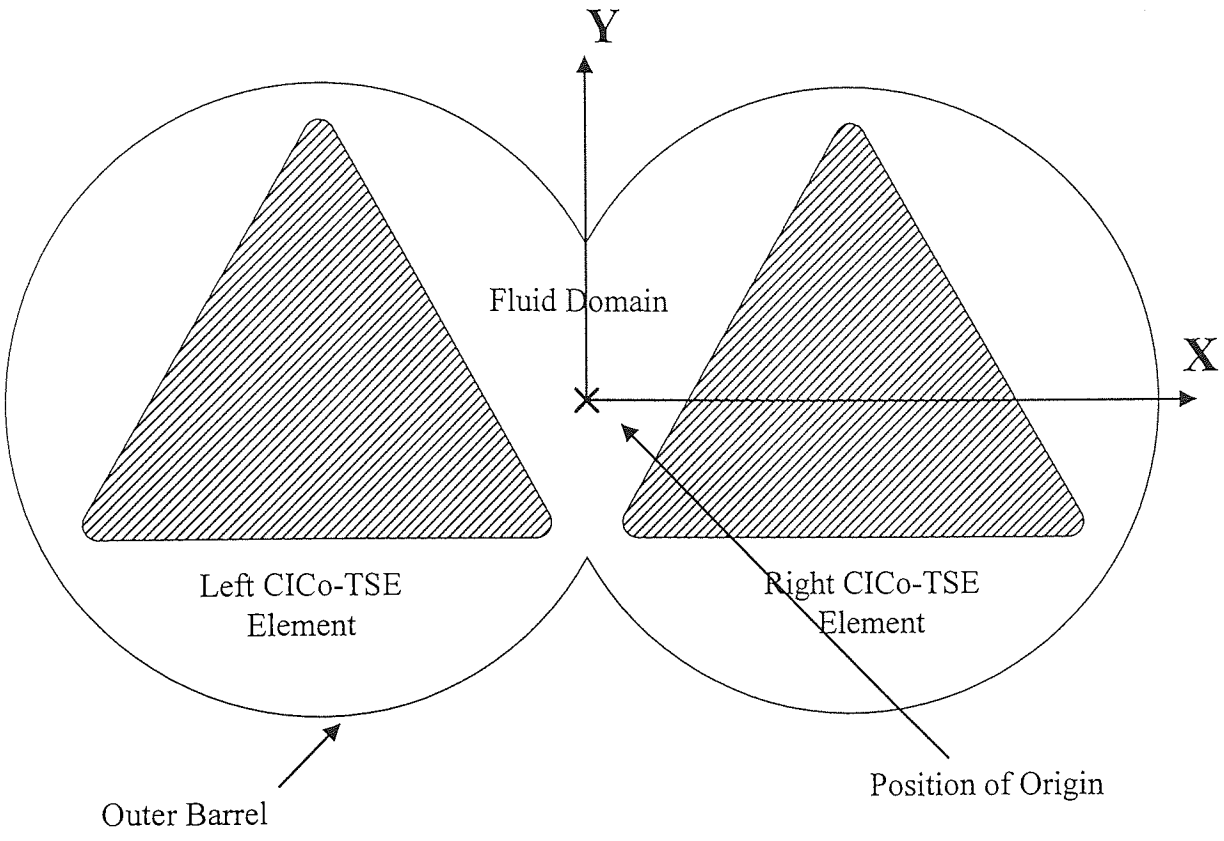

Figure 4-3: **2D Y-Z Simulations - Sign Convention**

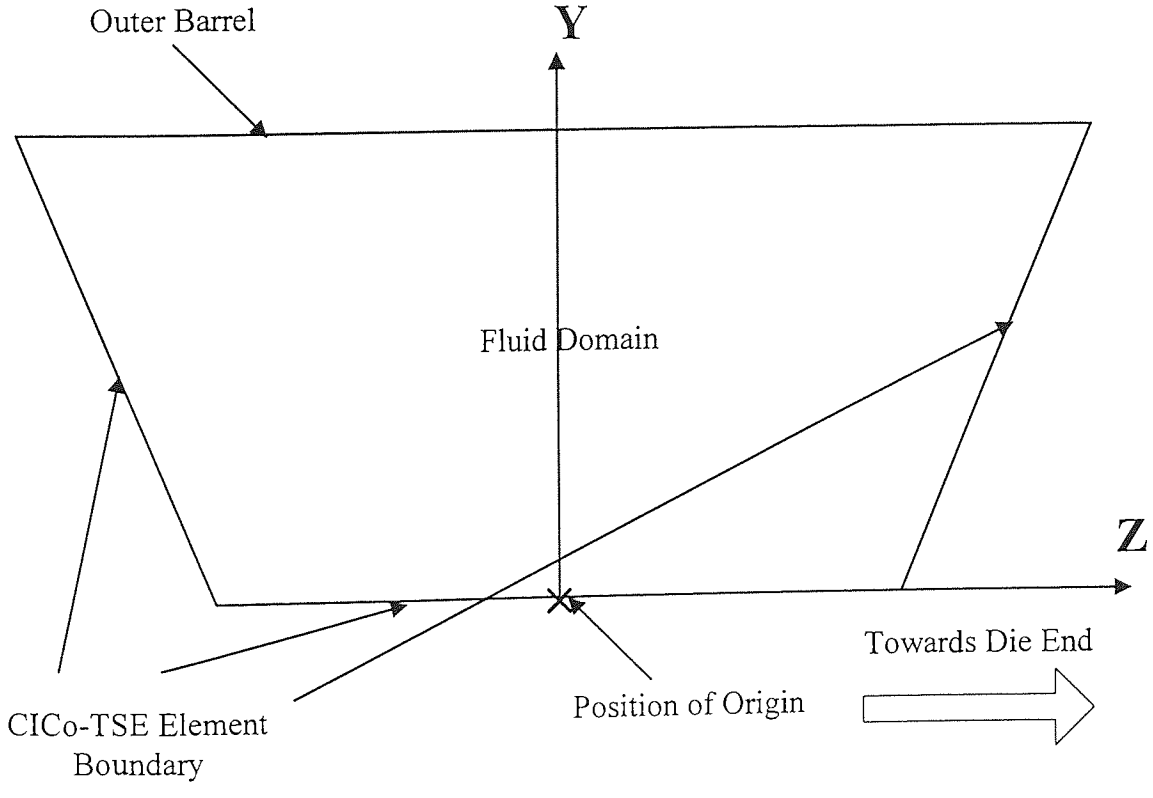

Figure 4-4:

3D Simulations - Sign Convention

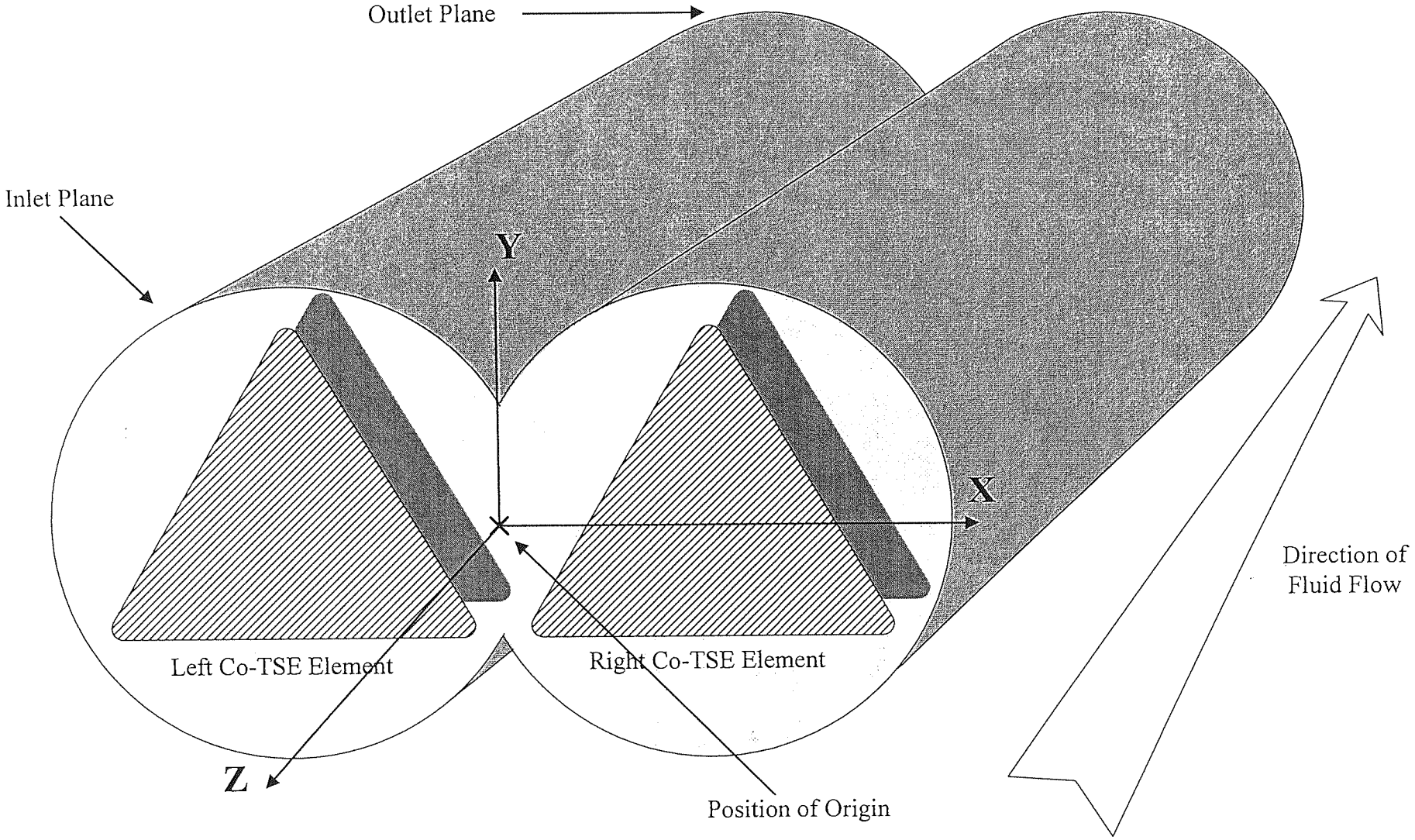

the construction of these 3D mixing zone meshes, ICEM-Polycem uses the convention that extrapolation of the Z-axis through the flow domain will always be negative. Thus if the origin lies within the inlet plane of a 3D mesh, then all co-ordinates contained within the flow domain will possess negative values of Z. This has the consequence of areas of back-mixing being represented by positive Z-velocity values, with velocity vectors visualised as coming out of the page towards the Reader. Construction of the 3D representations for the single-flighted, conveying screw element sections was different from that used for the construction of the two 3D mixing zones and special considerations had to be taken into account. Full description of the meshes constructed to represent the 3D single-flighted conveying screw element sections, are outlined in Chapter 6.

One of the benefits of using CFView-PF, as described in Chapter 3, is that cross sectional planes or spatial plots may be shown in three spatial directions in-situ within the 3D domain, using the CFView-PF default visualisation. This default is advantageous for comprehending the 3D domain as a whole as all three spatial directions are viewed in equal proportion, in relation to the flow domain. It is not, however, wholly appropriate for detailed or magnified representations. On many occasions it is advantageous to depict other aspects of the simulation by representation of the view in two spatial directions only (i.e. looking straight along a particular axis). Thus the default visualisation may be manipulated so as to illustrate a more detailed two directional visual orientation, along an axis. The convention used within this thesis for all 3D results, is to initially depict 2D cross sectional planes or spatial plots in-situ within the full 3D domain, so as to aid the clarity of visualisation, before magnified 2D representations along an axis or axes are shown. Full descriptions of all cross sectional orientations employed, will be given within the appropriate chapters.

4.4.2 Basic geometry of the Betol BTS40

The Betol BTS40 CICo-TSE possesses a figure-of-eight outer barrel consisting of two intermeshing chambers, each of 40.02 ± 0.01 mm diameter (20.01 mm average radius). The distance between the two chamber centres, called the centreline distance, is 35.01 mm. Using the co-ordinate system described previously, the centre of each CICo-TSE element will be at the position (-0.017505, 0, Z) for the left CICo-TSE element and at (0.017505, 0, Z) for the right element. From these properties a measure called the centreline ratio may be calculated, which is defined as follows;

$$\text{Centreline ratio, } \rho_c = \frac{\text{Centreline distance, } C_L}{\text{CICo} - \text{TSE Chamber radius, } R_S} \qquad (4\text{-}14)$$

For the Betol BTS40 CICo-TSE, this centreline ratio is calculated to be 1.7505 and for the BTS30, the value is 1.7000. This value of centreline ratio characterises the type of mixing that may be exhibited by the various CICo-TSE mixing elements and thus dictates whether the self wiping nature of a particular CICo-TSE element will be retained. In order to preserve the self wiping of material within a CICo-TSE, only specific mixing elements would be utilised depending on the value of the extruder's centreline ratio.

To describe fully the CICo-TSE geometries used within this research, each of the CICo-TSE elements examined are described separately at the beginning of each of their respective chapters. The following chapters will describe the following CICo-TSE elements;

- Chapter 6 - Single-flighted conveying screw elements.
- Chapter 7 - Staggered mixing disc zone.
- Chapter 8 - Kneading trilobal elements zone.

4.4.3 Fluid flow parameters and boundary conditions assigned

As there are many different parameters to investigate when considering the CICo-TSE simulation problem, it was decided that the same flow and material parameters would be applied to all three elements investigated within the Betol BTS40 CICo-TSE. Thus for all simulations performed within this research, results using the same rheological data are presented. Excluding the 2D time-dependent simulation of the conveying screw elements, the same boundary conditions and solution techniques were also employed. Most CICo-TSE processing is starve fed but for simplicity a filling factor of 1 was assumed for all meshes. This assumption is not that far removed from reality due to the fact that neither of the two mixing element zones, in the arrangements considered within this thesis, possess the ability to convey material, instead material progresses by pressure build-up. Unfortunately for the single-flighted conveying screw elements in both 2D and 3D, this assumption does not hold true as screw elements typically operate under partial fill conditions. However, as will be described in Chapter 6, combined experimental and computational investigation of partially full screw elements was beyond the scope of this research. Instead direct comparison between CFD and experimental results was achieved for full fill conveying screw element configurations only. Thus for all simulations performed during this research, the following flow parameters were assigned;

- The material was assumed to have idealised properties of polypropylene (PP). The ideal rheology of PP was represented using the power law viscosity model, given as follows.

$$\eta = K \dot{\gamma}^{n-1} \qquad (4\text{-}15)$$

where, $K = 4400\ N\ m^{-2}\ s^{0.5}$ and $n = 0.5$ [79]. It must be noted that the power law model does not predict the entire shear-rate/viscosity spectrum exhibited by a non-Newtonian fluid. For example, a typical flow curve for a non-Newtonian fluid is shown in Figure 4-5 and the power law region for this particular fluid would typically be between the approximate limits indicated (i.e. $10^{-3}\ s^{-1} \leq \dot{\gamma} \geq .10^{3}\ s^{-1}$). If the flow calculation encounters shear rate values outside of these limits, then their may be a risk of divergence or of inaccuracies. This is easily seen by inspection of Equation (4-15), because for very small values of $\dot{\gamma}$ the viscosity η will be extremely large and this may not be appropriate for the fluid under investigation (Figure 4-5 shows that the viscosity is at a plateau for both small and large values of shear rate). In this situation, the use of other viscosity laws may be more appropriate, such as using the Bingham law for low shear rate values or the Herschel-Bulkley law for large shear [30].

- The density of PP was taken to be $\rho = 800\ kg\ m^{-3}$, at a processing temperature of 200 °C [80].
- Each set of the mixing and conveying screw elements were set to rotate at 1 revolution per second (2π radian per second). This corresponds to a processing speed of 60 RPM.
- Non-slip boundary conditions were initially set for both the outer chamber walls and for the entire surface for each axial element. For 2D simulations involving the mixing discs and trilobal elements only, differing degrees of outer barrel slip were investigated.
- For all 3D simulations, Z-directional flow from the inlet to outlet was achieved by specifying a large arbitrary pressure profile between these two faces. The specification of a pressure profile for each 3D simulation was achieved by assigning a zero normal derivative on the velocity field at the outlet. i.e.

$$\frac{dv}{dp} = 0 \qquad (4\text{-}16)$$

This condition enables the assignment of one pressure value within the flow domain. The pressure value assigned for all 3D mixing zone simulations was $1x10^{5}$ Pa at the co-ordinate (0,0,0).

- An inlet volumetric flow rate of $5.20x10^{-7}\ m^{3}\ sec^{-1}$, corresponding to a feed rate of $25\ g\ min^{-1}$, was specified for all 3D meshes. Values of outlet volumetric flow rate were requested via Polyflow for correlation.

Figure 4-5:

Typical Flow Curve for a non-Newtonian Fluid, Showing the Power Law Shear Rate Range

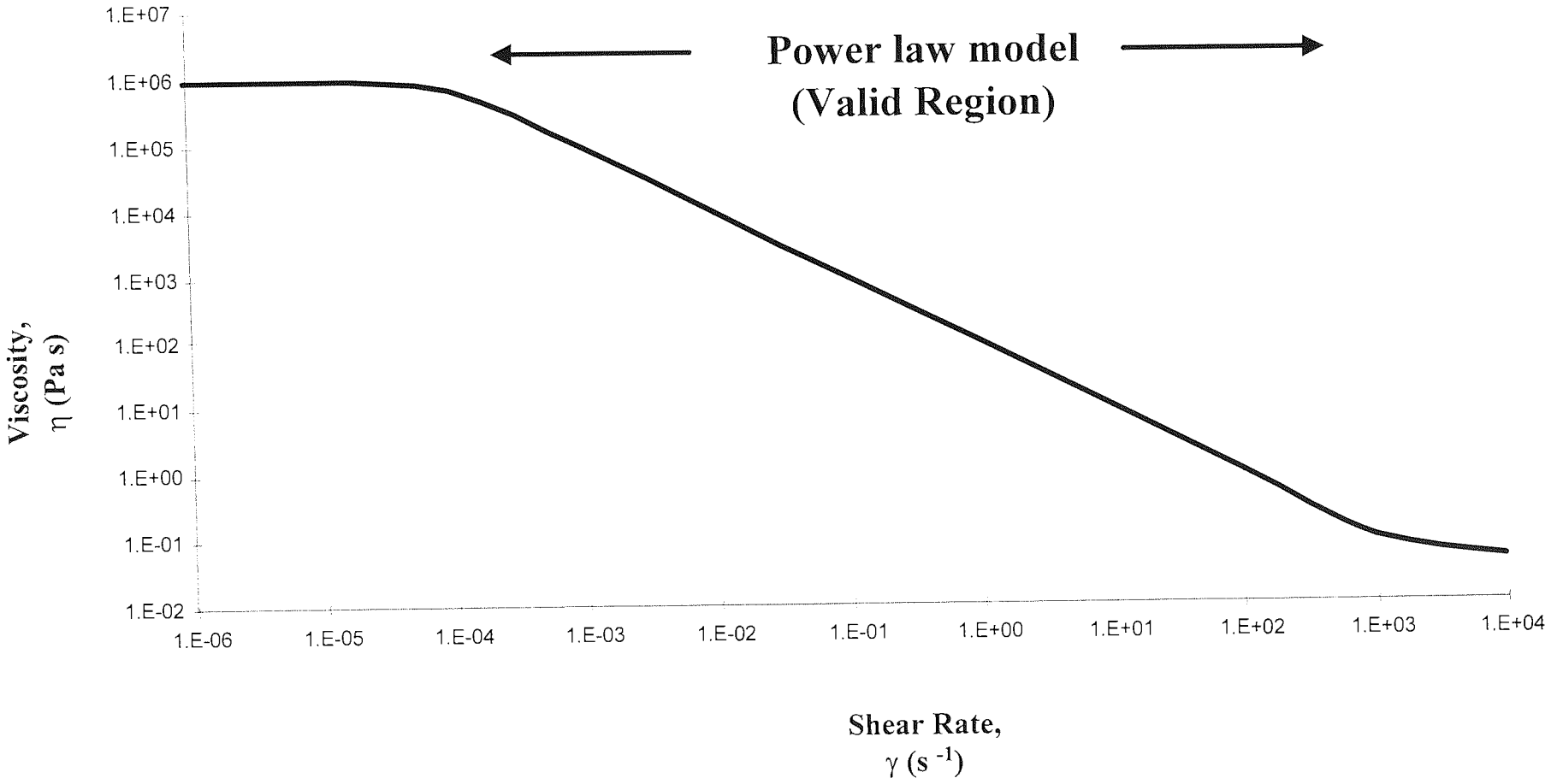

- A convergence criteria of 10^{-8} was specified for all simulations solved using the Silicon Graphics Indy workstation. Those simulations solved using the CRAY J90 supercomputer used less stringent convergence criteria and all values employed are given within the appropriate results section.
- For all simulations performed, the values for velocity, pressure, local shear rate, inelastic stress tensors and mixing efficiency (see below), as well as outlet volumetric flow rate for the appropriate 3D simulations, were calculated over each flow domain. In addition, average values were calculated for local shear rate, inelastic stress tensors and mixing efficiency and these average values were obtained by summing the product of the corresponding parameter in each element and the area of that element, as a fraction of the area of the entire flow domain. The calculation of these average flow parameter values was essential for the optimisation of each mesh used within this study. The procedure employed for mesh optimisation, involved the initial calculation of average values (and outlet volumetric flow rate for 3D simulations) for a particular mesh nodal distribution. The number of nodal points within this mesh was then increased and the average flow parameters re-calculated. This procedure was repeated until no significant change in average parameter values (and volumetric flow rate for 3D simulations) were obtained.

In order to quantify the elongational and rotational flow components and thus to define the character of the flow field, a parameter λ known as the mixing efficiency [58] was calculated for each simulation using the following equation;

$$\lambda = \frac{|d|}{|d|+|w|} \tag{4-17}$$

where $|d|$ represents the magnitude of the rate of deformation tensor and $|w|$ the magnitude of the vorticity tensor. From Equation (4-17) it may be seen that the value of λ will vary between 0 for $|d| \rightarrow 0$ (representing strong rotation) and 1 for $|w| \rightarrow 0$ (no rotation); 0.5 is typical for simple shear.

The full description of each of the Polydata .dat files used for the four different types of CICo-TSE simulations performed, as described in Section 4.4.1, are given in their shortened forms within Appendices F-M. The full .dat files used within Polydata (an example of which is shown in Appendix C) are very large and complex and little would be gained by including all of their contents. Instead the four intrinsic types of .dat file used within this research, describing the full flow conditions employed, are represented in each of the following two forms;

- Representations of each menu used, giving the relevant details seen onscreen as it appears within Polydata, collated chronologically.
- Flow parameters specified, summarised in a shortened form.

In the Author's opinion, both of the above representations of the .dat files employed within this research are useful. The first kind of representation is similar to that employed by Polyflow S.A. within their Examples Manuals [35], however this type of representation has the disadvantage of only being properly appreciated by Users who know the arrangement of menus within Polydata. Therefore, the second type of representation which summarises only the flow parameters used and is thus much more concise, is useful for all Readers. Thus the following .dat file representations were used for the following CICo-TSE simulations performed;

- Single-flighted conveying screw elements - Time-dependent simulations, for the 2D Y-Z screw channel flow (ΔX(time)). Appendices F and G.

  The same simulation was performed twice using different integration methods, for the purpose of comparing solution schemes. The two integration methods executed were the Crank-Nicholson method, utilising a precision of Δt^2 and the Implicit Euler method, utilising a precision of Δt.
- Single-flighted conveying screw elements - Steady state simulations for the 3D half profile. Appendices H and I.
- Mixing discs and trilobal element mixing zones - Steady state simulations for the 2D X-Y profiles ($\Delta Z = 0$ as elements rotate). Appendices J and K.
- Mixing discs and trilobal element mixing zones - Steady state simulations for the 3D mixing zones. Appendices L and M.

The simulations performed using the rheological data of PP, have assumed that the material is viscous and thus inertia terms may be ignored. However, as stated in Equation (4-2),

$$\rho \mathbf{v}.\nabla \mathbf{v} = 0 \qquad (4\text{-}18)$$

for cases when the Reynolds number, R_e, is very much less than one. The equation for calculating a representative Reynolds number is given as follows;

$$R_e = \frac{\rho v L}{\eta_o} \qquad (4\text{-}19)$$

and Equation (4-19) represents the ratio of the inertia forces to the viscous forces. To verify the previous statement, the following flow parameters utilised within the simulations may be used to calculate R_e. Thus for $\rho = 800$ kg m^{-3}, $v = 0.02$ m sec^{-1} (60 RPM and 0.02 m radius of outer barrel), $L = 0.05$ m (typical length of a CICo-TSE mixing zone under investigation) and kinematic viscosity of $\eta_o = 4400$ Poise (for $\dot{\gamma}^{n-1} = 1$), a Reynolds number of approximately $R_e = 2 \times 10^{-4}$ may be calculated. This value of Reynolds number is thus small enough to assume that inertia terms within the calculation may be ignored.

5 DESCRIPTION OF THE MECHANICAL MODEL UTILISED

5.1 Background

The work presented within this thesis is mainly concerned with the computational investigation of viscous fluid flow within the various sections of a CICo-TSE, using the CFD package Polyflow. The use of commercial CFD packages is becoming more prevalent within both academia and industry, this being due to the fact that, as these packages become more sophisticated and user-friendly, confidence in their use and reliability, and thus their application, is increasing. Each generation of commercial CFD package increases in sophistication. The CFD software houses have realised that the development and implementation of capabilities such as automatic correction and simulation verification, are in demand by the market. However, at this stage in the evolution of CFD, there has been little progress in developing these useful facilities in commercial packages. To have confidence, therefore, in the results from a commercial CFD package requires verification of the results by correlation with some other technique. Simple checking of the basis of the calculation and the consistency of the results is a sensible first step. Typical questions that need to be answered to give confidence in the CFD results are listed below;

- Are the units specified within the flow problem consistent and, if so, are the results obtained of the expected magnitude?
- If there are areas of symmetry within the flow domain, whereby identical flow conditions are being experienced by fluid within these regions, are the results obtained consistent with this symmetry?
- Are there any inconsistencies in the mesh utilised that may cause errors in the calculation, thus possibly leading to the invalidation of the conservation laws, such as mass balance?

The most valuable technique for verification of the appropriateness of the model is, of course, comparison of the outcome of the simulation with actual results obtained when using the modelled device and system. It is not possible to view mixing in-situ when processing using the Betol BTS range of CICo-TSEs (or within other processing devices, such as the Banbury or Brabender mixers) because of the metal casing. A transparent outer barrel casings would allow visual observation of the mixing process. Thus the investigation of the mixing of viscous material within the various elements of the CICo-TSE (or other processing machinery), would ideally, involve the following stages;

- Theoretical and computational investigation using CFD.
- Verification of predicted results using a mechanical model possessing transparent parts.

- Application of the verified predictive models on trials involving real life process machinery (laboratory and then full scale).

The discussion of how the predictive models, derived within this thesis, are to be applied in order to aid REX trials using the Betol BTS30, will be considered within the framework of other PPPG research programs. Many papers in the literature present experimental results for the continuous processing of immiscible or reactive viscous compounds and these materials may be either foodstuff or polymeric in nature. Those publications, however, which are of direct interest to this research program fall into two main categories;

- Papers that characterise and describe mixing within the CICo-TSE on a macro scale. Typically the attainment and application of parameters such as residence time distribution (RTD) and pressure profiles are discussed. Moreover, these types of paper discuss the implications for mixing when using different element configurations and also the effects on extruded product quality when applying varying processing conditions (such as a range of screw speeds, fill rate, temperature profile, etc.).
- Papers that describe local mixing within the various CICo-TSE sections. These types of paper portray either the mixing of bulk viscous material(s) or the behaviour of particulates and dyes through a CICo-TSE section over time.

J. L. White at the University of Akron at Ohio, USA, has presented results for the characterisation of flow, pressure and distribution of material within the Werner and Pfleiderer CICo-TSE as a whole, for different screw configurations [81-83]. Hornsby at Brunel University [14, 84] has done much experimental work with Betol CICo-TSEs again describing the effects of experimental parameters, such as screw speed, temperature profiles and screw configuration. Knowledge of RTDs for any continuous processing device is essential for controlling the property of an extruder product, such as the molecular weight distribution (MWD) of a plastic. RTD is also an important parameter for scale-up calculations and Todd [85] was one of the first to utilise experimental techniques to calculate RTDs. The particular technique described within his paper involved the injection of a radioactive tracer, namely activated MnO_2. Other techniques exist for monitoring in-situ mixing of material during processing. Bur and Gallant [86] describe a technique whereby fluorescence measurement was used to monitor polymer processing parameters within TSEs. Using specially developed optical fibre probes, which were inserted into the TSE barrel casings at various positions within the train, fluorescence radiation exhibited from a fluorescent dye added to the polymeric matrix at the feed port was monitored during processing.

Sinton *et al.* [87] however, describes a non-intrusive, non-invasive, 3D Nuclear Magnetic Resonance Imaging (NMRI) technique for monitoring mixing within TSEs. Whilst the results they describe within their paper are taken from samples extracted from different sections after the outer barrel casings have been removed, they conclude by stating that, within the next decade, it may be possible to use NMRI for on-line quality control during processing. Previous on-line analysis studies of mixing within extruders have usually involved monitoring the rheological properties of the extrudate, rather than its visualisation. Li *et al.* [88] and Gogos [89] both describe on-line measurement techniques. Li *et al.* [88] describes the application of torque-screw speed measurements to processing within the CICo-TSE. The technique outlined provides a means by which average shear rates, along the screw surfaces, may be derived using a geometry dependent shear rate constant, G_{sr} (derived within the paper) and angular velocity. Good correlation between theory and experimental measurements are reported and many advantages for using this technique are proposed. Gogos [89], however, describes the concept of Mixing Element Evaluators which are capable of evaluating, on-line, the morphology and rheology of immiscible polymer blends after they have been subjected to mixing by a specific mixing element sequence. Initially developed for the SSE, the paper describes the TSE evaluator which is essentially a specially designed data acquisition system incorporated into the modular outer barrel casings.

Papers that describe local mixing within the various CICo-TSE mixing sections are of greater immediate relevance to the work presented within this thesis, as visualisation of mixing within the different sections of a CICo-TSE may be compared directly to the CFD simulations presented here. Most of the published experimental results concentrate solely on the CICo-TSE conveying screw elements, with the most interesting publications supplied by Kalyon *et al.* [74, 90-91], Bigio [92-93], Ess and Hornsby [94] and Li *et al.* [95]. Kalyon *et al.* [74, 91] present, using the solidification technique, results from the processing of two different coloured viscous materials within the kneading block region. From the cross-sections revealed, the inference from these papers is that the flow fields exhibited in particular kneading block arrangements are similar to those exhibited within the double-flighted conveying screw elements. Karian [96] examines the influence of different kneading block arrangements on the processing of different PVC formulations within a CICo-TSE. The paper stresses the fact that the shearing action required for fusion of PVC particulates is separate from that of the kneading action which is required for thermal homogenisation of the molten phase. His investigation thus examined, using different coloured pigmented tracers added to the feedstock, the PVC powder-to-melt transition which takes place within the kneading blocks, for the different kneading block arrangements. Visualisation of the samples was achieved by dead-stopping the process and then opening the split outer barrel. A number of

papers have published results showing particle paths within clear viscous media. Szydlowski and White [97] compare their FAN simulations with videotape extracts of processing a small number of metal flakes within clear viscous Newtonian media. Though they claim good correlation, the video stills are unclear. Better images were obtained by Meijer and Elemans [98], who used clear glycerol to study the degree of screw channel fill within the screw elements of a CICo-TSE preceding the kneading blocks. Visualisation of flow within their CICo-TSE was achieved by employing a Plexiglas outer barrel wall and the images were obtained by use of a high speed camera. Bigio and Erwin [99] used an acid-dye extinguishment experiment to assess "mixedness" within the worst portions of the processing stream. The idea behind the technique was very simple, but effective and involves processing a clear bulk fluid, such as corn syrup, mixed with a clear acid such as acetic acid. Red basic dye solution was pumped into the acidified stream and at a certain pH, obtained by the successful agitation of the acid/base mix, the red colour of the dye would disappear. Bigio and Erwin's argument declares that any volume(s) containing red dye, illustrate regions of incomplete and hence inefficient mixing.

5.2 Mechanical model

Betol Machinery Limited provided one pair of screw shafts (length to diameter (L/D) ratio of 17:1) and an assortment of mixing discs and modular single-flighted conveying screw elements of differing pitch for the duration of this research. The CICo-TSE elements loaned were those from a Betol BTS40 CICo-TSE and were thus all of 40 mm outer diameter. The screw configuration used within this work is shown in Figure 5-1 and the arrangement of the CICo-TSE train, starting at the feed end, was configured as follows;

- Feed section:
  Feed screw elements, 1 pair of: 24 mm pitch, 120 mm length.
- Compression zone #1:
  Single-flighted screw elements, 1 pair of: 16 mm pitch, 80 mm length.
  Single-flighted screw elements, 1 pair of: 12 mm pitch, 80 mm length.
- Mixing disc zone #1:
  1 pair of long discs.
  3 pairs of short discs.
- Decompression zone:
  Single-flighted screw elements, 1 pair of: 24 mm pitch, 120 mm length.
- Compression zone #2:
  Single-flighted screw elements, 1 pair of: 18 mm pitch, 80 mm length.

Figure 5-1: **Schematic Diagram of the CICo-TSE Screw Elemental Train Arrangement Assigned Within the CICo-TSE Model Constructed**

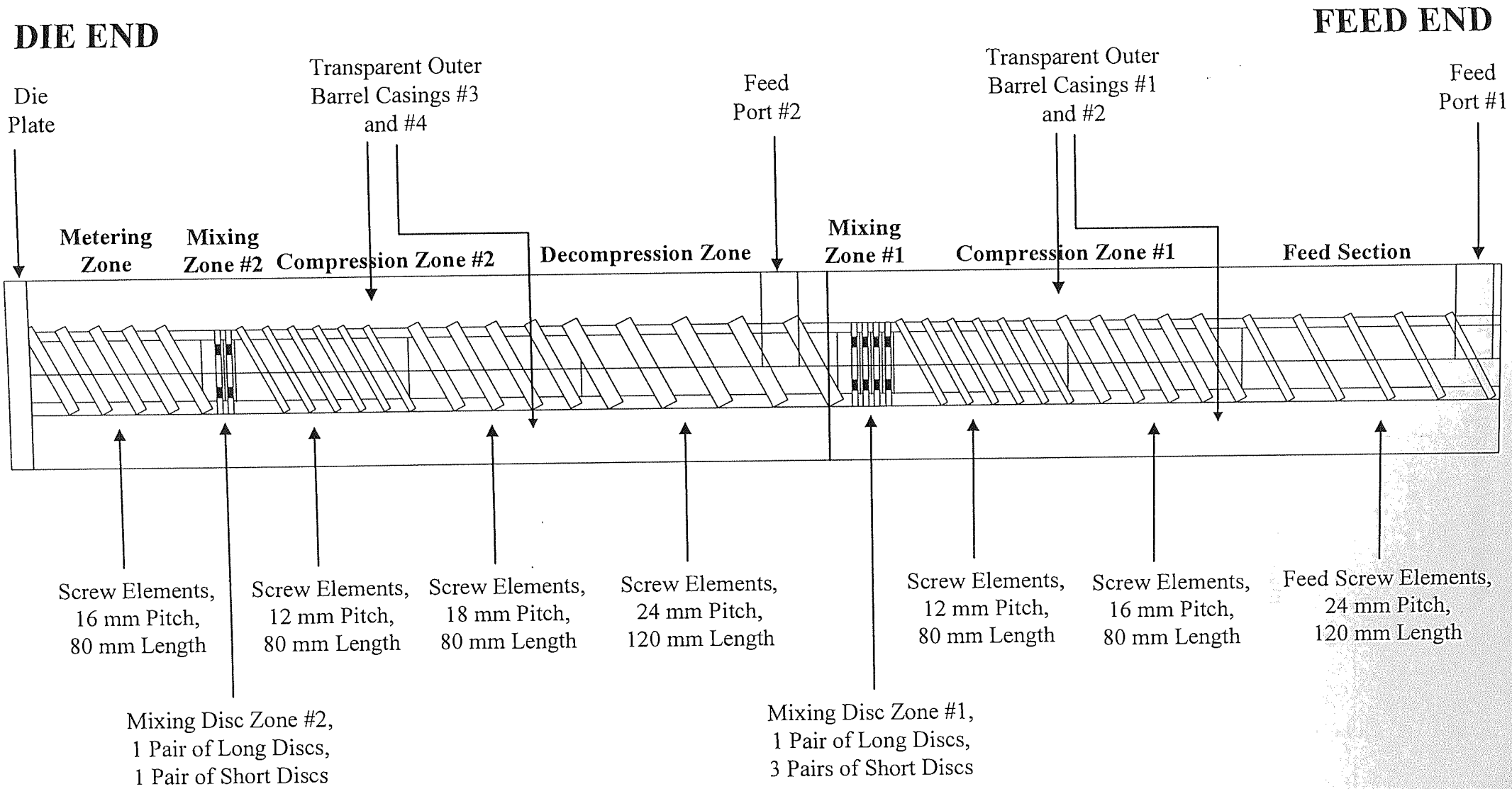

Single-flighted screw elements, 1 pair of: 12 mm pitch, 80 mm length.

- Mixing disc zone #2:

  1 pair of long discs.

  1 pair of short discs.

- Metering zone:

  Single-flighted screw elements, 1 pair of: 16 mm pitch, 80 mm length.

- Die plate:

The mechanical model constructed to accommodate this CICo-TSE train was of a simple design. Figure 5-2 shows the motor, and mechanical transmission used to co-rotate the two CICo-TSE screw shafts and elemental train. A better illustration is given by the schematic diagram of Figure 5-3. A full description of the components and their purpose is described as follows;

- A 9 kW motor, capable of rotating at a constant speed of 35 RPM and securely fixed to the workbench, rotates steel shaft 'A'.
- Steel shaft 'A' is connected to steel shaft 'B', via a flexible coupling. This flexible coupling serves the purpose of absorbing any shock caused by possible CICo-TSE element non-intermesh during processing.
- Steel shaft 'B' passes through a worm-gear box fixed to the workbench. This worm-gear box serves the purpose of regulating the rotation of shaft 'B'.
- Steel shaft 'B' is connected to steel shaft 'C', via another flexible coupling. Steel shaft 'C' is located within the main gear box housing.
- The portion of shaft 'C' contained within the main gear box, co-rotates, via two adjustable tension belts and a series of toothed wheels, steel shafts 'D' and 'E' together at the same rotational speed.
- Steel shafts 'D' and 'E' are connected in turn to the two CICo-TSE screw shafts, via two further flexible couplings.

The containment of the CICo-TSE train is provided by four modular transparent outer barrel casings, which are removable and made of Transpalite material, as supplied by Stanley Plastics Ltd. [100]. Two of these transparent casings form the fixed base beneath the CICo-TSE train. The remaining two casings cover the screw elements and are easily removable for inspection and sampling. Two feed ports were drilled into the two upper casings at the positions shown in Figure 5-1. In the Betol BTS range of CICo-TSEs, the screw element train is coupled to the drive shaft at the feed end only (as described in Chapter 1)

Figure 5-2:
Picture of the Motor and Gear Box Arrangement Utilised for the CICo-TSE Mechanical Model Constructed.

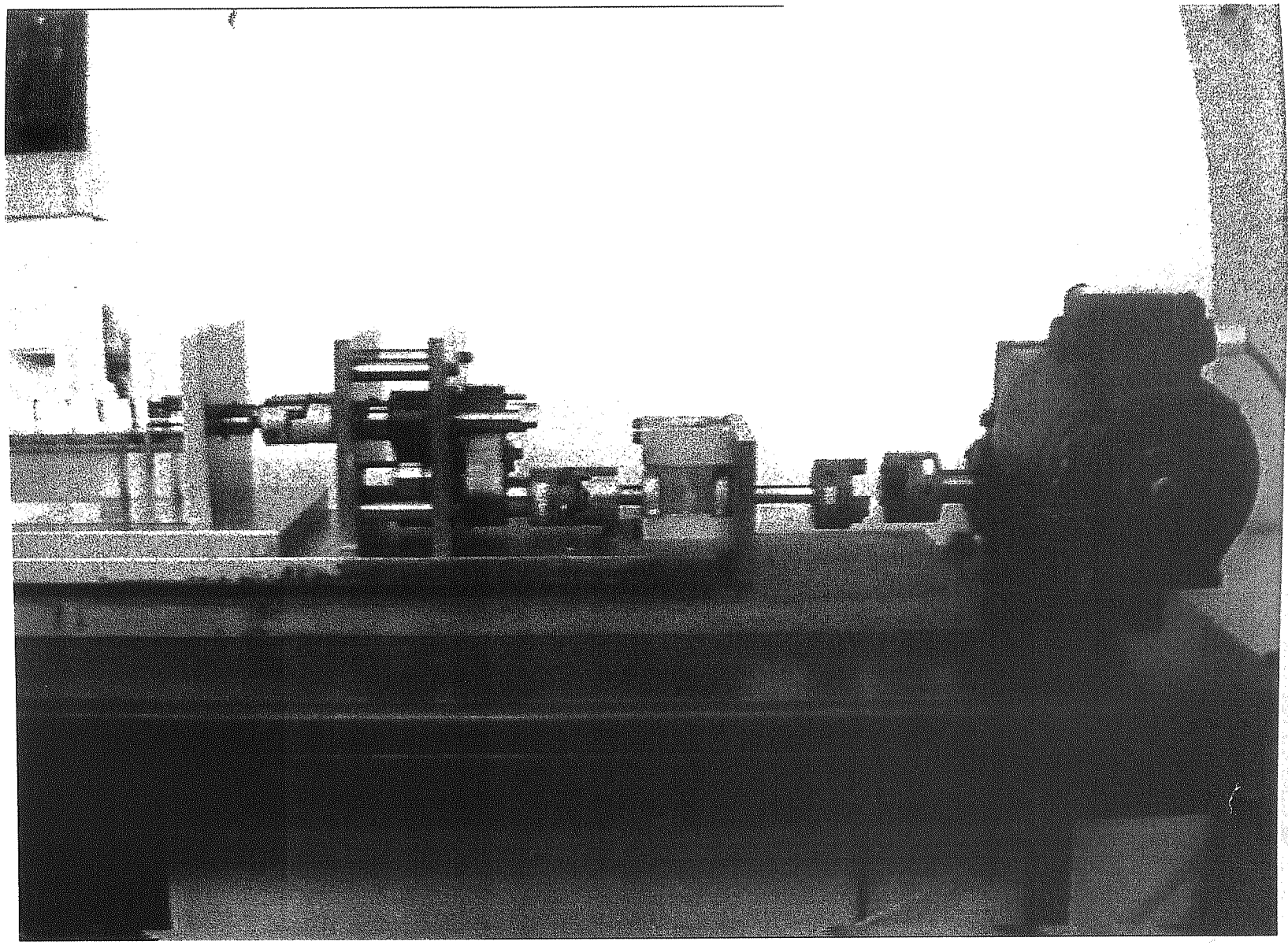

Figure 5-3: **Schematic Diagram of the Motor and Gear Box Arrangement Utilised Within the CICo-TSE Model Constructed**

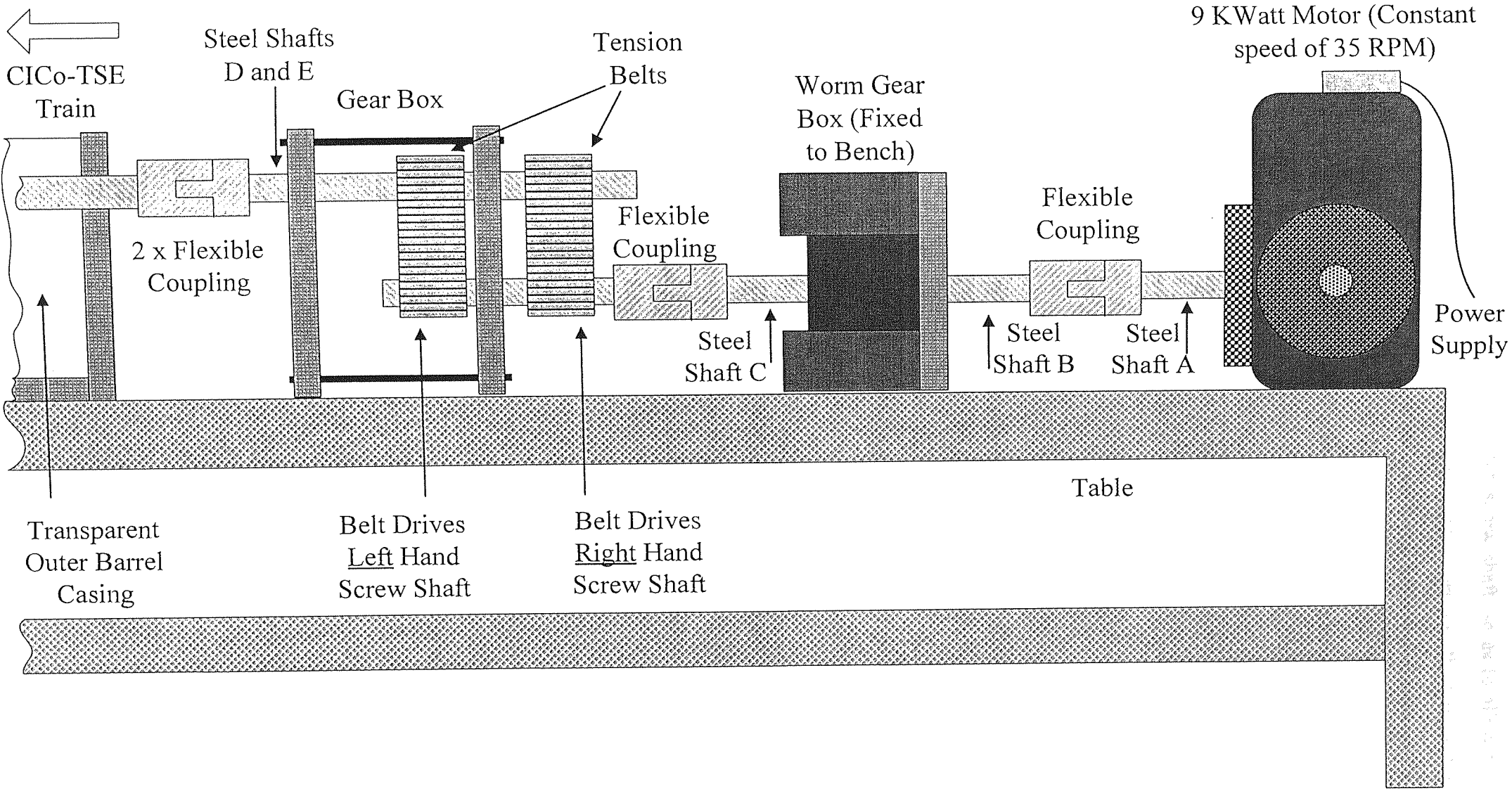

whilst at the die end there are conical tips attached to each screw shaft, so as to allow the creation of a chamber volume just before the die head. Consequently, because the CICo-TSE train is supported at the feed end only, the modular metal outer barrel casings also support the CICo-TSE train to some extent. Certainly, the CICo-TSE screw element train grinds against the outer barrel wall, which over time causes some degree of wear (Rauwandaal discusses this aspect in relation to screw flight clearance [10]). Thus, the data quoted in Chapter 4 for the clearance between the CICo-TSE elements and the outer barrel wall and used within the CFD simulations, are median values calculated from the tolerance values supplied by Betol Machinery Ltd. and consequently are considered as ideal clearance values. When construction of the mechanical model was undertaken, support of the CICo-TSE train at one end only would not have been practical due to the expectation that this would probably cause excessive wear of the Transpalite casings over a very short period of time. It was therefore decided that the solution would be to attach supports at the die end of each shaft, instead of conical tips, and then to rest these supports in guide holes drilled into the die plate. Due to the fact that this research program was not intended to consider flow within the die region, this arrangement was acceptable. Future research programs may need to modify this construction.

The mechanical model constructed and used in this research may only process material at moderate temperatures. The maximum temperature that could have been applied safely to the Transpalite material, (Transpalite being a form of poly(methyl methacrylate)) is of the order of 60 °C. Since processing of polypropylene or polyethylene requires temperatures of the order of 180 °C, these materials could not be used directly. Substitute materials which exhibited similar rheologies at room temperature needed to be identified. It was also intended to observe the distribution pattern of particulate additives within the flow field.

- To represent the bulk polymer matrix, different coloured "Playstuff" clay samples [101] were used. The use of "Playstuff" clay is advantageous because it comes in many different colours, is very malleable and its rheology may be controlled by the addition or removal of water. In addition, if a sample is left to dry, it becomes permanently hard and may thus be preserved (unfortunately some degree of shrinkage will also result). The use of "Playstuff" clay was suggested by the team at Polyflow S.A., who used the material for their experimental work on the investigation of mixing within the Kenics mixer [102] (by using different coloured "Playstuff" clay samples they have been able to observe good correlation between their simulations and their experimental results).
- To model the distribution of particulate matter, graphite particulates which are black, were dispersed in glycerol which is colourless. Other particulates such as small coloured beads were also employed, but with little success.

To enhance the visibility of, particularly, the particulates during processing, the screw elements and mixing discs were sprayed white. The processing of different coloured "Playstuff" samples was considered quite successful (as illustrated by the results in Chapters 6 and 7). Video-recording of the processing of particulates was less successful and this was due to a number of different factors which may be listed as follows;

- The video-camera used was not of sufficient quality for the capturing of fast moving images, such as those generated during the processing of particulates. To obtain satisfactory clarity of a process involving fast moving particulates, the acquisition of high quality cameras possessing high speed shutters will need to be considered.
- The path of particulates in both the top and bottom portions of the CICo-TSE train volume could not be tracked simultaneously. This is disadvantageous, for example, when trying to track particulates through the mixing zones, where particulate matter may fluctuate rapidly in either portion.

The results given in Chapter 6 for the single-flighted conveying screw elements using "Playstuff" clay, are similar to those of Kalyon for the double-flighted conveying screw elements [74, 90-91]. Kalyon, however, uses polymeric pigments and plasticised thermoplastic elastomer (TPE) tracers to characterise the cross channel and nip region flows fields. Avalosse and Crochet [102] use different coloured "Playstuff" clays in their work involving the Kenics mixer, however, they dilute the clay used in 200% of water. The purpose of this dilution is so as to enable the clay to be frozen for examination. After their clay samples have been processed, the reservoirs they have been collected in are removed and placed in a freezer. By freezing the clay samples, the chances of deforming the clay during sampling may be minimised (the clay will be very malleable at room temperature). This approach was attempted during the experimental trails using the CICo-TSE mechanical model, however, it was rejected due to the fact that prolonged contact of diluted clay against the body of the CICo-TSE elements, causes some degree of rusting.

5.3 Summary

A mechanical model has been described and the screw arrangement used within the work has been given. Reasons for the choice of materials used to represent viscous polymeric melt at room temperature have also been discussed.

6 INVESTIGATION OF VISCOUS FLOW WITHIN THE CICo-TSE SINGLE-FLIGHTED CONVEYING SCREW ELEMENTS

6.1 Single-Flighted Conveying Screw Elements - 2D Y-Z and 3D Geometries

Conveying screw elements, as described in Chapter 1, may be single- double- or triple-flighted in design and the full 3D geometries of the different closely intermeshing, conveying screw element sections are complex. By configuring different screw sections, each possessing different screw pitches, within a CICo-TSE train, selective use of compression and decompression of viscous material may be achieved. The flow of material through the geometrically simpler SSE screw element sections is well documented [10, 16, 103-104], however less is known about viscous flow within the various TSE screw sections.

Figure 6-1 shows a schematic diagram of the 24 mm pitched, single-flighted conveying screw element section, which is the particular screw section investigated within this work (when employed within the Betol BTS40 CICo-TSE, a 24 mm pitched screw section would typically be utilised within a decompression zone). As may be seen from this figure, the angle that the screw flights make with the vertical axis is 27° 4'. This angle is characteristic of that type and size of screw element and of that particular screw pitch, and it is found that different intermeshing screw elements of specified screw pitch will possess differing flight angles. The magnitude of screw flight angle is one of the many factors that determine conditions such as material throughput and degree of channel fill. Armstroff and Zettler [105] describes the relationship between screw flight angle and material throughput for SSE elements and then outlines how the SSE element equations may be modified for the quantification of TSE element throughputs.

It was Erdmenger [106] who first postulated that the flow path for the bulk of viscous melt through the CICo-TSE conveying screw elements, will be of a "figure-of-eight" nature. This description, however, is too simplistic as a number of factors, such as screw geometry and arrangement, effect the character of melt flow through the CICo-TSE conveying screw elements. To illustrate the possible flow paths, Figure 6-2 shows the result of pre-packing the channel of the right hand 24 mm pitched screw element with viscous "Playstuff" clay, shown as the bottom screw element in Figure 6-2, and rotating the shafts such that some of the material crosses over to the channel of the opposing left hand screw element, shown as the top screw element in Figure 6-2 (the "Playstuff" clay used within this experiment, as described in Chapter 4, is a water based viscous substance that is both malleable and easy to handle and its rheology at room temperature, which can be controlled with the addition or removal of water, is analogous to that of molten viscous polymer). It may be observed from Figures 6-1 and 6-2, that there are four distinct flow patterns by which material may progress and these are described as follows;

Figure 6-1:

Possible Routes for Viscous Melt Flow Within the 24mm Pitch, Single-Flighted Conveying Screw Elements

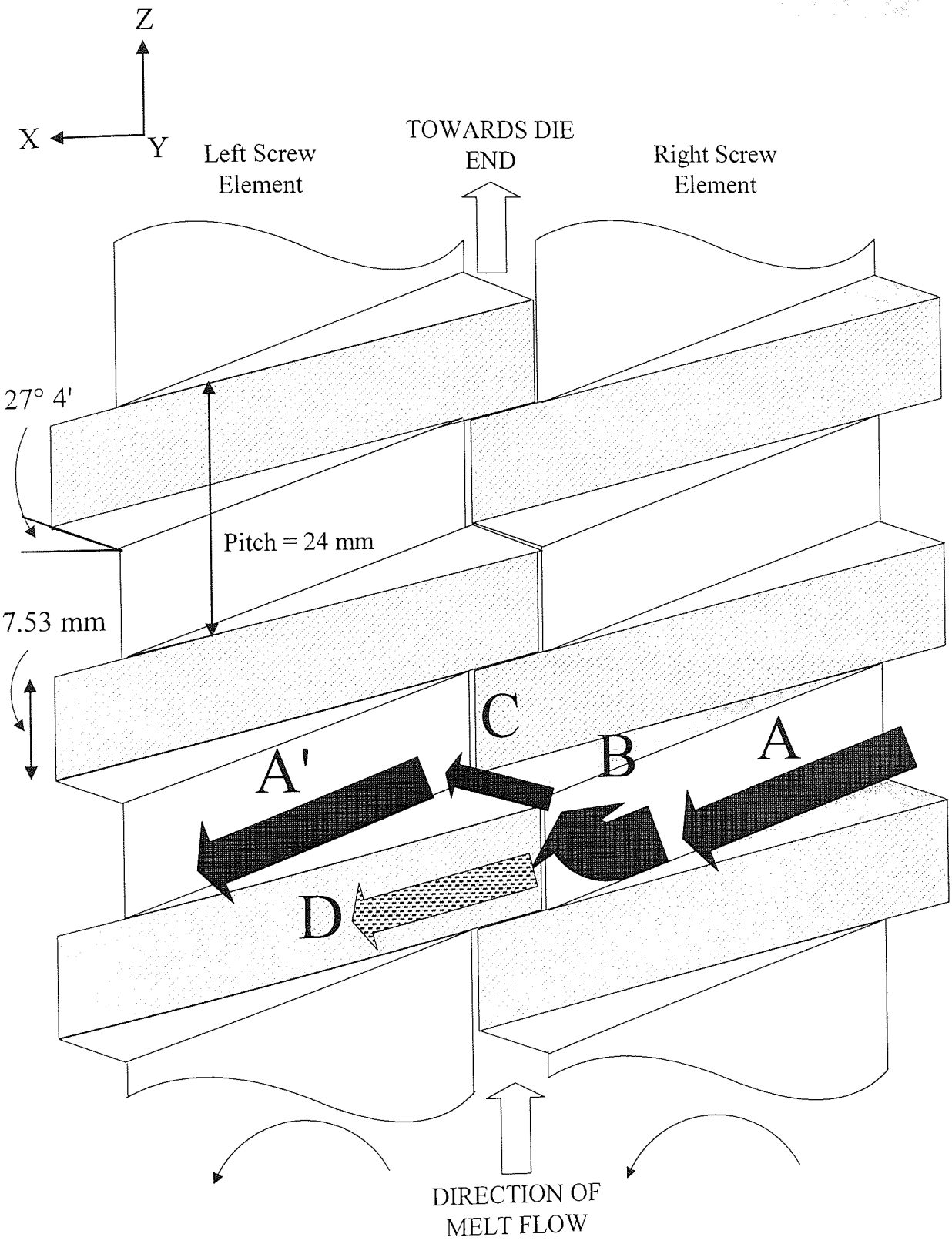

Figure 6-2:

Illustration of all Possible Material Flow Paths Within the 24 mm Pitched, Single-Flighted, Conveying Screw Element Section, Using Viscous "Playstuff" Clay as a Medium.

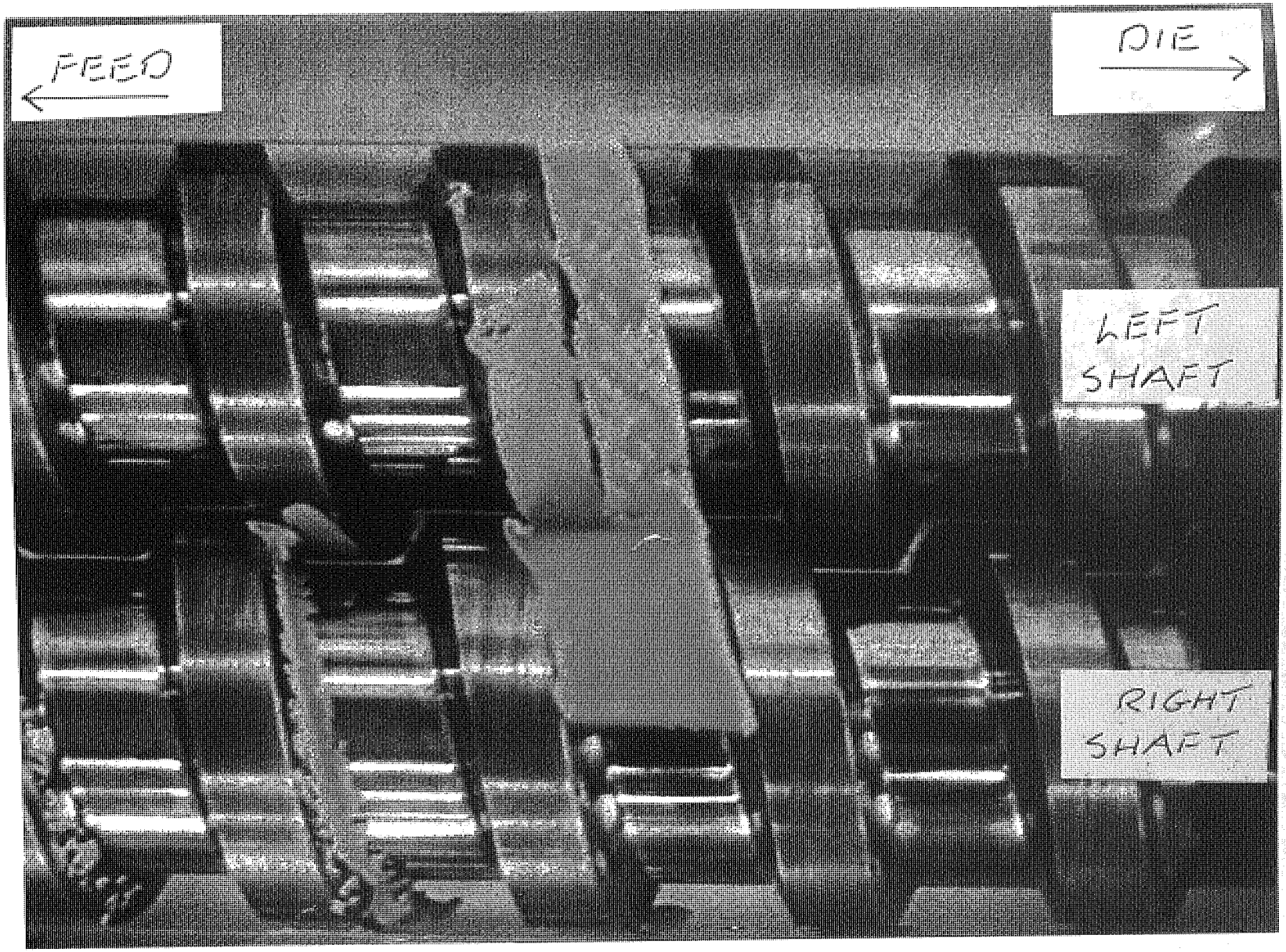

- Leakage flow

  CICo-TSE conveying screw elements intermesh, as their name suggests, very closely. However, in the regions where the screw flights intermesh, there are gaps through which material may leak. This is illustrated in Figure 6-2 by the thin line of clay that has adhered to the trailing flight of the right hand screw element. The degree of material leakage is dependent on the forwards and back pressures present within the screw zone and also on the screw geometry. Leakage flow is complex and will not be considered within this thesis, however other workers have published investigations on this topic elsewhere [10, 16, 107-108].

- Flow over the screw flights (shown as region D in Figure 6-1)

  Typically there is a relatively small clearance between the screw flights and the extruder barrel casing. Material will enter this region as shown in Figure 6-2. For the screw sections of the Betol BTS40 CICo-TSE, this distance is on average 0.145 mm. Any material contained within this region experiences very large shear stresses. Polyflow version 3.4.6 (Chapter 3) may be used simulate the processing of material where thin fabrication is needed, such as in film casting or film stretching problems. However, in solving these types of problem, the assumption made is that the film sheet is perfectly flat and thus contains no curvature. In addition, because the film thickness in relation to the sheet size is assumed to be very small, the film casting model used within Polyflow is 2D only. Hence the use of the Polyflow film casting module would be unsuitable for simulating the flow of material over the screw flights, as a significant amount of curvature is involved.

- Channel flow (shown as region A (and A') in Figure 6-1)

  For material being conveyed through a screw section, the bulk of that material (i.e. excluding that which has leaked) will reside for most of its time within the channel volumes of each screw element. The flow of viscous material through the screw channel of the 24 mm pitched single flighted, conveying screw element section has been studied within this work and the results of which are discussed in Section 6.2.

- Flow through the nip region (shown as regions B and C in Figure 6-1)

  Material crossing over from the channel of one screw element to the channel of the opposing screw element, is forced to pass through the intermeshing, screw nip region, where reorientation of material takes place. The number of nip regions present within a particular screw element section, depends on both the screw pitch and length of the modular screw elements. The flow of viscous material through the nip region of the 24 mm

pitched single-flighted, conveying screw element section has also been studied in this research program and the results are discussed in Section 6.3.

The experiment illustrated in Figure 6-2, allows the investigator to examine the behaviour of viscous fluid whilst it is being processed within the screw channels and also as it passes through the nip region. It must be noted however, that the pre-packing of a screw element, so as to achieve a screw channel which is fully filled, whilst it will account for the behaviour of viscous material within the aforementioned screw element regions, is not a complete representation of CICo-TSE processing at a steady state. This is due to the fact that in reality the various CICo-TSE screw element sections typically operate on a starve-filled basis (i.e. all screw channels will be only partially full). This is demonstrated by the end result of the processing shown in Figure 6-2, where the screw channel of the left hand element, shown to the top of Figure 6-2, is seen to be partially full. Partial fill conditions in that experiment, were created due to the location of the flight of the opposing screw element and this has caused a proportion of the clay in the full channel to be hindered in its progress to the channel of the opposing screw element. Furthermore, the amount of fill observed in the channel of the left hand screw element is the maximum allowed for this particular screw arrangement (if the effects of material swell are ignored) as is readily verified by inspection. A more thorough discussion of material screw element fill, with an explanation of why it not considered within this research, is given in Section 6-2.

Figure 6-3 illustrates the full 2D X-Y cross sectional outline through a pair of single-flighted conveying screw elements, illustrating the assignment of the following parameters as defined by Booy [109-110];

- The centre-line distance C_L.
- The radius of the outer barrel R_S.
- The screw tip angle θ.
- An angle ψ.

The angles θ and ψ are not screw pitch dependent, unlike the flight angle defined in Figure 6-1. Instead, each angle is dependent on the centreline ratio, as defined in Chapter 4 and each may be calculated using the following equations;

$$\theta = \frac{\pi}{n_s} - 2\cos^{-1}\left(\frac{\rho_c}{2}\right) \qquad (6\text{-}1)$$

Figure 6-3:

X-Y Cross-Sectional Plane Through the Single-Flighted, Conveying Screw Elements, Showing the Assignment of Certain Screw Parameters.

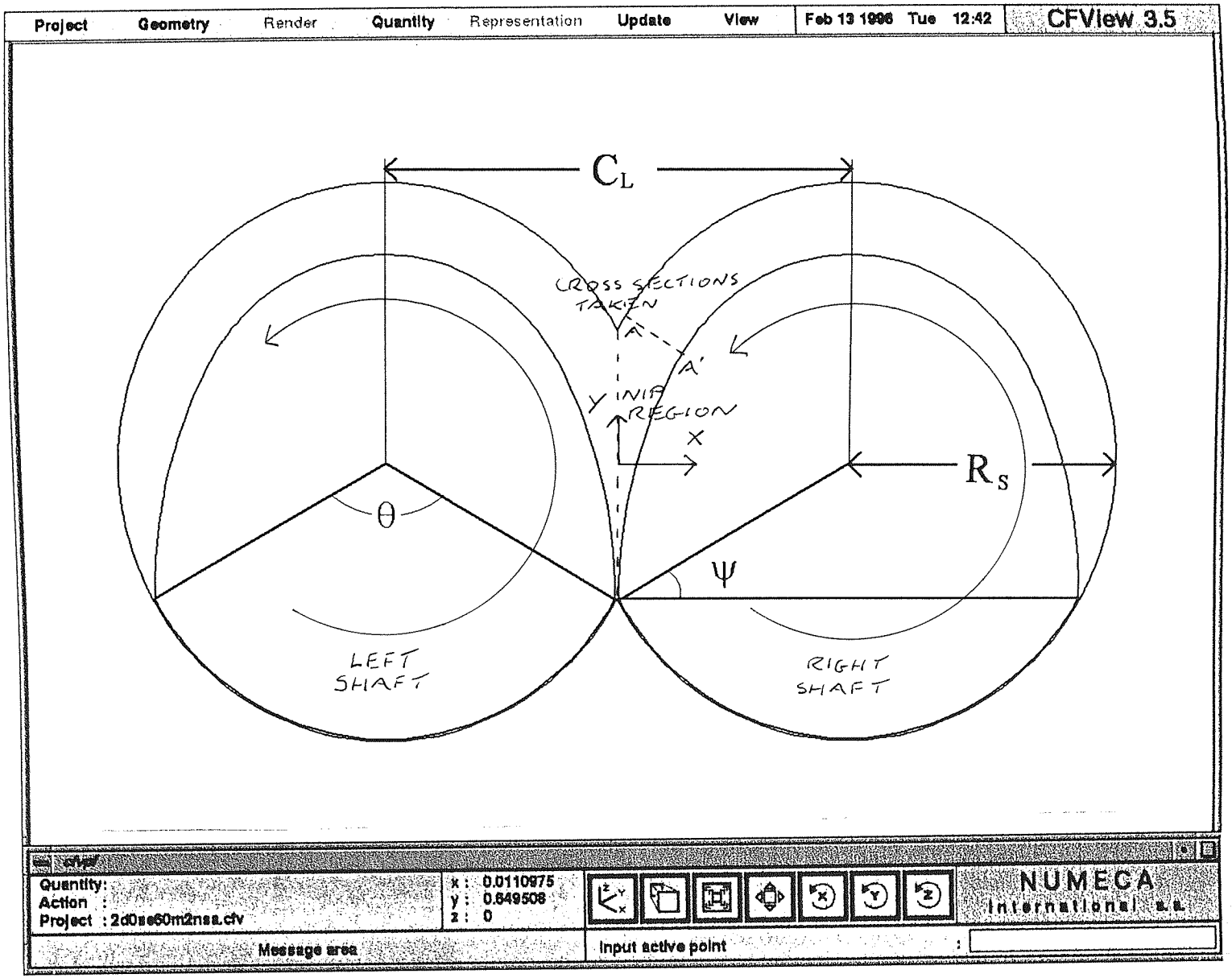

$$\psi = \cos^{-1}\left(\frac{\rho_c}{2}\right) \qquad (6\text{-}2)$$

where n_s is the number of screw tips. For the single-flighted conveying screw elements, $n_s = 1$. Thus, for the Betol BTS40 CICo-TSE examined within this work, it is found that the tip angle is $\theta = 122° 4'$ and $\psi = 28° 58'$.

To examine the flow of viscous material through the screw channel volume, a 2D mesh representing a cross section in the Y-Z plane was constructed. The full details for the construction of this mesh are given as follows;

- Macro-vertex co-ordinates:
  Appendix N.
- Macro-element numbering scheme:
  Appendix O.
- Sub-domain numbering scheme for the time-dependent problem:
  Appendix P.
- Details for the construction of the macro-elements:
  Appendix Q.
- Boundary numbering scheme:
  Appendix R.

The number of structured nodes contained within the 2D optimised mesh, representing the 24 mm single-flighted, conveying screw Y-Z cross section, was 1035 nodal points. The 2D mesh used for both the time-dependent and steady state simulations, is shown in Figure 6-4. From this figure it may be seen that mesh density has been increased about the regions close to the wall boundaries.

The 3D mesh constructed to represent flow through the nip region, posed the problem of how to incorporate the 27° 4' inclination of the screw flights into the mesh structure. This screw flight inclination meant that the axial length of the faces representing the outer barrel wall, were longer than those representing the screw collar (with all faces representing the screw flights thus inclining at an angle of 27° 4' to the Y-axis). The difference in length, given that the screw flight depth is 4.89 mm, is in fact given by the following calculation;

2 x 4.89 x tan (27° 4') mm

= 5.00 mm

Figure 6-4:

Mesh Utilised for the 2D Representation of the Y-Z Cross Section Through the 24 mm Pitched Single-Flighted, Conveying Screw Elements.

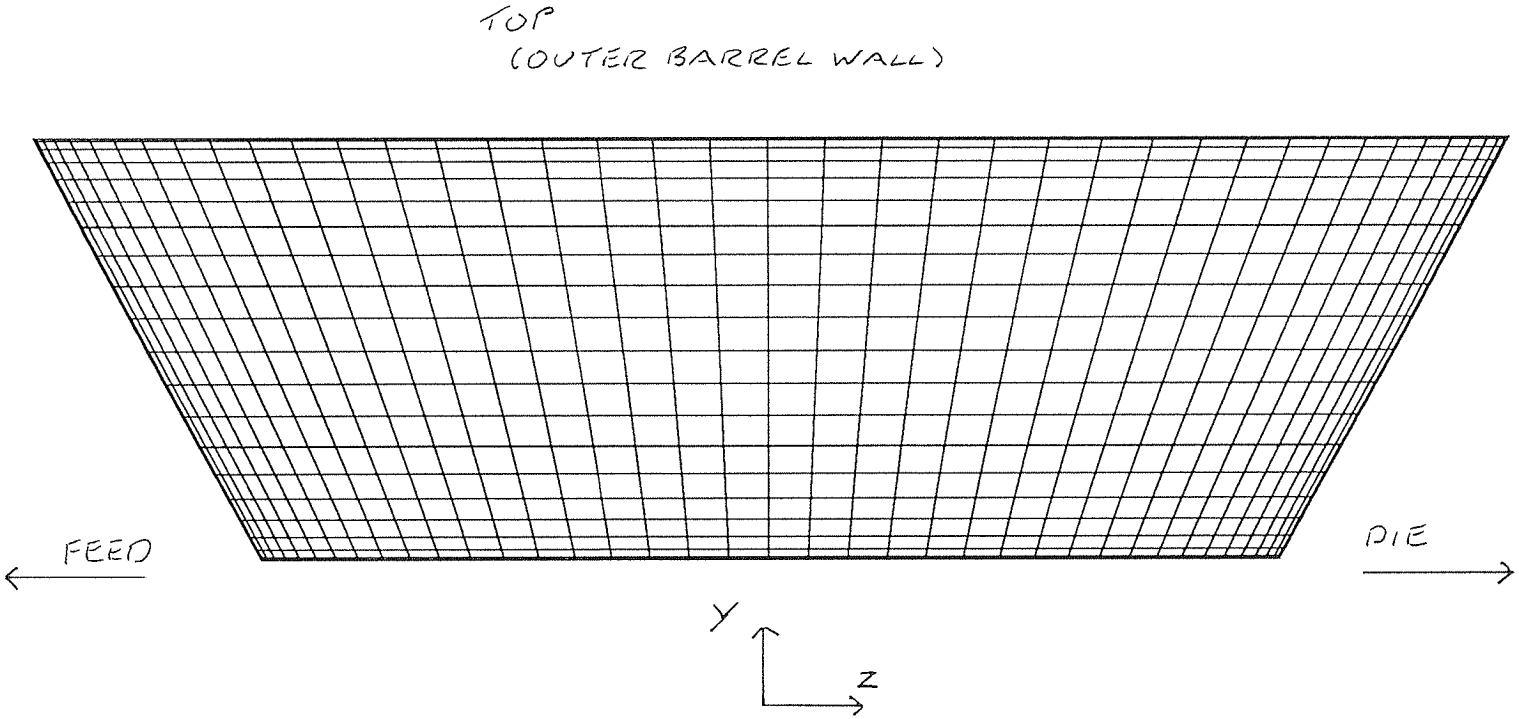

This difference in face lengths had to be manually created during mesh construction and this was achieved within the ICEM P-Cube module. In addition if the viscous clay sample shown in Figure 6-2 is inspected, it may be seen clearly that the line the sample makes with the X-axis is also 27° 4' (this is additionally illustrated in Figure 6.1). This subsequent condition was also manually incorporated into the mesh constructed using ICEM P-Cube. The actual mesh used for the simulation of processing viscous material through the nip region, similar to that shown in Figure 6-2 but excluding the flow of material over the screw flights, is shown in Figure 6-5. For this mesh, eight boundaries were ascribed and Figures 6-6 to 6-8 illustrate these assignments (the origin assigned for this mesh structure is indicated within these figures).

- Figure 6-6 shows the inlet face assigned as boundary number 1 (shown in red at the foreground of the structure) and the outlet face assigned as boundary number 8 (shown in blue at the background of the structure).
- Figure 6-7 shows the wall of the right hand screw element assigned as boundary number 2 (shown in green) and the wall of the left hand screw element assigned as boundary number 5 (shown in yellow).
- Figure 6-8 shows the wall of the outer barrel, assigned as boundary number 7 (shown in dark purple) and also the three faces located around the screw nip region. The flow parameters designated to these three boundaries are shown in Appendices H and I and their assigned boundary numbers are given as follows.

  Boundary number 3: shown in light blue.
  Boundary number 4: shown in dark blue.
  Boundary number 6: shown in pink.

  Boundary 6 was assigned for its rotational centre, the same co-ordinates as the centre of the left hand screw element. However, boundaries 3 and 4 were assigned for their rotational centres, Y co-ordinates of 19.8625 mm ($X = 0$ and $Z = Z_{\text{trailing flight}}$ and $Z_{\text{leading flight}}$). This particular value of Y assigned to the rotational centres of these two boundaries, is due to the radius of curvature of the arc possessed by boundary 3 (shown in Figure 6-8) and its position in relation to the origin chosen.

Table 6-1 catalogues the mesh parameters used and Graph 6-1 shows the Jacobian histogram for the mesh representing the 3D screw profile shown in Figure 6-5. The full theoretical discussion as to how the Jacobian histogram is constructed, is given in the ICEM

Figure 6-5:
Mesh Utilised for the 3D Half Profile of the 24 mm Pitched Single-Flighted, Conveying Screw Elements, Assuming Initial Full Fill Conditions in the Right Hand Screw Element Channel.

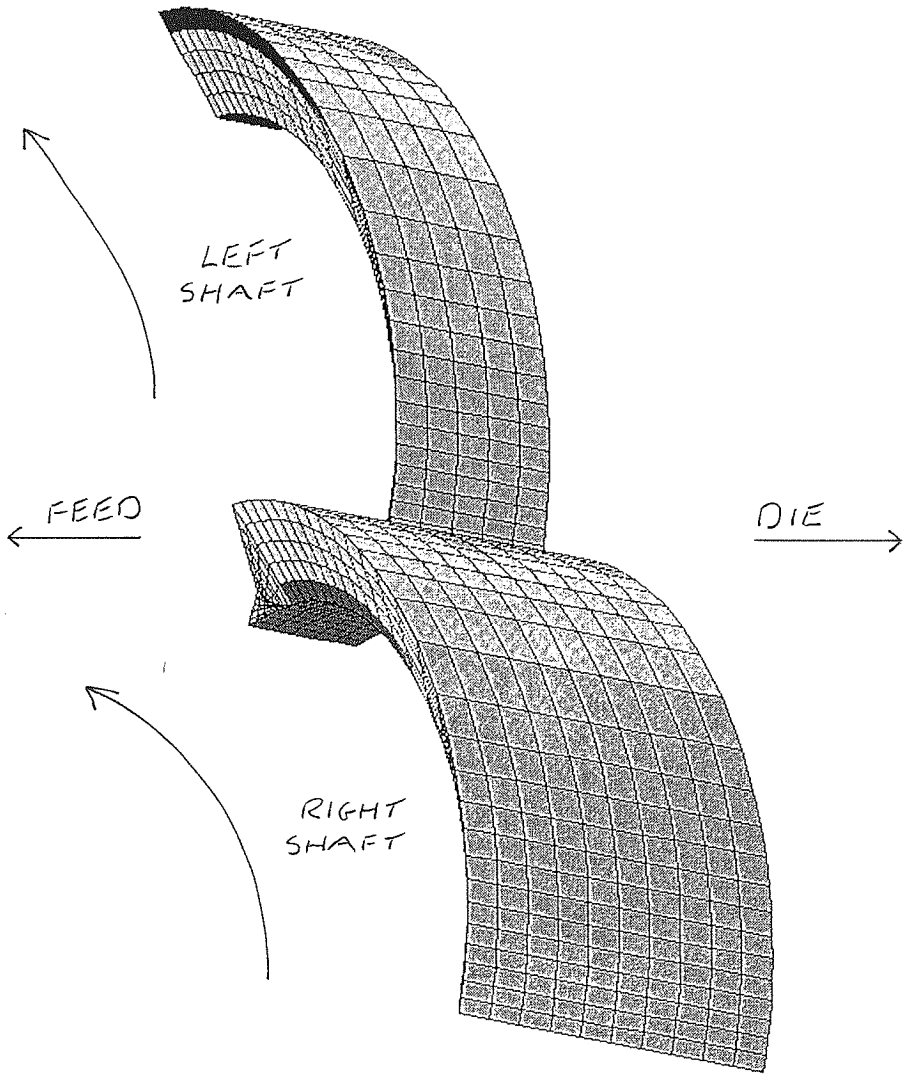

Figure 6-6:

Assignment of Boundaries 1 and 8 for the Mesh Shown in Figure 6-5.

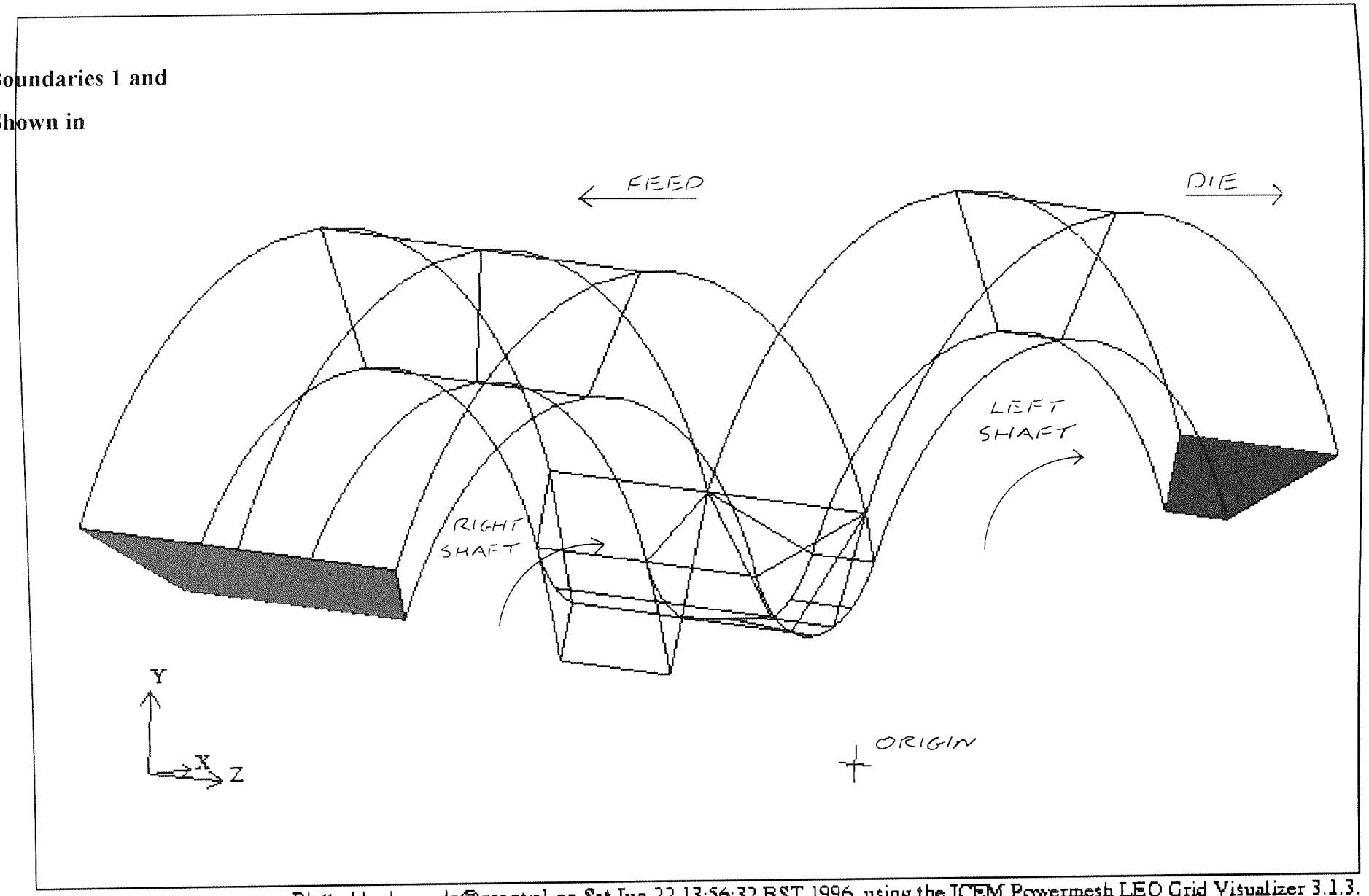

Figure 6-7:

Assignment of Boundaries 2 and 5 for the Mesh Shown in Figure 6-5.

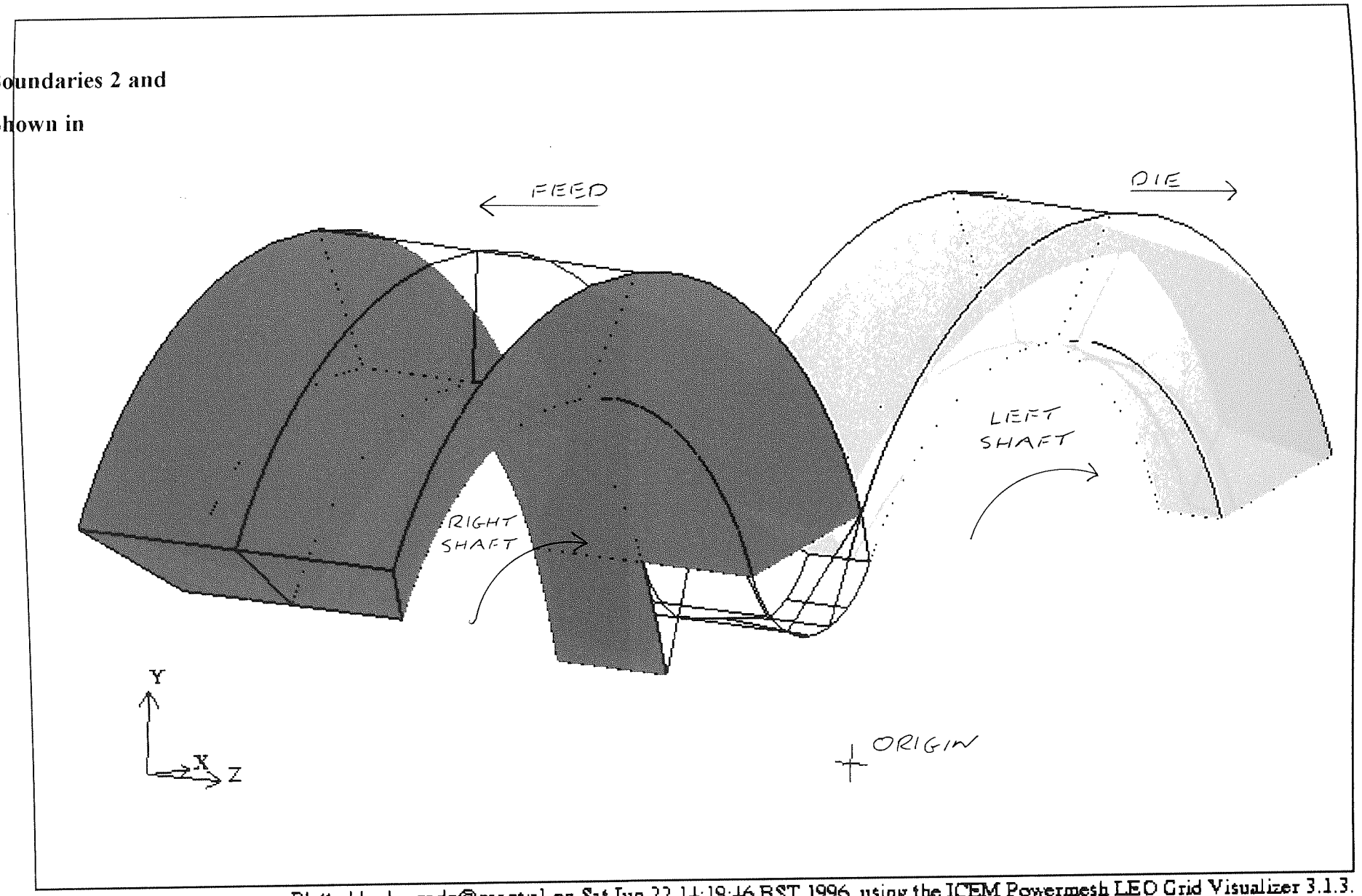

igure 6-8:
ssignment of Boundaries 3, 4, 6
nd 7 for the Mesh Shown in
igure 6-5.

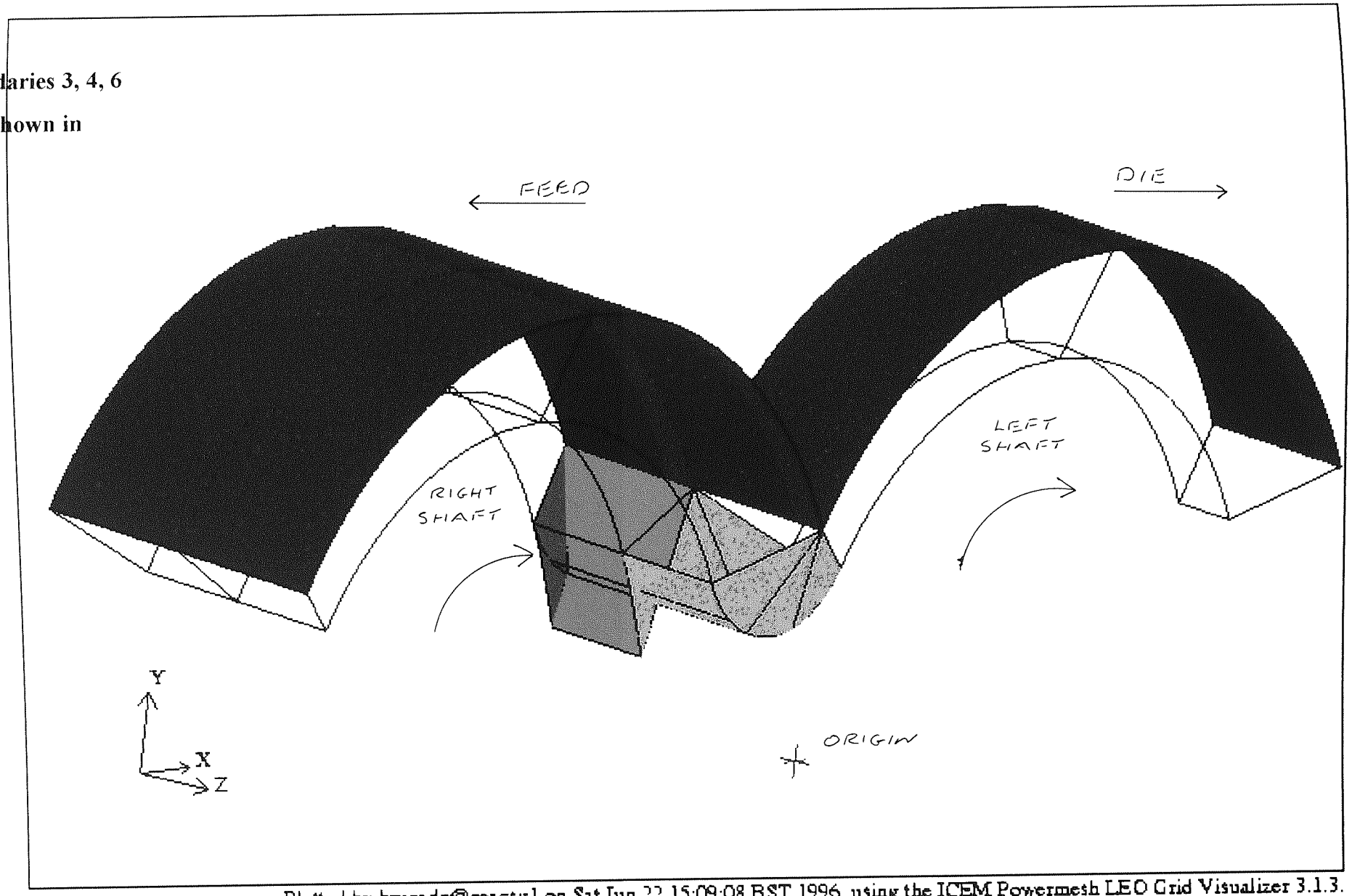

TABLE 6-1:

3D Parameters Table - Single-Flighted Conveying Screw Elements

Screw Pitch (mm)	No. of Domains	No. of Subfaces	No. of Edges	No. of Vertices	No. of BC's on Subfaces	Jacobian: Total	Jacobian: Mean	No. of Nodes on Inlet	No. of Nodes on BC2	No. of Nodes on BC3	No. of Nodes on BC4	No. of Nodes on BC5	No. of Nodes on BC6	No. of Nodes on BC7	No. of Nodes on Outlet
Full Fill Channel - Half Fill Channel:															
24	11	53	83	42	40 on 53	7765	91.1078	66 [1]	639 [1]	61 [1]	321 [1]	66 [1]	464 [1]	487 [1]	36 [1]

NOTE:

1 The assignments of boundaries 1-8 are illustrated in Appendices H & I

Graph 6-1:

Jacobian Distribution for the 3D Mesh Representing the 24 mm Pitched Single-Flighted, Conveying Screw Elements.

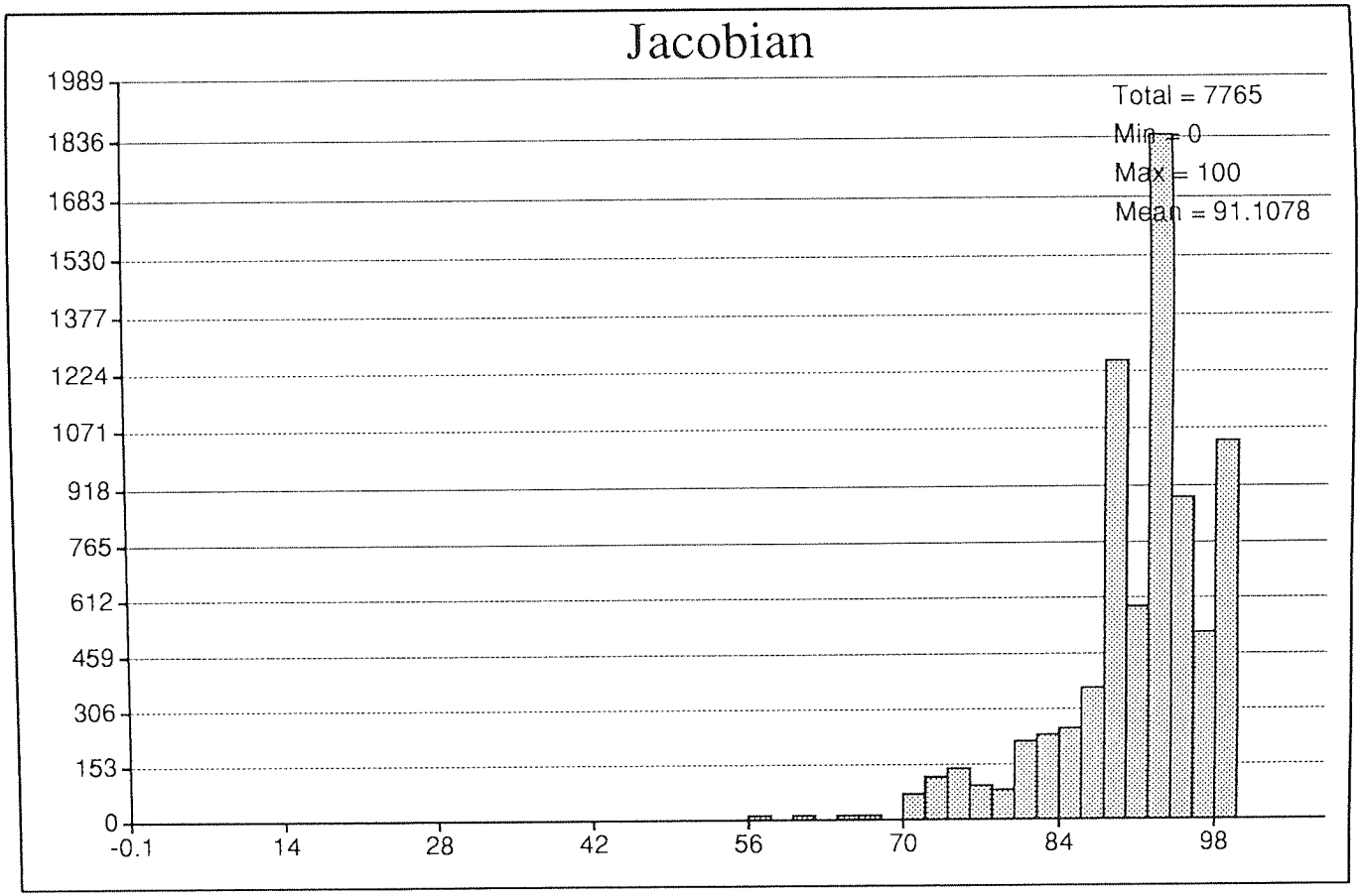

Systems manuals [42-44] and will not be repeated here. The Jacobian histogram gives some measure as to the quality of the mesh utilised (there are many other diagnostics that may additionally be performed). The procedure, executed via ICEM-LEO, inspects each finite element contained in the mesh and performs a diagnostic check on both the internal angles and opposing edges. For a finite element which is a perfect square containing internal angles of 90° (this structure being the computational ideal), the Jacobian value for this element is 100. Deviations from this ideal are then graded between the values 100 to 0. ICEM-LEO will also calculate a mean value for the entire mesh and mesh quality is improved, the closer this value is to 100 (for the Jacobian histogram shown in Graph 6-1, the mean is approximately 91 which is acceptable).

6.2 Results - 2D Y-Z profile to represent screw channel flow (ΔX(time))

A freeze-frame still taken during the processing of dilute "Playstuff" clay (single colour) within the single-flighted conveying screw element sections of a CICo-TSE, is shown in Figure 6-9. The image demonstrates that the steady state processing of viscous melt within the various sections of the single-flighted conveying screw elements, will result in the channels of each screw element being only partially full (as described previously). The closely intermeshing design of the single-flighted conveying screw elements dictates that once material has progressed through the nip region from one screw channel to the next, material will only occupy a fraction of that screw channel. This degree of screw channel fill is dictated by a number of factors including screw speed, feed rate and material rheology. Two further observations may be drawn from Figure 6-9 and these are described as follows;

- Some of the viscous melt contained within the partially filled screw channels orientates so as to be in contact with the trailing screw flights (in addition to the outer barrel wall). This implies that material contained within a flow boundary that is not in contact with either the trailing screw flights or the outer barrel wall, will possess a free surface.
- Material crossing over from one screw channel to the next has to progress through the screw nip region, as described previously. Thus as material enters the nip region, some of the melt will be forced around the flight of the opposing screw. However as is seen by the processing experiment illustrated in Figure 6-9, the back-pressure exerted by performing this reorientation of fluid, forces a non-uniform build-up of material about the nip region.

Quantification of mixing, in terms of being able to predict computationally, the location of particle paths and interfaces between the various phases, within the different CICo-TSE conveying screw element sections, involves a number of challenging problems. As previously

Figure 6-9:
Experimental Still From the Processing of Diluted "Playstuff" Clay Within the Screw Sections of a CICo-TSE.

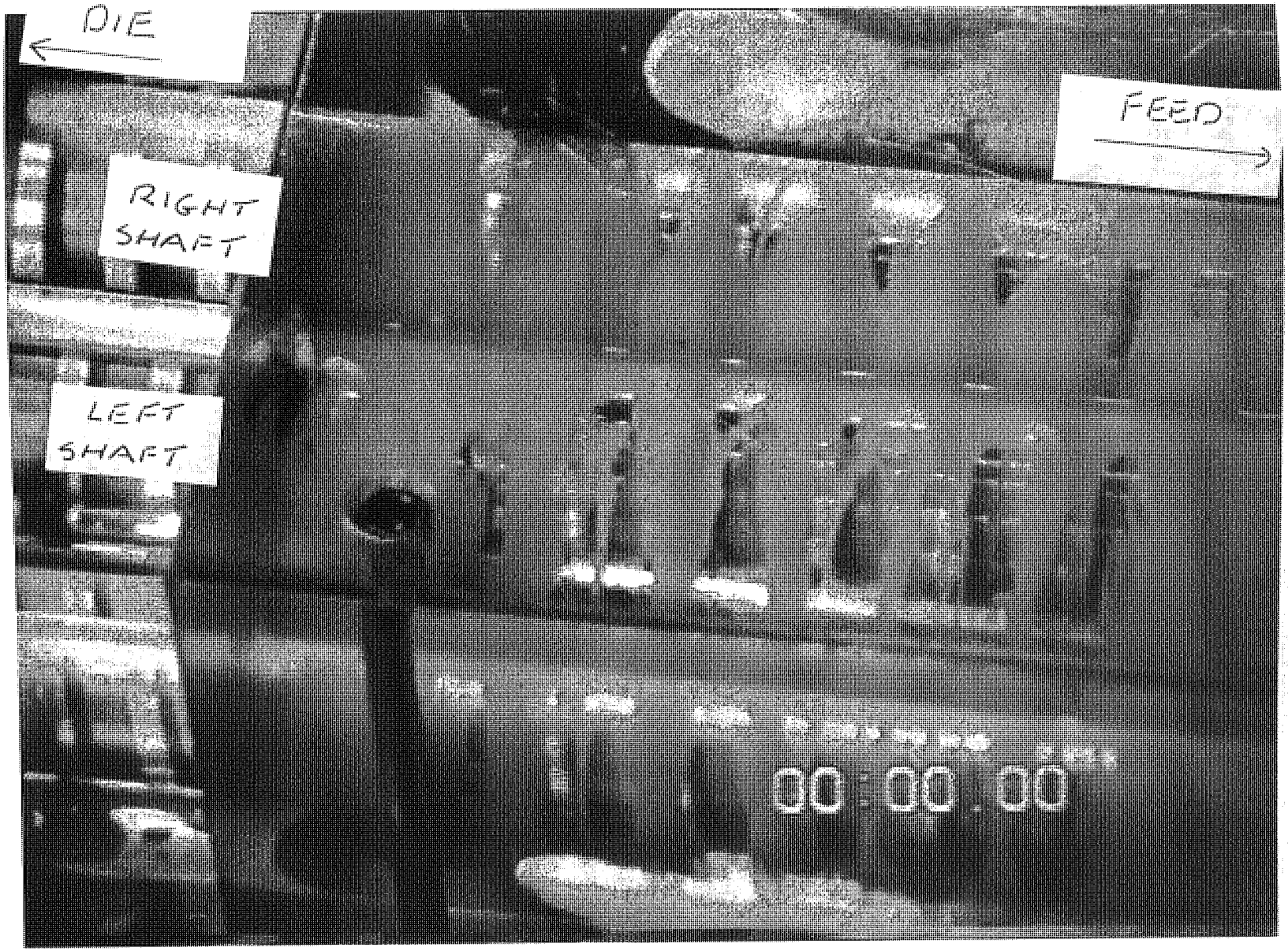

outlined, the CICo-TSE conveying screw elements when configured, possess two distinct domains; these are the channel flow volumes and the nip regions. As yet no acceptable unified theory exists for the prediction of mixing incorporating cross channel, down channel and nip region flow within the various CICo-TSE conveying screw element sections, that additionally takes into account different degrees of fill and free surface deformation. Many workers have tried to solve the screw flow problem by unwrapping the CICo-TSE screw channels [111, 112 and references therein], but this approach neglects both the nip region and the leakage of viscous material over the screw flights. Szydlowski and White in 1987 [113] included some additional terms to calculate the corrected fluid fluxes caused by the inclusion of the nip region, but no mention was made of the degree of mixing attained. Kalyon *et al* [52, 74, 90-91, 114] predicted mixing within the screw channel volumes by monitoring a deforming interface between two materials packed between the screw flights. Good correlation between the simulated and experimental results was reported for the double-flighted conveying screw elements, however, few quantitative results were given. In addition, the results reported in the work of Kalyon *et al*, were for fully filled screw channels only. The reason for considering only fully filled screw channels is simply explained; partially filled screw channels involve complex free surfaces which leads to some degree of uncertainty as to the exact locations of free surface boundaries, especially about the screw nip region. As outlined in Chapter 3, Polyflow possesses state-of-the-art modules for predicting free surface boundaries, however for this work, free surfaces are not considered. This thus dictates that for the work reported within this thesis on the simulation of flow within the single-flighted conveying screw elements, may be for fully filled screw channels only, thus excluding any consideration of free surface analysis.

Figure 6-10 shows an exposed cross section, significantly magnified and obtained as a result of processing two different coloured samples of "Playstuff" clay packed initially within the channel of the 24 mm pitched, right hand side single-flighted conveying screw element. The Y-Z cross sectional plane shown in Figure 6-10 was taken along the line A-A' as shown in Figure 6-3. The right hand side of the sample is seen to have been slightly deformed during sampling due to the softness of the clay used. At the start of each experiment a fixed volume of clay was packed into one screw channel, with, initially, purple clay occupying the left-hand-side of the screw channel and orange clay occupying the right. The results of the simulation of this same process using Polyflow, are shown in Figures 6-11 and 6-12, with Figure 6-11 showing the initial conditions at $t = 0$ and Figure 6-12 illustrating the predicted result after some time t. In both the predicted CFD result, shown in Figure 6-12, and the experimental result, shown in Figure 6-10, the section of sample surface in contact with the outer barrel wall, has travelled approximately the same axial distance. Comparison of the

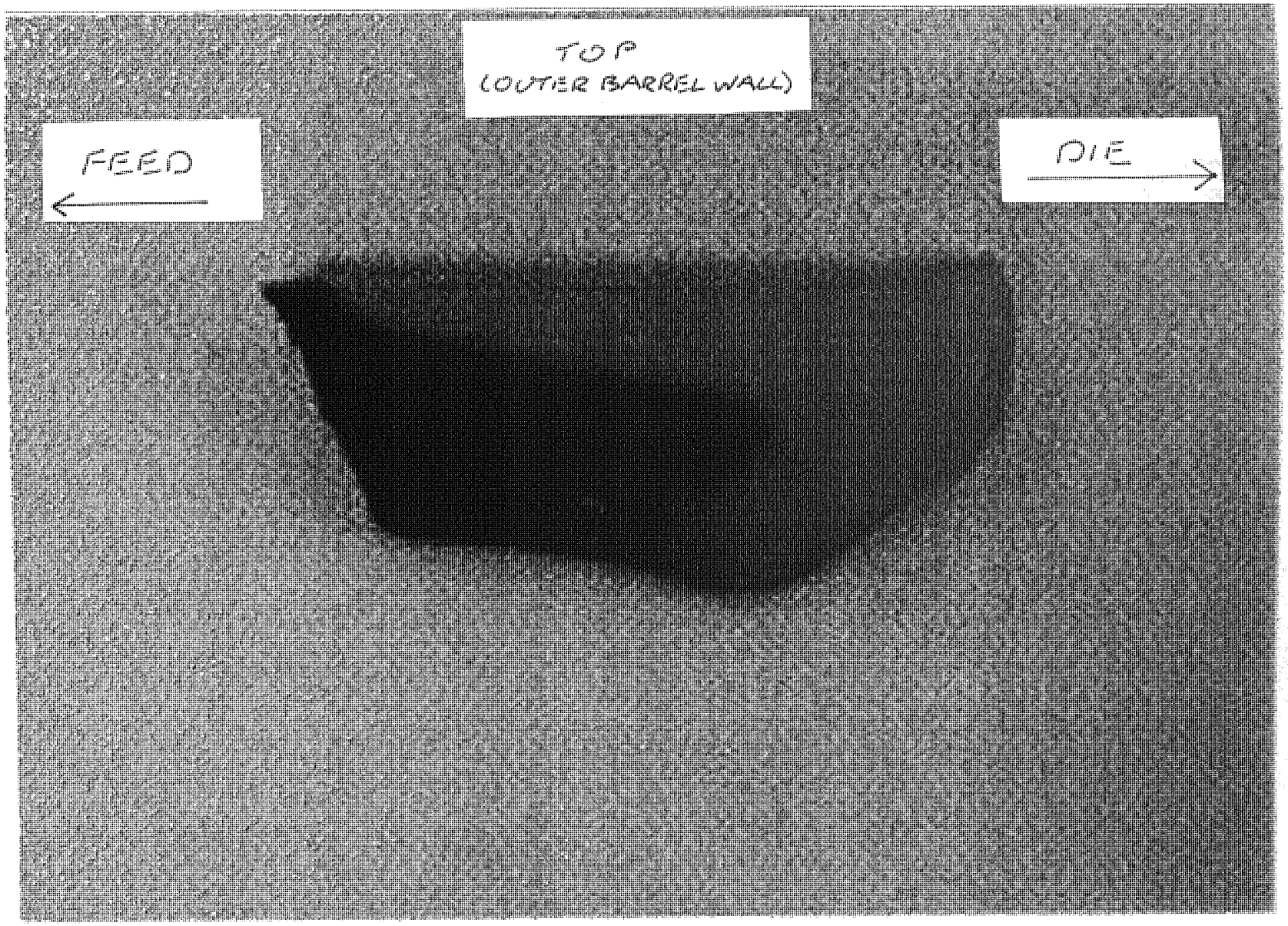

Figure 6-10:
Magnified Cross Section in the Y-Z Plane Taken at the Position Indicated Within Figure 6-3, as a Result of Processing Two Different Coloured "Playstuff" Samples Side-by-Side Within the Channel of a 24 mm Pitched Single-Flighted, Conveying Screw Element.

Figure 6-11:
Simulation of the Deformation of an Interface Between Two Viscous Materials Within the 24 mm Pitched Single-Flighted, Conveying Screw Elements; Initial Y-Z Cross Section.

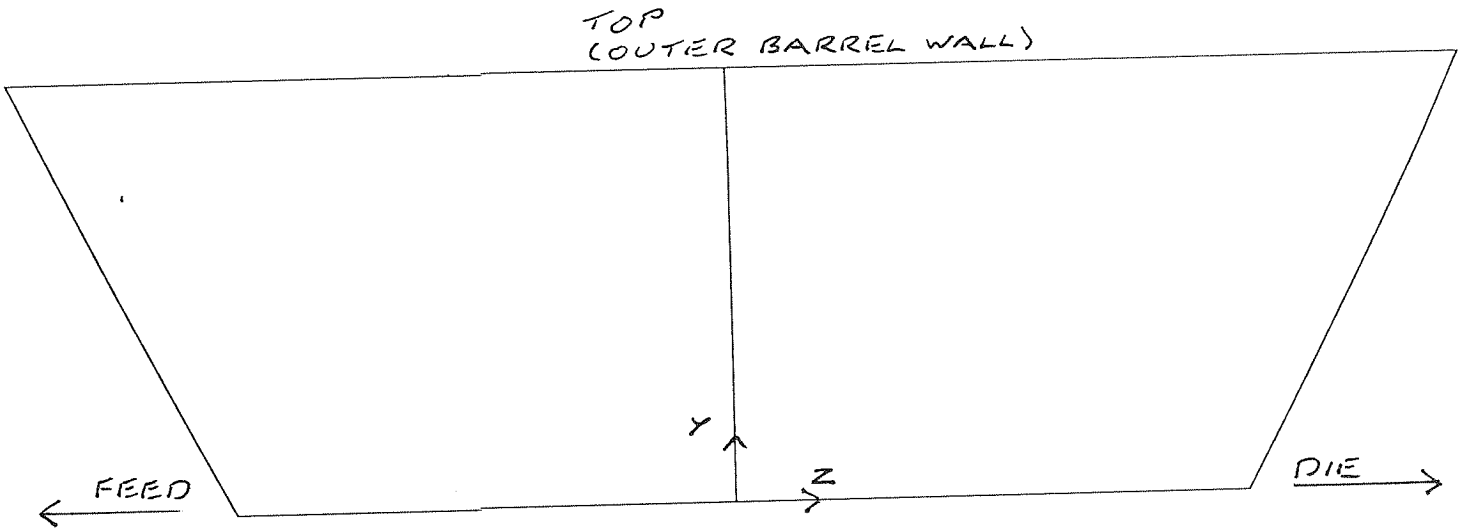

Figure 6-12:
Simulation of the Deformation of an Interface Between Two Viscous Materials Within the 24 mm Pitched Single-Flighted, Conveying Screw Elements; Final Y-Z Cross Section.

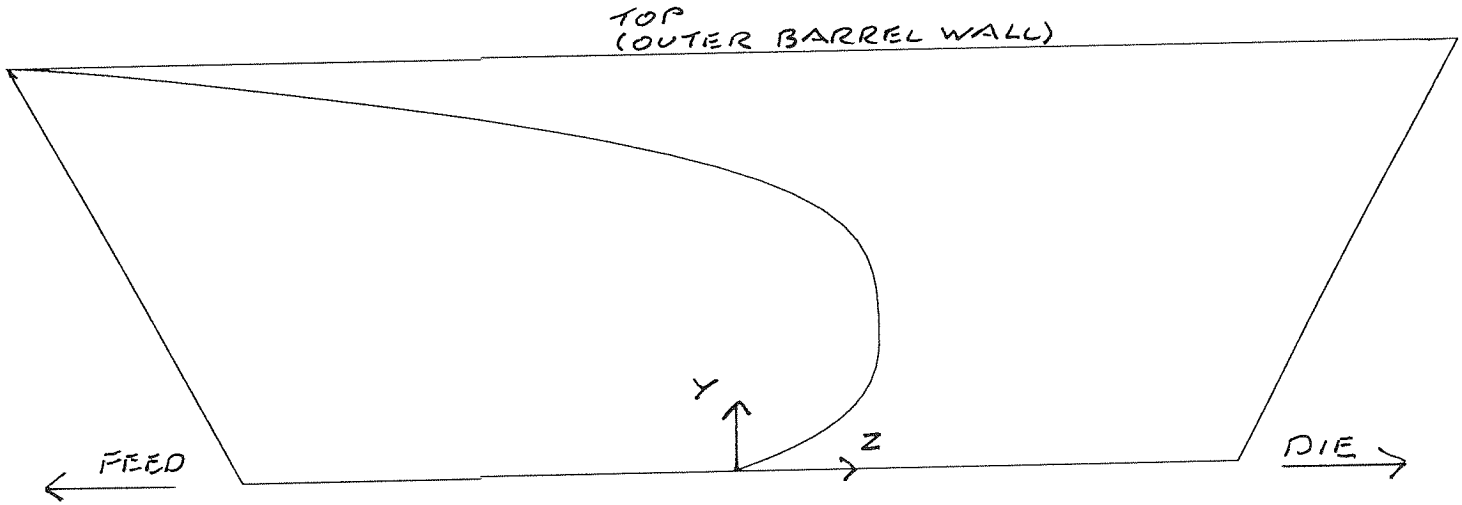

results shown in Figures 6-10 and 6-12 demonstrates a good correlation between experimental and simulated results. Before any sweeping conclusions are drawn about validity of the simulation model, however, a more rigorous appraisal of both the experimental and simulated processes and the assumptions behind the model needs to be undertaken.

6.2.1 Experimental Process

Figure 6-13 shows the sample remaining in the channel of the right hand screw element, after processing of the two, pre-packed viscous clay samples by approximately 2π revolutions. This number of revolutions corresponds to an axial progression along the barrel of approximately 24 mm (the exact sample position of the cross section shown in Figure 6-10 is also evident from this figure). However, the fraction of the sample surface in contact with the outer barrel wall for the predicted CFD result shown in Figure 6-12, has not progressed axially by 24 mm, instead it has been moved by a considerably less amount, calculated to be approximately 8 mm (this is shown in Figure 6-15). This discrepancy may be accredited to the presence of some degree of material slip between the viscous clay and the surface of the outer barrel wall. Due to the fact that material slip between the clay samples and the CICo-TSE mechanical model elements and outer barrel wall was not quantified experimentally, it will be assumed that the discussion of comparison between experimental and simulated models given in this chapter, will ignore the effects of material slip. It would be advantageous for future research programs to investigate and quantify experimental material slip for different viscous materials and to incorporate also, degrees of material slip within the time-dependent CFD simulations.

6.2.2 Computational Model

The results of the time-dependent simulation of the experiment shown in Figure 6-13, utilising the simulation techniques described in Chapter 4, are shown in Figures 6-14 to 6-17. For identical initial flow problem parameters and solution tolerances assigned, Figure 6-14 shows the outcome of using the Crank-Nicolson integration method for the discretisation of the flow problem, whilst Figure 6-15 shows the result of utilising the Implicit Euler integration method. As described in Chapter 3, for flow problems involving various shear-rate dependent viscosity models, computational solutions may be obtained by utilising either the Newton or Picard iteration scheme. The choice of iteration scheme depends upon the viscosity model chosen and, as a guide, it is usually more advantageous to utilise the Picard scheme for viscosity models involving high non-linearity. However, for problems where a solution could be obtained by using either of these two iteration schemes, even though the solutions obtained will be derived by different numerical routes, the results generated by either scheme are

Figure 6-13:

Total Remaining Sample in the Right Hand Screw Element Channel, Resulting From the Processing of Two Different Coloured "Playstuff" Samples Side-by-Side Within the 24 mm Pitched Single-Flighted Conveying Screw Elements.

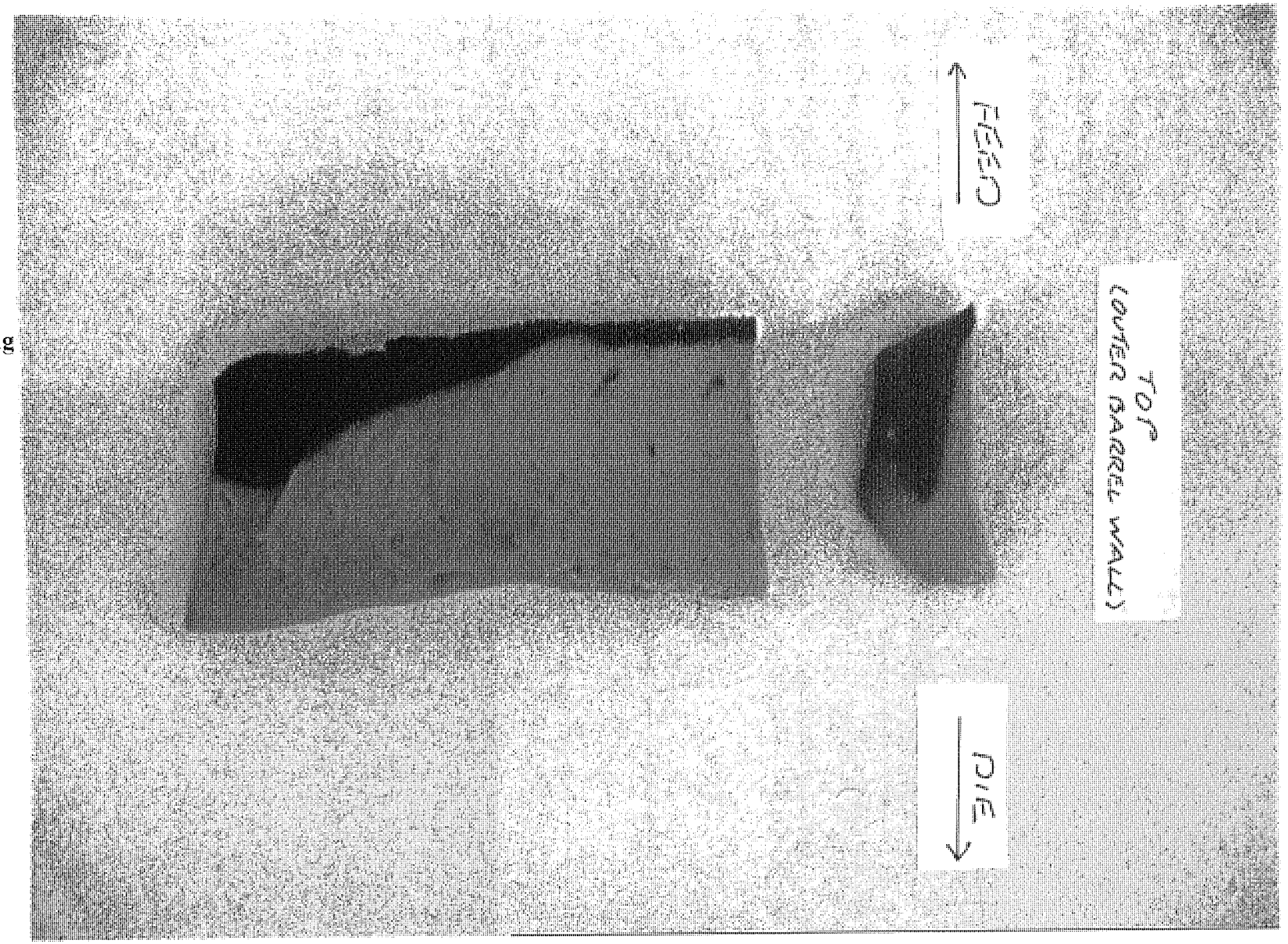

Figure 6-14:
Simulation Snapshots at Different Time Intervals for the Deformation of an Interface Between Two Viscous Materials, Processed Within the 24 mm Pitched Single-Flighted, Conveying Screw Elements; Results Using the Crank-Nicolson Integration Method.

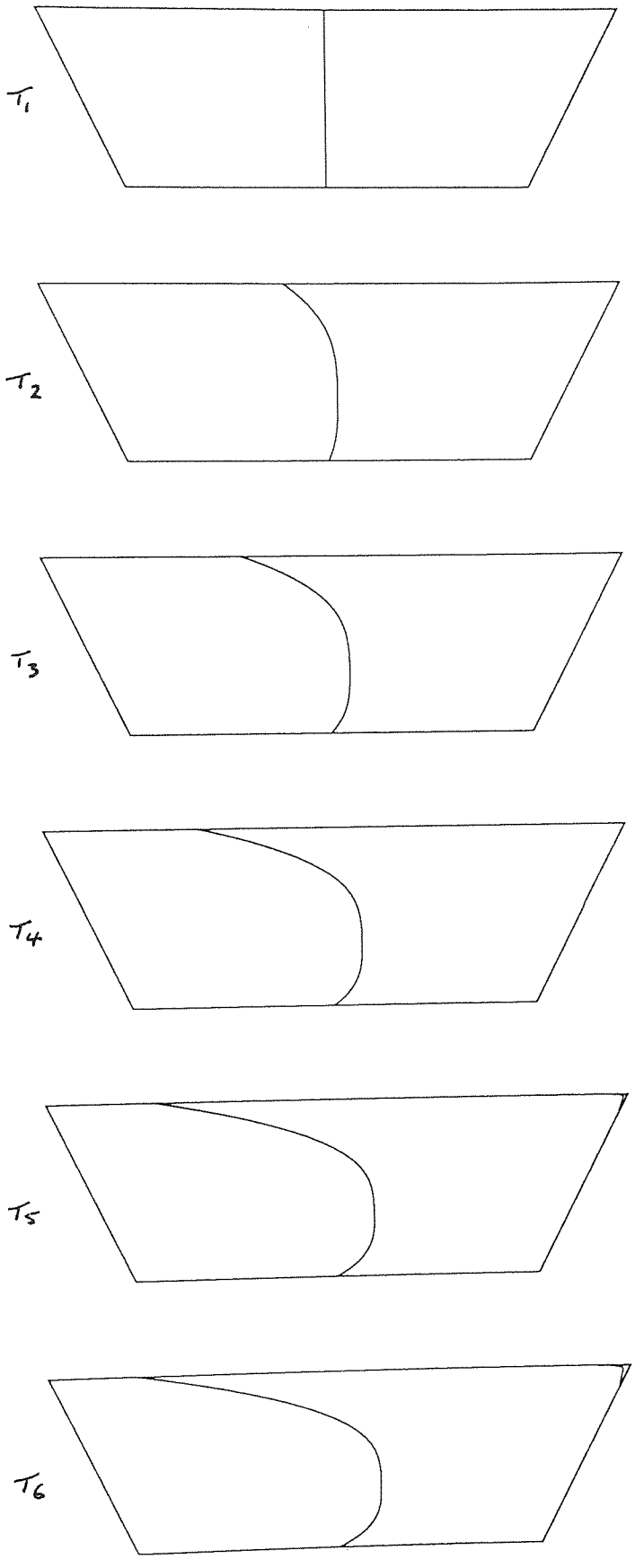

Figure 6-15:
Simulation Snapshots at Different Time Intervals for the Deformation of an Interface Between Two Viscous Materials, Processed Within the 24 mm Pitched Single-Flighted, Conveying Screw Elements; Results Using the Implicit Euler Integration Method.

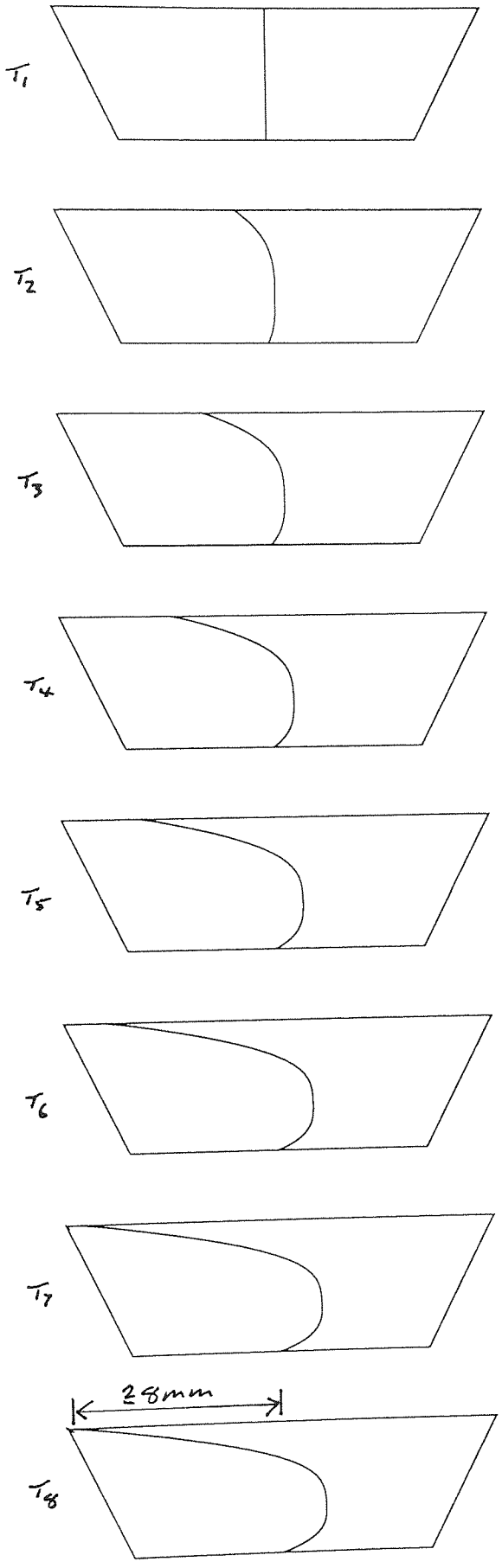

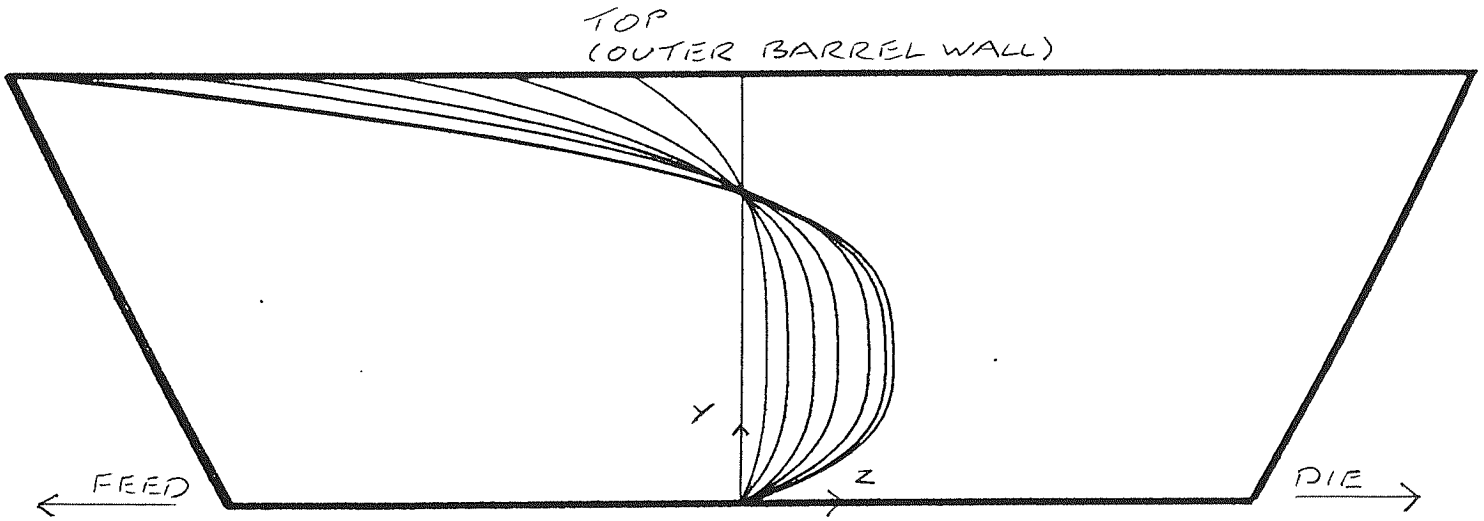

Figure 6-16:
Results Obtained in Figure 6-14 Overlaid so as to Illustrate the Position of the Pivot Point of the Deforming Interface With Time (Crank-Nicolson Integration Method).

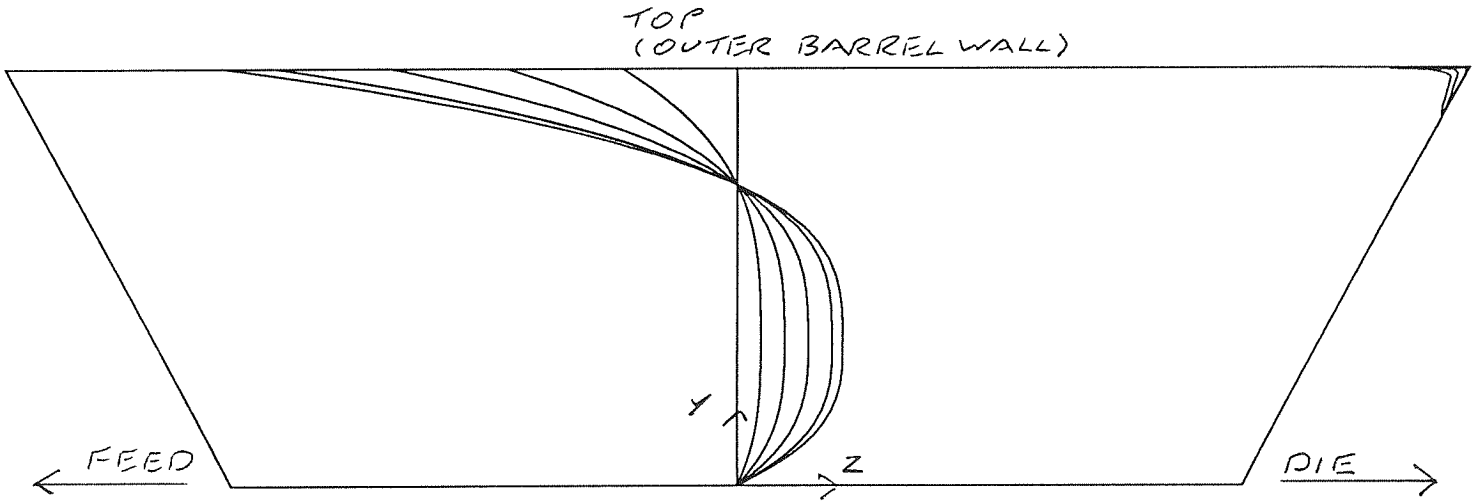

Figure 6-17:
Results Obtained in Figure 6-15 Overlaid so as to Illustrate the Position of the Pivot Point of the Deforming Interface With Time (Implicit Euler Integration Method)

always the same. This is also true for the utilisation of the various time-dependent integration methods. Identical results are obtained no matter which time integration method is chosen, however the suitability of the method is dependent upon both the accuracy needed and the stability of any solutions obtained.

The Crank-Nicolson and Implicit Euler schemes differ in their inherent precision tolerances and it is these tolerances that are used as a measure to assess the quality of the results obtained at each time integration step. The mathematical theories for the various time-dependent solution techniques are well documented [29-31] and they will not be reprinted here, however a brief discussion about time-dependent tolerance values follows. Numerical solution of any flow problem is greatly assisted by the incorporation of an initial guess into the flow calculation (the assignment of boundary conditions being part of this initial guess). For any time-dependent problem, it is clearly advantageous to firstly obtain a steady state solution of the flow problem, thus obtaining a solution to the flow problem at time $t = t_0$. Even though this steady state result is obtained by approximate numerical means, as described in Chapter 4, to all intents and purposes, this solution, together with the initial boundary conditions, may be considered as the exact solution at t_0. Consequently, this exact solution may be used as a subsequent initial guess, for obtaining the solution of the flow problem at time $t = t_1$, where t_1 represents some discrete time step. If a solution is found for t_1, then the results obtained for that time step may be considered as an exact solution and thus subsequently used as an initial guess for the solution of the flow problem at time $t = t_2$, and so on. To control the accuracy of any solutions obtained by using these discrete time steps, Polyflow allows the assignment of a tolerance value, which is utilised as a maximum admissible relative truncation error for the numeric solution of X_{n+1}, with reference to the exact solution. Thus when designating the Crank-Nicolson method within a particular time-dependent scheme, Polyflow inspects the square of the calculated truncation error in the time step with the user specified tolerance, whereas if the Implicit Euler scheme is used, Polyflow checks only the error. At the point when this truncation error between X_{n+1} and the exact solution exceeds the User's specified tolerance value, the calculation will automatically stop. The assignment of tolerance is important and, if it is specified at too high a value, then loss of accuracy will result. Moreover, too high a value would also result in unrealistically large time steps being used (the time steps utilised are not constant, instead the magnitude of each is increased automatically as a function of the number of successive solutions obtained), which would, in all probability, bring about a diverging solution. As a rule, it is advisable that the tolerance values assigned, should be between 0.001 and 0.01.

For the deforming interface problem presented within this chapter, used in the investigation of cross channel flow within the CICo-TSE 24 mm pitched, single-flighted conveying screw

elements, as the magnitude of the deformation of the interface between the two materials increases over time, the more difficult it becomes to obtain stable results for each subsequent time-marching step examined. For the two time integration schemes investigated, different critical values of time were reached whereby the relative truncation error between the last exact solutions and the solutions at these critical time values, exceeded the tolerance specified (the tolerance being 0.001 for both schemes). For the results shown in Figure 6-14 using the Crank-Nicolson method, the fifth time step shown at $t = 0.04000$ sec was the last exact solution obtained, whereas the sixth time-step shown at $t = 0.04453$ sec was the limiting one. However, for the results shown in Figure 6-15 using the Implicit Euler method, the seventh time step shown at $t = 0.06012$ sec was the last exact solution obtained, whereas the eighth time-step shown at $t = 0.06330$ sec was the limiting value. The difference in results is not that unexpected as the precision utilised by the Implicit Euler method is less stringent than that demanded by the Crank-Nicolson method.

The values of the time steps presented here seem quite small, however, their accuracy is easily verifiable. Let us examine the eighth time-step result from the Implicit Euler method (i.e. for $t = 0.06330$ sec). The velocity assigned at the outer barrel wall was 0.13 m sec^{-1}, thus the layer of fluid in contact with the outer barrel wall, possesses that value of velocity. Even though in reality the outer barrel wall is stationary, what has been assigned is the inverse problem whereby the screw shafts are stationary relative to a "moving" outer barrel wall. The value of 0.13 m sec^{-1} assigned for the wall velocity, corresponds to the velocity of the outer barrel wall, 0.020075 m away from the centre of the screw shafts, which are rotating at 2.06π rad sec^{-1} (61.8 RPM). For the eighth time-step, the fraction of the sample surface in contact with the outer barrel wall has travelled 0.008235 m from its initial position at t_0 (this distance is obtained by inspection of Figures 6-11 and 6-12, with reference to the dimensions specified within Appendix N). Thus the time taken to travel this distance may be calculated as follows;

$$\frac{0.008235\,\text{m}}{0.13\,\text{m}\,\text{sec}^{-1}}$$

$= \underline{0.06335\ \text{sec}}$ (compared to $t = 0.06330$ sec reported for time-step eight)

Figures 6-16 and 6-17 show the results of overlaying each of the respective time step findings presented within Figures 6-14 to 6-15 for the Implicit Euler and Crank-Nicolson methods respectively. What may be observed from both of these illustrations is the fact that there is a pivot point around which the interface is deformed by the shear rate profile generated. It is found that this pivot position corresponds to the centre of the swirl region

shown in Figure 6-18, which displays the velocity vector profile obtained from the steady state solution of the flow problem. Using the following formula;

$$\xi = \frac{y}{H} \tag{6-3}$$

where H is the channel depth (0.00489 m for the 24 mm pitched single-flighted conveying screw elements), the pivot point for the deforming interface between two (identical) power law fluids and thus the position for the centre of swirl, is obtained by inspection of Figures 6-16 and 6-17 and it is found to be at $\xi \approx 0.72$ (i.e. for a Y value of approximately 0.0035 m from the screw collar).

The length of the interface between the two power law fluids may be plotted against each time step taken within the calculation. The results obtained using the Implicit Euler scheme are tabulated within Table 6-2 and plotted in Graph 6-2 (the results obtained from using the Crank-Nicolson scheme are tabulated in Table 6-3). The shape of the interfaces obtained at each discrete time period using either the Implicit Euler or Crank-Nicolson scheme (shown in Figure 6-14 to 6-17), are of a complex parabolic nature. The plot of Graph 6-2, demonstrates that the growth of the interface with increasing time period, is not linear. Instead it is found that the interface deforms at different rates, dependent upon its position within the cross channel domain. This may be illustrated by Figure 6-19, which presents local shear rate isolines overlaid onto velocity vector profiles, for motion of the power law fluid described in Chapter 4, within the screw channel of the 24 mm pitched, single-flighted conveying screw element. For the sixth, seventh and eighth time steps obtained by using the Implicit Euler scheme (shown in Figure 6-15), there are portions of the interface which are contained within the region close to the trailing screw flight and the outer barrel wall. As is indicated in Figure 6-19, those portions of the interface incident within this region, undergo a more complex shearing mechanism. Indeed it is no surprise that the time-dependent calculation performed using the Implicit Euler scheme ceased once the eighth time step was reached, because the incorporation of these complex shear effects adds significantly to the uncertainty of the time-dependent calculation performed at that time step. Inspection of Figure 6-19 reveals that the position where the shear rate value is zero, is found to be at $\xi \approx 0.42$ (i.e. for a Y value of approximately 0.0021 m from the screw collar). Comparing this value with that found for the location of the centre of the swirling motion ($v_{xy} = 0$, $\xi \approx 0.72$) reveals that they are different. In fact the position where the shear rate is zero, is the location of the extremum of the velocity profile and this proposition will be confirmed later within this section.

Cross channel and down channel fluid flow within the screw channels of the SSE screw

Figure 6-18:

Velocity Vector Profiles for the Cross Channel Flow Within the Y-Z Plane of the 24 mm Pitched Single-Flighted, Conveying Screw Elements.

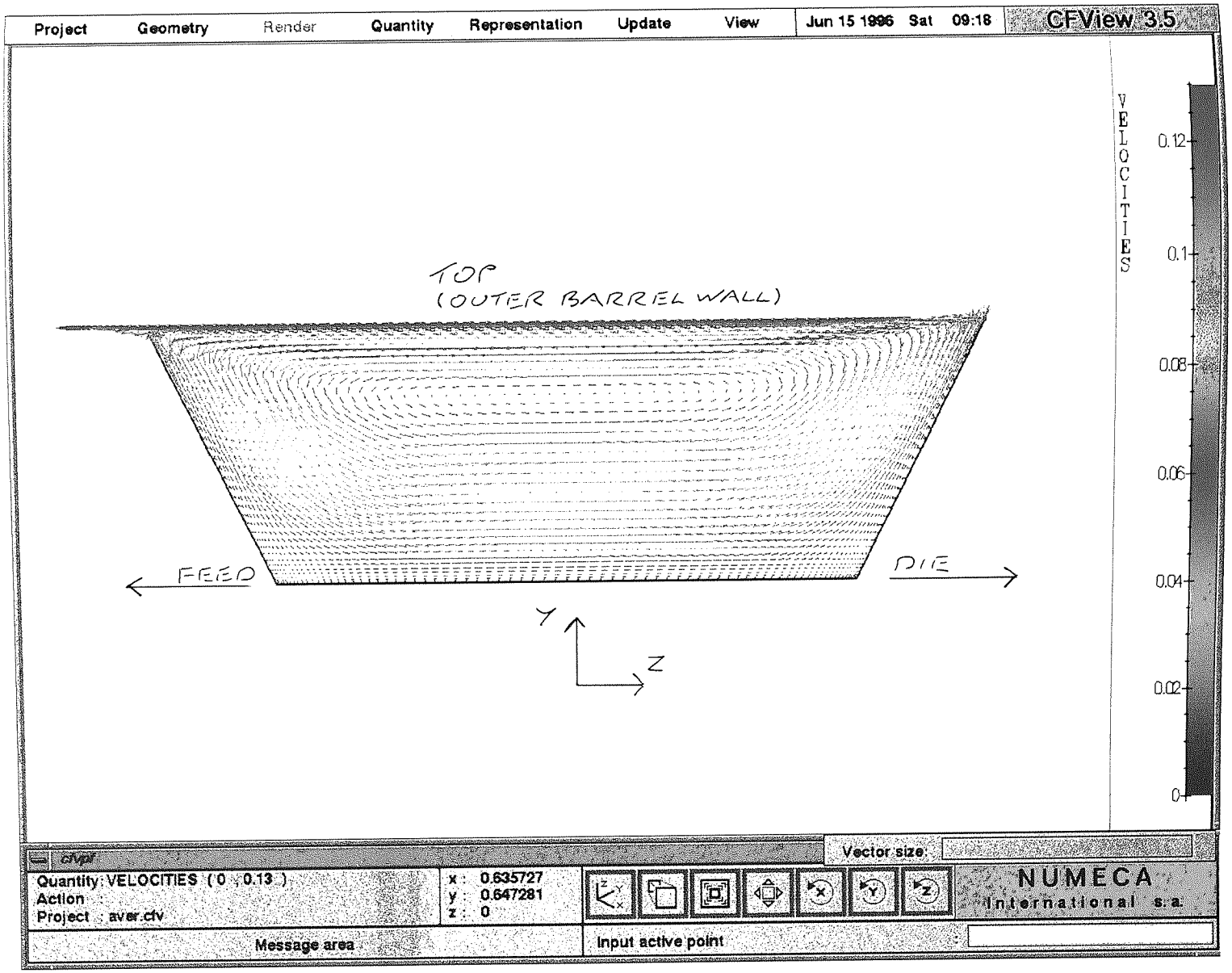

TABLE: 6-2

2D Time-Dependent Results Table (Single-Flighted Conveying Screw Elements) - Growth of the Interface Between Two Materials With Increasing Time, Obtained Using the Implicit Euler Scheme

Time Step	Time (sec)	Length of Interface (m)
1 (Time Zero)	0.000	0.00489
2	0.010	0.00551
3	0.020	0.00667
4	0.030	0.00827
5	0.040	0.00978
6	0.051	0.01165
7	0.060	0.01307
8 (Limiting Time)	0.063	0.01378

TABLE: 6-3

2D Time-Dependent Results Table (Single-Flighted Conveying Screw Elements) - Growth of the Interface Between Two Materials With Increasing Time, Obtained Using the Crank-Nicolson Scheme

Time Step	Time (sec)	Length of Interface (m)
1 (Time Zero)	0.000	0.00489
2	0.010	0.00551
3	0.020	0.00667
4	0.030	0.00827
5	0.040	0.00978
6 (Limiting Time)	0.045	0.01040

Graph 6-2:

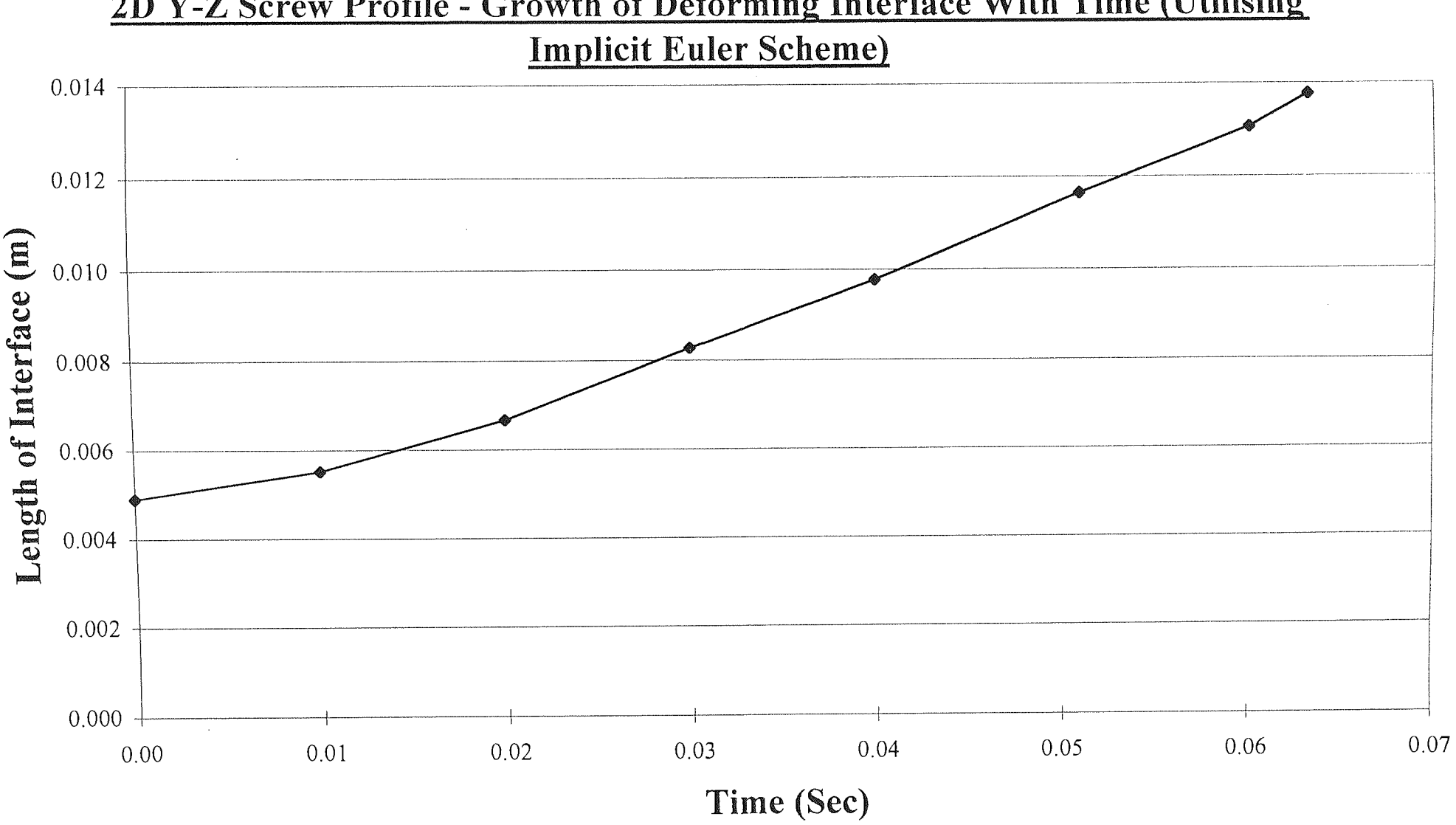
2D Y-Z Screw Profile - Growth of Deforming Interface With Time (Utilising Implicit Euler Scheme)
Length of Interface (m)
0.014
0.012
0.010
0.008
0.006
0.004
0.002
0.000
0.00
0.01
0.02
0.03
0.04
0.05
0.06
0.07
Time (Sec)

Figure 6-19:
Velocity Vector Profiles, Overlaid onto Local Shear Rate Isolines for the Cross Channel Flow Within the Y-Z Plane of the 24 mm Pitched Single-Flighted, Conveying Screw Elements; Power Law Fluid.

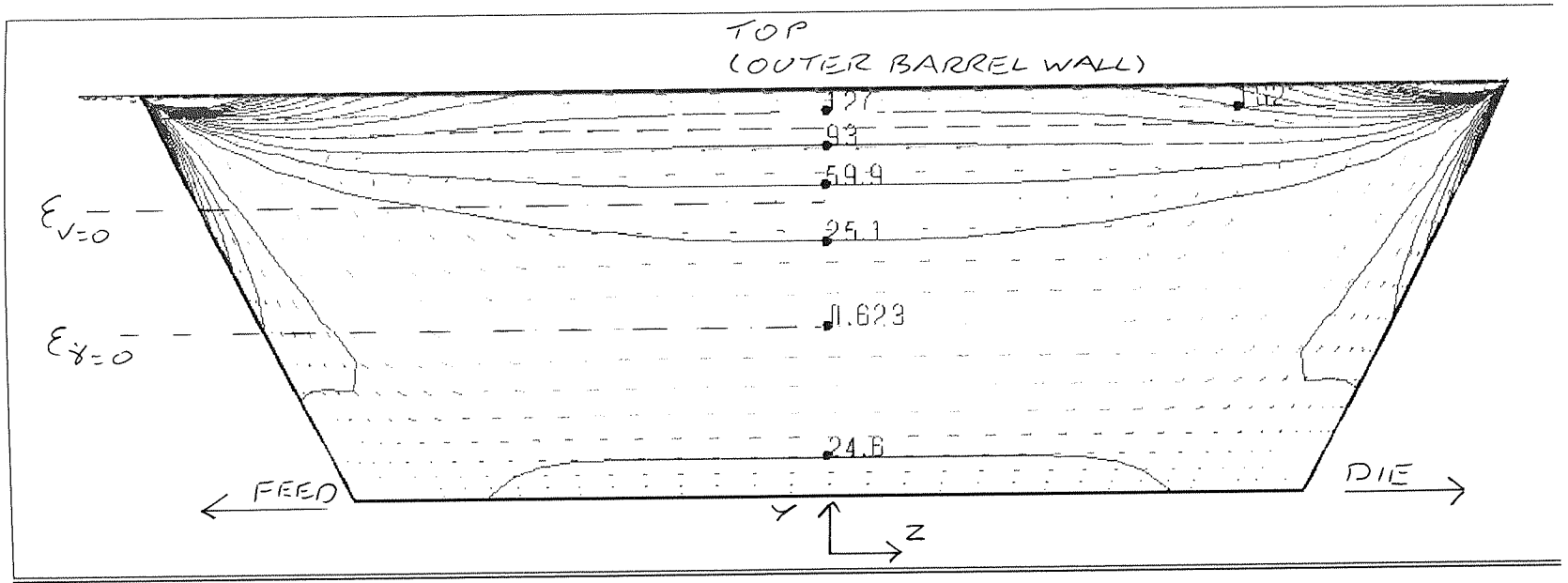

Figure 6-20:
Velocity Vector Profiles, Overlaid onto Local Shear Rate Isolines for the Cross Channel Flow Within the Y-Z Plane of an arbitrary SSE Screw Element; Power Law Fluid.

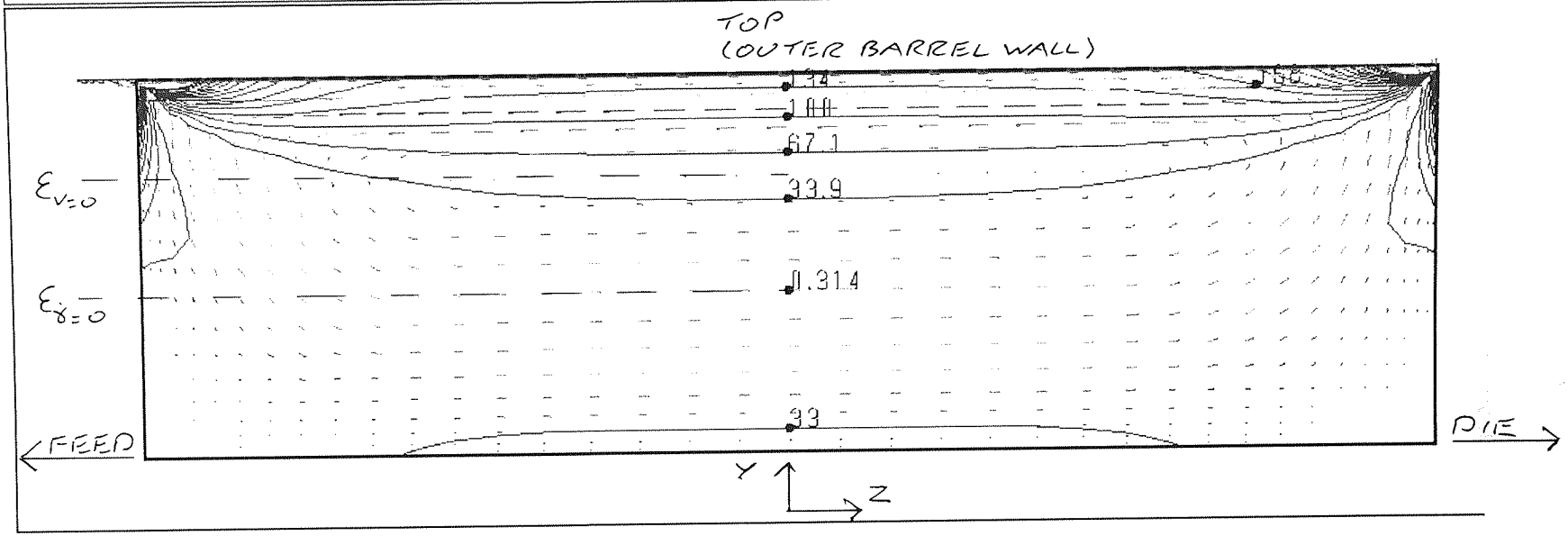

elements, may be predicted and quantified by known analytical and numerical means. Rauwendaal [10, 16] goes into much detail about Newtonian and power law fluid flow within the various regions of the SSE screw elements. Very little, however, has been published on the prediction of flow parameters, such as shear rate and velocity profiles, within the various CICo-TSE screw elements, probably due to the reasons highlighted previously. Figure 6-20 displays, for the identical parameters represented in Figure 6-19, the flow fields within the channel of an arbitrary SSE screw element, constructed with the same screw pitch and channel depth as the CICo-TSE screw element. Apart from the verticality of the flight faces, the cross channel geometries of each of these two screw types are not that dissimilar. Thus, it is reasonable to examine Rauwendaal's approach to flow analysis within the SSE screw elements, as applied to flow within the 24 mm pitched, CICo-TSE single-flighted conveying screw elements, already presented within this thesis (with the exclusion of flow within the CICo-TSE screw nip region, which is considered later within this chapter).

The approach derived by Rauwendaal, using the parallel plate approximation, for down channel flow of Newtonian fluid within the screw channels of the SSE, involves the use of different known pressure gradients. These down channel pressure gradients influence the nature of the down channel fluid velocities, dependent upon whether these pressure gradients are positive, negative or zero in value. They are related to the axial pressure and screw flight angle, such that;

$$g_x = g_a \sin\varphi \tag{6-4}$$

Because the CFD work on CICo-TSE screw elements presented within this thesis considers the deformation of an interface in the cross channel direction only and excludes pressure terms for the incorporation of down channel motion, the theory of cross channel flow only is considered here. Due to the fact that there is no net flow in the cross channel direction, it is necessary that cross channel pressure gradients for Newtonian fluids are derived instead using the following equation;

$$g_z = \frac{6\mu v_{bz}}{H^2} \tag{6-5}$$

As is seen in Equation 6-5, cross channel pressure gradient is dependent upon Newtonian viscosity. Rauwendaal [10] however, states that cross channel pressure gradient is unknown for non-Newtonian fluids, such as those showing power law behaviour and may be derived by approximate numerical means only. Because the prediction of flow parameters for a power

law fluid is complicated and because cross channel pressure gradient cannot be calculated by analytical means, non-Newtonian cross channel behaviour has not been further investigated in this study. Instead the analytical solutions for the flow of a Newtonian fluid derived by Rauwendaal are considered. Hence, Figures 6-21 and 6-22 show the local shear rate isolines overlaid onto velocity vector profiles, for cross channel motion of a Newtonian fluid ($\eta = \mu = 4400$ Pa sec, i.e. the viscosity obtained for n = 1 in the power law equation utilised) within the screw channels of the CICo-TSE and SSE screw elements respectively. The behaviour of the Newtonian fluid within the cross channel profile of the CICo-TSE single-flighted conveying screw elements shown in Figure 6-21, is similar (though not identical) to Newtonian flow within the screw channels of the SSE screw element shown in Figure 6-22. In addition, for the same values of ξ at positions about the centre of the screw channel, the value of shear experienced by the Newtonian fluid is virtually identical in each screw profile. Thus the equations that Rauwendaal [10, 16] derives for the prediction of velocity and shear rate of a Newtonian fluid about the central regions of the SSE screw element channels, may be utilised with reasonable confidence for the prediction of flow within the 24 mm pitched, CICo-TSE single-flighted conveying screw elements. They are as follows;

$$v_z(\xi) = v_{bz}(-2\xi + 3\xi^2) \tag{6-6}$$

$$\dot{\gamma}_{yz} = 2\frac{v_{bz}}{H}(-1 + 3\xi) \tag{6-7}$$

Thus various values of ξ were introduced into equations 6-6 and 6-7 and estimates for cross channel velocity, v_z and shear rate, $\dot{\gamma}_{yz}$ calculated; the results obtained are shown in Tables 6-4 and 6-5 and plotted in Graphs 6-3 and 6-4 respectively. The positions where the velocity and shear rate values are zero, may be calculated using these two equations and they are found to be at $\xi = 2/3$ for $v_z = 0$ (corresponding to a Y value of 0.00326 m from the screw collar) and $\xi = 1/3$ for $\dot{\gamma}_{yz} = 0$ (corresponding to a Y value of 0.00163 m from the screw collar). These values are identical to those obtained via the CFD simulations, as may be verified by inspection of Figures 6-21 and 6-22. In addition, as previously stated, the position where $\dot{\gamma}_{yz} = 0$, corresponds to the same position where the maximum negative value of v_z is to be found and this as shown in Graph 6-3. Again the results obtained from the CFD simulations display the same effect as shown in Figures 6-21 and 6-22. The following table summarises these results for ease of comparison;

Figure 6-21:
Velocity Vector Profiles, Overlaid onto Local Shear Rate Isolines for the Cross Channel Flow Within the Y-Z Plane of the 24 mm Pitched Single-Flighted, Conveying Screw Elements; Newtonian Fluid.

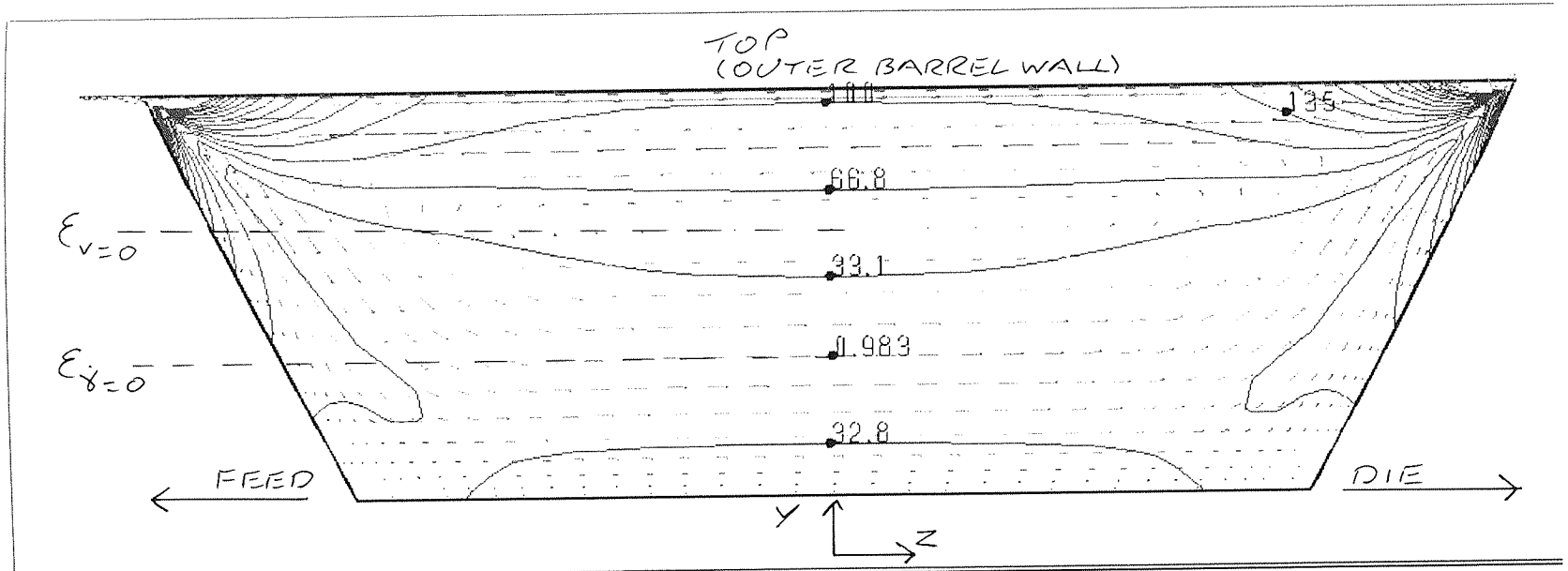

Figure 6-22:
Velocity Vector Profiles, Overlaid onto Local Shear Rate Isolines for the Cross Channel Flow Within the Y-Z Plane of an arbitrary SSE Screw Element; Newtonian Fluid.

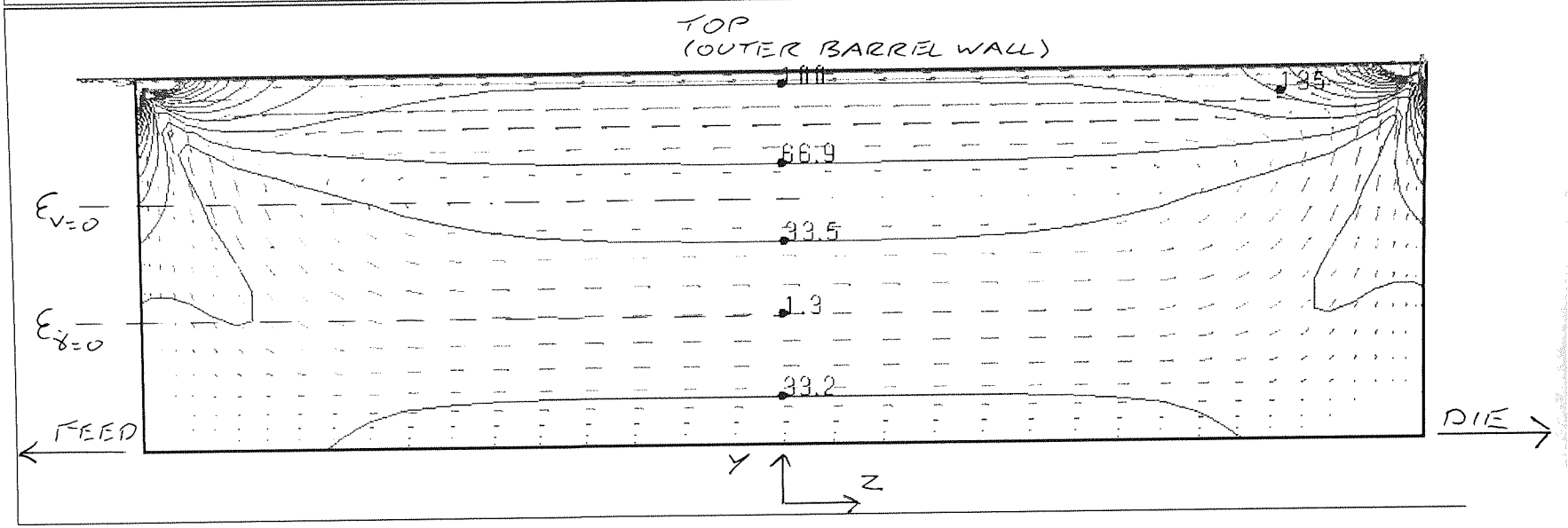

TABLE: 6-4

2D Time-Dependent Results Table (Single-Flighted Conveying Screw Elements) - Cross Channel velocity as a Function of Distance From Screw Collar for a Newtonian Fluid (Using Parallel Plate Approximation)

Dimensionless Length ξ	Distance From Screw Collar Y Value (m)	Cross Channel Velocity (m sec^{-1})
1.0000000	0.0048900	0.1300000
0.9202454	0.0045000	0.0910083
0.8179959	0.0040000	0.0482768
0.6666667	0.0032600	0.0137002
0.7157464	0.0035000	0.0000000
0.6134969	0.0030000	-0.0127216
0.5112474	0.0025000	-0.0309885
0.4089980	0.0020000	-0.0411005
0.3333333	0.0016300	-0.0433333
0.3067485	0.0015000	-0.0430577
0.2044990	0.0010000	-0.0368600
0.1022495	0.0005000	-0.0225074
0.0000000	0.0000000	0.0000000

TABLE: 6-5

2D Time-Dependent Results Table (Single-Flighted Conveying Screw Elements) - Local Shear Rate as a Function of Distance From Screw Collar for a Newtonian Fluid (Using Parallel Plate Approximation)

Dimensionless Length ξ	Distance From Screw Collar Y Value (m)	Shear Rate $\dot{\gamma}_z$ (sec^{-1})
1.0000000	0.0048900	106.3394683
0.9202454	0.0045000	93.6178755
0.8179959	0.0040000	77.3081411
0.6666667	0.0032600	53.1697342
0.7157464	0.0035000	60.9984067
0.6134969	0.0030000	44.6886723
0.5112474	0.0025000	28.3789379
0.4089980	0.0020000	12.0692035
0.3333333	0.0016300	0.0000000
0.3067485	0.0015000	-4.2405309
0.2044990	0.0010000	-20.5502653
0.1022495	0.0005000	-36.8599997
0.0000000	0.0000000	-53.1697342

Cross Channel Velocity as a Function of Distance From Screw Collar (Using Parallel Plate Approximation)

Graph 6-3:

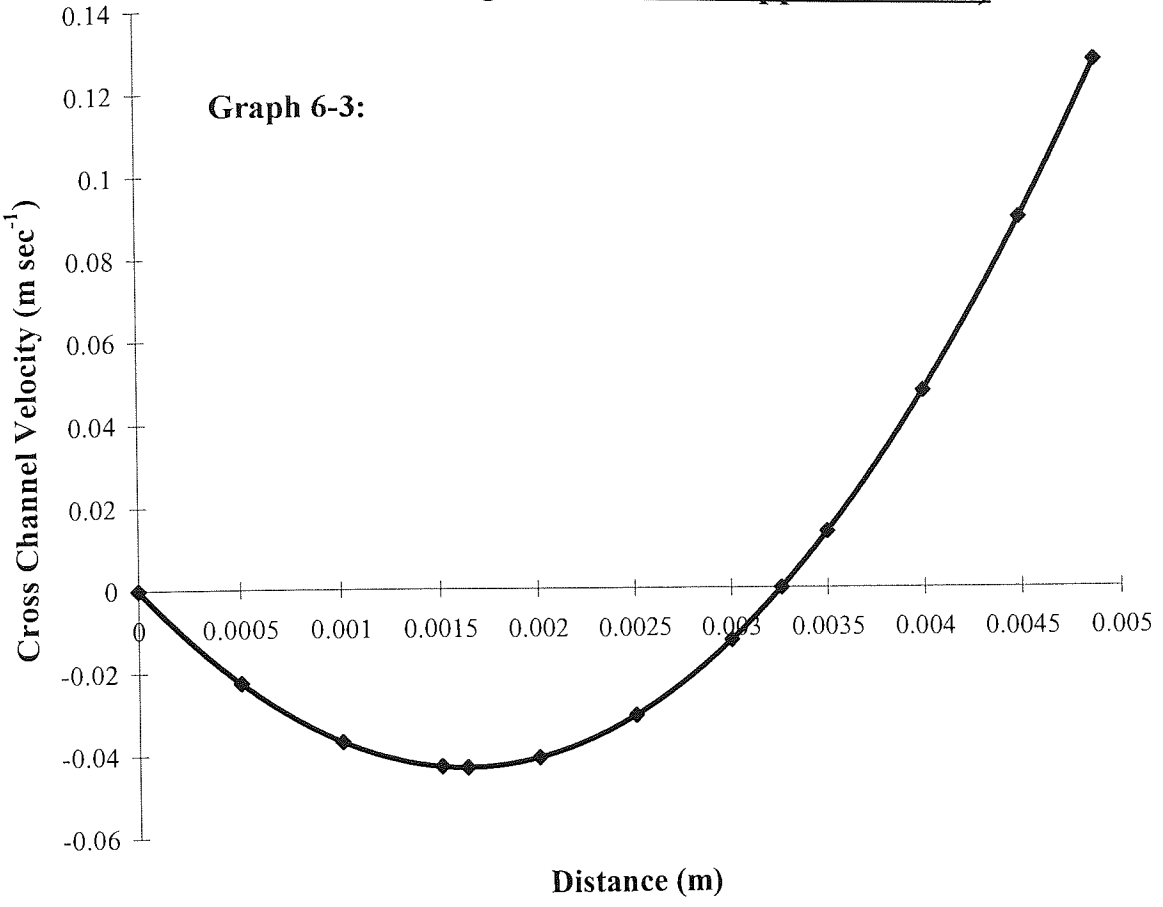

Local Shear Rate as a Function of Distance From Screw Collar (Using Parallel Plate Approximation)

Graph 6-4:

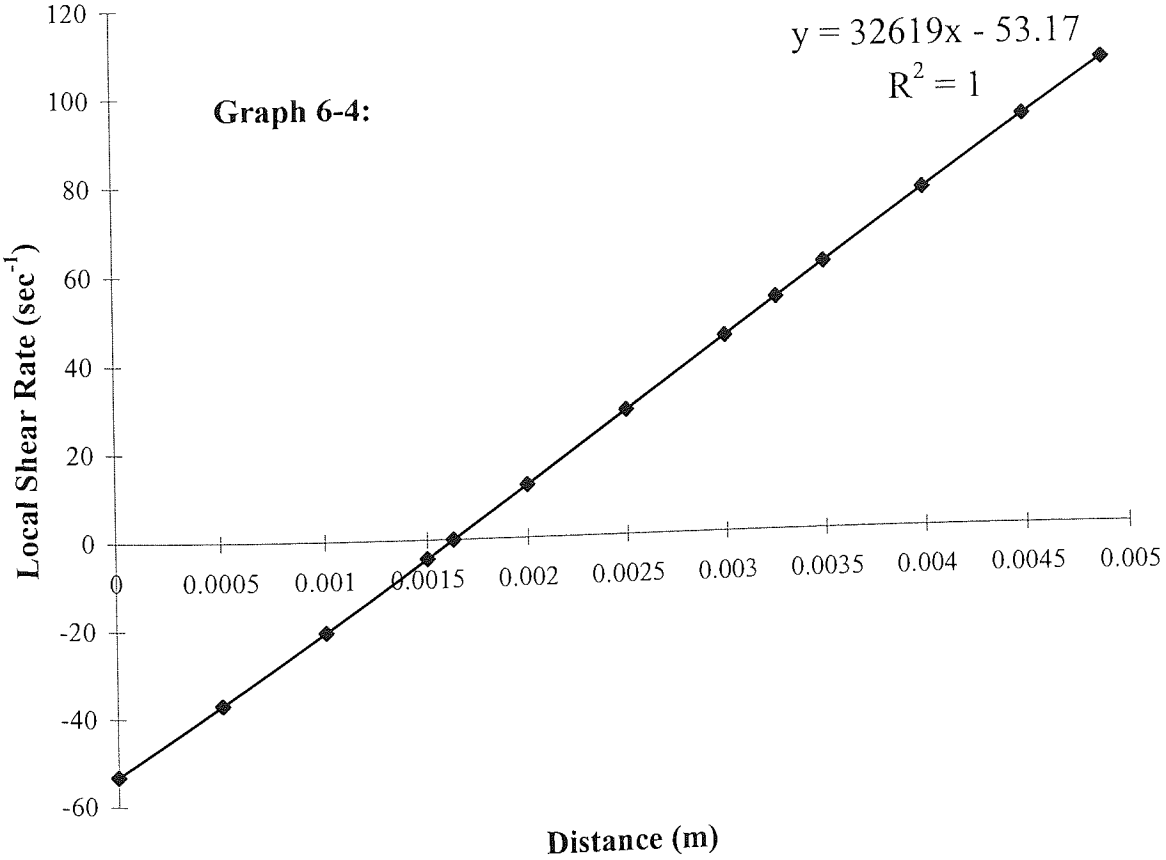

	Power Law Fluid		Newtonian Fluid		Experiment
	CICo-TSE Screw Element	SSE Screw Element	CICo-TSE Screw Element	SSE Screw Element	CICo-TSE Screw Element
$v_z = 0$	$\xi \approx 0.73$	$\xi \approx 0.74$	$\xi = 0.67$	$\xi = 0.67$	$\xi \approx 0.7$
$\dot{\gamma}_{yz} = 0$	$\xi \approx 0.43$	$\xi \approx 0.43$	$\xi = 0.35$	$\xi = 0.35$	-

Rauwendaal [16] also proposed that, due to the geometry of the screw elements of the SSE, two distinct flow regions exist within the cross channel domain. These two regions are known as the inner and outer recirculatory flow regions and material within either of these two regions experiences differing shear effects. Assuming Newtonian fluid flow only, the loci of these two regions are approximately the same for both the SSE screw elements and the CICo-TSE single-flighted, conveying screw elements. If we consider the deformation of a small cube as it travels around the cross channel domain, then Figure 6-23 speculates how this cube might deform within the outer recirculatory flow region over time and Figure 6-24 the deformation within the inner region. Due to both the position where $\dot{\gamma}_{yz} = 0$ and the cross channel velocity profile created within each of these two regions, the cube deforms by different mechanisms as it circulates.

- Outer recirculating flow region

  The cube when in the lower portion, travels in the direction of the shear force, but experiences drag, created by the non-slip boundary condition specified at the shaft wall and thus deforms as shown in steps 1 to 3. However, once the cube is located in the upper portion of the outer recirculating flow region, it travels in the direction of the shear force, but experiences no drag effect and thus it deforms as shown in steps 4 to 6.

- Inner recirculating flow region

  The cube whilst in the lower portion of the inner recirculating flow region, travels in the opposite direction to the shear force, thus it deforms as shown in steps 1 to 3, until it enters the upper portion where it travels in the same direction as the shear force, where it deforms as shown in steps 4 to 6.

It may be noted in Figures 6-23 and 6-24 that the shape of the cube (assuming the same

Figure 6-23: **2D Screw Channel Flow - Shearing Within the Outer Recirculating Flow Region**

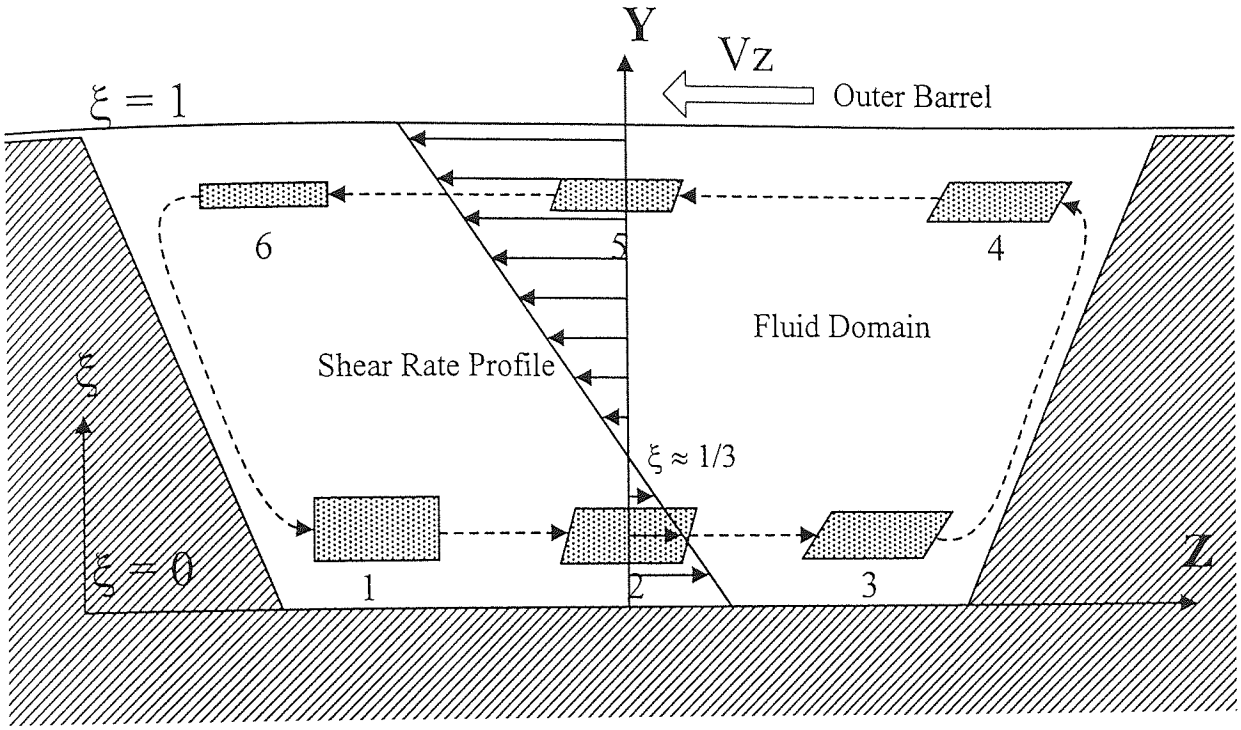

Figure 6-24: **2D Screw Channel Flow - Shearing Within the Inner Recirculating Flow Region**

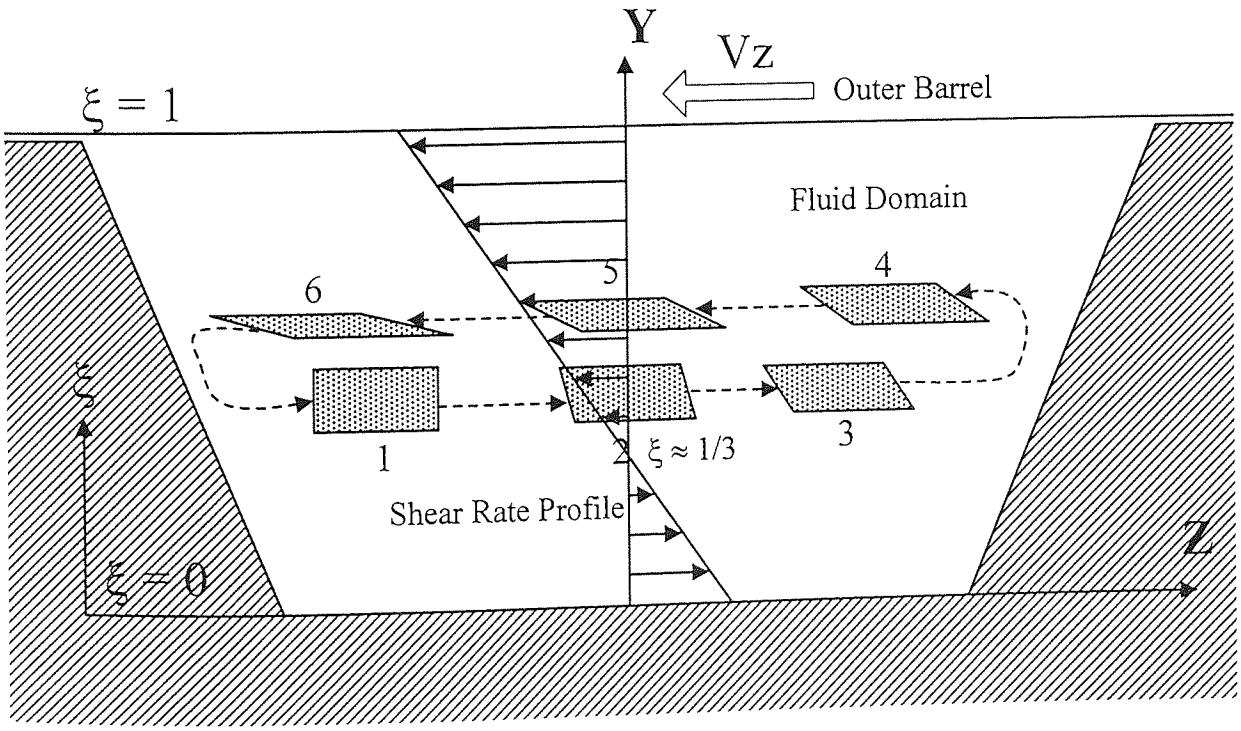

initial forms) at position 6 within each recirculatory flow region, is different. These speculations have not been experimentally verified and such verification is recommended for future research.

6.3 Results - 3D half profile, representing flow through the nip region

For the experiment represented by Figure 6-13 (two viscous materials pre-packed into a CICo-TSE screw channel and then processed), after viscous material had travelled along a screw channel volume, it inevitably had to pass through a screw nip region in order to progress into the screw channel of the opposing screw element. This flow pattern has been simulated except in one aspect. A small amount of material passed through the small clearance between the screw flight and the outer barrel wall and this clearance is assumed to be zero in the simulation. For this experiment, Figure 6-25 shows the cross sectional sample taken directly through the screw nip region, after progression along the screw volume (the position where the cross section shown in Figures 6-13 has been taken, is also indicated). The resultant flow patterns within the cross section shown in Figure 6-25, illustrate an added complexity of the viscous flow problem exhibited within the CICo-TSE conveying screw elements. As material approaches the screw nip region, the cross channel motion described in Section 6.2.2 becomes less prominent. Instead, the rotational motion of the screw flight belonging to the opposing screw element and the pressure build-up within material which is forced to move along this screw channel, both govern the nature of the flow fields generated (this description of the nip region may be readily visualised from the picture shown in Figure 6-2). The pattern displayed in Figure 6-25, reveals a small zone of orange clay, which has been detached from the body of the main orange clay sample. To perform time-dependent deforming interface simulations to predict this is, at this stage in the development of CFD, impossible due to the interfacial deformations involved. Instead, a 3D steady state simulation representing the flow of viscous material from one screw channel to the opposing screw channel, thus including the nip region (as described in Chapter 4), was performed. Figure 6-26 displays velocity vector profiles on all boundaries assigned within the 3D domain constructed, for the steady state simulation described. If a cross sectional cut is taken through the exact position of the nip region, as indicated in Figure 6-3, then the profile shown in Figure 6-27 is obtained. The orientation presented in Figure 6-27 is that of the cross section viewed from the position of the right hand screw element, thus looking towards the channel volume of the left hand screw element. From the velocity vectors plotted on the cross section shown, an area of swirl is predicted towards the top left hand corner of the domain close to the outer barrel wall. The position where this area of swirl is predicted, is the same approximate location as that of the isolated orange zone observed in Figure 6-25. The X-velocity isoline plot in Figure 6-28,

Figure 6-25:
Cross Section Taken in the Y-Z Plane Directly Through the Nip Region as Indicated Within Figure 6-3, Resulting From the Processing of Two Different Coloured "Playstuff" Samples, Side-by-Side Within the 24 mm Pitched Single-Flighted, Conveying Screw Elements.

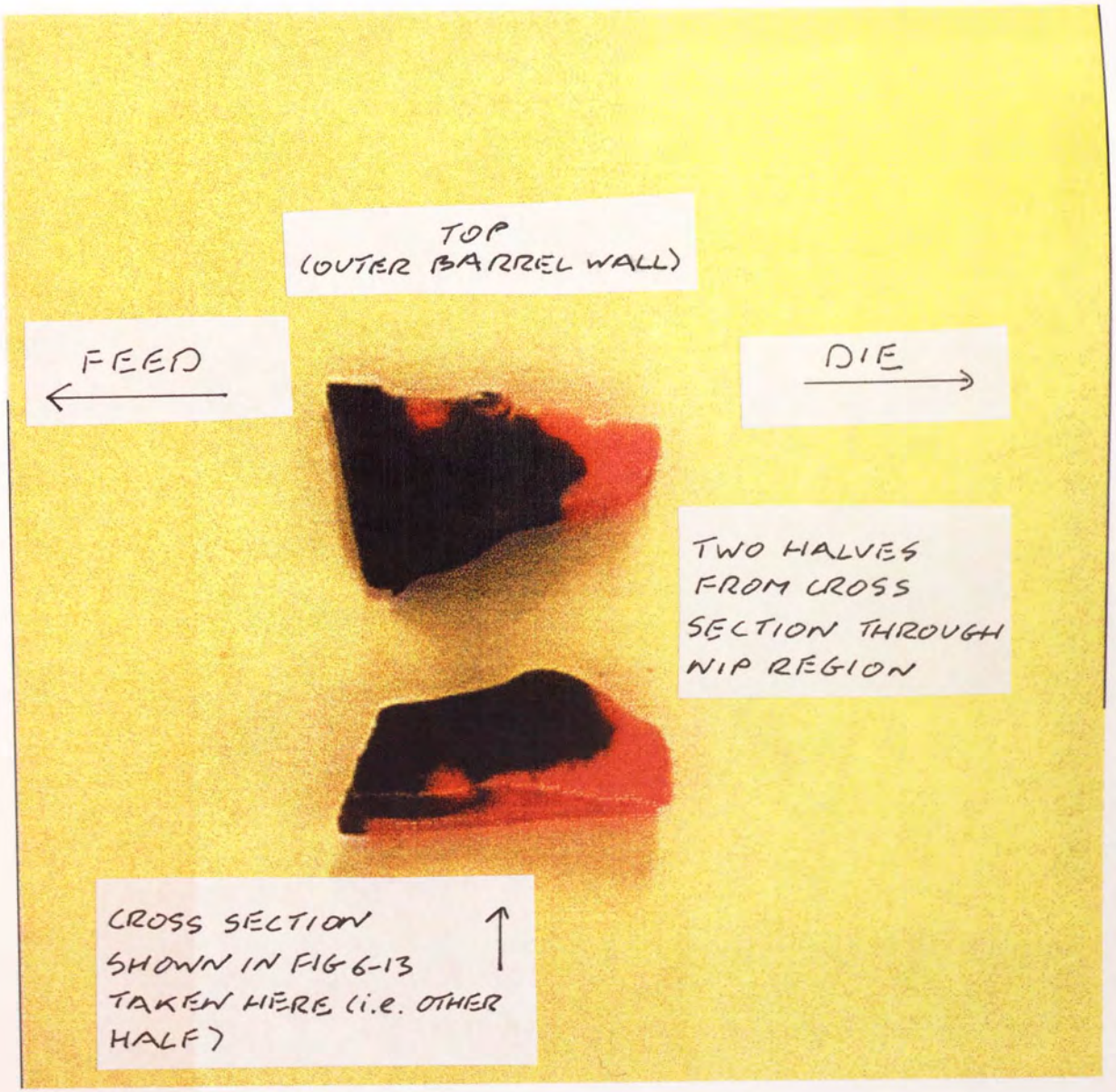

Figure 6-26:
Velocity Vector Profiles Present at the Boundaries for the 3D Half Profile of the 24 mm Pitched Single-Flighted, Conveying Screw Elements.

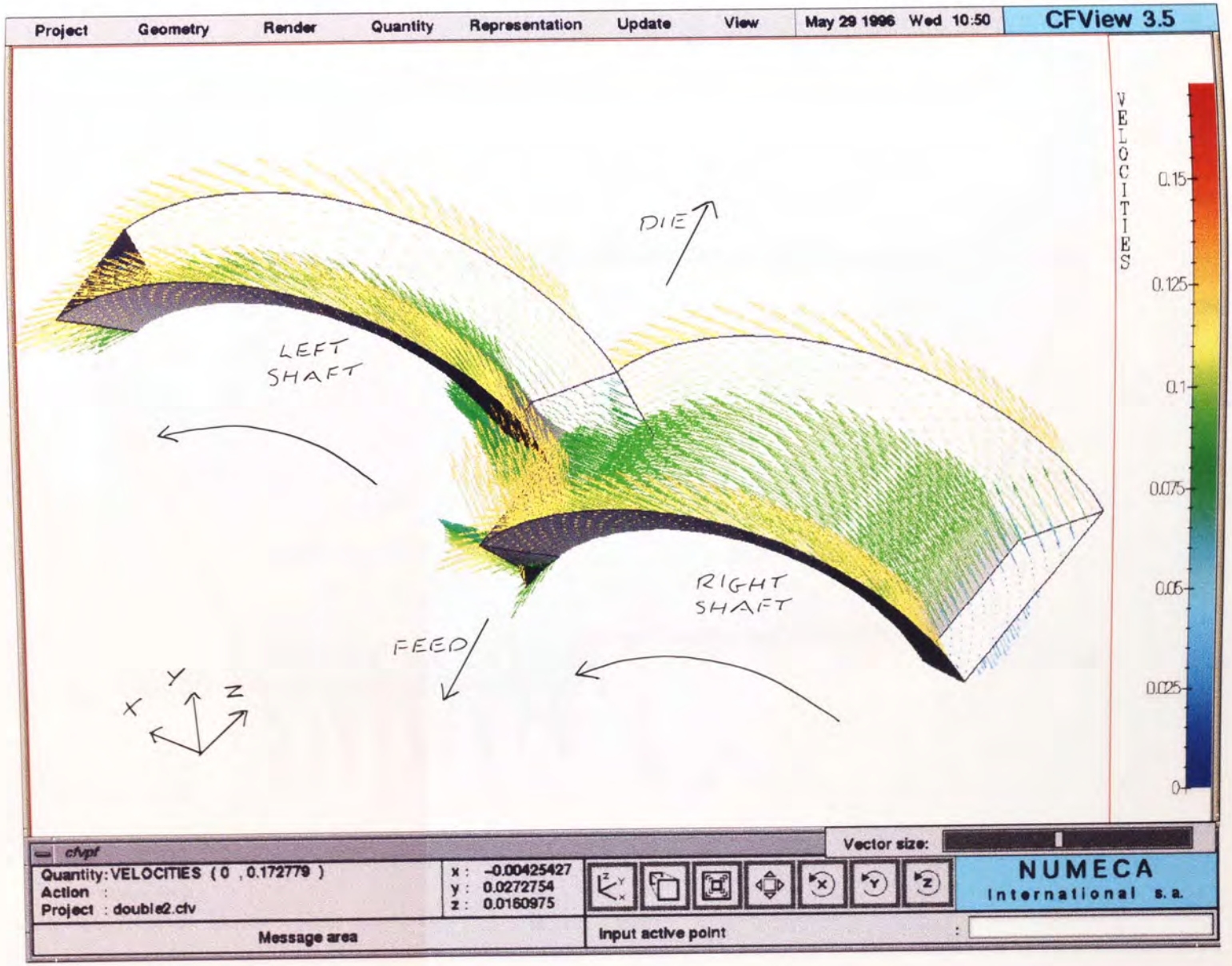

Figure 6-27:
Velocity Vector Profiles on the Y-Z Cross-Sectional Plane Taken Through the Nip Region, Within the 24 mm Pitched Single-Flighted, Conveying Screw Elements.

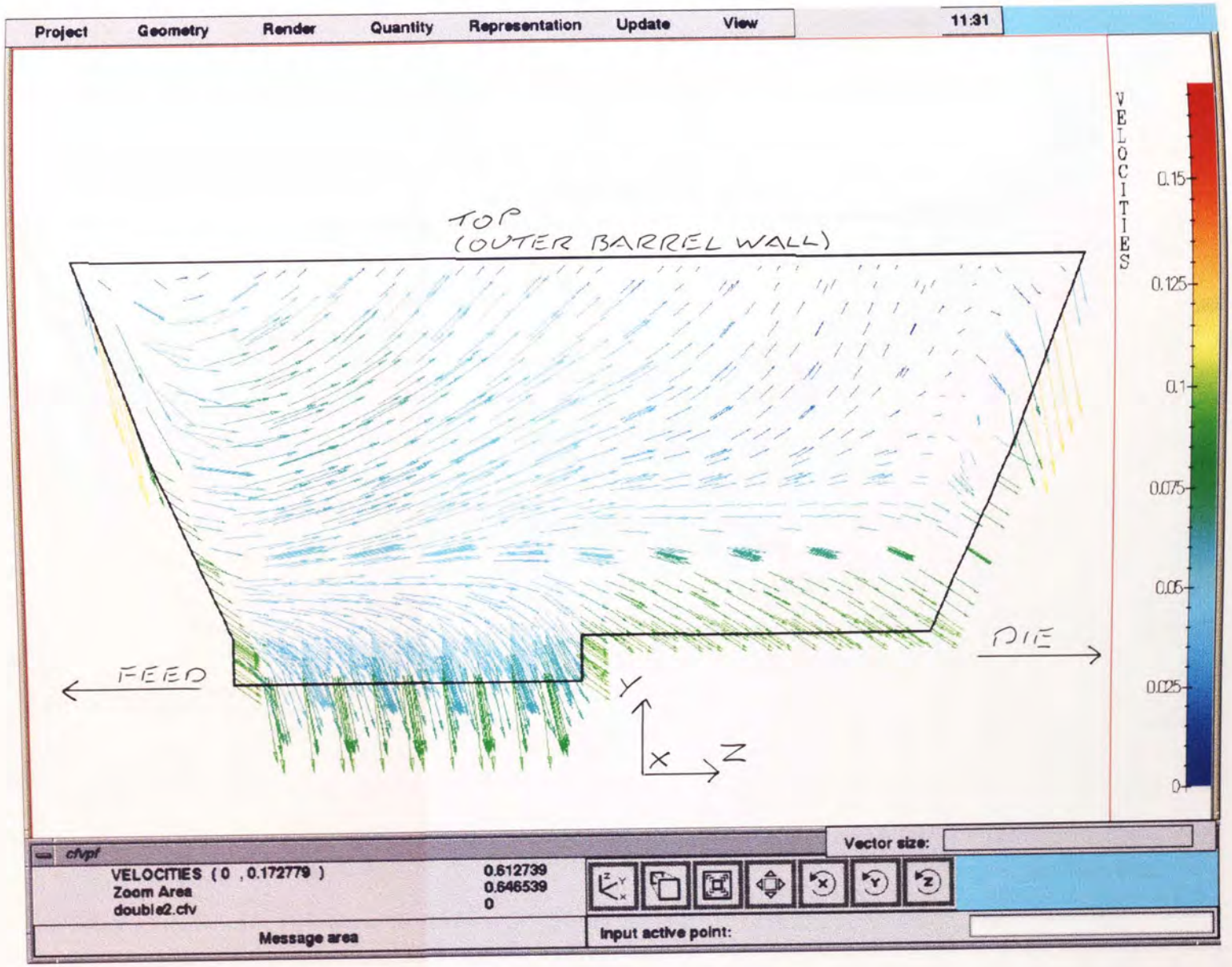

Figure 6-28:
X-Velocity Isolines on the Y-Z Cross-Sectional Plane Taken Through the Nip Region, Within the 24 mm Pitched Single-Flighted, Conveying Screw Elements.

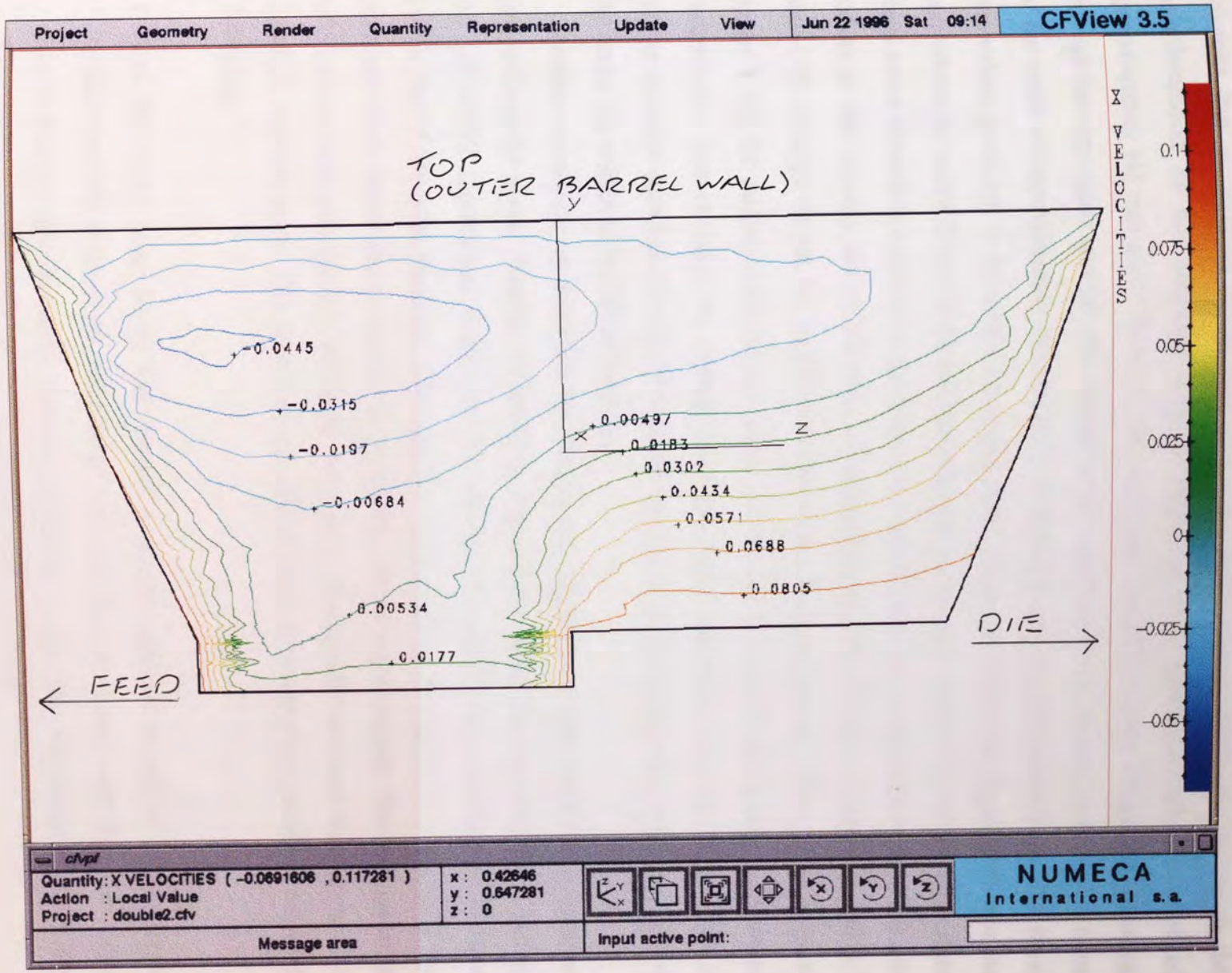

suggests that the motion of the opposing screw flight causes backwards motion in the neighbourhood of the predicted area of swirl, up to a maximum velocity value of approximately |45 mm sec^{-1}|. However, the maximum forward velocity of material crossing through the nip region and into the channel of the opposing screw element, is predicted to be of the order of approximately |80 mm sec^{-1}|, so forward motion will predominate. The shear rate values predicted in the screw nip region cross section are shown in Figure 6-29. For the area where the screw flight of the left hand element comes very close to the collar of the right hand screw element (contained in the bottom left hand side of the cross section), the shear rate values in this locality are of the order of approximately 150-250 sec^{-1}. Tables 6-6 and 6-7 show, the average values for local shear rates $\dot{\gamma}$, the X-Y components of the inelastic stress tensor **T** and the mixing efficiencies λ, calculated for the 2D and 3D steady state calculations respectively. Interestingly, the average shear rate value calculated over the 3D domain, is higher than that calculated for the 2D domain and this is most probably due to the inclusion of the screw nip region in the 3D calculation.

Another approach, as described by Kalyon [52, 73-74], was also used and it involved pre-packing the screw channels as shown in Figure 6-30. When this was processed through the CICo-TSE mechanical model for two viscous "Playstuff" clay materials of different colour but of identical rheology, a sample such as that shown in Figures 6-31 and 6-32 was obtained (each figure shows a different perspective of the same sample). The passage of the two viscous materials through the screw nip region, dramatically increased the length of the interface between them. The growth of this interface may be credited to a combination of the following;

- Zero slip at the outer barrel wall induced a velocity gradient across the screw channel volume between fluid at the outer barrel wall and fluid in contact with the screw collar. Due to the fact that the initial interface defined in the problem was assigned in the same plane as this velocity gradient, the interfacial length increased.
- Progression of material through the nip region caused a change in flow direction, which increased the deformation rate and shear stresses and, consequently, the interfacial length [74].

It would be advantageous to quantify, and predict using Polyflow, the growth of this interfacial length between the two clay materials, as a function of progression through the screw nip region. Figure 6-33 shows the initial construction of the interface between two viscous materials, inside the channel volume of a 24 mm pitched CICo-TSE conveying screw element preceding the nip region (i.e. a simplified version of the initial desired problem,

Figure 6-29:

Local Shear Rate Isolines on the Y-Z Cross-Sectional Plane Taken Through the Nip Region, Within the 24 mm Pitched Single-Flighted, Conveying Screw Elements. Local Shear Rate Cartesian Plots, as a Function of Spatial Distance, for the Values Encountered Along the Lines Indicated.

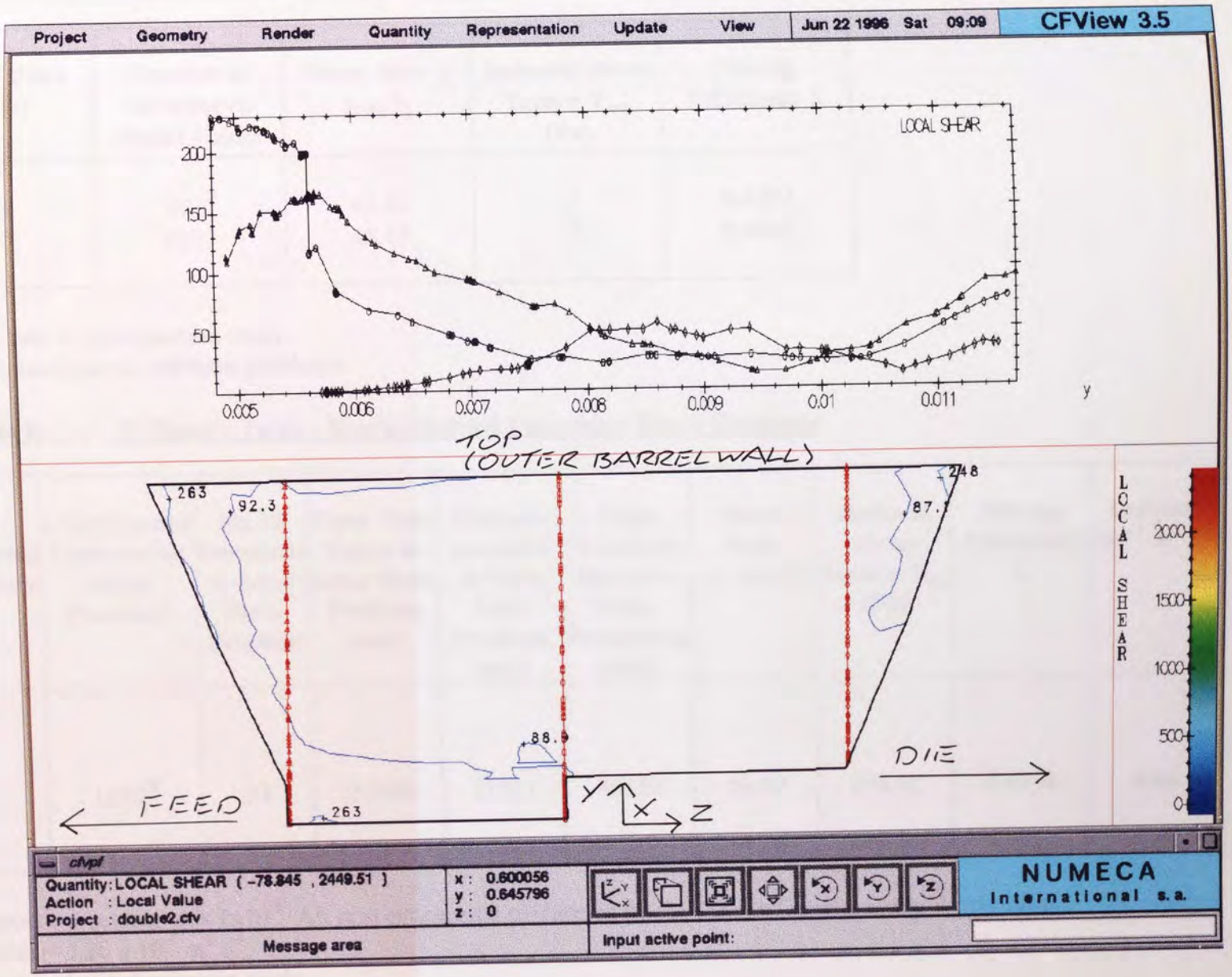

TABLE:6-6 2D Time-Dependent Results Table - Single-Flighted Conveying Screw Elements

Screw Pitch (mm)	Number of Structured Nodal Points	Shear Rate $\dot{\gamma}$ (sec^{-1})	Inelastic Stress Tensor T_{x-y} (Pa)	Mixing Efficiency λ
24	861[1]	45.81	-[2]	0.4855
"	1035	45.85	-[2]	0.4866

1 Additional simulation performed as part of optimisation study.
2 Inelastic stress tensor values not obtained due to software problems

TABLE:6-7 3D Results Table - Single-Flighted Conveying Screw Elements

Screw Pitch (mm)	Computer Used for Solving Problem	No. of Unstructured Nodal Points	Convergence Criteria for Main Problem [1]	No. of Iterations to Solve Main Problem	Total Time Taken to Solve Main Problem (sec)	Time per Iteration to Solve Main Problem (sec)	Time Taken to Solve for Post-Processing (sec)	Shear Rate $\dot{\gamma}$ (sec^{-1})	Inelastic Stress Tensor T_{x-y} (Pa)	Mixing Efficiency λ	Output [2] (10^{-7} m^3 s^{-1})
3D Half Profile	Silicon Graphics Indy Workstation										
24		3762	$1x10^{-8}$	24	751956	31331	40150	56.00	390.02	0.4916	4.08
24 [3]		2045	$1x10^{-8}$	-	-	-	-	54.60	410.88	0.4925	5.76

1 Convergence criteria used for all post-processing was $1x10^{-8}$. All post-processing performed on the Silicon Graphics Indy Workstation.
2 Original volumetric flow rate at inlet = 5.20×10^{-7} m^3 s^{-1}.
3 Additional simulation performed as part of optimisation study.

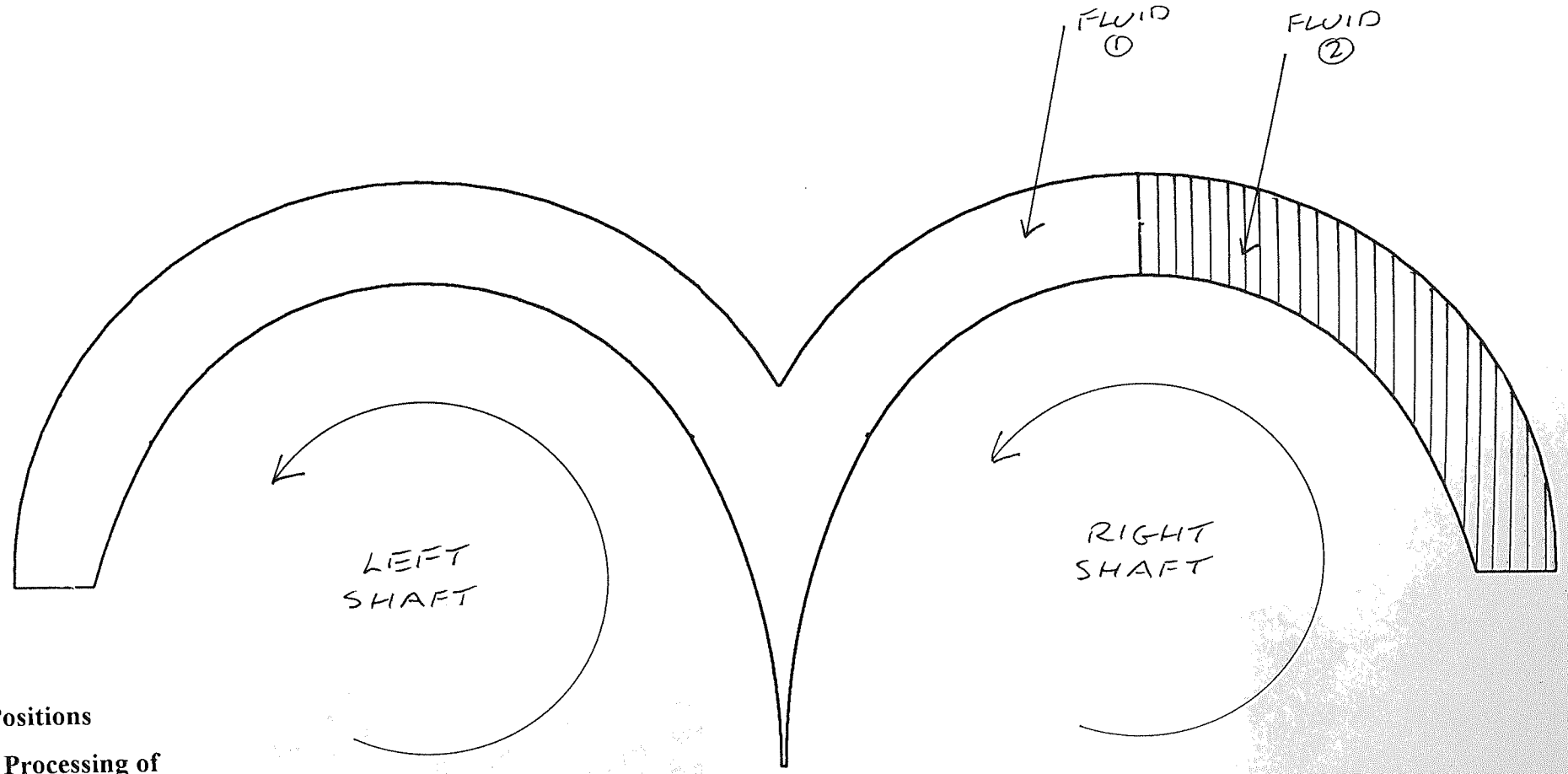

Figure 6-30:
Initial Starting Positions Assigned for the Processing of Two Different Coloured "Playstuff" Samples, One Behind the Other, Within the Channel of a 24 mm Pitched Single-Flighted, Conveying Screw Elements.

Figure 6-31:
Result of Processing the Experiment Described Within Figure 6-30; Sample Viewed From Die End.

Figure 6-32:
Result of Processing the Experiment Described Within Figure 6-30; Sample Viewed From Feed End.

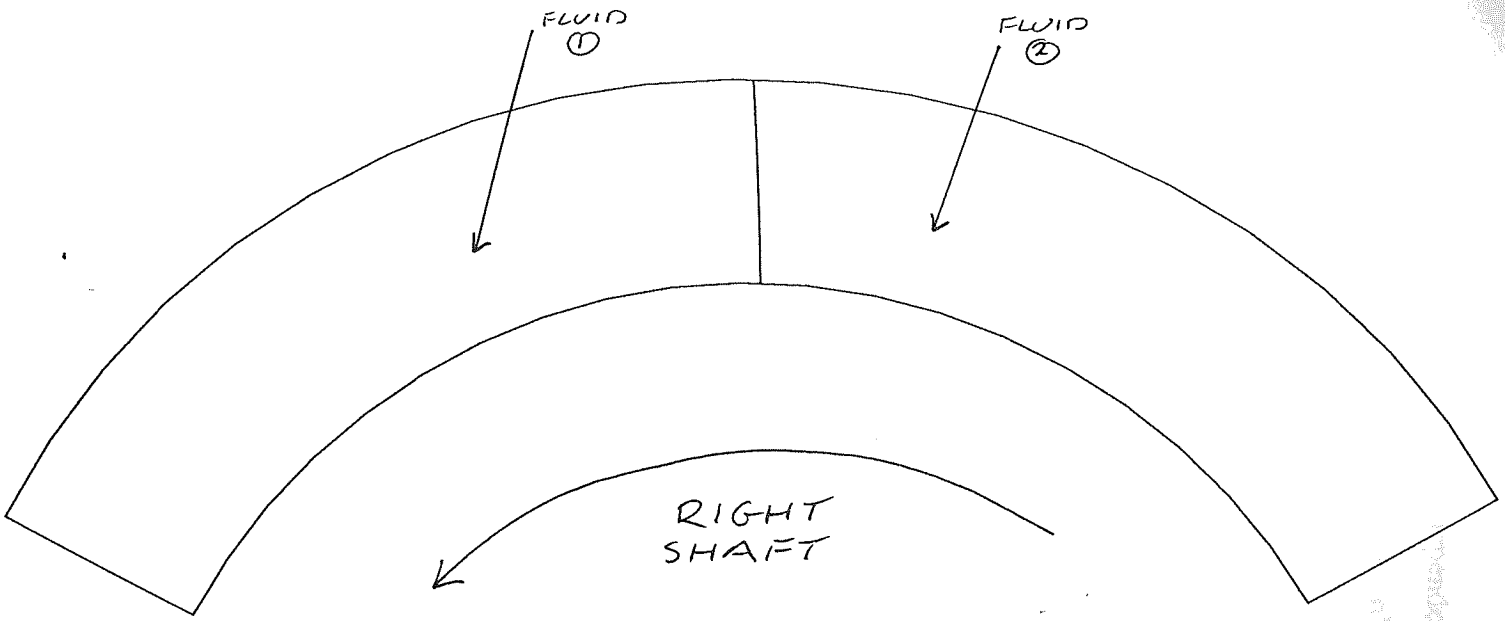

Figure 6-33:
Initial Starting Positions Assigned for the Simulation of the Deforming Interface Between Two Different Coloured "Playstuff" Samples, One Behind the Other, Within the Channel of a 24 mm Pitched Single-Flighted, Conveying Screw Elements.

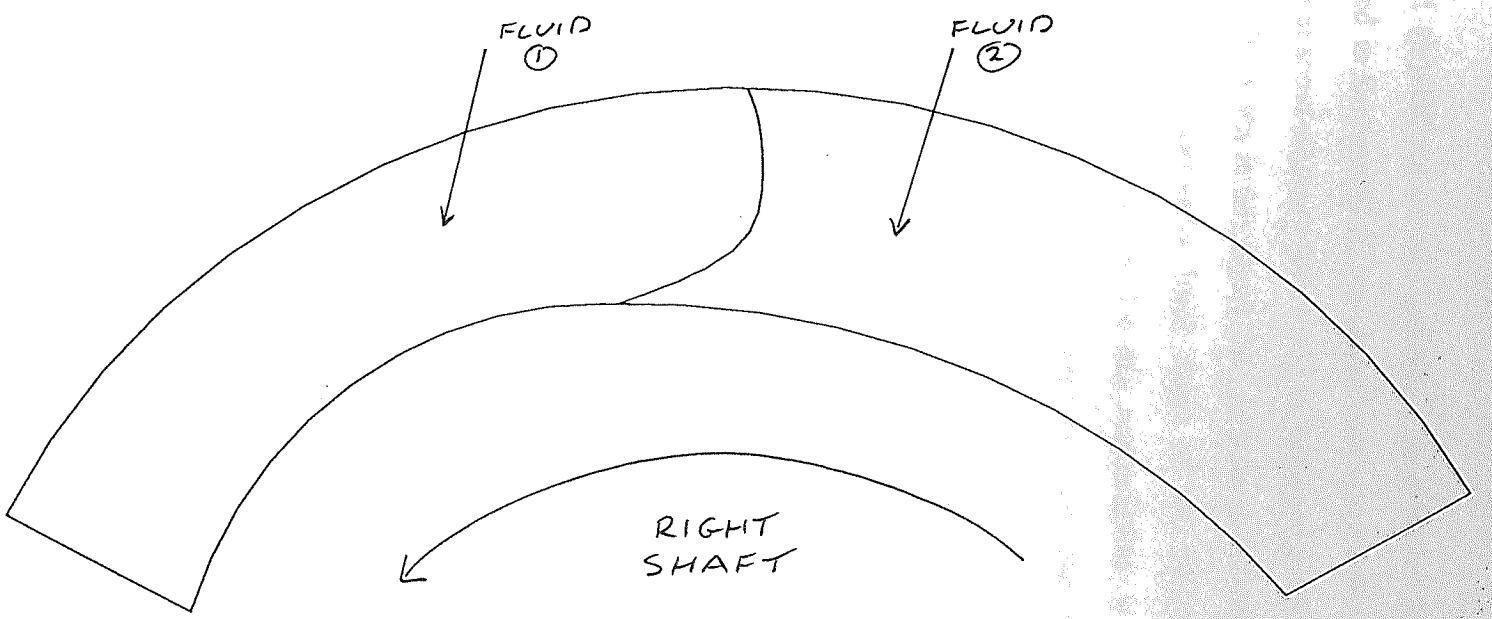

Figure 6-34:
Result of Performing the Simulation Described in Figure 6-33, After Some Time t.

shown in Figure 6-30). If time dependent simulations on this structure, identical to those performed for cross channel flow described in Section 6.2.2, are carried out using Polyflow version 3.4.6, then a typical result obtained at some arbitrary time t may be obtained as shown in Figure 6-34. It may be seen from the result shown in this figure that, as well as deforming the interface, the simulation predicts that the supposedly fixed shape of the boundary representing the screw collar wall also deforms. The reason for this contradiction is the remeshing technique used to recalculate the new shape of the mesh at each time step. Unfortunately the Method of Spines technique (described in Chapter 3) used to calculate the deformation of the interface, also recalculates the shape of the adjacent boundaries connected to the deforming interface. This condition is usually acceptable for most simulation problems assigned, however, because the screw collar boundary connected to the moving interface is both curved and possesses a tangential velocity, Polyflow cannot treat this boundary as being of a fixed shape over the entire period of the marching time simulation. It is hoped that future versions of Polyflow will possess improved facilities that may overcome this particular problem.

7 INVESTIGATION OF VISCOUS FLOW WITHIN THE STAGGERED MIXING DISCS ZONE

7.1 Mixing Discs - 2D X-Y geometries

The mixing discs are a type of CICo-TSE mixing element, modular in design and which possess six "U" shaped apertures cut into the outer perimeter at 60° intervals. The discs may be either long or short in classification, this referring to the relative lengths of the collars on either side of each disc as shown in the upper and lower outlines of Figure 7-1. The dimensions of the long and short disc for use within the Betol BTS40 CICo-TSE are also shown in Figure 7-1. To create a mixing disc zone, adjacent discs are staggered between alternate screw shafts. Two long discs must be present within each mixing disc zone for a particular CICo-TSE configuration, such that one long disc is placed at the entrance and one at the exit. These two long discs must be located on opposing screw shafts, the choice of which being dependent upon the direction of rotation. Figure 7-2 illustrates the arrangement where one long disc is placed at the entrance on the right hand shaft, as viewed from the feed end, followed by pairs of short discs staggered in sequence and culminating with the remaining long disc on the left hand shaft, at the exit section of the zone. The convention shown in Figure 7-2 is for a right handed screw arrangement with the rotation of shafts counter-clockwise. This mixing zone, containing three short and one long pair of discs, if situated within the Betol BTS40 CICo-TSE would typically be 45 mm in length. For the staggered mixing disc zone, there are three independent 2D X-Y cross sections that may be taken at any point along the zone and these are listed as follows;

- Outline of mixing disc in left CICo-TSE chamber and outline of disc collar in the right chamber.
- Outline of disc collar in both the left and right chambers.
- Outline of disc collar in left chamber and outline of mixing disc in the right chamber.

Because of the influence of pressure gradients resulting in forward and backward fluid motion from each staggered disc, the second option from the above list may only sensibly be examined using 3D analysis. When considering the flow field exhibited by the remaining two possible 2D X-Y cross sections, the symmetry within the mixing disc zone allows the following assumptions to be made;

- The flow fields exhibited within the first and third cross sections described above will be similar (though not identical) due to their symmetry. In view of this expected similarity in exhibited fluid flow, only one cross section needs to be examined and it was thus decided

FIGURE 7-1

Diagrammatic Representations of both the Long Mixing Disc (Upper Diagram) and Short Mixing Disc (Lower)

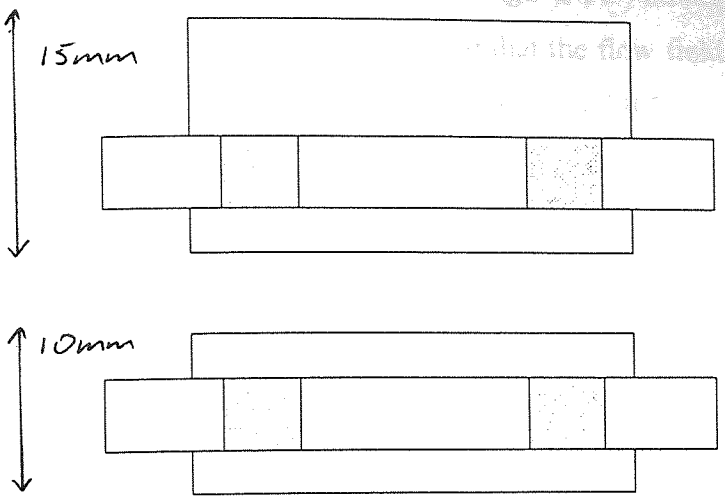

FIGURE 7-2

Diagrammatic Representation Illustrating the Placement of Long Mixing Discs, in Accordance With the Anti-Clockwise Co-Rotation of Screw Shafts

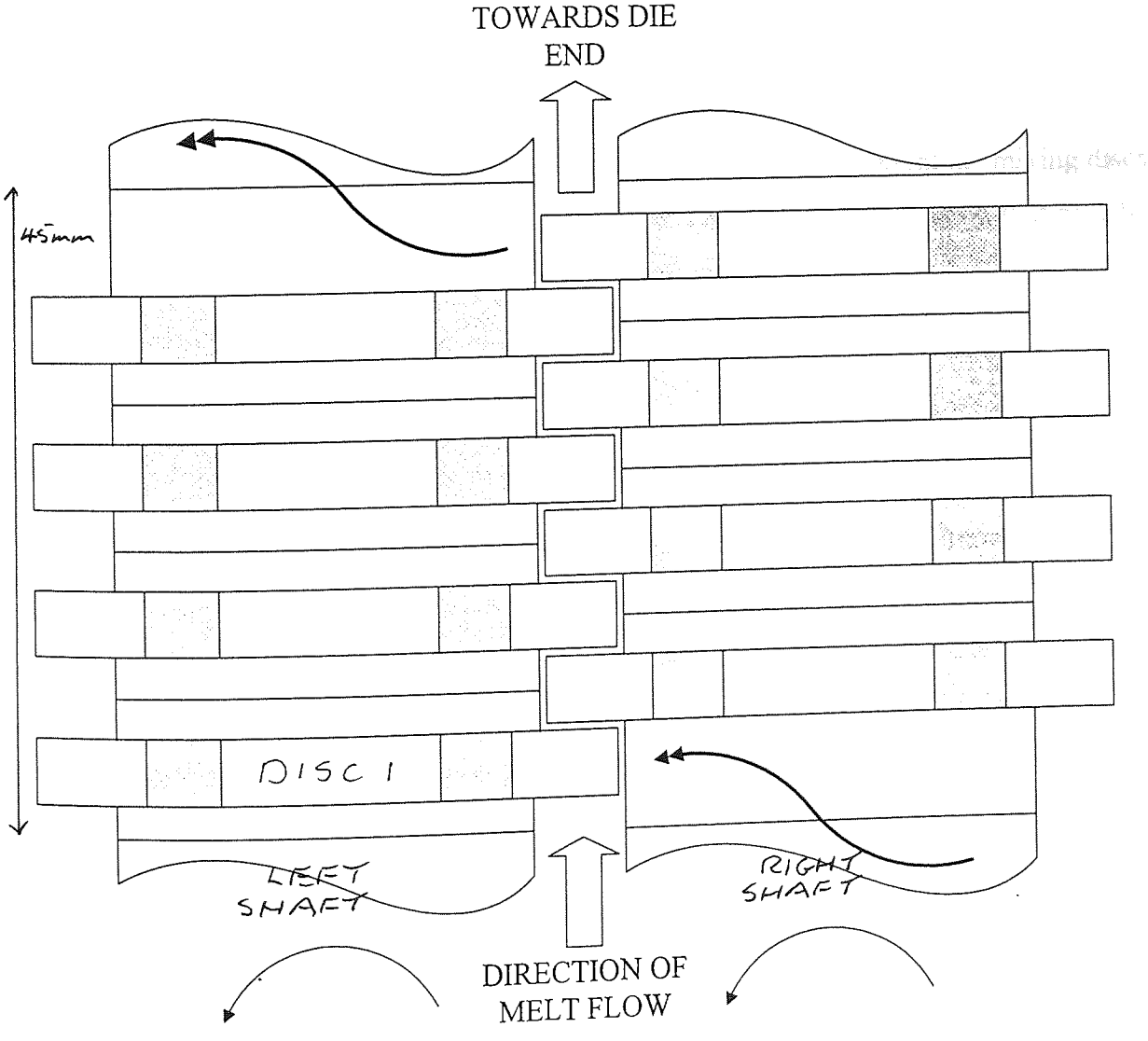

that rotated configurations of the first option would be investigated (outline of mixing disc in left chamber).

- The chosen cross section was examined through a 30° mixing cycle only, due to the repetition of the configuration. It was assumed that the flow fields exhibited by the mixing discs over a full rotation are periodic with a frequency of 30°.

The partial mixing cycle investigated is shown in Figure 7-3 from the $\alpha = 0°$ (top left) to the $\alpha = 30°$ (bottom right) rotated configuration. For the mixing discs, α represents the angle between the centre of the furthest right hand aperture of the disc in the left chamber, referred to as the central aperture and the horizontal axis. The position within the domain that this central aperture occupies is referred to as the intermeshing region. The physical construction of each mesh at 5° intervals, in terms of global nodal positions, will change through this partial mixing cycle. However, it is found that groups of meshes may be classified as being of the same macro-element construction. This is explained by the following illustration. For rotated configurations where the central aperture of the left hand disc partly coincides with the upper bridge region (for example the $\alpha = 30°$ configuration, bottom right in Figure 7-3), the macro-element construction of these meshes is different from those meshes that represent configurations where this central aperture does not coincide with the bridge region (for example, the remaining three configurations in Figure 7-3). Thus to represent the mixing discs in 2D, it is found that there are two discrete sets of macro-element construction that may be used. These are for the following sets of rotated configurations;

Set 1: $0° \leq \alpha \leq 20°$ $\Delta\alpha = 5°$

Set 2: $25° \leq \alpha \leq 30°$ $\Delta\alpha = 5°$

The full macro-element details for each mesh contained within each of these two rotated configuration sets specified, are as follows;

Set 1:

- Number of macro-vertices within each mesh: 46
- Number of macro-elements within each mesh: 25

Set 2:

- Number of macro-vertices within each mesh: 48
- Number of macro-elements within each mesh: 27

Figure 7-3:

Partial Mixing Cycle Examined for the Investigation of the Mixing Disc Zone Progressing From the a = 0° (Top Left) to the a = 30° (Bottom Right) Rotated Configuration.

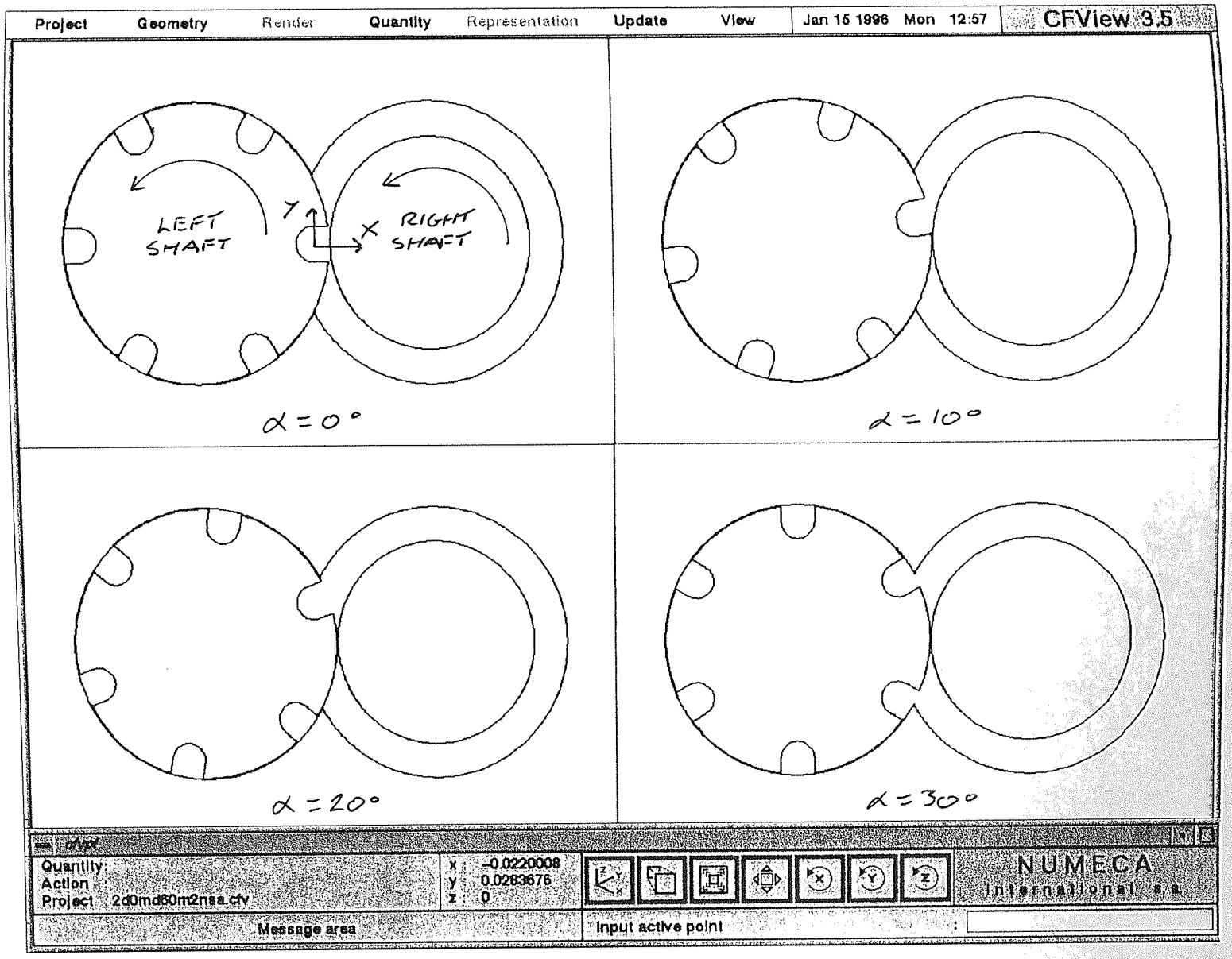

The full details for the construction of each mesh within each of the two mixing disc rotated configuration sets, are as follows;

Set 1:

- Macro-vertex numbering scheme:
  Appendix S.
- Macro-vertex co-ordinates for each mesh contained within Set 1:
  Appendices T1 - T5.
- Macro-element numbering scheme:
  Appendix U.
- Details for the construction of all macro-elements contained within each mesh of Set 1:
  Appendix V.
- Boundary numbering scheme:
  Appendix W.

Set 2:

- Macro-vertex numbering scheme:
  Appendix X.
- Macro-vertex co-ordinates for each mesh contained within Set 2:
  Appendices Y1 - Y2.
- Macro-element numbering scheme:
  Appendix Z.
- Details for the construction of all macro-elements contained within each mesh of Set 2:
  Appendix AA.
- Boundary numbering scheme:
  Appendix AB.

The number of structured nodes contained within each mesh pertaining to each of the two macro-element construction sets, are as follows;

Each mesh within Set 1: 2905
Each mesh within Set 2: 2905

An example of a typical 2D mixing disc mesh, illustrating the mesh density within the flow domain, is given in Figure 7-4. From this figure it may be seen that the areas of greatest mesh density are for the intermeshing and upper and lower bridge regions.

Figure 7-4:

Typical Mesh Utilised for the 2D Representation of the Mixing Disc Zone in the X-Y Plane (Rotated Configuration $\alpha = 30°$).

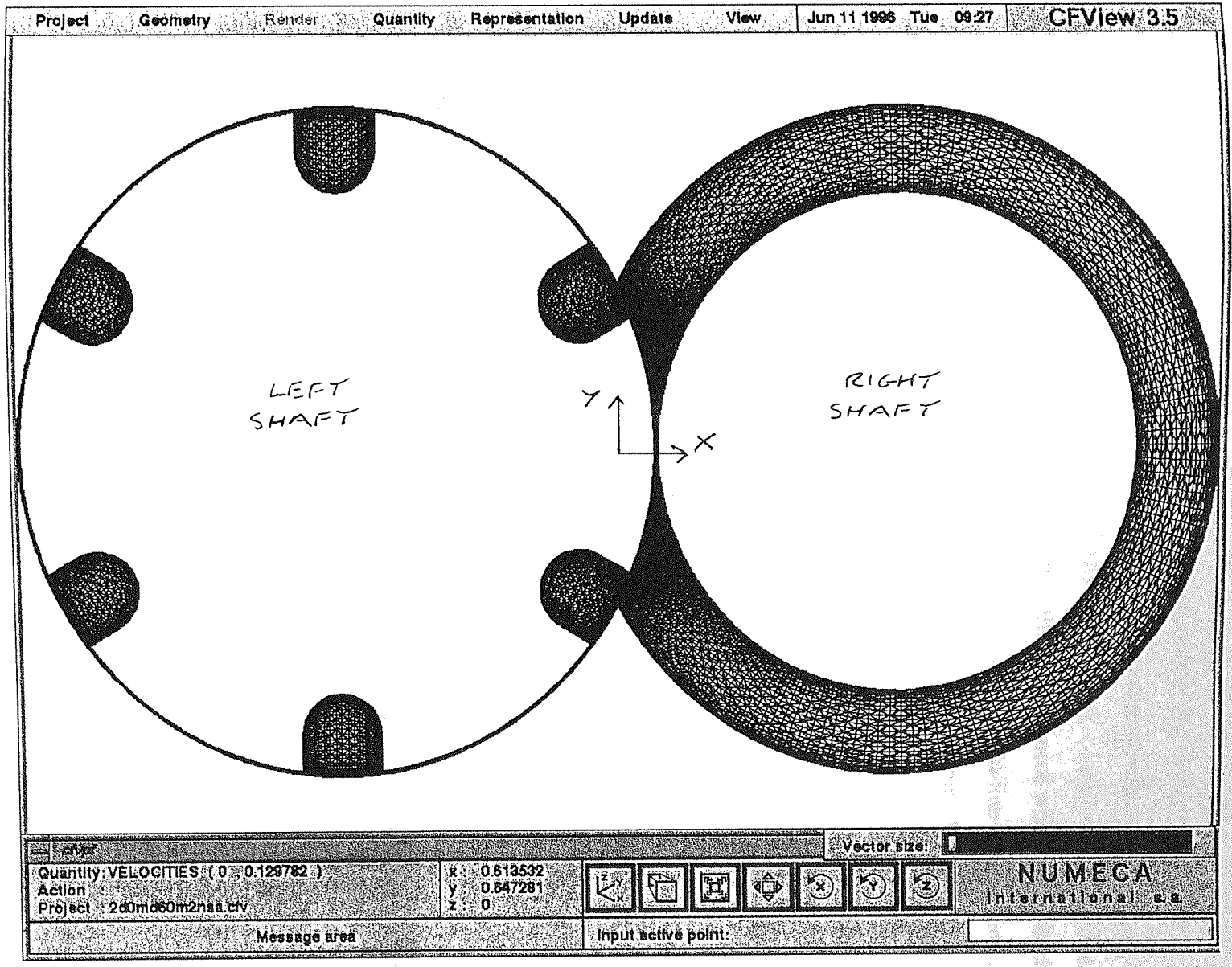

7.2 Mixing Discs - 3D geometries

The staggered arrangement of apertures within a typical mixing disc zone, may either be in-line when viewed along the barrel, or each disc may be offset consecutively by 30°, to give a continuous off-line aperture geometry. The emphasis of the work contained within this thesis is concerned with the in-line geometry only, as it is this arrangement which is utilised by the PPP group in our Betol BTS30 CICo-TSE. An example of the in-line arrangement, in-situ within a mechanical model of the BTS40 CICo-TSE, is shown in Figure 7-5.

The 3D construction of a mesh representing parts of the mixing disc zone is a complex task. The approach made was that, initially, possible areas of symmetry were scrutinised in order to try to reduce the complexity of construction. Figure 7-6 shows a 3D construction for a pair of mixing discs meshed for the top half of the zone only (i.e. for values of $Y \geq 0$). Whilst this construction is a correct representation of the symmetry involved, because the mixing discs co-rotate, once the symmetrical results are mirrored for the $Y \leq 0$ fluid domain to give a complete structure, the directions of flow do not correspond (as shown in Figure 7-6). This is unfortunate and implies that the simulation of the mixing disc zone in 3D, must involve meshes that represent the mixing disc flow domain completely.

The number of discs required within a mixing disc zone is, to a certain extent, based on an educated guess. Enough discs must be present so as to adequately mix material passing through, however, the inclusion of too many discs is obviously inefficient in terms of energy consumption. The mixing disc zone shown in Figure 7-5 contains three short and one long pair of discs. Direct simulation of viscous flow through this number of discs by CFD, is unfortunately not feasible using current software. It was thus decided to break down the problem by simulating more simple arrangements. The mixing disc arrangements examined within this work were as follows;

- One half pair of discs, obtained by using the same 2D mixing disc cross sections as described in Section 7.1 and shown in Figure 7-3, but by projecting each domain in the Z-direction by 4.6 mm.
- One full pair of long discs, including the separation plane between each disc.

The meshes used for the simulation of one half pair of discs are shown in Figures 7-7 and 7-8 for the $\alpha = 0°$ and 30° rotated configurations respectively. A point of interest to note from Figure 7-8 is the increased nodal point density about the two bridge regions where the two apertures coincide, in anticipation of the increased flow activity within these areas. The meshes used for the simulation of one full pair of long mixing discs are shown in Figure 7-9 to 7-11 for the $\alpha = 0°$, 15° and 30° rotated configurations respectively. These three meshes

Figure 7-5:
Typical CICo-TSE Staggered Mixing Disc Zone, Containing Four Pairs of Discs in the In-Line Arrangement.

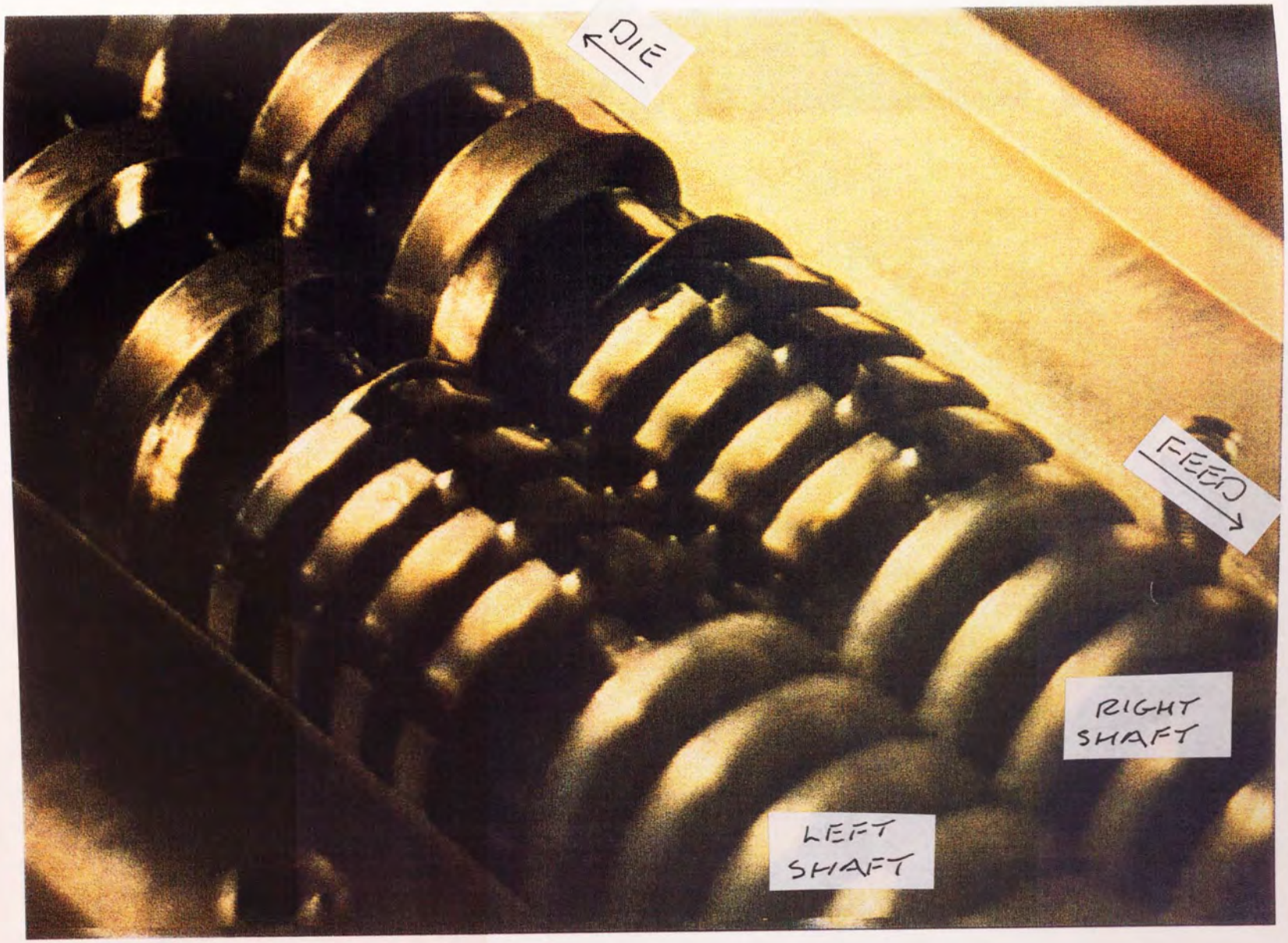

Figure 7-6:

3D Construction for a Pair of Mixing Discs in the In-Line Arrangement, Meshed for the Top Half of the Zone Only ($Y \geq 0$).

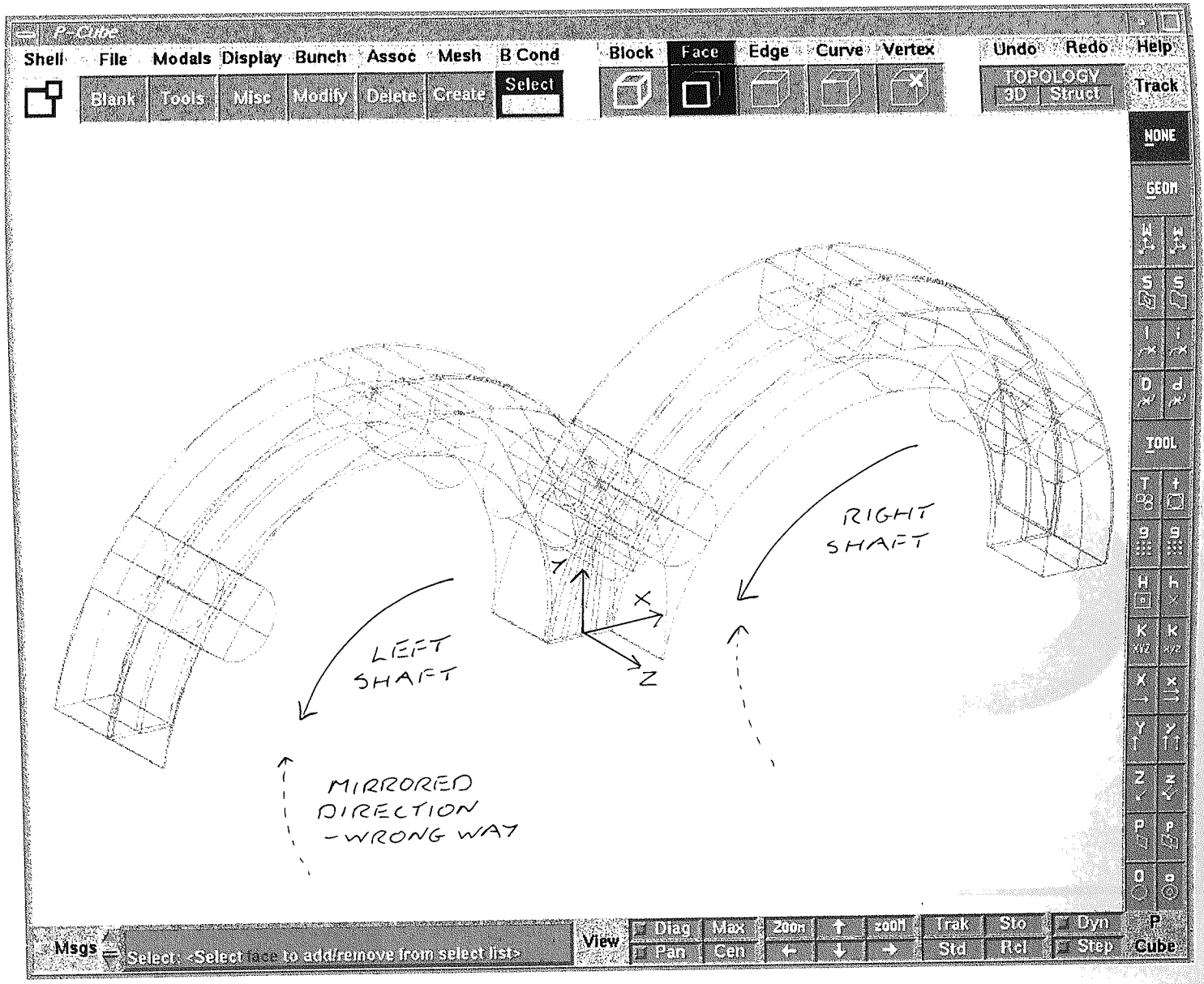

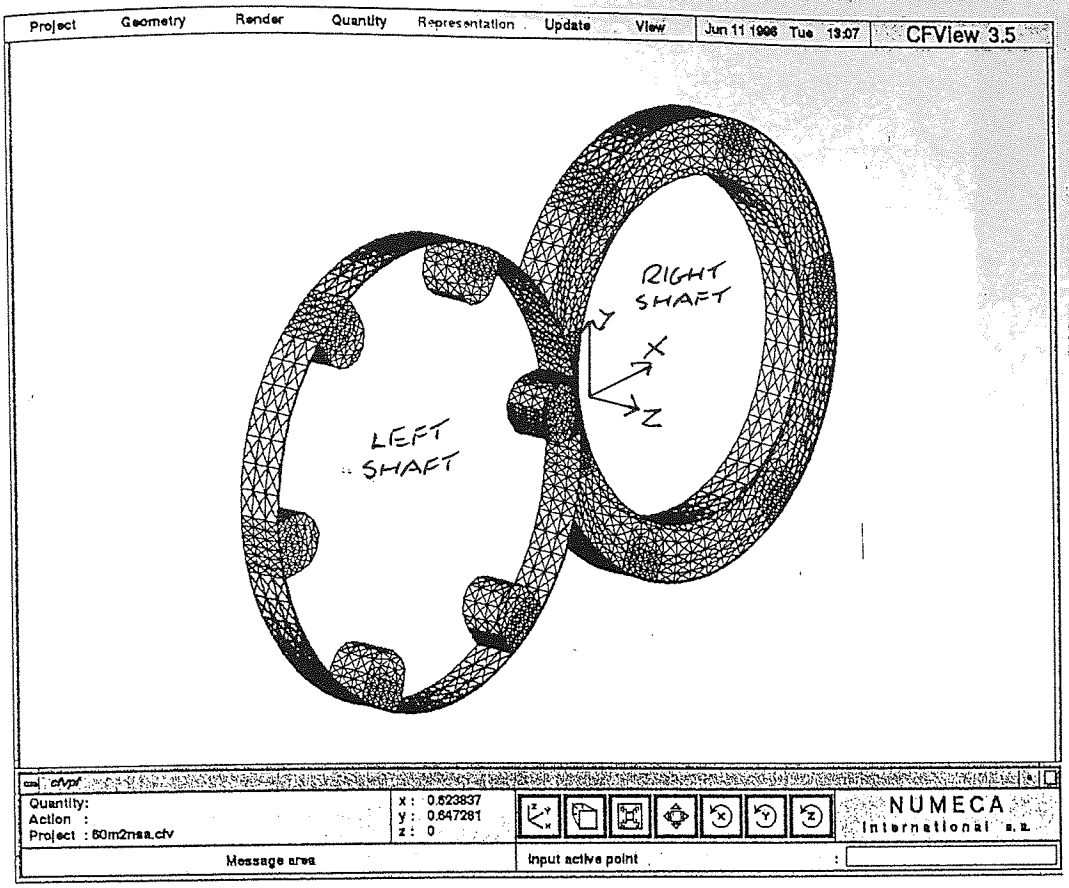

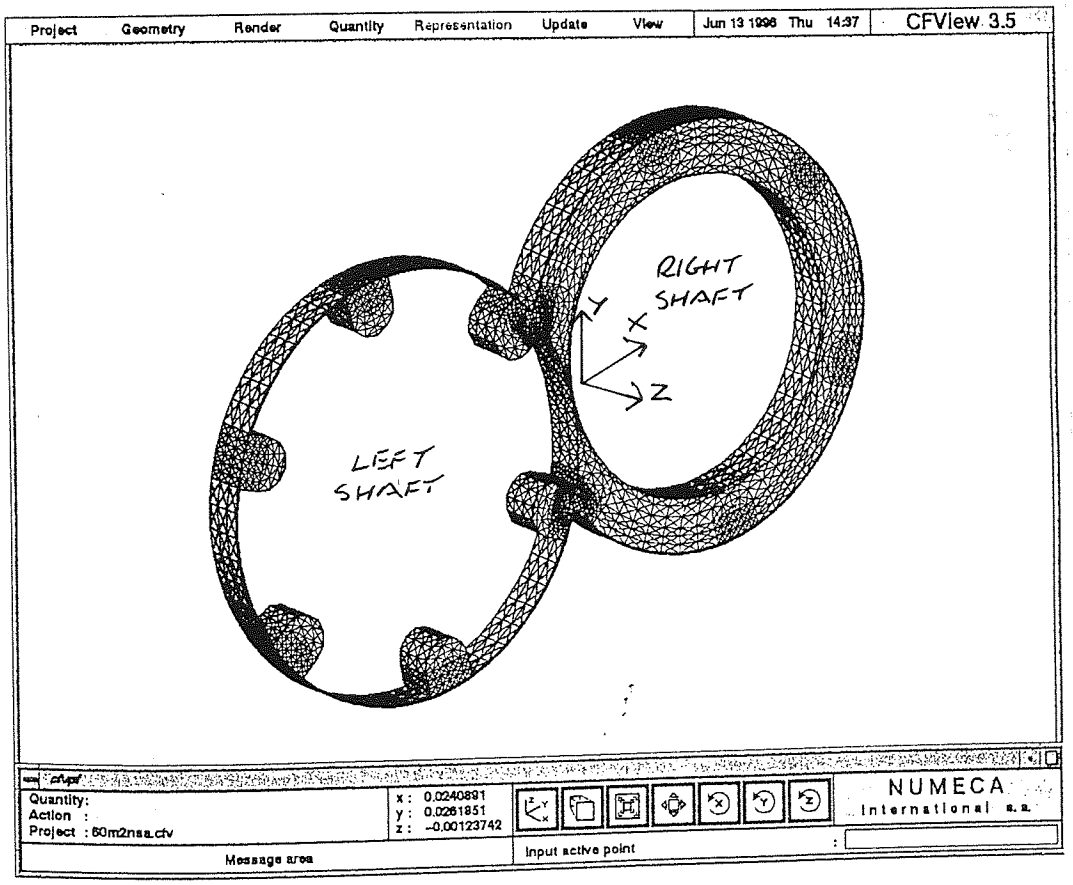

Figure 7-7 (Upper): Mesh Utilised for the Representation of One Half Pair of Mixing Discs (Rotated Configuration $\alpha = 0°$).

Figure 7-8 (Lower): Mesh Utilised for the Representation of One Half Pair of Mixing Discs (Rotated Configuration $\alpha = 30°$).

Figure 7-9:

Mesh Utilised for the Representation of One Full Pair of Mixing Discs, in the In-Line Arrangement (Rotated Configuration $\alpha = 0°$).

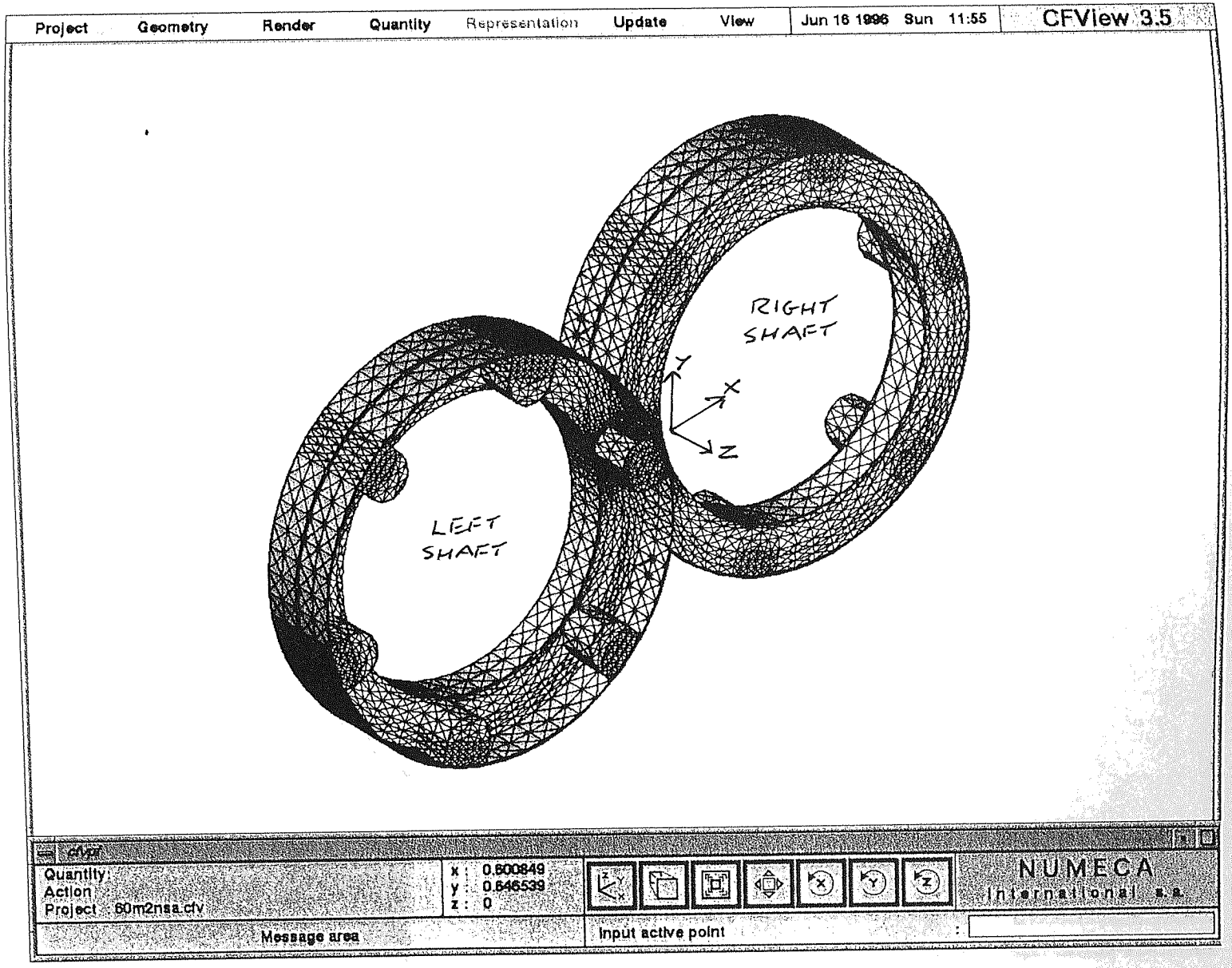

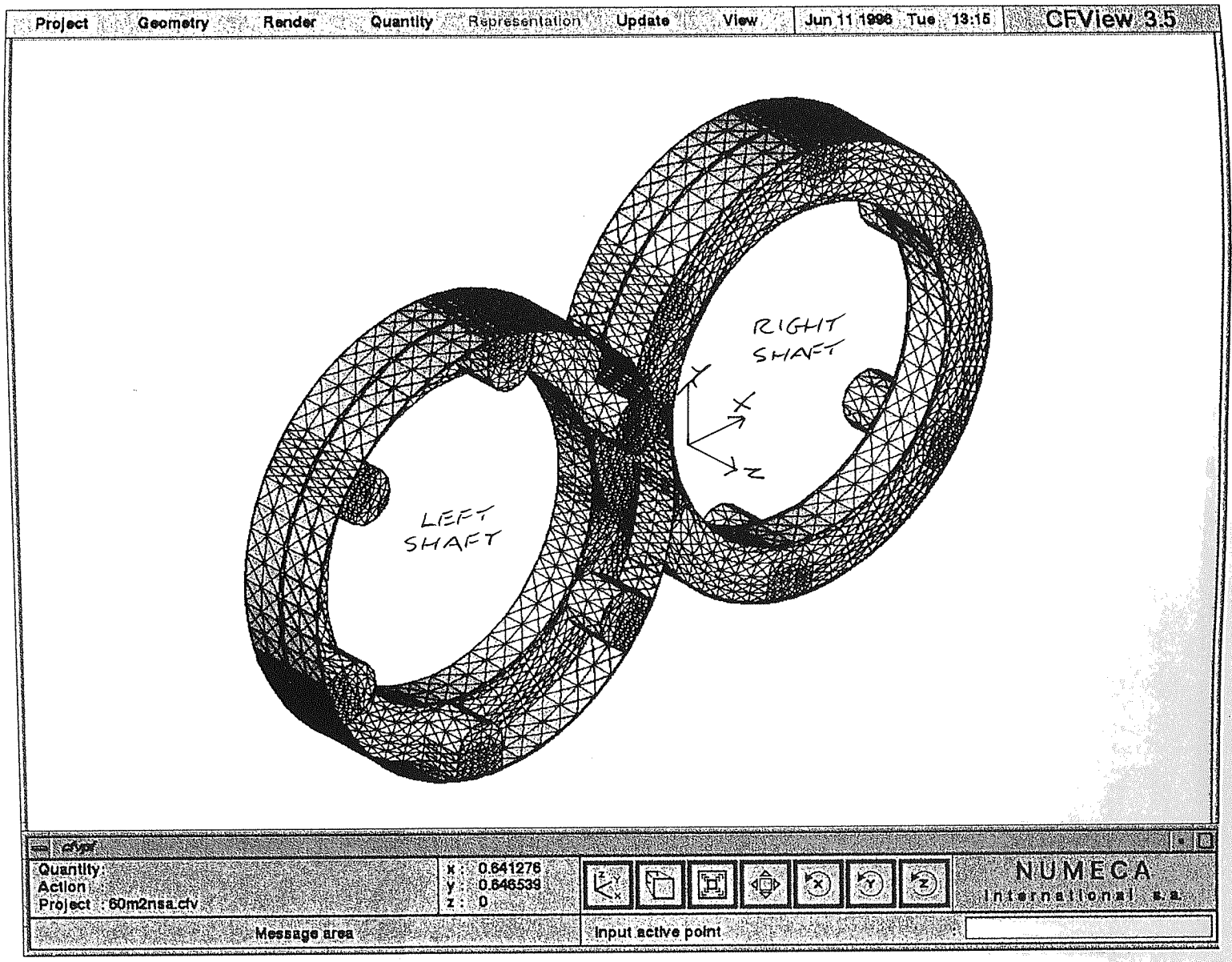

Figure 7-10:

Mesh Utilised for the Representation of One Full Pair of Mixing Discs, in the In-Line Arrangement (Rotated Configuration $\alpha = 15°$).

Figure 7-11:
Mesh Utilised for the Representation of One Full Pair of Mixing Discs, in the In-Line Arrangement (Rotated Configuration $\alpha = 30°$).

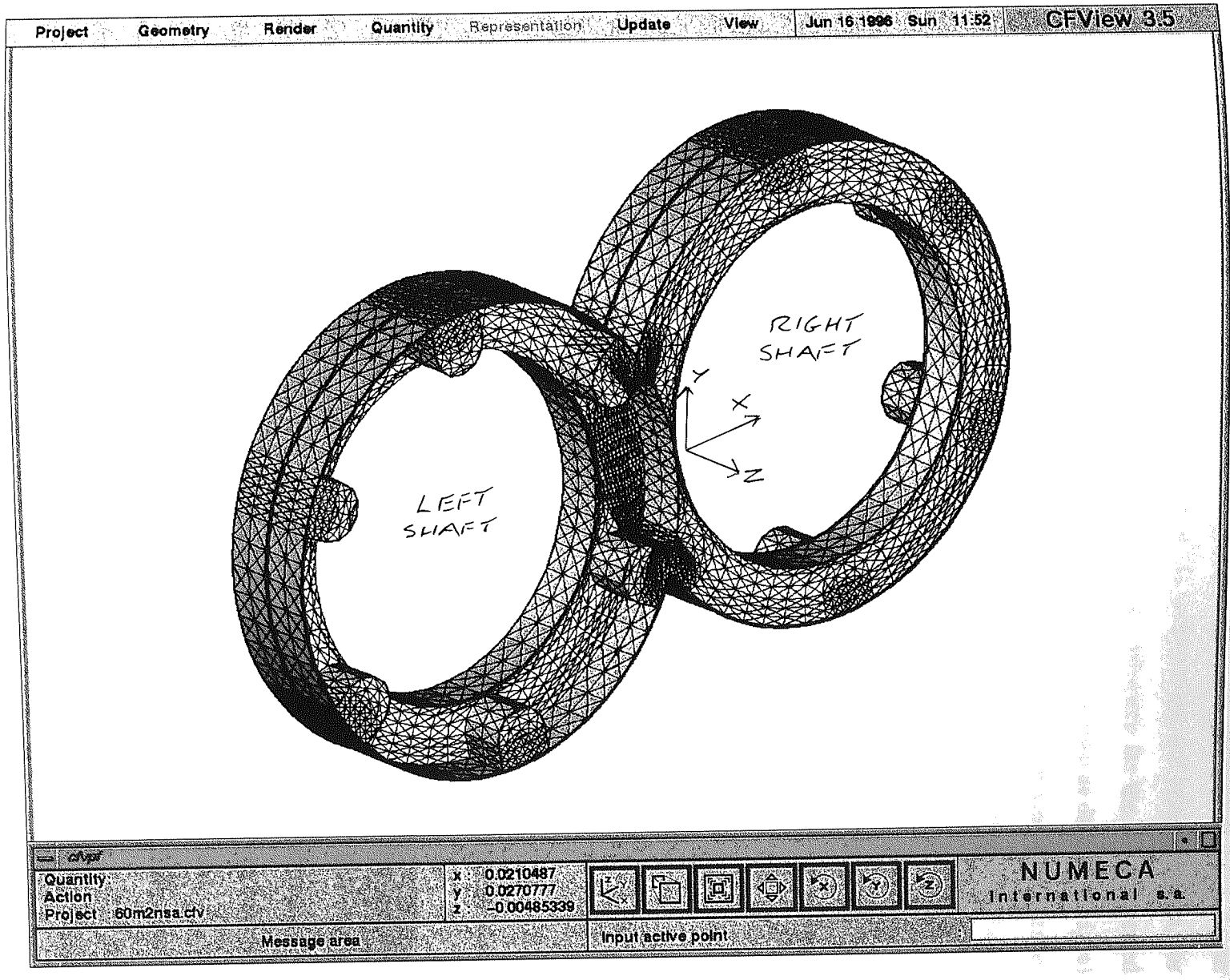

were constructed in an identical manner to those representing the one half pair of discs. Again the nodal point densities have been increased about the intermeshing and bridge regions, for all three rotated configurations. An example of the domain structure for the $\alpha = 0°$ rotated configuration is shown in Figure 7-12, illustrating also the Master (shown as dark blue edges) and Slave (shown as light blue edges) distributions employed. For all mixing disc meshes constructed (and for all trilobal element meshes as described in Chapter 8), five boundaries were ascribed and Figures 7-13 to 7-15 illustrate these assignments.

- Figure 7-13 shows the inlet face assigned as boundary number 1 (shown in red at the foreground of the structure) and the outlet face assigned as boundary number 5 (shown in pink at the background of the structure).
- Figure 7-14 shows the wall of the left disc assigned as boundary number 2 (shown in green) and the wall of the right disc assigned as boundary number 3 (shown in blue).
- Figure 7-15 shows the wall of the outer barrel, assigned as boundary number 4 (shown in light blue).

Table 7-1 catalogues all mesh parameters used, for each of the three rotated configurations constructed representing either the one half pair or one full pair of discs respectively. As can be seen from this table, the number of domains pertaining to the three configurations representing one half pair of discs (approximately 80 domains) is a lot less than that used for the three configurations representing one full pair of discs (approximately 280 domains). This is due to the large number of domains needed to mesh the separation plane between each long mixing disc. Graphs 7-1 to 7-6 show the Jacobian histograms for each mesh used. As may seen from each of these graphs, their general form is approximately the same and this implies that the construction of each 3D mixing disc mesh was consistent. This condition is important if comparisons of flow parameters are to be made between rotated configurations. The average Jacobian values obtained are approximately 94, which is good.

7.3 Viscous flow Within the 3D Staggered Mixing Disc Zone

Results from the simulation of 2D cross sections, chosen to represent particular mixing disc zone profiles, are shown in Figures 7-16 to 7-17. These 2D profiles, created at sequential rotated geometries so as to represent rotation of the discs about their fixed axes (as described in Chapter 4) are of limited benefit when used for the investigation of CICo-TSE mixing elements. Figure 7-16 shows the velocity vector profiles for the 2D rotated configuration of $\alpha = 30°$. Quite correctly, the results shown in Figure 7-16 demonstrate that material located within the apertures of the left disc, experiences much greater relative velocity than that of

Figure 7-12:
P-Cube Master and Slave Distribution Assigned to the Mesh Utilised for the Representation of One Full Pair of Mixing Discs, in the In-Line Arrangement (Rotated Configuration α = 0°).

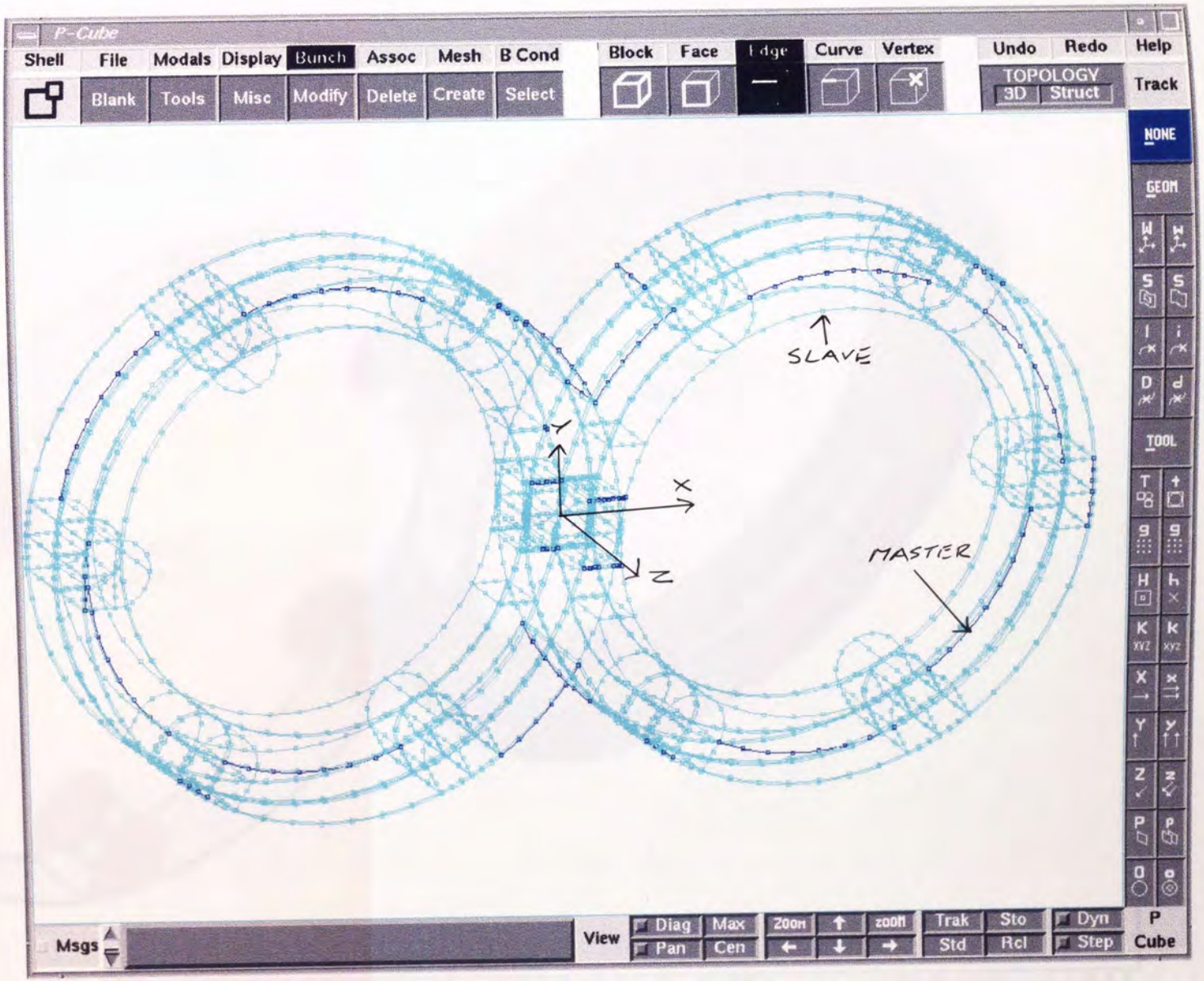

Figure 7-13:
Assignment of Boundaries 1 and 5 for the Mesh Shown in Figure 7-11.

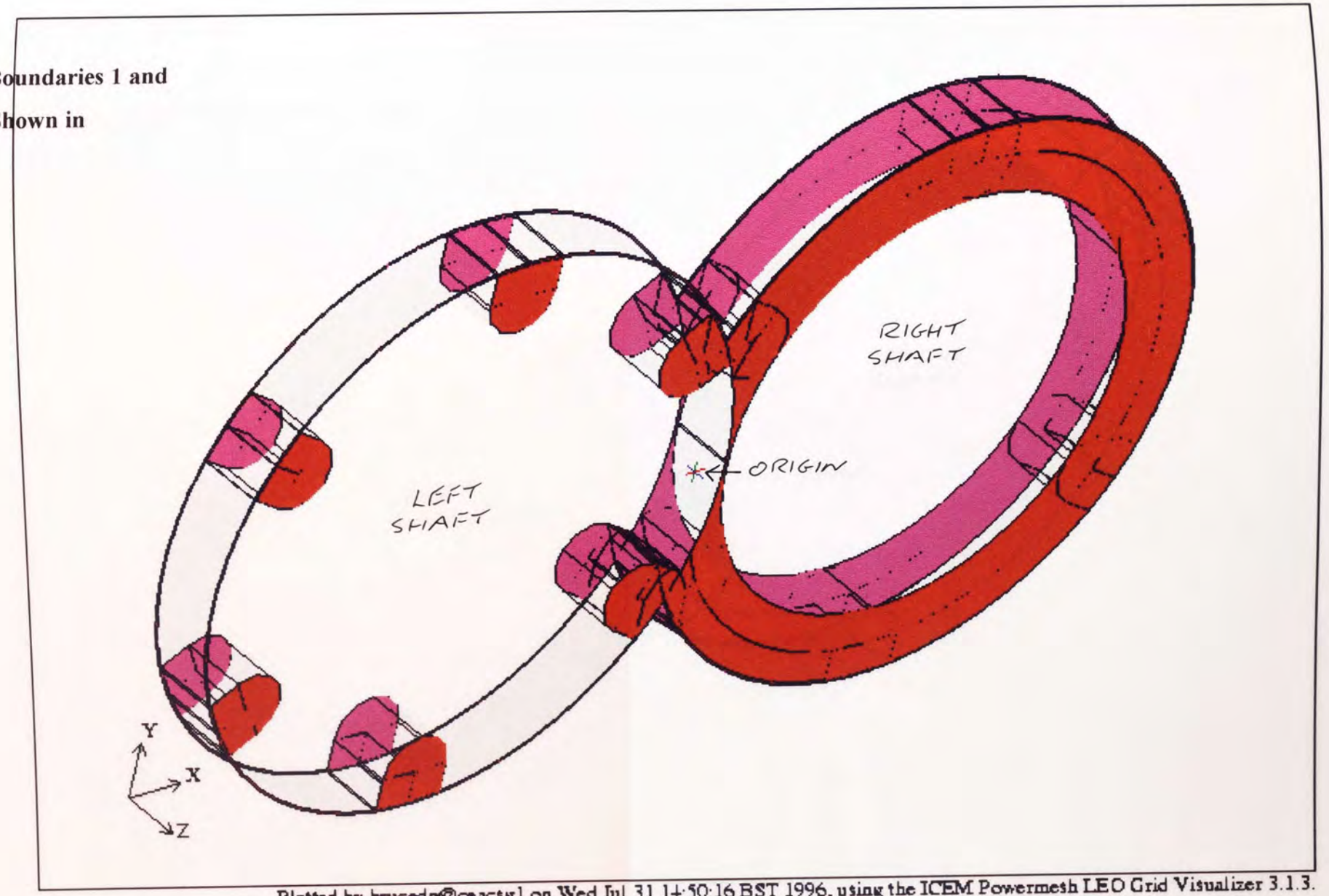

Figure 7-14:
Assignment of Boundaries 2 and 3 for the Mesh Shown in Figure 7-11.

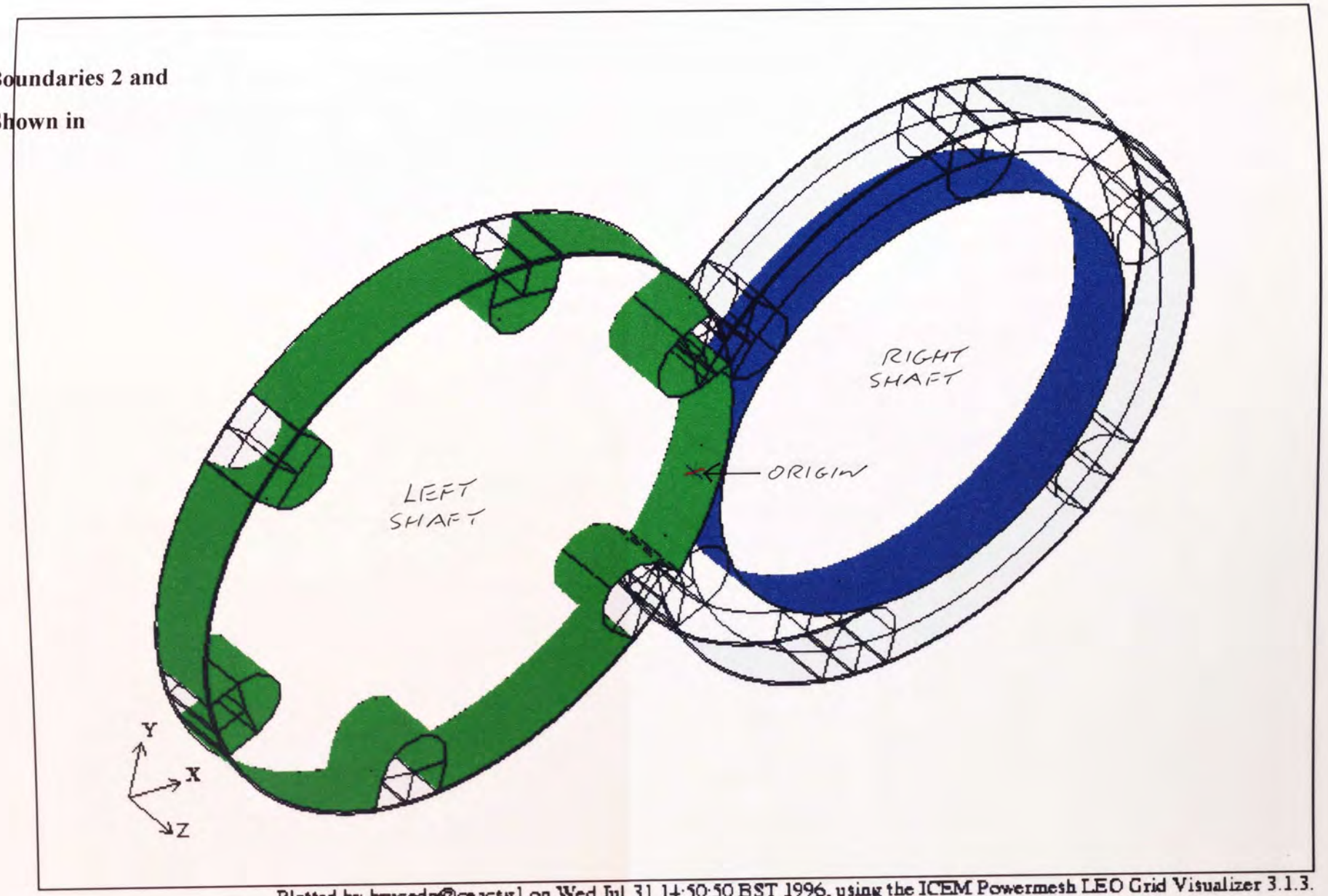

Figure 7-15:
Assignment of Boundary 4 for the Mesh Shown in Figure 7-11.

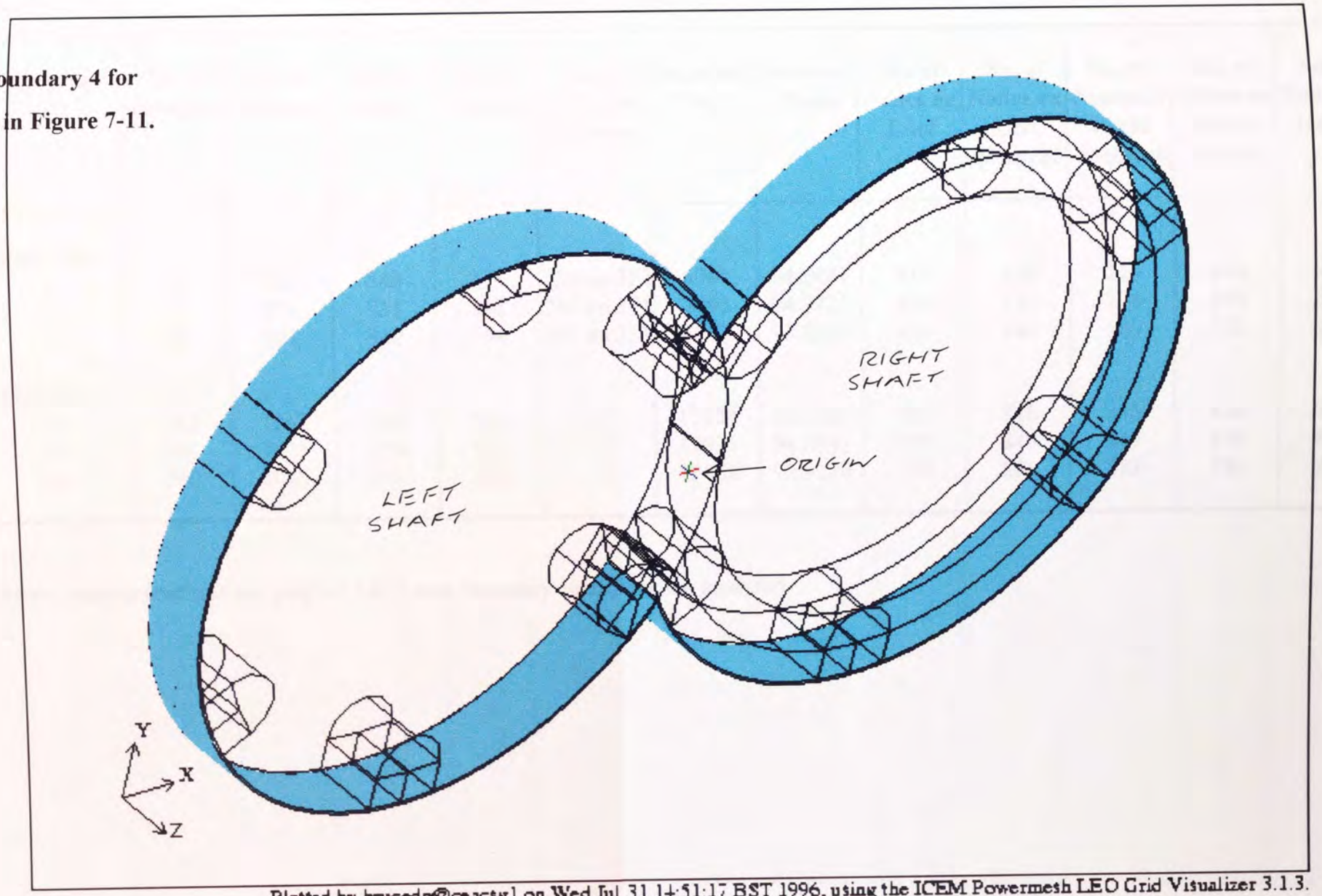

TABLE 7-1

3D Parameters Table - Staggered Mixing Discs

Configuration ($\alpha°$)	No. of Domains	No. of Subfaces	No. of Edges	No. of Vertices	No. of BC's on Subfaces	Jacobian: Total	Jacobian: Mean	No. of Nodes on Inlet	No. of Nodes on Left Element	No. of Nodes on Right Element	No. of Nodes on Outer Barrel	No. of Nodes on Outlet
Half Pair:												
0	86	382	543	246	250 on 382	8084	94.2081	911	528	216	544	911
15	83	371	531	242	244 on 371	7793	94.7725	879	532	196	544	879
30	86	381	540	244	246 on 381	8213	93.2329	920	540	180	520	920
One Pair:												
0	282	1062	1301	520	- [1]	15334	93.3885	901	846	846	816	901
15	272	1025	1256	502	- [1]	14991	94.2145	879	849	849	816	879
30	280	1044	1267	502	- [1]	15858	92.9228	920	873	873	780	920

NOTES:

1 Problems too large to load into the program LEO, thus boundary conditions not analysed.

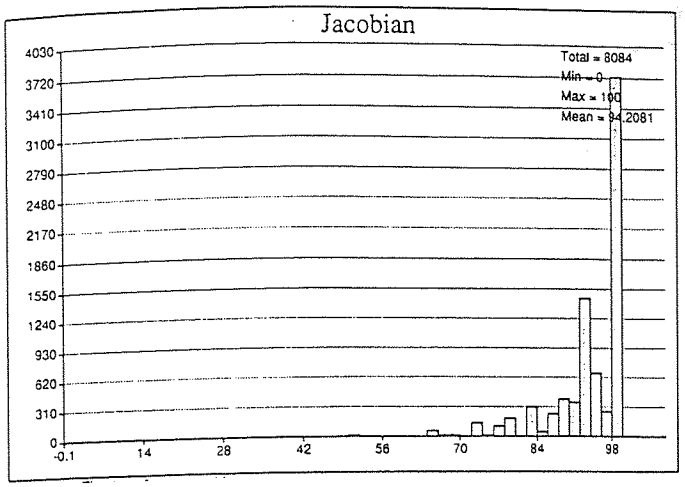

Graph 7-1:

Jacobian Distribution for the 3D Mesh Representing the Half Pair of Mixing Discs at Rotated Configuration $\alpha = 0°$.

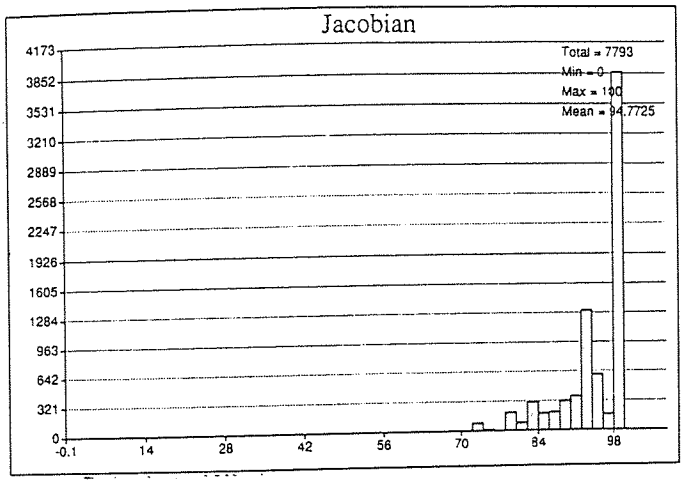

Graph 7-2:

Jacobian Distribution for the 3D Mesh Representing the Half Pair of Mixing Discs at Rotated Configuration $\alpha = 15°$.

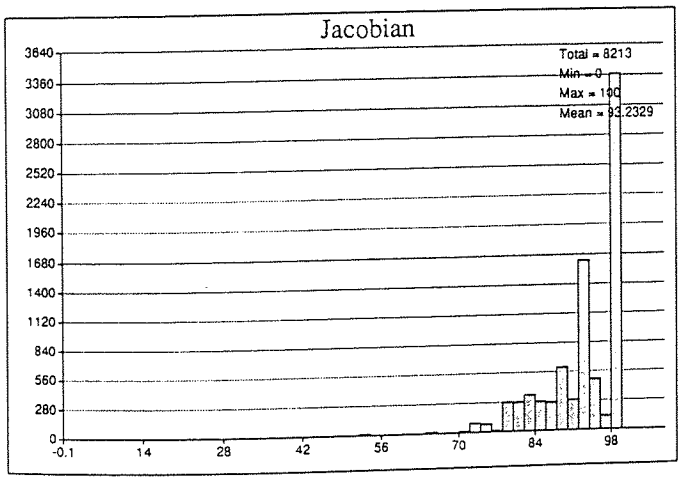

Graph 7-3:

Jacobian Distribution for the 3D Mesh Representing the Half Pair of Mixing Discs at Rotated Configuration $\alpha = 30°$.

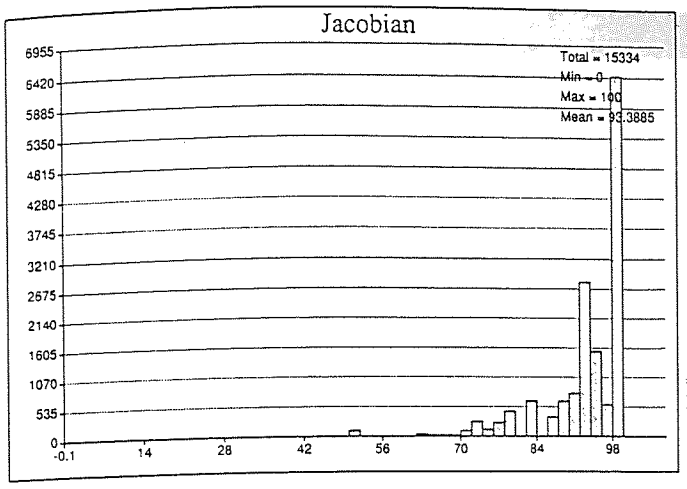

Graph 7-4:

Jacobian Distribution for the 3D Mesh Representing One Full Pair of Mixing Discs in the In-Line Arrangement, at Rotated Configuration $\alpha = 0°$.

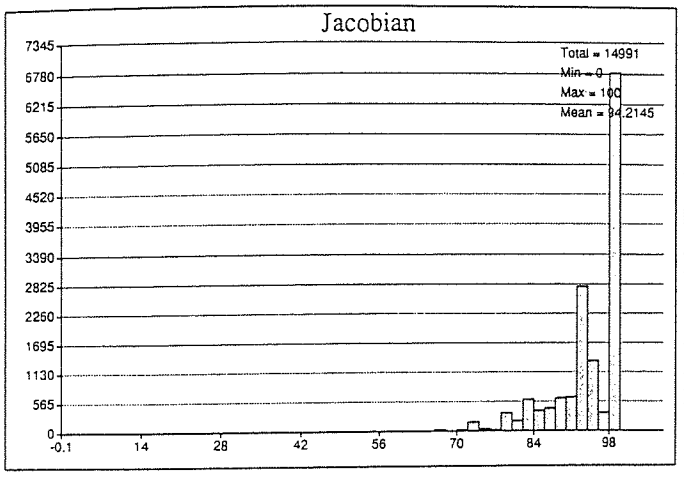

Graph 7-5:

Jacobian Distribution for the 3D Mesh Representing the One Full Pair of Mixing Discs in the In-Line Arrangement, at Rotated Configuration $\alpha = 15°$.

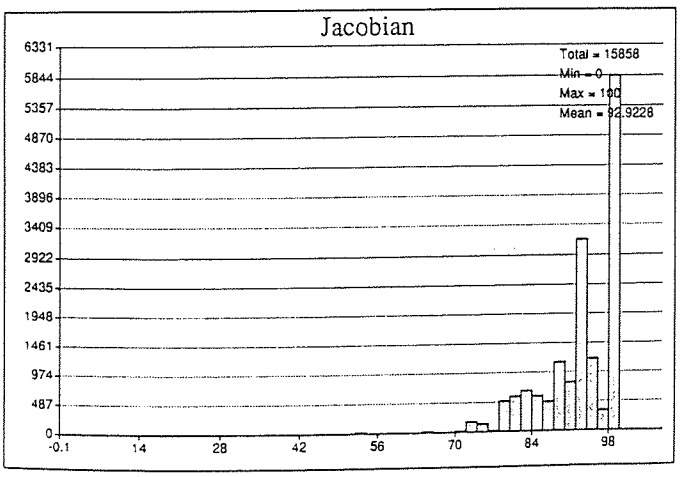

Graph 7-6:

Jacobian Distribution for the 3D Mesh Representing the One Full Pair of Mixing Discs in the In-Line Arrangement, at Rotated Configuration $\alpha = 30°$.

Figure 7-16:
Velocity Vector Profiles for the 2D Representation of the Mixing Discs in the X-Y Plane, at the Rotated Configuration $\alpha = 30°$.

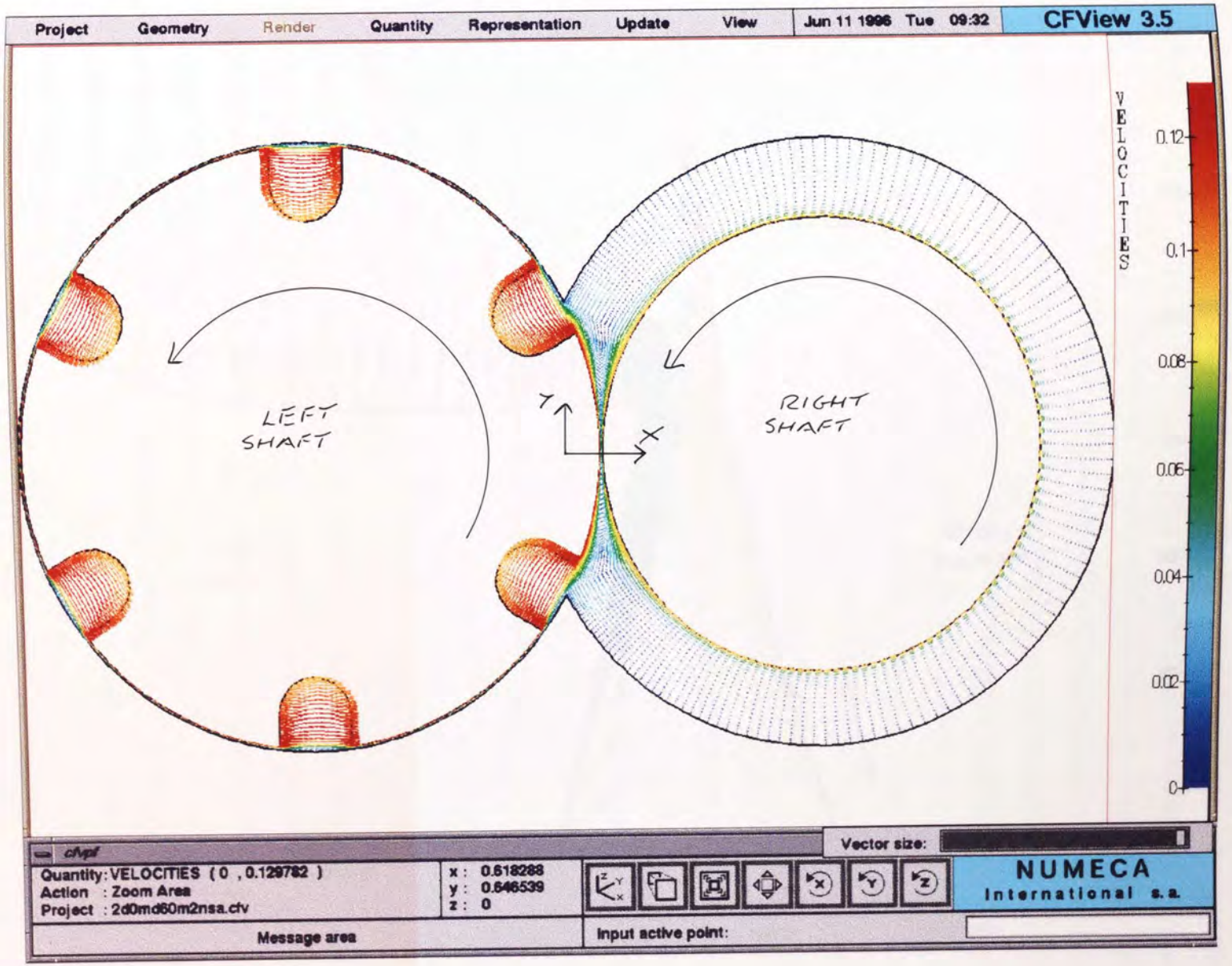

Figure 7-17:
Velocity Vector Profiles, Overlaid onto Local Shear Rate Colour Contours ($\dot{\gamma} \geq 400\ sec^{-1}$) for the 2D Representation of the Mixing Discs in the X-Y Plane, at the Rotated Configuration $\alpha = 0°$ (Magnified View).

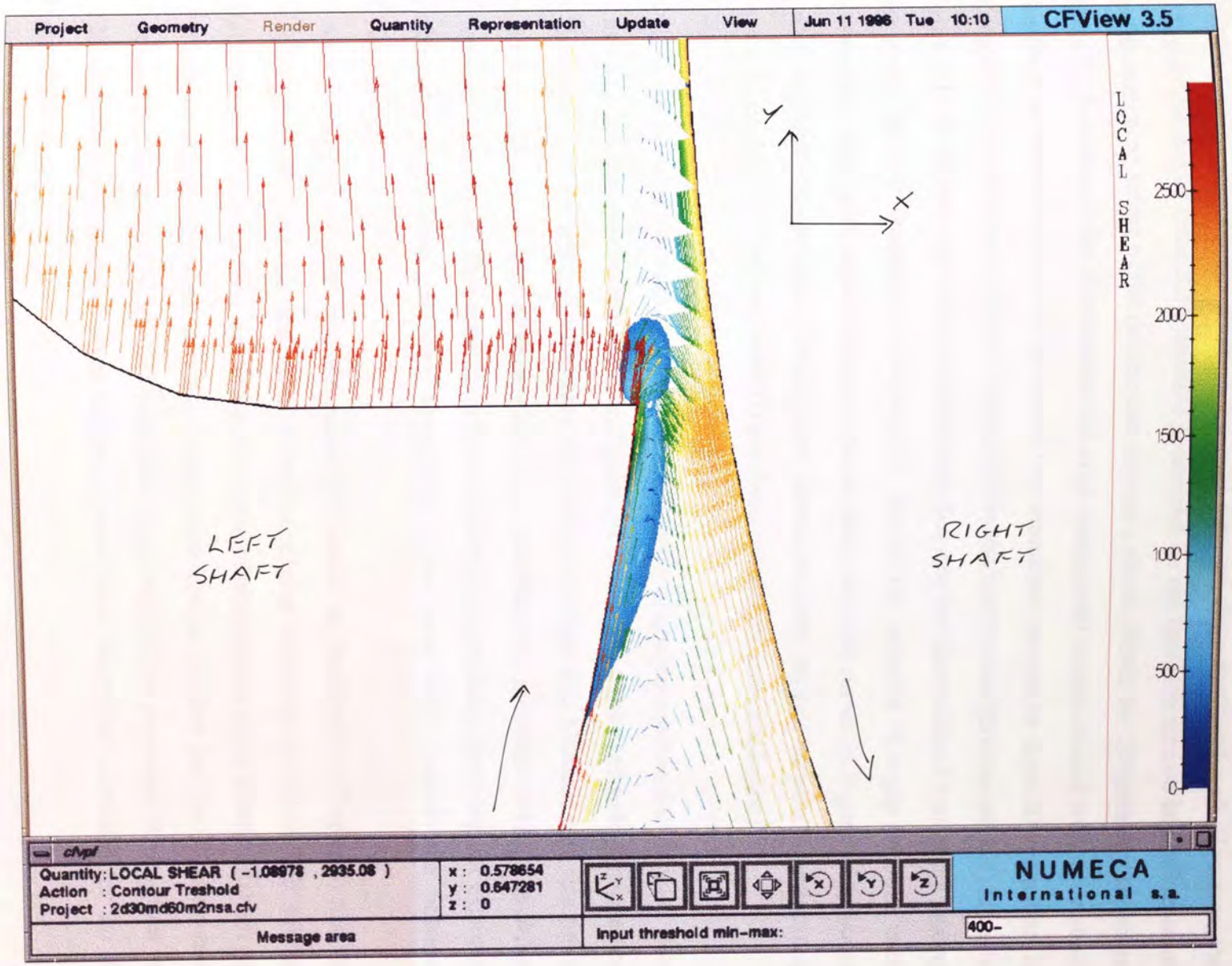

material located between the collar of the right disc and the outer barrel wall. However, the CFD calculations of these 2D sequential geometries do not take into account any influence of the 3D staggered nature of the mixing disc zone as a whole. Hence the 2D geometry shown in Figure 7-16 does not take into account the axial elongational motion created within the zone. This leads to the conclusion that the overall flow simulation picture for these 2D geometries is incomplete. The situation is further complicated by the fact that the 2D cross section shown in Figure 7-16 is not the only type of cross section that may be taken within a typical 3D mixing disc zone. As was described in Section 7.1, due to the presence of a gap between each intermeshing disc, additional 2D cross sections other than that shown in Figure 7-16, would need to be taken into account. Despite these limitations there are real benefits to performing these 2D calculations compared with 3D and these benefits are indicated below;

- Nodal point densities may be increased significantly at positions where fine detailed flow examination is required. For example, Figure 7-17 illustrates the area of swirl generated by the aperture of the left disc adjacent to the collar of the right disc. Overlaid onto this figure is the colour contour plot of areas where local shear rates are in excess of 400. The ability to obtain this kind of fine detail is useful when designing processes involving, for example, thermally degradable polymers where high shear rates might degrade the polymer significantly.
- Average values summed over the entire 2D domain (as described in Chapter 4) may be obtained at 5° intervals and used to predict mixing trends as the CICo-TSE mixing elements rotate about their fixed axes. This type of examination gives relative (though not absolute) changes between sequential geometries. Due to the fact that the 3D sequential geometries have been taken at 15° intervals, the averaged flow parameter results from the 2D simulations will give a more detailed representation than those calculated for the 3D simulations.

The remainder of this chapter describes the results obtained solely from the 3D simulation of the partial mixing cycle for one full pair of staggered mixing discs, arranged in the in-line configuration only (as described in Chapter 4). The average flow parameters calculated from the 2D simulations, such as local shear rates, inelastic stress tensors and mixing efficiencies and the 2D studies involving outer barrel slip, are discussed in relation to the 2D trilobal element results, at the end of Chapter 8. In addition comparisons are made between the average flow parameter results obtained from the simulation of viscous material through both the half pair and full pair of mixing discs.

Velocity vector profiles generated upon the five boundaries assigned (i.e. the inlet and

outlet faces and the surfaces of the right and left element and outer barrel walls), for a pair of mixing discs at the rotated configuration of $\alpha = 30°$, are shown in Figure 7-18. This result confirms some of the boundary values used within Polydata for the definition of initial flow boundary parameters (for example, no fluid slip at the outer barrel walls, where $v_s = v_n = 0$). However, the velocity vector profile on the inlet face of Figure 7-18 is seen to be complex, especially at the bridge regions. Thus to further expose the complex 3D fluid motion represented within the volumetric computational flow domain as a whole, various 2D cuts along different planes may be taken. Figures 7-19 to 7-21 display the velocity vector profiles, overlaid onto Z-velocity contours plots corresponding to both the inlet (foreground) and outlet (background) cross sections, for the mixing disc rotated configurations of $\alpha = 0°$, 15° and 30° respectively. As may be seen from the sequence through Figures 7-19 to 7-21, areas of forward and back mixing are prominent at all aperture cross sections contained within the inlet and outlet planes. The apertures that are located centrally either close to the disc on the opposing screw shaft (referred to as the intermeshing area) or neighbouring either of the two bridge regions, exhibit the most flow activity, as regards forward and back mixing behaviour. Material within the apertures that passes via the top bridge region experiences back mixing, whilst material within the apertures rotating past the bottom bridge is forced forward through the mixing zone due to the pressure drop created by the counter-clockwise, co-rotation of the mixing discs.

Examination of the apertures that are not within the locality of either of the two bridge regions or at the disc intermesh, suggests that forward and back mixing is also taking place, to some extent, within these regions. To investigate this proposition further, a cross section may be taken through the aperture which is furthest from the disc intermesh region for the $\alpha = 0°$ configuration, as shown in Figure 7-22. Inspection of the Z-velocity contour plot on this cross section leads to the conclusion that any forward and back mixing being generated is minimal. Magnification and orientation along the X-axis of this cross section, shown in Figure 7-23, confirms this observation. Material contained within this region would almost certainly not be undergoing mixing to any significant level. Instead, mixing behaviour is mostly being exhibited within the volume which encompasses both bridge regions and disc intermesh region.

Figures 7-24 to 7-26 show a sequence of Y-Z cross sections along the axial length of the barrel for the rotated configurations, $\alpha = 0°$, 15° and 30° respectively. All points contained within each cross sectional plane shown, possesses an $X = 0$ mm co-ordinate value. Figure 7-24, representing the $\alpha = 0°$ rotated configuration, shows fluid flow when the two apertures from opposing discs coincide to give a fully in-line aperture arrangement at the very core of the mixing zone. Since a fluid "tunnel" has been created by this aperture alignment,

Figure 7-18:

Velocity Vector Profiles Present at the Boundaries for the 3D Mixing Disc Zone Containing One Pair of Discs in the In-Line Arrangement, at the Rotated Configuration $\alpha = 30°$.

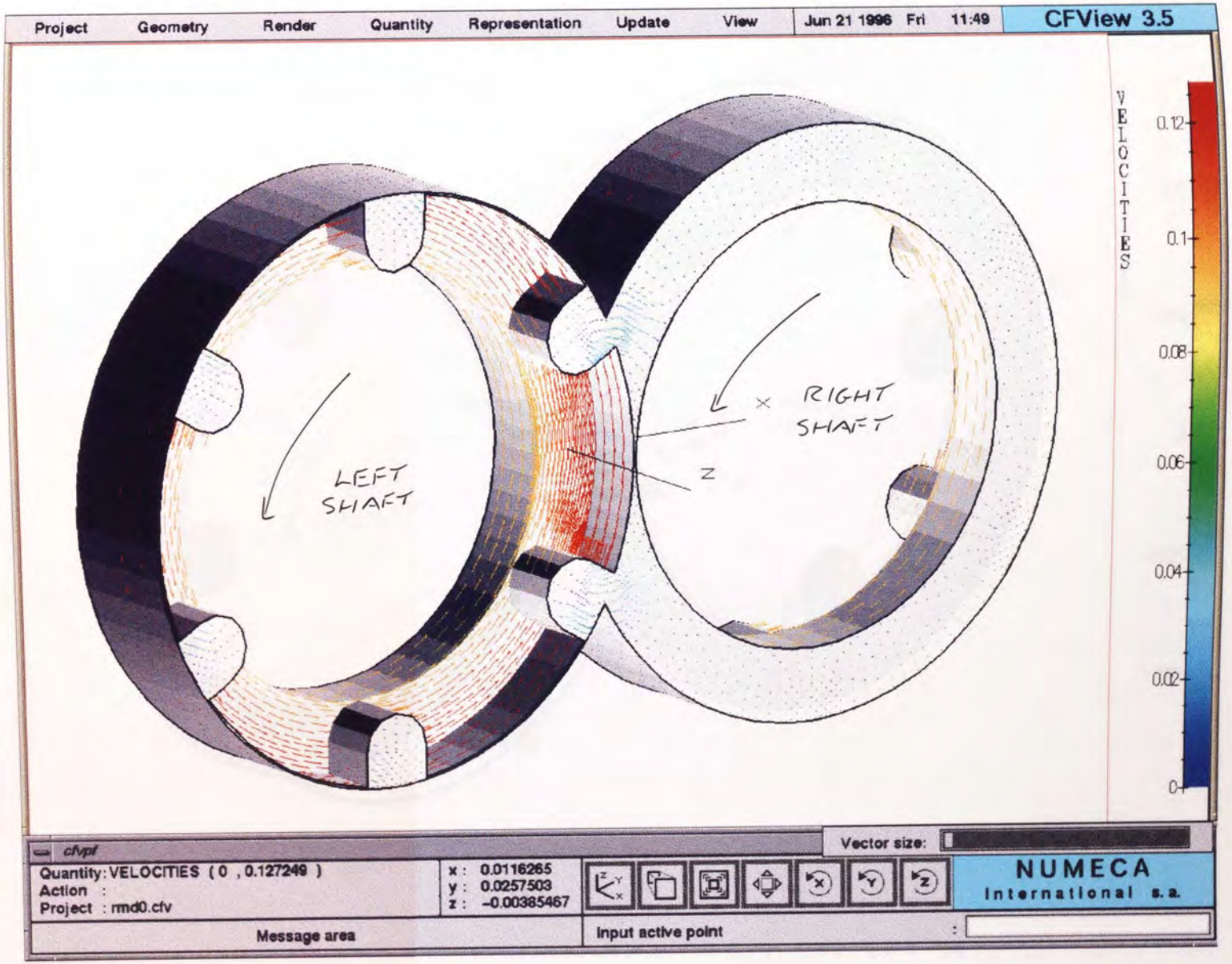

Figure 7-19:
Velocity Vector Profiles, Overlaid onto Z-Velocity Colour Contours at Both the Inlet (Foreground) and Outlet (Background) X-Y Planes, for the 3D Mixing Disc Zone Containing One Pair of Discs in the In-Line Arrangement, at the Rotated Configuration $\alpha = 0°$.

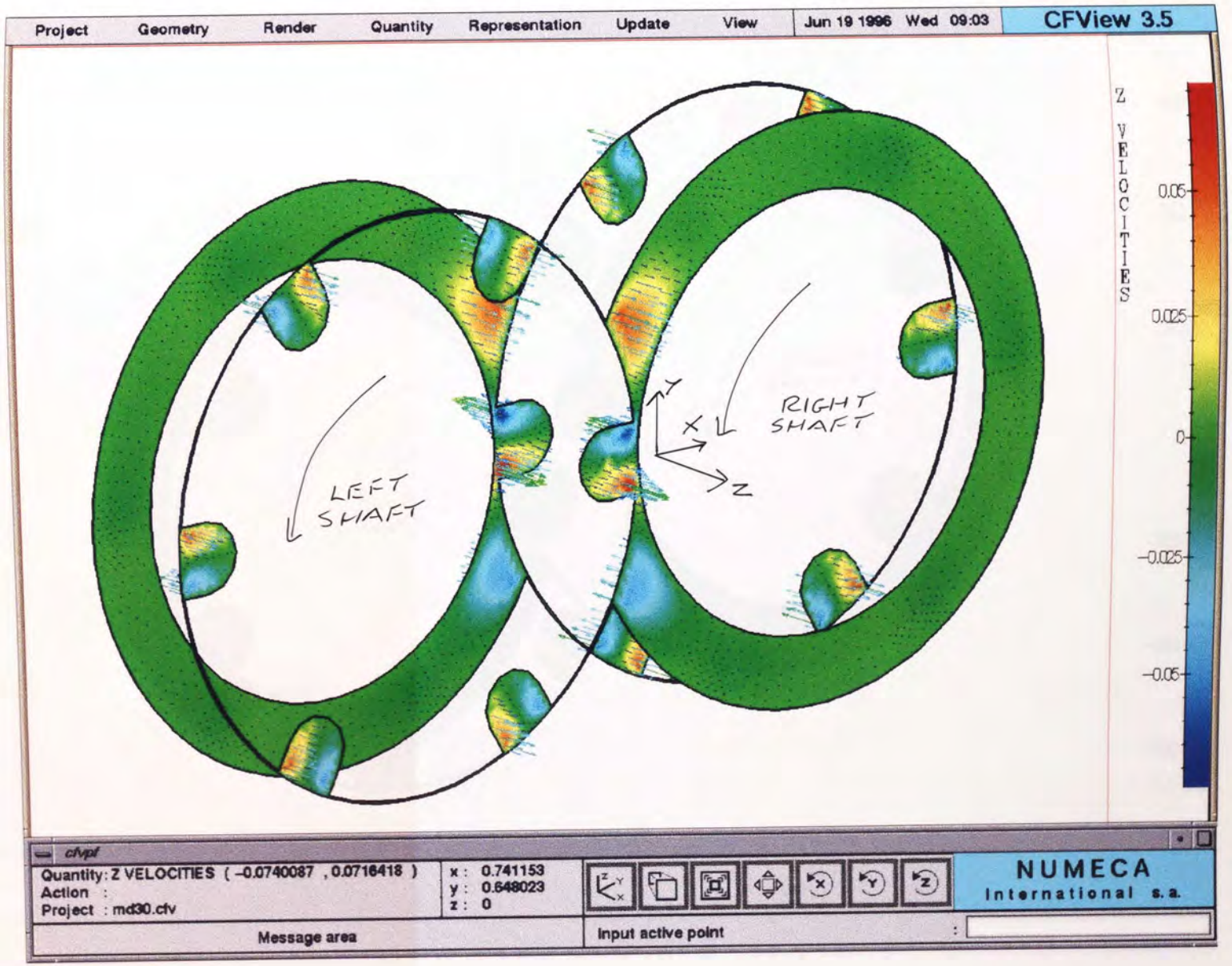

Figure 7-20:

Velocity Vector Profiles, Overlaid onto Z-Velocity Colour Contours at Both the Inlet (Foreground) and Outlet (Background) X-Y Planes, for the 3D Mixing Disc Zone Containing One Pair of Discs in the In-Line Arrangement, at the Rotated Configuration $\alpha = 15°$.

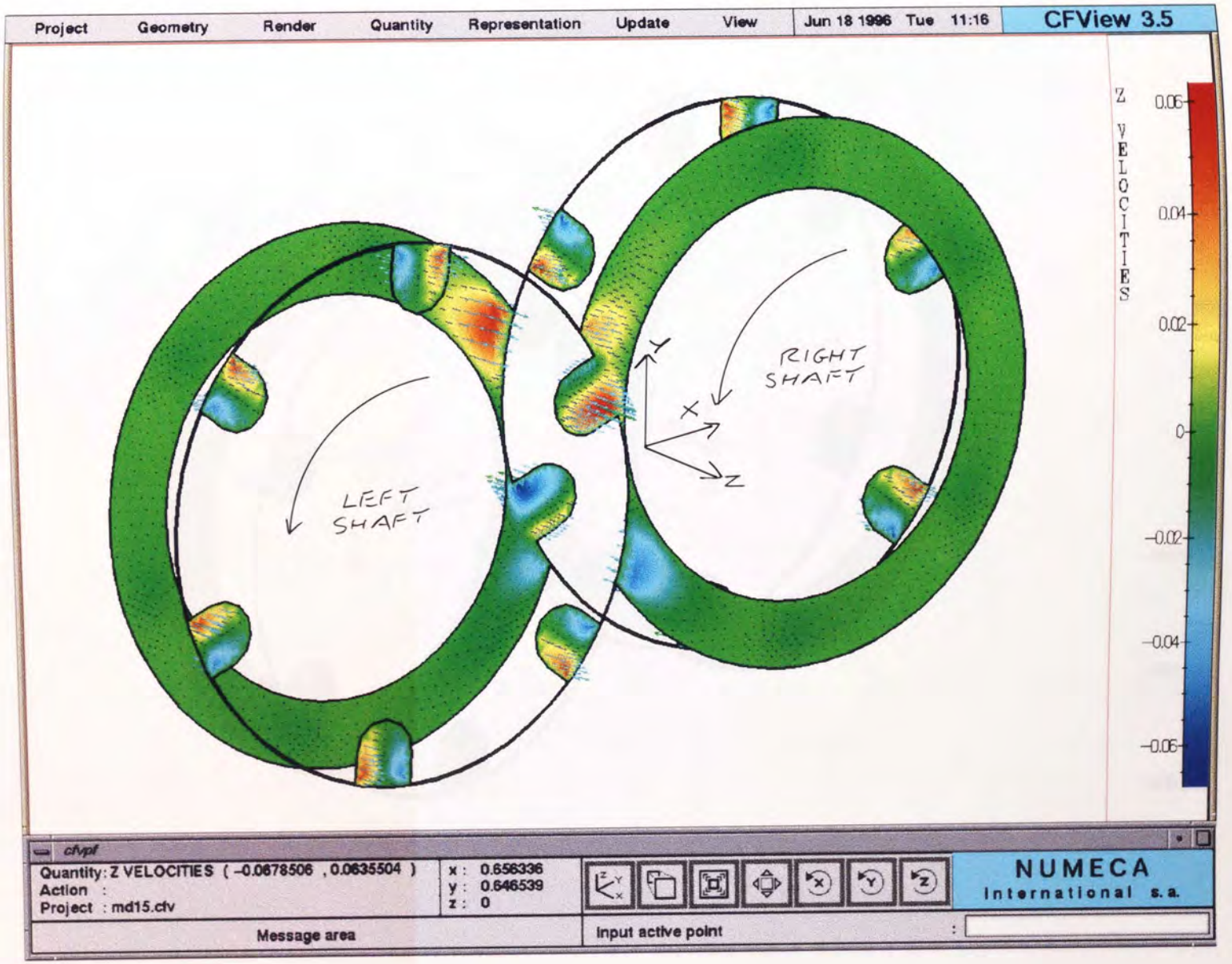

Figure 7-21:

Velocity Vector Profiles, Overlaid onto Z-Velocity Colour Contours at Both the Inlet (Foreground) and Outlet (Background) X-Y Planes, for the 3D Mixing Disc Zone Containing One Pair of Discs in the In-Line Arrangement, at the Rotated Configuration $\alpha = 30°$.

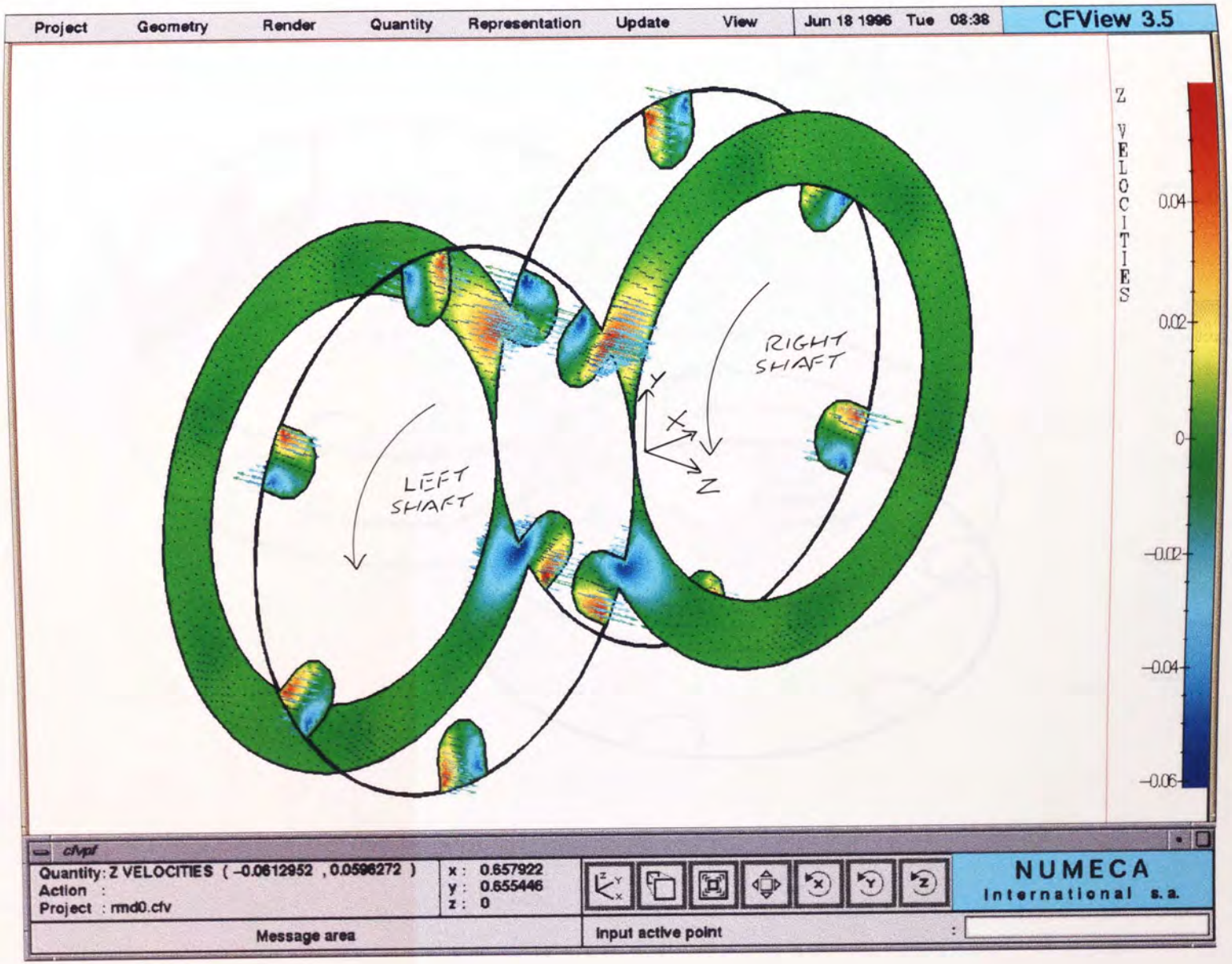

Figure 7-22:

Z-velocity Contour Plot on a Cross Section in the Y-Z Plane Taken Through the Aperture Furthest From the Disc Intermesh Region, for the 3D Mixing Disc Zone Containing One Pair of Discs in the In-Line Arrangement, at the Rotated Configuration a = 0°.

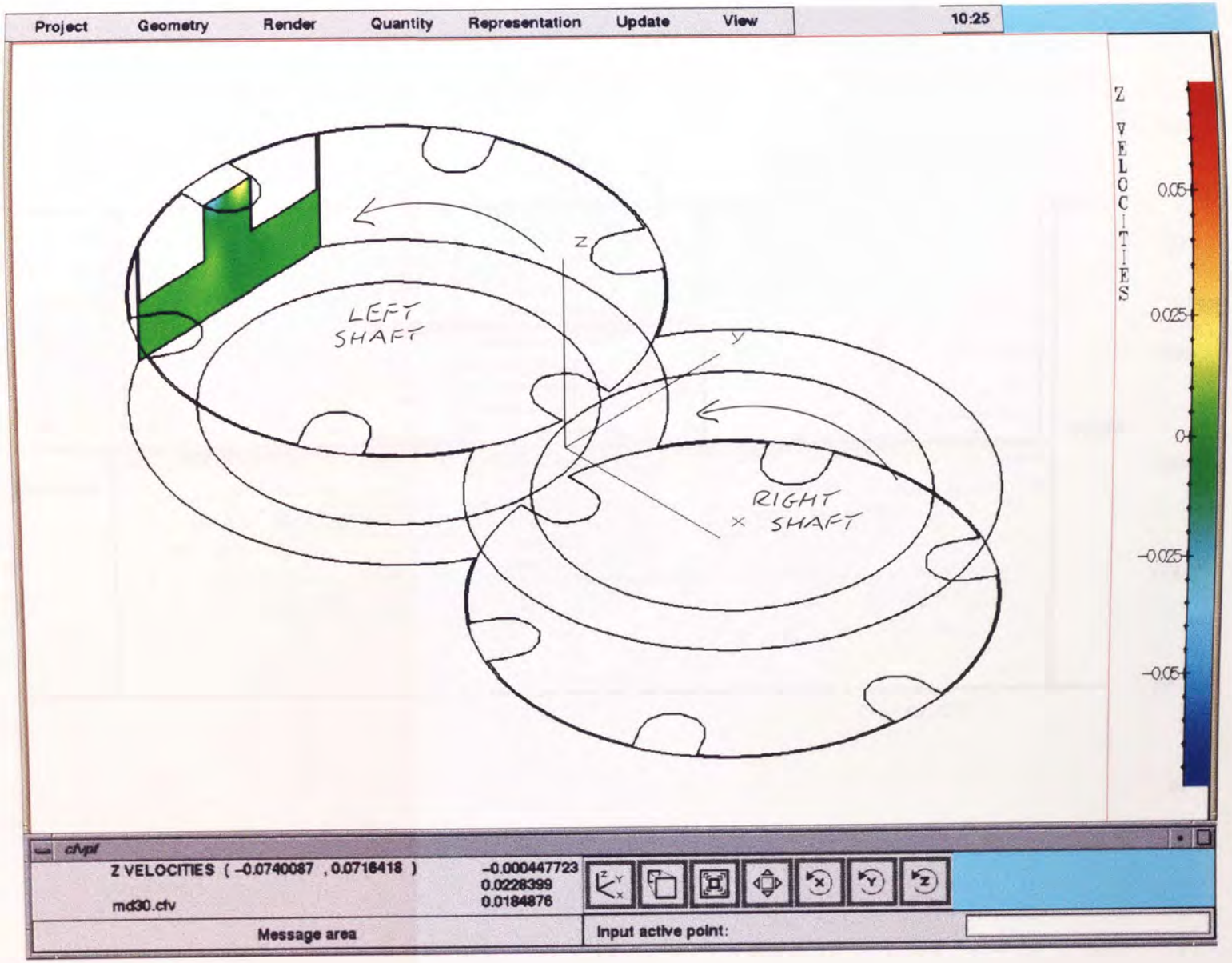

Figure 7-23:
Velocity Vector Profiles on the Cross Section Described in Figure 7-22, Viewed Along the X-Axis (Magnified View).

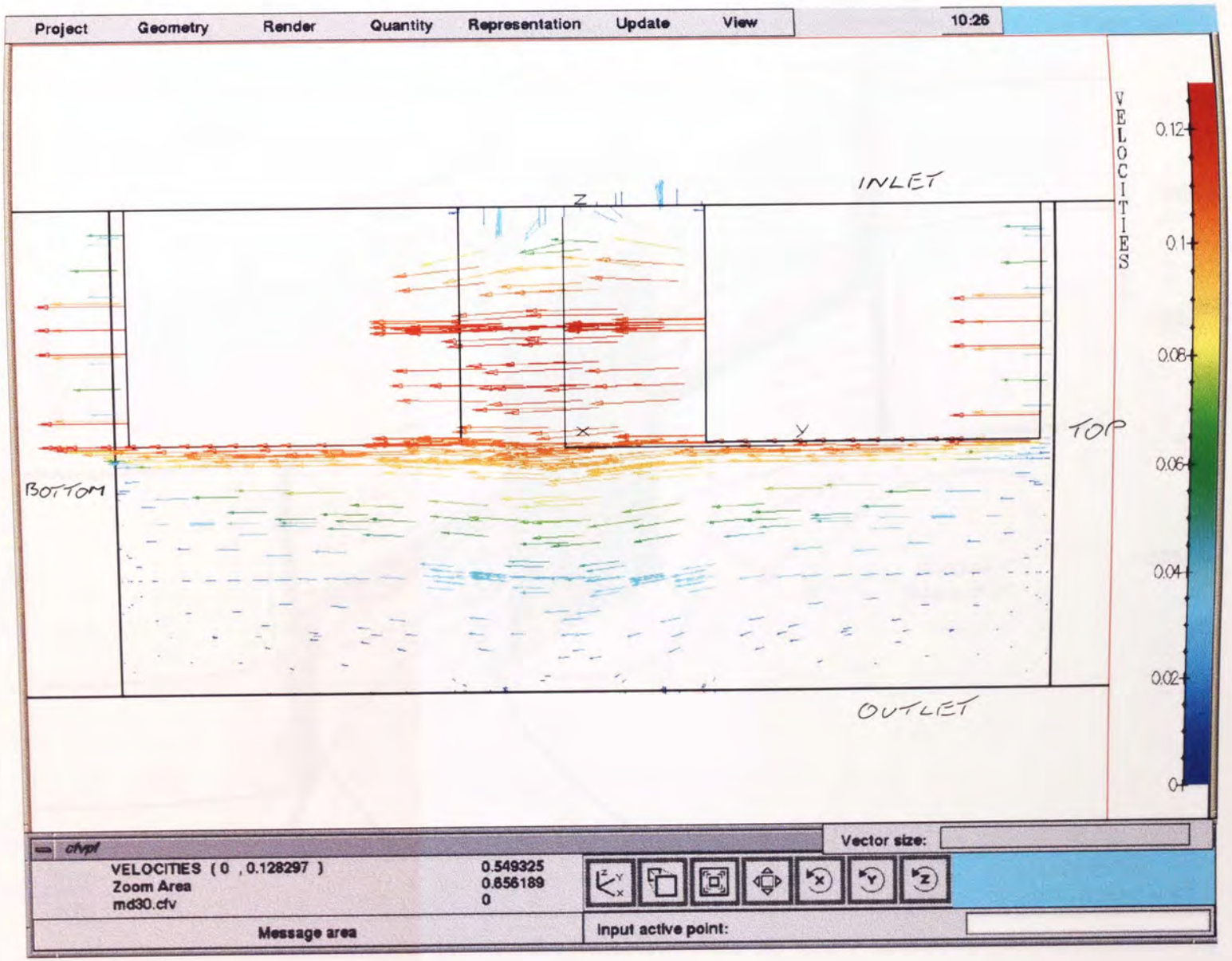

Figure 7-24:
Velocity Vector Profiles, Overlaid onto Z-Velocity Colour Contours for the Cross Section Created Centrally in the Y-Z Plane, for the 3D Mixing Disc Zone Containing One Pair of Discs in the In-Line Arrangement, at the Rotated Configuration $\alpha = 0°$ (Magnified View).

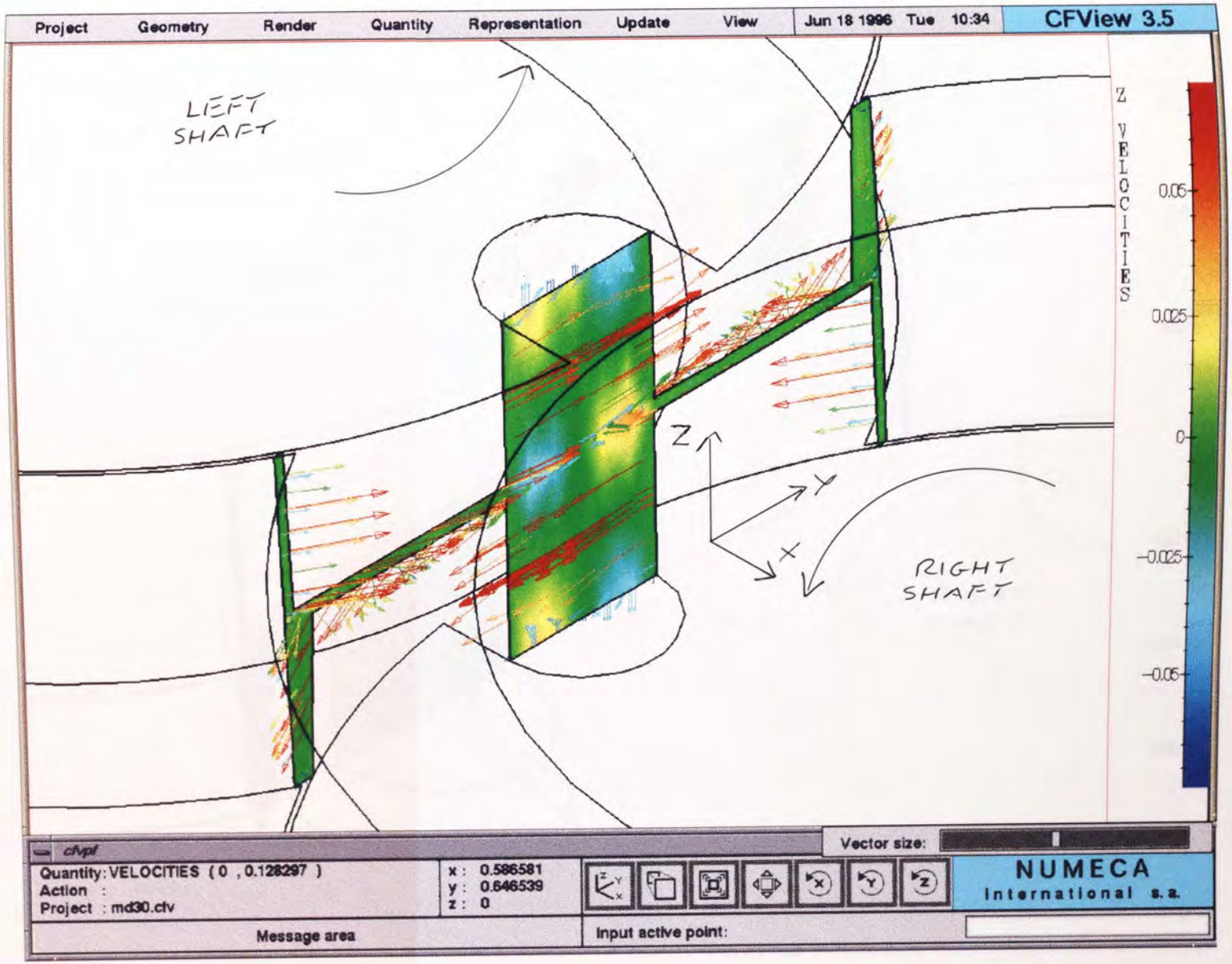

Figure 7-25:
Velocity Vector Profiles, Overlaid onto Z-Velocity Colour Contours for the Cross Section Created Centrally in the Y-Z Plane, for the 3D Mixing Disc Zone Containing One Pair of Discs in the In-Line Arrangement, at the Rotated Configuration α = 15° (Magnified View).

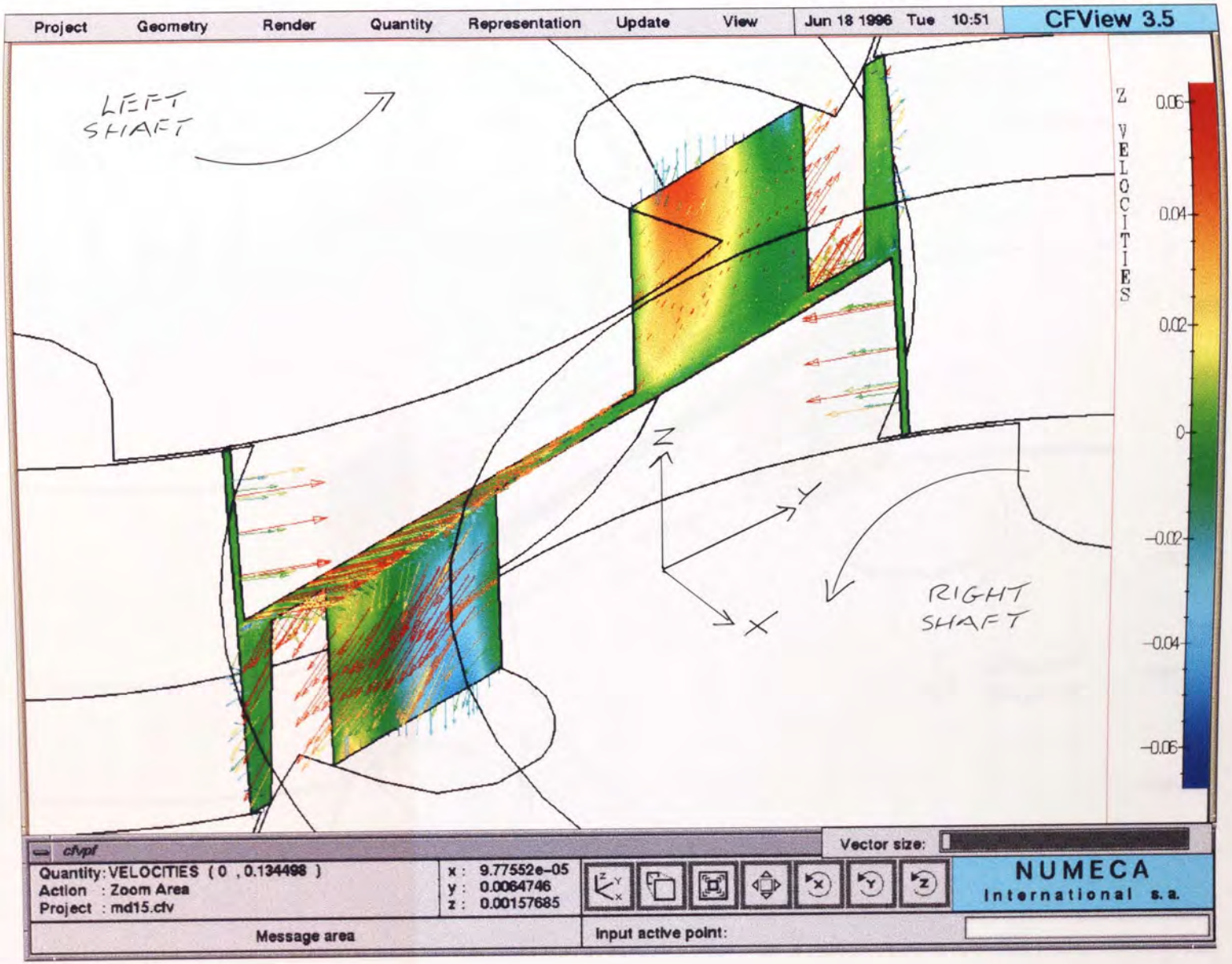

Figure 7-26:
Velocity Vector Profiles, Overlaid onto Z-Velocity Colour Contours for the Cross Section Created Centrally in the Y-Z Plane, for the 3D Mixing Disc Zone Containing One Pair of Discs in the In-Line Arrangement, at the Rotated Configuration $\alpha = 30°$ (Magnified View).

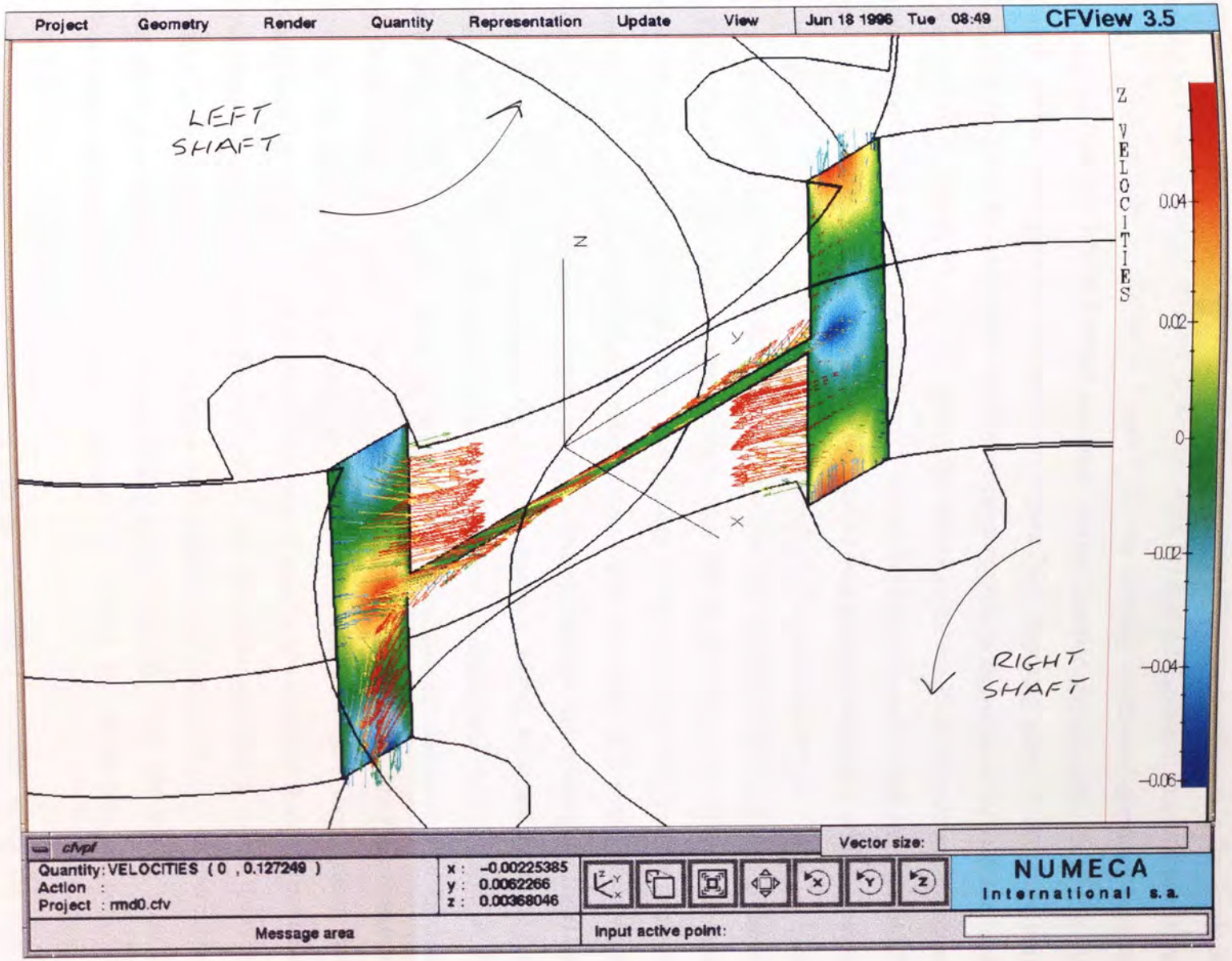

there is a significant drop in pressure gradient and thus a subsequent reduction in the levels of forward and back mixing displayed. However, when the disc configuration rotates towards the $\alpha = 15°$ configuration, as shown in Figure 7-25, the centrally positioned apertures become fully out of line and hence forward and back mixing increase significantly. Finally at the $\alpha = 30°$ rotated configuration, as shown in Figure 7-26, opposing pairs of apertures only partially coincide at both the upper and lower bridge regions, with sustained forward and back mixing being exhibited. Figure 7-27 shows the experimental result of pre-packing the screw elements preceding the mixing disc zone, with two different coloured undiluted "Playstuff" clay samples (initially one of each coloured sample was packed exclusively within separate screw element channels - referred to as Experiment 1). The picture shown in Figure 7-27 has been taken so as to expose the fluid "tunnel" mentioned in relation to the cross section shown in Figure 7-24 and the orientation presented is such that the entrance to the mixing disc zone is to the right of the image as viewed and the exit to the left. From the processed sample shown in Figure 7-27, cross-sectional samples were taken in both the Y-Z plane, as shown in Figure 7-28 (i.e. contrasting component mixing at different axial positions along the zone) and in the X-Y plane, as shown in Figure 7-29 (i.e. for observing mixing exhibited about the disc collar regions). Figure 7-28, shows an increased "degree of mixedness" from material at the mixing zone entrance (material to the left of the picture as viewed) and material at the zone exit (material to the right). The cross-sectional sample shown in Figure 7-29, however, suggests that material flowing around each disc collar volume undergoes simple shear, with no localised rotational motion evident. This type of behaviour is implied from the predicted simulation results shown within Figures 7-19 to 7-21 (i.e. rotational motion within the collar volumes is only apparent once material approaches either bridge region). Experimental quantification of the degree of mixing undergone by material within the mixing zone by pre-packing of the preceding screw elements, is difficult for the reasons explained in Chapter 5.

It is interesting to note from Figures 7-24 to 7-26 that at locations along the central apertures where the separation plane is encountered, localised areas of forward and back mixing are observed. To study the disc separation plane further, X-Y cross sectional planes exactly half way along the mixing disc pair, at the Z co-ordinate values of 4.8 mm, were investigated (the separation length between the two discs is 0.4 mm, which means that the separation volume lies within the region $4.4 \text{ mm} \leq Z \leq 4.8 \text{ mm}$). Figures 7-30 to 7-32 show the velocity vector profiles for X-Y cross sections midway through the staggered mixing disc pair, obtained for the $\alpha = 0°$, 15° and 30° configurations respectively. Each of these three cross sections thus display the exact centre of the separation plane between the two intermeshing discs. For the $\alpha = 0°$ configuration shown in Figure 7-30, the coincidence of the

Figure 7-27:
Results of Pre-Packing the Screw Elements Preceding a Mixing Disc Zone Containing Four Pairs of Discs in the In-Line Arrangement, With Two Different Coloured "Playstuff" Clay Samples and Then Processing (Experiment 1). View Within the Intermeshing Region Shown.

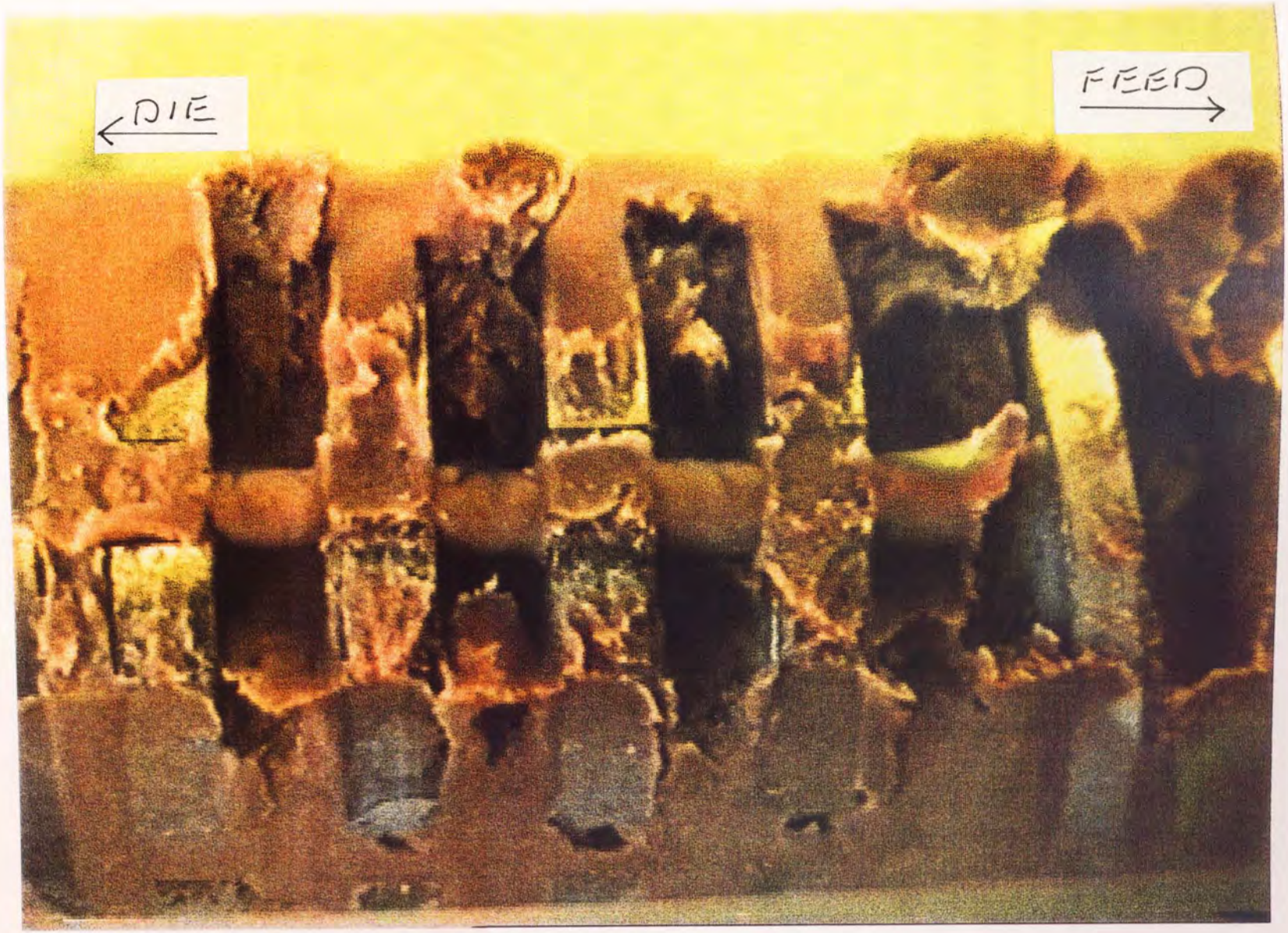

Figure 7-28:
Cross-Section of Part of the Sample Shown Within Figure 7-27 Taken in the Y-Z Plane, Illustrating Mixing Along the Mixing Zone.

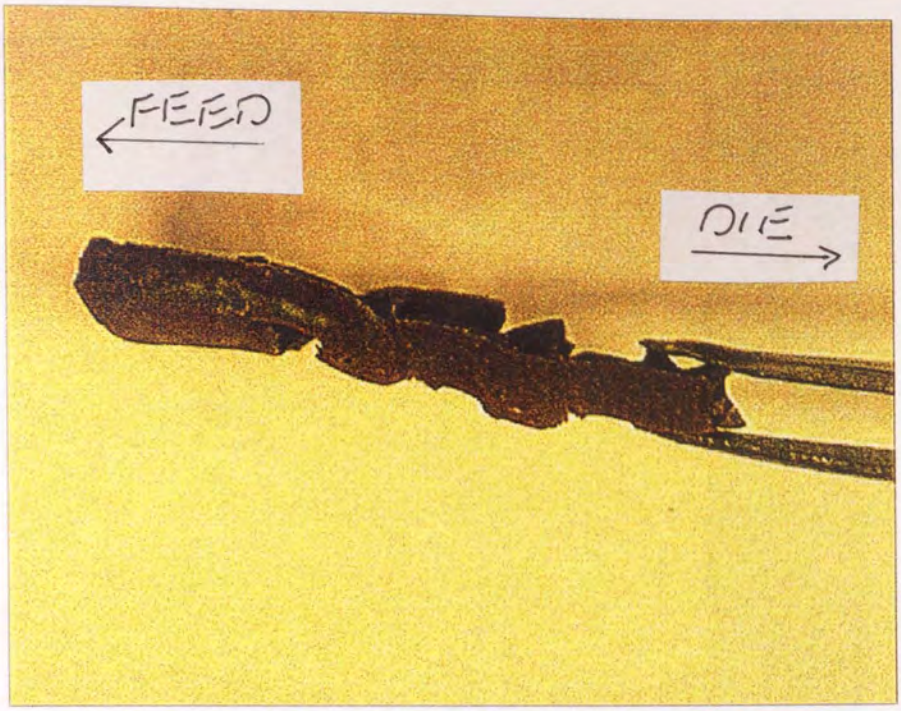

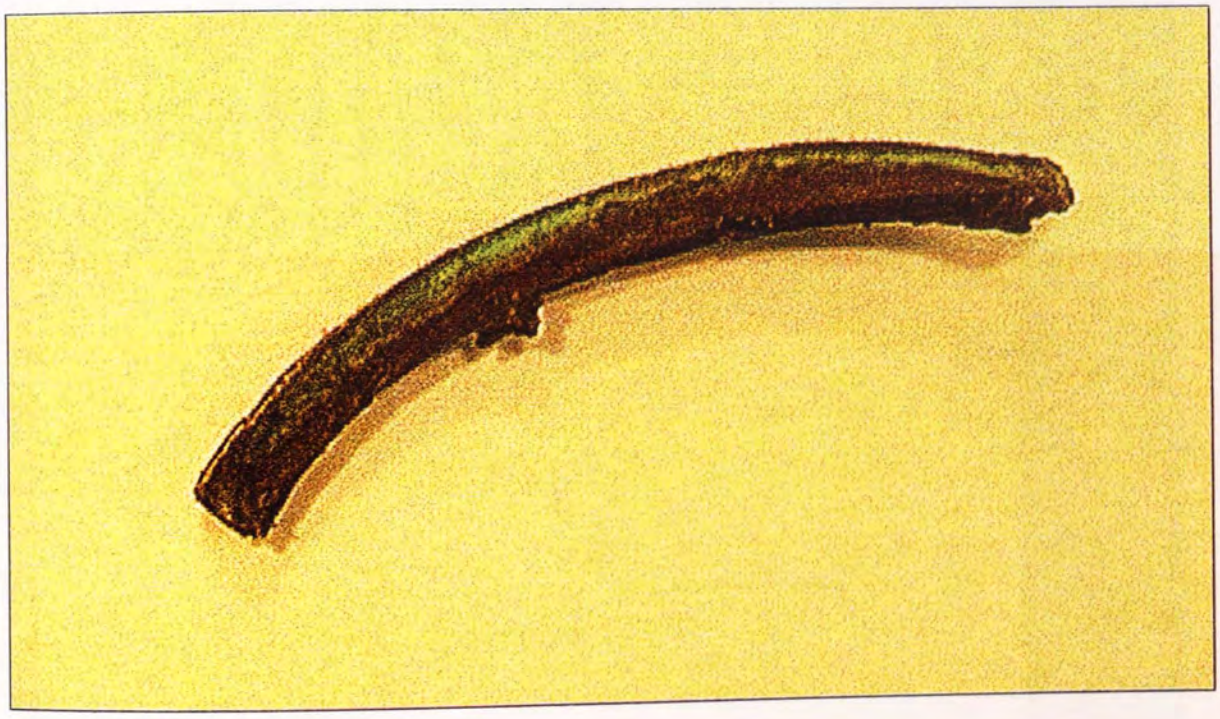

Figure 7-29:
Cross-Section of Part of the Sample Shown Within Figure 7-27 Taken in the X-Y plane, Illustrating Mixing About the Disc Collar Region.

Figure 7-30:
Velocity Vector Profiles on the Cross Section Created Exactly Half Way Along the Zone (Z = 4.8 mm) in the X-Y Plane, for the 3D Mixing Disc Zone Containing One Pair of Discs in the In-Line Arrangement, at the Rotated Configuration α = 0° (Magnified View).

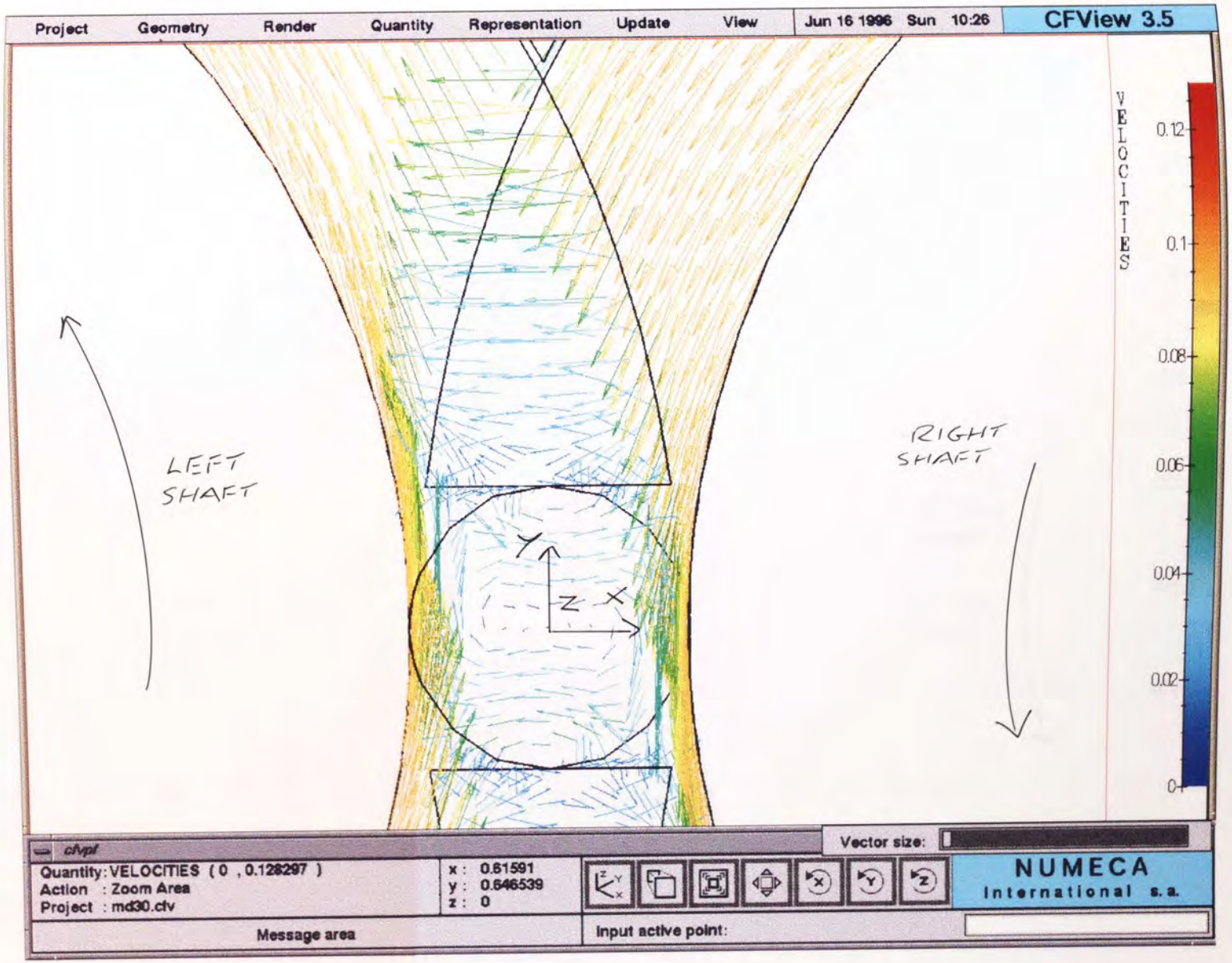

Figure 7-31:
Velocity Vector Profiles on the Cross Section Created Exactly Half Way Along the Zone (Z = 4.8 mm) in the X-Y Plane, for the 3D Mixing Disc Zone Containing One Pair of Discs in the In-Line Arrangement, at the Rotated Configuration α = 15° (Magnified View).

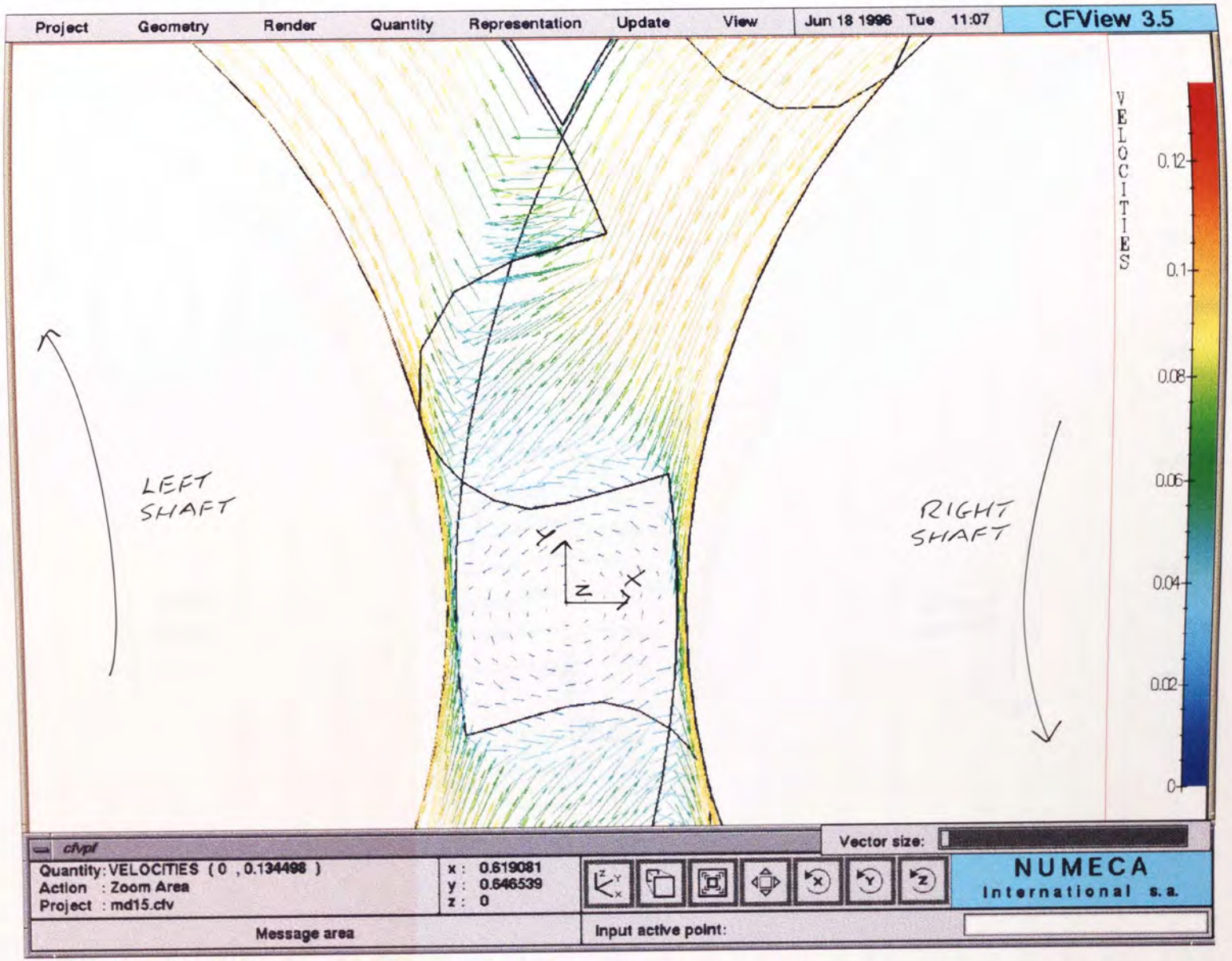

Figure 7-32:
Velocity Vector Profiles on the Cross Section Created Exactly Half Way Along the Zone (Z = 4.8 mm) in the X-Y Plane, for the 3D Mixing Disc Zone Containing One Pair of Discs in the In-Line Arrangement, at the Rotated Configuration α = 30° (Magnified View).

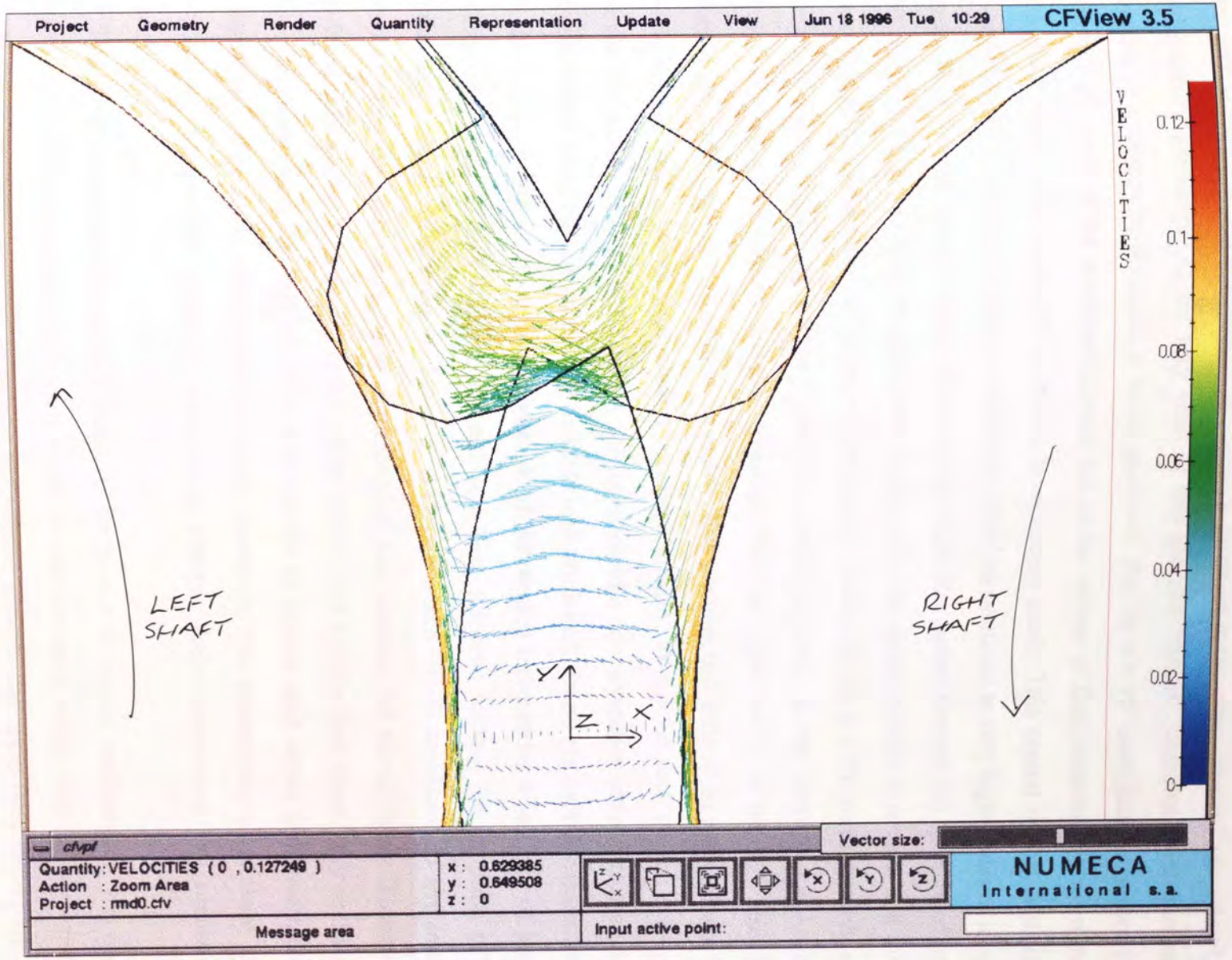

two central apertures, each moving in the opposite direction to the other, creates large velocity and pressure gradients. At the very heart of this aperture "tunnel", complex spiral motion rotating in a clockwise direction, is being generated. For the $\alpha = 15°$ configuration shown in Figure 7-31, none of the apertures coincide and so the volume of fluid contained between the two discs where they centrally intermesh, is extremely small. This central region, with its evident swirling motion, is where viscous melt would be subjected to very high values of local shear. Near the top bridge region, fluid from the right disc passes through the aperture of the left disc. However, as may be seen from Figure 7-31, the abrupt change in motion that this crossover of material produces is quite pronounced. Finally for the $\alpha = 30°$ configuration, as shown in Figure 7-32, two apertures partially coincide at both the top (shown) and lower bridge regions. This causes material crossing from the right cavity to the left also to experience abrupt changes in motion. In reality, it is possible that little or no material would be contained within the disc separation volume. Certainly, as will be seen for the average parameter values reported in Chapter 8, the inclusion of a disc separation plane increases the average local shear rates significantly and this may artificially distort the overall calculation. In the Author's opinion though, construction of the meshes representing a full pair of long mixing discs within this study, could not have been achieved without the inclusion of a separation volume. In general, inclusion or exclusion within a CFD simulation of any small volume separating most processing elements leads to a dilemma and this is clearly illustrated in Wang and Manas-Zlocower's investigation of the CTM [72]. In their paper, they excluded the separation plane between the stator and rotor for all meshes used within their study, thus simplifying the mesh construction problem. However, the assumption to exclude the separation volume then leads to discrepancies between their experimental and simulated results.

The 2D cross section shown in Figure 7-33 for the $\alpha = 0°$ rotated configuration, has been presented to illustrate more clearly the swirling motion contained within both the two central apertures when they coincide and within the volume close to the upper (and lower) bridge region. This cross section has been represented in all three spatial directions. The orientation shown in Figure 7-33 is that looking down from the top of the mixing zone along the Y-axis. This cross section, however, is more effectively viewed along the Z-axis, as shown in Figure 7-34, such that the velocity vectors on the right hand side of the cross section as shown are towards the inlet section, whilst those vectors to the left hand side lie towards the outlet. As may be illustrated from this cross section, the intensity of swirling for the volume of viscous fluid contained within the two coinciding apertures, increases the closer the fluid progresses to the centre (i.e. towards the disc separation volume). It may be also seen from this figure that the predicted direction of rotational motion, from the perspective of the feed

Figure 7-33:

Velocity Vector Profiles on the Cross Section Created in All Three Spatial Directions, so as to Illustrate the Swirling Motion Contained Within Both the Two Central Apertures When They Coincide and Within the Volume Close to the Upper Bridge Region, for the 3D Mixing Disc Zone Containing One Pair of Discs in the In-Line Arrangement at the Rotated Configuration $\alpha = 0°$ and Viewed Along the Y-Axis.

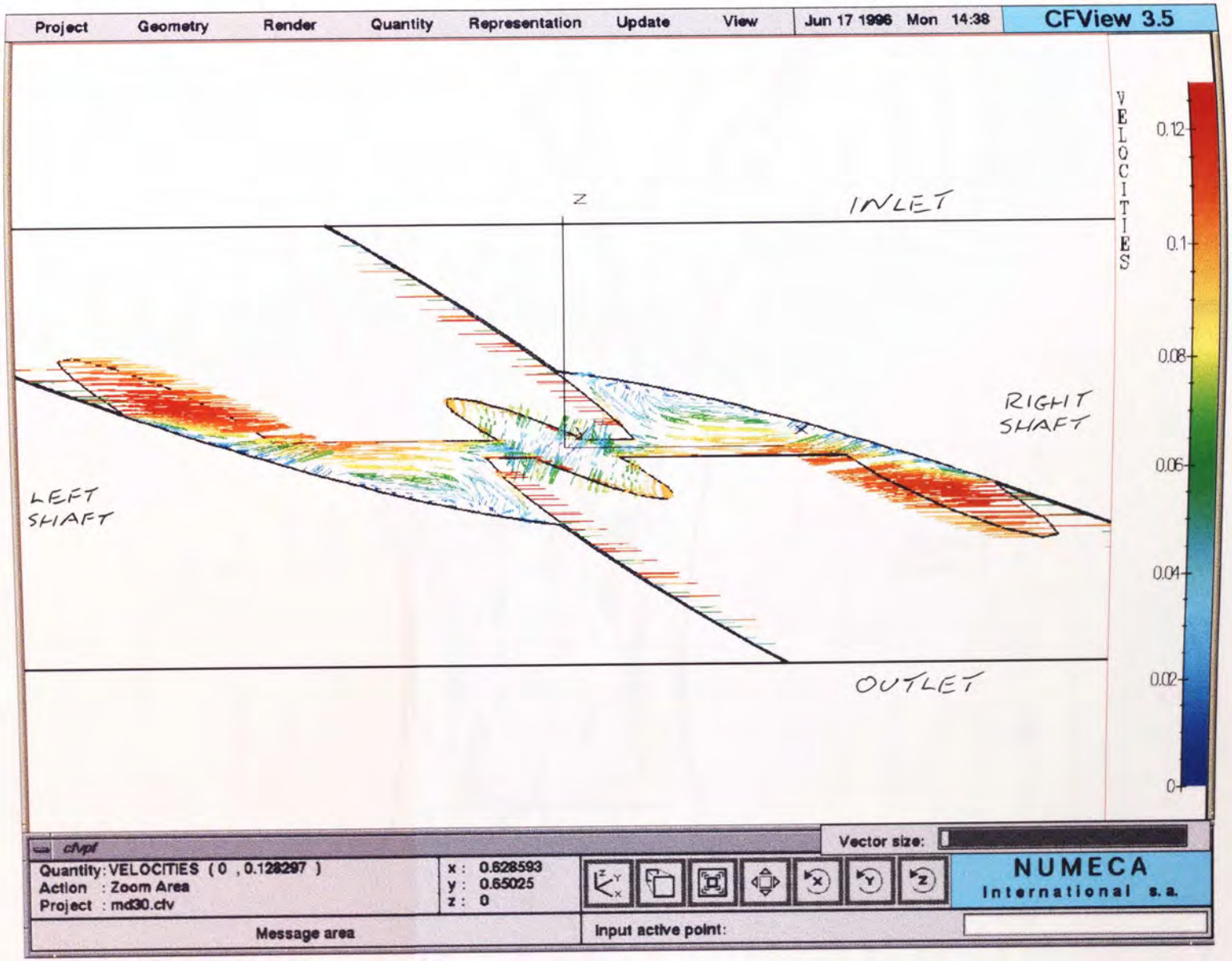

Figure 7-34:
Velocity Vector Profiles on the Cross Section Described in Figure 7-33, Viewed Along the Z-Axis (Magnified View).

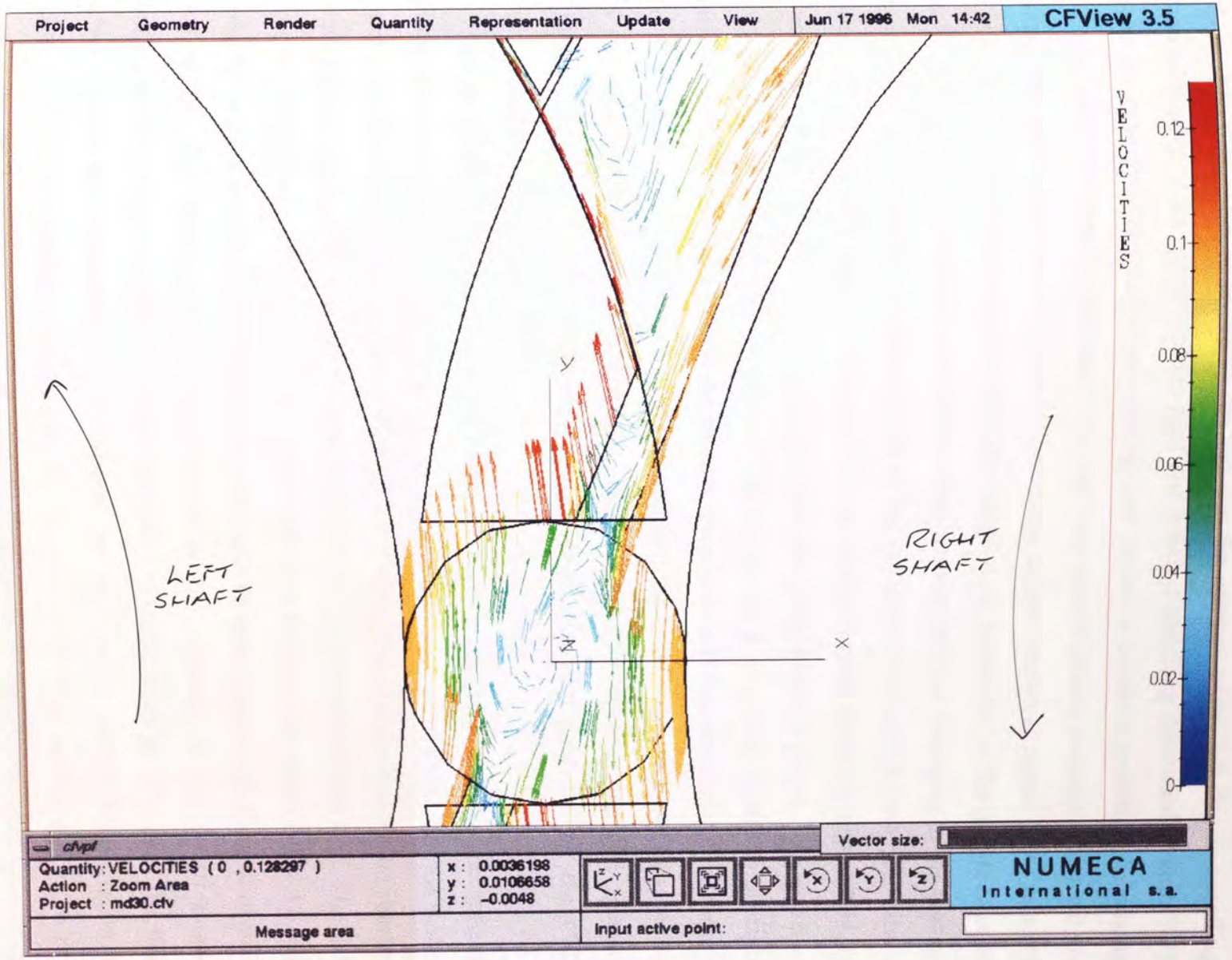

end, is clockwise. This is caused by the fact that the aperture of the left disc is travelling upwards relative to the aperture of the right disc which is travelling downwards. Figure 7-35 shows the experimental result of pre-packing both the screw elements preceding the mixing disc zone with one coloured undiluted "Playstuff" clay sample (shown as orange clay) and the mixing disc zone itself with a different coloured clay sample (shown as purple clay - referred to as Experiment 2). The small cylindrical appendage to the bottom left of the sample as seen, has been extracted from the centrally located intermeshing aperture belonging to the disc on the left hand shaft, which is located closest to the entrance of the mixing zone; this disc is indicated as Disc 1 in Figure 7-2. In relation to the predicted result shown in Figure 7-34, to which this experimental sample is to be compared, the view shown in Figure 7-35 is that of looking along the positive X-axis such that the inlet of the mixing zone is seen to the right hand side of the picture as seen and the outlet is towards the left (the remainder of the sample shown within Figure 7-35 has been extracted from the disc collar volume). It can be seen that the two different coloured clays materials, located within the intermeshing disc aperture volume, have swirled in a clockwise manner, identical to that predicted by the CFD simulation shown in Figure 7-34.

Fluid or particulate matter positioned within the upper bridge region, swirls and remains within this domain until the apertures of the opposite disc start to coincide with the bridge region (i.e. for rotating configurations with $20° \leq \alpha \leq 40°$). This is illustrated by the velocity vector profiles drawn for the $\alpha = 30°$ rotated configuration, as shown in Figure 7-36. The X-Y cross section shown, viewed along the Z-axis, has been taken at the position $Z = 3.6$ mm along the mixing zone from the inlet. As may be observed from Figure 7-36, the area of swirl seen in the right cavity, is not as pronounced as that observed for the $\alpha = 0°$ rotated configuration shown in Figure 7-34. This small area of swirl ceases to exist once the fluid arrives within the separation volume (shown for the $\alpha = 30°$ rotated configuration in Figure 7-32). The Z-velocity isolines plot for this same X-Y cross section at $Z = 3.6$ mm given in Figure 7-37, shows that material in the right cavity is being forced back towards the inlet, with a maximum velocity of approximately 10 mm sec^{-1} (shown as positive Z-contours). However, once material has progressed into the aperture of the left disc, it progresses forward through the domain with a maximum velocity of approximately 20 mm sec^{-1} (shown as negative Z-contours). Swirling motion within either the upper or lower bridge region could, under certain circumstances, be considered undesirable as it may cause an increase in residence times. To examine this hypothesis, experimental trials were conducted using the mechanical model whereby graphite particles, possessing diameters in the range of approximately 1-3 mm, were processed through the mixing disc zone by using glycerol as a conveyor. It was observed from these trials that for particulates within the collar volumes,

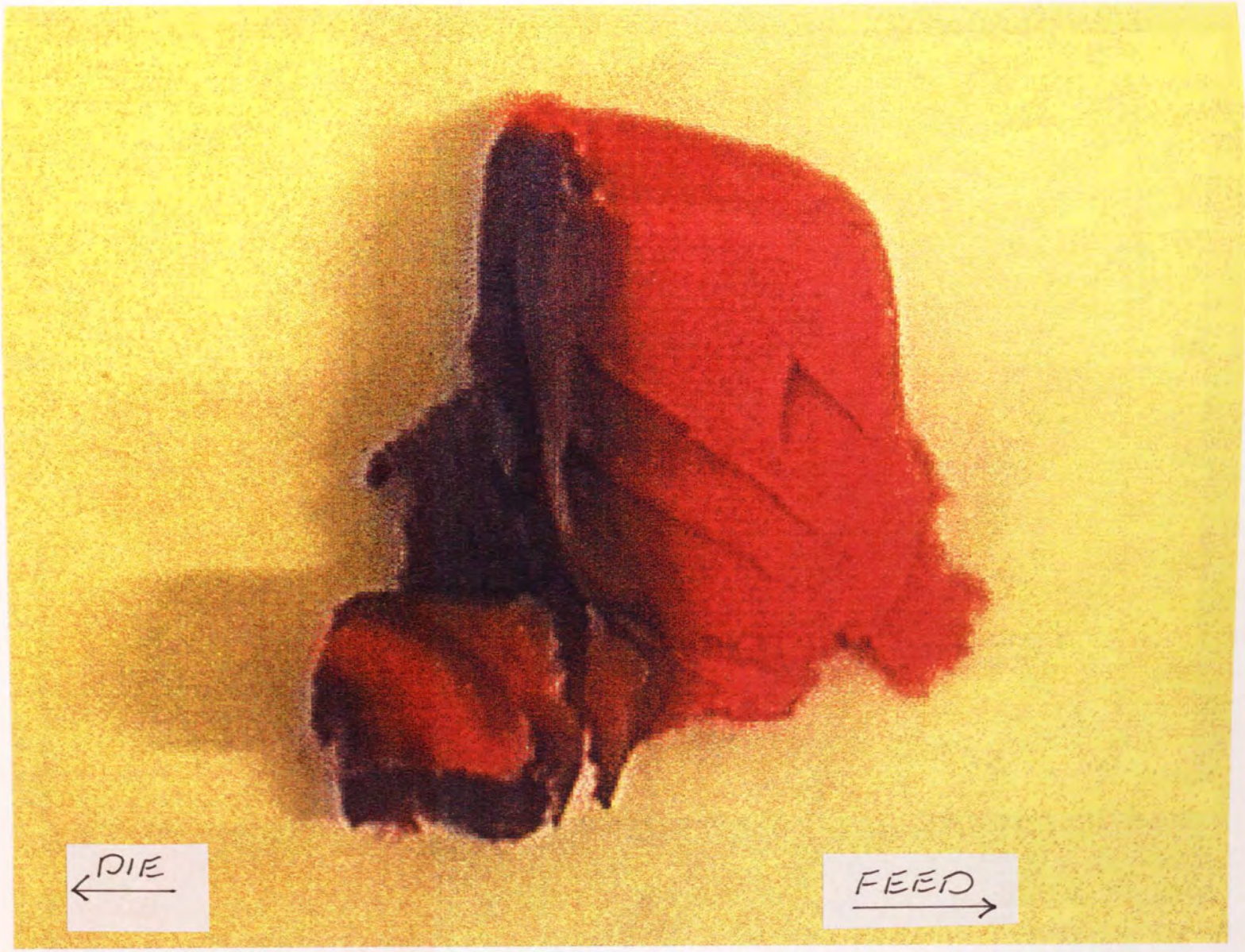

Figure 7-35:
Results of Pre-Packing Both the Screw Elements Preceding a Mixing Disc Zone Containing Four Pairs of Discs in the In-Line Arrangement, and the Mixing Zone Itself With Two Different Coloured "Playstuff" Clay Samples and Then Processing (Experiment 2). View Within the Intermeshing Region Shown.

Figure 7-36:
Velocity Vector Profiles on the Cross Section Created at Z = 3.6 mm Along the Zone and in the X-Y Plane, for the 3D Mixing Disc Zone Containing One Pair of Discs in the In-Line Arrangement, at the Rotated Configuration α = 30° (Magnified View).

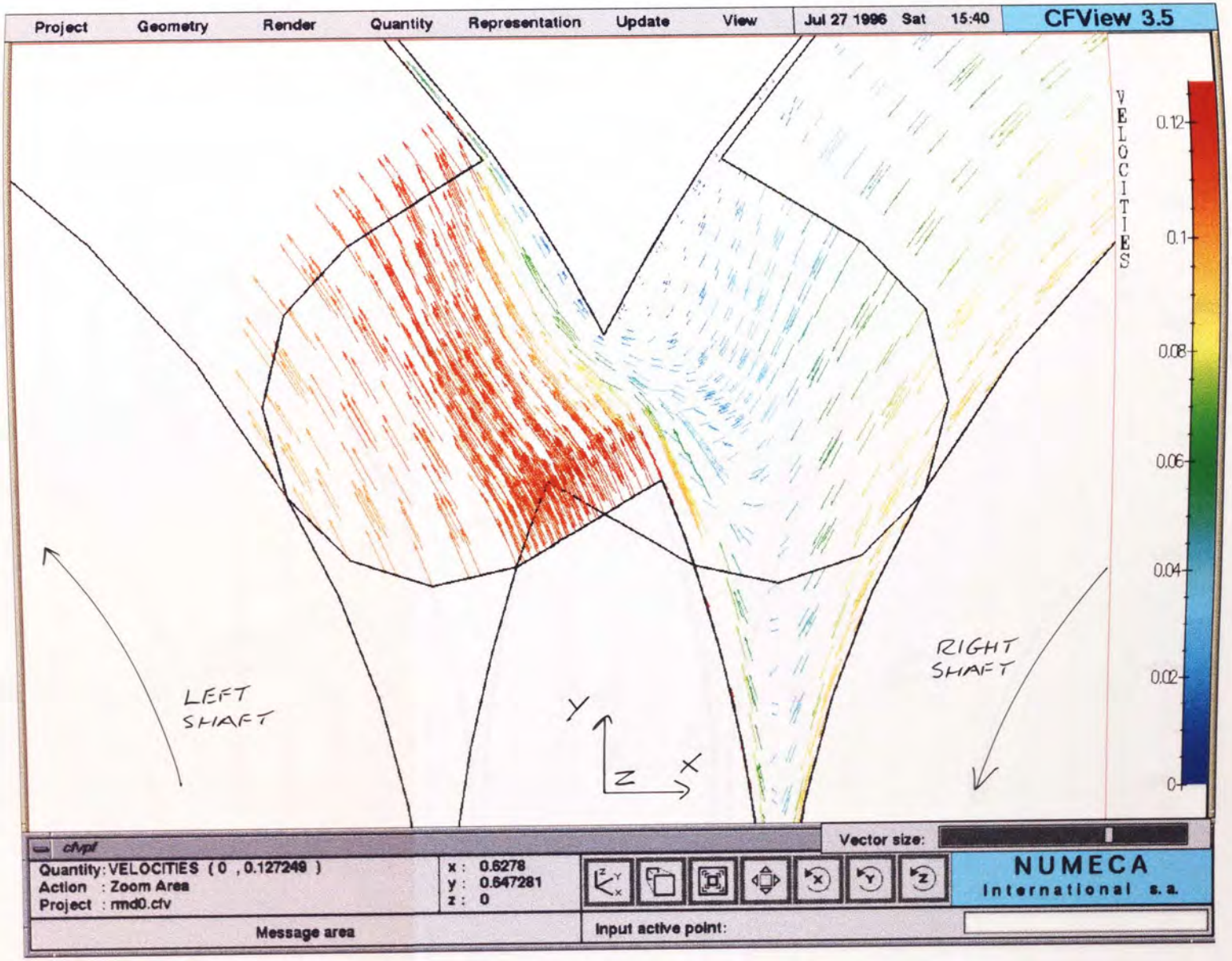

Figure 7-37:

Z-Velocity Isolines on the Cross Section Created at Z = 3.6 mm Along the Zone and in the X-Y Plane, for the 3D Mixing Disc Zone Containing One Pair of Discs in the In-Line Arrangement, at the Rotated Configuration α = 30° (Magnified View).

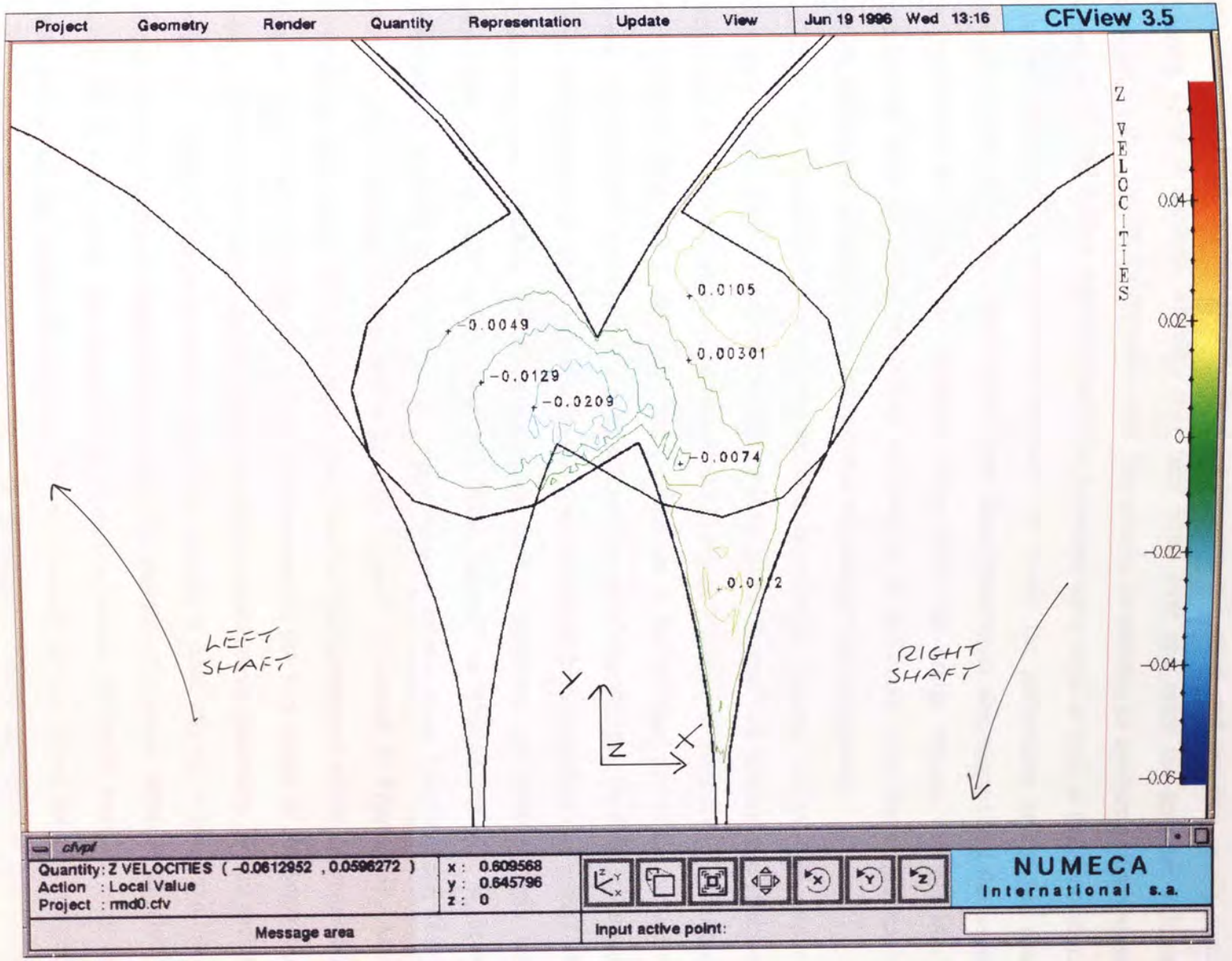

upon entering either bridge region, these particulates will swirl and oscillate axially until chancing upon a location whereby they may cross over and enter the aperture volume belonging to the disc on the opposite shaft. The criteria for entering an aperture volume when located within the bridge region seems to be dependent upon axial as well as radial position, with the likelihood of progression increased the closer the particulates are to the disc separation plane. However, observations from these experiments also suggest that the larger the particulate, the longer the residence times within the bridge regions will be. More experimental trials involving particulates will need to be performed in the future, preferably with the utilisation of high quality, freeze-frame camcorder/video equipment.

Due to the importance of the cross sections described in Figures 7-24 to 7-26, further discussion of the results obtained for them will be given. Figure 7-38 displays the effect of obtaining a side view of the cross section shown in Figure 7-24 ($\alpha = 0°$ rotated configuration), by orientation along the X-axis (such that the inlet lies to the left-hand side of the picture as viewed and the outlet to the right). The significant change of direction that the fluid undergoes within the separation volume between the two discs is evident from inspection of Figure 7-38. In addition, the opposite directions in which the two apertures are moving imply that distributive mixing will occur along this fluid "tunnel" as viscous material is being consecutively severed at the separation volume between the two discs. Magnification of this cross section, focusing on the central aperture "tunnel", is shown in Figure 7-39. As is illustrated in this figure, the 180° reorientation that the fluid undergoes within the separation volume significantly reduces its velocity. Furthermore, at the very centre of the separation volume, the velocity vectors shown imply that fluid is momentarily stationary. Within each of these two centrally located apertures, very little forward or back mixing is being exhibited. Instead, for this particular rotated configuration, the majority of material seems to be rotating around the Z-axis, rather than along it. As these simulations performed were for only one rotational speed and under the influence of one pressure profile across the mixing zone, further operating conditions would need to be investigated before any sensible conclusions might be drawn. Incidentally, what may also be observed from Figure 7-39, is the fact that the velocity vectors shown seem to be amassed along the centre of each aperture. The explanation for this is illustrated in Figure 7-40, which displays the computational mesh on which the flow problem was solved for that particular cross section shown within Figure 7-38. This mesh reveals a non-uniform distribution of nodal points within the cross section taken resulting from the automatic unstructured mesh generation used within ICEM-Polycem. The Z-velocity isolines for the $\alpha = 0°$ central cross section shown in Figure 7-41, show that maximum Z-velocities near both the inlet and outlet planes are of the order of ± 20 mm sec^{-1}. Material within the separation volume, however, is experiencing a much larger forward and back

Figure 7-38:
Velocity Vector Profiles on the Cross Section Described in Figure 7-24, Viewed Along the X-Axis.

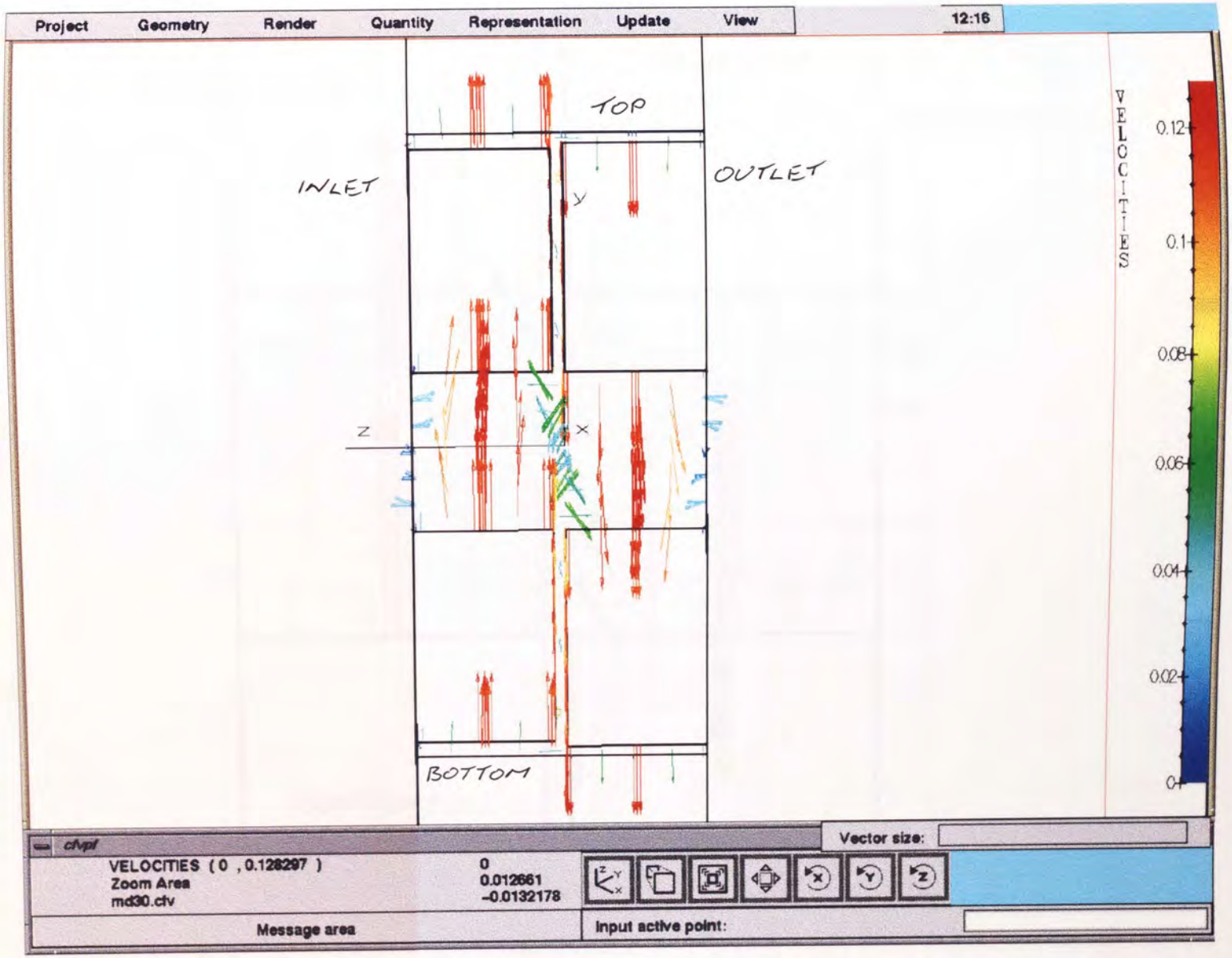

Figure 7-39:
Velocity Vector Profiles on the Cross Section Described in Figure 7-24, Viewed Along the X-Axis (Magnified View).

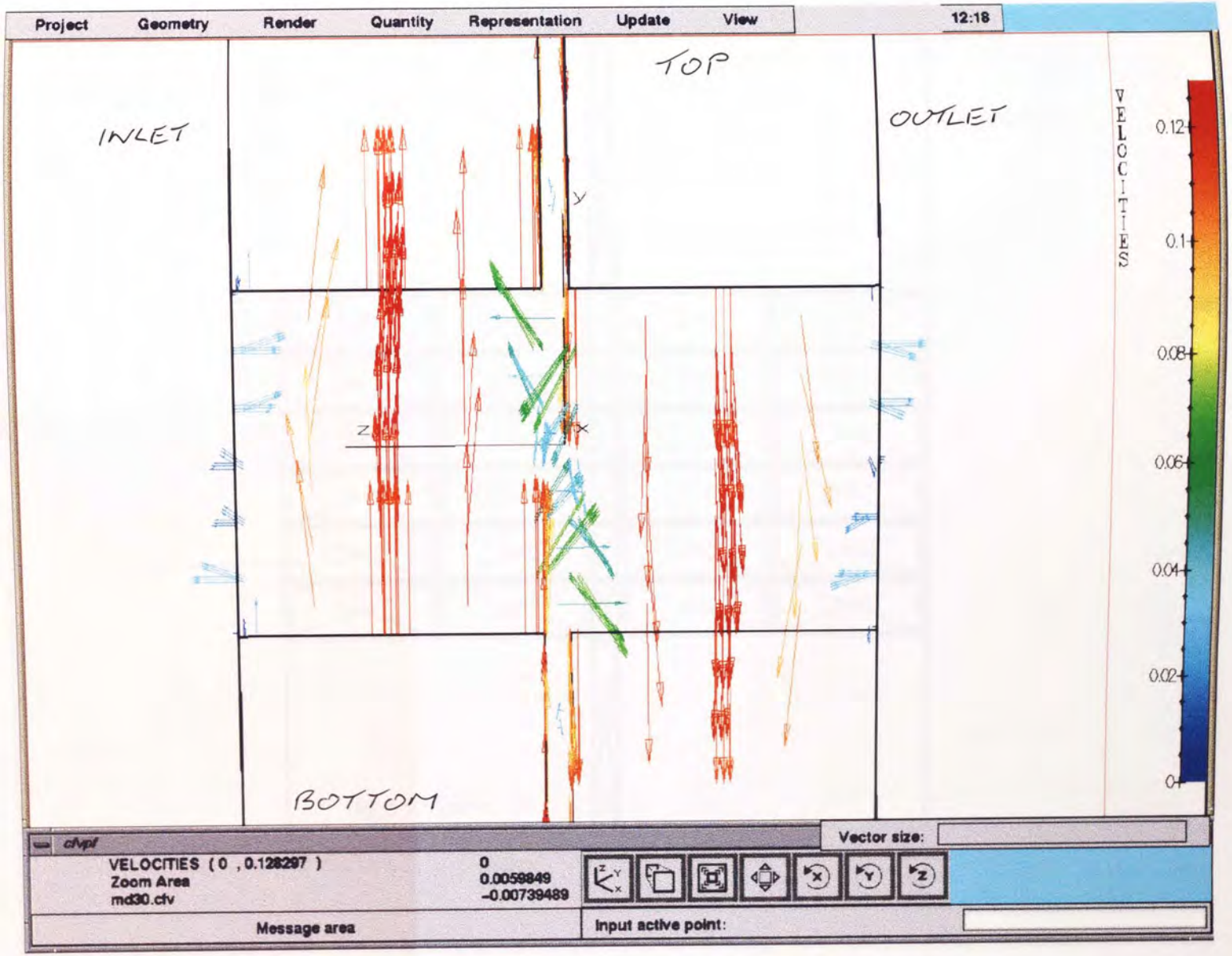

Figure 7-40:

Unstructured Mesh for the Cross Section Described in Figure 7-24, Viewed Along the X-Axis (Magnified View).

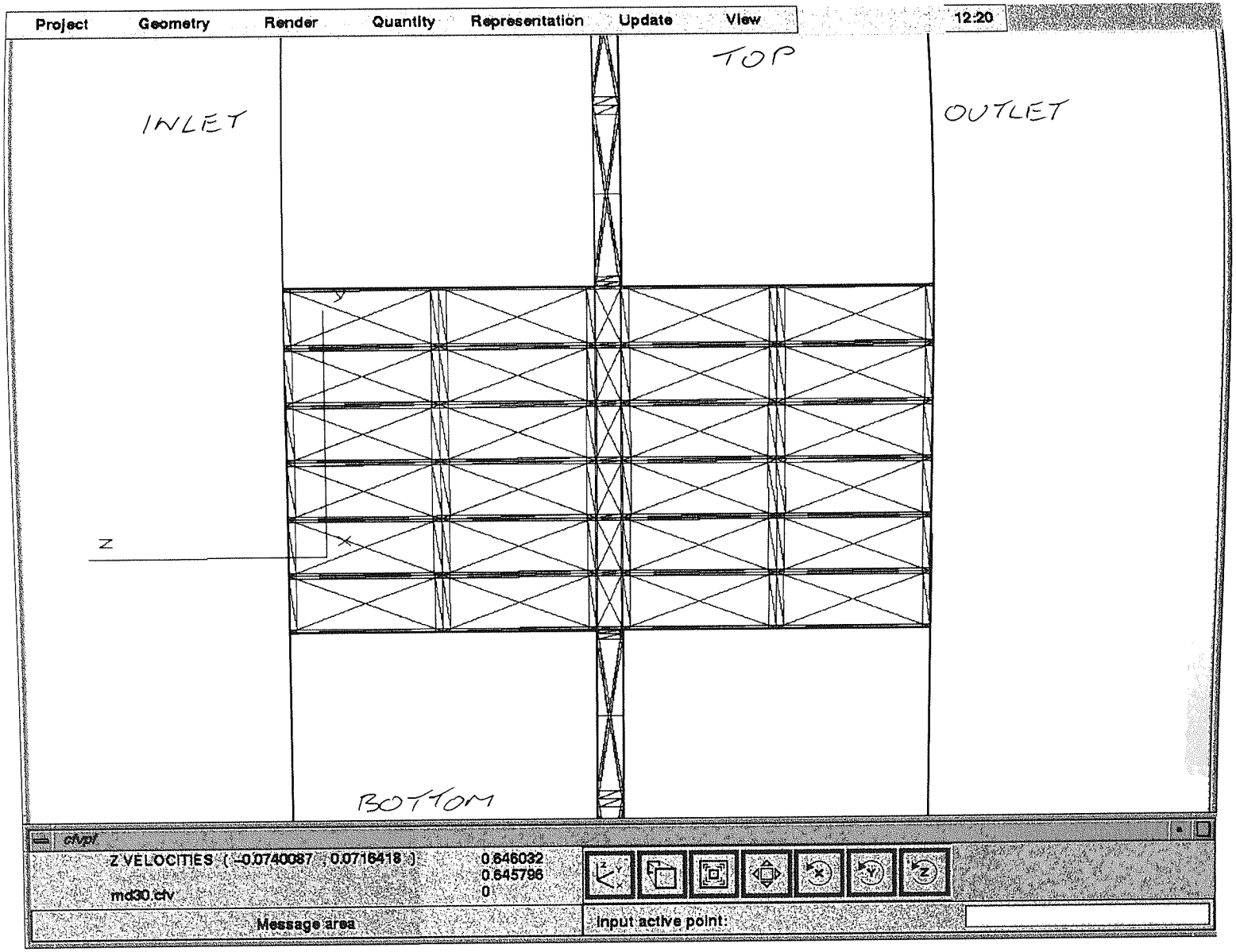

Figure 7-41:
Z-Velocity Isolines on the Cross Section Described in Figure 7-24, Viewed Along the X-Axis (Magnified View).

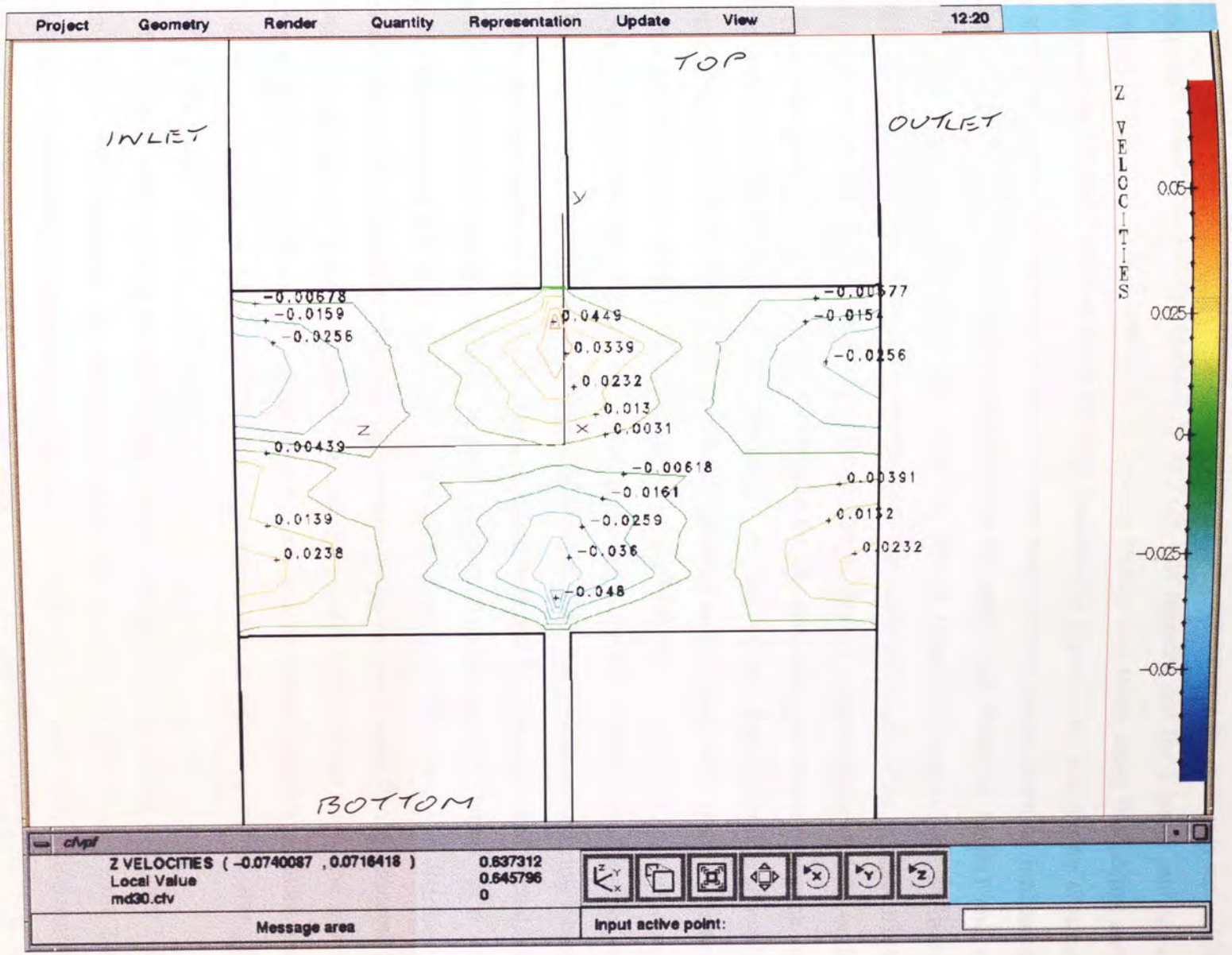

mixing effect, travelling axially at velocities up to approximately ± 45 mm sec^{-1}. The experiment described within Figures 7-27 to 7-29 was repeated but for a lesser number of revolutions (referred to as Experiment 3). A cross section was taken along the mixing zone intermeshing "tunnel", created along the edge indicated in Figure 7-42. The sample obtained is shown in Figure 7-43 and it is the result of both magnification (actual physical dimensions of the sample shown are approximately 45 mm in length and 5 mm in height) and of artificially enhancing the colours by using the Silicon Graphics "ImageView" software. Orientation of the sample shown is presented such that material located at the entrance of the mixing zone lies to the right hand side of the picture as viewed, whereas material at the outlet is to the left. The two initial colours of clay used for this particular experiment were pink and blue, which mix together to give a purple matrix. As may be seen from the profile shown in Figure 7-43, there is a "degree of mixedness" gradient commencing with material present within the mixing zone entrance. As shown in Figures 7-38 and 7-39, pairs of apertures, once they coincide within the intermeshing region, move in the opposite direction to each other and this effect produces a consecutive chopping of material, with the position of severing located within the disc separation volume. Thus, because material is consecutively severed and relocated once the rotated configuration forms the intermeshing aperture "tunnel" at $\alpha = 0°$ with a frequency of $\pi/3$, then this mechanism may be characterised as being of a distributive nature. Hence the accumulation of this agglomerate chopping mechanism through successive intermeshing regions, is the creation of successively smaller agglomerates along the mixing zone as shown within Figure 7-43. Consequently, it would be highly desirable in future work to derive expressions for the quantification of agglomerate size at different positions along the mixing disc zone.

The central cross section for the $\alpha = 15°$ rotated configuration, as shown in Figure 7-25, may be further examined by orientation along the X-axis, as shown in Figure 7-44. Magnification has been enhanced for this figure by displaying the cross section horizontally (such that the inlet lies to the top of the picture as viewed and the outlet to the bottom). Velocity vectors displayed on this central cross section, clearly show that a much greater forward and back mixing effect is exhibited. The Z-velocity isolines for this same central cross section in Figure 7-45, show that maximum Z-velocities near both the inlet and outlet are of the order of approximately ± 45 mm sec^{-1}. However, due to the non-coincidence of disc apertures, axial motion diminishes within the separation plane for this cross section.

Finally, the central cross section for the $\alpha = 30°$ rotated configuration, as shown in Figure 7-26, may also be further examined by orientation along the X-axis, as shown in Figure 7-46. Again for this orientation, magnification has been enhanced for this figure by displaying the cross section horizontally. As explained previously, material located near the

Figure 7-42:

Results of Pre-Packing Only the Screw Elements Preceding a Mixing Disc Zone Containing Four Pairs of Discs in the In-Line Arrangement, With Two Different Coloured "Playstuff" Clay Samples and Then Processing (Experiment 3). View of Sample in Contact With the Outer Barrel Wall Shown.

Figure 7-43:

Cross-Section of Part of the Sample Shown Within Figure 7-39 Taken in the Y-Z Plane, Illustrating Mixing Along the Mixing Zone.

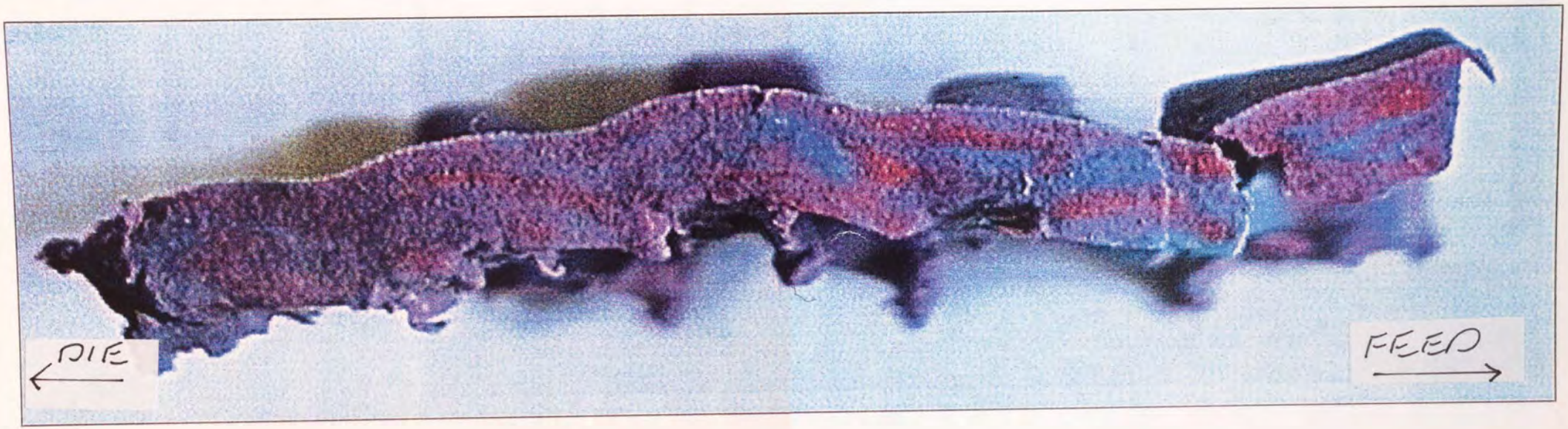

Figure 7-44:
Velocity Vector Profiles on the Cross Section Described in Figure 7-25, Viewed Along the X-Axis.

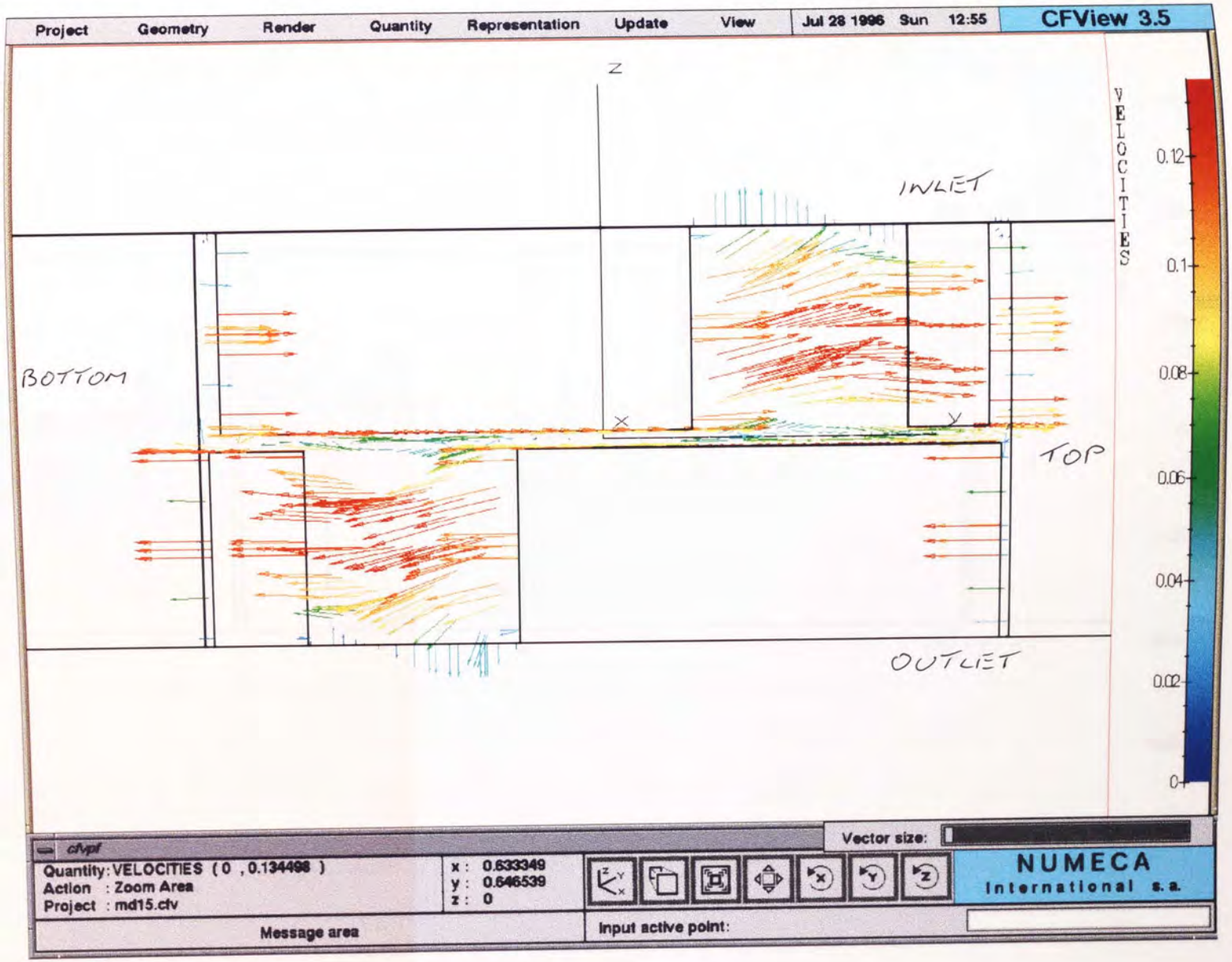

Figure 7-45:

Z-Velocity Isolines on the Cross Section Described in Figure 7-25, Viewed Along the X-Axis.

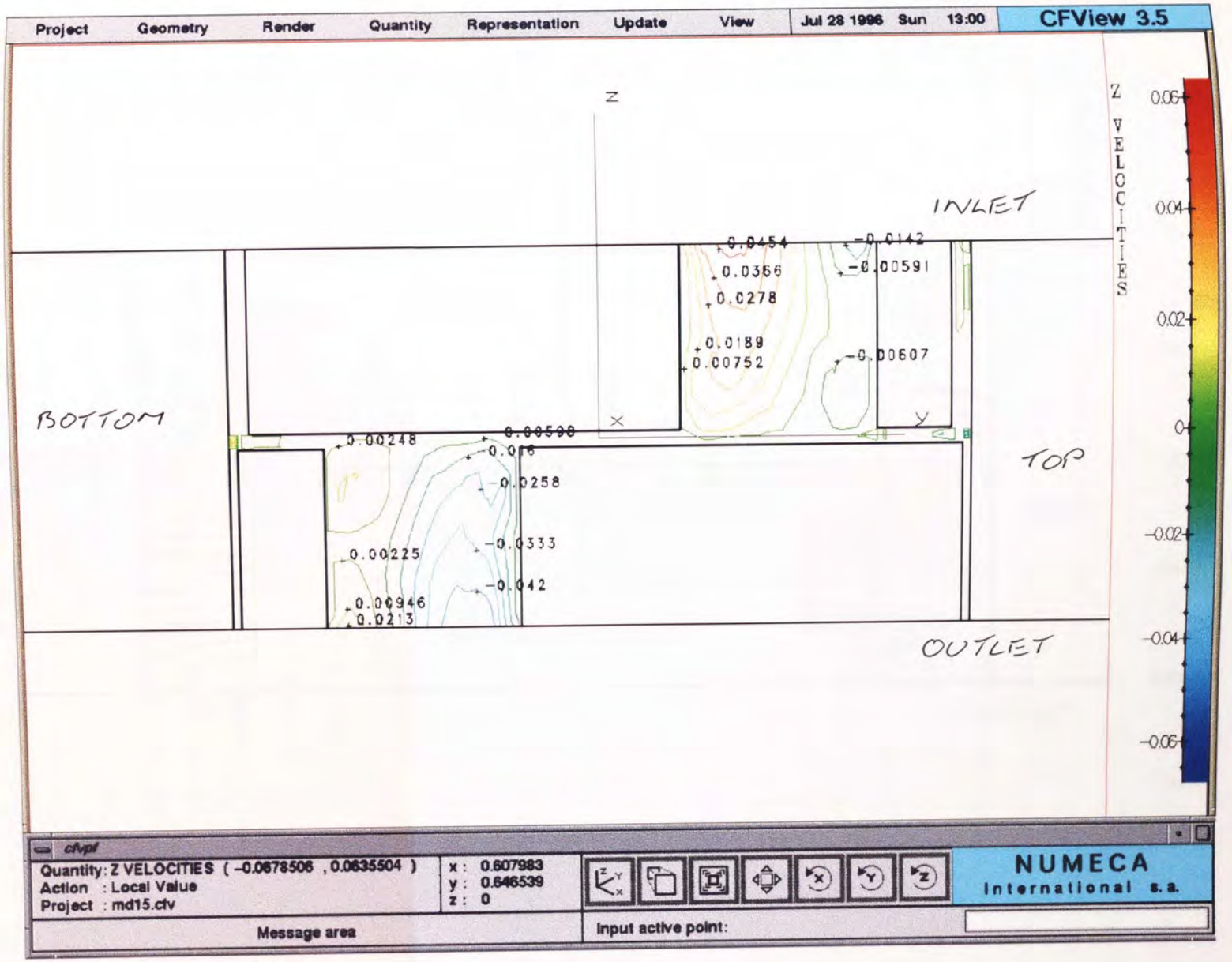

Figure 7-46:

Velocity Vector Profiles on the Cross Section Described in Figure 7-26, Viewed Along the X-Axis.

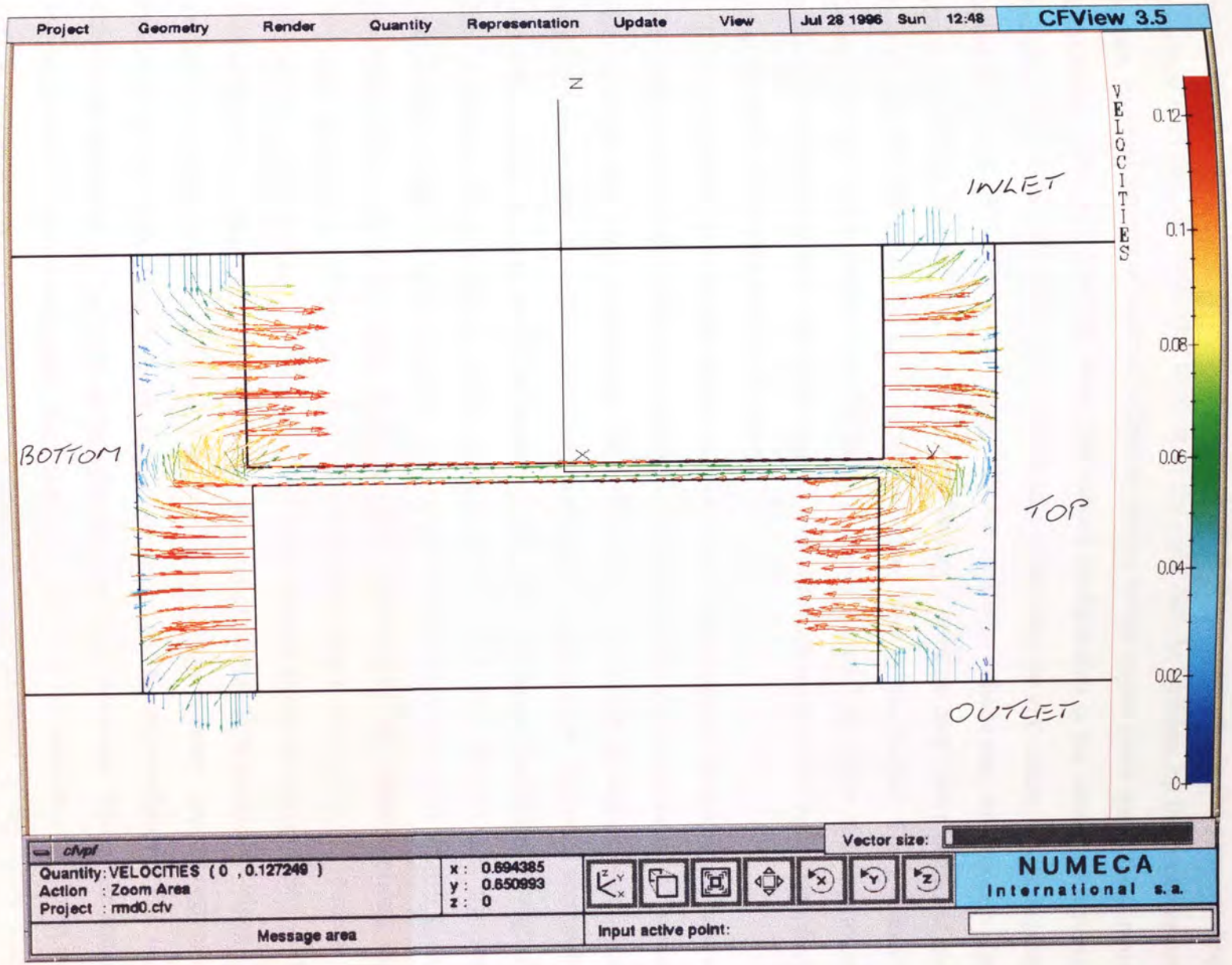

bottom bridge region is sucked into the flow domain at the inlet, due to the pressure drop associated with the anti-clockwise rotation of the right disc. In addition, by the conservation of mass, an equal amount of material within the bottom bridge region flows out of the domain at the outlet. What is interesting about this rotated configuration is the motion of material emerging from within the separation volume near to both the top and bottom bridge regions within the mixing zone. Material emerging from the separation volume near the bottom bridge region, is flowing into the area which is experiencing a pressure drop. More details of the fluid motion for this particular cross section are given later in this chapter. The Z-velocity isolines for this same central cross section, given in Figure 7-47, show that maximum Z-velocities at both the inlet and outlet regions, and at the entrances of the separation plane, are of the order of approximately $\pm$ 45 mm sec^{-1}.

Having described fluid motion at each of these three cross sections, it would be informative to compare calculated flow parameters such as pressure profiles, local shear rates and mixing efficiencies on each cross section also. Figures 7-48 to 7-51 display pressure isolines, with spatial Cartesian plots for each of the three central cross sections taken. The cross section for the rotated configuration of $\alpha = 0°$ is shown in Figure 7-48. The spatial line drawn through the domain (shown in red), along which pressure points have been plotted, has the start co-ordinates, in mm, of approximately (0, 0, 0) and the end co-ordinates of (0, 0, 9.6). All subsequent lines drawn for other Cartesian plots representing the various mixing disc calculated parameters, always start at $Z = 0$ (inlet) and always end at $Z = 9.6$ (outlet). In addition, the graphs drawn are all plotted such that the distance along the mixing zone (i.e. the Z co-ordinate) is plotted along the horizontal axis and calculated flow parameters along the vertical. The Cartesian plot drawn in Figure 7-48, shows a large pressure drop for regions at, and close to, the inlet. This pressure drop seems large but the explanation for this is as follows. As described in Chapter 4, at the inlet face, the initial developed flow at the start of the simulation is *a priori* unknown. The values of v_x and v_y at the surfaces of all three wall boundaries though, are known due to the specified rotational speed of the screw shafts. However, axial motion must be described also for material to progress through the mixing zone (neither the mixing discs nor the trilobal elements in the arrangements examined can convey material, instead, material progression through the domain is achieved by a pressure profile). Thus combined volumetric flow rate and pressure profile along the zone, must be specified for material to advance through the zone. For the 3D results described, these values are 5.2×10^{-7} m^3 sec^{-1} (corresponding to a fill rate of 25 g min^{-1}) and 1×10^5 Pa at the co-ordinates (0, 0, 0) respectively. In addition, at all points contained within the outlet plane, $F_n = 0$ N. As is observed from Figure 7-48, the value of pressure plotted at $Z = 0$ on the inlet face is approximately 0.9×10^5 Pa. At $Z = 2.4$ mm (approximately half way along the first

Figure 7-47:

Z-Velocity Isolines on the Cross Section Described in Figure 7-26, Viewed Along the X-Axis.

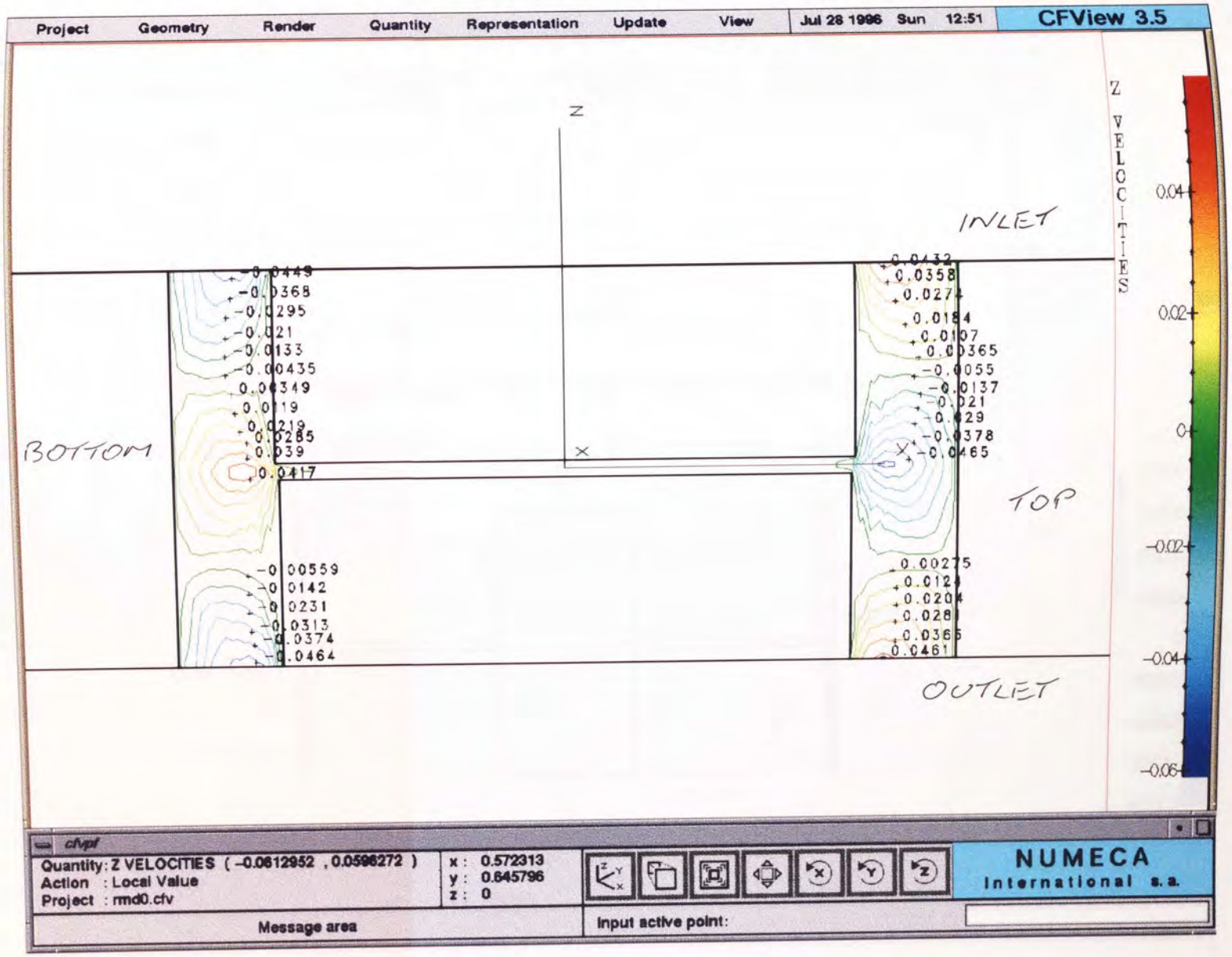

Figure 7-48:

Pressure Isolines on the Cross Section Described in Figure 7-24, Viewed Along the X-Axis. Pressure Cartesian Plot, as a Function of Spatial Distance, for the Values Encountered Along the Line Indicated.

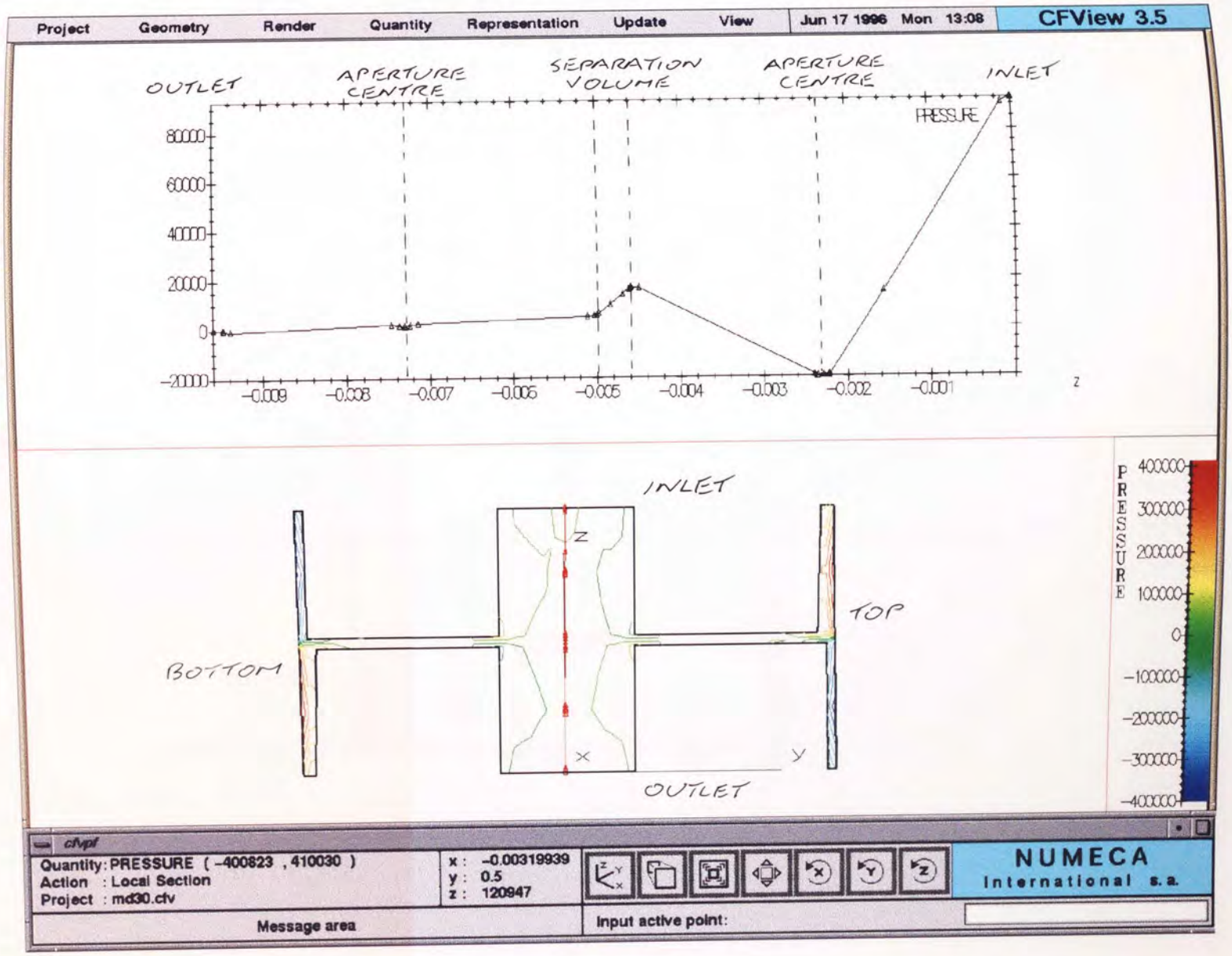

Figure 7-49:

Pressure Isolines on the Cross Section Described in Figure 7-25, Viewed Along the X-Axis. Pressure Cartesian Plots, as a Function of Spatial Distance, for the Values Encountered Along the Lines Indicated.

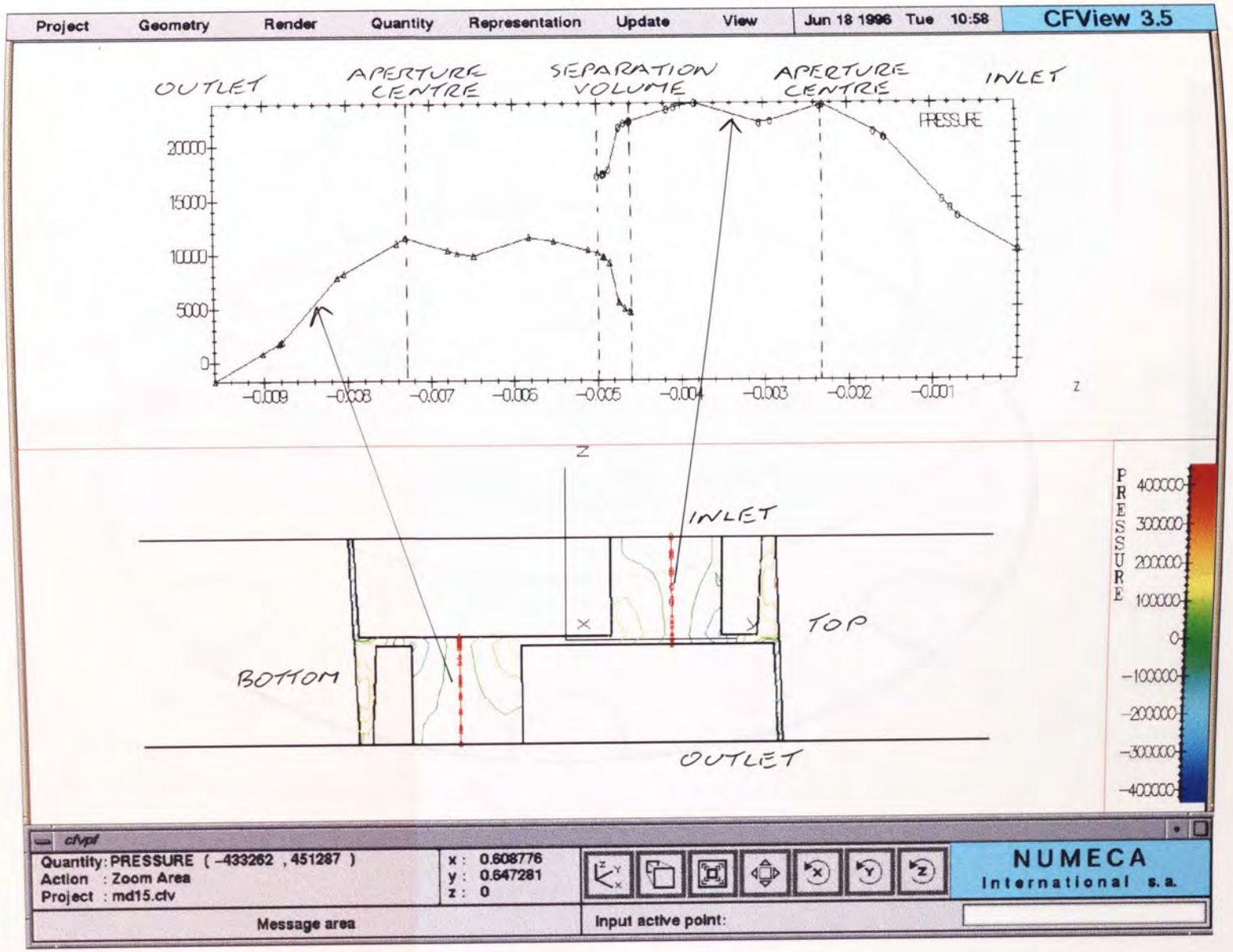

Figure 7-50:

Pressure Isolines on the Outlet Plane, for the 3D Mixing Disc Zone Containing One Pair of Discs in the In-Line Arrangement, at the Rotated Configuration α = 15° (Magnified View).

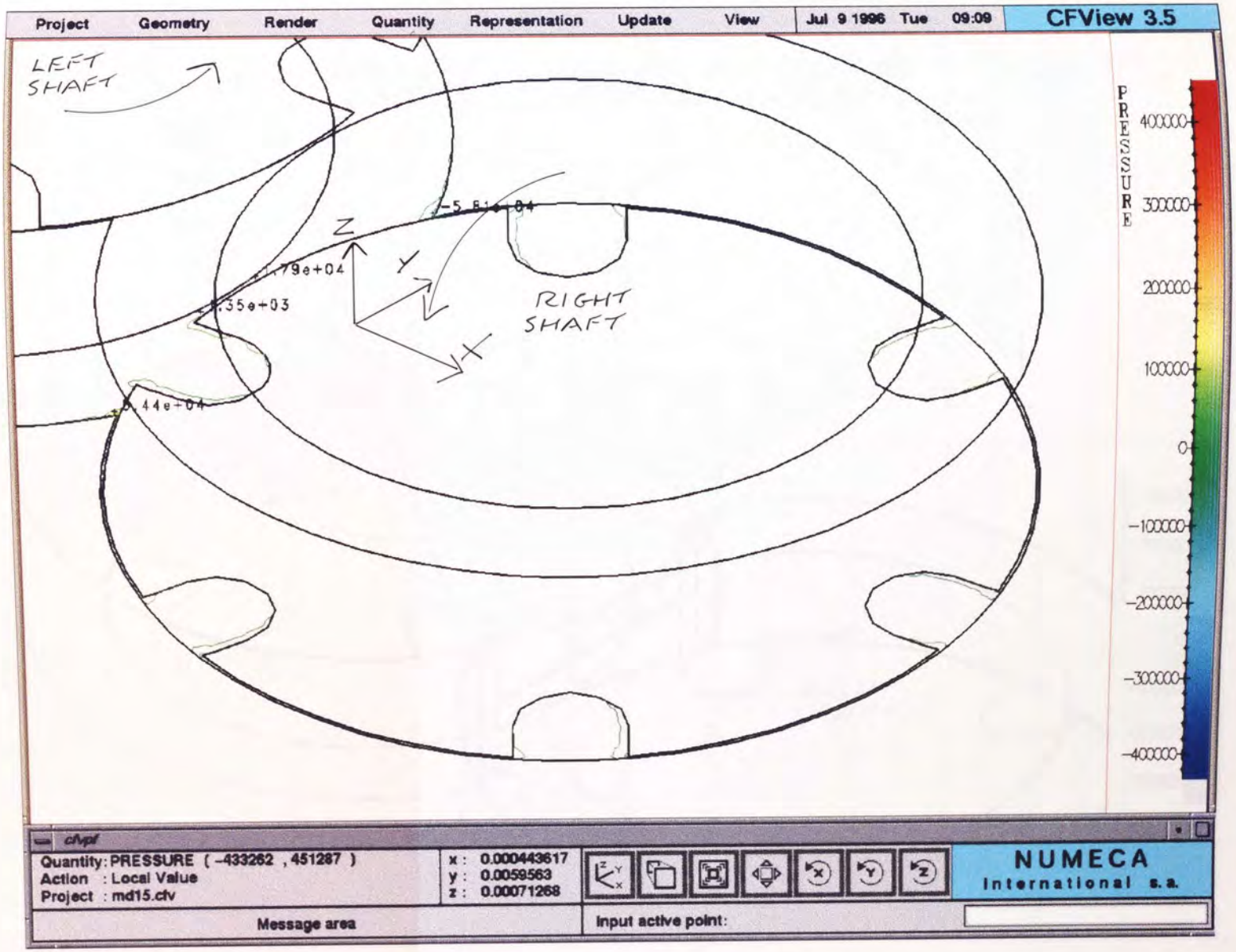

Figure 7-51:

Pressure Isolines on the Cross Section Described in Figure 7-26 (Magnified View). Pressure Cartesian Plots, as a Function of Spatial Distance, for the Values Encountered Along the Lines Indicated.

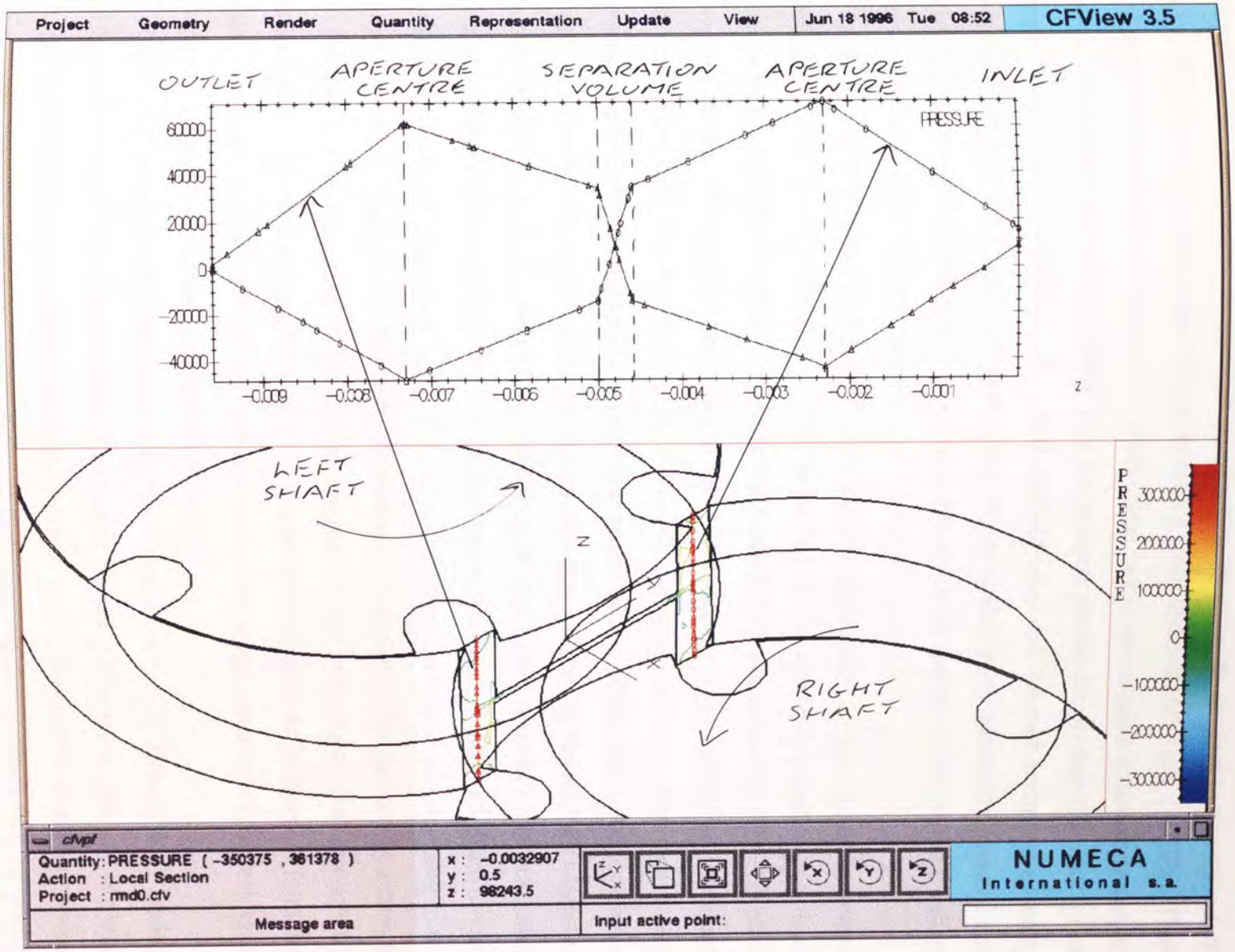

aperture of the disc nearest to the inlet plane) the pressure value has dropped to approximately -0.2×10^5 Pa which is a very steep drop over such a small distance ($\Delta P = |1.1 \times 10^5|$ Pa). Thus further pressure profiles will need to be investigated before any sensible conclusions can be drawn. One refinement to the method used for pressure profile designation that may be of benefit, would be the assignment of a global pressure value over the inlet surface as a whole, instead of the assignment of a pressure value at one spatial point within the domain. For Polyflow version 3.4.6 used within this study, this ability to specify global pressure values was not available at the time of research.

Pressure isolines for the central cross section pertaining to the $\alpha = 15°$ rotated configuration are shown in Figure 7-49. Due to the fact that the apertures are not in-line, there is no straight path from the inlet to the outlet that material may take, hence two Cartesian plots have been drawn. The first line begins at the inlet of the aperture nearest the top bridge region and progresses into the domain, ending within the separation volume. The second line however, starts within the separation volume nearest the bottom bridge region and progresses further into the domain, ending at the outlet face. The area enclosed by the aperture nearest to the bottom bridge region is subjected to lower pressure than that of material contained within the upper aperture. From the velocity vectors observed within Figure 7-44, the forward mixing of material contained within the lower aperture is a result of the drop in pressure seen in the Cartesian plot of Figure 7-49. However, the pressure value plotted for this configuration at $Z = 9.6$ mm (i.e. at the outlet of the bottom aperture) is non-zero. Figure 7-50 displays the pressure isolines on the outlet, for the $\alpha = 15°$ rotated configuration. As is observed from this figure, there are regions around the aperture perimeters where pressure $\neq 0$ Pa and these discrepancies may be artefacts of the flow calculation.

Figure 7-51 shows the pressure isolines for the central cross section of the $\alpha = 30°$ rotated configuration. Due to the fact that, for this particular rotated configuration, pairs of apertures partially coincide at the top and bottom bridge regions, two Cartesian plots of pressure values were drawn, one for each region. These two graphs depicting the pressures will be used to explain the complex fluid motion observed in Figure 7-46. Fluid motion within the aperture located within the top bridge region only is considered, with the assumption that fluid motion in the region nearest the bottom bridge is identically equal but opposite in direction. Thus there are five different stages going from the inlet to the outlet that need to be considered.

- Region 1 - Material contained within the region $0 \leq Z \leq 2.3$ mm (forward of the inlet and up to the centre of the first aperture).

  There is a linear increase in pressure over this region of approximately $\Delta P = |0.5 \times 10^5|$ Pa. As may be observed from Figure 7-46, the result of this pressure

increase means that material within this region is back mixing.

- Region 2 - Material contained within the region $2.3 \leq Z \leq 4.6$ mm (forward of the centre of the first aperture, to the beginning of the separation volume).

  Over this region there is a linear decrease in pressure of approximately $\Delta P = |0.3 \times 10^5|$ Pa. As is seen from Figure 7-46, the result of this pressure decrease implies that material within this region is moving forwards, towards the outlet. It is also interesting to note from this plot, the local maximum of the net pressure is at the very centre of the first aperture, where material is rotating about the Z-axis in the X-Y plane only.

- Region 3 - Material within the separation volume, $4.6 \leq Z \leq 5.0$ mm.

  Within this short distance there is a large pressure decrease of approximately $\Delta P = |0.6 \times 10^5|$ Pa. Thus, as is illustrated by the orange velocity vectors shown in Figure 7-46, the result of this pressure decrease for material within the locality of the separation volume is that forward motion is being intensified.

- Region 4 - Material contained within the region $5.0 \leq Z \leq 8.3$ mm (forward of the separation volume and up to the centre of the second aperture).

  Over this region there is a linear decrease in pressure of approximately $\Delta P = |0.3 \times 10^5|$ Pa, similar to that being experienced within Region 2. This implies that material within this region will move forwards, towards the outlet.

- Region 5 - Material contained within the region $8.3 \leq Z \leq 9.6$ mm (forward of the centre of the second aperture and up to the outlet plane).

  Similar to Region 1, there is a linear increase in pressure of approximately $\Delta P = |0.5 \times 10^5|$ Pa. As may be observed from Figure 7-46, the result of this pressure increase implies that material is being forced into the flow domain from the outlet.

Figures 7-52 to 7-54 illustrate the local shear isolines, whilst Figures 7-55 to 7-57 show the mixing efficiency isolines, with spatial Cartesian plots for each of the three central cross sections under investigation. Each of the local shear rate graphs, suggest the same trends for each of the three rotated configurations under investigation. Maximum local shear rates for these particular cross sections are of the order of several hundred sec^{-1}, with regions at the inlet, outlet, separation plane and towards the edges of the apertures experiencing the largest shear. As would be expected, material contained within the centre of each aperture is experiencing minimal shear. The graphs plotted for the mixing efficiency values for each of

Figure 7-52:

Local Shear Rate Isolines on the Cross Section Described in Figure 7-24, Viewed Along the X-Axis. Local Shear Rate Cartesian Plot, as a Function of Spatial Distance, for the Values Encountered Along the Line Indicated.

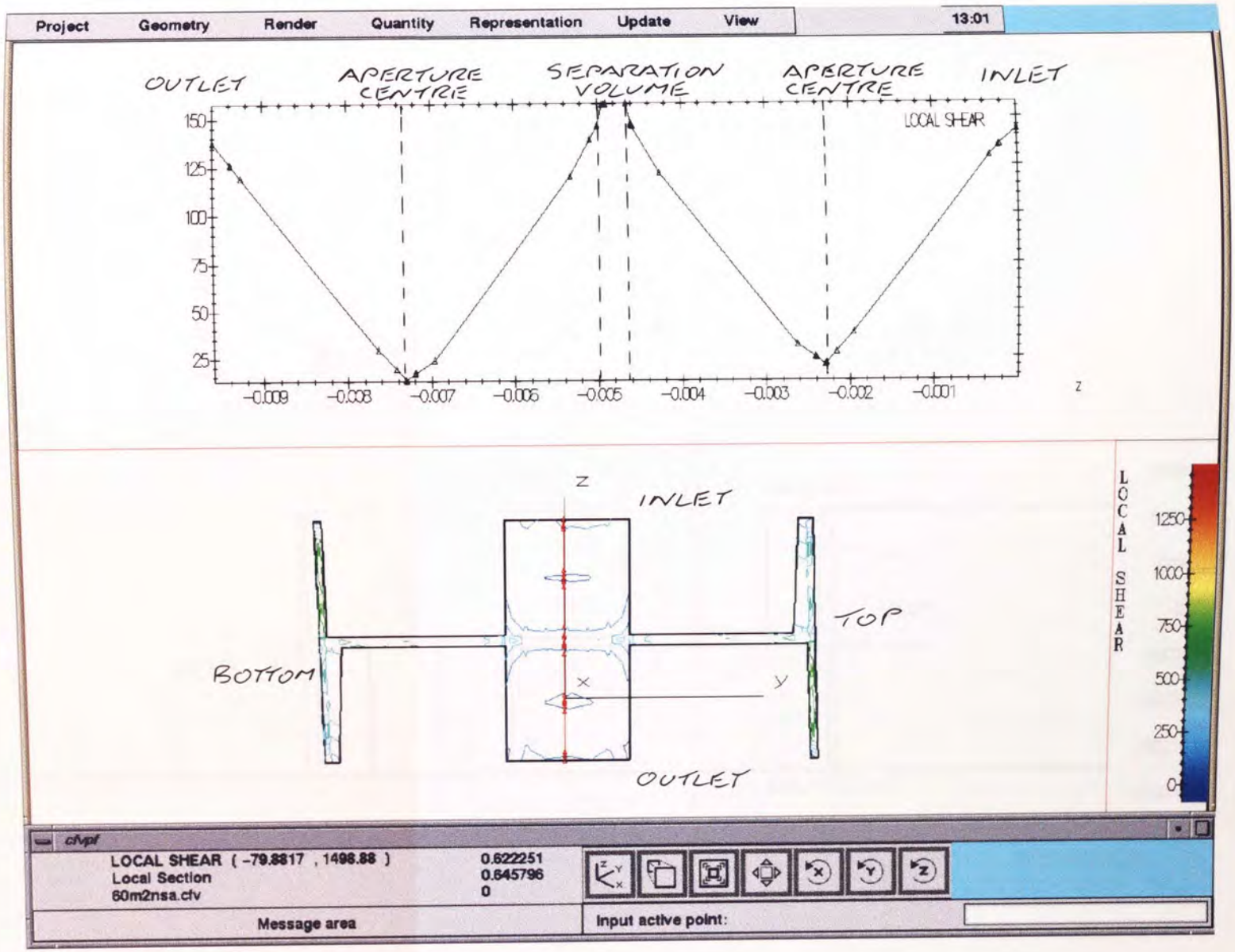

Figure 7-53:

Local Shear Rate Isolines on the Cross Section Described in Figure 7-25, Viewed Along the X-Axis. Local Shear Rate Cartesian Plots, as a Function of Spatial Distance, for the Values Encountered Along the Lines Indicated.

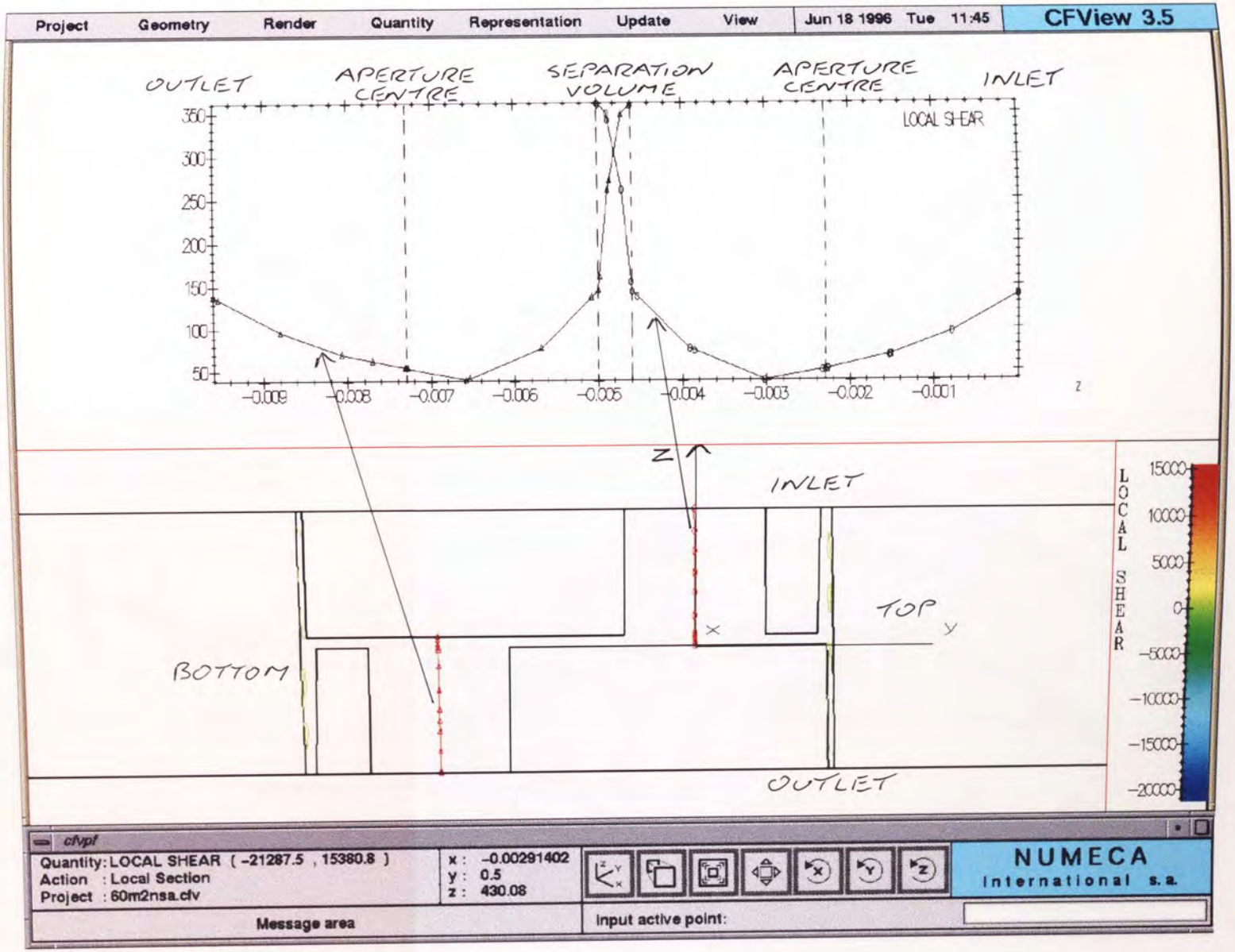

Figure 7-54:

Local Shear Rate Isolines on the Cross Section Described in Figure 7-26 (Magnified View). Local Shear Rate Cartesian Plots, as a Function of Spatial Distance, for the Values Encountered Along the Lines Indicated.

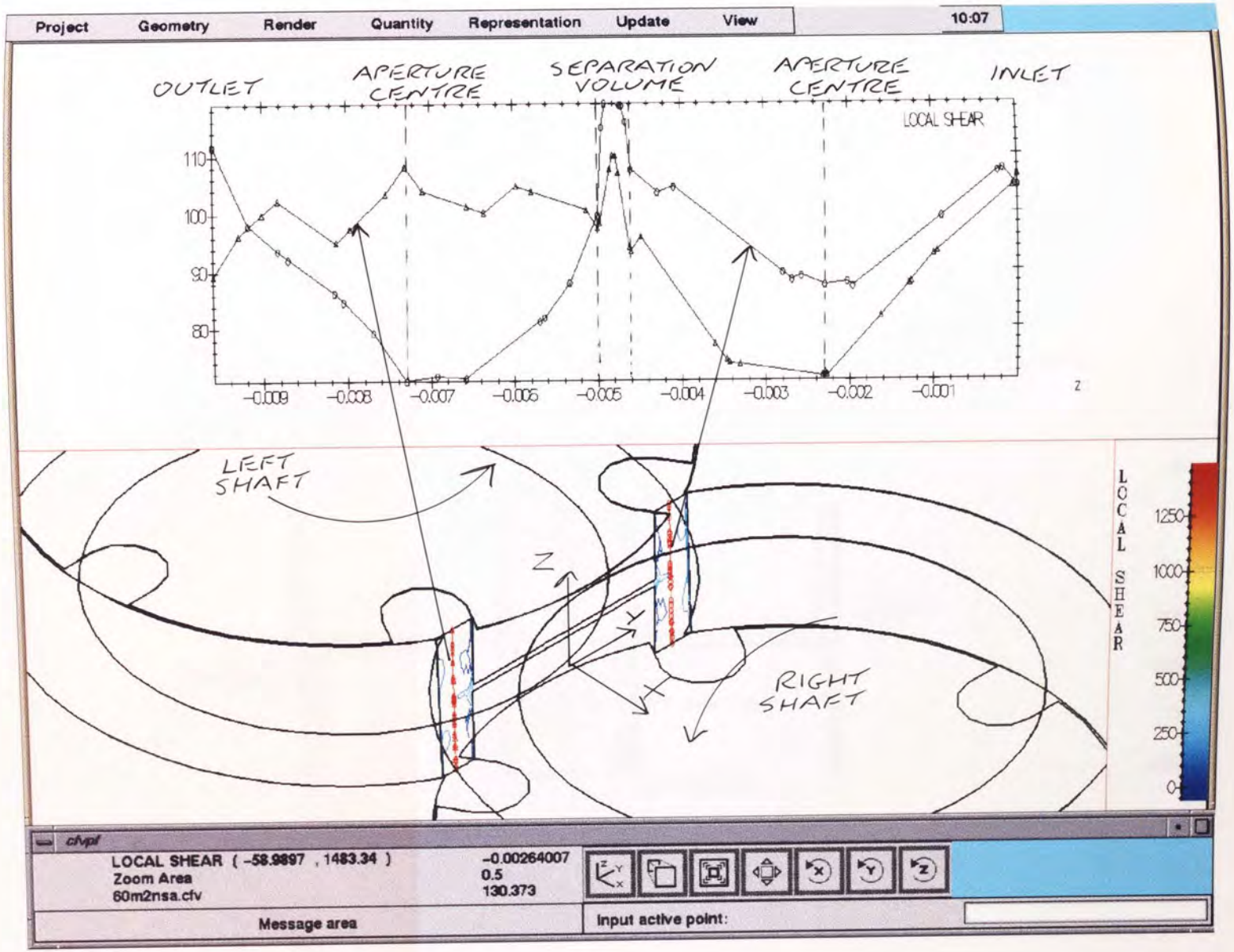

Figure 7-55:

Mixing Efficiency Isolines on the Cross Section Described in Figure 7-24, Viewed Along the X-Axis. Mixing Efficiency Cartesian Plot, as a Function of Spatial Distance, for the Values Encountered Along the Line Indicated.

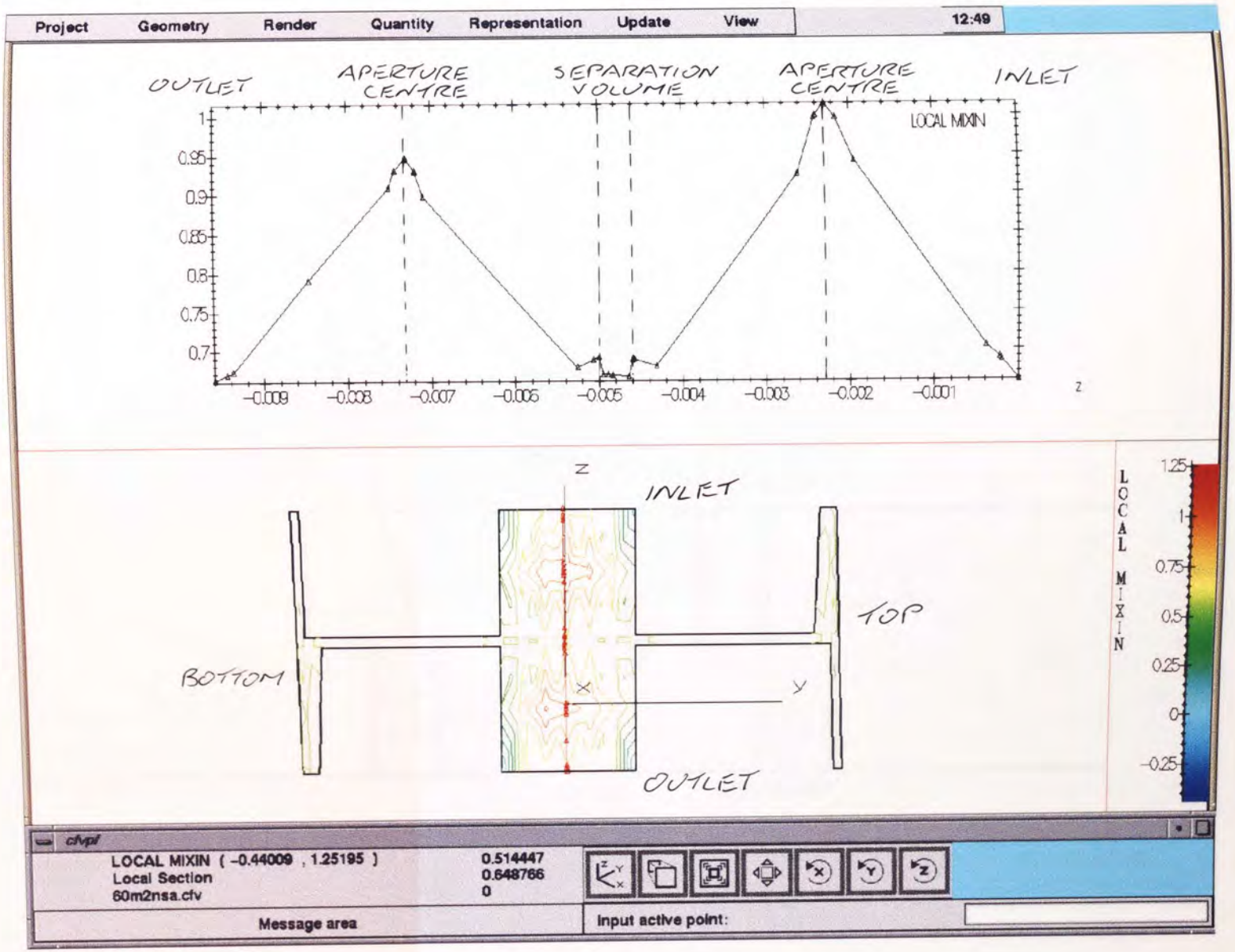

Figure 7-56:

Mixing Efficiency Isolines on the Cross Section Described in Figure 7-25, Viewed Along the X-Axis. Mixing Efficiency Cartesian Plots, as a Function of Spatial Distance, for the Values Encountered Along the Lines Indicated.

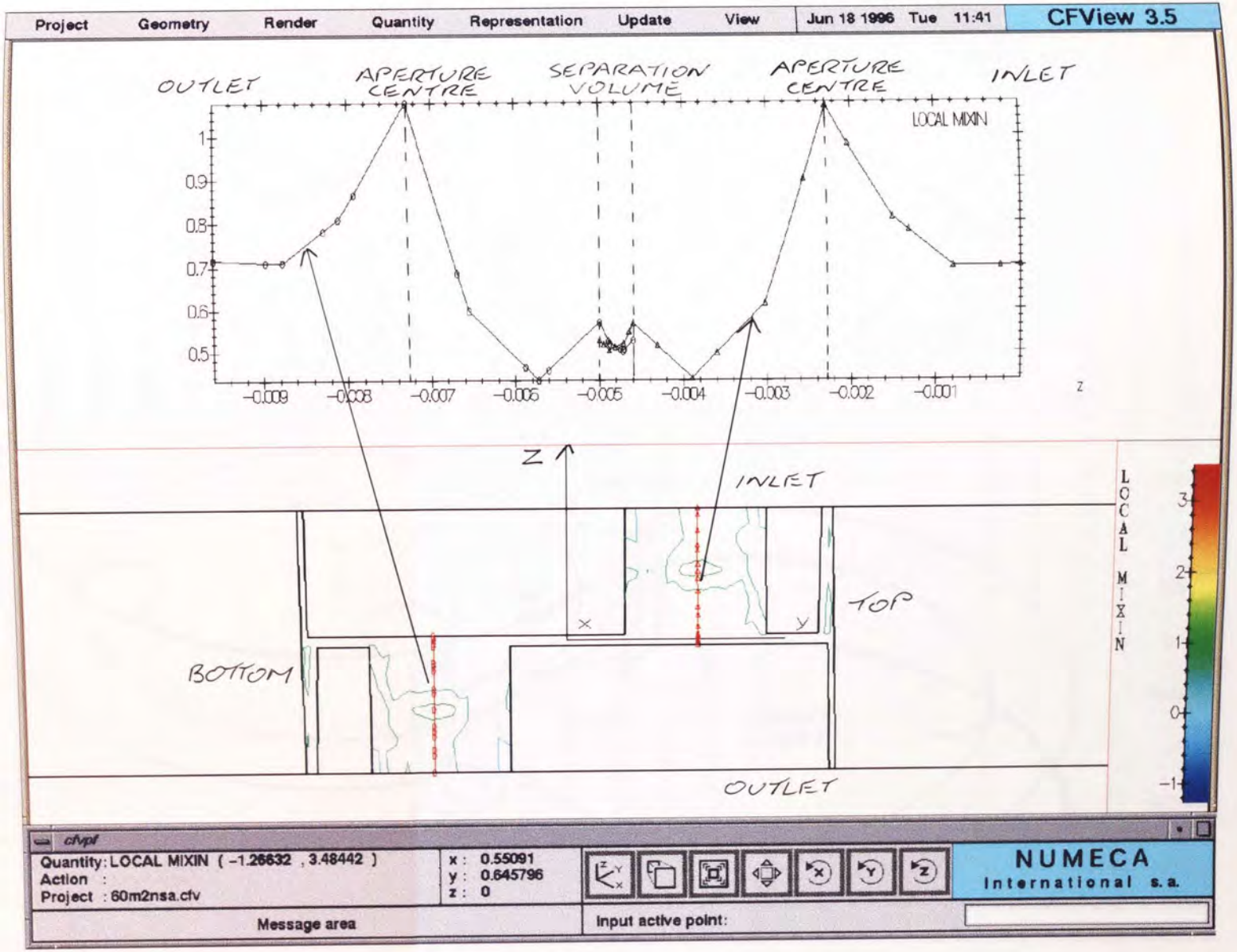

Figure 7-57:

Mixing Efficiency Isolines on the Cross Section Described in Figure 7-26 (Magnified View). Mixing Efficiency Cartesian Plots, as a Function of Spatial Distance, for the Values Encountered Along the Lines Indicated.

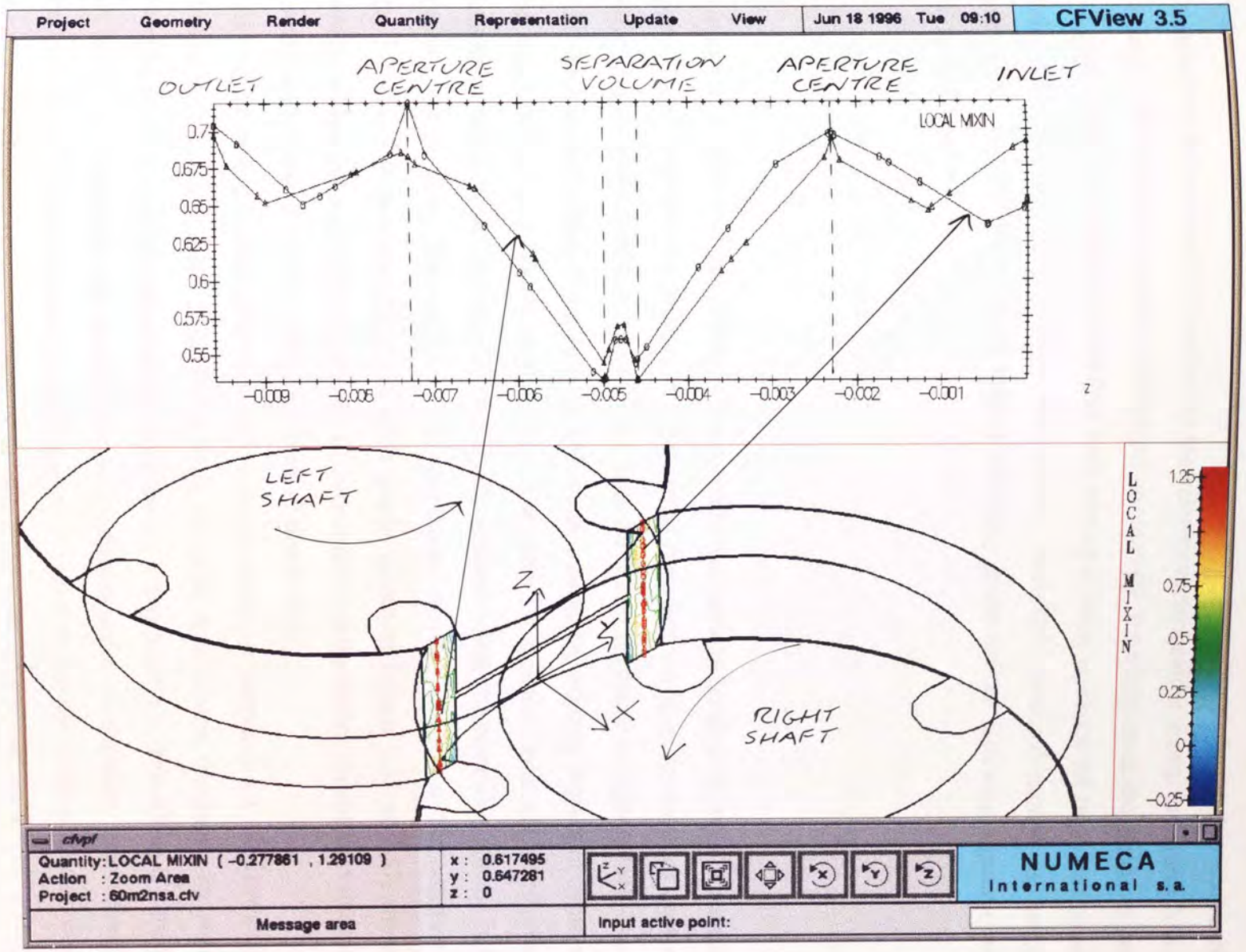

the three rotated configurations examined, also suggest a shared trend. At the very centre of each aperture, as previously illustrated by the velocity vector profiles shown in Figures 7-41, 7-44 and 7-46, material is mostly, though not exclusively, travelling about the Z-axis in the X-Y plane only (i.e. minimal forward or back mixing is being exhibited for those particular spatial co-ordinates). This implies that locally, minimum rotational motion is being experienced. By the definition of mixing efficiency given for the following equation, as defined in Chapter 4,

$$\lambda = \frac{|d|}{|d|+|w|} \qquad (7\text{-}1)$$

values of λ approaching 1 possess a low value for the vorticity component, $|w|$. Thus at the centre of each aperture contained within the central cross sections taken for the three rotated configurations investigated, values of λ are high. As is also illustrated in Figures 7-41, 7-44 and 7-46, material within the separation volume is undergoing differing degrees of forward and back mixing (i.e. the v_z components of motion for material contained within the separation volume $\neq 0$). This implies that locally material within the separation volume will possess some vorticity. This vorticity component dictates that the value of λ will be much less than 1. Indeed, inspection of the Cartesian graphs shown in Figures 7-55 to 7-57, shows material within the separation volume for all three rotated configurations, exhibiting values of λ which lie between 0.5 to 0.6, which is typical of simple shear.

As indicated in Chapter 4, the value of λ in theory should lie between $1 \leq \lambda < 0$. However, because Polyflow calculates λ indirectly using the mean least squares technique, for areas where large velocity gradients are being experienced, λ may possess a value which is outside this range. Unfortunately, for the mixing disc geometries under investigation, large velocity gradients were being calculated and imaginary λ values at certain nodal positions were produced within the domain. For the mixing efficiency values obtained for the $\alpha = 15°$ rotated configuration and shown in Figure 7-56, a manual count of the total number of nodes possessing a value outside the permitted range was performed. The number of imaginary values found where $\lambda > 1$ was 62 out of a total of 39099 nodal points (0.16 %), whereas the number for which $\lambda < 0$ was found to be 217 out of a total of 39099 nodal points (0.56 %). Thus the total percentage of nodal points where λ was calculated to have a value outside the permitted range, for the simulation represented in Figure 7-56, was 0.72 %.

The sequence of cross sections shown in Figures 7-24 to 7-26 and the subsequent description of flow parameters associated with them, demonstrate clearly the mixing behaviour exhibited within the very heart of the mixing disc zone. Each of the three

aforementioned cross sections were created such that the intersection of each plane with the outer barrel wall was through both the top and bottom bridge brows. However, because the discs are co-rotating about their fixed axes, the relative X-Y co-ordinates of the disc apertures in space, will change at different stages through the mixing cycle. As a result of this, the three aforementioned cross-sections taken in Figures 7-24 to 7-26 have intersected the central apertures at different localities. To describe further the mixing of viscous material within other regions inside the flow domain, additional cross sections along the Z-axis, but going away from the bridge regions will be described (i.e. for cross sections where $x \neq 0$). Figures 7-58 and 7-59 display Z-velocity contour plots on cross sections offset towards the right hand disc, such that the values of the X co-ordinates within each respective cross section, are the same. The intersections with the flow domain, for each cross section shown, are complex. The cross sectional plane shown in Figure 7-58 intersects four apertures at various spatial positions, whereas the cross sectional plane shown in Figure 7-59, has been created so as to intersect only two of the apertures (those of the right hand disc). The results obtained for these cross sectional planes are more effectively viewed using magnification and orientation along an axis. Thus Figures 7-60 and 7-61 show velocity vector profiles on each respective cross section, viewed along the X-axis, such that the inlet lies to the left of each image as viewed and the outlet to the right. What is interesting about the velocity profile shown in Figure 7-61 is that for material contained within the neighbourhood of the outer perimeter of the left disc and the collar of the right disc, complex swirling motion is exhibited.

Figure 7-58:

Z-Velocity Colour Contours on the First Cross Section Created in the Y-Z Plane, Offset Towards the Right Hand CICo-TSE Chamber, for the 3D Mixing Disc Zone Containing One Pair of Discs in the In-Line Arrangement at the Rotated Configuration $\alpha = 30°$.

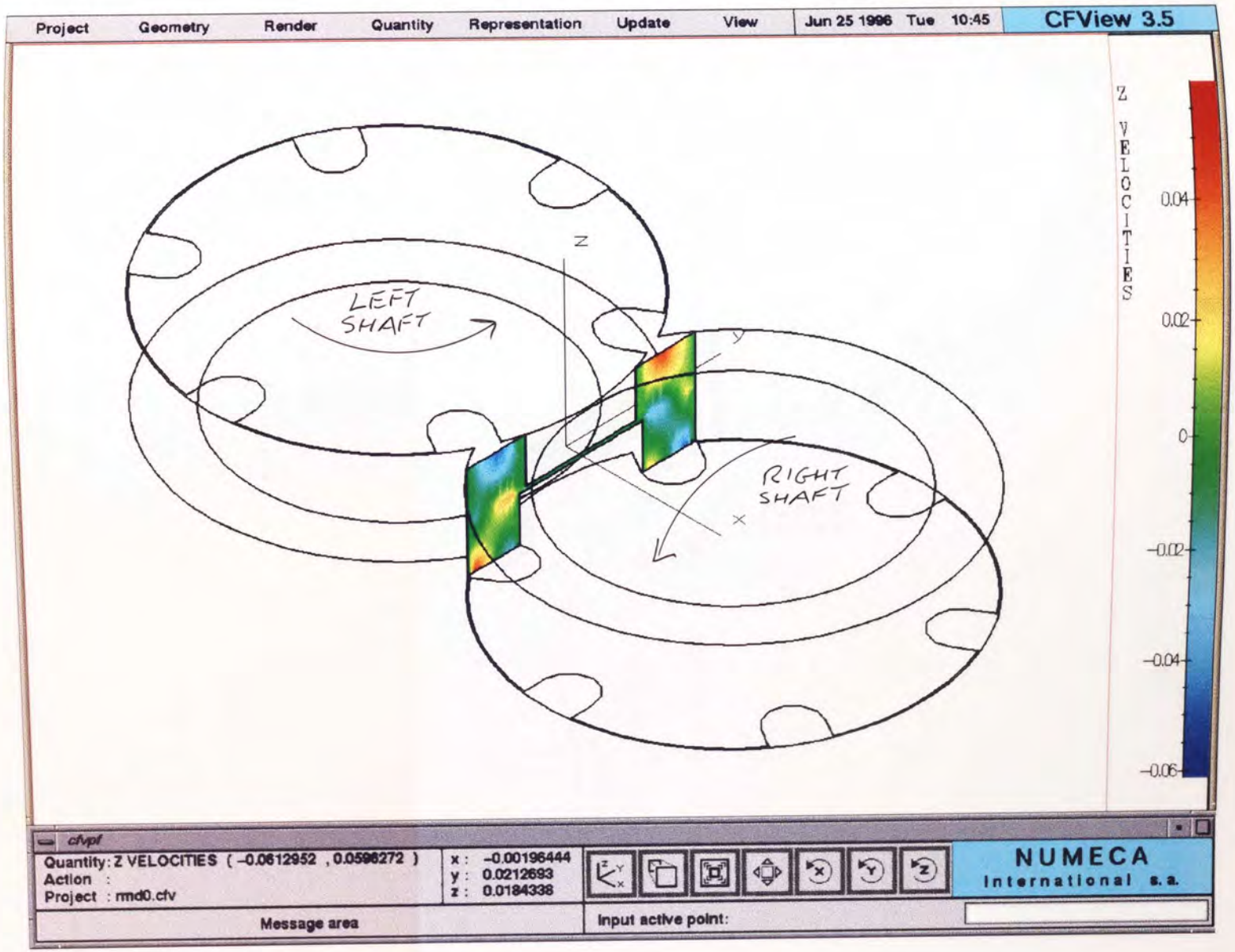

Figure 7-59:

Z-Velocity Colour Contours on the Second Cross Section Created in the Y-Z Plane, Offset Towards the Right Hand CICo-TSE Chamber, for the 3D Mixing Disc Zone Containing One Pair of Discs in the In-Line Arrangement at the Rotated Configuration $\alpha = 30°$.

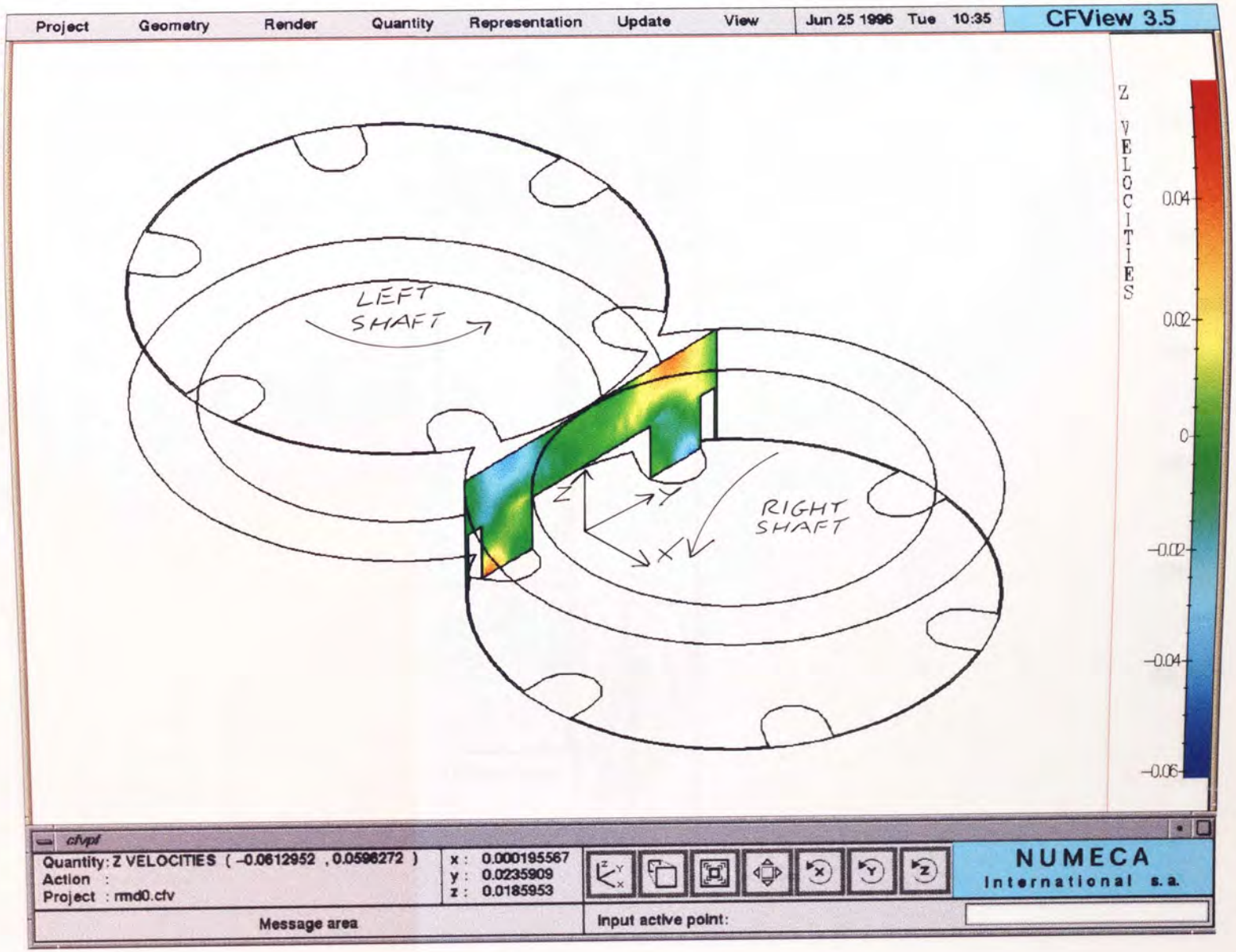

Figure 7-60:

Velocity Vector Profiles on the Cross Section Described in Figure 7-58, Viewed Along the X-Axis.

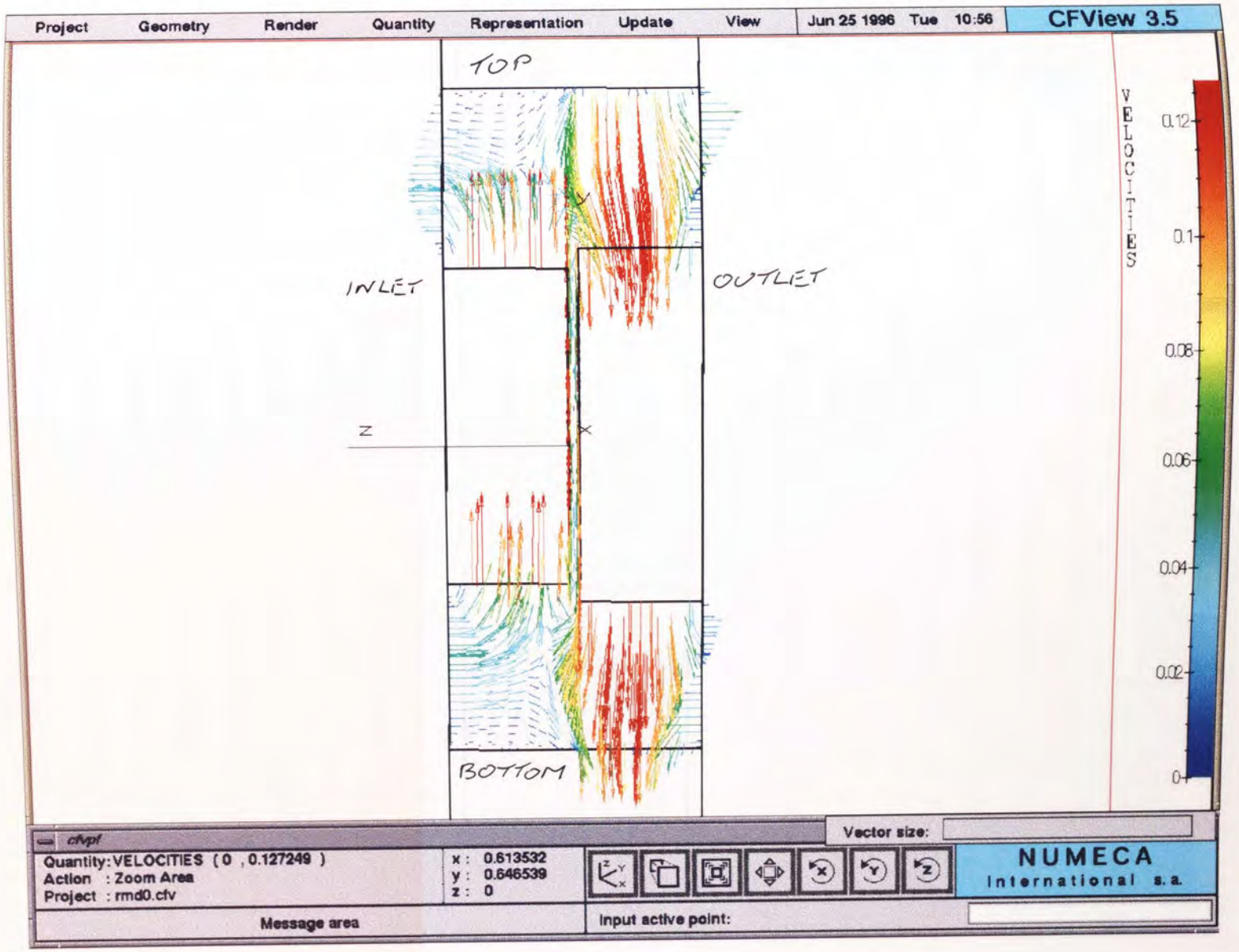

Figure 7-61:

Velocity Vector Profiles on the Cross Section Described in Figure 7-59, Viewed Along the X-Axis.

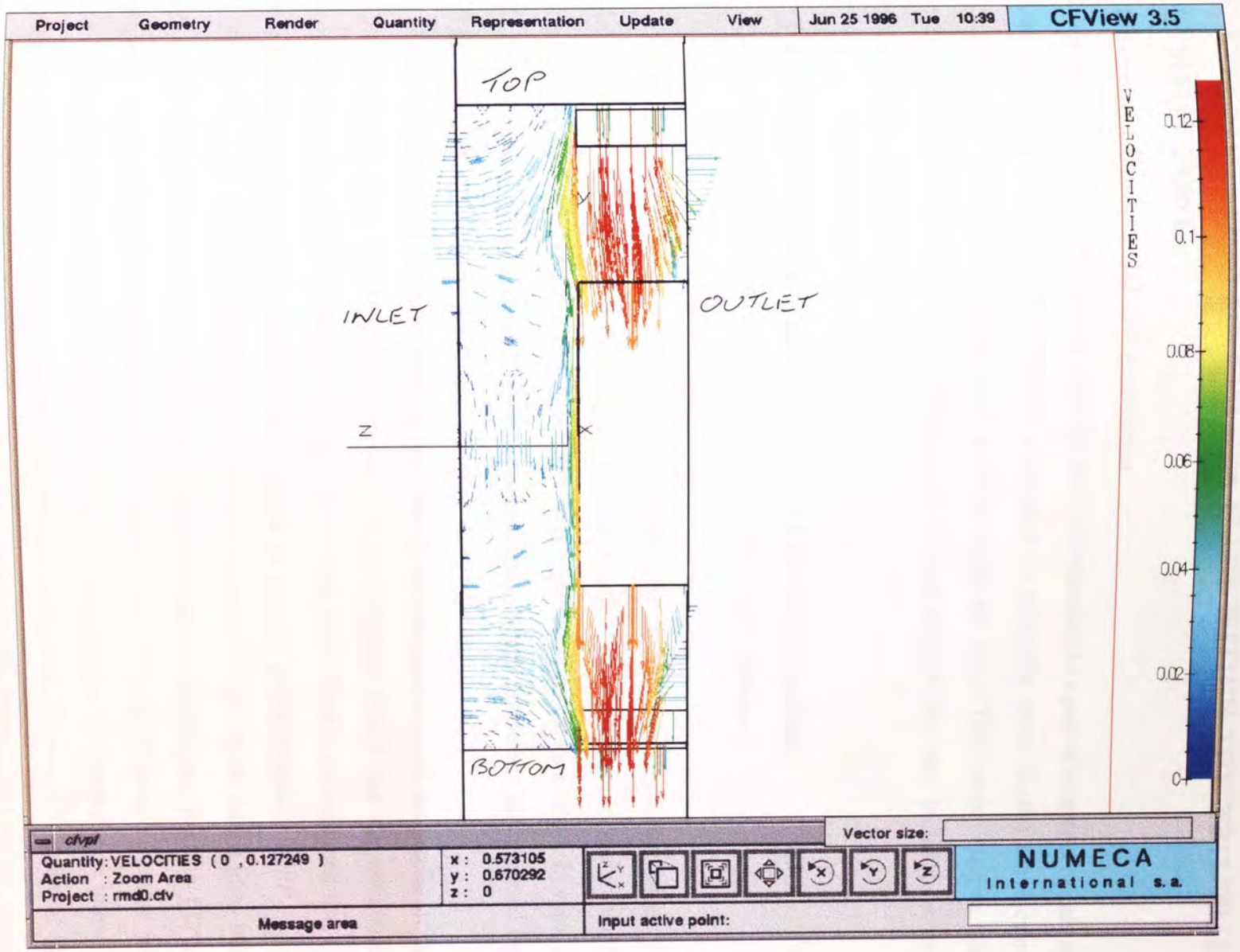

8 INVESTIGATION OF VISCOUS FLOW WITHIN THE TRILOBAL ELEMENT ZONE

8.1 Trilobal Elements - 2D X-Y geometries

For the trilobal element mixing zone, the trilobes belonging to a pair of elements (a pair of elements being defined as two trilobes positioned on opposing screw shafts) are located alongside each other at the same axial position along the CICo-TSE barrel. Due to this arrangement, there are only two independent X-Y cross sections that may be taken at any point along the zone and they show,

- The profiles of the trilobal elements in both the left and right chambers.
- The profiles of the element collars in both the left and right chambers.

The collar gap between each trilobal element pair is very small (of the order of 0.1 - 0.2 mm). Ideally this gap should be as small as possible, as its presence is detrimental to the progression of any material caught between pairs of elements on the same shaft. In view of this the simulation of the trilobal element zone presented within this thesis has assumed that the gap between element pairs is negligible and thus disregarded.

When performing a 2D simulation of the flow fields exhibited around the profile of the trilobal element pair, the repeated symmetry of the elements meant that the simulation analysed be examined for a rotation through a 30° mixing cycle. Thus it was assumed that the flow fields exhibited by the trilobal elements would be periodic with a frequency of 30°.

The partial mixing cycle investigated is shown in Figure 8-1. The cycle shown goes from the $\alpha = 0°$ (top left) to the $\alpha = 30°$ (bottom right) rotated configuration. For the trilobal elements, α represents the angle between the right hand tips belonging to each element pair and the horizontal axis. The physical construction of each mesh at 5° intervals, in terms of global nodal positions, changes through this partial mixing cycle. However, it is found that groups of meshes may be classified as being of the same macro-element construction, similar to that of the mixing discs as outlined in Chapter 7. For the trilobal elements this need arises due to the trilobal tips coinciding with the bridge regions for certain rotated configurations, as may be seen in Figure 8-1. Thus for representing the trilobal elements in 2D, it was found that there are two discrete sets of macro-element construction that may be used. These are for the following sets of rotated configurations;

Set 1: $0° \leq \alpha \leq 25°$

Set 2: $\alpha = 30°$

Figure 8-1:

Partial Mixing Cycle Examined for the Investigation of the Trilobal Element Mixing Zone, Progressing From the a = 0° (Top Left) to the a = 30° (Bottom Right) Rotated Configuration.

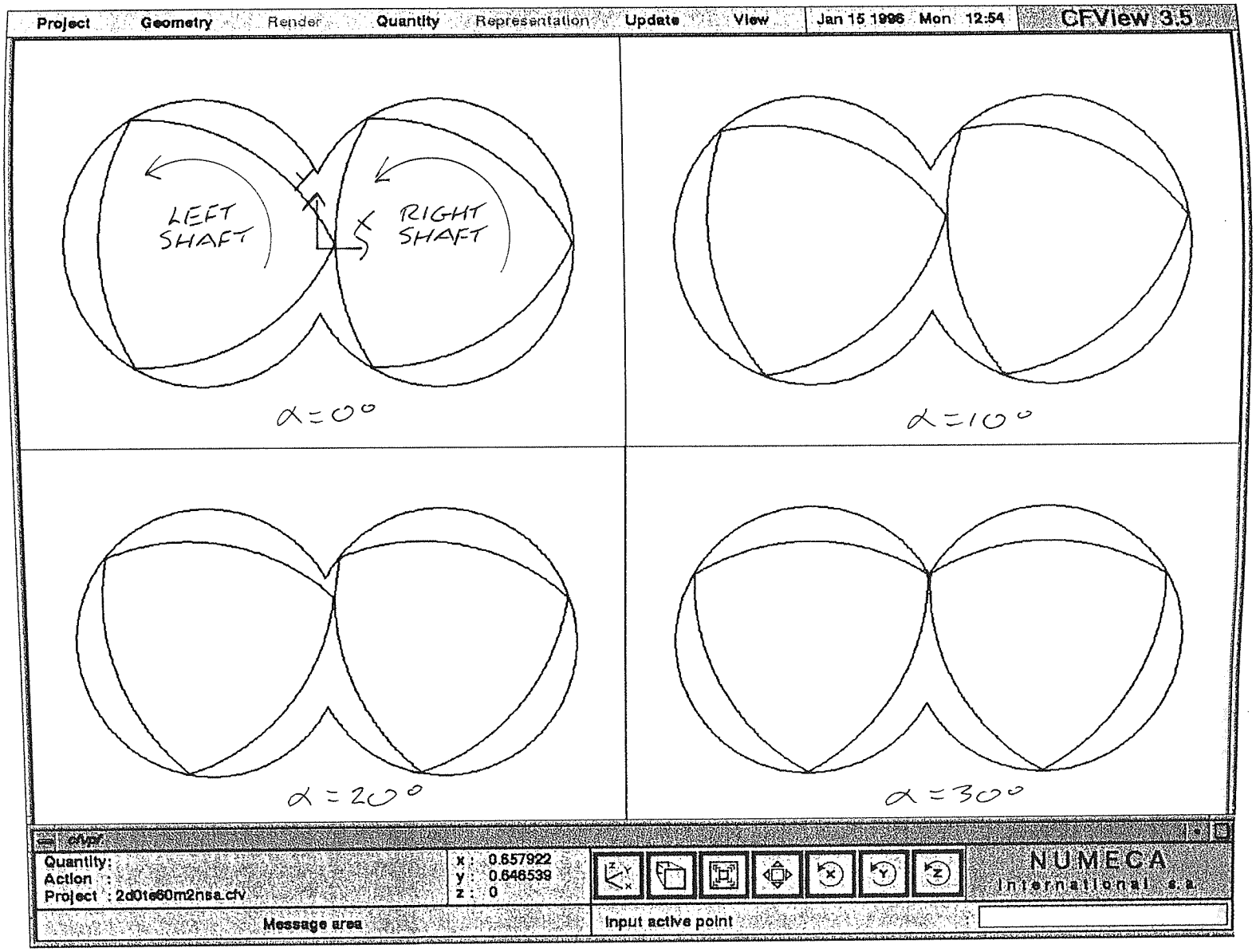

The full macro-element details for each mesh contained within each of these two rotated configuration sets specified, are as follows;

Set 1:

- Number of macro-vertices within each mesh: 19
- Number of macro-elements within each mesh: 11

Set 2:

- Number of macro-vertices within each mesh: 18
- Number of macro-elements within each mesh: 10

The full details for the construction of each mesh within each of the two trilobal element rotated configuration sets, are as follows;

Set 1:

- Macro-vertex numbering scheme:
  Appendix AC.
- Macro-vertex co-ordinates for each mesh contained within Set 1:
  Appendices AD1- AD6.
- Macro-element numbering scheme:
  Appendix AE.
- Details for the construction of all macro-elements contained within each mesh of Set 1:
  Appendix AF.
- Boundary numbering scheme:
  Appendix AG.

Set 2:

- Macro-vertex numbering scheme:
  Appendix AH.
- Macro-vertex co-ordinates for the $\alpha = 30°$ mesh:
  Appendices AI.
- Macro-element numbering scheme:
  Appendix AJ.
- Details for the construction of the $\alpha = 30°$ mesh:
  Appendix AK.

- Boundary numbering scheme:

  Appendix AL.

The number of structured nodes contained within each mesh pertaining to each of the two macro-element construction sets, are as follows;

Each mesh within Set 1: 3642

Each mesh within Set 2: 3641

An example of a typical 2D trilobal element mesh, illustrating the mesh density within the flow domain, is given in Figure 8-2. From this figure it may be seen that the greatest mesh density areas are around all trilobal tips.

8.2 Trilobal Elements - 3D geometries

Similar to the kneading blocks described in Chapter 1, the trilobal elements may be arranged with different stagger angles between adjacent element pairs. The stagger angles typically employed within different CICo-TSE arrangements are 15°, 30°, 45° and 60° (neutral). Essentially, the use of different stagger angles gives rise to the following three distinct classification of zone arrangement, each imposing different mixing mechanisms on the viscous melt;

- Right-handed arrangements, which convey material in the same direction as the melt flow.
- Neutral (60°) arrangement which induces equal forward and back mixing within the zone.
- Left-handed arrangements, which forces material back against the direction of melt flow.

The schematic diagrams shown in Figure 8-3 show the principles of viscous fluid flow within each of these three different elemental arrangements [16]. The particular arrangement utilised by the PPPG at Aston within the Betol BTS30 CICo-TSE is the neutral arrangement and thus it is results from this particular arrangement which are presented within this thesis. Figure 8-4 depicts the neutral arrangement for a mixing zone containing a set of five trilobal element pairs.

Similar to the construction of the mixing disc zone, the number of trilobal pairs that are needed within a trilobal element mixing zone is, to a certain extent, an educated guess. The trilobal element mixing zones utilised by the PPPG within the Betol BTS30 CICo-TSE, contain five pairs of trilobal elements arranged as shown in Figure 8-4. Direct simulation of this number of element pairs by CFD is feasible using Polyflow, however it would be very

Figure 8-2:

Typical Mesh Utilised for the 2D Representation of the Trilobal Element Mixing Zone in the X-Y Plane (Rotated Configuration $\alpha = 0°$).

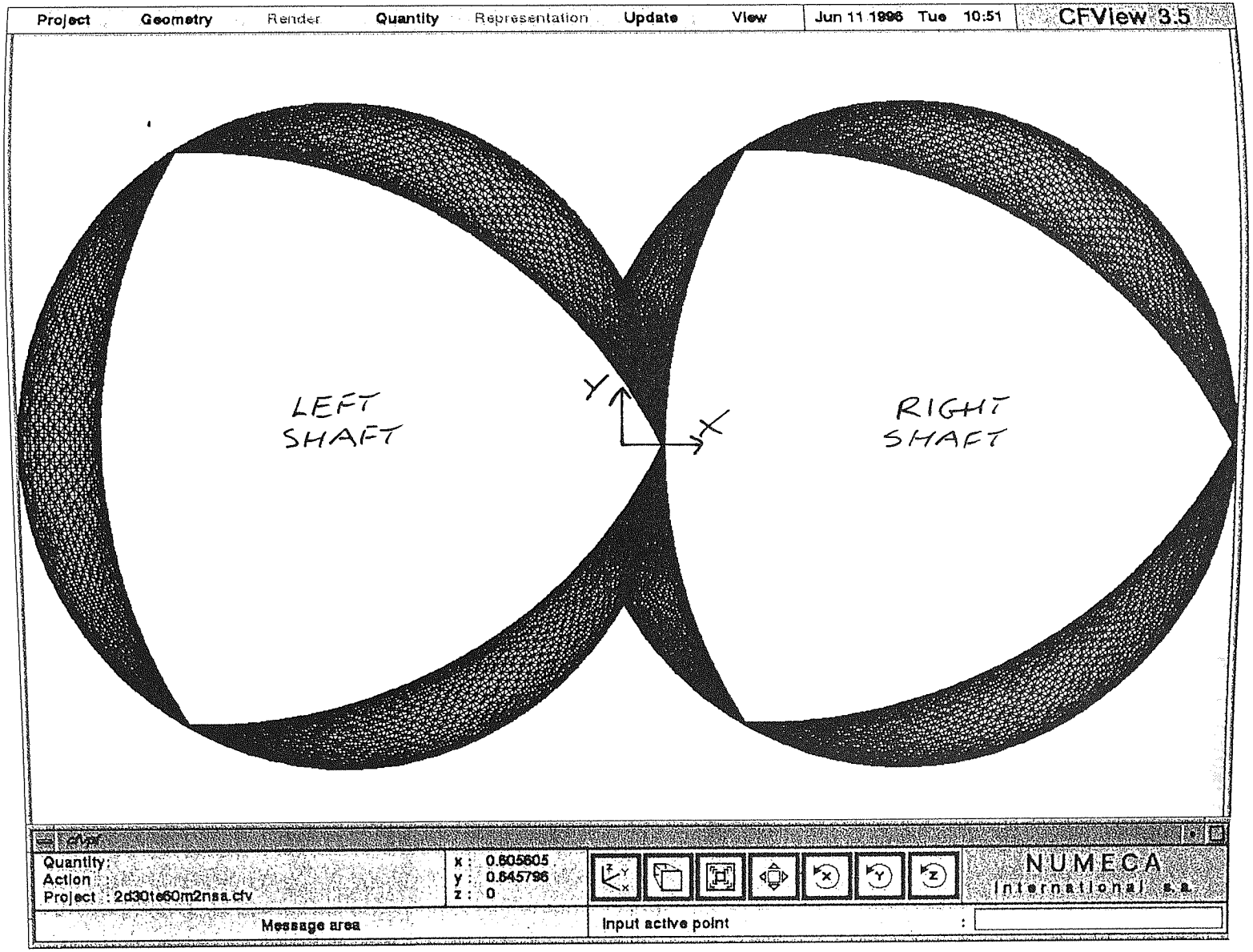

FIGURE 8-3

Different Stagger Angle Arrangements for the Trilobal Element Mixing Zone

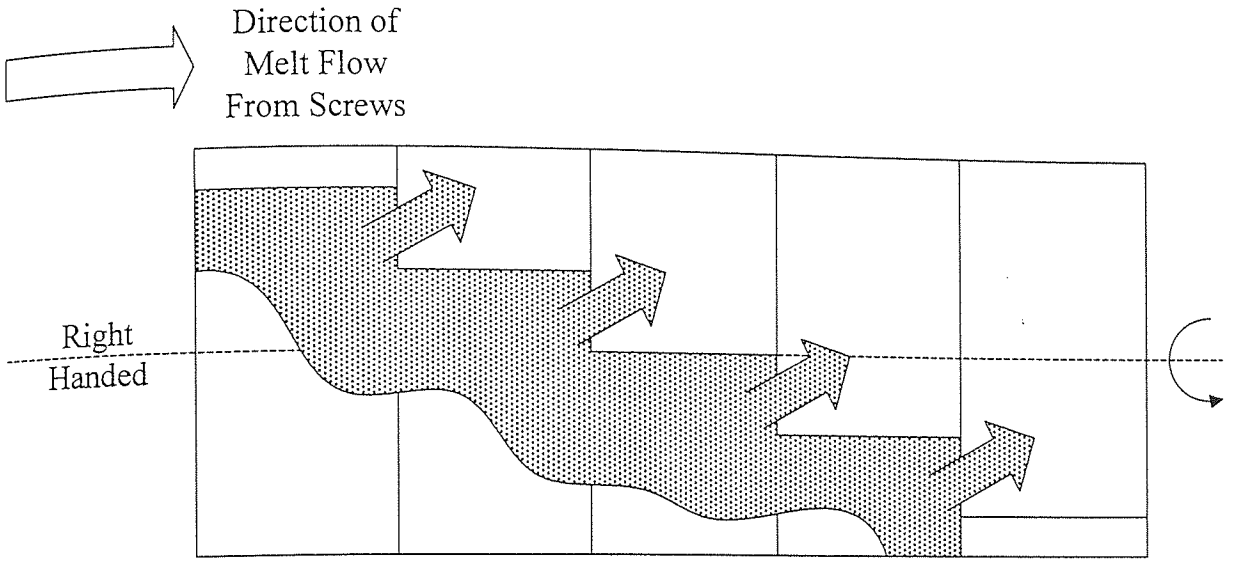

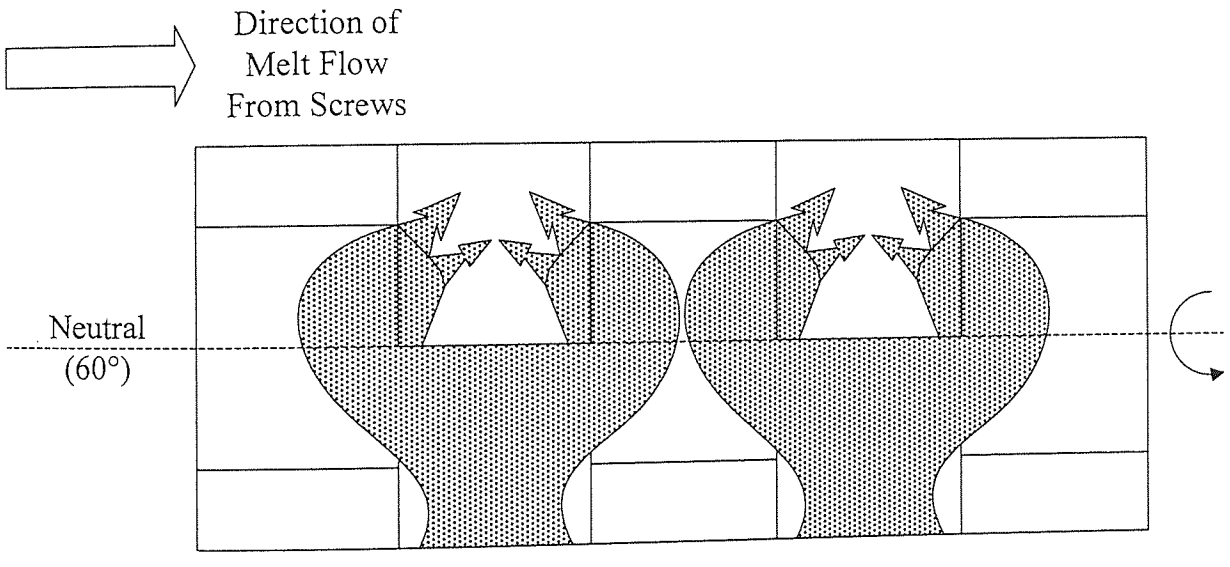

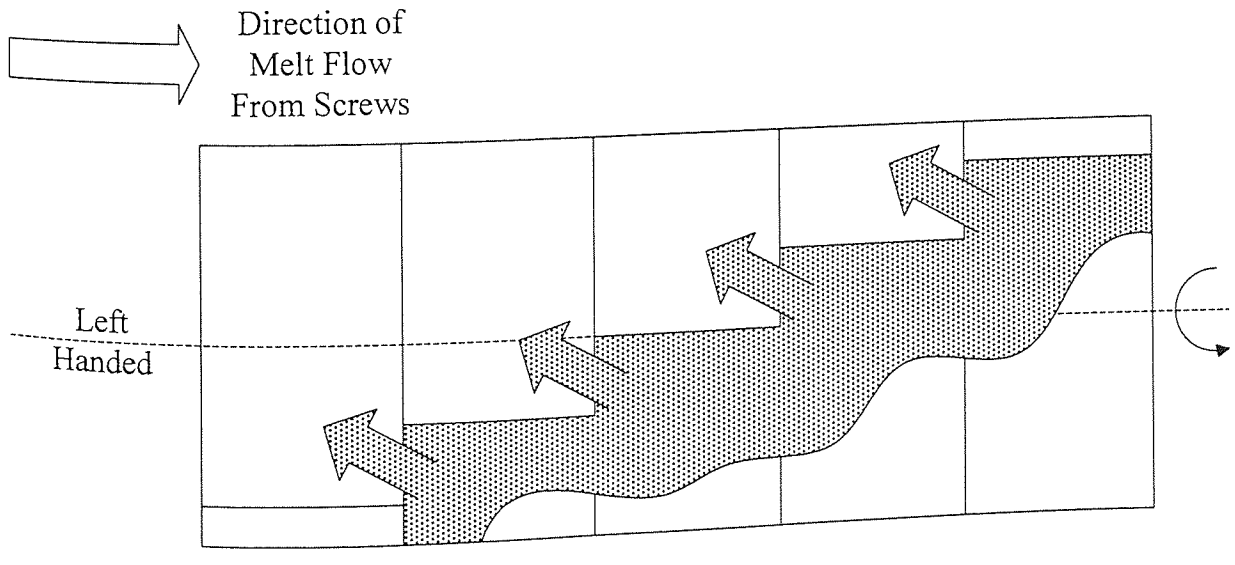

Figure 8-4:

Schematic Diagram Illustrating the Placement of Elements Within a Typical Trilobal Element Mixing Zone, Containing Five Pairs of Elements in the Neutral Arrangement (Anti-Clockwise, Co-Rotation of Shafts).

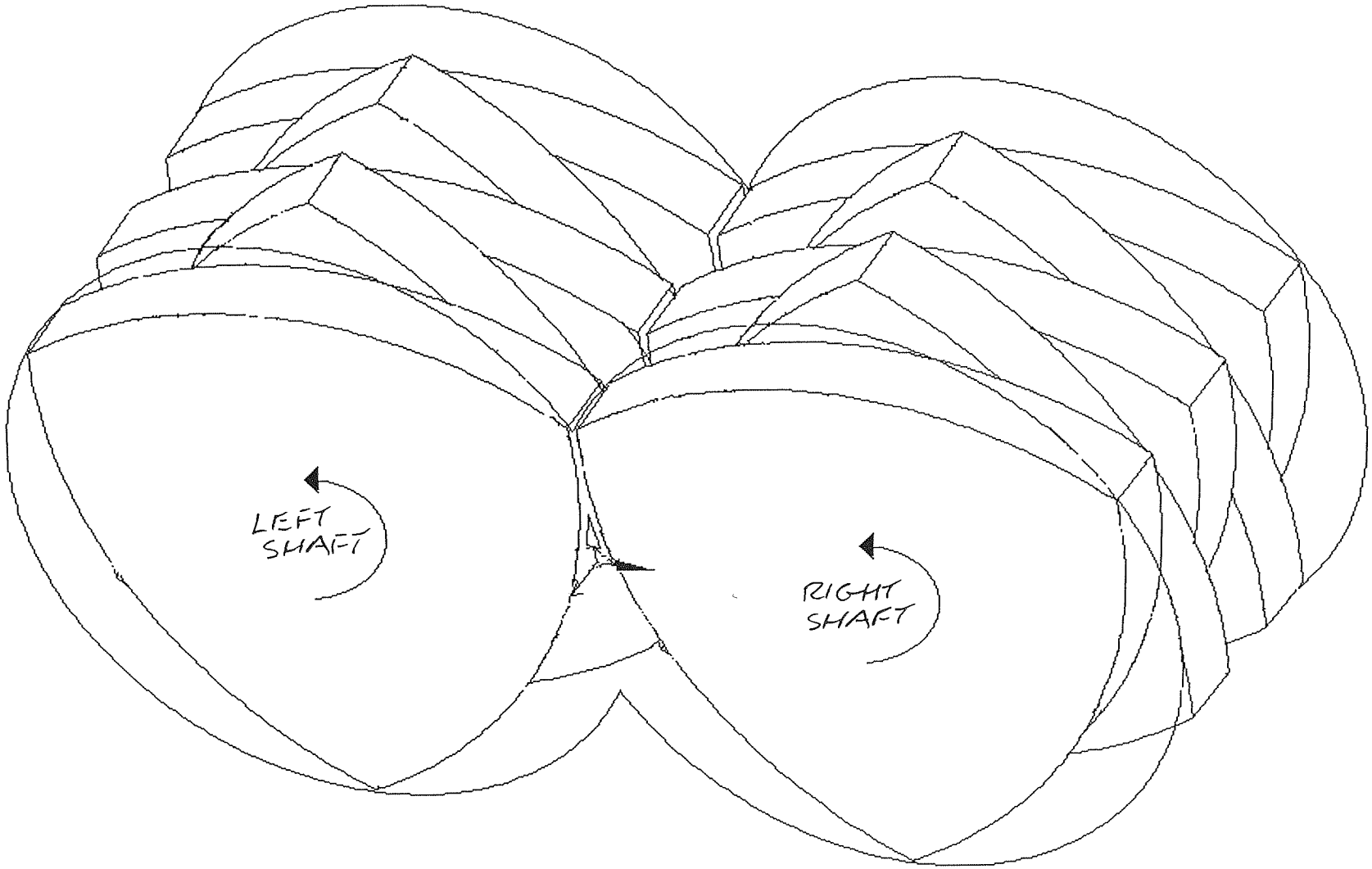

expensive in terms of CRAY CPU time needed to solve the problem. During the course of this research a successful application of Class 3 computing time was awarded and this amounted to an allocation of 40 hours of CRAY J90 CPU time. This amount of CRAY J90 CPU time would not have been sufficient to solve the flow problem within a mixing zone containing five pairs of trilobal elements. Unfortunately, an application for extensive allocation of CRAY J90 CPU time, known as a Class 1 allocation, was not allowed for this particular level of research. Thus it was decided to degenerate the flow problem by simulating one pair of trilobal elements at each stage, building the problem up until the CRAY J90 CPU time taken to potentially solve the flow problem became too high. Consequently it was found that results could only be obtained for the simulation of one, two and three pairs of trilobal elements. The meshes used for the simulation of one pair of trilobal elements are shown in Figures 8-5 and 8-6 for the $\alpha = 0°$ and 30° rotated configurations respectively. However, the results obtained from meshes representing one pair of trilobal elements are not very interesting, as the influence of the stagger angles between the adjacent elemental pairs is omitted. Therefore, meshes representing mixing zones containing two and three pairs of elements are described in the following paragraphs.

As mentioned previously, one of the assumptions made for the construction of meshes representing the trilobal element mixing zone, was that the small collar gap between each pair of staggered elements is omitted. Unfortunately, there are rotated configurations for which the tips from opposing trilobal elements coincide and it is at these configurations that opposing trilobal tips very nearly touch each other. Thus to accommodate the omission of the collar gap between trilobal element pairs, an assumption was made for these rotated configurations such that at those particular instances, the trilobal tips do touch and therefore no material is contained within the space between each tip. To illustrate this assumption more clearly, one may inspect the meshes used for the simulation of two pairs of trilobes as shown in Figures 8-7, 8-8 and 8-10 for the $\alpha = 0°$, 15° and 30° rotated configurations respectively. At the centre of the mesh shown in Figure 8-7 for the $\alpha = 0°$ configuration, there is a rectangular "hole". This "hole" corresponds to the position for the coincidence of two tips, one from the left trilobe of the foreground trilobal element pair and the other tip from the right trilobe of the background pair. Opposing trilobal pairs for the $\alpha = 15°$ rotated configuration also coincide, however this cannot be visualised from its mesh which is shown in Figure 8-8. Instead the coincidence of trilobal pairs may be clearly seen only at the very centre of the mesh outline shown in Figure 8-9. For the $\alpha = 30°$ rotated configuration shown in Figure 8-10, no coincidence of trilobal element pairs takes place.

An example of the domain structure for the $\alpha = 0°$ rotated configuration is shown in Figure 8-11, illustrating also the Master (shown as dark blue edges) and Slave (shown as light

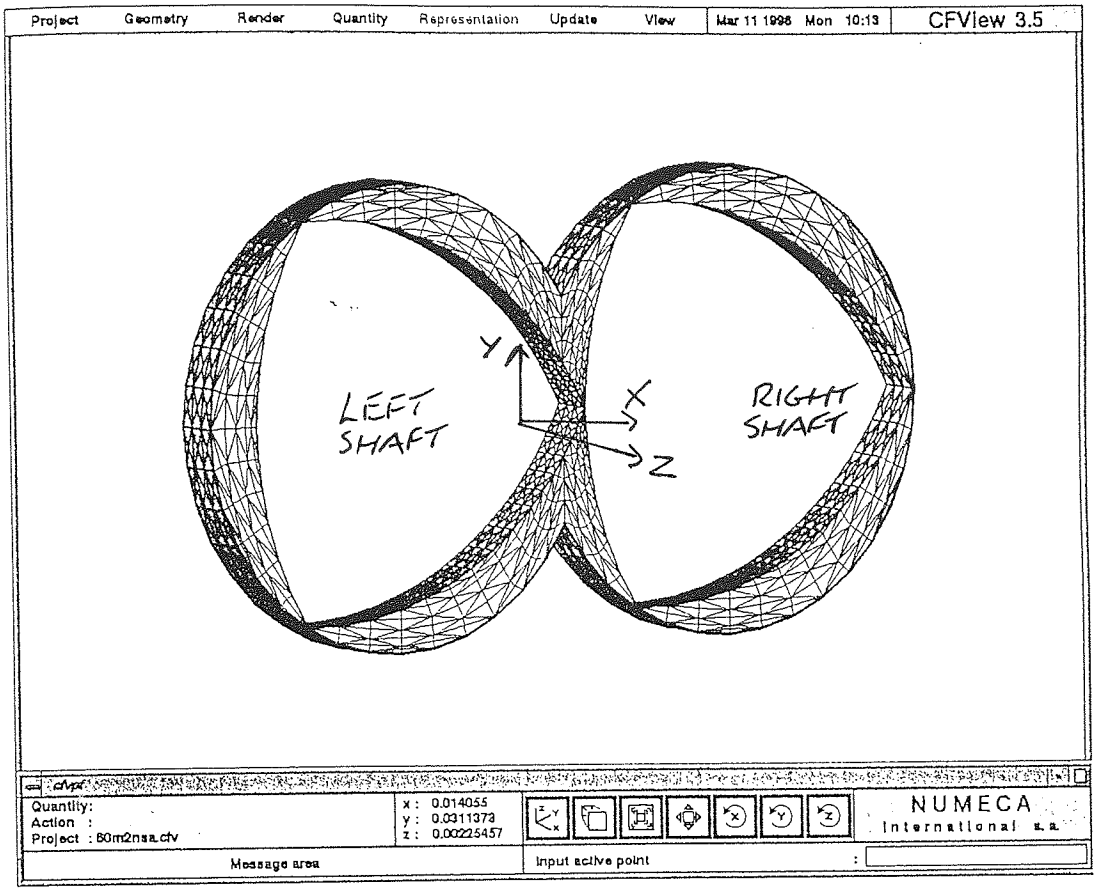

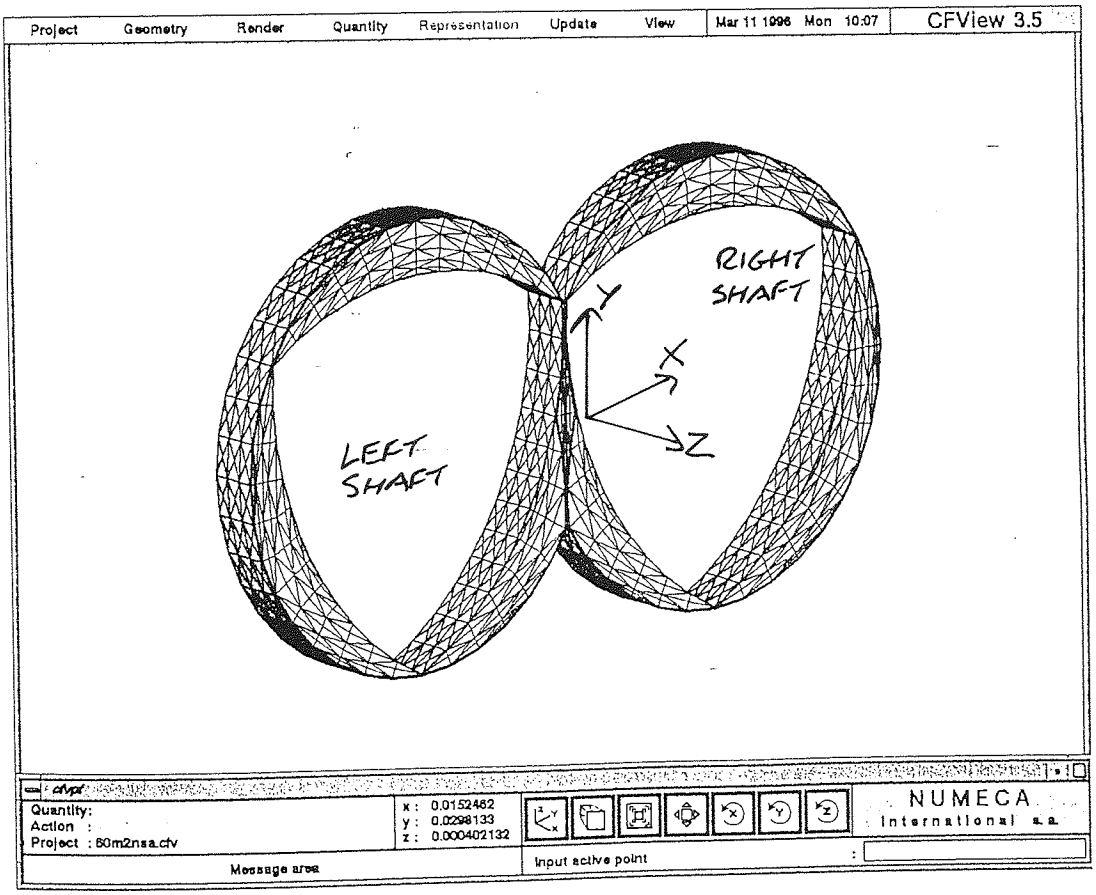

Figure 8-5 (Upper): Mesh Utilised for the Representation of One Pair of Trilobal Elements (Rotated Configuration $\alpha = 0°$).

Figure 8-6 (Lower): Mesh Utilised for the Representation of One Pair of Trilobal Elements (Rotated Configuration $\alpha = 30°$).

Figure 8-7:
Mesh Utilised for the Representation of Two Pairs of Trilobal Elements in the Neutral Arrangement (Rotated Configuration $\alpha = 0°$).

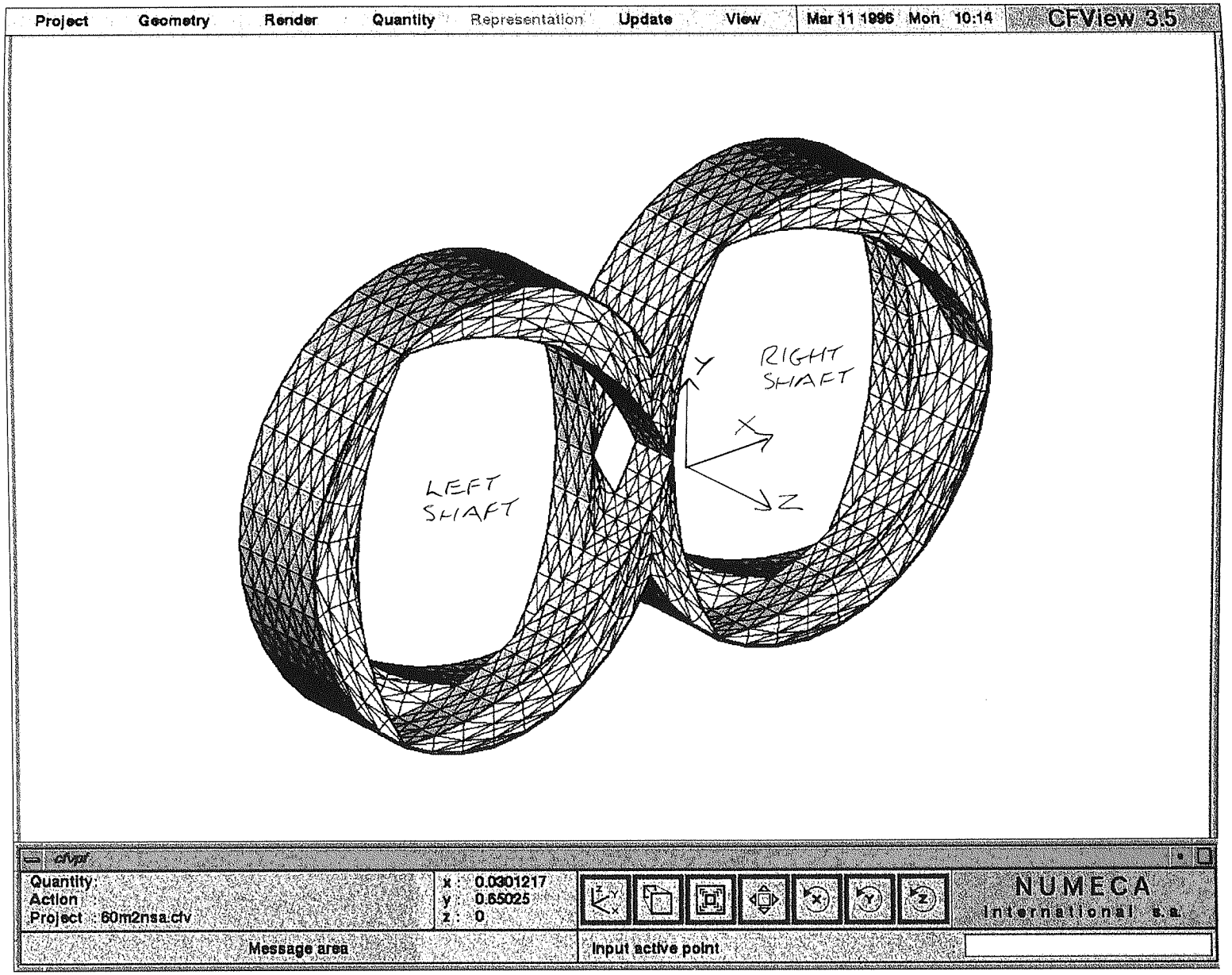

Figure 8-8:
Mesh Utilised for the Representation of Two Pairs of Trilobal Elements in the Neutral Arrangement (Rotated Configuration $\alpha = 15°$).

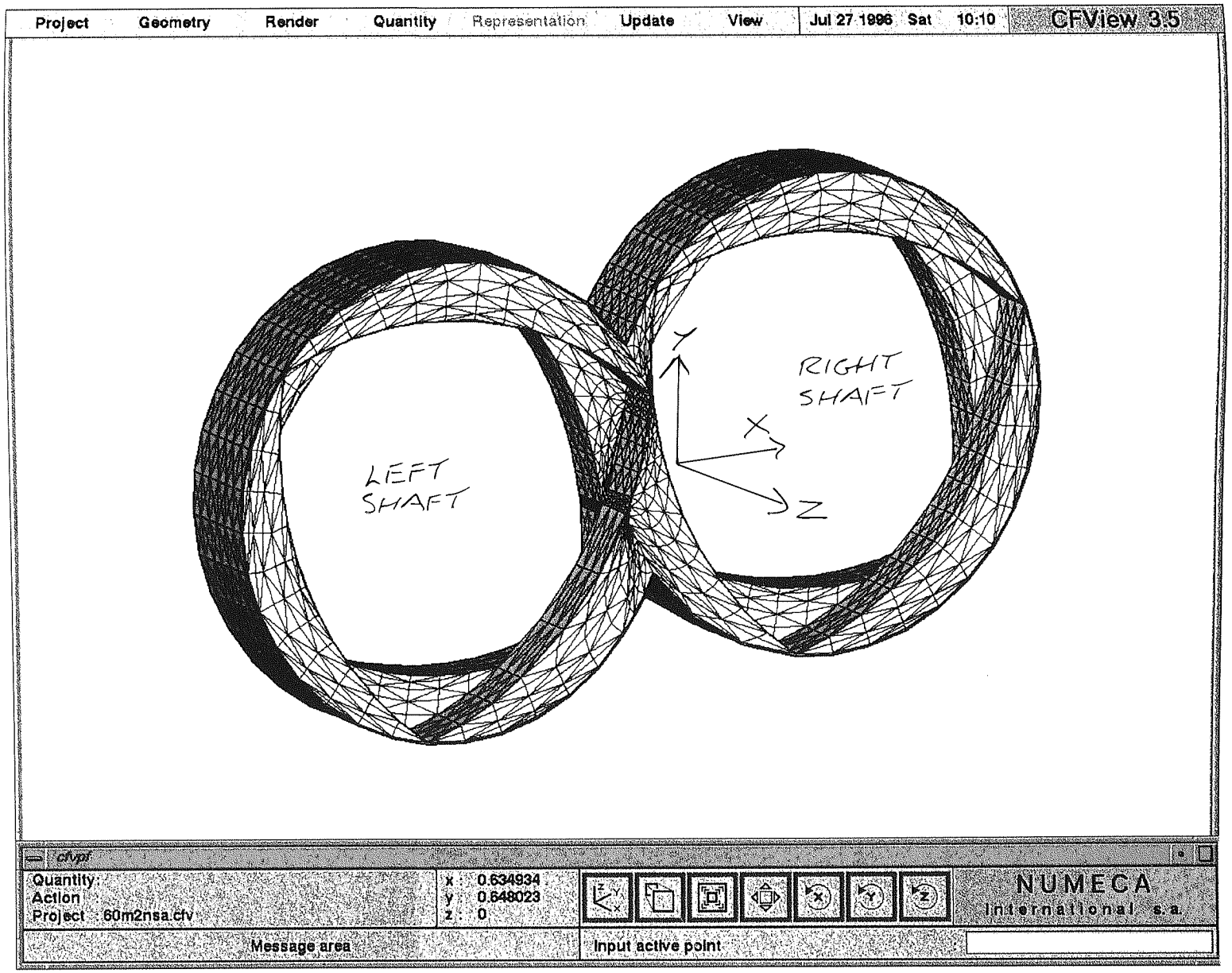

Figure 8-9:

Mesh Outline Illustrating the Coincidence of Trilobal Pairs for the Representation of Two Pairs of Trilobal Elements in the Neutral Arrangement, at the Rotated Configuration $\alpha = 15°$.

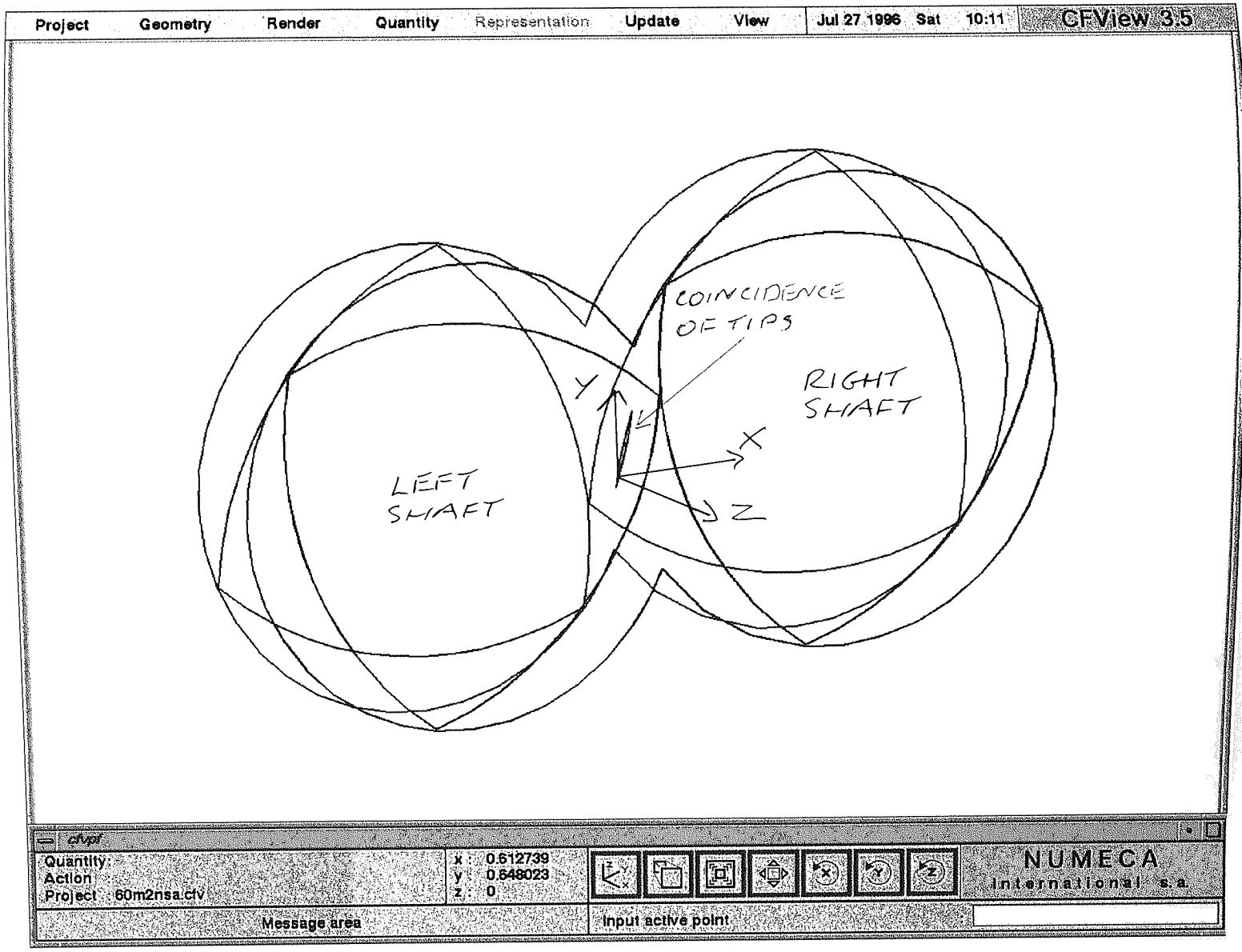

Figure 8-10:
Mesh Utilised for the
Representation of Two Pairs of
Trilobal Elements in the Neutral
Arrangement (Rotated
Configuration $\alpha = 30°$).

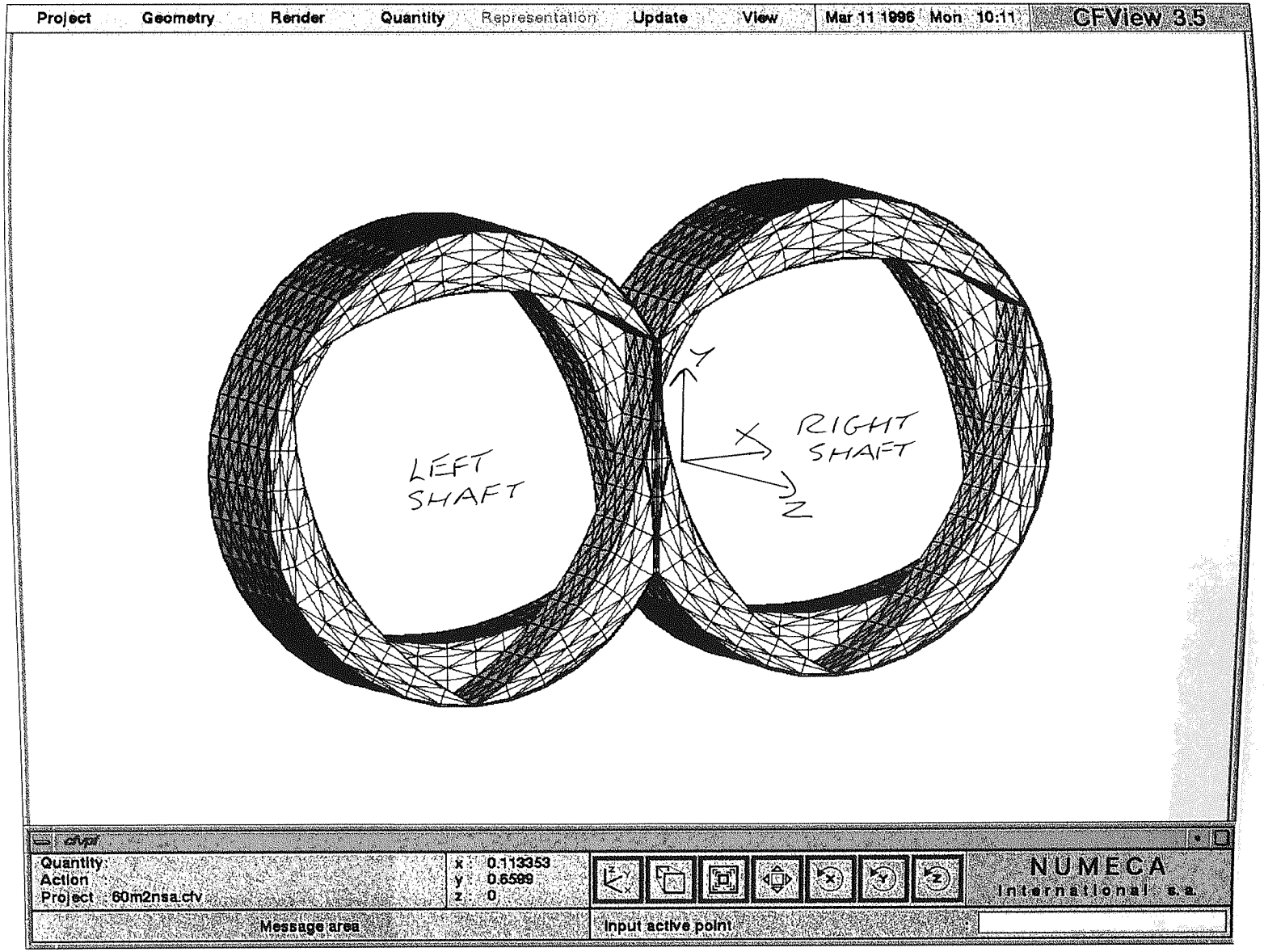

Figure 8-11:
P-Cube Master and Slave Distribution Assigned to the Mesh Utilised for the Representation of Two Pairs of Trilobal Elements in the Neutral Arrangement (Rotated Configuration $\alpha = 0°$).

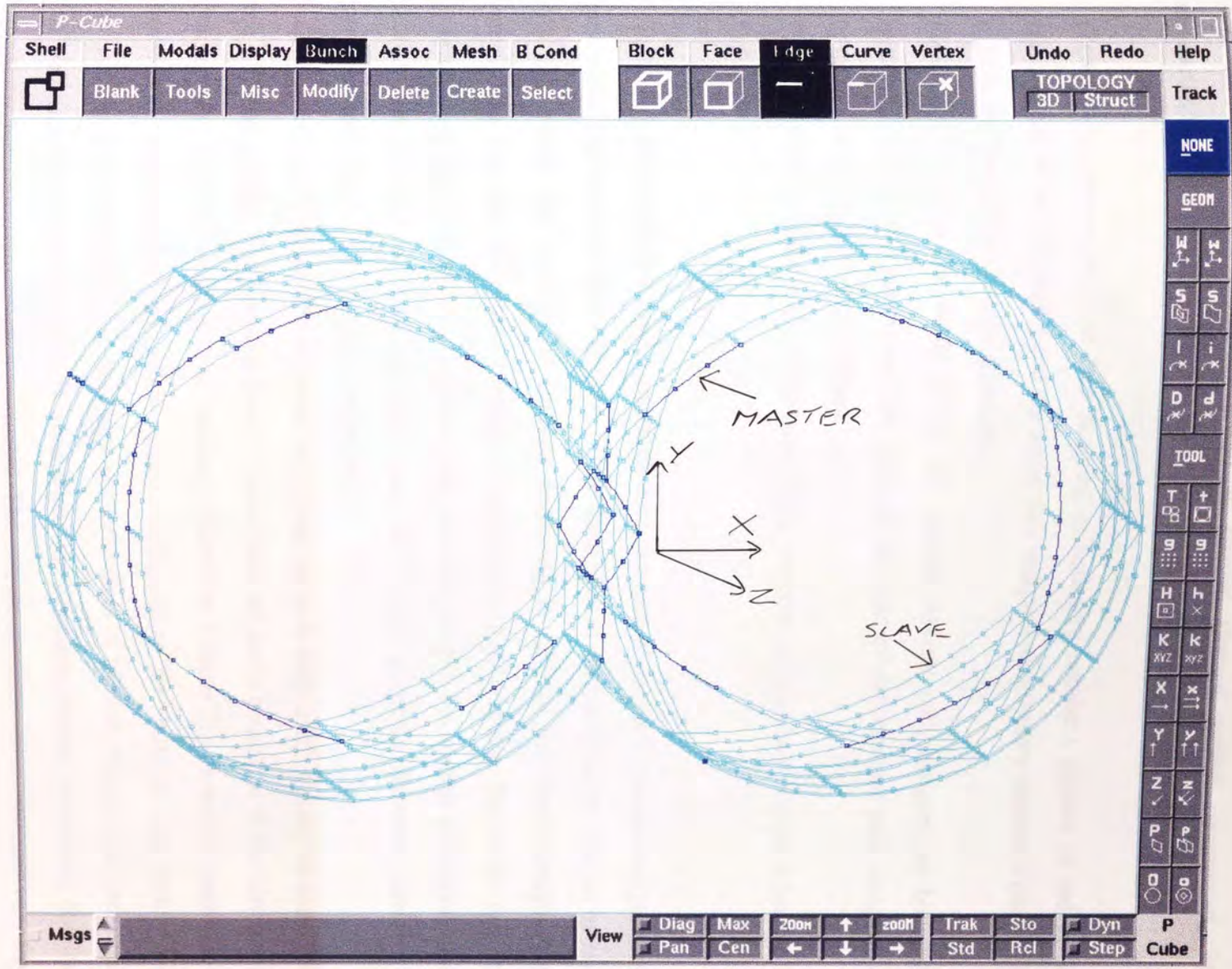

blue edges) distributions employed. For all trilobal element meshes constructed, five boundaries were ascribed and Figures 8-12 to 8-14 illustrate these assignments;

- Figure 8-12 shows the inlet face assigned as boundary number 1 (shown in red at the foreground of the structure) and the outlet face assigned as boundary number 5 (shown in pink at the background of the structure).
- Figure 8-13 shows the walls of the left trilobal element pair, assigned as boundary number 2 (shown in green) and the walls of the right trilobal element pair, assigned as boundary number 3 (shown in blue).
- Figure 8-14 shows the wall of the outer barrel, assigned as boundary number 4 (shown in light blue).

Table 8-1 catalogues all mesh parameters used, for each of the three rotated configurations constructed representing either the one, two or three pairs of trilobal elements. As can be seen from this table, the number of domains pertaining to each of the three configurations representing one pair of trilobal elements is approximately 40 domains. Due to the fact that the separation plane between each trilobal pair has been omitted, the number of domains used for the construction of two and three pairs of trilobal elements increases linearly to approximately 80 and 120 domains respectively.

Graphs 8-1 to 8-9 show the Jacobian histograms for each mesh used. As may be seen from each of these graphs, their general form is varied (they are not as consistent as the histograms obtained for the 3D mixing disc meshes, shown in Chapter 7). However, each mesh constructed representing the same rotated configuration for each of the three zone configurations investigated (i.e. one, two and three pairs of trilobal elements) is consistent. This inconsistency must be borne in mind when one compares average parameters obtained through the partial mixing cycle investigated. The average Jacobian values obtained vary from approximately 90 to 94.

8.3 Flow within the Trilobal Element Zone

Results from the simulation of 2D trilobal element cross sections are shown in Figures 8-15 to 8-18. Similarly to the mixing disc simulation results reported in Chapter 7, a series of 2D cross sections representing various regions within the 3D trilobal element mixing zone, does not provide the whole flow picture. The significance of axial pressure, giving rise to various degrees of forward and back mixing along the length of the mixing zone, is lost. However, by using 2D meshes possessing large mesh refinement within areas of intense flow activity, a clearer picture of the fluid motion within those regions is gained. Figure 8-15

Figure 8-12:
Assignment of Boundaries 1 and
for the Mesh Shown in
Figure 8-8.

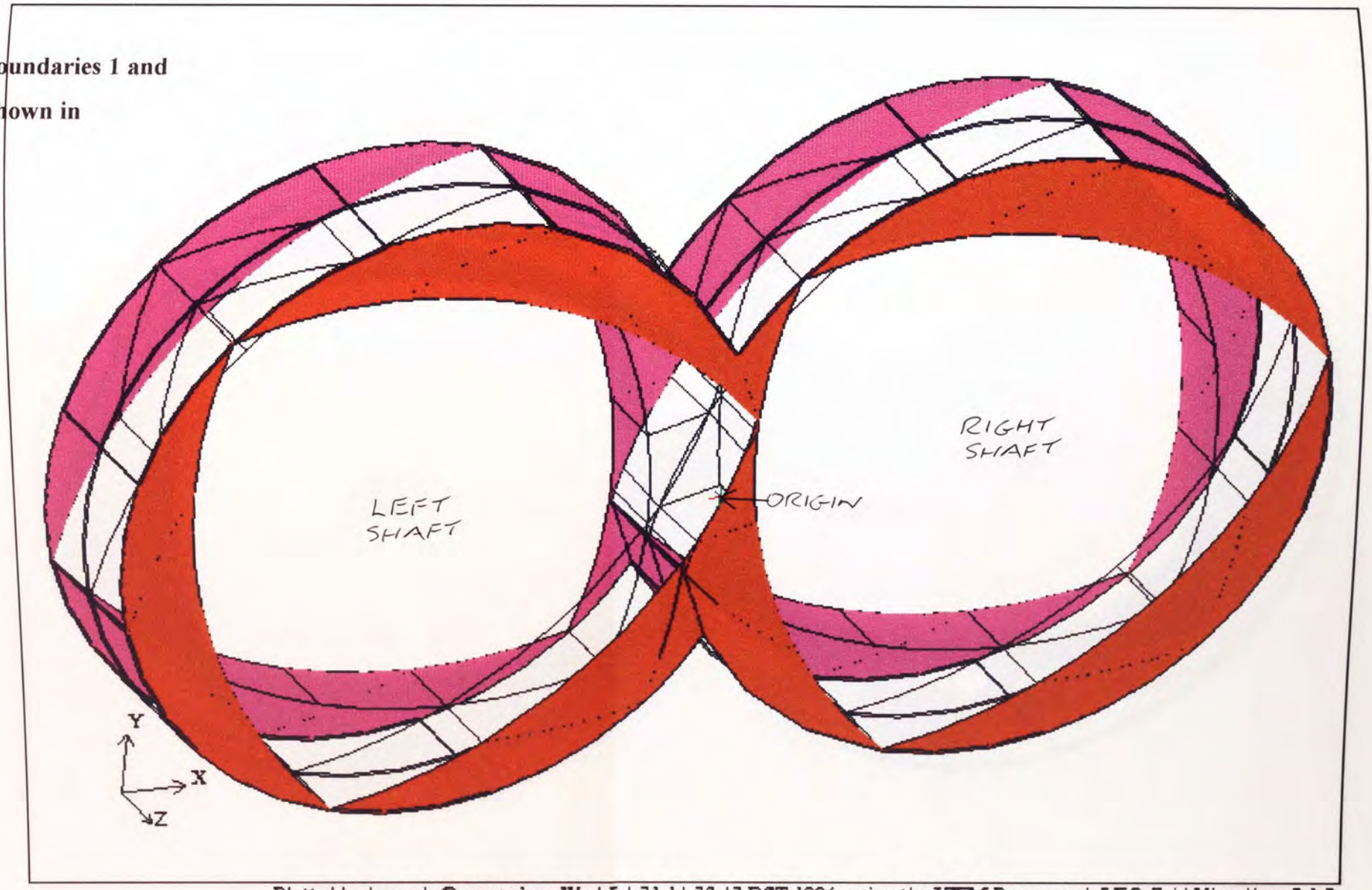

Figure 8-13:
Assignment of Boundaries 2 and
for the Mesh Shown in
Figure 8-8.

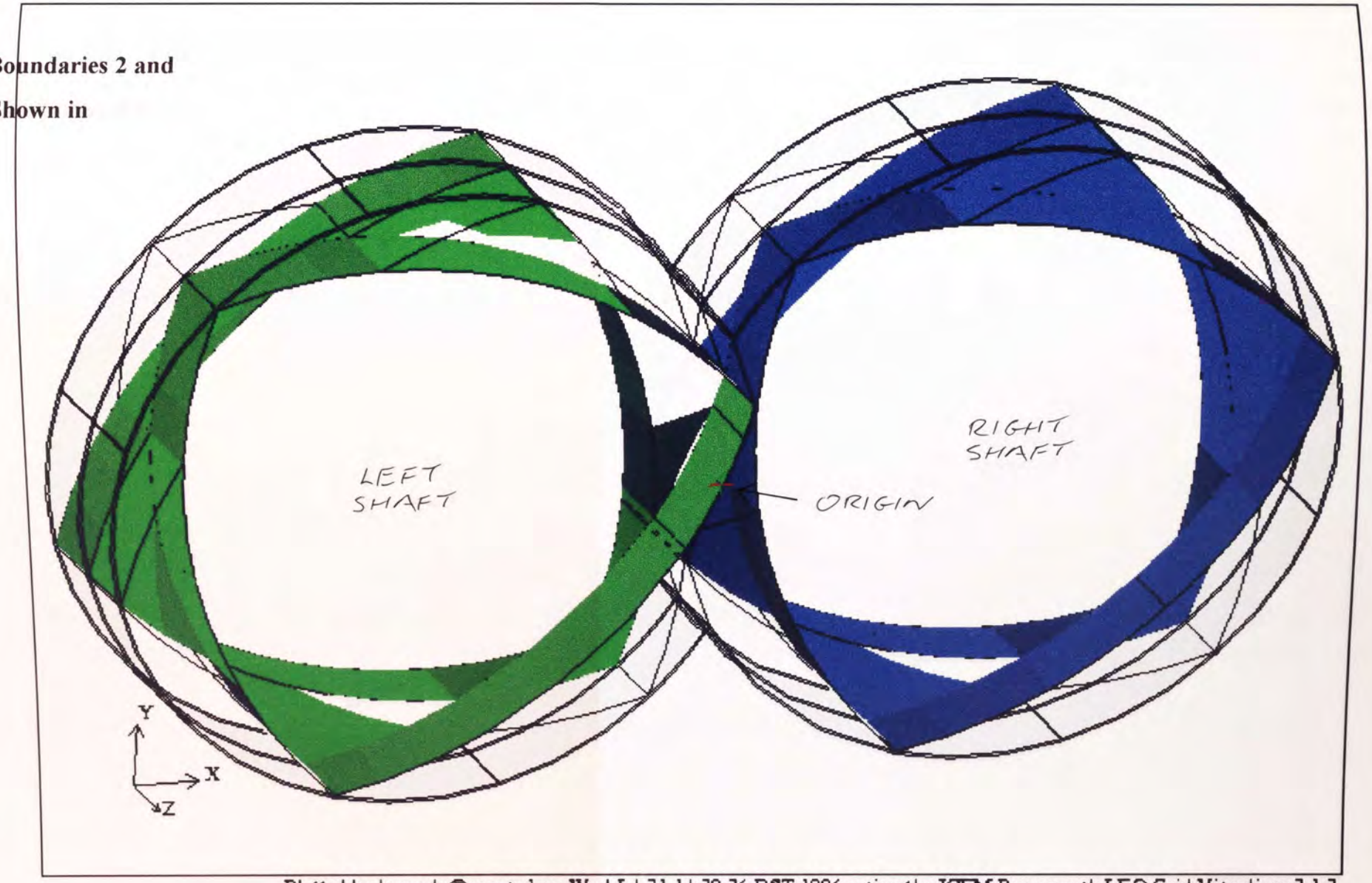

Plotted by bruced@ceacsg1 on Wed Jul 31 14:39:36 BST 1996, using the ICEM Powermesh LEO Grid Visualizer 3.1.3.

Figure 8-14:
Assignment of Boundary 4 for the Mesh Shown in Figure 8-8.

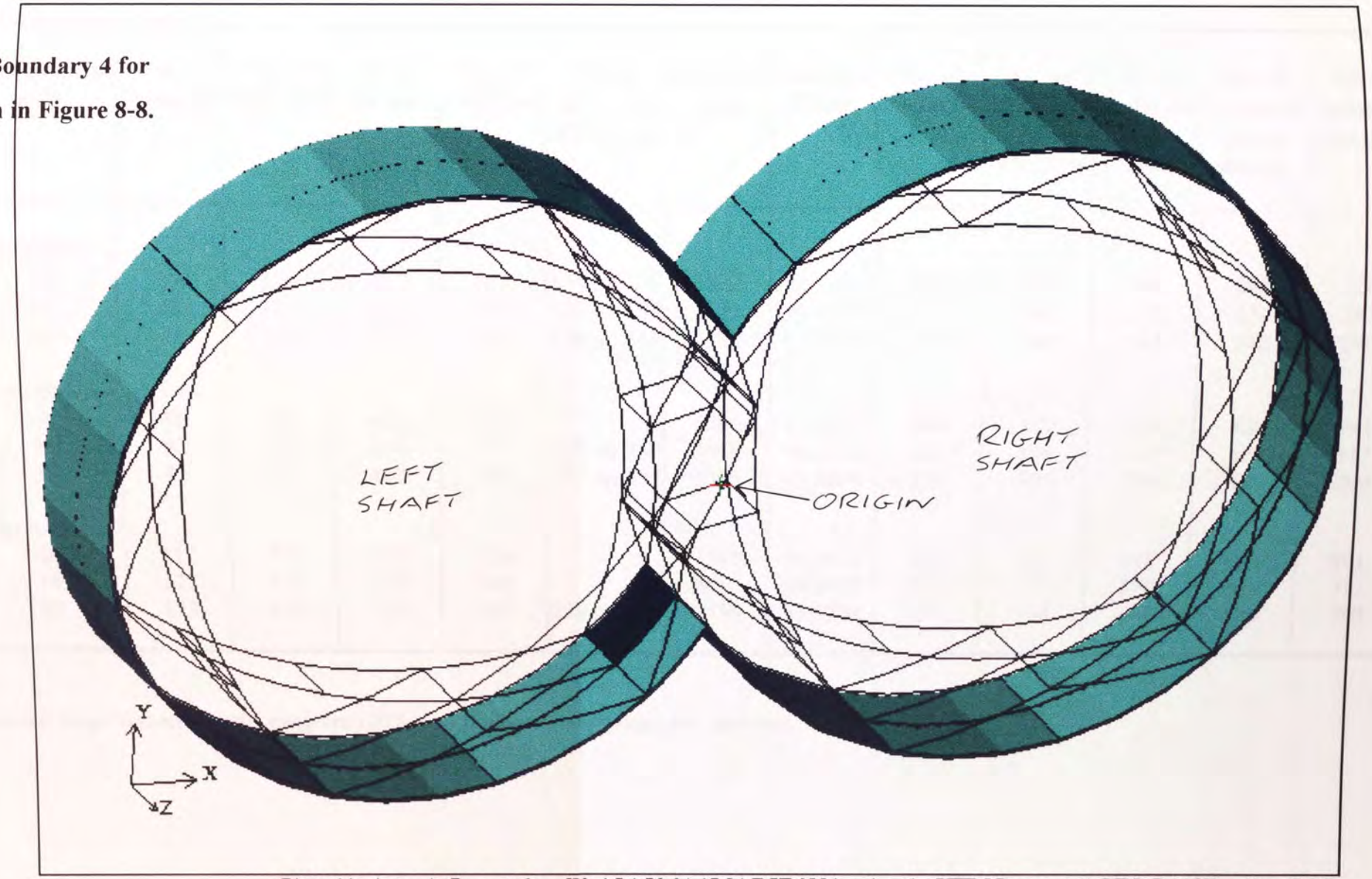

Plotted by brucedp@ceacsg1 on Wed Jul 31 14:40:26 BST 1996, using the ICEM Powermesh LEO Grid Visualizer 3.1.3.

TABLE 8-1

3D Parameters Table - Trilobal Elements

Configuration (α°)	No. of Domains	No. of Subfaces	No. of Edges	No. of Vertices	No. of BC's on Subfaces	Jacobian: Total	Jacobian: Mean	No. of Nodes on Inlet	No. of Nodes on Left Element	No. of Nodes on Right Element	No. of Nodes on Outer Barrel	No. of Nodes on Outlet
One Pair:												
0	39	179	263	122	124 on 179	2637	92.9370	299	168	144	240	299
15	41	187	273	126	128 on 187	2621	91.5208	293	140	148	232	293
30	41	186	270	124	126 on 186	2592	93.8584	290	144	144	240	290
Two Pairs:												
0	78	326	440	190	-[1]	4986	93.0925	291	319	319	420	291
15	82	340	454	194	188 on 340	5448	90.9279	317	338	338	420	317
30	82	337	448	192	182 on 337	5013	93.8604	290	306	306	420	290
Three Pairs:												
0	117	473	617	258	-[1]	7395	93.0852	291	502	478	600	291
15	123	493	635	262	-[1]	9410	90.4898	372	578	570	640	372
30	123	488	626	260	238 on 488	7434	93.8758	290	468	468	600	290

NOTES:

1 Problems too large to load into the program LEO, thus boundary conditions not analysed.

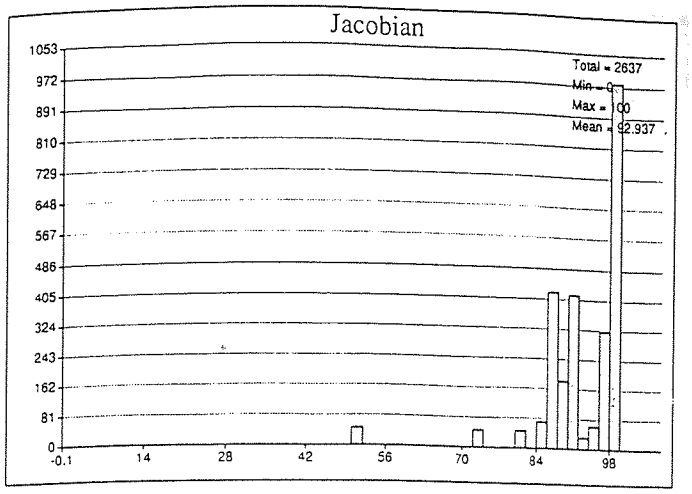

Graph 8-1:

Jacobian Distribution for the 3D Mesh Representing One Pair of Trilobal Elements at Rotated Configuration $\alpha = 0°$.

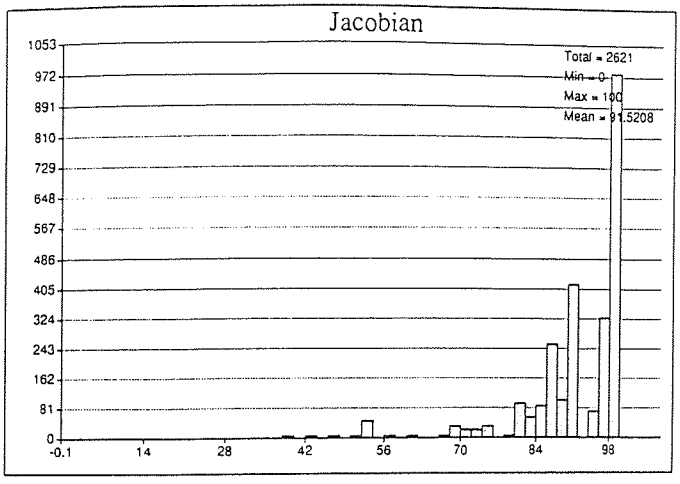

Graph 8-2:

Jacobian Distribution for the 3D Mesh Representing One Pair of Trilobal Elements at Rotated Configuration $\alpha = 15°$.

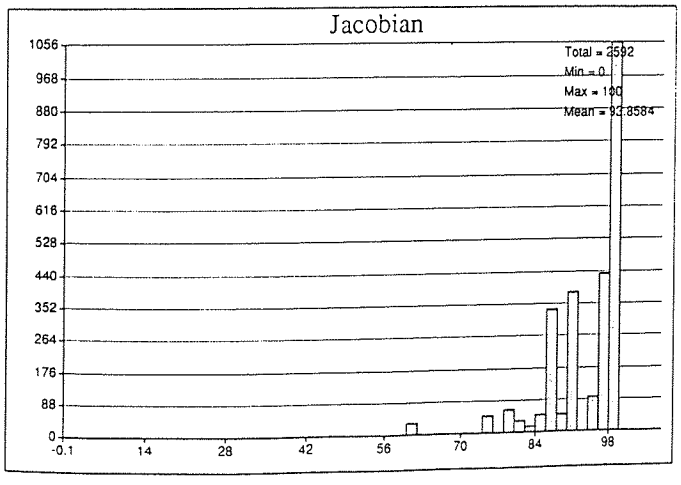

Graph 8-3:

Jacobian Distribution for the 3D Mesh Representing One Pair of Trilobal Elements at Rotated Configuration $\alpha = 30°$.

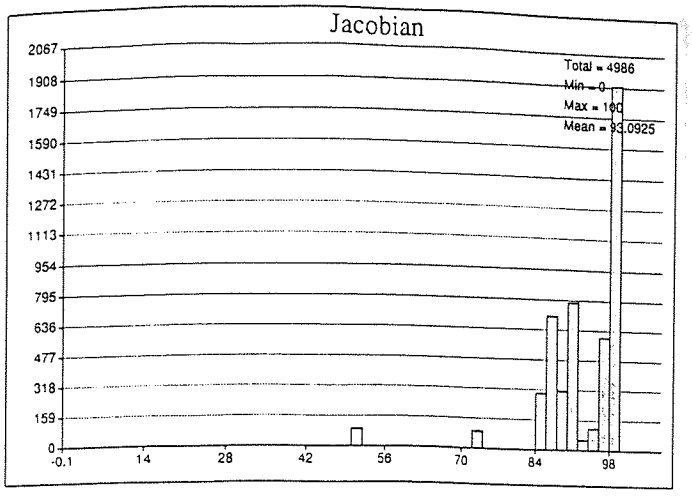

Graph 8-4:

Jacobian Distribution for the 3D Mesh Representing Two Pairs of Trilobal Elements in the Neutral Arrangement, at Rotated Configuration $\alpha = 0°$.

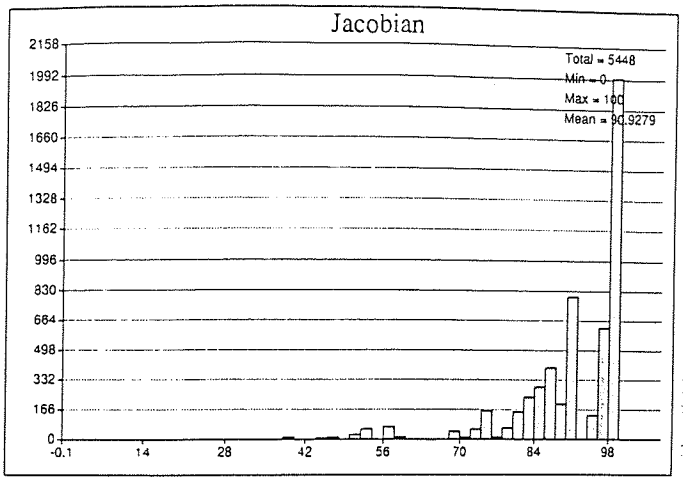

Graph 8-5:

Jacobian Distribution for the 3D Mesh Representing Two Pairs of Trilobal Elements in the Neutral Arrangement, at Rotated Configuration $\alpha = 15°$.

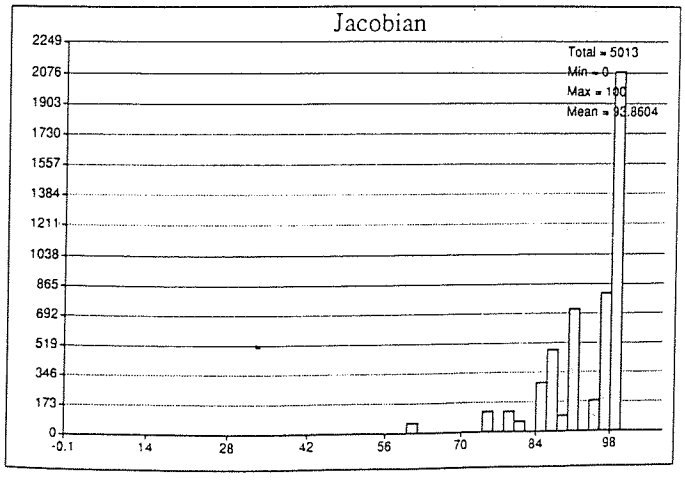

Graph 8-6:

Jacobian Distribution for the 3D Mesh Representing Two Pairs of Trilobal Elements in the Neutral Arrangement, at Rotated Configuration $\alpha = 30°$.

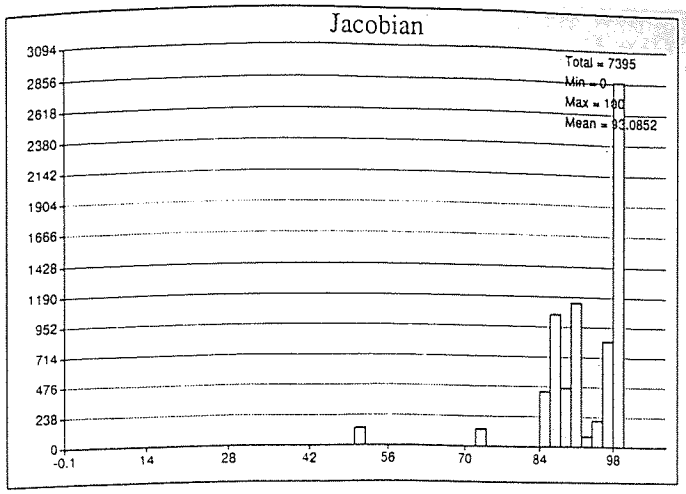

Graph 8-7:

Jacobian Distribution for the 3D Mesh Representing Three Pairs of Trilobal Elements in the Neutral Arrangement, at Rotated Configuration $\alpha = 0°$.

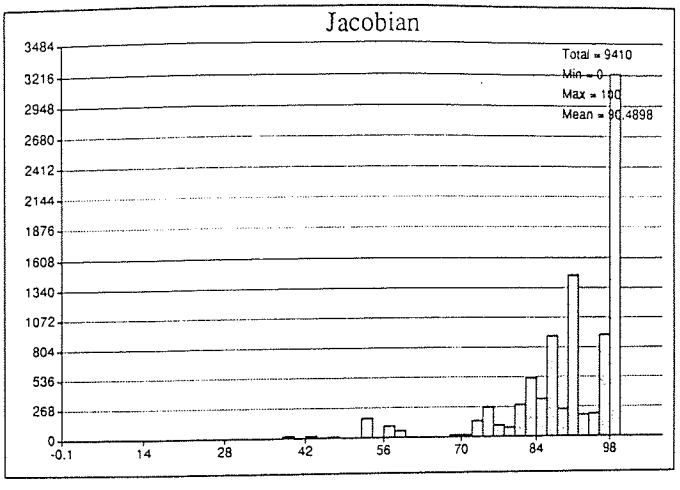

Graph 8-8:

Jacobian Distribution for the 3D Mesh Representing Three Pairs of Trilobal Elements in the Neutral Arrangement, at Rotated Configuration $\alpha = 15°$.

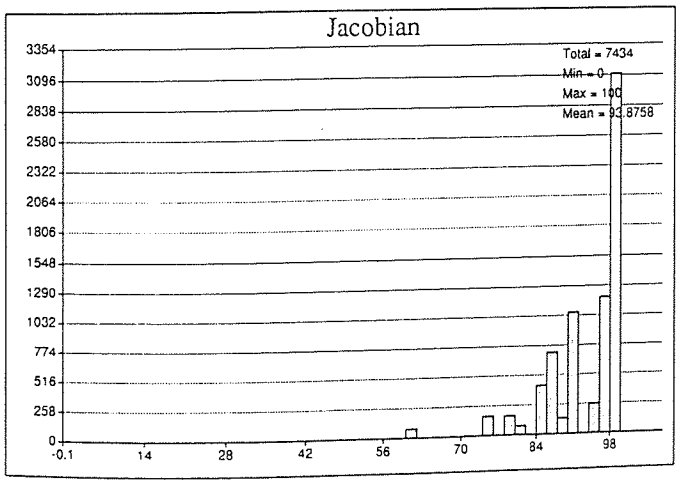

Graph 8-9:

Jacobian Distribution for the 3D Mesh Representing Three Pairs of Trilobal Elements in the Neutral Arrangement, at Rotated Configuration $\alpha = 30°$.

Figure 8-15:

Velocity Vector Profiles for the 2D Representation of the Trilobal Elements in the X-Y Plane, at the Rotated Configuration $\alpha = 15°$.

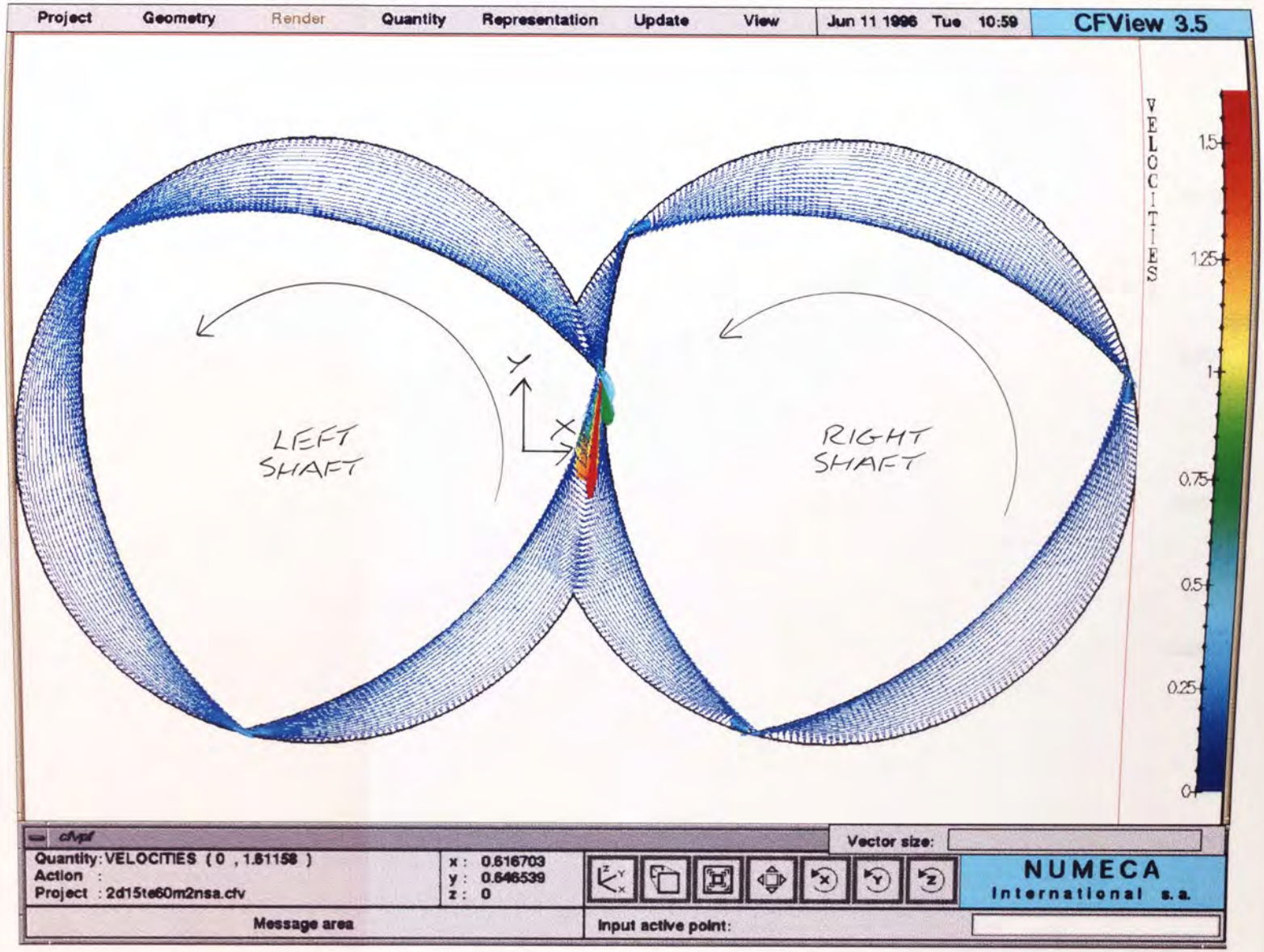

Figure 8-16:

Local Shear Rate Colour Contours ($\dot{\gamma} \geq 200$ sec^{-1}) for the 2D Representation of the Trilobal Elements in the X-Y Plane, at the Rotated Configuration $\alpha = 15°$.

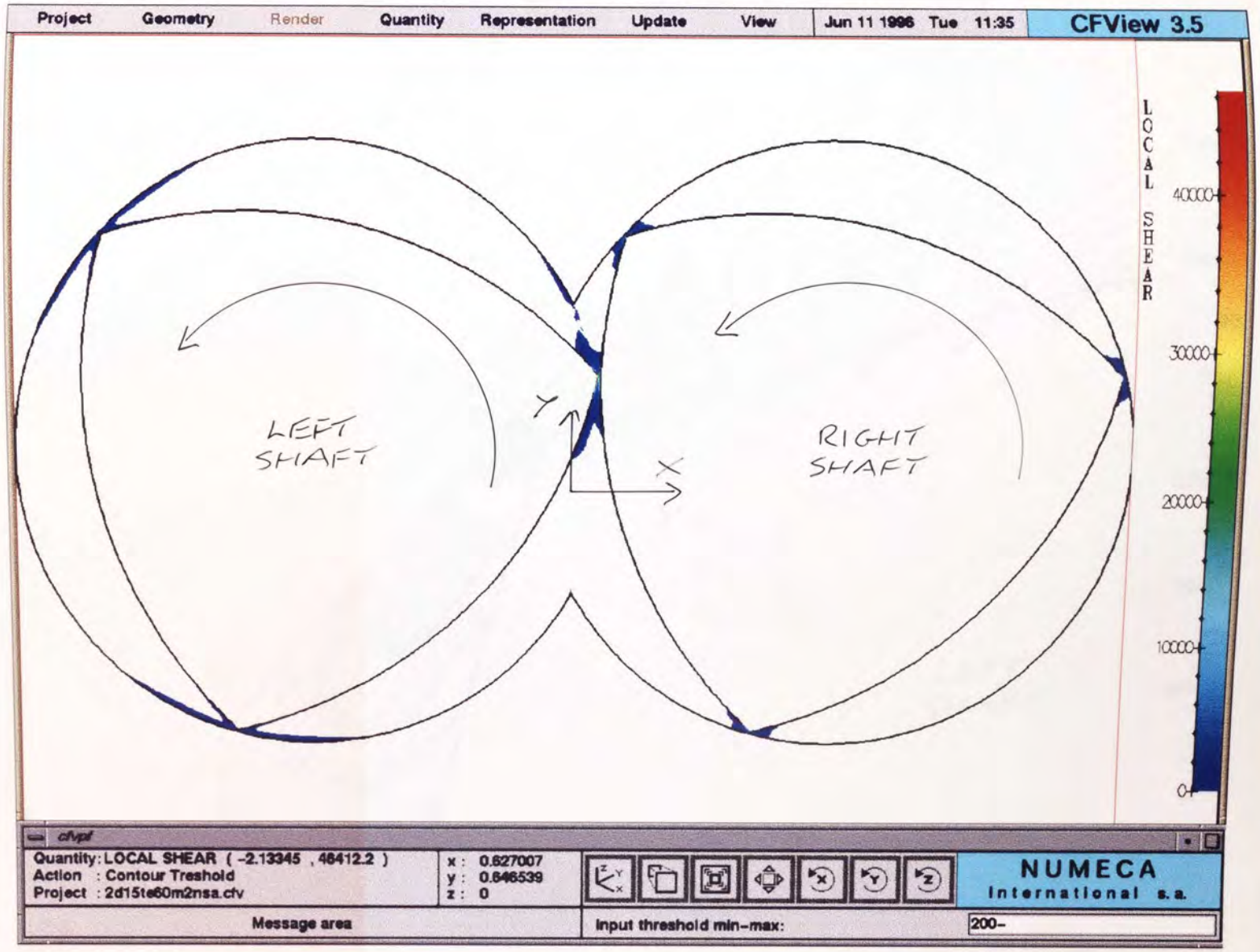

Figure 8-17:

Velocity Vector Profiles in the Neighbourhood of the Upper Trilobe Tip of the Left Element, for the 2D Representation of the Trilobal Elements in the X-Y Plane, at the Rotated Configuration $\alpha = 15°$.

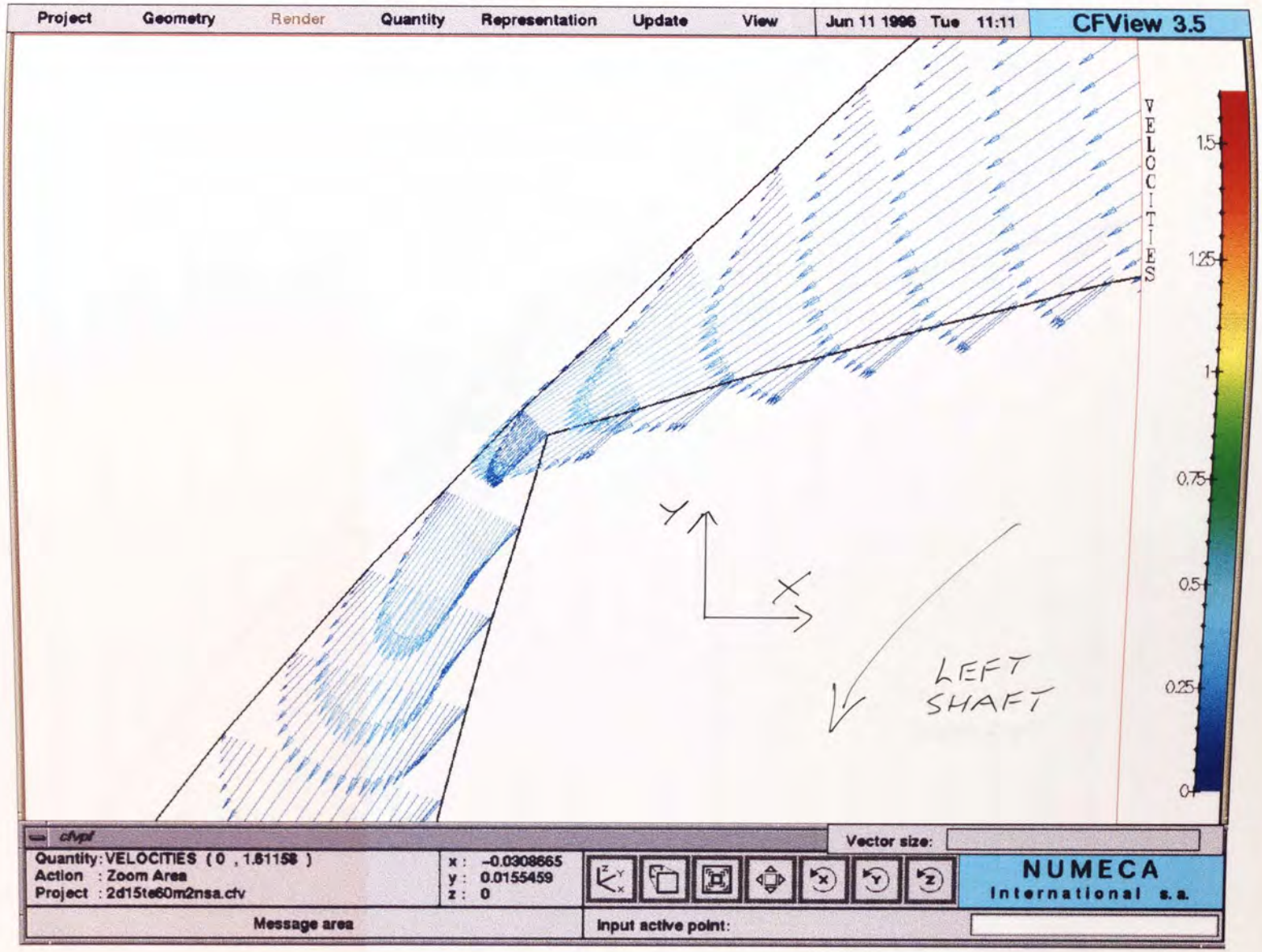

Figure 8-18:

Velocity Vector Profiles in the Neighbourhood of the Upper Trilobe Tip of the Right Element, for the 2D Representation of the Trilobal Elements in the X-Y Plane, at the Rotated Configuration $\alpha = 15°$.

321

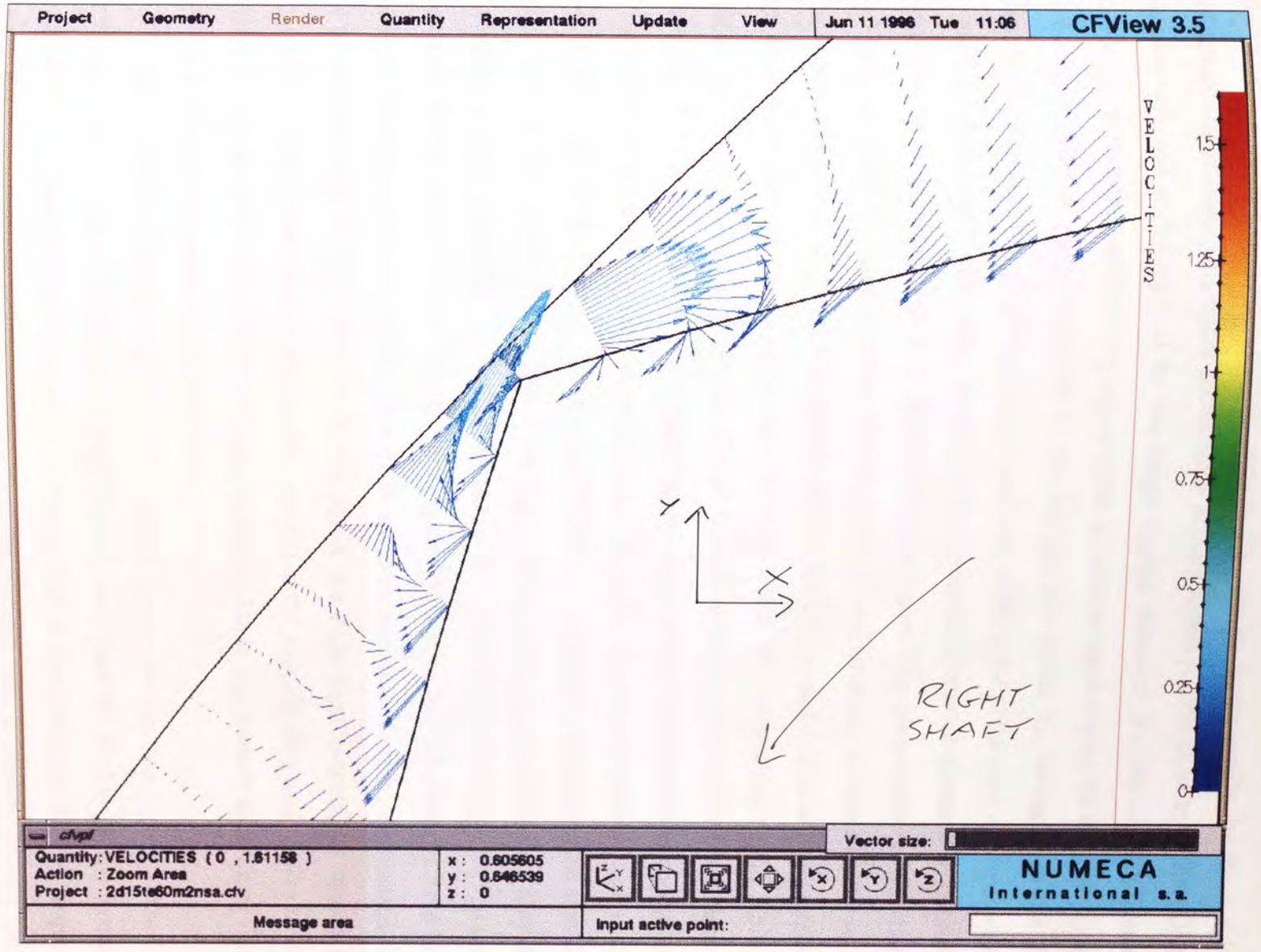

shows, for a particular trilobal element section, the velocity vector profile for the $\alpha = 15°$ rotated configuration. This figure shows much activity within regions close to all six trilobal element tips and within each of the two bridge regions. However, it is the centrally located trilobe tip within the intermeshing region which is inducing most activity on the melt within that region. This is partly explained by the fact that this trilobe tip, belonging to the left element, is moving upwards relative to the incidence of the brow of the right element, which is moving downwards. The effect of this local movement of trilobal elements in opposite directions, is to generate large local shear within this region. This phenomenon is illustrated by Figure 8-16, which gives a contour plot of regions of local shear rate in excess of 200 sec^{-1}. The values of local shear rate within regions close to the remaining five trilobal tips are much less than the values obtained close to the trilobe tip within the intermeshing region. This is due to the fact that each of these five trilobal tips are moving relative to wall boundaries, where the fluid in contact with each wall is stationary (i.e. non-slip wall boundary condition). What is interesting from the plot shown in Figure 8-16 is the observation that fluid near to the two trilobal tips of the left element are experiencing much greater shear rates than that for fluid close to the three trilobal tips of the right element. This interesting effect may be explained by the velocity vector profiles shown in Figures 8-17 to 8-18. Figure 8-17 shows the upper trilobe tip of the left element from Figure 8-16 and, as may be observed from this figure, all fluid within this region is moving in the same direction. However, for material in the neighbourhood of the uppermost trilobe tip of the right hand element, as shown in Figure 8-18, some fluid within that region is flowing in the opposite direction relative to the motion of the tip itself. This observed effect is probably due to the pressure build-up of fluid exerted at the nearby uppermost bridge region.

To take account of axial pressure within the trilobal element mixing zone, results of the 3D simulations involving a configuration consisting of three pairs of trilobes in the neutral arrangement, as described in Section 8.2, are presented in the remainder of this chapter. Figures 8-19 to 8-21 display velocity vector profiles, overlaid onto Z-velocity contour plots corresponding to the inlet (foreground) and outlet (background) cross sections, for the trilobal element rotated configurations of $\alpha = 0°$, 15° and 30° respectively. As may be seen in these figures, areas of forward and back mixing are evident at each one of the tips contained within the inlet and outlet planes. The forward and back mixing shown within Figures 8-19 to 8-20, are greatest for fluid contained within the intermeshing regions close to the centrally located trilobe tips. However, as the trilobal elements rotate about their fixed axes, the forward and back mixing exhibited by these central tips diminishes as the tips approach either bridge region. Figure 8-21 depicts the $\alpha = 0°$ rotated configuration, showing clearly this diminished effect for the centrally located trilobal tips.

Figure 8-19:
Velocity Vector Profiles, Overlaid onto Z-Velocity Colour Contours at Both the Inlet (Foreground) and Outlet (Background) X-Y Planes, for the 3D Trilobal Element Mixing Zone Containing Three Pairs of Elements in the Neutral Arrangement, at the Rotated Configuration $\alpha = 0°$.

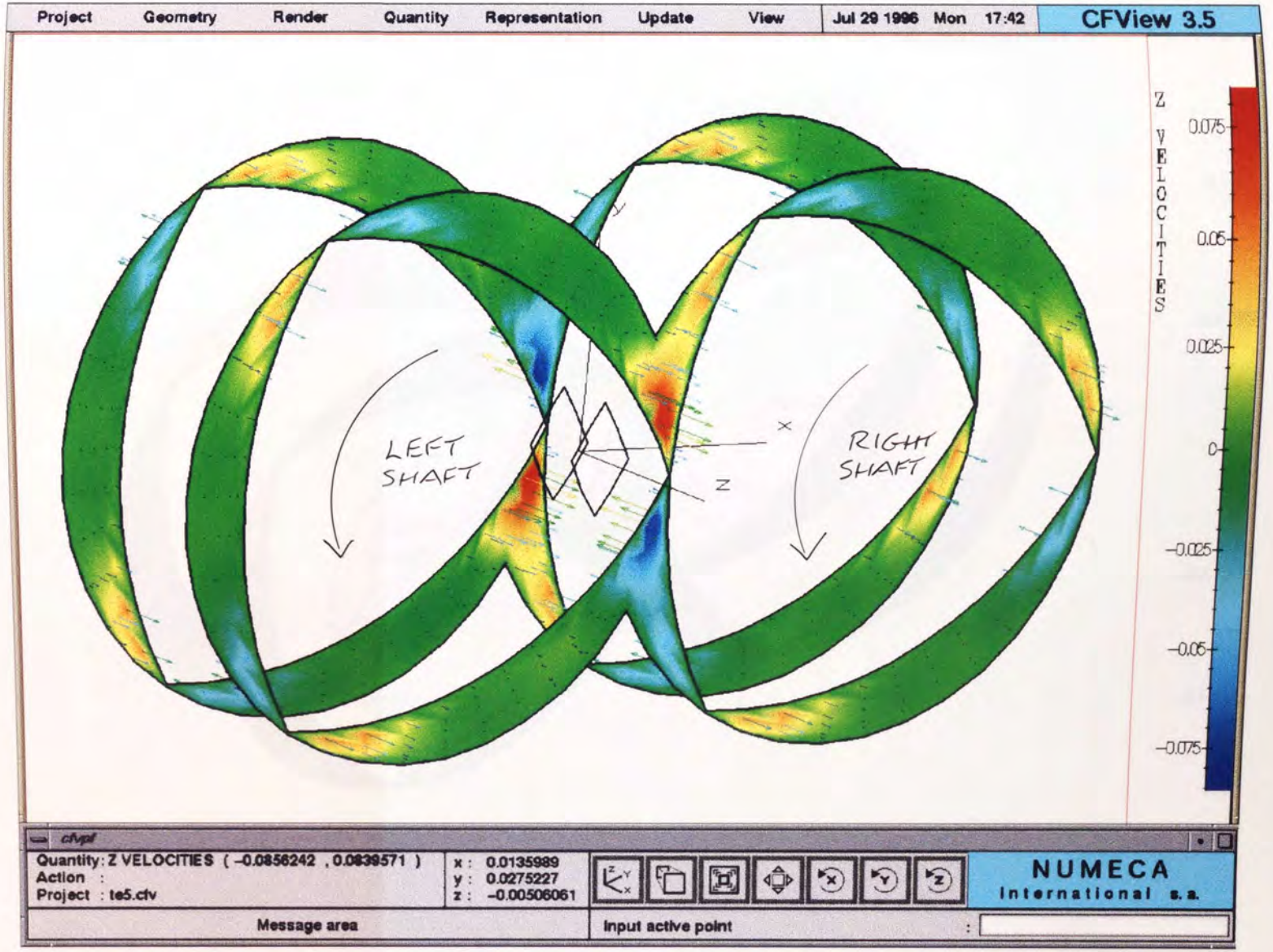

Figure 8-20:

Velocity Vector Profiles, Overlaid onto Z-Velocity Colour Contours at Both the Inlet (Foreground) and Outlet (Background) X-Y Planes, for the 3D Trilobal Element Mixing Zone Containing Three Pairs of Elements in the Neutral Arrangement, at the Rotated Configuration α = 15°.

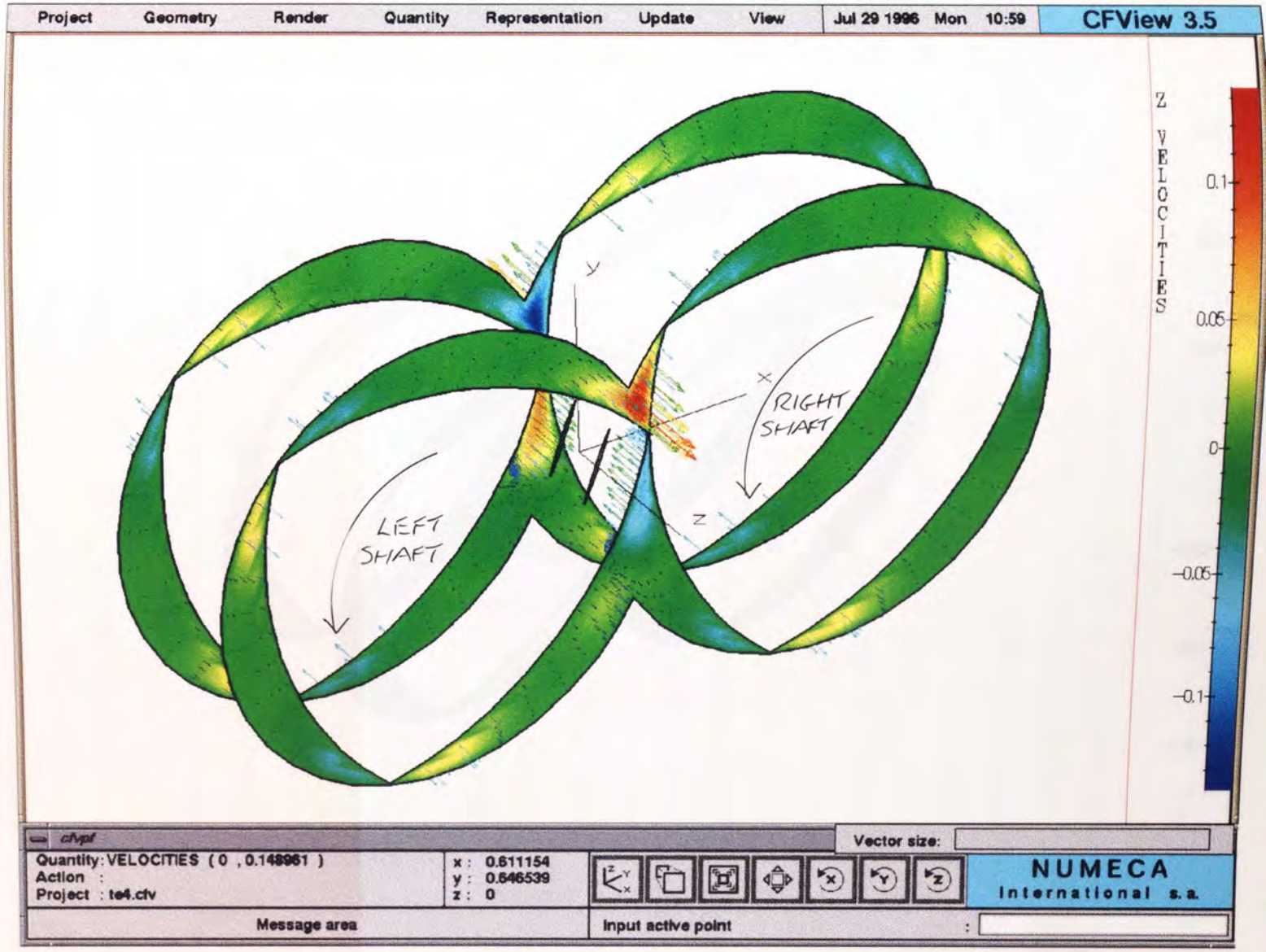

Figure 8-21:
Velocity Vector Profiles, Overlaid onto Z-Velocity Colour Contours at Both the Inlet (Foreground) and Outlet (Background) X-Y Planes, for the 3D Trilobal Element Mixing Zone Containing Three Pairs of Elements in the Neutral Arrangement, at the Rotated Configuration $\alpha = 30°$.

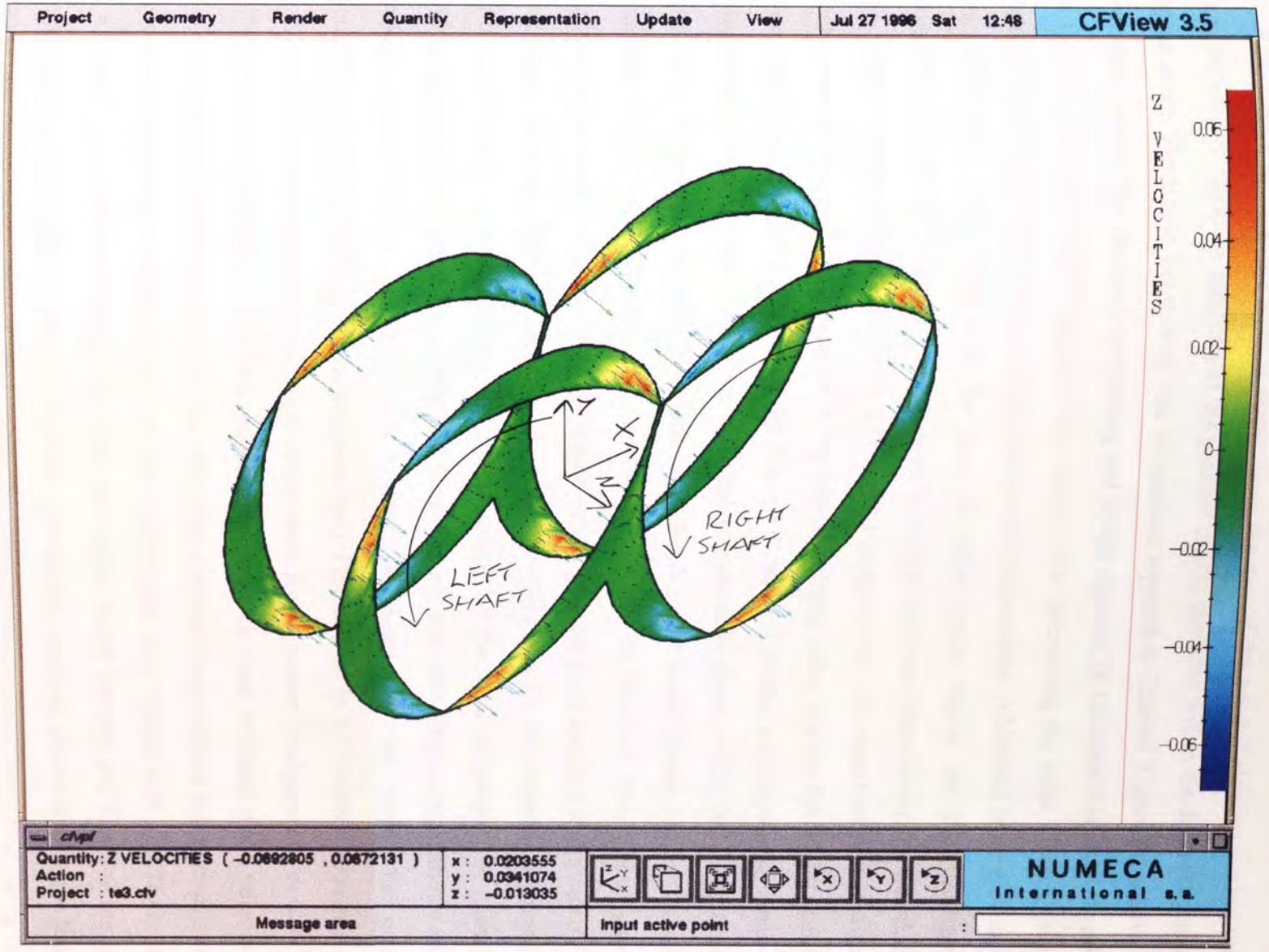

A sequence of cross sections at points along the axis of the trilobal element mixing zone may be used to build-up a picture of the possible effects exhibited within the different regions of the zone. Similar to the mixing disc simulations reported in Chapter 7, greatest activity is exhibited within the central intermeshing and bridge regions. To illustrate this cross sections in the Y-Z plane along the length of the mixing zone intersecting the brow of each bridge region, are presented for the three different rotated configurations. Additional cross sections in the X-Z plane, coinciding with the brow of either bridge region, are also illustrated. Figures 8-22 to 8-24 illustrate a sequence of Y-Z cross sectional planes along the barrel, for the rotated configurations of $\alpha = 0°$, 15° and 30° respectively. All points contained within each cross sectional plane possess an X = 0 mm co-ordinate value. For the Z-velocity contour plots shown in Figures 8-22 to 8-23 for the $\alpha = 0°$ and 15° rotated configurations, areas of intense forward and back mixing are exhibited at various locations within the domain. The epicentres of these axial mixing regions lie at the inlet and outlet planes and at the axial positions of Z = -5.0 and -10.0 mm respectively. As may be observed from these figures, regions of forward and back mixing alternate across the zone from the inlet to the outlet for both cross sections. Figure 8-24 however, shows the Y-Z plane for the rotated configuration of $\alpha = 30°$ and it is evident from this representation that the axial progression of material within this particular plane has diminished to very nearly zero (the diagram itself shows only velocity vectors, as a solid Z-velocity contour plot shows only one colour, i.e. green signifying zero Z-velocity, over the entire surface). Figures 8-25 to 8-27 show a sequence of X-Z cross sections along the axial length of the barrel for the rotated configurations of $\alpha = 0°$, 15° and 30° respectively. All points contained within each cross sectional plane possess a Y = 9.7 mm co-ordinate value, such that each cross sectional plane created just intersects the brow of the uppermost bridge region. As may be observed from Figures 8-25 to 8-26 for the $\alpha = 0°$ and 15° rotated configurations only, the regions where forward and back mixing are being predicted are many. However, for both of these cross sectional planes shown, the brow line of the upper bridge region going along the mixing zone is clearly seen. It is along this brow line that fluid in contact with the outer barrel wall will be stationary and this is a result of the non-slip boundary condition predetermined at the outset of the simulation. However, similar to the Y-Z cross section shown within Figure 8-24, the X-Z cross section for the $\alpha = 30°$ rotated configuration shown in Figure 8-27, again displays minimal forward and back mixing activity. Thus it may be concluded from the results shown within these preceding cross sectional planes, that the trilobal elements in their neutral arrangement display possible periodic mixing effects as the elements rotate. This conclusion has also been drawn by Szydlowski and White [97] who state that the trilobal element mixing zone exhibits an axial peristaltic pumping mechanism, with a frequency which is equal to three times the screw

igure 8-22:
-Velocity Colour Contours for
e Cross Section Created
entrally in the Y-Z Plane, for
e 3D Trilobal Element Mixing
one Containing Three Pairs of
lements in the Neutral
rrangement, at the Rotated
Configuration $\alpha = 0°$ (Magnified
iew).

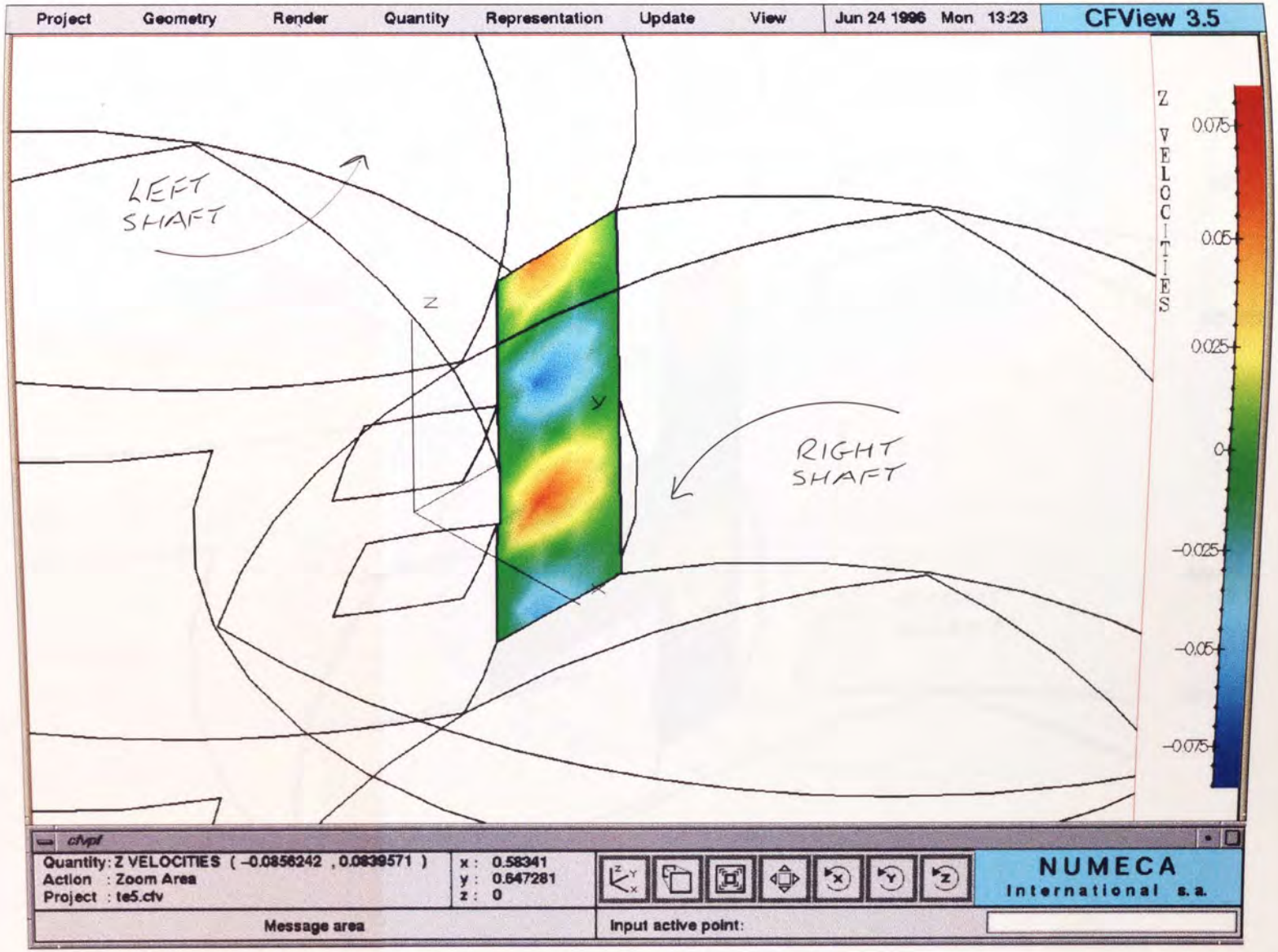

Figure 8-23:

Z-Velocity Colour Contours for the Cross Section Created Centrally in the Y-Z Plane, for the 3D Trilobal Element Mixing Zone Containing Three Pairs of Elements in the Neutral Arrangement, at the Rotated Configuration α = 15° (Magnified View).

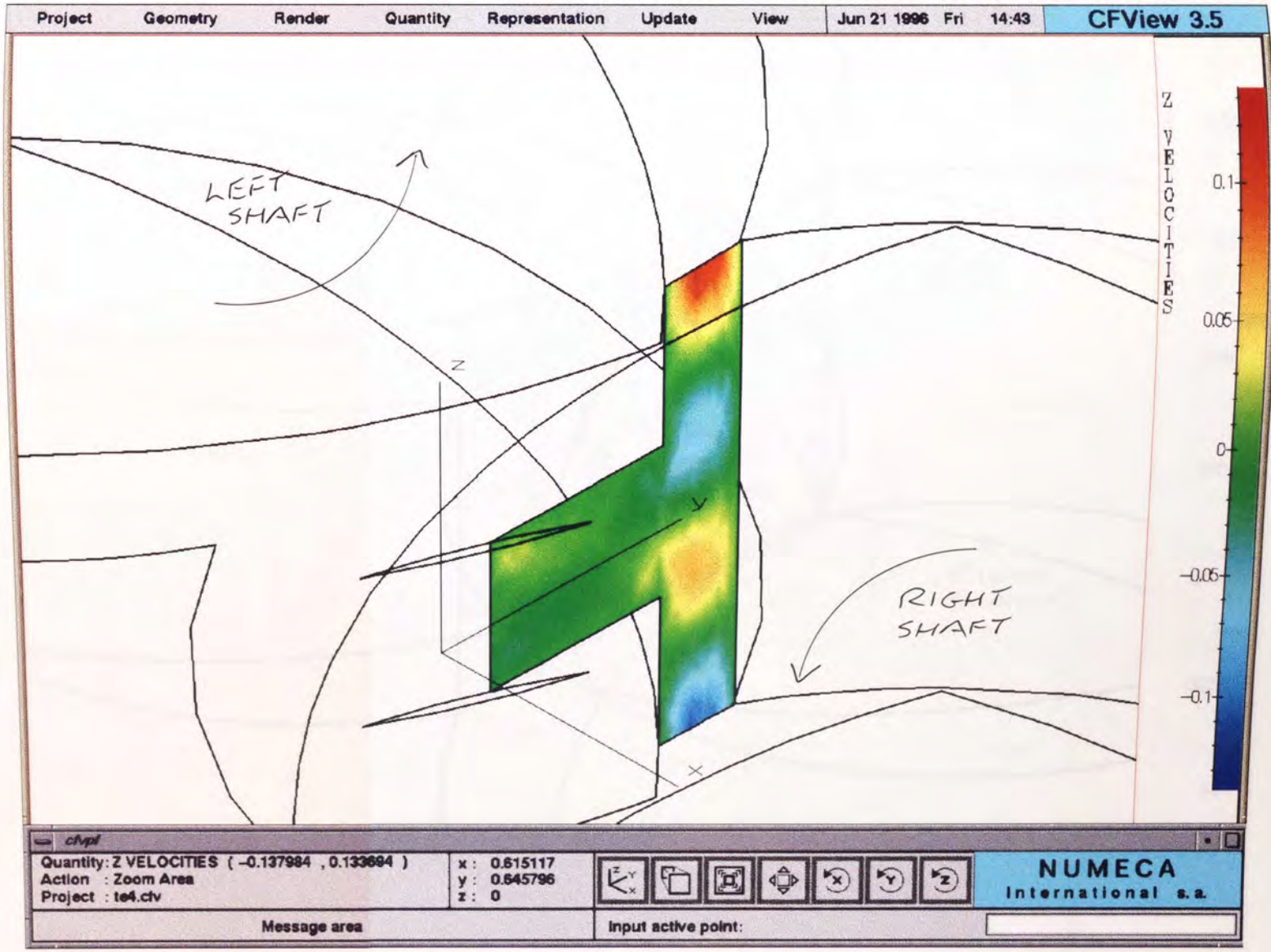

Figure 8-24:

Velocity Vector Profiles for the Cross Section Created Centrally in the Y-Z Plane, for the 3D Trilobal Element Mixing Zone Containing Three Pairs of Elements in the Neutral Arrangement, at the Rotated Configuration $\alpha = 30°$ (Magnified View).

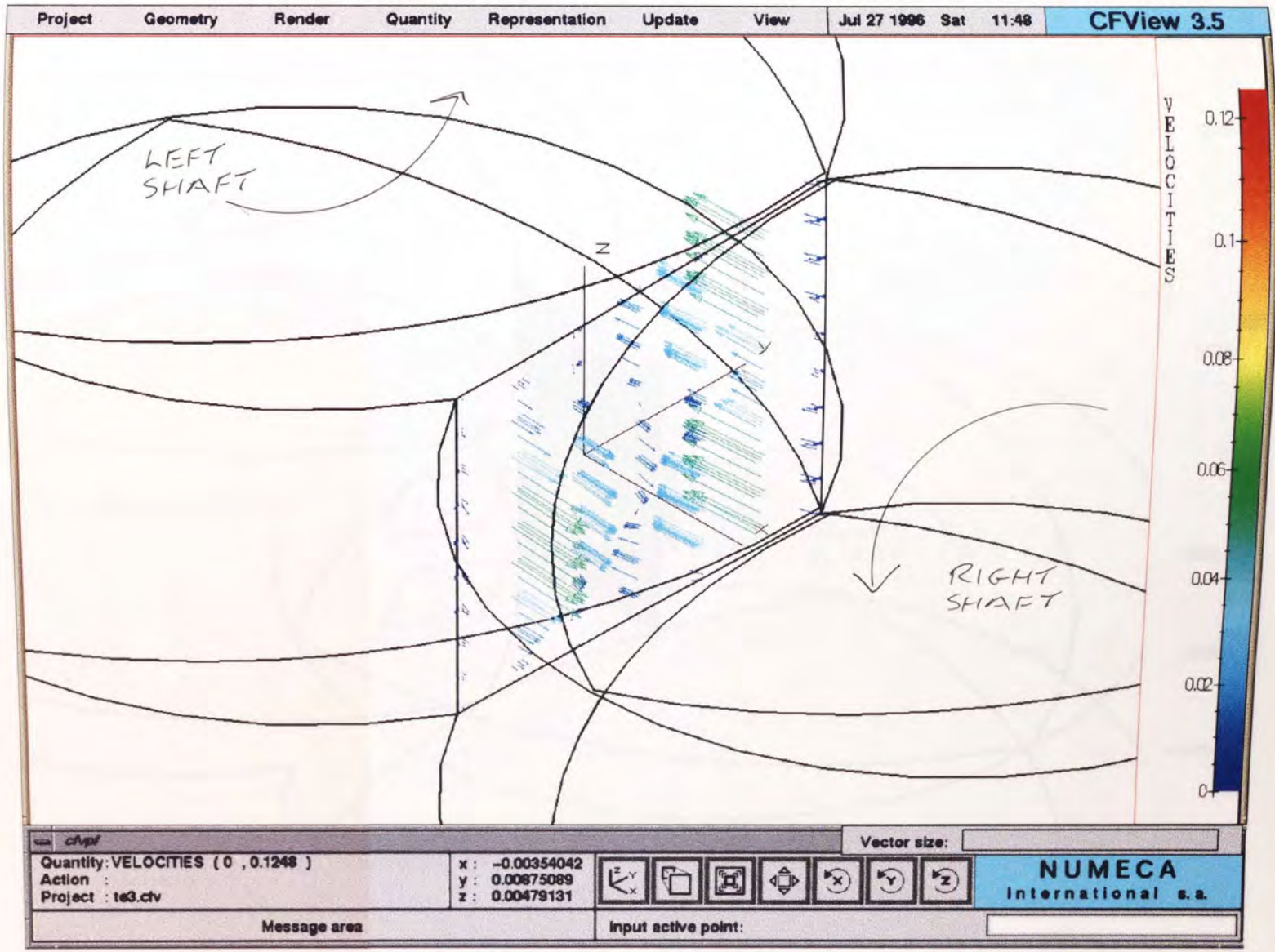

Figure 8-25:

Z-Velocity Colour Contours for the Cross Section Created in the X-Z Plane and Intersecting the Brow of the Uppermost Bridge Region (Y = 9.7 mm), for the 3D Trilobal Element Mixing Zone Containing Three Pairs of Elements in the Neutral Arrangement, at the Rotated Configuration α = 0° (Magnified View).

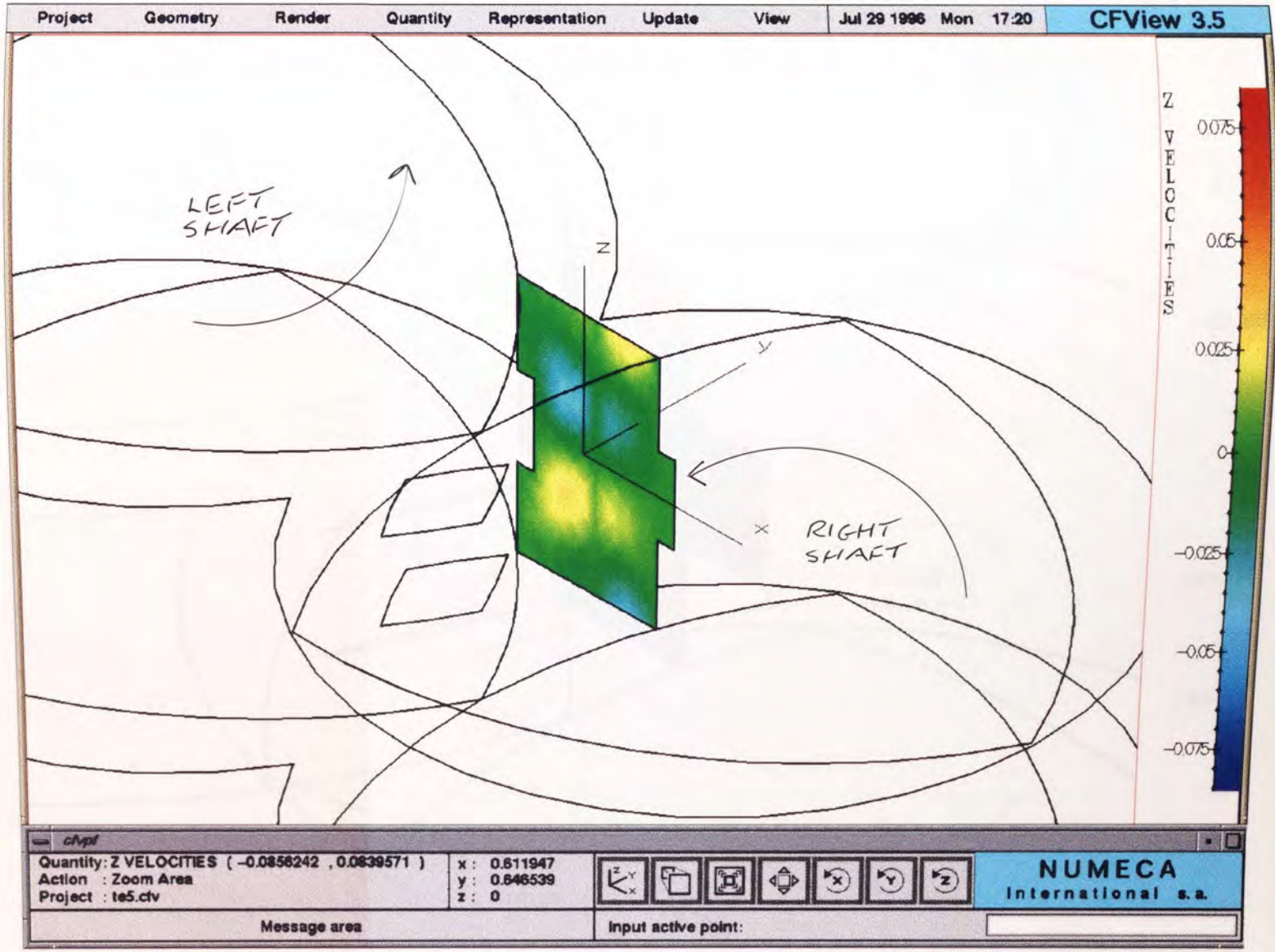

Figure 8-26:

Z-Velocity Colour Contours for the Cross Section Created in the X-Z Plane and Intersecting the Brow of the Uppermost Bridge Region (Y = 9.7 mm), for the 3D Trilobal Element Mixing Zone Containing Three Pairs of Elements in the Neutral Arrangement, at the Rotated Configuration α = 15° (Magnified View).

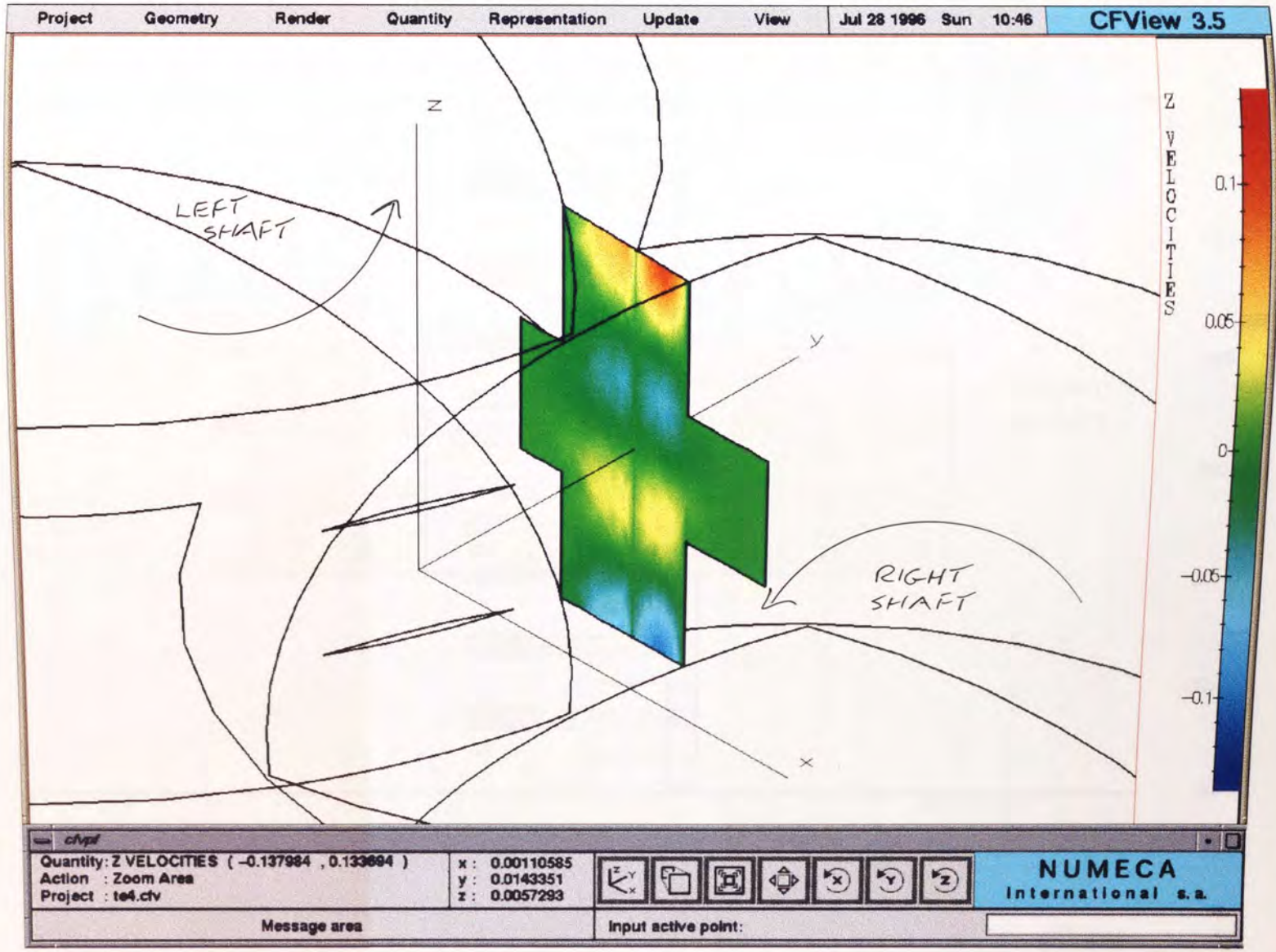

Figure 8-27:

Velocity Vector Profiles for the Cross Section Created in the X-Z Plane and Intersecting the Brow of the Uppermost Bridge Region (Y = 9.7 mm), for the 3D Trilobal Element Mixing Zone Containing Three Pairs of Elements in the Neutral Arrangement, at the Rotated Configuration α = 30° and Viewed Along the Y-Axis.

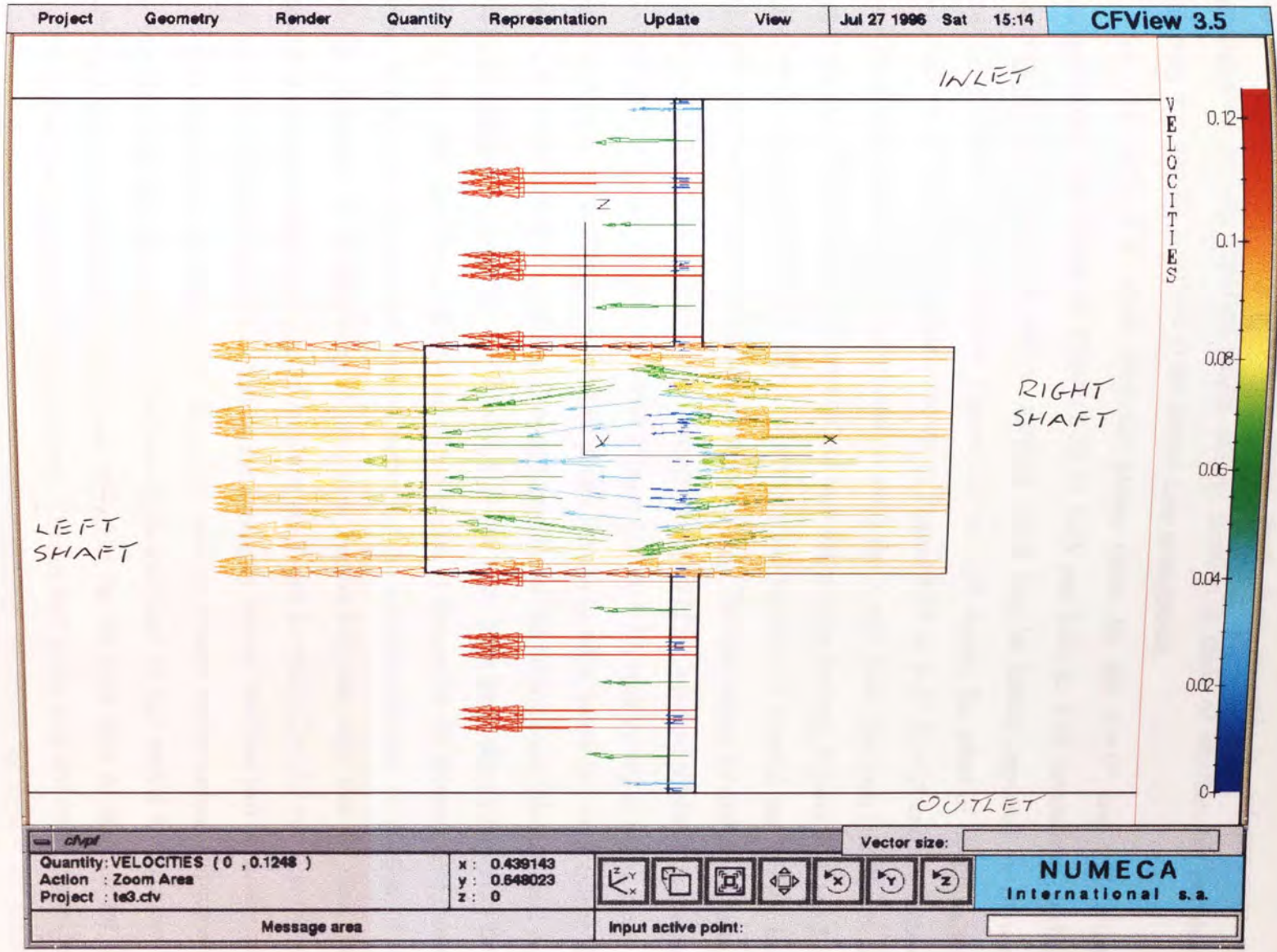

rotation. However, this observation drawn from their research is unfortunately not substantiated by any reported results and no mention is made of whether this peristaltic pumping mechanism is unique to the neutral zone arrangement.

The Y-Z and X-Z cross sectional planes taken for the $\alpha = 0°$ and 15° rotated configurations, as shown in Figures 8-22 to 8-23 and 8-25 to 8-26 respectively, exhibit complex forward and back mixing motions which may be further inspected by showing additional magnified orientations. Figures 8-28 to 8-29 display the affect of obtaining side zone views of the cross sections shown in Figures 8-22 to 8-23 ($\alpha = 0°$ and 15° rotated configurations respectively), by orientation along the X-axis (such that each inlet lies in the upper portion of each picture as viewed and each outlet to the bottom). Figures 8-28 and 8-29 illustrate a maximum leakage effect, whereby equal amounts of material are flowing both forwards and backwards through the mixing zone [16]. The inlet planes for each cross section shown in Figures 8-28 to 8-29 are located above the tip of the left-hand trilobe from the first element pair. As may be observed from Figures 8-28 to 8-29, back mixing is taking place at each inlet face. If similar cross sectional planes were to be taken below this same trilobe tip, then at the inlet, material would be flowing forwards into the mixing zone; this statement may easily be verified by inspection of Figures 8-19 and 8-20. Thus the relative direction of fluid flow at the inlet face within the intermeshing region, is dictated by the pressure drop created below the tip of the left-hand trilobe caused by the counter-clockwise, co-rotation of the trilobal elements. It is interesting to note from Figures 8-28 and 8-29, that the fluid flow pattern is mirrored about the line drawn along the Y-axis for which Z = -7.5 mm (i.e. exactly half way into the flow domain). Plotting the Z-velocity isolines for these two cross sections, shown in Figures 8-30 to 8-31 for the $\alpha = 0°$ and 15° rotated configurations respectively, again illustrates the periodicity of the flow fields exhibited for this neutral arrangement of rotating trilobal elements. The maximum velocities for the axial flow of material for the $\alpha = 0°$ rotated configuration is approximately $\pm$ 50 mm sec^{-1} at the inlet and outlet planes and at the axial positions of Z = -5.0 and -10.0 mm respectively. However, for the $\alpha = 15°$ rotated configuration, the maximum axial velocities at both the inlet and outlet planes are approximately $\pm$ 100 mm sec^{-1}, which is very large increase from that experienced at the $\alpha = 0°$ rotated configuration. As stated previously, once the elements rotate further to the $\alpha = 30°$ configuration, the axial motion at both the inlet and outlet planes diminish quite markedly.

For the X-Z cross sections intersecting the brow of the uppermost bridge region (shown in Figures 8-25 to 8-26 for the $\alpha = 0°$ and 15° rotated configuration respectively), Figures 8-32 to 8-33 display the views looking down onto the mixing zone along the Y-axis (such that each inlet face lies in the upper portion of the picture as viewed and each outlet to the bottom).

Figure 8-28:

Velocity Vector Profiles on the Cross Section Described in Figure 8-22, Viewed Along the X-Axis.

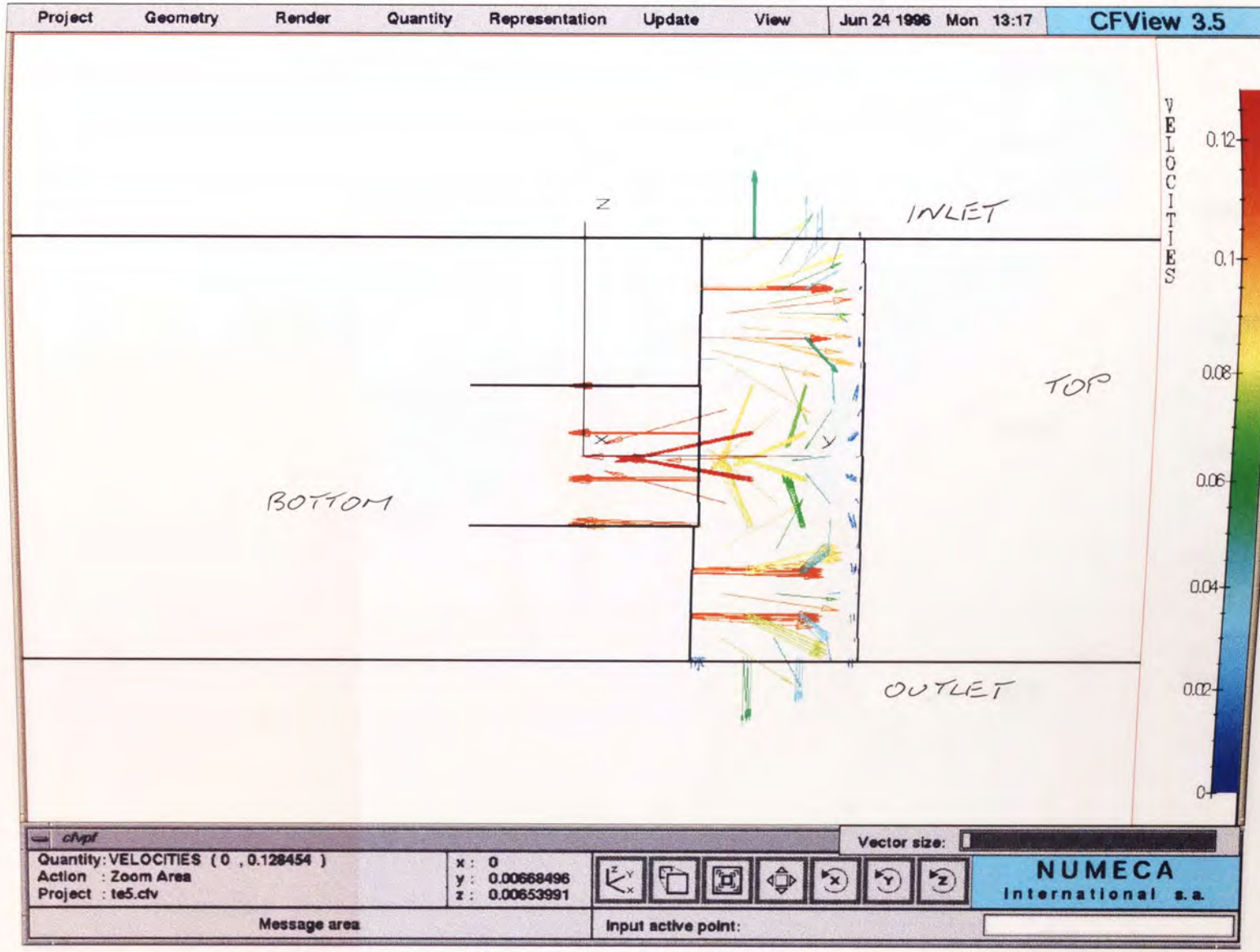

Figure 8-29:

Velocity Vector Profiles on the Cross Section Described in Figure 8-23, Viewed Along the X-Axis.

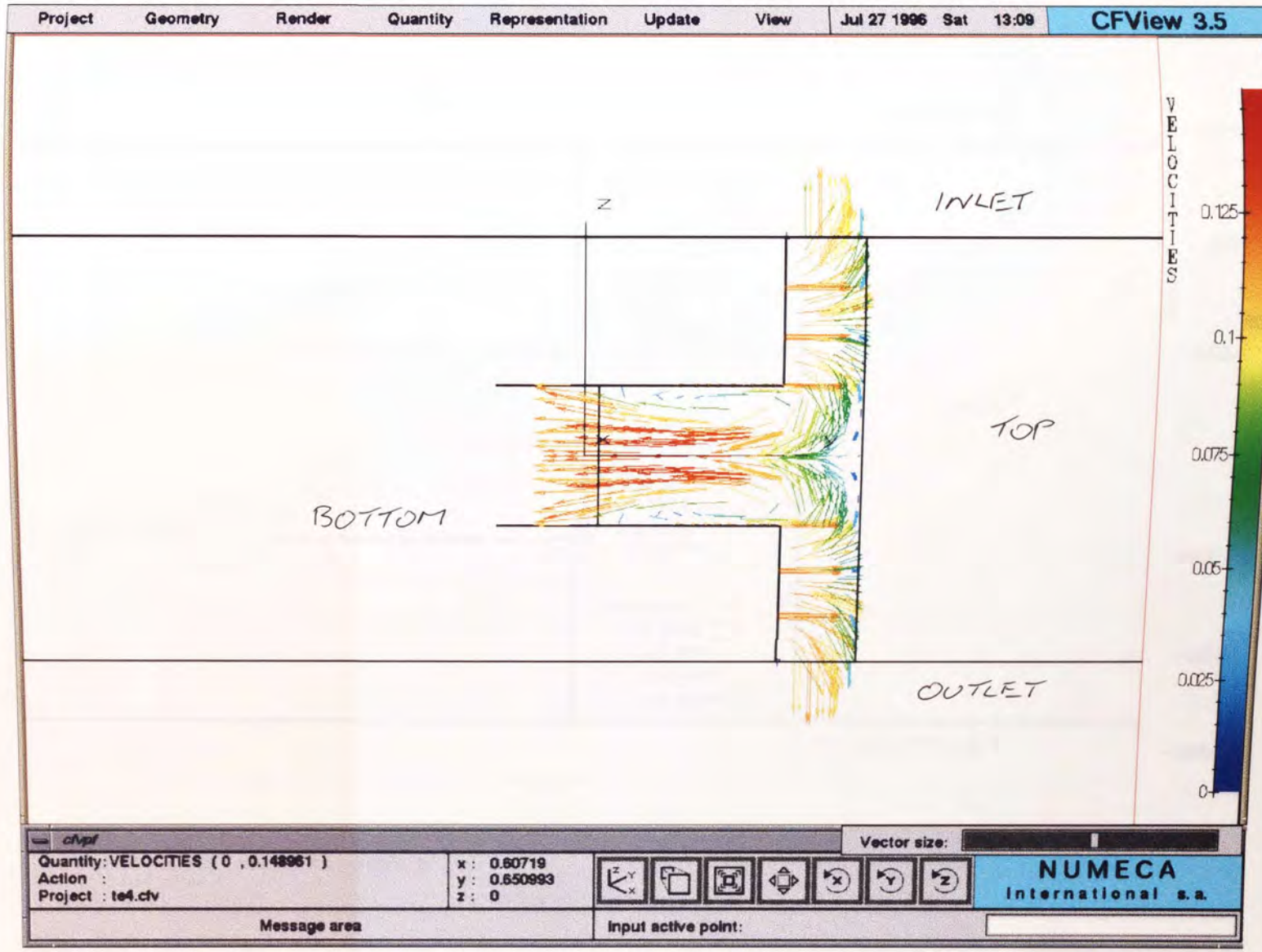

Figure 8-30:

Z-Velocity Isolines on the Cross Section Described in Figure 8-22, Viewed Along the X-Axis.

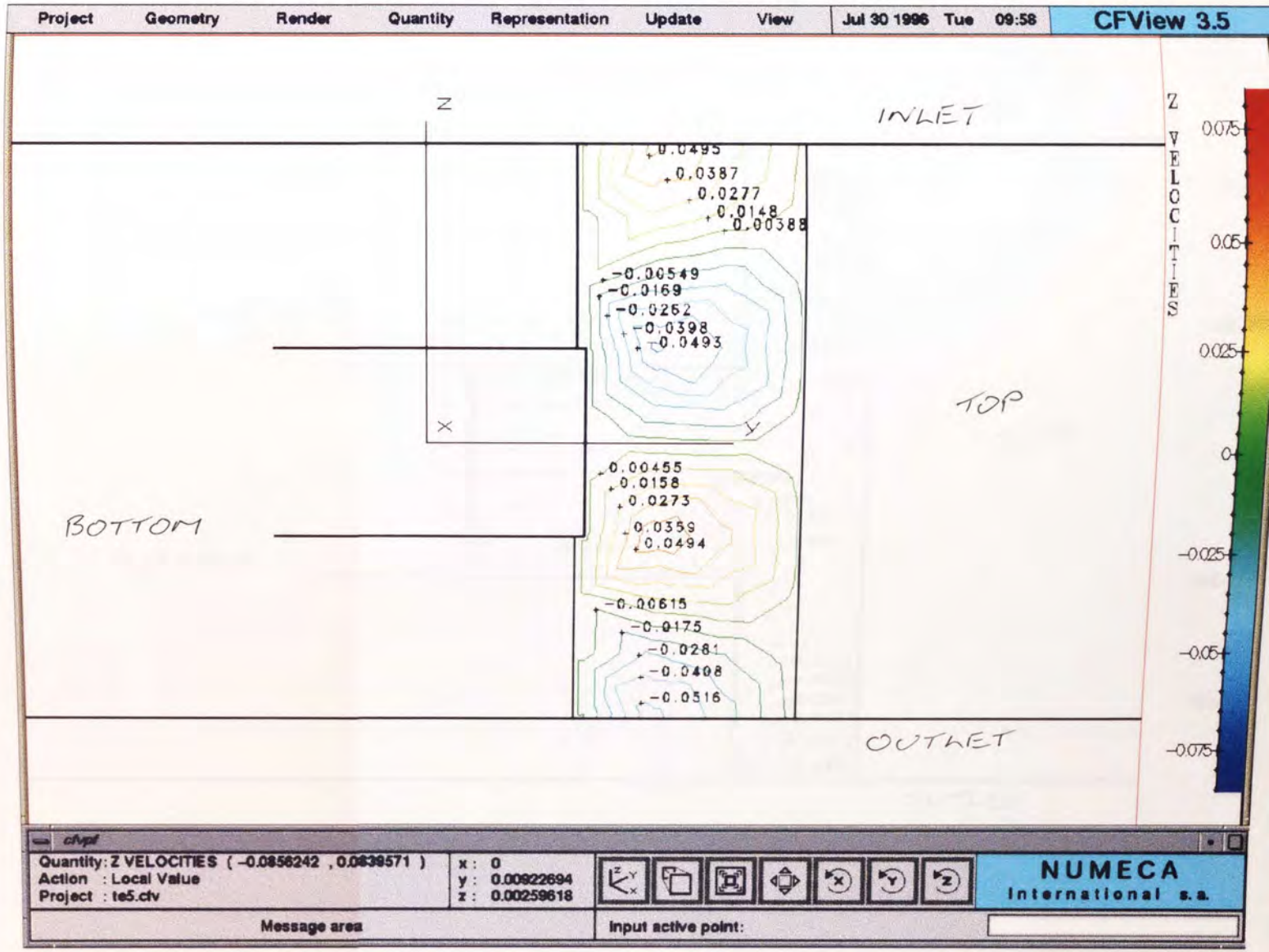

Figure 8-31:

Z-Velocity Isolines on the Cross Section Described in Figure 8-23, Viewed Along the X-Axis.

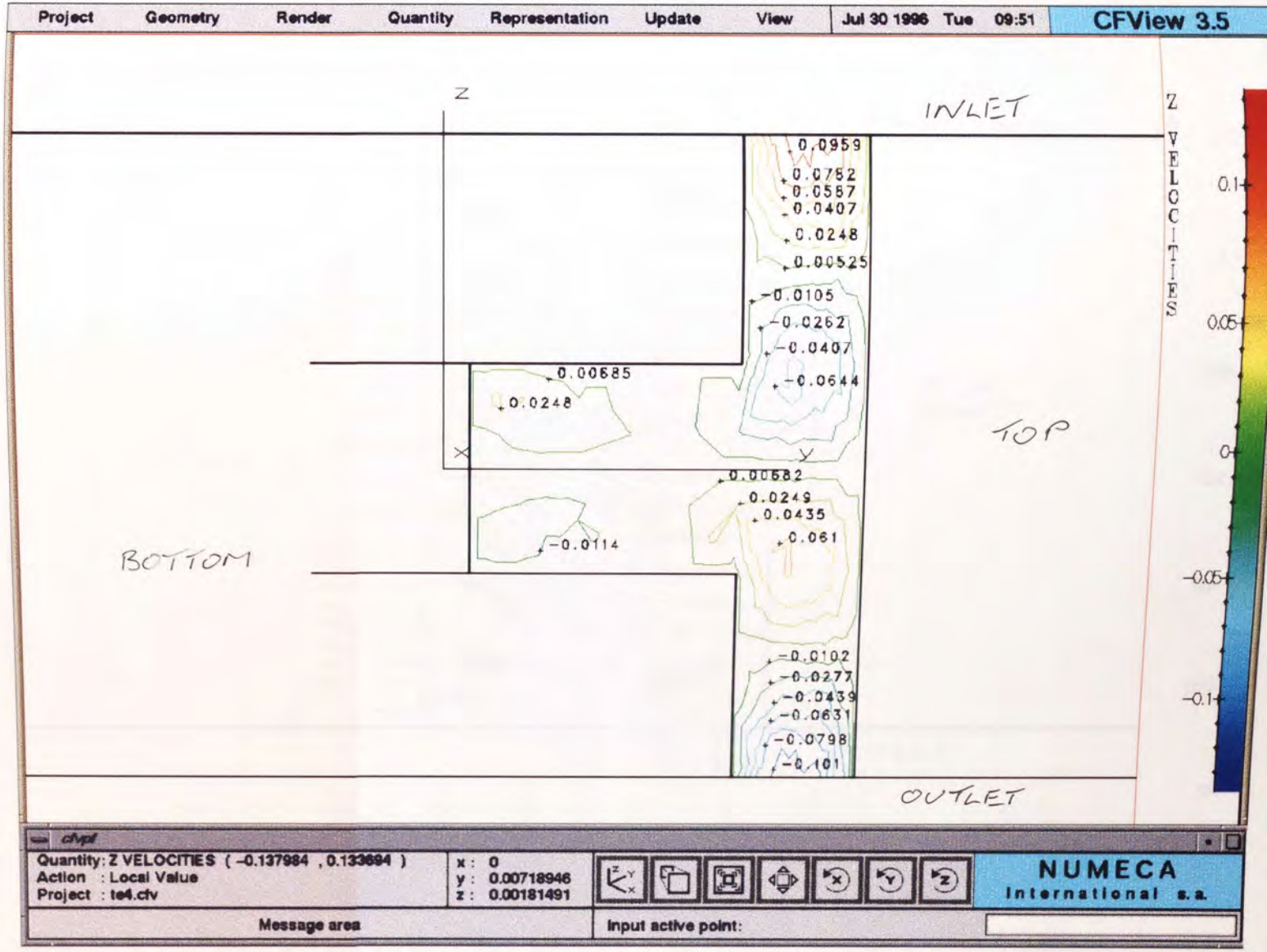

Figure 8-32:

Velocity Vector Profiles on the Cross Section Described in Figure 8-25, Viewed Along the Y-Axis.

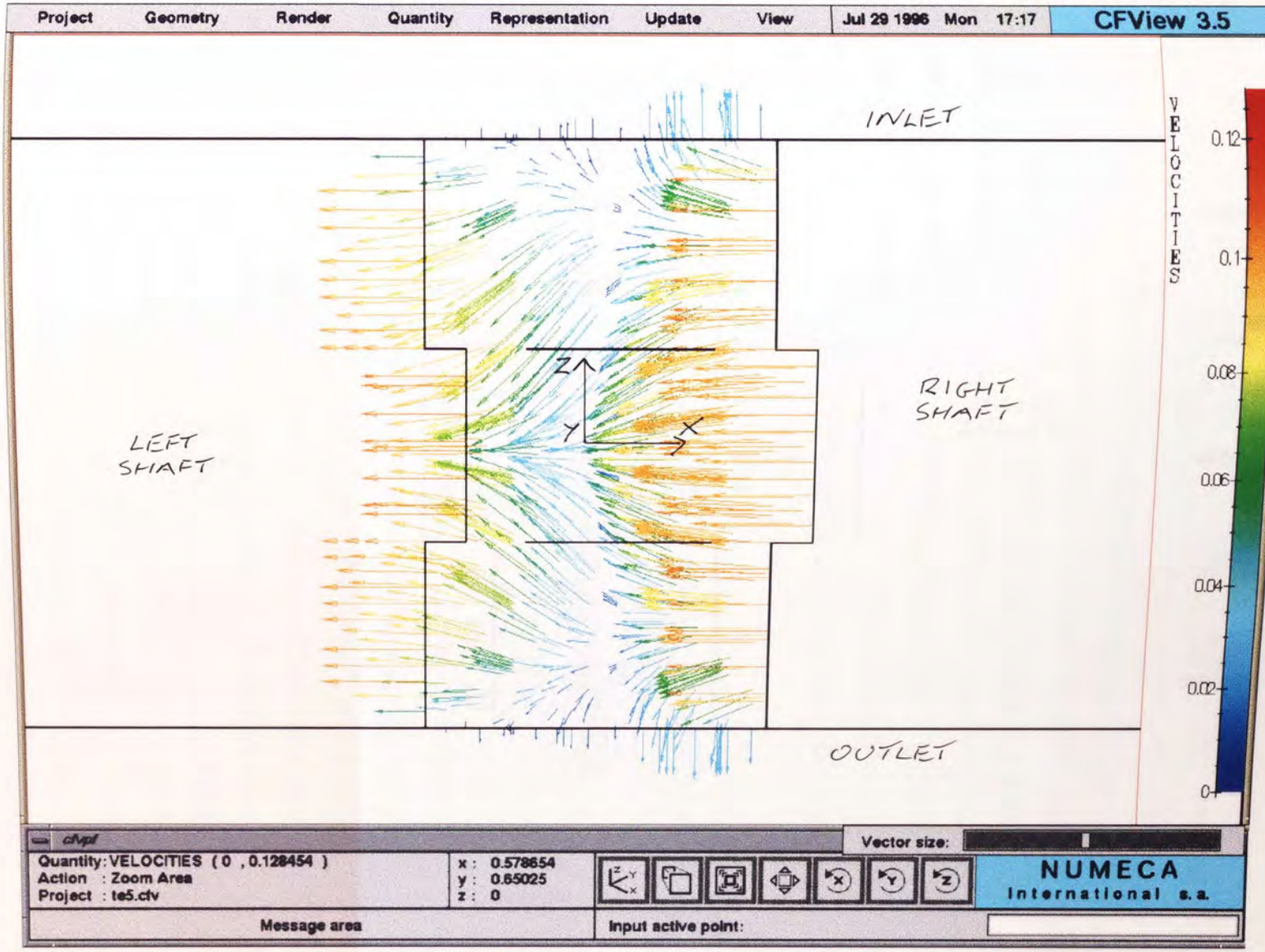

Figure 8-33:

Velocity Vector Profiles on the Cross Section Described in Figure 8-26, Viewed Along the Y-Axis.

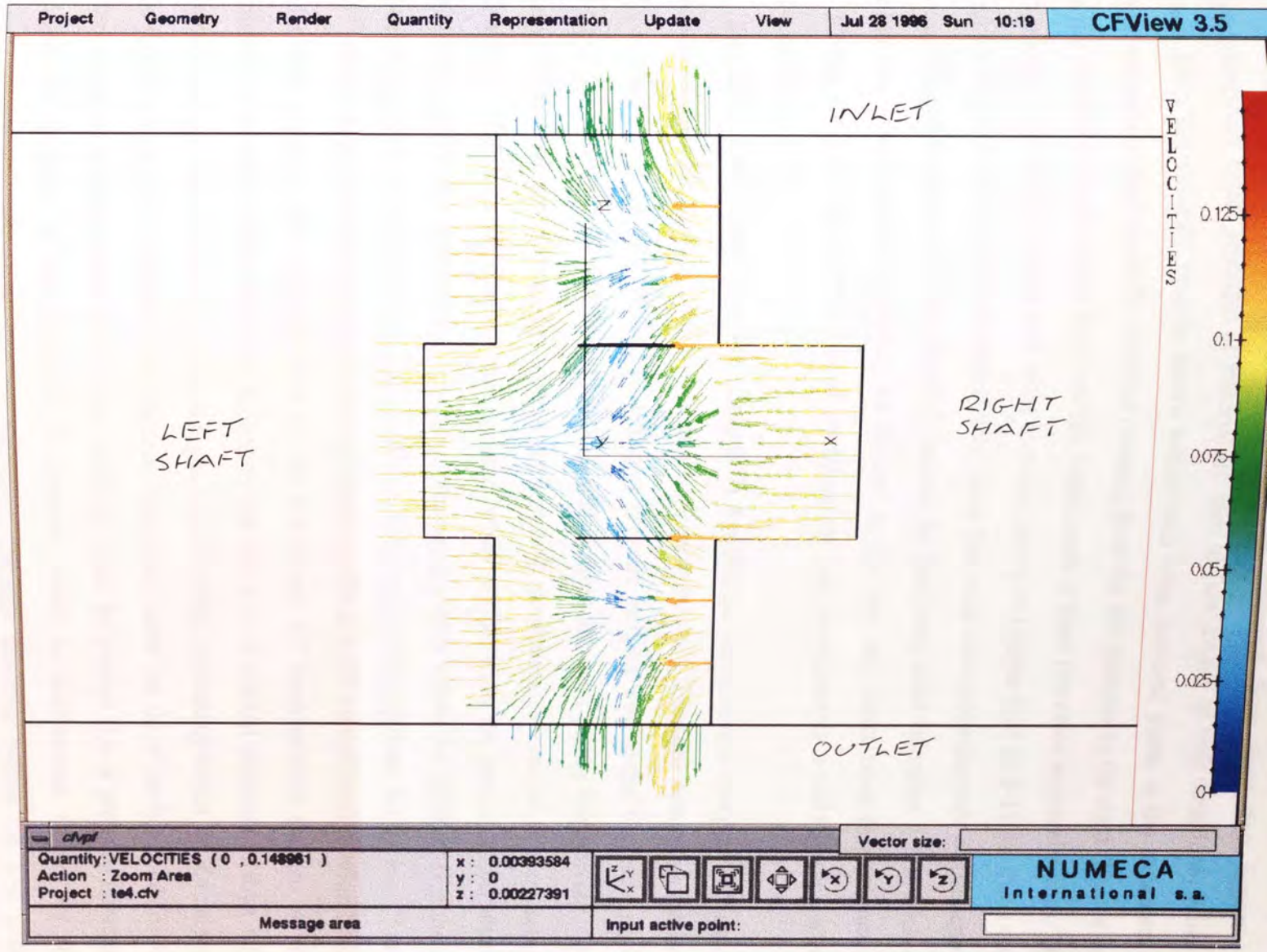

Again the affect of maximum leakage may be observed from these two figures as approximately equal amounts of material are seen to flow axially in both directions. What is clear from the velocity vectors shown within each cross sectional plane, is the reduction in fluid velocities undergone by material crossing from the left chamber to the right. This is due to the presence of the bridge brow section within each of these two cross sectional planes. The Z-velocity isolines for these two cross sections, shown in Figures 8-34 to 8-35 for the $\alpha = 0°$ and 15° rotated configurations respectively, show that axial velocities either side of the central intermeshing region are much reduced. Instead the maximum axial velocities within each of these two cross sectional planes, are located at the inlet and outlet faces (approximately $\pm$ 30 mm sec^{-1} for the $\alpha = 0°$ rotated configuration and approximately $\pm$ 100 mm sec^{-1} when $\alpha = 15°$).

Similar to the mixing disc zone (Chapter 7), it would be informative to compare calculated flow parameters in each of the cross sectional planes previously described within this section. Figures 8-36 to 8-38 and 8-39 to 8-41 display pressure isolines, with spatial Cartesian plots, for the previous three Y-Z and three X-Z central cross sectional planes respectively. The convention used for plotting the trilobal element flow parameters, is identical to that used in Chapter 7. The trilobal element mixing zone, when configured in the neutral arrangement, presents a geometry that creates very large pressure gradients within the different regions of the mixing zone. These large pressure gradients, however, are only apparent for the $\alpha = 0°$ and 15° rotated configurations, with pressure gradients for the $\alpha = 30°$ rotated configuration being relatively modest. The general trend for the $\alpha = 0°$ and 15° cross sections chosen, is that pressure increases within the flow domain of the first pair of trilobal elements, it then falls sharply within the domain of the second pair, before finally increasing within the domain of the third pair. Again if similar cross sections were taken below the tip of the left-hand trilobe from the first element pair, the reverse situation would be evident (i.e. a pressure decrease within the domain of the first pair of elements would be encountered, caused by the counter-clockwise co-rotation of the elements). Pressure gradients within the Y-Z cross sections shown in Figures 8-36 to 8-37 are of the order of $\Delta P = |0.9 \times 10^5|$ Pa and $\Delta P = |1.5 \times 10^5|$ Pa for the $\alpha = 0°$ and 15° rotated configurations respectively. Similar pressure gradients are experienced in the X-Z cross sections shown in Figures 8-39 to 8-40 (of the order of $\Delta P = |0.7 \times 10^5|$ Pa and $\Delta P = |1.5 \times 10^5|$ Pa for the $\alpha = 0°$ and 15° rotated configurations respectively).

Investigation of the mixing of viscous material within other regions of the trilobal elements flow domain, is also of interest. The two previous sets of cross sectional planes presented, have illustrated the mixing of material within both the central intermeshing and bridge regions. However, the two cross sectional planes outlined in the following section, will

Figure 8-34:

Z-Velocity Isolines on the Cross Section Described in Figure 8-25, Viewed Along the Y-Axis.

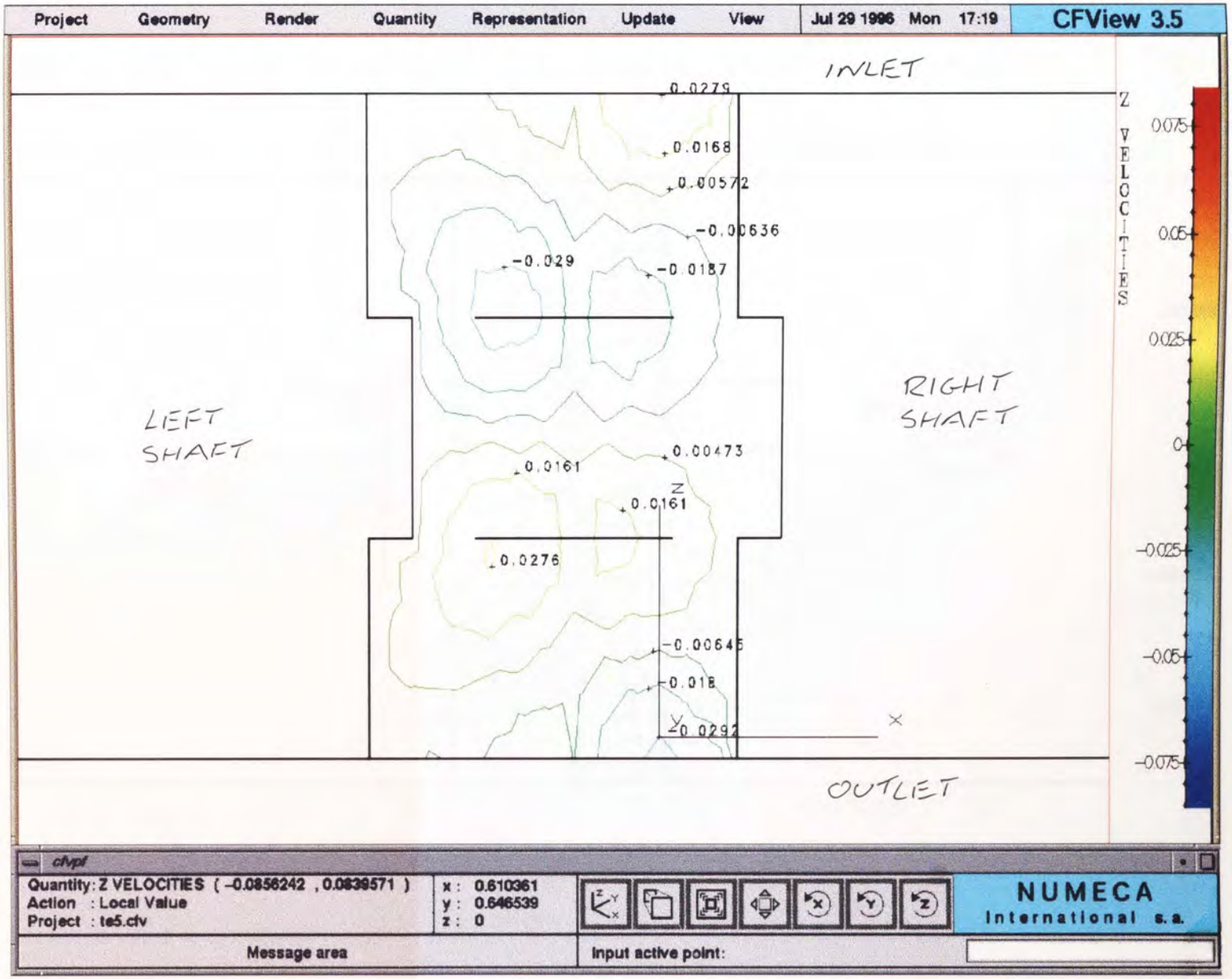

Figure 8-35:

Z-Velocity Isolines on the Cross Section Described in Figure 8-26, Viewed Along the Y-Axis.

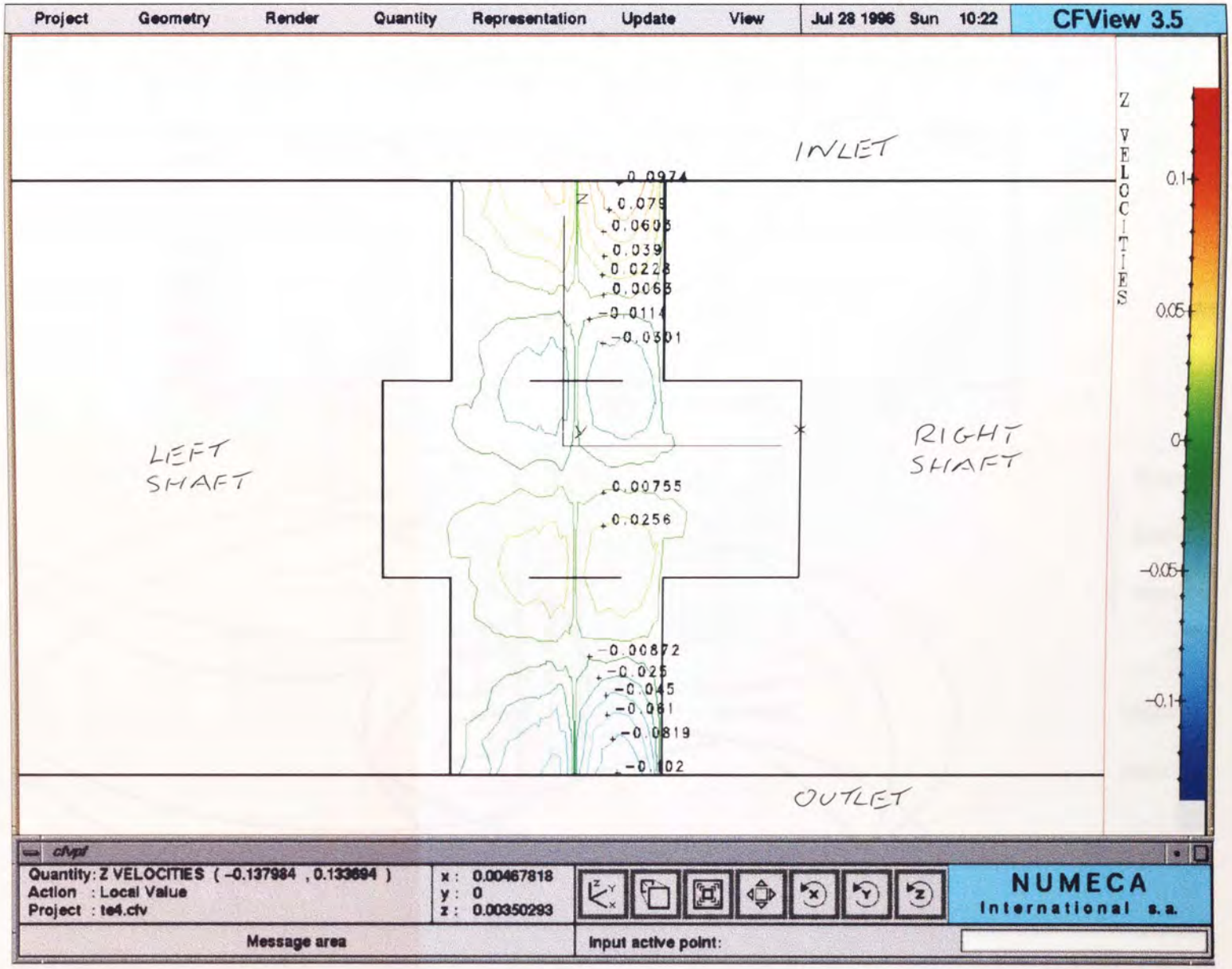

Figure 8-36:

Pressure Isolines on the Cross Section Described in Figure 8-22 (Magnified View). Pressure Cartesian Plot, as a Function of Spatial Distance, for the Values Encountered Along the Line Indicated.

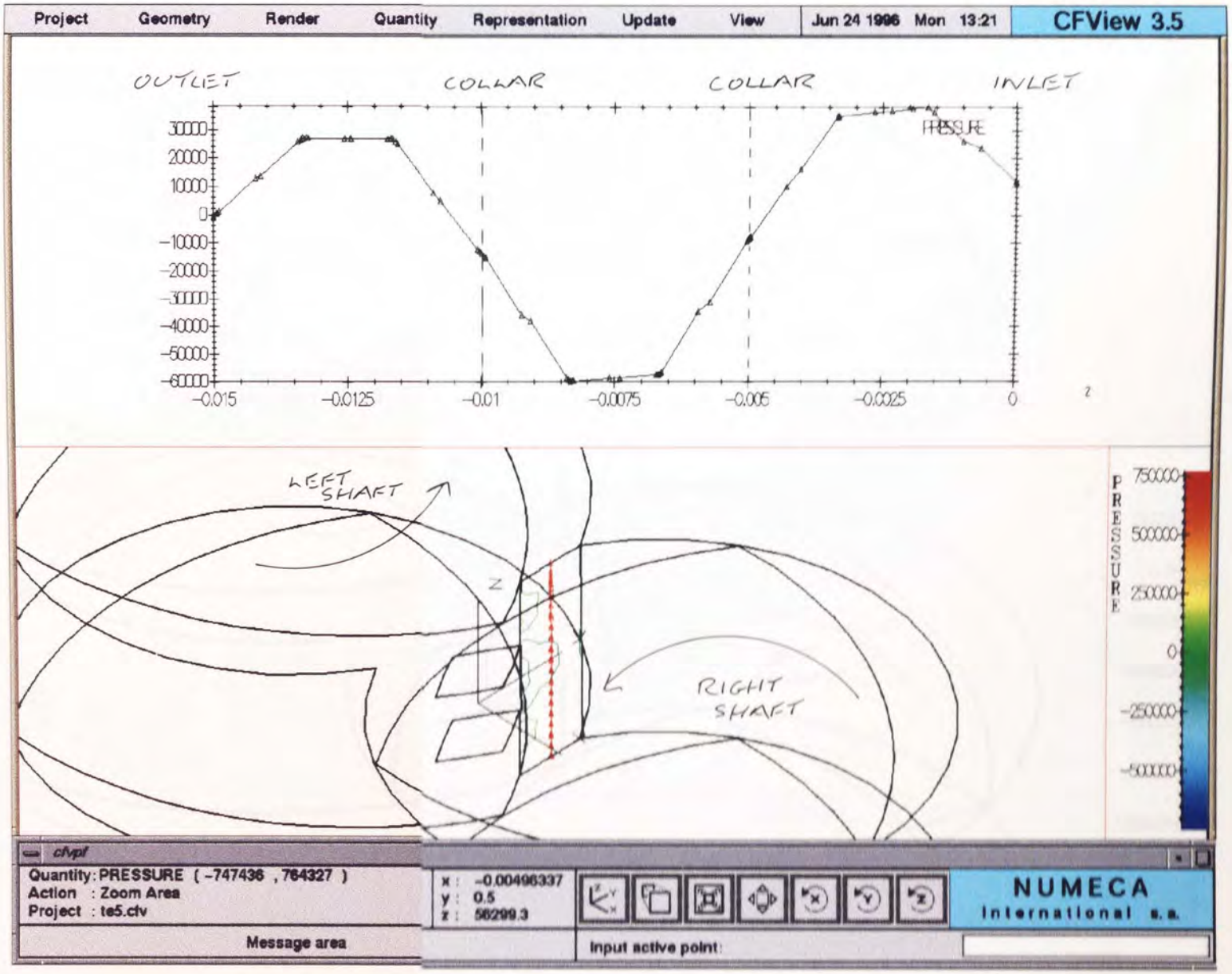

Figure 8-37:

Pressure Isolines on the Cross Section Described in Figure 8-23 (Magnified View). Pressure Cartesian Plot, as a Function of Spatial Distance, for the Values Encountered Along the Line Indicated.

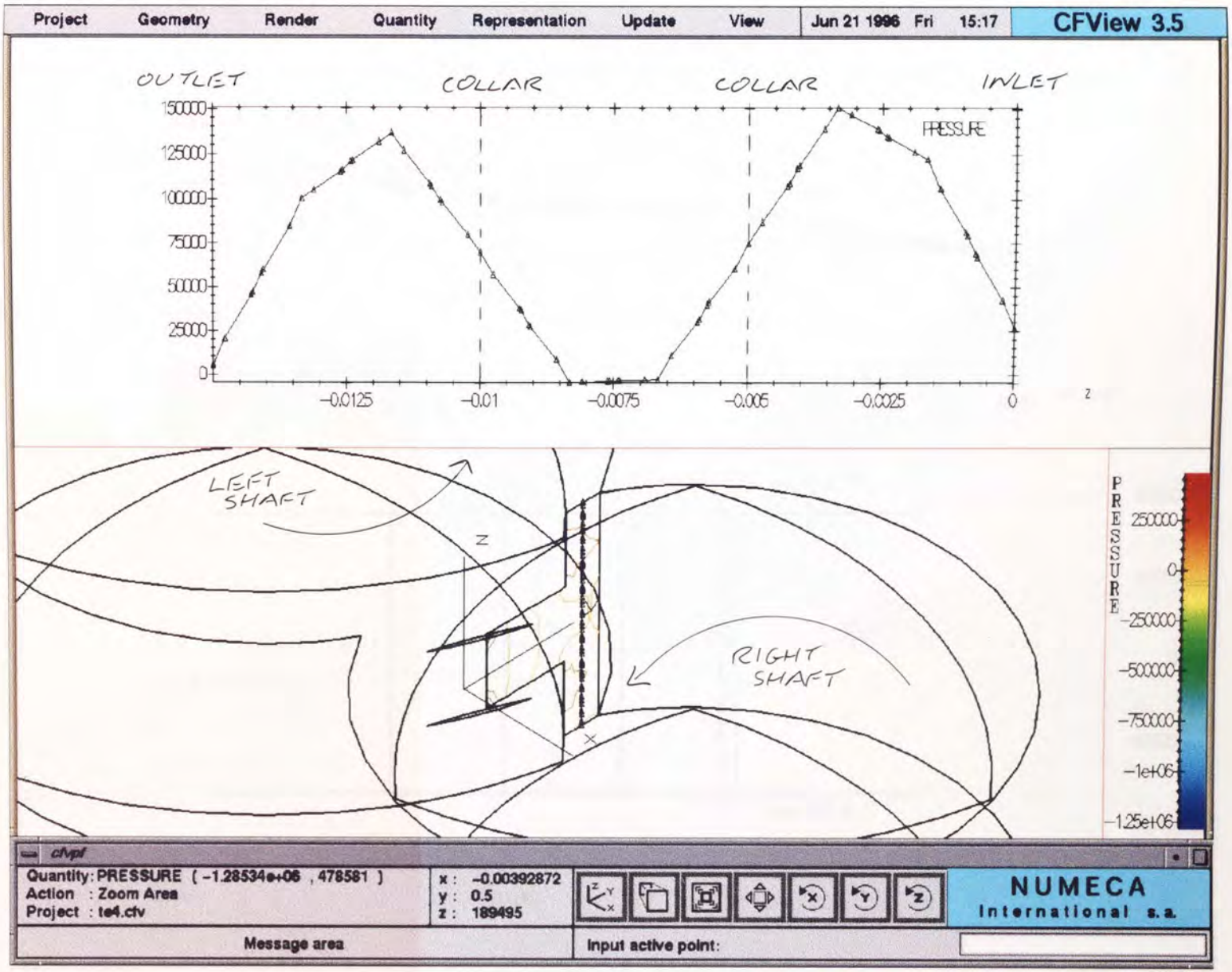

Figure 8-38:

Pressure Isolines on the Cross Section Described in Figure 8-24, Viewed Along the X-Axis. Pressure Cartesian Plots, as a Function of Spatial Distance, for the Values Encountered Along the Lines Indicated.

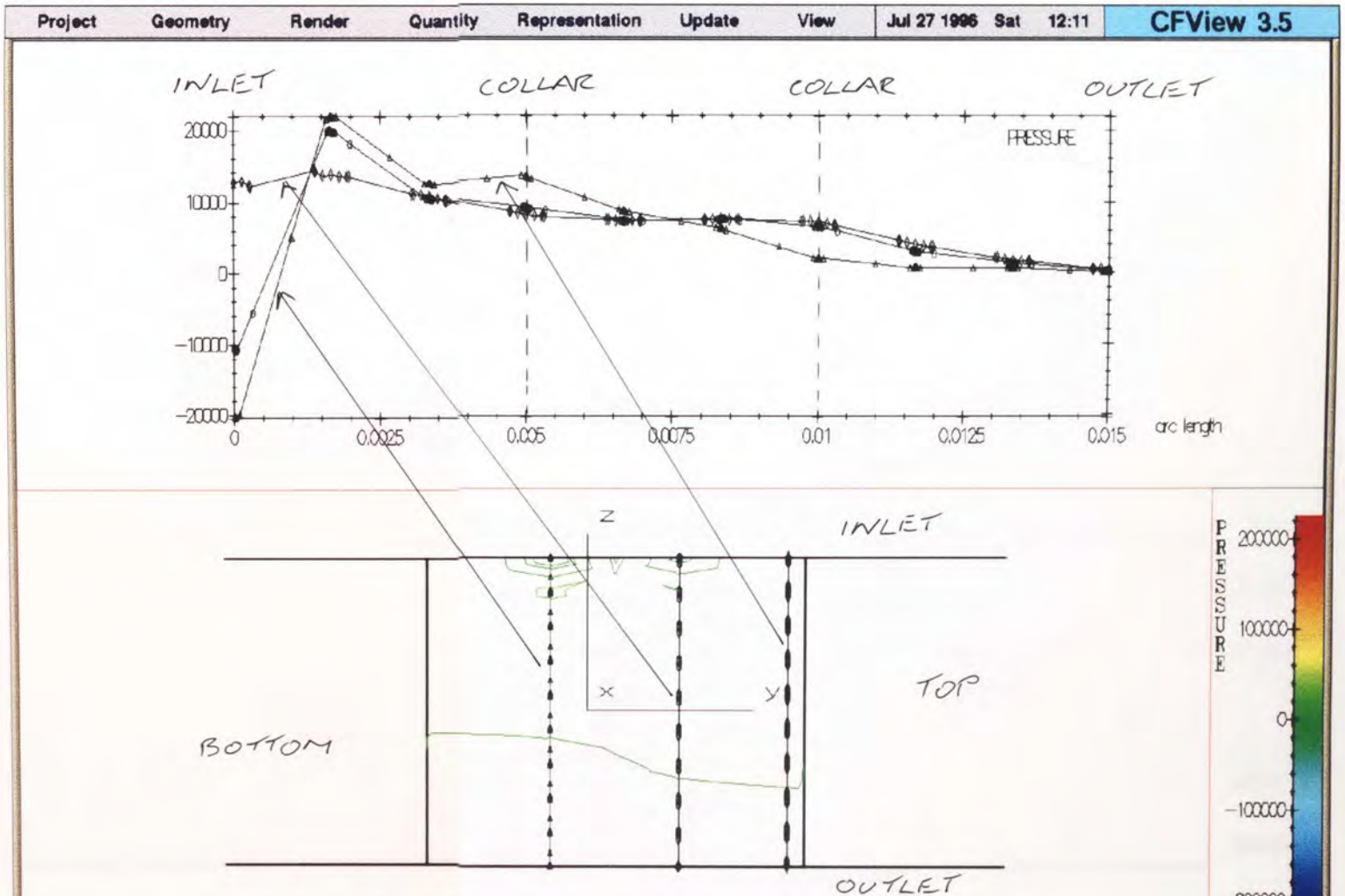

Figure 8-39:

Pressure Isolines on the Cross Section Described in Figure 8-25, Viewed Along the Y-Axis. Pressure Cartesian Plot, as a Function of Spatial Distance, for the Values Encountered Along the Line Indicated.

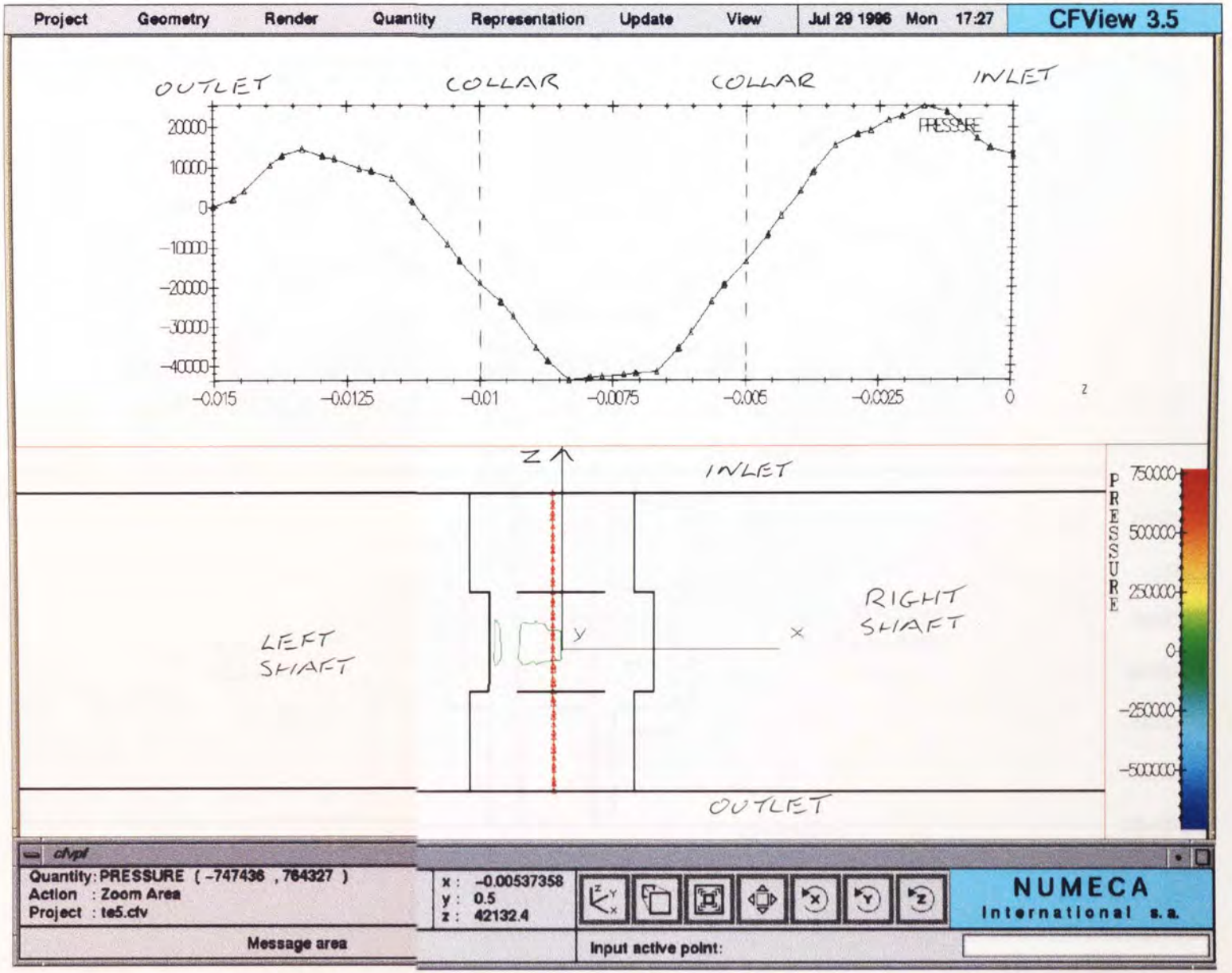

Figure 8-40:

Pressure Isolines on the Cross Section Described in Figure 8-26, Viewed Along the Y-Axis. Pressure Cartesian Plots, as a Function of Spatial Distance, for the Values Encountered Along the Lines Indicated.

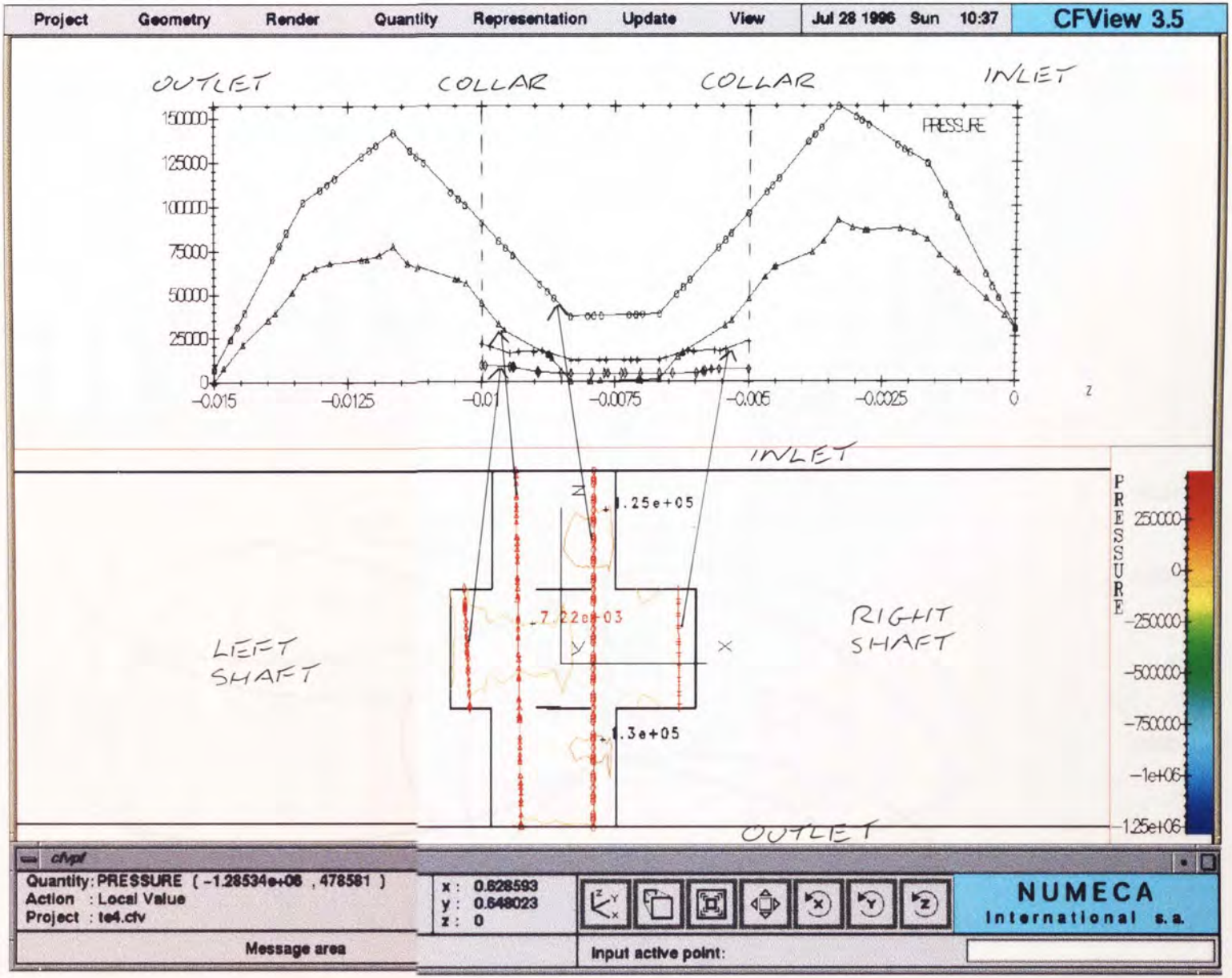

Figure 8-41:

Pressure Isolines on the Cross Section Described in Figure 8-27 (Magnified View). Pressure Cartesian Plot, as a Function of Spatial Distance, for the Values Encountered Along the Line Indicated.

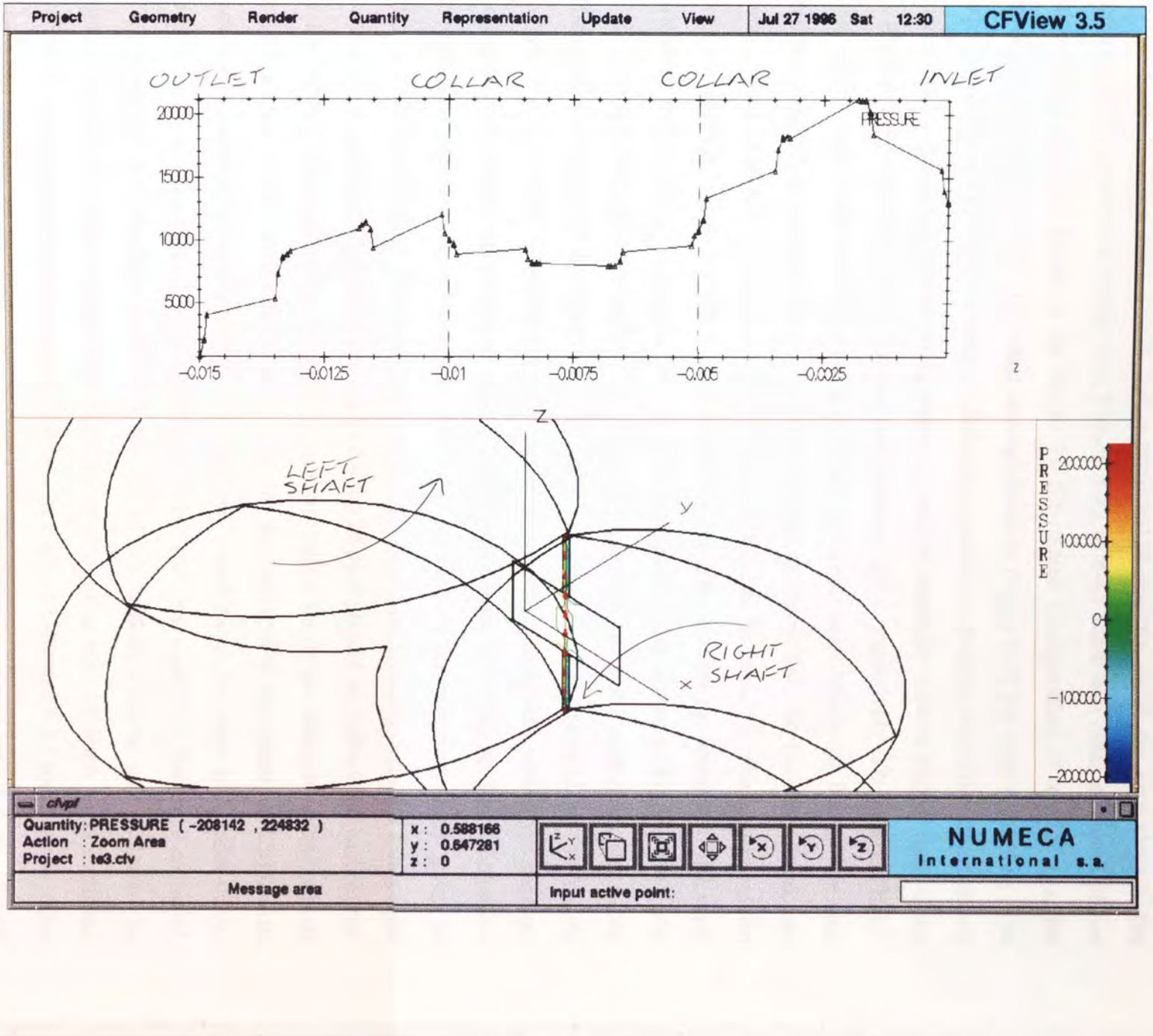

illustrate the vigorous fluid motion that is predicted at regions which are very close to the three centrally positioned trilobal tips. Figures 8-42 to 8-43 show two cross sectional planes taken along the axial length of the barrel, for the rotated configuration of $\alpha = 15°$ (i.e. for cross sections where $X \neq 0$). The cross section shown in Figure 8-42 has been created so as to expose regions close to the two central trilobal tips, which are located within the intermeshing region for this particular rotated configuration. These two centrally located trilobal tips belong to the left trilobe of each of the first and third element pairs respectively. The central "hole" seen within this cross section, is the area where the right hand trilobe of the middle pair intersects the plane created. The cross section shown in Figure 8-43 on the other hand, has been created so as to show regions close to the third trilobal tip, which is also located within the intermeshing region for this rotated configuration. This trilobal tip belongs to the right trilobe of the middle element pair. The Z-velocity contour plots shown in Figures 8-42 and 8-43, illustrate complex axial motions within the flow domain and at the inlet and outlet faces. They also show that the fluid flow pattern is mirrored about the line drawn along the Y-axis for which Z = -7.5 mm, identical to other cross sectional planes examined within this chapter. To depict more clearly the motion of the fluid flow within these two cross sections, each view is magnified and orientated along the X-axis. Thus each of the representations given in Figures 8-44 to 8-45 show the cross sectional planes viewed horizontally from the side of the mixing zone, such that each inlet face lies to the top of each picture as viewed and each outlet to the bottom. Greatest axial motion is exhibited within the cross sectional plane which intersects close to the two centrally located trilobal tips (referred to henceforth as CS1), with maximum velocities of approximately $\pm$ 80 mm sec^{-1} resulting at the inlet and outlet faces. Maximum axial velocities of approximately $\pm$ 50 mm sec^{-1} are evident in the cross sectional plane close to the centrally located trilobal tip of the middle element pair (referred to henceforth as CS2). The velocity vector profiles overlaid onto each of these cross sectional planes are quite spectacular and they are shown in Figures 8-46 and 8-47 respectively. The associated pressure isolines plots for CS1 and CS2 are shown in Figures 8-48 to 8-49. Due to the complex nature of the motion exhibited within each of these two cross sectional planes, each will be explained separately as follows;

- Flow within CS1 (intersecting two trilobal tips)

  Three pressure plots, labelled as lines A1, B1 and C1, have been taken along the Z-axis, as shown in Figure 8-48, for the following three fluid flow regions-

  <u>About the line A1 (towards the lower bridge region):</u>

  Very little axial flow is exhibited in this region as reflected by the small pressure gradient

Figure 8-42:
Z-Velocity Colour Contours on the First Cross Section Created in the Y-Z Plane, Offset Towards the Right Hand CICo-TSE Chamber, for the 3D Trilobal Element Mixing Zone Containing Three Pairs of Elements in the Neutral Arrangement at the Rotated Configuration $\alpha = 15°$.

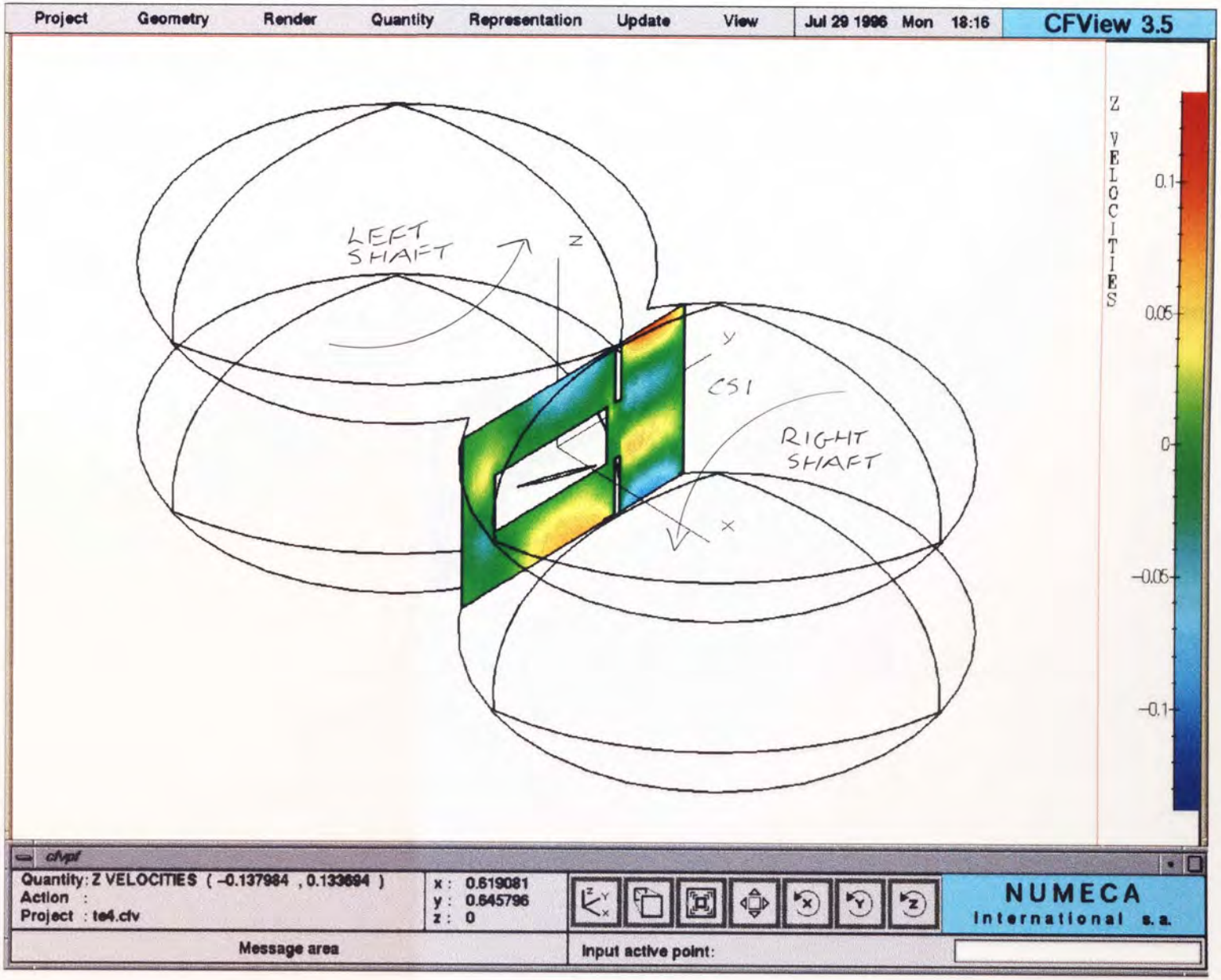

Figure 8-43:
Z-Velocity Colour Contours on the Second Cross Section Created in the Y-Z Plane, Offset Towards the Left Hand CICo-TSE Chamber, for the 3D Trilobal Element Mixing Zone Containing Three Pairs of Elements in the Neutral Arrangement at the Rotated Configuration $\alpha = 15°$.

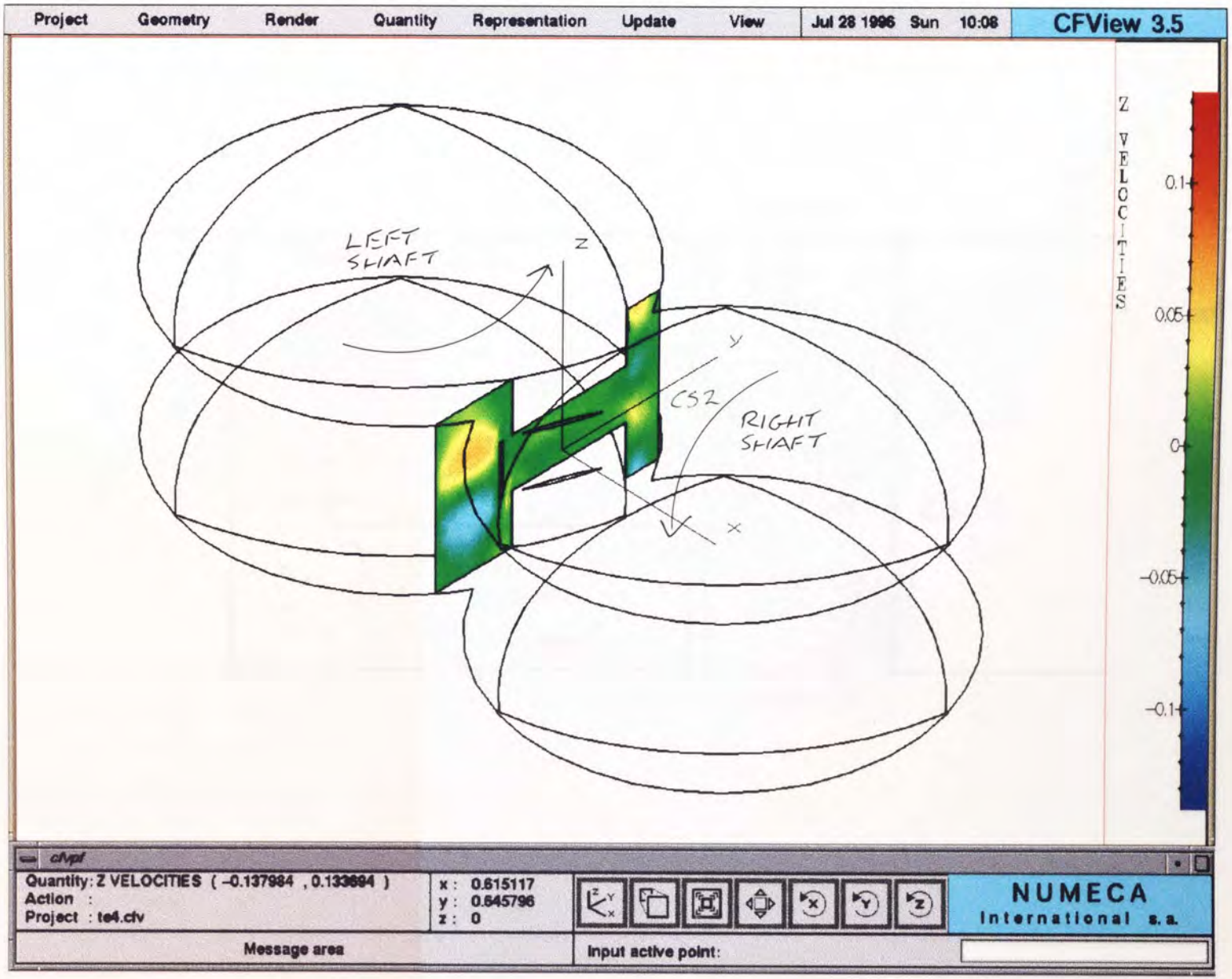

Figure 8-44:

Z-Velocity Isolines on the Cross Section Described in Figure 8-42, Viewed Along the X-Axis.

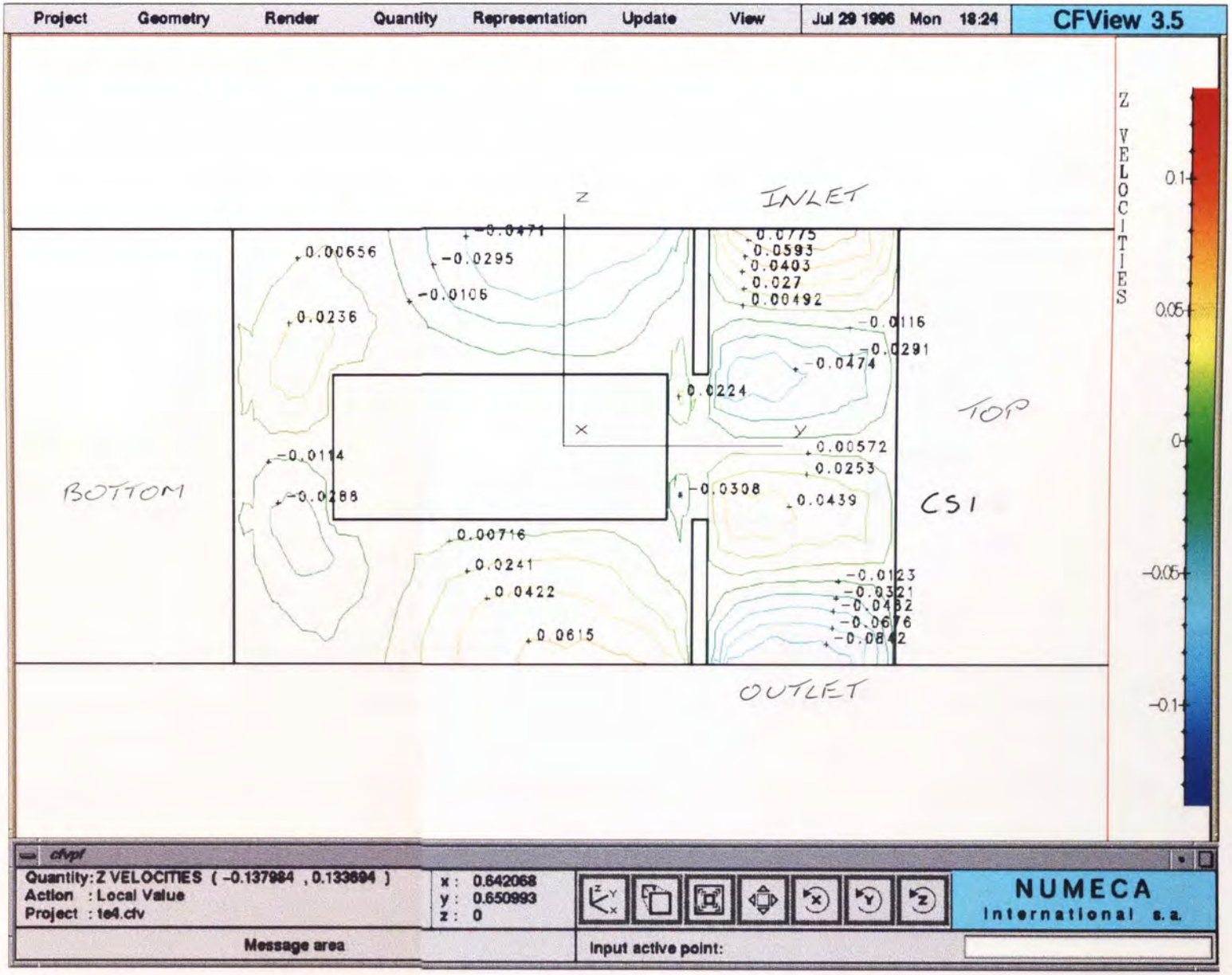

Figure 8-45:

Z-Velocity Isolines on the Cross Section Described in Figure 8-43, Viewed Along the X-Axis.

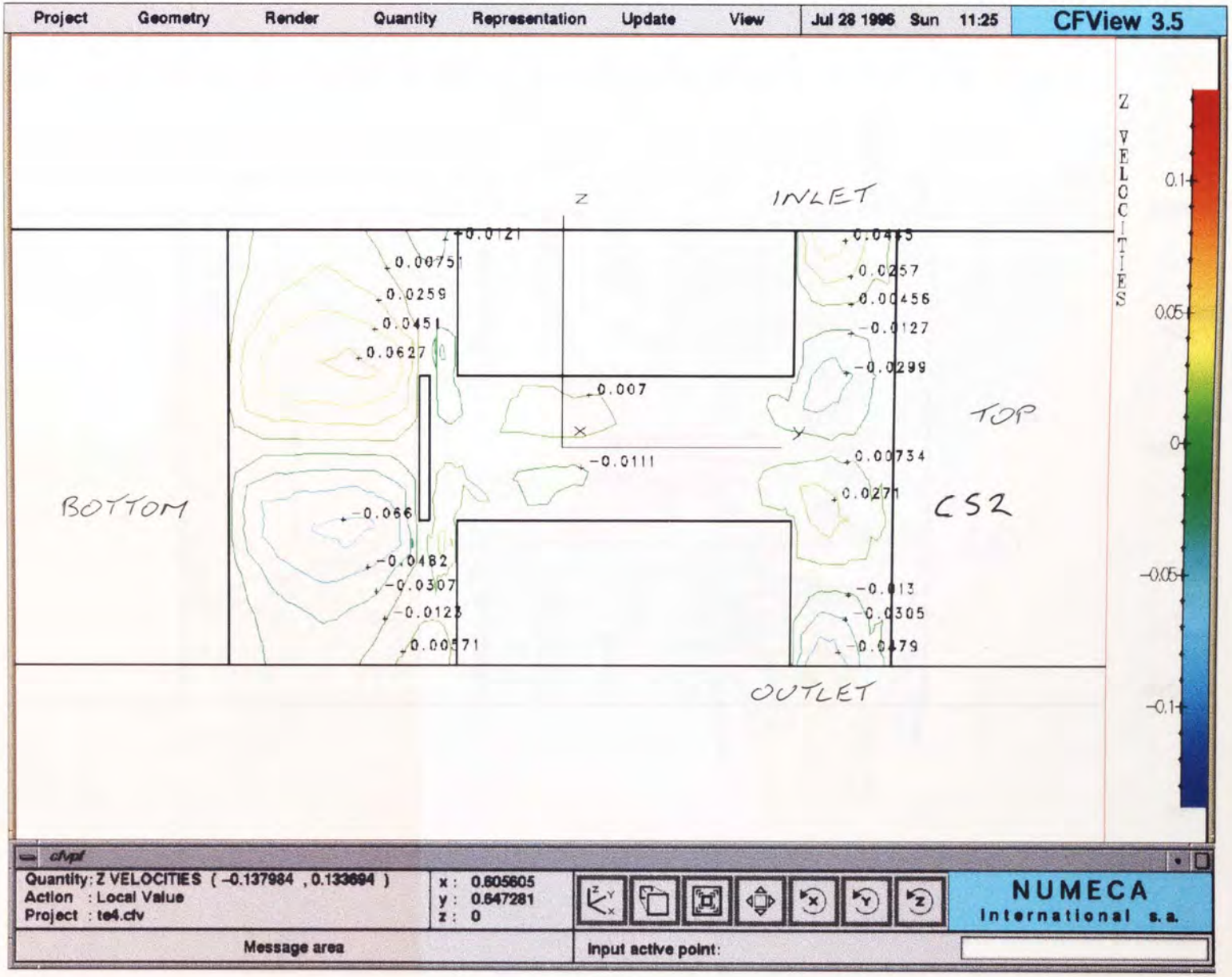

Figure 8-46:
Velocity Vector Profiles on the Cross Section Described in Figure 8-42, Viewed Along the X-Axis.

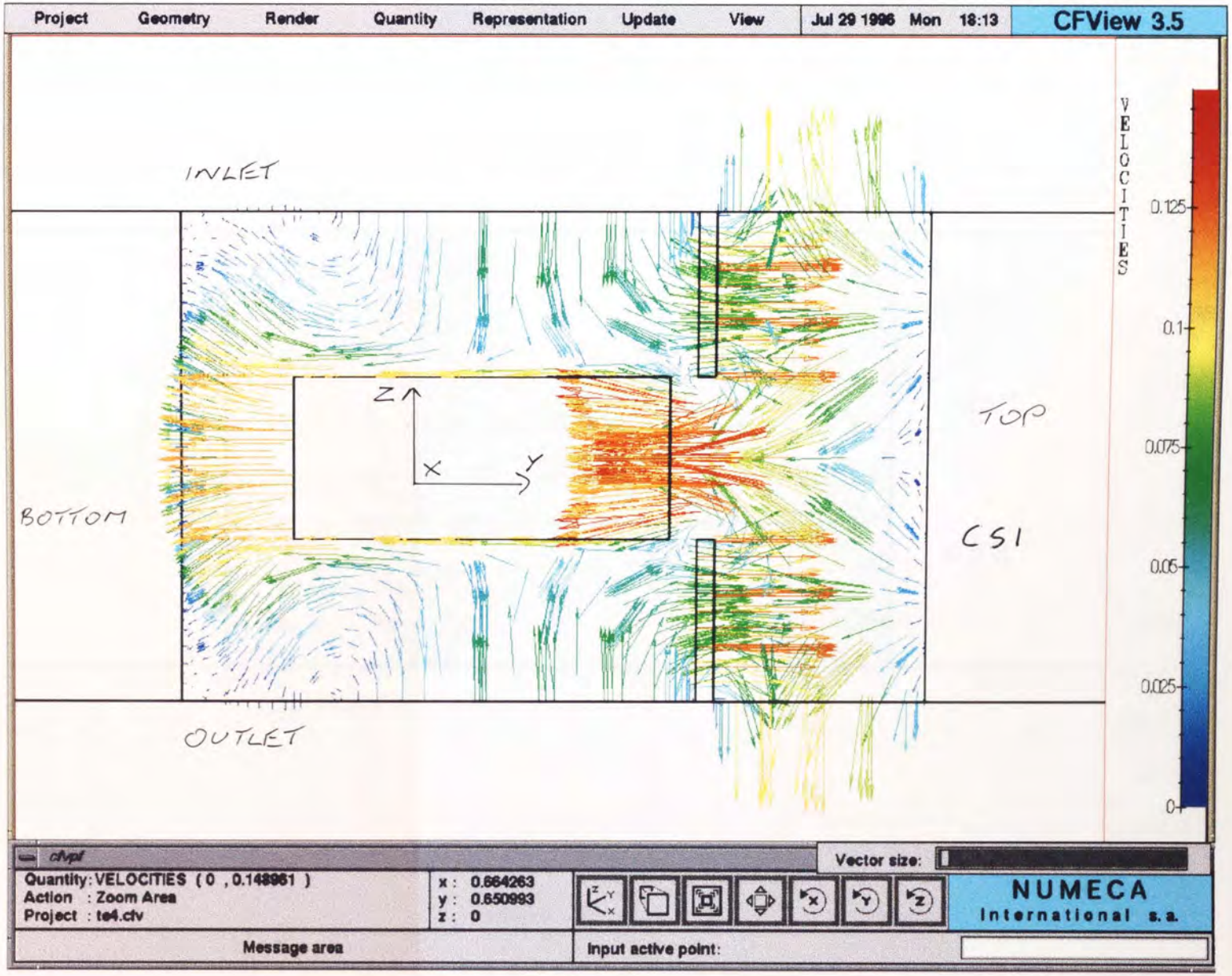

Figure 8-47:
Velocity Vector Profiles on the Cross Section Described in Figure 8-43, Viewed Along the X-Axis.

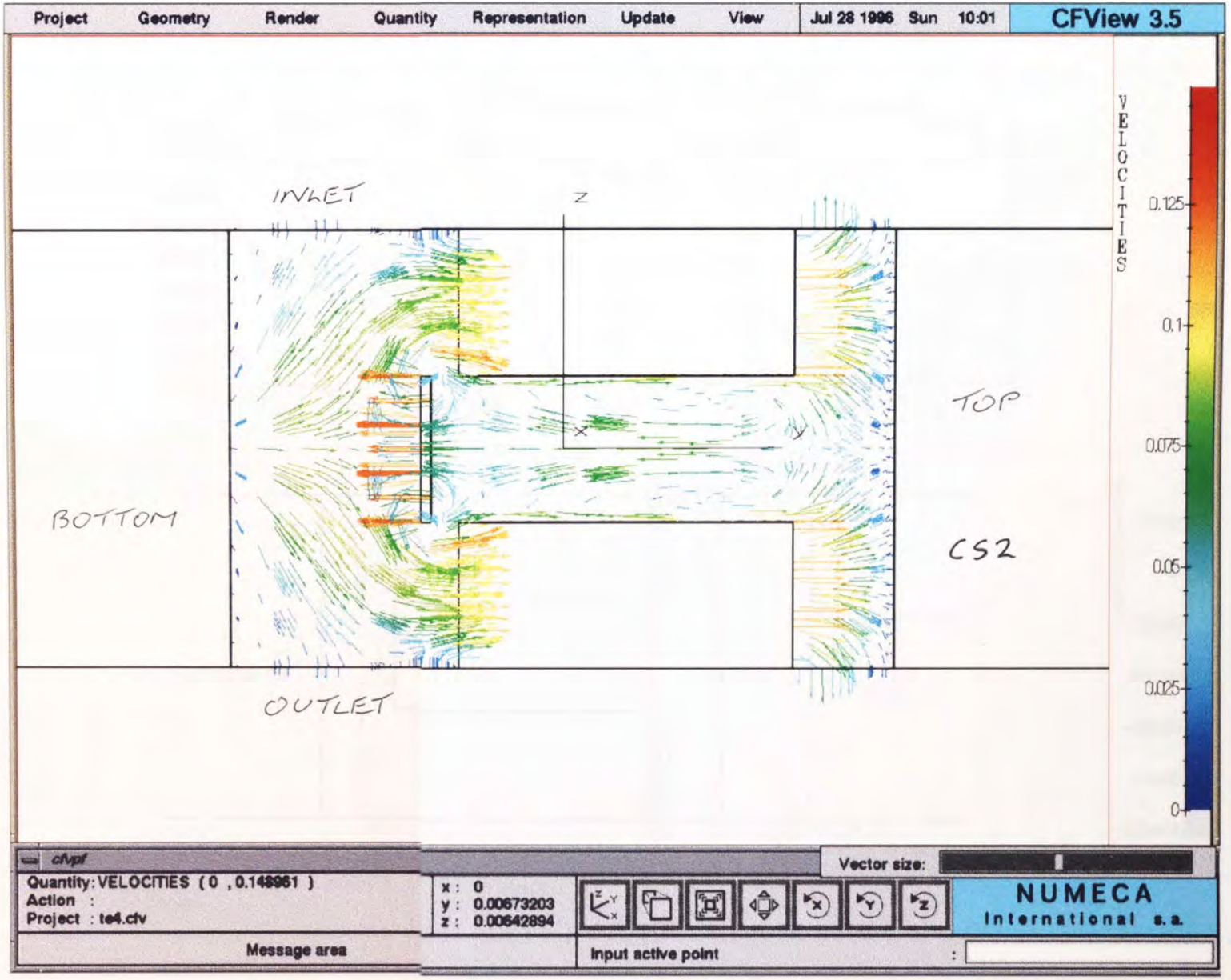

Figure 8-48:

Pressure Isolines on the Cross Section Described in Figure 8-42, Viewed Along the X-Axis. Pressure Cartesian Plots, as a Function of Spatial Distance, for the Values Encountered Along the Lines Indicated.

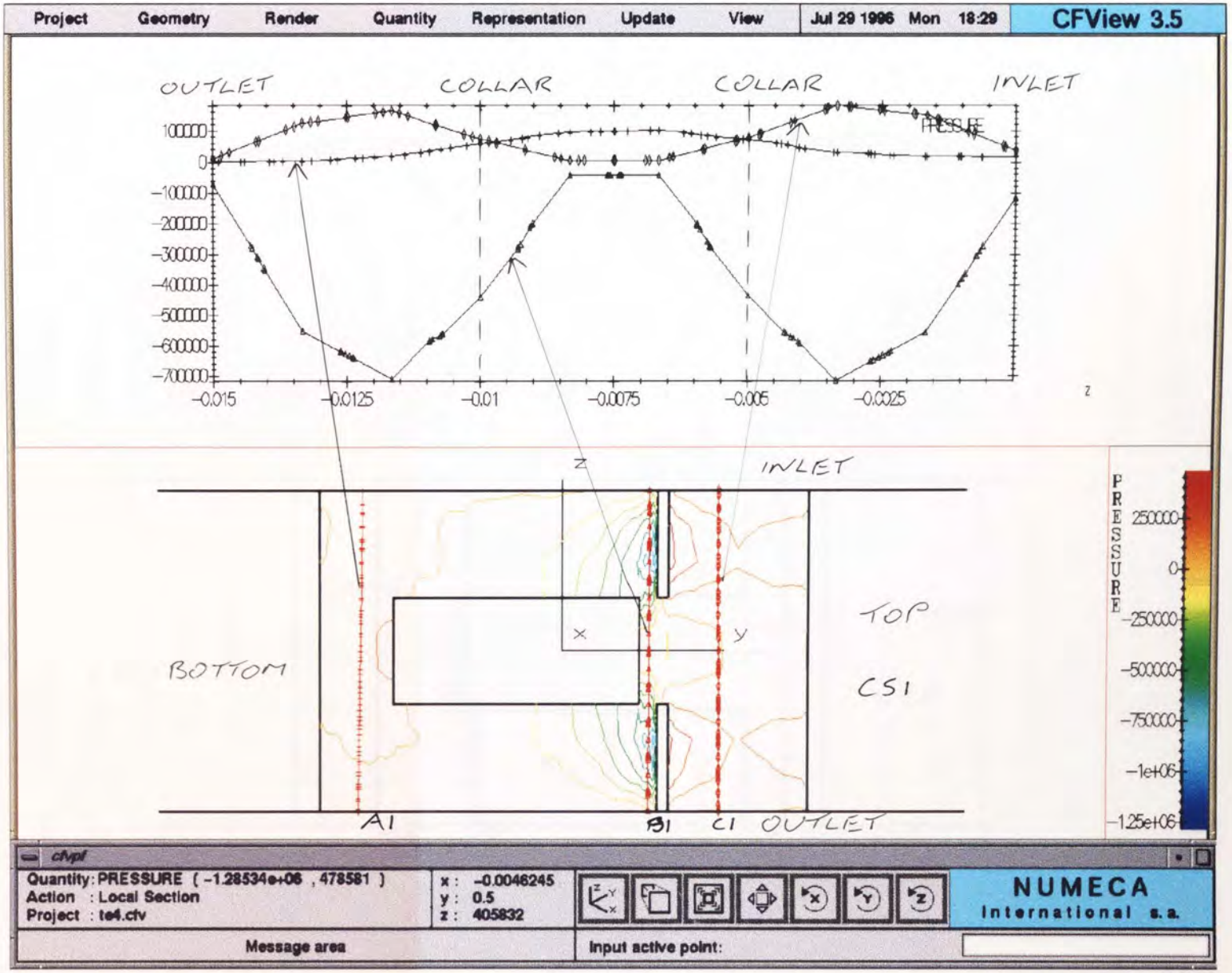

Figure 8-49:

Pressure Isolines on the Cross Section Described in Figure 8-43, Viewed Along the X-Axis. Pressure Cartesian Plots, as a Function of Spatial Distance, for the Values Encountered Along the Lines Indicated.

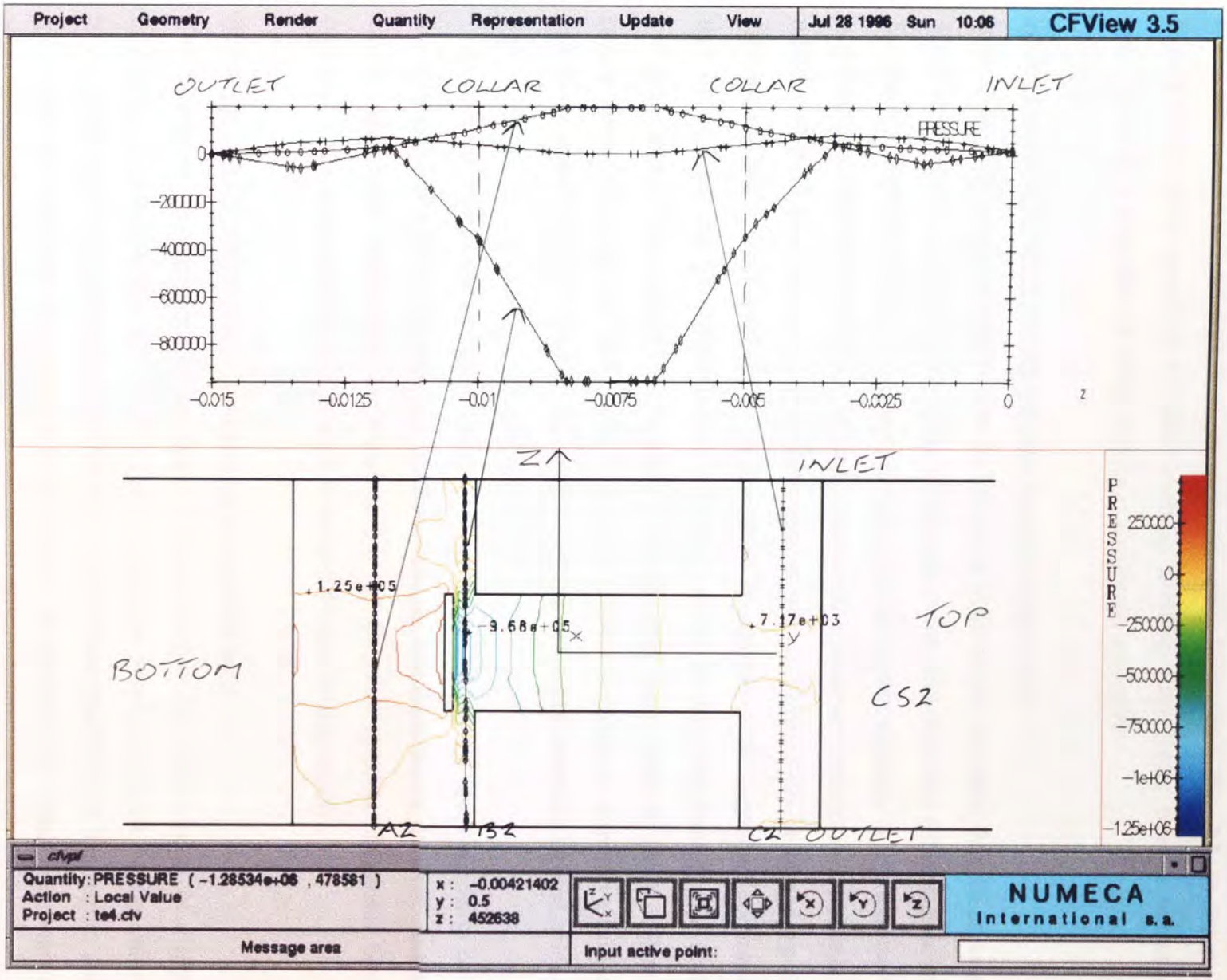

along line A1. Indeed for regions at the inlet and outlet faces above line A1, as shown in Figure 8-46, there seems to be slow moving swirling flow fields over a radius of approximately 5 mm, each of which possesses a stagnant epicentre.

About the line B1 (below the two centrally located trilobal tips):

Inspection of the pressure plot for line B1 shown in Figure 8-48, indicates that the pressure difference between material close to the trilobal tip of the first and third element pair and for material contained within the domain occupied by the middle element, is approximately of the order of $\Delta P = |7.0 \times 10^5|$ Pa. The magnitude of this pressure gradient and the violent rotation of fluid flow about the two trilobal tips, as seen in Figure 8-46, is caused by the fact that the two trilobal tips intersecting this plane are moving in the opposite direction to that of the body of the middle trilobal element, which is also intersecting this cross sectional plane. Consequently, this high pressure drop over such a short distance (approximately 5 mm) and small area, is likely to induce significant dispersive mixing effects on material contained within the neighbourhood of the two centrally located trilobal tips.

In addition, within the two regions below each of these two trilobal tips, material at both the inlet and outlet faces is drawn into the flow domain. The direction of the fluid motion within these two regions may be explained by the fact that pressure decreases have occurred as a result of the two tips moving towards the upper bridge region.

About the line C1 (above the two centrally located trilobal tips):

The maximum pressure gradient encountered along the line C1, whilst being of a high magnitude (approximately $\Delta P = |1.5 \times 10^5|$ Pa) is modest when compared to the values being experienced along the line B1. However, the pressure gradients in this region still gives rise to significant forward and back mixing. In addition, the equal amounts of forward and backward movement exhibited, as shown in Figure 8-46, illustrates the maximum leakage effect which was outlined previously within this chapter.

- Flow within CS2 (intersecting one trilobal tip)

  Three pressure plots, labelled as lines A2, B2 and C2, have been taken along the Z-axis, as shown in Figure 8-49, for the following three fluid flow regions-

  About the line A2 (below the centrally located trilobal tip):

  The maximum pressure gradient encountered along the line A2, is approximately $\Delta P = |1.5 \times 10^5|$ Pa and this is associated with forward and back mixing. As may be observed in Figure 8-47, the motion of material within this region is dictated by the speed

and direction of the middle trilobal tip, which is moving towards the bottom bridge region.

About the line B2 (above the centrally located trilobal tip):

For this particular rotated configuration ($\alpha = 15°$) and about both the regions where the lines B1 and B2 have been drawn, the simulation predicted that the most vigourous mixing of material will take place. The pressure difference along the line B2 as shown in Figure 8-49, between material contained within the domains of the first and third element pairs and for material close to the trilobal tip of the middle element pair, is approximately $\Delta P = |10.0 \times 10^5|$ Pa. These huge pressure gradients predicted over such small distances, are associated with very intense swirling flows fields within regions close to each corner of the middle trilobal tip. Similar to the regions close to the line B1 shown within Figure 8-48, this magnitude of pressure difference along line B1 is likely to induce significant dispersive mixing of material in the vicinity of the domain occupied by the middle trilobal tip.

About the line C2 (towards the upper bridge region):

Very modest pressure gradients are experienced along the line C2, associated with some axial mixing. Interestingly as shown in Figure 8-47, the simulation predicts two elongated swirling flow fields in the central region contained within the middle element pair domain (i.e. above the central trilobal tip and below the line C2).

Along the same two sets of three lines for which pressure values were plotted, as shown in Figures 8-48 to 8-49, graphs for local shear rate and mixing efficiencies have also been drawn. Figures 8-50 to 8-51 display the local shear rate values and Figures 8-52 to 8-53 the mixing efficiencies, for the cross sectional planes of CS1 and CS2 respectively. The local shear rates predicted in the regions very close to all three centrally located trilobal tips for the $\alpha = 15°$ rotated configuration, are of the order of approximately 1000 - 2000 sec^{-1}, which is extremely high. These values may be compared with those encountered in the mixing disc simulations described in Chapter 7, where the maximum local shear rate values predicted for regions contained within the mixing disc flow domain, are of a significantly lower order of several hundred sec^{-1}. This marked difference in terms of the maximum local shear rate values being predicted, illustrates the difference between the flow fields exhibited by each of these two CICo-TSE mixing zones. The mixing efficiency values are shown in Figures 8-52 to 8-53.

8.4 CICo-TSE Mixing zones - Comparison Analysis

One of the benefits of performing 2D simulations for the two Betol BTS40 CICo-TSE

Figure 8-50:

Local Shear Rate Isolines on the Cross Section Described in Figure 8-42, Viewed Along the X-Axis. Local Shear Rate Cartesian Plots, as a Function of Spatial Distance, for the Values Encountered Along the Lines Indicated.

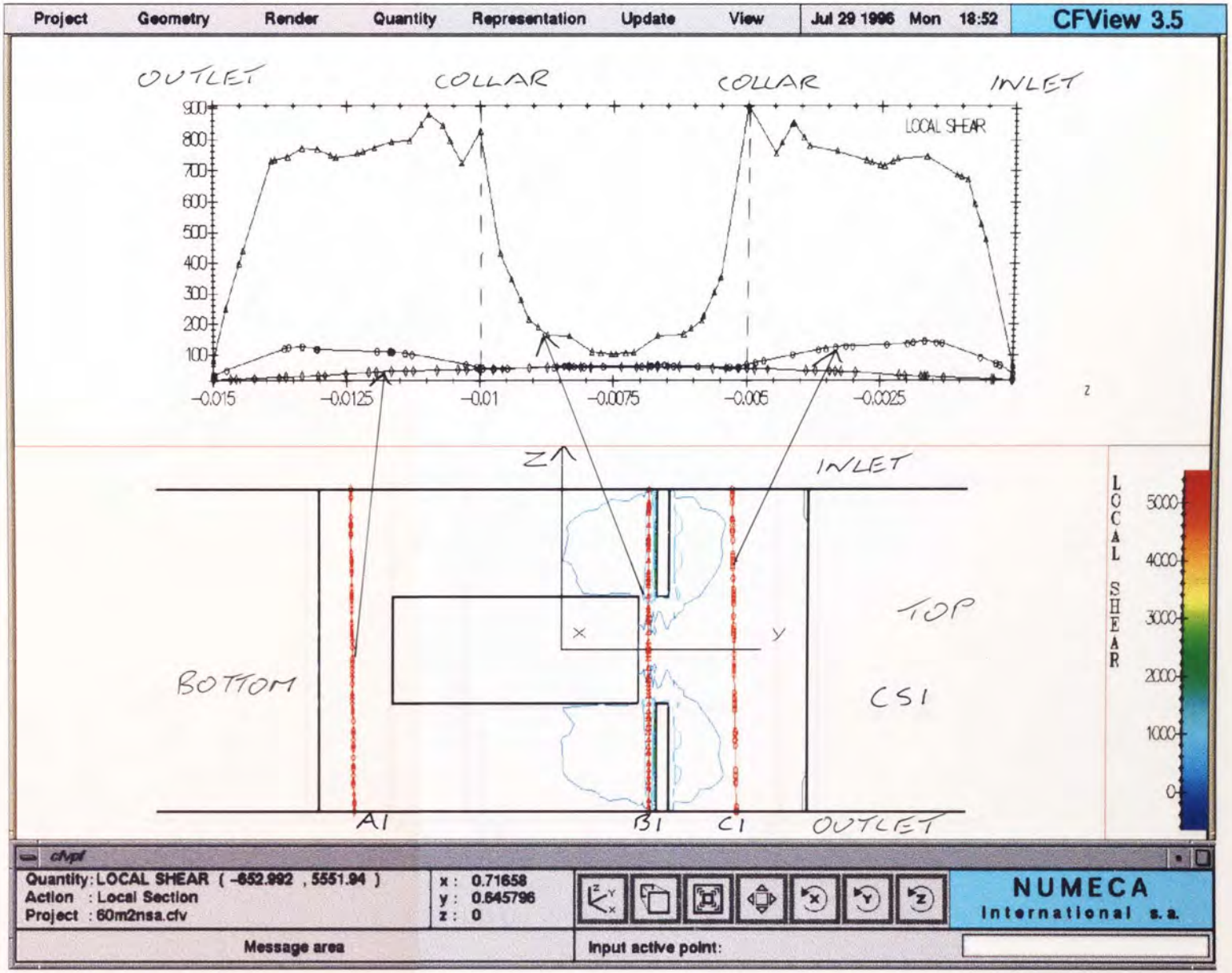

Figure 8-51:

Local Shear Rate Isolines on the Cross Section Described in Figure 8-43, Viewed Along the X-Axis. Local Shear Rate Cartesian Plots, as a Function of Spatial Distance, for the Values Encountered Along the Lines Indicated.

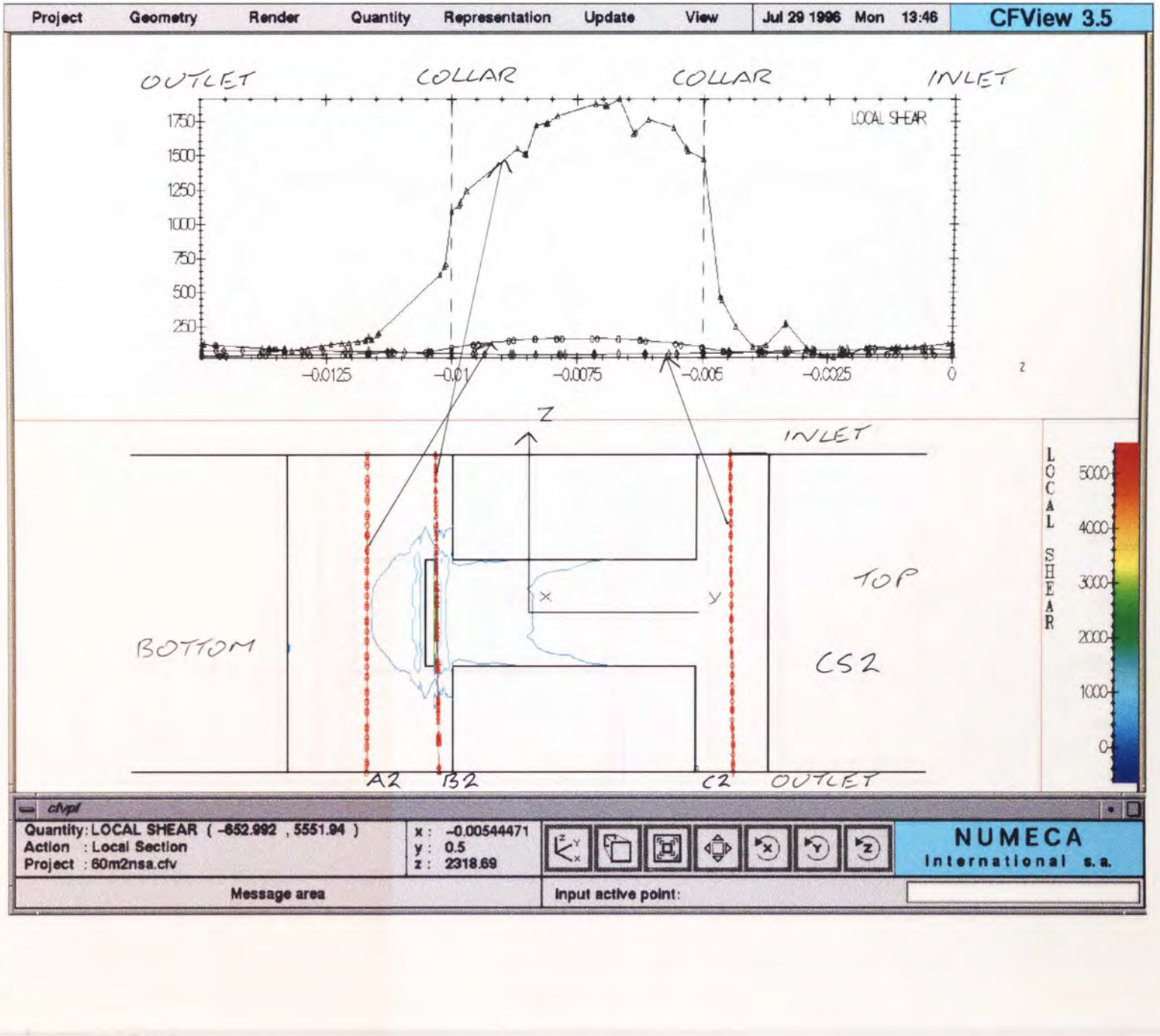

Figure 8-52:

Mixing Efficiency Isolines on the Cross Section Described in Figure 8-42, Viewed Along the X-Axis. Mixing Efficiency Cartesian Plots, as a Function of Spatial Distance, for the Values Encountered Along the Lines Indicated.

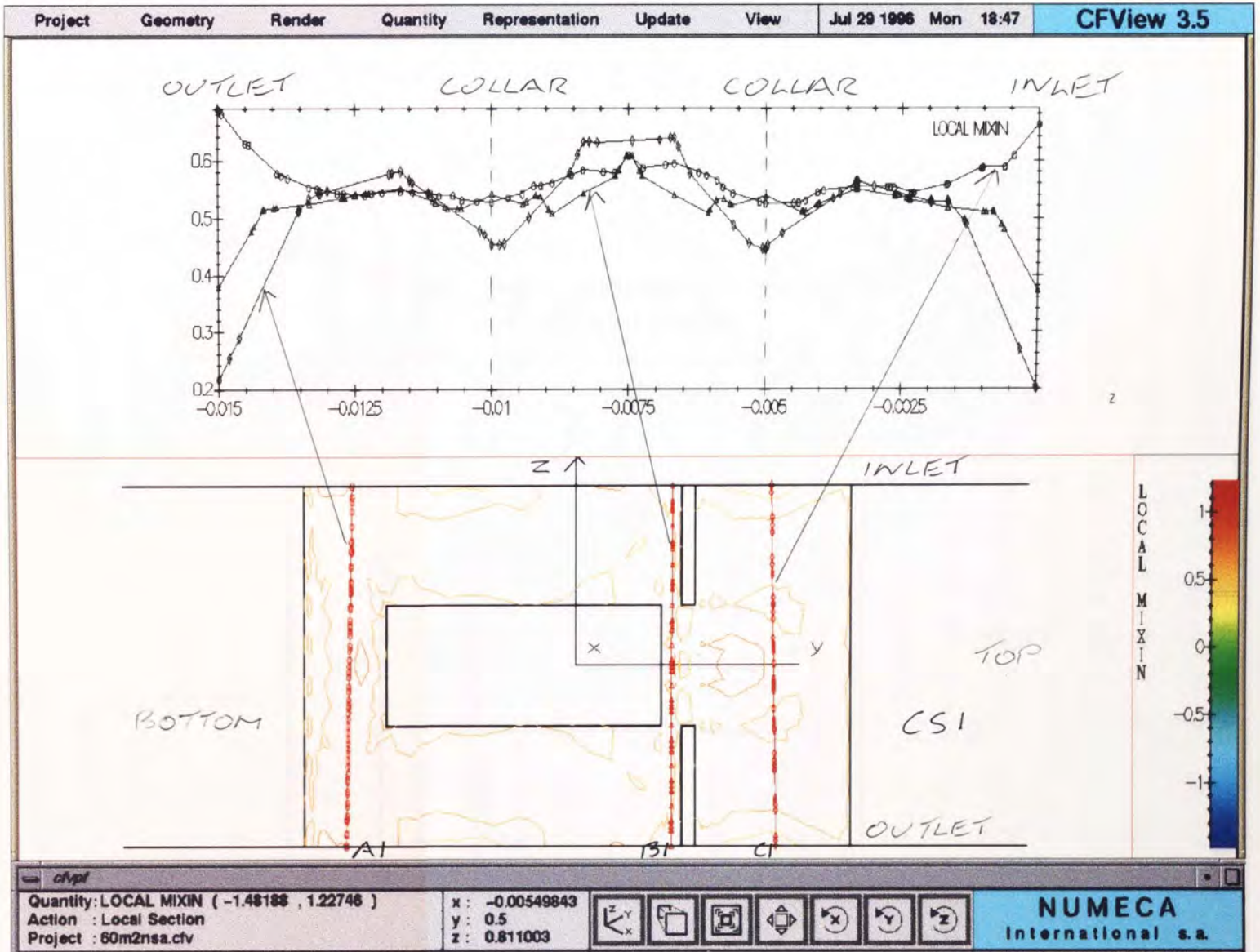

Figure 8-53:

Mixing Efficiency Isolines on the Cross Section Described in Figure 8-43, Viewed Along the X-Axis. Mixing Efficiency Cartesian Plots, as a Function of Spatial Distance, for the Values Encountered Along the Lines Indicated.

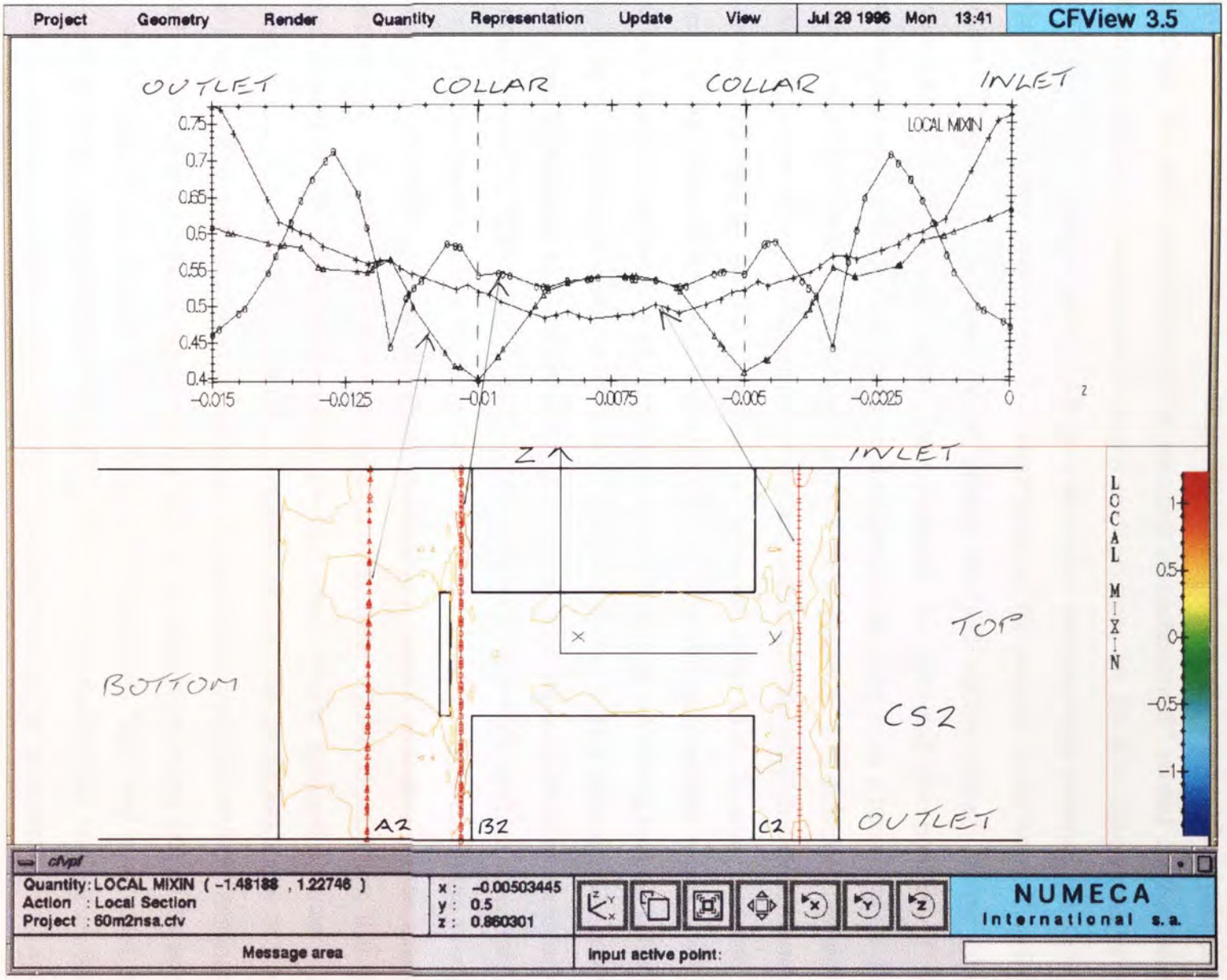

mixing zones under consideration within this thesis, is that the average flow parameters calculated for each simulation may be obtained at successive 5° rotated configurations. Obtaining solutions at successive 5° rotated configurations for 3D flow simulations, is not feasible. Tables 8-2 and 8-3 show, for each of the rotated configurations indicated, the average values for local shear rates $\dot{\gamma}$, the X-Y components of the inelastic stress tensor $\mathbf{T}$ and the mixing efficiencies λ, calculated for the mixing disc and trilobal element mixing zones respectively. These average values were obtained by summing the product of the corresponding parameter in each element and the area of that element as a fraction of the area of the entire flow domain. The trilobal elements are designed to give enhanced dispersive mixing whilst the mixing discs control melting and distributive blending. In order to achieve dispersive mixing, the trilobal elements must generate large shear stresses in order to overcome the adhesion forces that bind agglomerates. The average shear rate values given in Tables 8-2 and 8-3 are depicted in Graph 8-10 and they show an interesting contrast between the types of mixing mechanisms exhibited by these two sets of mixing elements. The results for the trilobal elements reinforce the notion of a periodic pumping mechanism as the shearing action observed in Table 8-3 seems to oscillate between a maximum average shear rate at $\alpha = 0°$ and a minimum at $\alpha = 30°$. Thus the pumping action and the magnitude of the average shear rates obtained are dependent on the instantaneous rotated orientation of the trilobal element tips. For any particular rotated configuration, those trilobal element tips that are wholly incident with the outer barrel wall, generate steep velocity gradients as material is forced between each trilobal tip and the outer barrel wall. For the configuration $\alpha = 0°$ there are a total of five tips which are fully incident with the outer barrel wall with the remaining sixth trilobe tip smearing material against the body of the adjacent element. Due to the angle at which this sixth tip interacts with the body of its neighbour, high local shear rates are generated. For the configuration $\alpha = 30°$, though, there are only four trilobal tips that are fully incident with the outer barrel wall whilst the remaining two tips are in alignment with each other. This alignment greatly reduces the smearing achieved by these two tips. By contrast, the mixing achieved by the mixing discs does not depend on the smearing of material against the outer barrel (though some smearing will be present) and, as is shown in Graph 8-10, the average shear rate values calculated remain relatively stable throughout the partial mixing cycle. The average X-Y components of the inelastic stress tensor and the average mixing efficiency values are shown in Graphs 8-11 and 8-12 respectively. The spread of mixing efficiency values obtained for each of the two mixing zones is small ($\Delta\lambda \approx 0.02$) and it may thus be concluded that average mixing efficiency values are constant, for both mixing zones, over the partial mixing cycles investigated.

To further illustrate both the different types of mixing mechanisms and the extent to which

TABLE:8-2 2D Results Table - Mixing Discs

Configuration ($\alpha°$)	Number of Structured Nodal Points	Shear Rate $\dot{\gamma}$ (sec^{-1})	Inelastic Stress Tensor T_{x-y} (Pa)	Mixing Efficiency λ
0	2905	45.28	-309.64	0.4884
5	"	46.71	-451.28	0.4832
10	"	47.03	-460.38	0.4820
15	"	46.93	-464.58	0.4770
20	"	46.89	-443.08	0.4761
25	"	47.14	-439.66	0.4818
30	"	47.09	-480.75	0.4845

TABLE:8-3 2D Results Table - Trilobal Elements

Configuration ($\alpha°$)	Number of Structured Nodal Points	Shear Rate $\dot{\gamma}$ (sec^{-1})	Inelastic Stress Tensor T_{x-y} (Pa)	Mixing Efficiency λ
0	3642 or 3641	73.04	47.62	0.4786
5	"	72.71	49.50	0.4793
10	"	71.64	56.97	0.4809
15	"	69.48	74.40	0.4815
20	"	65.07	105.47	0.4803
25	"	56.31	107.27	0.4727
30	"	50.05	-35.99	0.4705

GRAPH 8-10 **2D Average Local Shear Rate Values**

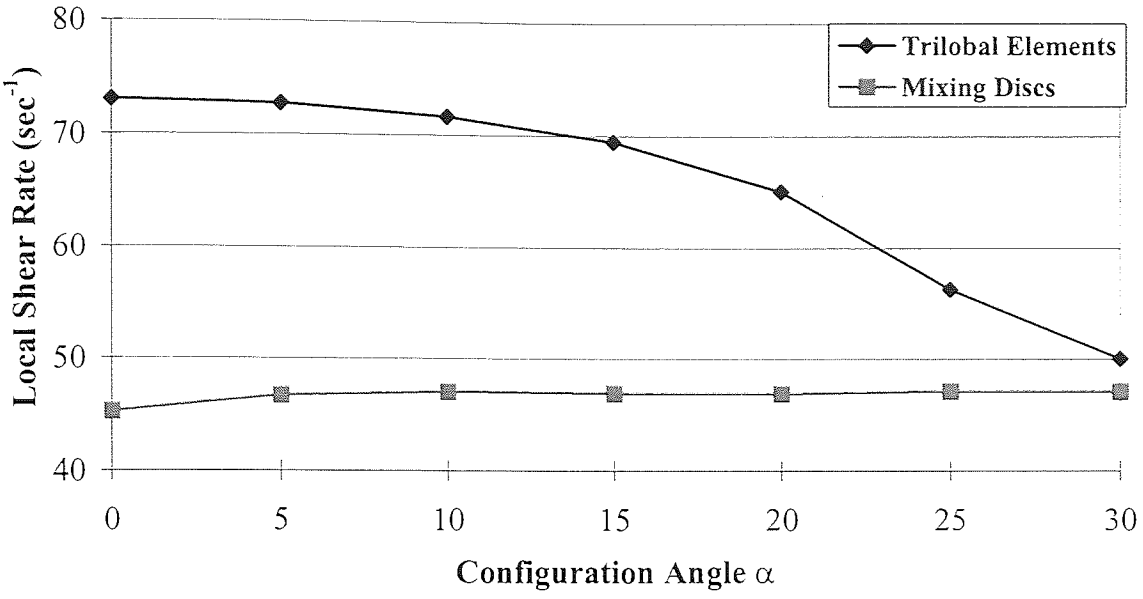

GRAPH 8-11 **2D Average Inelastic Stress Tensor Values**

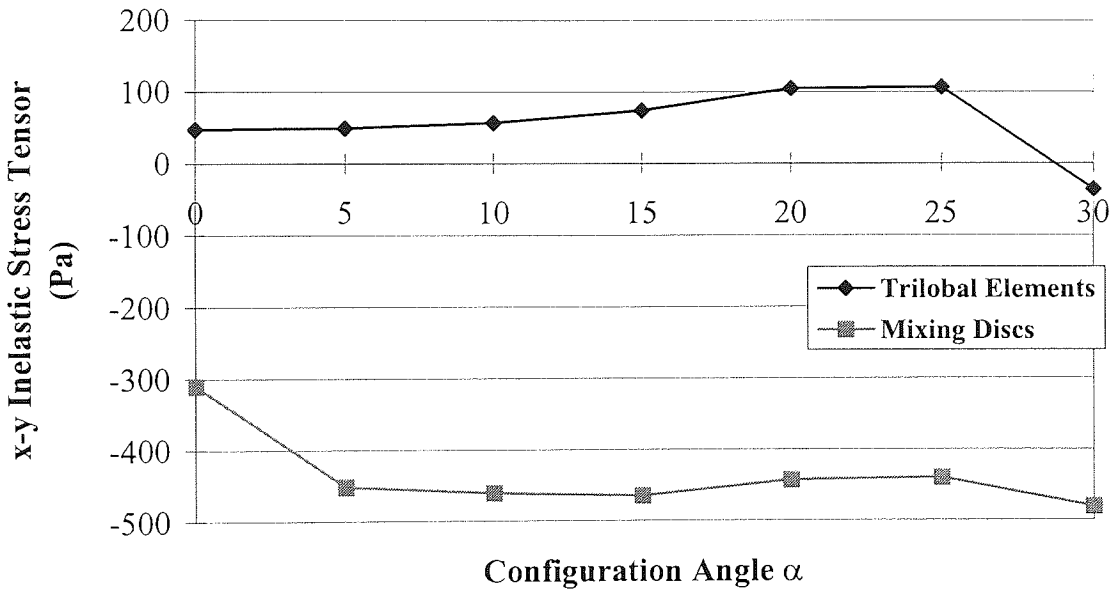

GRAPH 8-12 **2D Average Mixing Efficiency Values**

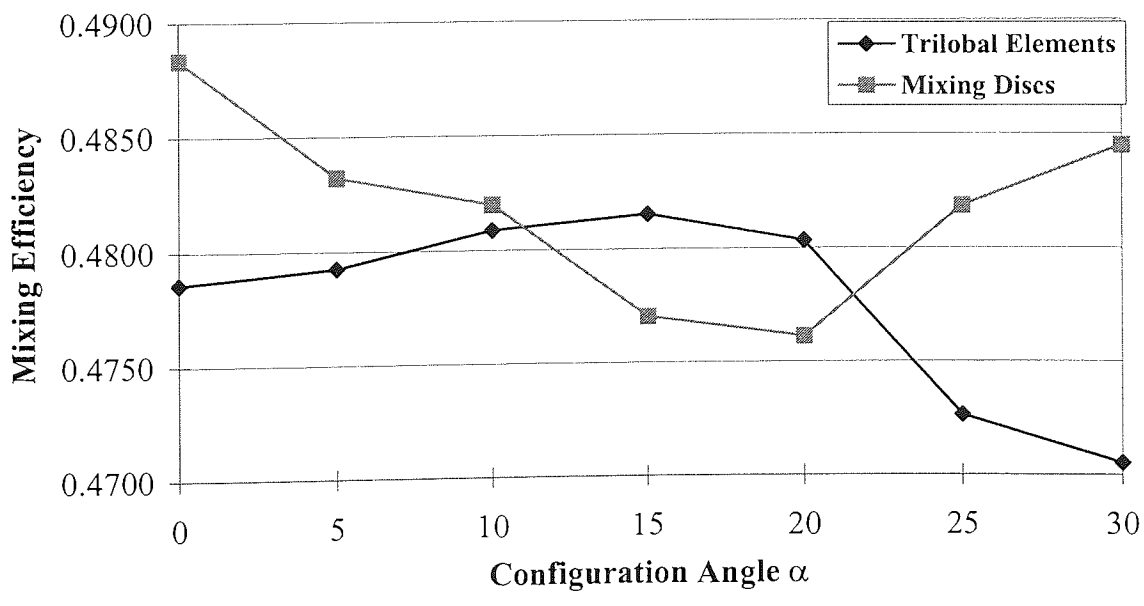

mixing depends on the smearing of material against the outer barrel wall for these two CICo-TSE mixing zones, variation of the degree of slip at the outer barrel wall was investigated. An arbitrary rotated configuration was chosen for both the mixing disc ($\alpha = 5°$) and trilobal element mixing zones ($\alpha = 15°$) and simulations were performed for both the non-slip case and for three values of the outer barrel slip. The values chosen for outer barrel slip employed within each simulation, were calculated as follows;

- If the angular rotational speed of each of the two mixing elements is given by Ω_r (assigned within the simulations as 2π rad sec^{-1} or 1 revolution sec^{-1}) and the outer barrel radius is given by R_s, (calculated to be 20.0075 mm for the Betol BTS40 CICo-TSE), then the tangential angular velocity component v_s at the outer barrel wall, is given by the following expression.

$$v_s = S\Omega_r R_s \qquad (8\text{-}1)$$

where S is some slip factor such that non-slip conditions apply when $S = 0$ and full slip conditions when $S = 1$ (full slip in reality would be meaningless, as this would imply free surface conditions). Thus the values of outer barrel slip investigated were for assigned values of $S = 0$, such that $v_s = 0$ (i.e. non-slip conditions) and of $S = 0.25$, 0.50 and 0.75 respectively.

The results obtained for the separate mixing disc and trilobal element rotated configurations investigated are given in Tables 8-4 and 8-5 respectively. It is evident from the results shown in these tables, that certain trends are followed as the degree of slip at the outer barrel wall is increased. These flow parameter trends are better represented graphically and the rationale for each is as follows;

- Average local shear rate values, depicted in Graph 8-13.
  The average local shear rate values for the mixing discs remain virtually constant as outer barrel slip is increased. The average values calculated for the trilobal elements, however, decrease linearly over the reducing slip range indicated. This suggests that smearing of material against the outer barrel wall, plays a significant role in the mixing mechanism exhibited by the trilobal elements. Colour contour plots showing regions where $\dot{\gamma} \geq 100$ sec^{-1} for the simulation results representing the four values of S investigated, are shown for the 2D mixing disc and trilobal element mixing zones in Figures 8-54 and 8-55 respectively. The reduction in the levels of shear realised at the outer barrel wall as slip is

TABLE: 8-4 2D Slip Results Table - Mixing Discs

Configuration ($\alpha°$)	Slip Coefficient S	Number of Structured Nodal Points	Shear Rate $\dot{\gamma}$ (sec^{-1})	Inelastic Stress Tensor T_{x-y} (Pa)	Mixing Efficiency λ
5	0.00	2905	46.71	-451.28	0.4832
"	0.25	"	46.10	-1159.62	0.4812
"	0.50	"	46.28	-1643.74	0.4627
"	0.75	"	46.76	-2056.57	0.4491

TABLE: 8-5 2D Slip Results Table - Trilobal Elements

Configuration ($\alpha°$)	Slip Coefficient S	Number of Structured Nodal Points	Shear Rate $\dot{\gamma}$ (sec^{-1})	Inelastic Stress Tensor T_{x-y} (Pa)	Mixing Efficiency λ
15	0.00	3642	69.48	74.40	0.4815
"	0.25	"	60.00	-237.85	0.4843
"	0.50	"	51.05	-571.97	0.4989
"	0.75	"	43.05	-1035.08	0.5402

GRAPH 8-13 **2D Slip - Average Local Shear Rate Values**

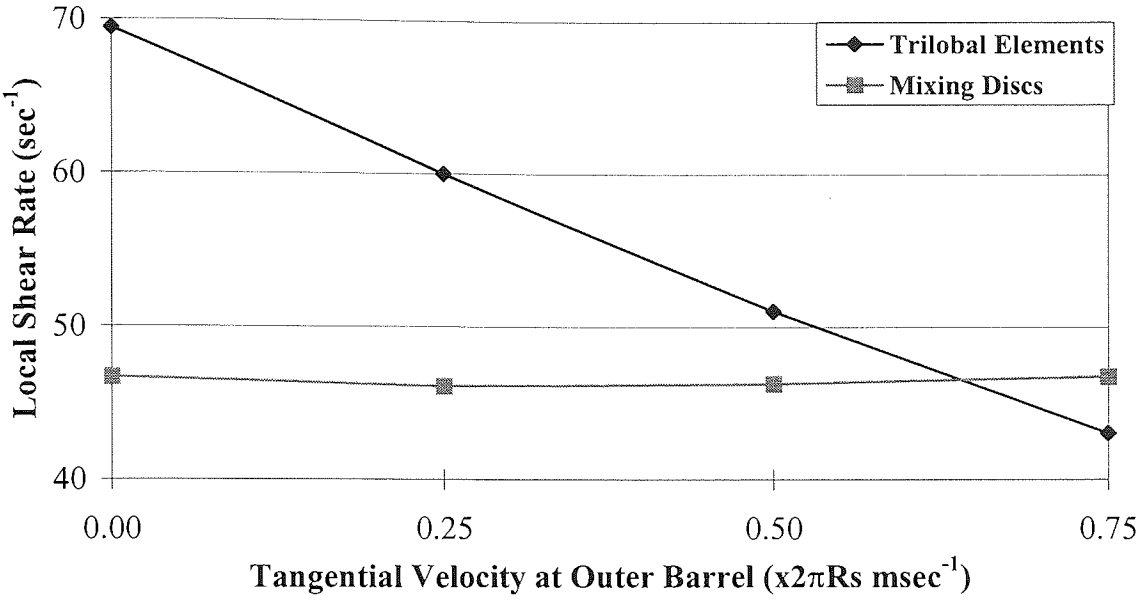

GRAPH 8-14 **2D Slip - Average Inelastic Stress Tensor Values**

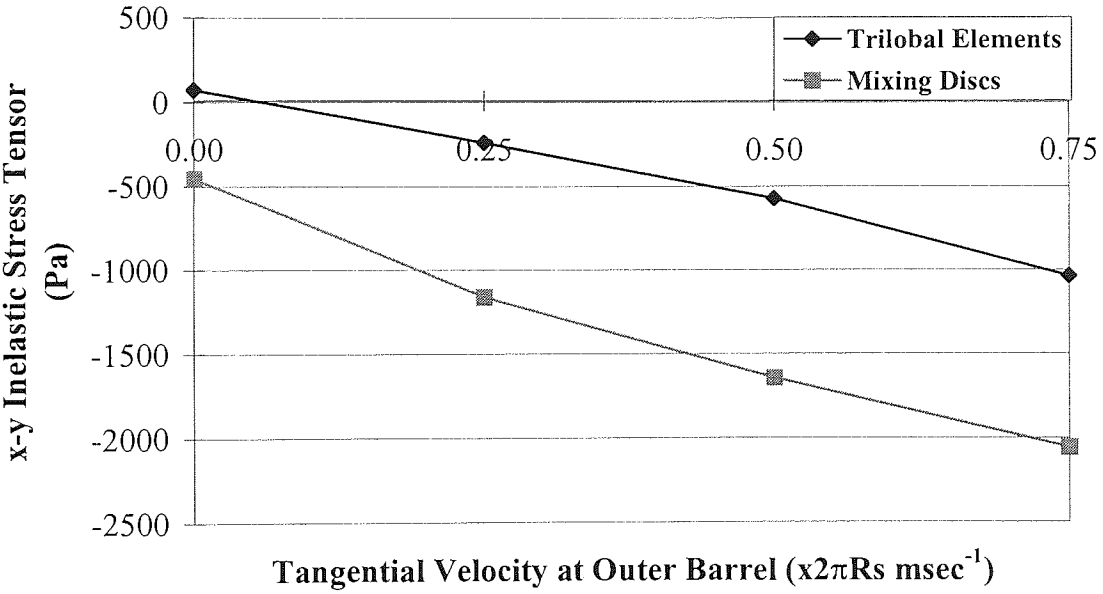

GRAPH 8-15 **2D Slip - Average Mixing Efficiency Values**

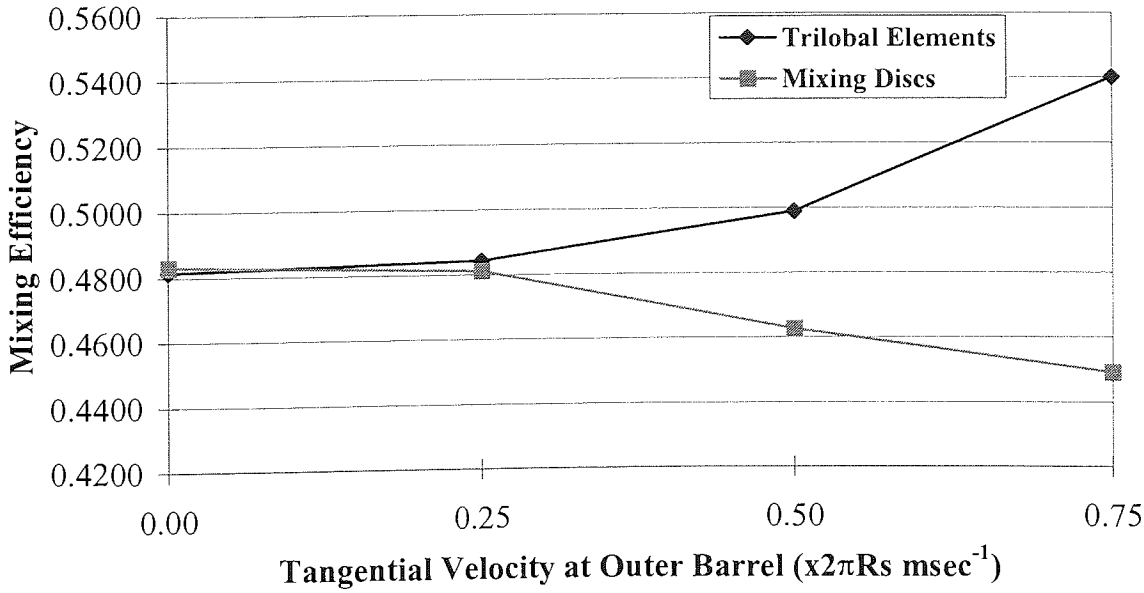

Figure 8-54:

Local Shear Rate Colour Contours ($\dot{\gamma} \geq 100\ sec^{-1}$) for 2D Representations of the Mixing Discs in the X-Y Plane, at the Rotated Configuration $\alpha = 5°$, for Differing Values of Outer Barrel Slip.

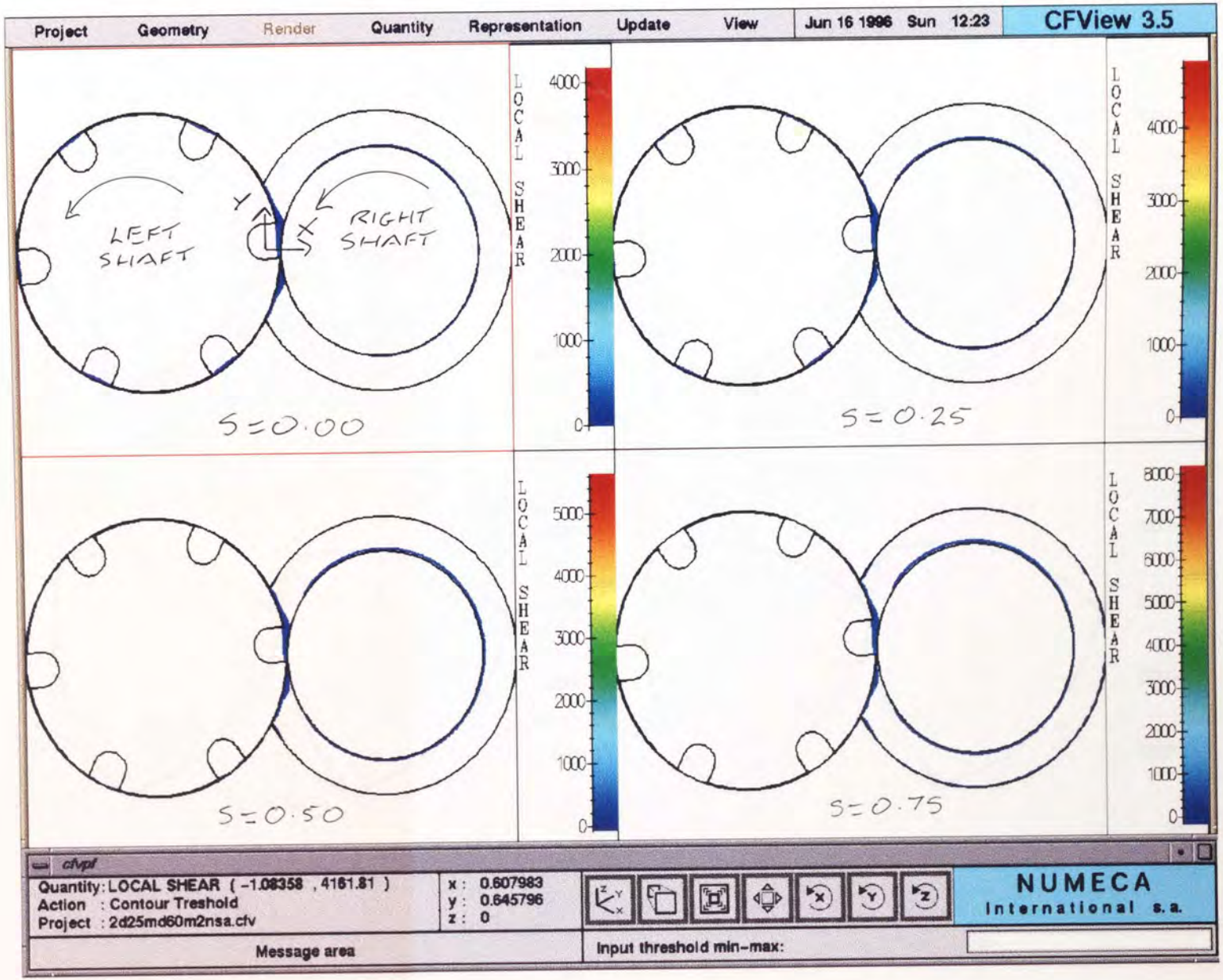

Figure 8-55:

Local Shear Rate Colour Contours ($\dot{\gamma} \geq 100\ sec^{-1}$) for 2D Representations of the Trilobal Elements in the X-Y Plane, at the Rotated Configuration $\alpha = 15°$, for Differing Values of Outer Barrel Slip.

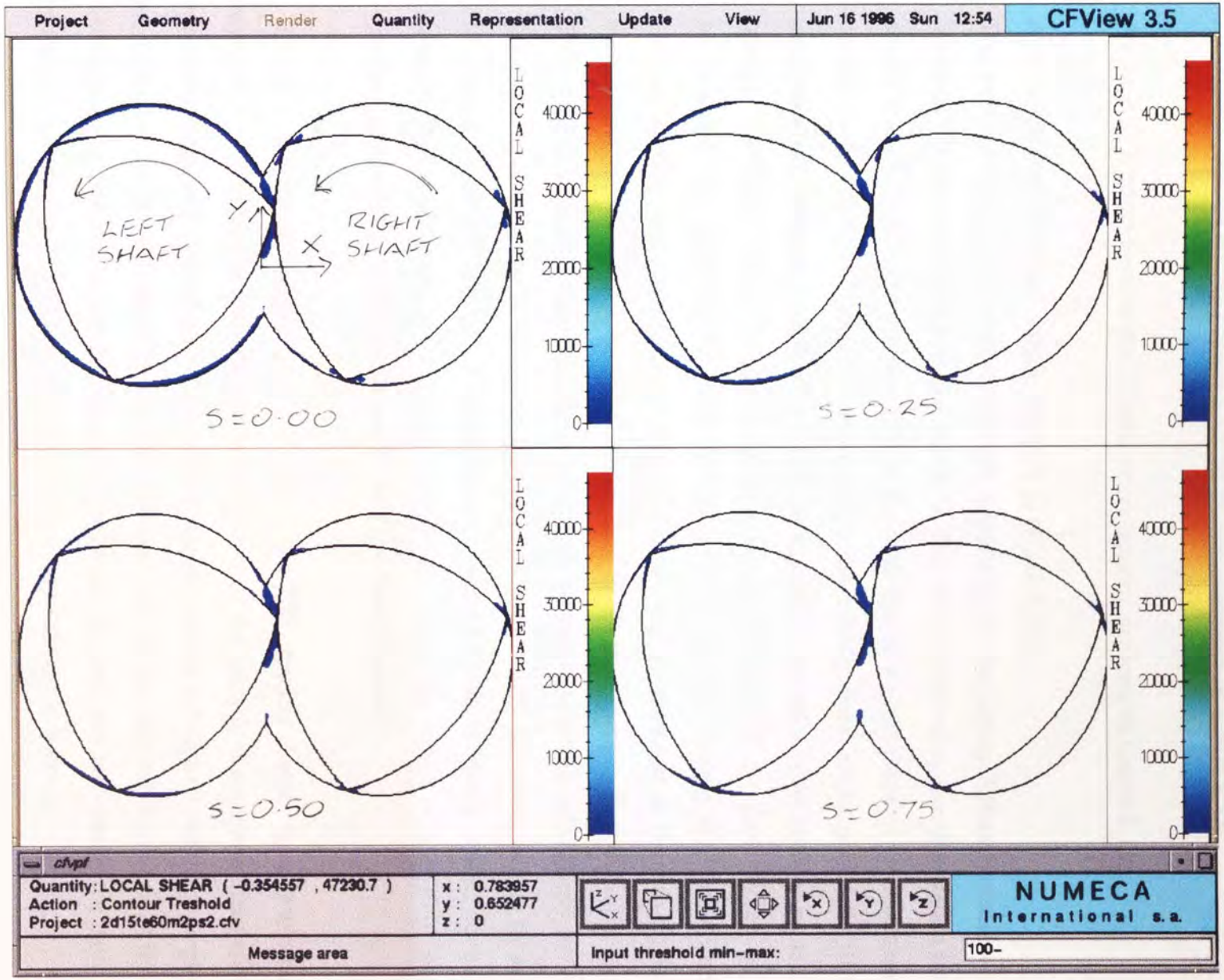

introduced, may be readily observed for the trilobal elements in Figure 8-55.

- Average X-Y component of the inelastic stress tensors, depicted in Graph 8-14.

- Average mixing efficiency values, depicted in Graph 8-15.
  The average mixing efficiency values are interesting in displaying different trends with increasing values of outer barrel slip factor, S. This may be related to the observation that, as slip is introduced at values over 25% at the outer barrel wall, material is predominantly rotated within the flow domain when mixed by the mixing discs, whilst material will be predominantly elongated when mixed with the trilobal elements. Colour contour plots for mixing efficiency values for the simulation results of each of the four values of S investigated, are shown in Figures 8-56 and 8-57 for the 2D mixing disc and trilobal element mixing zones respectively. As outer barrel slip is increased in the mixing disc simulations, the values of λ exhibited within each of the disc aperture flow domains $\rightarrow 0$. This trend corresponds to a situation where much greater magnitudes of vorticity |w| are generated in comparison to the values for rate of deformation |d|. However, as may be seen in Figure 8-57, for the 2D trilobal element mixing zone a much more complex phenomenon is observed. As outer barrel slip is increased, the values of λ exhibit larger gradients, especially within the domain of the right hand chamber.

The 3D simulations representing the two CICo-TSE mixing zones, were performed progressively. This meant that, for the investigation of the mixing discs zone, simulations representing one half pair of discs were solved and the results scrutinised before attempting the simulation of one full pair of discs. This was also true for the investigation of the trilobal element mixing zone where simulations were performed for one, two and then three pairs of elements respectively. The reasons for pursuing this approach are as follows;

- It is more advantageous to perform optimisation studies on smaller meshes (in this work the smaller meshes are typified by the half pair of mixing discs and the one pair of trilobal elements) and then to extrapolate those results to optimise the much larger meshes, than it is to perform optimisation studies on the large meshes directly. Due to the fact that the allocation of CRAY J90 CPU time for this research was both limited and valuable and that the meshes representing one pair of mixing discs and three pairs of trilobal elements could only be solved using the CRAY J90 supercomputer, optimisation of these large meshes could not have been achieved any other way.
- Trends may be examined as further pairs of mixing elements are added. For example,

Figure 8-56:

Mixing Efficiency Colour Contours for 2D Representations of the Mixing Discs in the X-Y Plane, at the Rotated Configuration α = 5°, for Differing Values of Outer Barrel Slip.

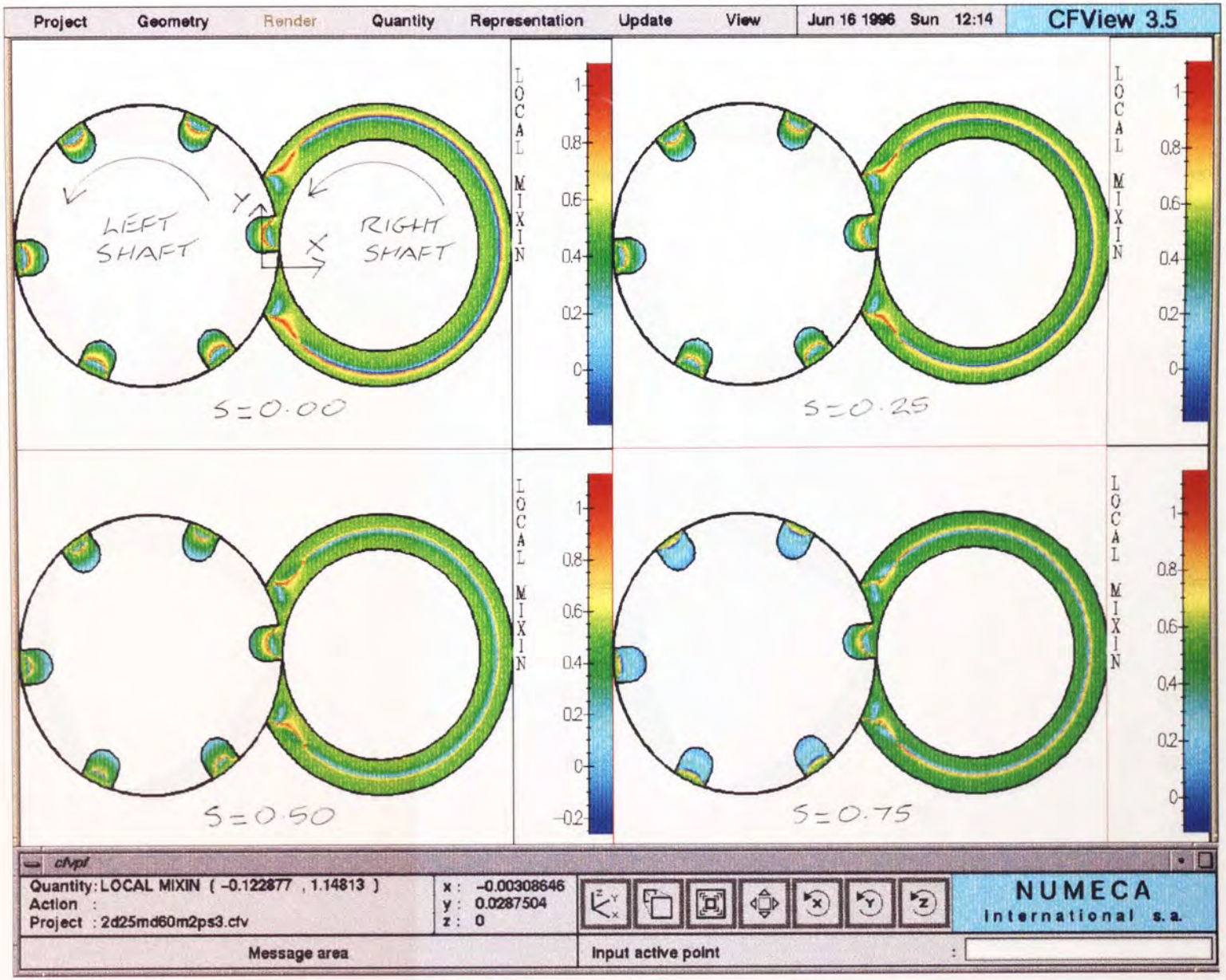

Figure 8-57:

Mixing Efficiency Colour Contours for 2D Representations of the Trilobal Elements in the X-Y Plane, at the Rotated Configuration α = 15°, for Differing Values of Outer Barrel Slip.

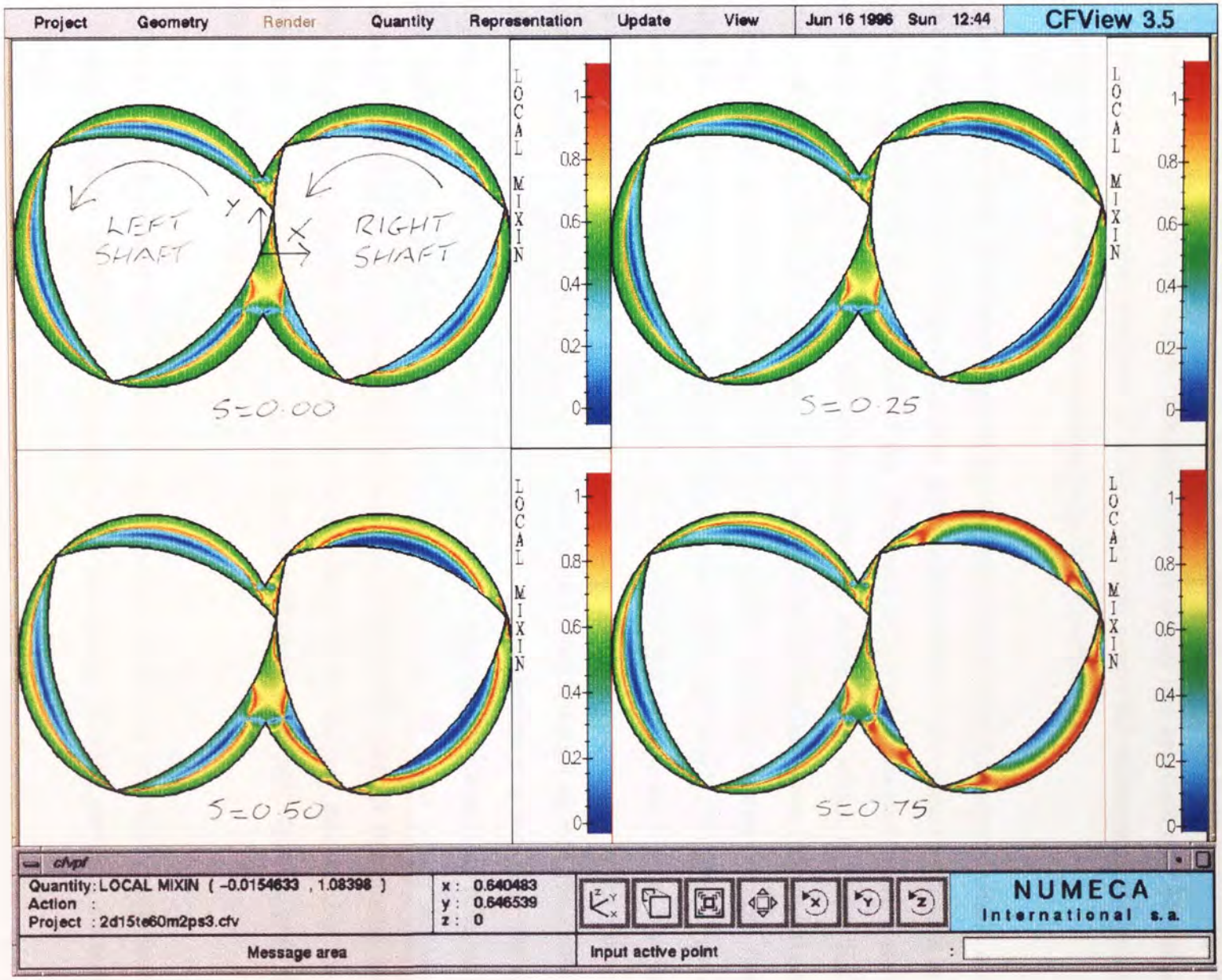

possible effects on mixing behaviour may be compared for a mixing zone containing two trilobal element pairs and a zone containing three. In theory this approach may be utilised to estimate the optimum numbers of mixing elements where the subsequent addition of elemental pairs would not improve mixing behaviour significantly.

Table 8-6 tabulates the number of nodal points, convergence criteria employed within each simulation, the number of iterations taken to solve each problem to the respective criteria and the various CPU times taken for each of the 3D mixing disc simulations performed. Results for the optimisation of one half pair of discs are also shown from which it was initially estimated that each of the meshes depicting the various rotated configurations for one full pair of discs, should possess approximately 8000 nodal points. However, as may be seen from Table 8-6, the three mixing disc meshes actually solved using the CRAY J90 supercomputer possessed approximately 6000 nodal points. The reason for the reduced mesh sizes was that the meshes containing 8000 nodal points would have generated temporary swap files of approximately 2.5 Gigabytes in size. For Polyflow version 3.4.6 installed on the CRAY J90 at RAL at the time of research, this size of temporary file generation was too large for the program to execute. Thus the three mixing disc meshes constructed were suitably reduced in size, until solutions were obtainable for the reduced number of nodal points assigned. Table 8-7 tabulates all the average flow parameters obtained for each of the mixing disc simulations performed. The procedure for optimisation of the mixing disc meshes, was performed by increasing the number of nodal points throughout each mesh domain, until the following two criteria were satisfied;

- The calculated average flow parameters, such as local shear rate and mixing efficiency, ceased to change significantly between meshes containing differing numbers of nodal points.
- The flow rate calculated at the outlet approached the value assigned at the inlet (i.e. for all simulations performed, inlet flow rate = 5.2×10^{-7} m^3 sec^{-1}, which corresponds to a feed rate of 25 g min^{-1}). If the domain volume is assumed to be constant and the simulated fluid incompressible, then by the conservation of mass, the flow rates at the inlet should match those obtained at the outlet. However, because the FEM is an approximate solution technique, discrepancies in the flow calculation do occur and these are partly accredited to the quality of the mesh being used. If these discrepancies are minimised or cancelled out completely, then this is an indication of how "good" the mesh being utilised actually is.

As may be seen from the optimisation study performed for the meshes representing one

TABLE 8-6

3D Results Table - Staggered Mixing Discs

Configuration ($\alpha°$)	Computer Used for Solving Problem	No. of Unstructured Nodal Points	Convergence Criteria for Main Problem [1]	No. of Iterations to Solve Main Problem	Total Time Taken to Solve Main Problem (sec)	Time per Iteration to Solve Main Problem (sec)	Time Taken to Solve for Post-Processing (sec)
Half Pair:	Silicon Graphics						
0	Indy Workstation	3644	$1x10^{-8}$	24	154779	6449	8888
15		3516	$1x10^{-8}$	25	123049	4922	7336
30		3680	$1x10^{-8}$	23	189065	8220	10262
0 [2]		1401	$1x10^{-8}$	-	-	-	-
15 [2]		1404	$1x10^{-8}$	-	-	-	-
30 [2]		1449	$1x10^{-8}$	-	-	-	-
30 [2]		2796	$1x10^{-8}$	-	-	-	-
One Pair:	CRAY J90						
0	Super-computer	5994	$1x10^{-3}$	9	46238 [4]	5138	113082
15	at RAL	5880	$1x10^{-3}$	20 [3]	90270 [4]	4514	79103
30		6186	$1x10^{-3}$	9	47763 [4]	5307	92235

NOTES:

1 Convergence criteria used for all post-processing was $1x10^{-8}$. All post-processing performed on the Silicon Graphics Indy Workstation.

2 Additional simulations performed as part of optimisation study.

3 Divergence occurred, periodic solution obtained. Best convergence 10^{-2} .

4 CRAY J90 computational times given are those for the total CPU time for solving each problem using four parallel processors simultaneously.

TABLE 8-7 **3D Results Table (Cont.) - Staggered Mixing Discs**

Configuration ($\alpha°$)	No. of Unstructured Nodal Points	Shear Rate $\dot{\gamma}$ (sec^{-1})	Inelastic Stress Tensor T_{x-y} (Pa)	Mixing Efficiency λ	Pressure Gradient (Pa)	Output [1] (10^{-7} m^3 s^{-1})
Half Pair:						
0	3644	50.48	249.04	0.5188	2932.27	5.30
15	3516	50.32	368.56	0.5188	2896.01	5.20
30	3680	49.88	344.03	0.5184	2957.09	5.21
0 [2]	1401	47.83	276.11	0.5210	-	5.41
15 [2]	1404	47.57	373.97	0.5204	-	5.22
30 [2]	1449	47.22	319.91	0.5188	-	5.22
30 [2]	2796	49.96	322.53	0.5187	-	5.22
One Pair:						
0	5994	56.76	398.19	0.5166	10832.37	5.30
15	5880	56.75	539.72	0.5175	13025.93	5.18
30	6186	56.23	464.00	0.5163	12481.08	5.21

NOTES:

1 Original volumetric flow rate at inlet = 5.20×10^{-7} m^3 s^{-1}.

2 Additional simulations performed as part of optimisation study.

half pair of discs, both of the above criteria have been satisfied (the number of nodal points were increased from approximately 1400 nodal points initially, to the final optimised amount of approximately 3500 nodal points).

Comparisons between the results obtained for both sets of rotated configurations for the half pair and full pair of discs, may be made from the graphs plotted in Graphs 8-16 to 8-18, which represent the average local shear rates, X-Y components of the inelastic stress tensor and mixing efficiency values respectively. The average local shear rates obtained for the meshes representing the full pair of mixing discs, as depicted in Graph 8-16, are much higher ($\approx$ 10 %) than those obtained for the meshes representing the half pair of discs. This is due to the presence of the separation volume between the two discs of the full pair arrangement, which generates high shear rate (the separation volume is absent from the meshes representing one half pair of discs). The average mixing efficiency results shown in Graph 8-18 demonstrate that, whilst the local shear rates obtained differ depending on the number of discs present, the average mixing efficiency values are approximately the same (i.e. independent of the number of discs utilised).

Table 8-8 shows the number of nodal points, convergence criteria employed within each simulation, the number of iterations taken to solve each problem to the respective criteria and the various CPU times taken for each of the 3D trilobal element simulations performed. As may be seen from Table 8-8, the number of nodal points assigned increased approximately linearly as a function of the number of trilobal element pairs contained within each mixing zone. However, doubling the number of nodal points from approximately 1000 to 2000 for meshes representing one and two pairs of trilobal elements respectively, does not necessarily signify a similar doubling in the CPU times taken to solve each flow problem. It was found that the CPU time needed to solve a flow problem on a mesh, is not dependent on the number of nodes contained within that mesh, instead it is given by the following expression;

CPU time (Computer Hardware Used)

$$= (\text{Constant}) \times (\text{No. of Flow Problem Variables}) \times (\text{Frontal Width}) \qquad (8\text{-}2)$$

where the constant in Equation (8-2) is computer hardware dependent (obviously CPU times will differ depending on the type of computer utilised). The frontal widths for all simulations performed are given in Appendices AM-AO for the single-flighted conveying screw element, mixing disc and trilobal element meshes used. Frontal widths depend upon the numbering arrangement of the finite elements assigned within the mesh (as described in Chapter 3) and not necessarily on the number of nodal points contained. Two identically constructed meshes containing the same number of nodal points may possess radically

GRAPH 8-16 **3D Average Local Shear Values - Mixing Discs**

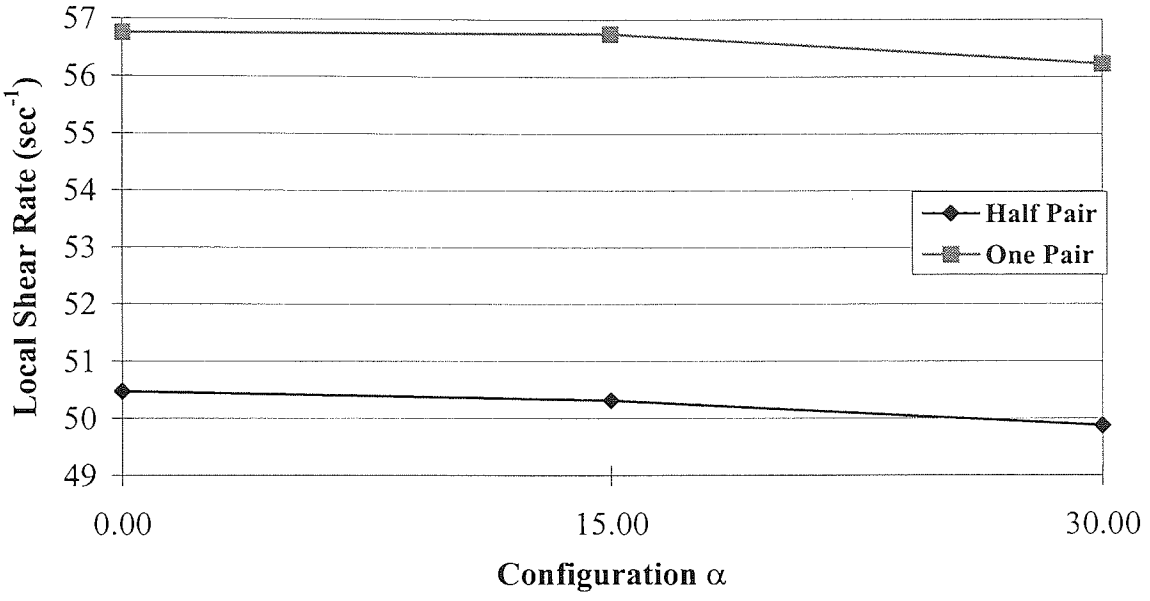

GRAPH 8-17 **3D Average Inelastic Stress Tensor Values - Mixing Discs**

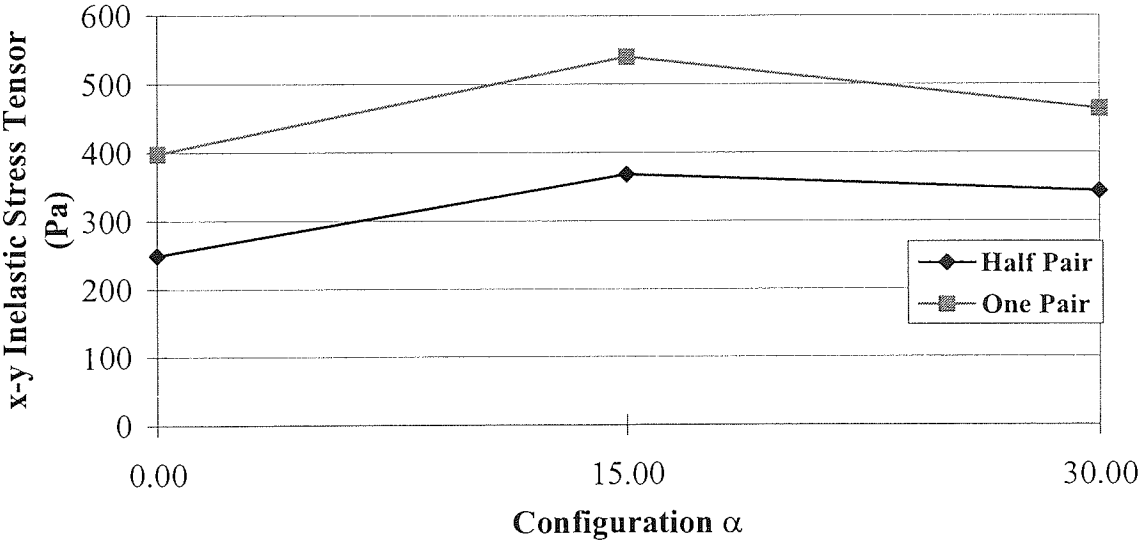

GRAPH 8-18 **3D Average Mixing Efficiency Values - Mixing Discs**

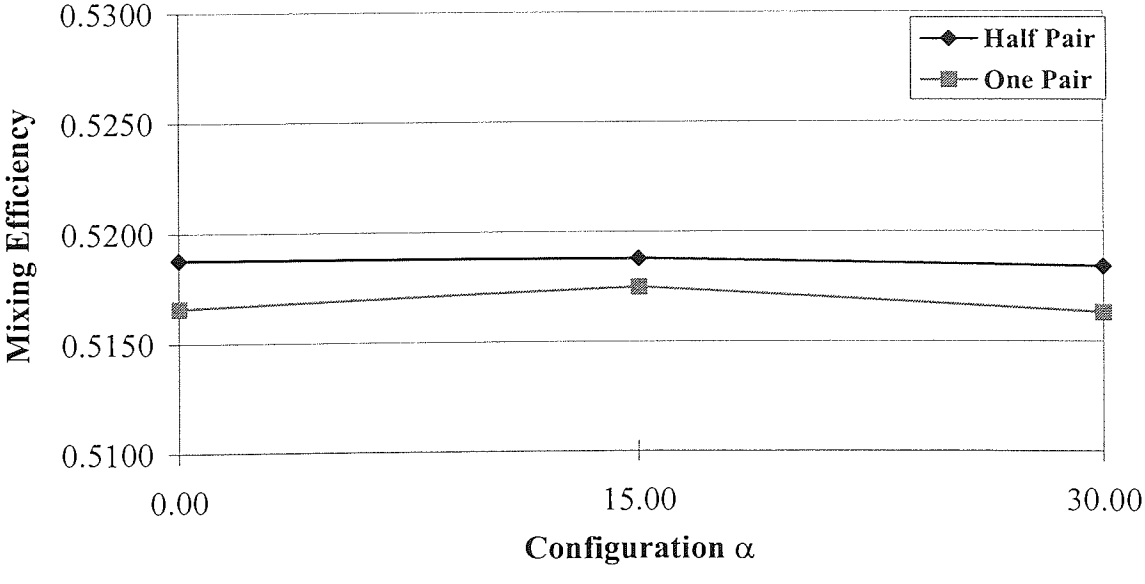

TABLE 8-8

3D Results Table - Trilobal Elements

Configuration ($\alpha°$)	Computer Used for Solving Problem	No. of Unstructured Nodal Points	Convergence Criteria for Main Problem [1]	No. of Iterations to Solve Main Problem	Total Time Taken to Solve Main Problem (sec)	Time per Iteration to Solve Main Problem (sec)	Time Taken to Solve for Post-Processing (sec)
One Pair:	Silicon Graphics						
0	Indy Workstation	1196	$1x10^{-8}$	23	18785	817	1724
15		1172	$1x10^{-8}$	24	21407	892	1807
30		1160	$1x10^{-8}$	22	14584	663	1087
15 [2]		2908	$1x10^{-3}$	9	74520	8280	17352
Two Pairs:	Silicon Graphics						
0	Indy Workstation	2094	$1x10^{-8}$	23	153610	6679	11638
15		2278	$1x10^{-8}$	24	271354	11306	16541
30		2084	$1x10^{-8}$	22	116267	5285	8665
Three Pairs:	CRAY J90						
0	Super-computer	3024	8 Iterations	8	13818 [3]	1727	36172
15	at RAL	3860	6 Iterations	6	29240 [3]	4873	64858
30		3008	$1x10^{-6}$	15	20972 [3]	1398	22658

NOTES:

1 Convergence criteria used for all post-processing was $1x10^{-8}$. All post-processing performed on the Silicon Graphics Indy Workstation.

2 Additional simulation performed as part of optimisation study.

3 CRAY J90 computational times given are those for the total CPU time for solving each problem using four parallel processors simultaneously.

different frontal widths. Inspection of Appendices AN and AO, indicates that the trilobal element meshes possess larger frontal widths than those of the mixing discs, for meshes which contain approximately the same amount of nodal points. In addition, the CPU times taken to solve each iteration for flow problems using meshes representing two trilobal element pairs, were approximately nine times greater than for those meshes representing one pair of elements. Thus, due to the prohibitive increases in the CPU times taken to solve subsequent flow problems on meshes constructed to accommodate successive elemental pairs, the decision was taken to use trilobal element meshes within this study that were not fully optimised. As may be seen from Table 8-8, only one optimisation study was performed for the mesh representing one pair of elements at a rotated configuration of $\alpha = 15°$. This optimised mesh contained approximately 3000 nodal points. Extrapolation of this distribution of nodal points to those meshes representing three pairs of elements, meant that to achieve optimisation, each mesh would need to contain of the order of 9000 nodal points. As outlined previously when describing the mixing discs results in Chapter 7, meshes containing this number of nodal points would not have been soluble using Polyflow version 3.6.4.

Table 8-9 tabulates all the average flow parameters obtained for each of the three sets of trilobal element simulations performed. As may be seen from this table, the average local shear rate and mixing efficiency values obtained for the two meshes representing one pair of trilobal elements (meshes containing 1172 and 2908 nodal points respectively) do not differ significantly. The addition of nodal points however, predicts a value for the volumetric output which is more consistent with the volumetric input. Evidence for the periodic pumping action of the trilobal elements may be further seen in the results obtained for the average shear rate values. The effect is more marked for mixing zones containing two or three trilobal element pairs. The average local shear rates obtained for meshes representing one, two and three pairs of trilobal elements, are depicted in Graph 8-19. Two conclusions may be drawn from the lines plotted in this graph.

- Increasing the mixing zone from one to two pairs of trilobal elements increases the average local shear rates obtained over the partial mixing cycle. A further increase in the number of trilobal element pairs does not significantly alter the average shear rates achievable.
- The omission of the collar volume between element pairs has almost certainly reduced the values of the shear rates predicted. Inspection of the results for the mixing disc zone in Chapter 7 for one half pair (no collar) and one full pair of discs (separation volume considered) supports this argument.

Kneading blocks are elements with two tips to each lobe, as shown in Chapter 1, which

TABLE 8-9

3D Results Table (Cont.) - Trilobal Elements

Configuration ($\alpha°$)	No. of Unstructured Nodal Points	Shear Rate $\dot{\gamma}$ (sec^{-1})	Inelastic Stress Tensor T_{x-y} (Pa)	Mixing Efficiency λ	Pressure Gradient (Pa)	Output [1] (10^{-7} m^3 s^{-1})
One Pair:						
0	1196	45.77	785.20	0.5601	2366.86	5.35
15	1172	45.65	793.34	0.5592	2500.71	5.41
30	1160	44.64	743.23	0.5581	2383.62	5.33
15 [2]	2908	45.86	820.84	0.5590	-	5.27
Two Pairs:						
0	2094	48.19	990.28	0.5428	8672.82	5.22
15	2278	49.08	1183.20	0.5426	10527.22	6.92
30	2084	46.92	975.02	0.5414	7287.01	5.32
Three Pairs:						
0	3024	48.33	1102.49	0.5520	14665.38	5.22
15	3860	49.78	1348.71	0.5531	17704.51	8.37
30	3008	46.74	998.76	0.5529	11864.22	5.31

NOTES:

1 Original volumetric flow rate at inlet = 5.20 x 10^{-7} m^3 s^{-1}.

2 Additional simulations performed as part of optimisation study.

GRAPH 8-19

3D Average Local Shear Values - Trilobal Elements

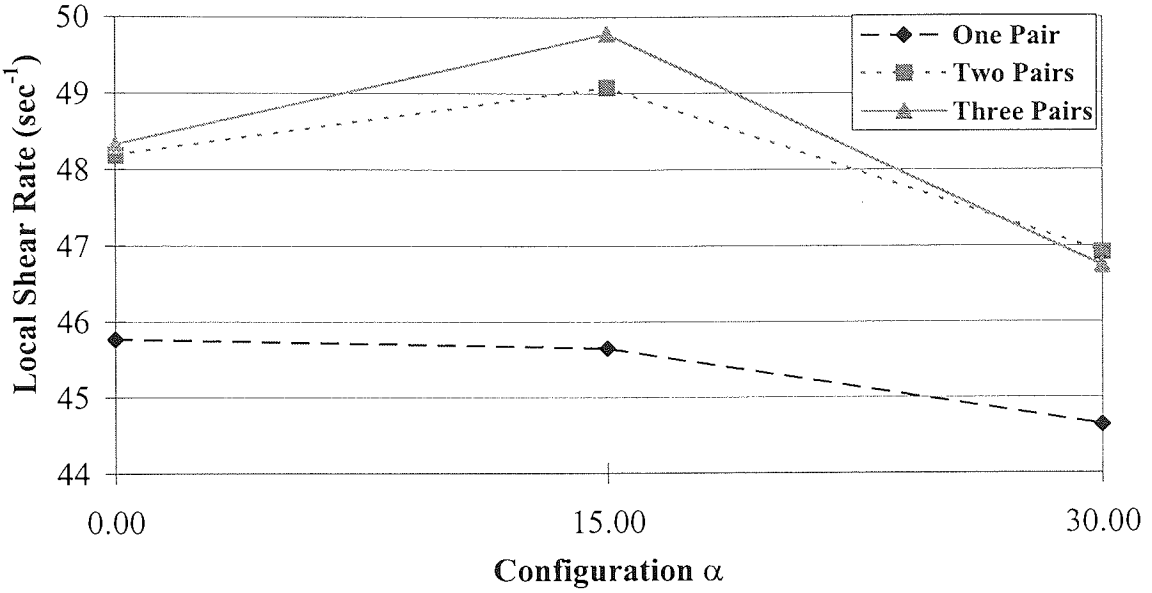

GRAPH 8-20

3D Average Inelastic Stress Tensor Values - Trilobal Elements

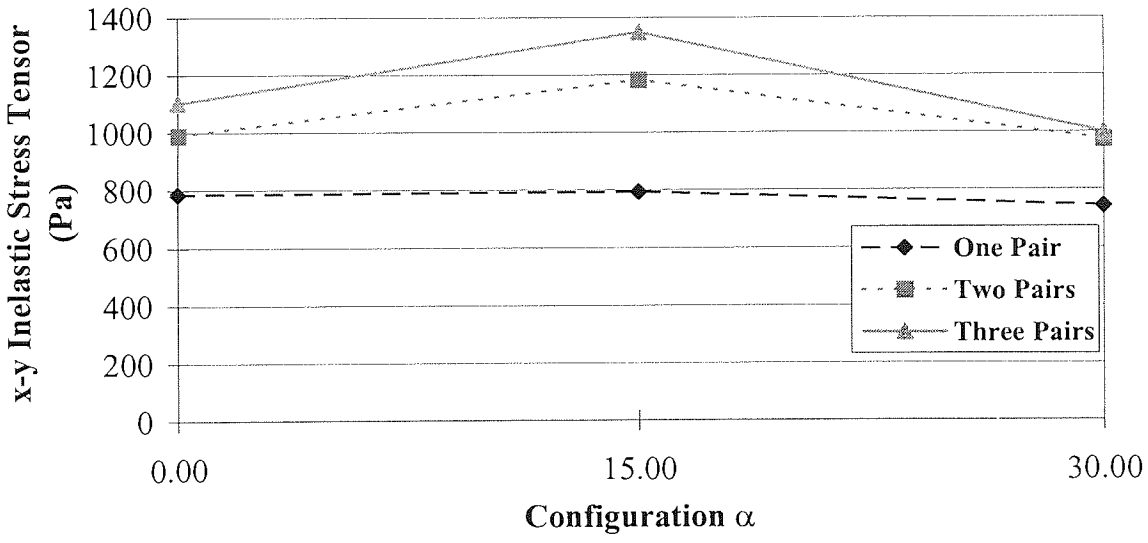

GRAPH 8-21

3D Average Mixing Efficiency Values - Trilobal Elements

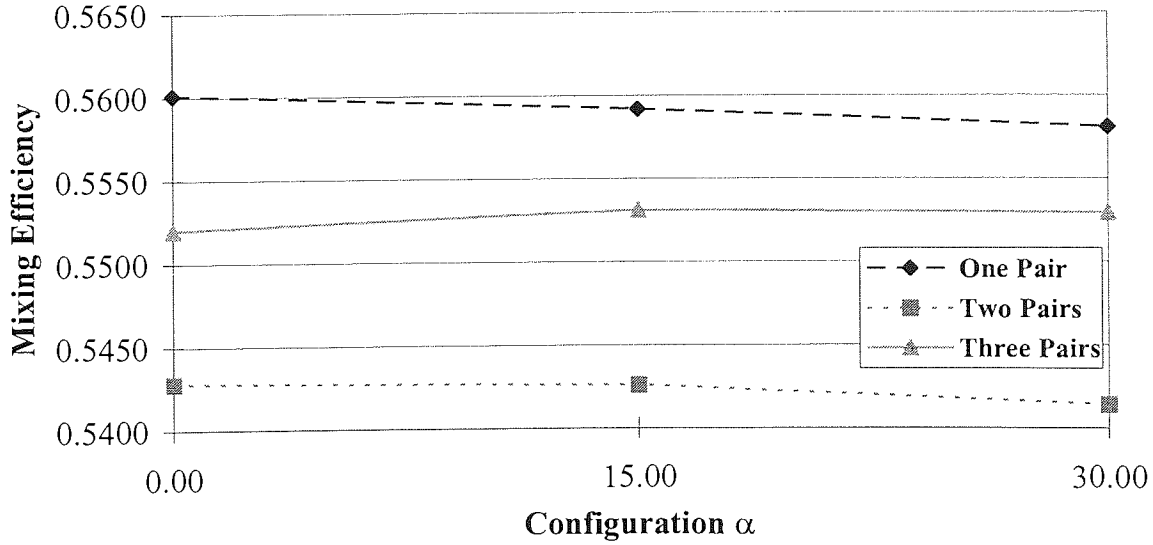

impose dispersive mixing mechanisms on the viscous melt and Manas-Zloczower [57-58], Kiani [51, 77] and Kaylon [73-74] have all studied viscous fluid flow within the CICo-TSE kneading block mixing zone. However, each of these papers make no mention as to whether their respective simulations have included the collar volume between each block or not. Manas-Zloczower [57-58] declares average shear rate values for the partial mixing cycle of a kneading block zone containing five pairs of kneading blocks configured at a successive 45° forward (positive displacement) stagger angle. The values reported are of the order of approximately 90 sec^{-1}. These values are much higher than those calculated for the trilobal element mixing zone in the neutral arrangement reported within this thesis. It is difficult to conclude, however, whether these discrepancies are due to the different number of tips possessed by each respective mixing element, the different stagger angle arrangements of each mixing zone, the different number of element pairs investigated or whether the meshes used within Manas-Zloczower's paper have taken into account the collar volumes between each kneading block.

The average X-Y components of the inelastic stress tensor and mixing efficiency values are shown in Graphs 8-20 and 8-21 respectively. The average mixing efficiency values reported within Graph 8-21 display a trend that is quite surprising. Firstly, the average mixing efficiency values, for each of the three mixing zone arrangements investigated, remain virtually constant as the trilobal pairs rotate. This result is in stark contrast to that obtained for the average shear rate and x-y component of the inelastic stress tensor values calculated (as shown in Graphs 8-19 and 8-20), which suggests that a periodic effect is being exhibited. Furthermore, an additional observation may be drawn from the average mixing efficiency values shown in Graph 8-21. The approximate magnitude of the average values obtained for configuring one pair of trilobes is 0.559 and when a further pair of trilobes is introduced into the calculation, the average values obtained reduces to approximately 0.542. However, introduction of an additional pair of trilobes to give a total of three pairs, increases the approximate magnitude of the average values to 0.553. The manner of the average mixing efficiency values obtained, suggest that configuring pairs of elements at successive stagger angles of 60°, so as to obtain a neutral arrangement of elements, causes the introduction of successive regions which possess alternate high and low average mixing efficiency values. For example, for meshes representing one pair of trilobes, the average mixing efficiency values obtained over the areas representing both the inlet and outlet planes, will, it is assumed, be the same and so let this value be known as x for all rotated configurations. The average mixing efficiency value obtained from the volume occupied by this trilobal pair, however, will be different, so we will let this value be known as y for all rotated configurations. Thus, for the mixing zone containing one pair of trilobes, we can propose the following relationship;

$$\frac{2x + y}{3} \approx 0.559 \tag{8-3}$$

What is found though, for introducing the second pair of trilobes arranged at a stagger angle of 60° into the simulation, is that the average mixing efficiency values obtained over the entire domain are reduced. Therefore, it is assumed that the average values in the volume occupied by this second pair are different to those obtained within the domain occupied by the first trilobe pair and we will let this value be known as z for all rotated configurations. Hence it follows that;

$$\frac{2x + y + z}{4} \approx 0.542 \tag{8-4}$$

Introducing a third pair of trilobes into the mixing zone at a stagger angle of 60°, creates a geometry whereby this third pair of trilobes is of an identical arrangement to that of the first pair of trilobes (this is illustrated within Figure 8-4). Thus, the average mixing efficiency values obtained within the domain occupied by the third pair of trilobes will be the same as those obtained within the domain occupied by the first pair (i.e. a value of y for all rotated configurations). So it follows that the average values over the entire flow domain will increase in value.

$$\frac{2x + 2y + z}{5} \approx 0.553 \tag{8-5}$$

These simple algebraic Equations 8-3 to 8-5, may be solved to yield values for x, y and z, thus giving a predictive measure of average mixing efficiency value within the domain, dependent upon the number of trilobal pairs present. However, it must be stressed that the simulations presented within this chapter, have only been performed for up to three trilobe pairs and it would thus be most advisable to perform further simulations in the future for zones containing more trilobal pairs before any firm conclusions may be drawn.

9 CONCLUSIONS

The work outlined in this thesis has been concerned with the prediction and verification of viscous melt flow through the various sections of the Betol BTS40 CICo-TSE and the following issues have been described;

- The simulation of viscous melt flow has been modelled and predicted using the commercial CFD package Polyflow, which employs the FEM. Polyflow was chosen because of its specific application to modelling rheologically complex fluid flow in complicated domains such as those found in the various sections of a CICo-TSE. A review of other commercially available CFD packages was also undertaken.
- The verification of some of the predictions generated by using Polyflow was achieved, with limited success, by the utilisation of a mechanical CICo-TSE model possessing transparent outer barrel casings. This model has been described and its usefulness and limitations outlined. Results are presented for the processing, at room temperature, of various coloured viscous "Playstuff" clay samples, which has enabled the clear visualisation of some of the mixing patterns exhibited.

The specific regions of the Betol BTS40 CICo-TSE which have been investigated in this work, are listed as follows;

- Single-flighted conveying screw elements.
- Staggered mixing disc zone.
- Trilobal element mixing zone.

The investigation of viscous melt flow through each of these regions by the utilisation of CFD, has been achieved by a combination of steady state and time-dependent methods. A summary of how the investigation of each CICo-TSE region was undertaken and a brief resume of the results obtained, are given as follows;

- Single-flighted conveying screw element section.

A description of the various possible routes for viscous melt flow through the CICo-TSE screw elements has been given. Of these possible routes, cross channel flow and flow through the intermeshing screw nip region were investigated and the results presented. The ideal rheological behaviour for polypropylene characterised by a power law model constitutive equation was used. For the 24 mm pitched, single-flighted conveying screw elements, cross channel flow for a Newtonian and power law fluid has been presented. Cross channel flow

within the CICo-TSE screw elements was assumed to be approximately the same as SSE channel flow, but only for material which is located away from the screw nip region. The results for the prediction of cross channel flow, were obtained by time-dependent schemes and the utilisation of two of these schemes were assessed. Visualisation of cross channel flow was achieved computationally and experimentally by monitoring a deforming interface between two viscous fluids during processing and some degree of correlation was achieved. Analytical solutions to the prediction of velocities and shear at different dimensionless heights within the screw channel for the Newtonian fluid were given.

Screw nip regional flow was investigated computationally by the use of the steady state method. It has been found that significant fluid reorientation occurs due to the design and location of the intermeshing screw flights. The reasons why deforming interfacial flow through the screw nip region could not be predicted using Polyflow, have been given.

- Staggered mixing disc zone.

Results for the investigation of viscous melt flow through a pair of staggered mixing discs in the in-line aperture configuration have been presented. The results have been obtained by using unstructured meshes containing up to 7000 nodal points, with the simulation problems being solved using the CRAY J90 supercomputer at RAL. To overcome the problem of the time dependent flow boundaries as the respective elements rotate about their fixed axes, incremental sequential geometries were selected so as to represent a time sequence of the process. Assuming steady state, isothermal conditions and ignoring the effects of inertia, the overall process was deduced from the results obtained separately for successive sequential geometries. Due to the symmetry of the mixing disc zone, three rotated states were investigated. Comparisons have been made for the results obtained from the investigation of one pair of discs, containing a separation volume between each disc, and from those obtained for the simulation of a half pair of discs. It has been found that the inclusion of the separation volume adds significantly to the shear levels predicted and to the degree of forward and back mixing behaviour. It has also been found that as the discs rotate, flow behaviour in terms of shear and mixing characteristics remain steady. More work, however, is needed to investigate mixing behaviour within zones containing more than one pair of discs and on mixing zones which are configured in the off-line aperture arrangement.

- Trilobal element mixing zone.

The same steady state method as described for the mixing disc zone, was applied to the simulation of melt flow through a trilobal element zone containing three pairs of elements arranged in the neutral configuration, with a stagger angle of 60° used between consecutive

trilobal element pairs. Due to the fact that the separation volume between consecutive axial pairs of trilobes is very small and that the probability of material residing between trilobes on the same shaft is very low, it was assumed that the separation volume could be neglected. It was found from the CFD simulations that as the trilobes rotate around their central axis, a periodic pumping effect is exhibited. The simulations also confirmed that the trilobes configured in the neutral arrangement exhibit a maximum leakage effect, whereby equal amounts of material flow in both the forward and backward directions. The behaviour of viscous melt within other trilobal arrangements was discussed and these different arrangements should be investigated in future work programs.

Average values for mixing efficiency, shear rate and shear stress were determined for each of the three rotated states examined, for both CICo-TSE mixing zones. A comparison analysis was undertaken to contrast the flow fields exhibited by the mixing disc and trilobal element zones and marked differences were found. The effect of fluid slip at the outer barrel wall was investigated for 2D meshes pertaining to each of the two mixing zones. It was found that the mixing levels predicted for the trilobal elements, is directly linked to the degree of slip assigned, however, for the mixing discs the value of fluid slip at the outer barrel wall has a negligible effect on the shear levels predicted.

9.1 Future possible work

As stated in Section 1.8, there are some limitations of using CFD in the simulation of real life flow problems, such as those posed by processing rheologically complex fluids within the CICo-TSE. These limitations may be grouped into the following two categories;

- Incorporation of all real life flow conditions into the same flow calculation

As stated previously, the flow problems investigated within this work were simplified by the utilisation of a set of carefully considered assumptions and this was done for the following two reasons. Firstly, by considering steady state, isothermal conditions, within fully filled elements for a single, generalised Newtonian fluid, the probability of obtaining converged solutions to the flow problems specified was quite good. Secondly, the computer memory requirements and the CPU times needed to solve these simplified flow problems, were much less than those requirements needed for more complex flow problems, especially those involving viscoelastic fluids. Real life flow processes within the CICo-TSE, however, typically involve viscoelastic, multi-component, multi-phased reacting species, processed under complex, partial fill, non-isothermal flow conditions. It would be highly advantageous to be able to specify all of these parameters for solution, if it were known that a converged

solution would be attainable.

- Consideration of the entire CICo-TSE flow domain

The results presented in this thesis, and in some of the literature described, are for small, discrete sections of the total CICo-TSE configuration. Sophisticated screw configurations utilised in certain complex REX processes may contain a combination of many modular screw sections - which act to either feed, compress, devolatilize or meter the viscous matrix - several mixing sections, each of which may possibly utilise different types of mixing element and, depending on the product form, a complex shaped die. Ideally the whole CICo-TSE domain, irrespective of size, should be represented within the same simulation.

At this stage in the development of both CFD and of computer hardware, which is of equal importance, the simulation of the flow fields within the CICo-TSE may only be obtained for simplified flow problems within discrete machine sections. Whilst simplified simulations, such as those outlined in this thesis do give useful insights into mixing behaviour within the CICo-TSE, one of the eventual goals of using CFD should be for the full simulation of any real life CICo-TSE process without restriction of either flow conditions, fluid rheology, or size and complexity of the flow domain. It is difficult to speculate when a CFD package, such as Polyflow, could be used to simulate an extrusion process as a whole, from the introduction of the powdered or pelletised feedstock to the final extrusion of a complex die profile. Instead it would be far more instructive to outline immanent and near future developments as regards the improvement of Polyflow and, in addition, to describe very recent, relevant, research developments by other workers.

In July of 1996, Polyflow S.A. released version 3.5 of its software package. This release gave the User the opportunity to use many advanced features and to model new flow concepts that were previously unavailable. A summary of these new Polyflow features is given as follows;

- The Polydata menu system has been converted to a GUI based system. The conversion to GUI greatly assists the User as it is now more straightforward to use Polydata 3.5 for the creation of data files. In addition, the full visualisation of a mesh whilst a data file is being created, is now provided. This type of facility is advantageous for, amongst other things, identifying boundaries whilst applying conditions.
- A new flow analyser called Polystat has been installed. Polystat is an interactive post-processor analyser which performs quantitative statistical analysis on a User defined set of trajectories obtained from a flow simulation. One of its benefits for this particular

work is that it may be used to plot, at different time intervals, the dispersion of particulates in a viscous processing domain such as the CICo-TSE.

- A new reactive systems module. This ability to analyse and predict properties from systems involving chemically reacting species, may be applied for the simulation of many process applications, including REX. It would thus be advantageous to use this module in future work programs, to investigate REX within the various sections of a CICo-TSE. Some of the reactive systems module's other potential applications include, chemical foaming, polymer ageing, tire curing and thermosets.

Other areas of research involving further aspects of the simulation of viscous flow within the various sections of a CICo-TSE, that have not been investigated in this particular research program but have been investigated by other workers, include the following subjects;

- Non-isothermal analysis
- Simulation of viscoelastic fluids.
- Modelling the conveying of melting particles (such as in the feed section).

Non-isothermal simulations involving non-Newtonian fluid flow within the CICo-TSE, have been published. However, White and Chen [115] explicitly point out that while simulation of non-isothermal flow in SSEs has been investigated since the 1960's, non-isothermal studies for TSEs are few. Their approach for analysis is to calculate heat build-up through a CICo-TSE barrel, by presuming each element to be isothermal and then, starting at a predefined element, calculate a temperature rise associated with that element and extrapolate stepwise for all other elements. Min and Fukuoka [116] use the FAN method to simulate non-isothermal flow for a non-Newtonian fluid in a non-intermeshing, counter-rotating TSE, however, a very interesting paper by Chiruvella *et al.* [117] gives results for the simulation of fluid flow and heat transfer in a CICo-TSE by means of the finite volume method. The reason why this paper stands out, is for its use of the finite volume method for simulating viscous fluid flow and they achieve results for flow through the screw nip region by the use of a crude 2D "V" shaped mesh.

The amount of papers that investigate the simulation of the flow of viscoelastic fluids in processing devices such as a CICo-TSE are few, because to achieve the successful simulation of viscoelasticity on meshes which are complex, would be very demanding. Loh *et al.* [118] explain that poor solutions of numerical simulations at a contraction have often been attributed to the numerical scheme used, however, the solution of a numerical simulation is also highly dependent on the constitutive equation used. In their paper they illustrate results

for various viscoelastic fluids through a 4:1 die exit using the FEM. Finally, some papers have been published on the examination of melt conveyance within complex processing devices. Carrot *et al.* [119] describe a technique for modelling the conveying of solid polymer in the feed zone of a CICo-TSE. They achieve their results by an approach which is commonly used for SSEs, but with modification to take account of the special geometry of the CICo-TSE screw elements. Potente *et al.* [120] also describe a technique which models solid melt flow within both a SSE and TSE, for the purpose of designing extruder elements.

REFERENCES

1. Tzoganakis, C., Reactive Extrusion of Polymers: A Review, *Adv. Polym. Tech.*, **9**, 4, p321-330 (1989).
2. Jackson, S. M. and Dreiblatt, A., Application of Twin Screw Extruders for Reactive Processing, *Plant/Operations Prog.*, **9**, 4, p220-225 (1990).
3. Todd, D. B., Consider Reactive Extrusion, *Chem. Eng. Prog.*, 8, p72-74 (1992).
4. Scott, G. and Al-Malaika, S., *US Patent 4,956,410* (1990).
5. Scott, G. and Al-Malaika, S., *US Patent 5,382,633* (1995).
6. Scott, G., Al-Malaika, S. and Sheena, H. H., *Int. Patent appl. No PCT/Gb 96/01380* (1996).
7. Betol Machinery Limited, 187 Camford Way, Sundon Park, Luton, Bedfordshire, LU3 3AN, England.
8. Cheng, J. J. and Manas-Zloczower, I., Hydrodynamic Analysis of a Banbury Mixer - 2D Flow Simulations for the Entire Mixing Chamber, *Polym. Eng. Sci.*, **29**, 15, p1059-1065 (1989).
9. Morton-Jones, D. H., Polymer Processing, Chapman and Hall, London and New York (1989).
10. Rauwendaal, C., Polymer Extrusion, Hanser, New York (1986).
11. Illing, G., Direct Extrusion of Nylon Products From Lactams, *Mod. Plas.*, 8, p70-76 (1969).
12. Martelli, F., Twin Screw Extruders - A Separate Breed, *SPE Journal*, **27**, 1, p25-30 (1971).
13. Mack, W. A. and Herter, R., Extruder Reactors for Polymer Production, *Chem. Eng. Prog.*, **72**, 1, p64-70 (1976).
14. Hornsby, P. R., Design and Application of a Laboratory Twin-Screw Compounding Extruder, *Plas. Comp.*, 4, p65-71 (1983).
15. White, J. L., Twin Screw Extrusion: Technology and Principles, Hanser Publications, New York (1990).
16. Manas-Zloczower, I. and Tadmor, Z, Mixing and Compounding of Polymers; Theory and Practise, Hanser Publishers, Munich (1994).
17. Werner and Pfleiderer, a Company of the Krupp Group, Theodorstrasse 10, D-70469 Stuttgart, Germany.
18. Eise, K., Herrmann, H., Jakopin, S., Werner, H. and Burkhardt, U., An Analysis of Twin-Screw Extruder Mechanisms, *Adv. Polym. Tech.*, **1**, 2, p18-39 (1981).
19. Erdmenger, R., *German Patent 813 154* (1951).

20. Boden, H., Ocker, H., Pfaff, G., and Worz. W., *US Patent 3 305 894* (1967).
21. Polyflow S.A., Place de L'Universite 16, B-1348 Louvain-la-Neuve, Belgium.
22. Szydlowski, W., Brzoskowski, R., and White, J. L., Modelling Flow in an Intermeshing Co-Rotating Twin Screw Extruder: Flow in Kneading Discs, *Intern. Polym. Process.*, **1**, 4, p207-214 (1987).
23. Bruce, D. P., Characterisation and Scale-up of Reactive Processing Within a Twin-Screw Extruder, Internal Report, University of Aston in Birmingham (1994).
24. Boyson, H., Future Directions in CFD, *Expanding the Boundaries of CFD Analysis*, IBM, London (1994).
25. Crochet, M. J. and Walters, K., Computational Rheology: a New Science, *Endeavour*, **17**, 2, p64-77 (1993).
26. Bschorer, S. and Schierholz, W., Simulation Programs for Non-Newtonian Fluids, *Rheology 93*, p198-201 (1993).
27. Polyflow S.A., Louvain-la-Neuve, Belgium, 2D Polymesh User's Manual (1991).
28. Polyflow S.A., Louvain-la-Neuve, Belgium, 3D Polymesh User's Manual (1989).
29. Polyflow S.A., Louvain-la-Neuve, Belgium, Polyflow Theoretical Background (1989).
30. Polyflow S.A., Louvain-la-Neuve, Belgium, Polyflow User's Manual - Version 3.4.0 (1995).
31. Polyflow S.A., Louvain-la-Neuve, Belgium, Polyflow Reference Manual - Version 3.4.0 (1995).
32. Polyflow S.A., Louvain-la-Neuve, Belgium, Polyflow Basic Training Manuals - Volumes 1 and 2 (1992).
33. Polyflow S.A., Louvain-la-Neuve, Belgium, Polyflow Super-User Manual (1992).
34. Polyflow S.A., Louvain-la-Neuve, Belgium, Polyplot User's Manual (1987).
35. Polyflow S.A., Louvain-la-Neuve, Belgium, Polyflow Example Manuals I-V (1991-1995).
36. Control Data, St Paul, MN, USA, ICEM Introduction and System Controls - Version 3.1 (1992).
37. Control Data, St Paul, MN, USA, ICEM Data Management - Version 3.1 (1992).
38. Control Data, St Paul, MN, USA, ICEM Basic Construction - Version 3.1 (1992).
39. Control Data, St Paul, MN, USA, ICEM Advanced Design - Version 3.1 (1992).
40. Control Data, St Paul, MN, USA, ICEM IGES Translators - Version 3.1 (1992).
41. Polyflow S.A., Louvain-la-Neuve, Belgium, Polycem Training Example Manual (1995).
42. ICEM Systems GmbH, ICEM CFD Powermesh Manual - Versions 2.0 (1995).
43. ICEM Systems GmbH, ICEM CFD Powermesh Manual - Versions 3.0 and 3.1 (1996).
44. ICEM Systems GmbH, ICEM CFD P-Cube User's Manual - Version 3.0 (1996).

45. Polyflow S.A., Louvain-la-Neuve, Belgium, CFView-PF Tutorial Manual - Version 3.5 (1993).

46. Control Data Systems, Inc., ICEM Marketing, ARH290, 4201 Lexington Avenue North, Arden Hills, MN 55126-6198, USA.

47. Numeca International S.A., 22 Rue de la Concorde, 1050 Brussels, Belgium.

48. Oden, J. T., Kennon, S. R., Tworzydlo, W. W., Bass, J. M. and Berry, C., Progress on Adaptive *hp*-Finite Element Methods for the Incompressible Navier-Stokes Equations, *Comp. Mech.*, **11**, p421-432 (1993).

49. Potts, I. and Anderson, A., An Undergraduate Introductory Course on Computational Fluid Dynamics, *Proc. Instn. Mech. Engrs.*, **205**, p3-10 (1991).

50. Aston, J. G. L, Computational Fluid Dynamics Without Complex Mathematics: the Advantages for Thermofluids Education, *Proc. Instn. Mech. Engrs.*, **205**, p11-23 (1991).

51. Kiani, A., Grald, E. W. and Subbiah, S., Spectral Element Analysis of the Mixing Characteristics of Twin Screw Extruders, *AIChE Symposium on Numerical Simulation of Mixing Phenomena*, (1992).

52. Kalyon, D. M., Gotsis, A. D., Yilmazer, U., Gogos, C. G., Sangani, H., Aral, B. and Tsenoglou, C., Development of Experimental Techniques and Simulation Methods to Analyze Mixing in Co-Rotating Twin Screw Extrusion, *Adv. Polm. Tech.*, **8**, 4, p337-353 (1988).

53. Szydlowski, W. and White, J. L., A Non-Newtonian Model of Flow in a Kneading Disc Region of a Modular Intermeshing Co-rotating Twin Screw Extruder, *J. Non-Newtonian Fluid Mech.*, **28**, p29-46 (1988).

54. Tadmor, Z., Broyer, E. and Gutfinger, C., Flow Analysis Network (FAN) - A Method for Solving Flow Problems in Polymer Processing, *Polym. Eng. Sci.*, **14**, 9, p660-665 (1974).

55. Wong, T. H. and Manas-Zloczower, I., Numerical Studies of the Flow Field in Partially Filled Mixing Equipment, *SPE ANTEC Tech. Papers*, **38**, p1788-1795 (1992).

56. Yang, H. H. and Manas-Zloczower, I., 3D Flow Field Analysis of a Banbury Mixer, *Int. Polym. Process.*, **7**, 3, p195-203 (1992).

57. Yang, H. H. and Manas-Zloczower, I., Flow Field Analysis of the Kneading Discs Region in a Corotating Twin Screw Extruder, *Fourth FIDAP Users Conference* (1991).

58. Yang, H. H. and Manas-Zloczower, I., Flow Field Analysis of the Kneading Disc Region in a Co-Rotating Twin Screw Extruder, *Polym. Eng. Sci.*, **32**, 19, p1411-1417 (1992).

59. Wilson, M. P., Al-Malaika, S., Generalis, S. and Bruce, D. P., Non-Newtonian Flow Field Analysis of Some Mixing and Conveying Element Regions Within a Closely

Intermeshing, Co-Rotating Twin-Screw Extruder, *British Applied Mathematics Colloquium,* **38**, p8 (1996).

60. Wilson, M. P., Al-Malaika, S. and Bruce, D. P., Flow Field Analysis of the Trilobal Elements Region Within an Intermeshing Co-Rotating Twin-Screw Extruder *IChemE Research Event*, **74**, 1, p367-369 (1996).

61. Bruce, D. P., Flow Field Analysis of Some Mixing and Conveying Screw Element Regions Within a Closely Intermeshing, Co-Rotating Twin-Screw Extruder, *IChemE Fluid Mixing Subject Group - Competition for Research Students* (1996).

62. Wilson, M. P., Al-Malaika, S., Generalis, S. C. and Bruce, D. P., Flow Field Analysis of Some Mixing and Conveying Element Regions Within a Closely Intermeshing, Co-Rotating Twin-Screw Extruder, *Fluid Mixing V (IChemE Symposium Series No. 140): The UK Conference on Mixing*, p237-248 (1996).

63. Wilson, M. P., Al-Malaika, S., Generalis, S. C. and Bruce, D. P., Flow Field Analysis of Some Mixing Element Regions Within a Closely Intermeshing, Co-Rotating Twin-Screw Extruder *AIChE Fifth World Congress of Chemical Engineering*, **4**, p509-514 (1996).

64. Bruce, D. P., Co-TSE Modelling, *ATLAS, Newsletter of Department for Computing and Information, RAL*, **4**, p3 (1996).

65. Bruce, D. P., Flow Field Analysis of Some Mixing and Conveying Element Regions Within a Closely Intermeshing, Co-Rotating Twin-Screw Extruder, *Polyflow Promotional Meeting* (1996).

66. Harries, A. and Bruce, D. P., Investigation of Wall Slip Within Some Mixing and Conveying Element Regions for a Closely Intermeshing, Co-Rotating Twin-Screw Extruder, *IChemE Jubilee Research Event*, **75** (1997). In press.

67. Bruce, D. P., Wilson, M. P. and Generalis, S. C., Flow Field Analysis of Both the Trilobal Element and Mixing Disc Zones Within a Closely Intermeshing, Co-Rotating Twin-Screw Extruder, *Journ. Polym. Proc.* (1997). Submitted.

68. Bruce, D. P., Harries, A. M., Wilson, M. P. and Generalis, S. C., Isothermal Non-Newtonian Flow Within the Different Sections of a Closely Intermeshing, Co-Rotating Twin-Screw Extruder, *Fifth Annual Conference of the Computational Fluid Dynamics Society of Canada*, (1997). In press.

69. Nguyen, K. T. and Lindt, J. T., Finite Element Modeling of a Counter-Rotating, Non-Intermeshing Twin Screw Extruder, *Polym. Eng. Sci.*, **29**, 11, p709-714 (1989).

70. Bigio, D. and Zerafati, S., Parametric Study of a 2-D Model of the Nip Region in a Counter-Rotating, Non-Intermeshing Twin Screw Extruder, *Polym. Eng. Sci.*, **31**, 19, p1400-1410 (1991).

71. Li, T. and Manas-Zloczower, I., Flow Field Analysis of an Intermeshing Counterrotating Twin Screw Extruder, *Polym. Eng. Sci.*, **34**, 7, p551-558 (1994).

72. Wang, C. and Manas-Zloczower, I., Flow Field Analysis of a Cavity Transfer Mixer, *Polym. Eng. Sci.*, **34**, 15, p1224-1230 (1994).

73. Gotsis, A. D., Ji, Z. and Kalyon, D. M., 3-D Analysis of the Flow in Co-Rotating Twin Screw Extruders, *SPE ANTEC Tech. Papers*, **36**, p139-142 (1990).

74. Lawal, A. and Kalyon, D. M., Mechanisms of Mixing in Single and Co-Rotating Twin Screw Extruders, *Polym. Eng. Sci.*, **35**, 17, p1325-1338 (1995).

75. Van der Wal, D. J., Goffart, D., Klomp, E. M., Hoogstraten, H. W. and Janssen, L. P. B. M., Three-Dimensional Flow Modeling of a Self-Wiping Corotating Twin-Screw Extruder. Part II: The Kneading Section, *Polym. Eng. Sci.*, **36**, 7, p912-924 (1996).

76. Cuvelier, C., Segal, A. and van Steenhoven, A. A., Finite Elements and Navier-Stokes Equations, D. Reidel Publishing Co., The Netherlands (1986).

77. Kiani, A., Modeling of Twin Screw Extruders Using Nekton, *Fluent Europe Users' Meeting*, (1992).

78. Nekton Package, Fluent Europe Ltd., Holmwood House, Cortworth Road, Sheffield, S11 9LP, England.

79. Bird, R. B., Armstrong, R. C. and Hassager, O., Dynamics of Polymeric Liquids, Volume 1: Fluid Mechanics, John Wiley and Sons, Inc., New York (1987).

80. Wilkes, G. L., and Maxwell, B., Recent Advances in Polymer Science, John Wiley and Sons, Inc., New York (1974).

81. Wang, Y., White, J. L. and Szydlowski, W., Flow in a Modular Intermeshing Co-Rotating Twin Screw Extruder, *Intern. Polym. Process.*, **4**, 4, p262-269 (1989).

82. White, J. L., Montes, S. and Kim, J. K., Experimental Study and Practical Engineering Analysis of Flow Mechanisms in a Modular Intermeshing Corotating Twin Screw Extruder, *Kautschuk und Gummi Kunstsoffe*, **43**, 1, p20-25 (1990).

83. Lim, S. and White, J. L., Influence of a Compatibilizing Agent on the Phase Morphology of a Polyethylene-Polyamide 6 Blend in a Modular Intermeshing Corotating Twin-Screw Extruder, *Polym. Eng. Sci.*, **34**, 3, p221-228 (1994).

84. Hornsby, P. R., Short Communication - Flow and Mixing Phenomena in a Co-Rotating Intermeshing Twin-Screw Extruder, *Plastics Rubber Appl.*, **7**, 4, p237-240 (1987).

85. Todd, D. B., Residence Time Distribution in Twin-Screw Extruders, *Polym. Eng. Sci.*, **15**, 6, p437-443 (1975).

86. Bur, A. J. and Gallant, F. M., Fluorescence Monitoring of Twin Screw Extrusion, *Polym. Eng. Sci.*, **31**, 19, p1365-1371 (1991).

87. Sinton, S. W., Crowley, J. C., Lo, G. A., Kalyon, D. M. and Jacob, C., Nuclear Magnetic

Resonance Imaging Studies of Mixing in a Twin-Screw Extruder, *SPE ANTEC Tech. Papers,* **36**, p116-119 (1990).

88. Li, Y., Lu, Q., Huff, H. E. and Hsieh, F., On-Line Rheological Properties Measurements on a Co-Rotating Self-Wiping Twin-Screw Extruder, *Trans IChemE,* **74**, p149-158 (1996).
89. Gogos, C. G., The Single and Twin-Screw Mixing Element Evaluators: On-Line Performance Evaluation of Extrusion Mixing Elements, *Paper presented at the Advances in Additives and Modifers for Polymer Blends,* (1994).
90. Gotsis, A. D. and Kalyon, D. M., Simulation of Mixing in Co-Rotating Twin Screw Extruders, *SPE ANTEC Tech. Papers*, **35**, p44-48 (1989).
91. Kalyon, D. M. and Sangani, H. N., An Experimental Study of Distribution Mixing in Fully Intermeshing Co-Rotating Twin Screw Extruders, *Polym. Eng. Sci.*, **29**, 15, p1018-1026 (1989).
92. Bigio, D. and Erwin, L., Mixing Studies in Co-Rotating Twin Screw Extruders, *SPE ANTEC Tech. Papers*, **31**, p45-48 (1985).
93. Bigio, D., New Studies on Mixing With Implications on Polymer Blending and Equipment Selection, *Paper presented at the Advances in Additives and Modifiers for Polymer Blends*, (1994).
94. Ess, J. W. and Hornsby, P. R., Twin-Screw Extrusion Compounding of Mineral Filled Thermoplastics: Dispersive Mixing Effects, *Plastics Rubber Appl.*, **8**, 3, p147-156 (1987).
95. Li, Y., Senouci, A., Lai-Fook, R. A. and Smith, A. C., Mixing in a Self-Wiping Co-Rotating Twin-Screw Extruder, An Experimental Study, *Plastics Rubber Appl.*, **11**, 4, p207-214 (1989).
96. Karian, H. G., Co-Rotating Twin Screw Compounding Studies of PVC Formulations, *J. Vinyl Tech.*, **7**, 4, p154-159 (1985).
97. Szydlowski, W. and White, J. L., Improved Model of Flow in the Kneading Disc Region of an Intermeshing Co-Rotating Twin Screw Extruder, *Intern. Polym. Process.*, **2**, 3, p142-150 (1988).
98. Meijer, H. E. H. and Elemans, P. H. M., The Modeling of Continuous Mixers. Part I: The Corotating Twin-Screw Extruder, *Polym. Eng. Sci.*, **28**, 5, p275-290 (1988).
99. Bigio, D. and Erwin, L., The Effect of Axial Pressure Gradient on Extruder Mixing Characteristics, *Polym. Eng. Sci.,* **32,** 11, p760-765 (1992).
100. Stanley Plastics Ltd., Holmbush Industrial Estate, Midhurst, West Sussex, GU29 9HX
101. Peter Pan Playthings, Swindon, England.
102. Avalosse, Th. and Crochet, M. J., Finite Element Simulation of Mixing. Part 3: 3D Flow

Through a Kenics Mixer, Submitted (1995).

103. Griffith, R. M., Fully Developed Flow in Screw Extruders, *IEC Fund.*, **1**, 3, p180-187 (1962).

104. Maheshri, J. C. and Wyman, C. E., Mixing in an Intermeshing Twin Screw Extruder Chamber: Combined Cross and Down Channel Flow, *Polym. Eng. Sci.*, **20**, 9, p601-607 (1980).

105. Armstroff, O. and Zettler, H. D., Formulas for the Design of Twin-Screw Extruders - Determination of the Pressure Loss of Kneading Elements and of the Back-Up Length of Pressure Build-Up Regions in Twin Screw Extruders, *Kunststofftechnik*, **12**, p240-243 (1973).

106. Erdmenger, R., Mehrwellen - Schnecken in der Verfahrenstechnik, *Chem. Ing. Tech.*, **36**, 3, p175-185 (1964).

107. Chen, L., Hu, G. H. and Lindt, J. T., Residence Time Distribution in Non-Intermeshing Counter-Rotating Twin-Screw Extruders, *Polym. Eng. Sci.*, **35**, 7, p598-603 (1995).

108. Kajiwara, T., Nagashima, Y., Nakano, Y. and Funatsu, K., Numerical Study of Twin-Screw Extruders by Three-Dimensional Flow Analysis - Development of Analysis Technique and Evaluation of Mixing Performance for Full Flight Screws, *Polym. Eng. Sci.*, **36**, 16, p2142-2152 (1996).

109. Booy, M. L., Geometry of Fully Wiped Twin-Screw Equipment, *Polym. Eng. Sci.*, **18**, 12, p973-984 (1978).

110. Booy, M. L., Isothermal Flow of Viscous Liquids in Corotating Twin Screw Devices, *Polym. Eng. Sci.*, **20**, 18, p1220-1228 (1980).

111. Denson, C. D. and Hwang, B. K., The Influence of the Axial Pressure Gradient on Flow Rate for Newtonian Liquids in a Self Wiping, Co-Rotating Twin Screw Extruder, *Polym. Eng. Sci.*, **20**, 14, p965-971 (1980).

112. Wang, Y. and White, J. L., Non-Newtonian Flow Modelling in the Screw Regions of an Intermeshing Corotating Twin Screw Extruder, *J. Non-Newtonian Fluid Mech.*, **32**, p19-38 (1989).

113. Szydlowski, W. and White, J. L., An Improved Theory of Metering in an Intermeshing Corotating Twin-Screw Extruder, *Adv. Polym. Tech.*, **7**, 2, p177-183 (1987).

114. Gotsis, A. D. and Kalyon, D. M., Simulation of Mixing in Co-Rotating Twin Screw Extruders, *SPE ANTEC Tech. Papers*, **35**, p44-48 (1989).

115. White, J. L. and Chen, Z., Simulation of Non-Isothermal Flow in Modular Co-Rotating Twin Screw Extrusion, *Polym. Eng. Sci.*, **34**, 3, p229-237 (1994).

116. Fukuoka, T. and Min, K., Numerical Nonisothermal Flow Analysis of Non-Newtonian Fluid in a Nonintermeshing Counter-Rotating Twin Screw Extruder, *Polym. Eng. Sci.*,

34, 13, p1033-1046 (1994).

117. Chiruvella, R. V., Jaluria, Y., Karwe, M. V. and Sernas, V., Transport in a Twin-Screw Extruder for the Processing of Polymers, *Polym. Eng. Sci.*, **36**, 11, p1531-1540 (1996).
118. Loh, K. W. L., Tay, A. A. O. and Teoh, S. H., Effect of Constitutive Models on the Numerical Simulation of Viscoelastic Flow at an Entry Region, *Polym. Eng. Sci.*, **36**, 15, p1990-2000 (1996).
119. Carrot, C., Guillet, J., May, J. F. and Puaux, J. P., Modeling of the Conveying of Solid Polymer in the Feeding Zone of Intermeshing Co-Rotating Twin Screw Extruders, *Polym. Eng. Sci.*, **33**, 11, p700-708 (1993).
120. Potente, H., Hanhart, W. and Reski, T., Design and Processing Optimization of Extruder Screws, *Polym. Eng. Sci.*, **34**, 11, p937-945 (1994).

NOMENCLATURE

Lower Case Roman Characters

a, b, c, d	Material coefficients used in the calculation of Cp(T) and k(T)
d	Rate of deformation tensor
|d|	Magnitude of the rate of deformation tensor
f	External body force per unit mass
f_n	Normal force
f_s	Tangential force
g	Gravity
g_a	Axial pressure gradient
g_x	Down channel pressure gradient
g_z	Cross channel pressure gradient
k(T)	Thermal conductivity as a function of temperature
n	Power law index
n_s	Number of screw tips
p	Pressure
q	Heat flux
q_c	Constant heat flux
r	Heat generated per unit volume by external source
t	Time
t'	Historic time
tr	Second invariant, such that tr $\mathbf{d}^2 \equiv \mathbf{D}:\mathbf{D}$
v	Velocity
v_{bz}	Velocity of fluid in contact with the outer barrel wall
v_{yz}	Cross channel velocity
v_n	Normal velocity
v_s	Tangential velocity
w	Vorticity tensor
|w|	Magnitude of the vorticity tensor
x, y, z	Spatial directions

Upper Case Roman Characters

A	Model-dependent tensor function for differential viscoelastic model
C_L	Centreline distance
Cp(T)	Heat capacity per unit mass as a function of temperature

Ex_{slip}	Slip power index
F^a	Finite element approximation of the function F
F_{slip}	Slip coefficient
H	Screw channel depth
L	Characteristic length
M(t-t')	Integral viscoelastic memory models
P_e	Peclet number
R	Gaussian curvature of a surface
R_e	Reynolds number
R_S	CICo-TSE chamber radius
S	Slip factor
$\mathbf{S}_t$	Deformation-dependent tensor
T	Temperature
$\mathbf{T}$	Stress tensor
$\mathbf{T}_1$	Viscoelastic stress tensor
$\mathbf{T}_2$	Purely viscous stress tensor
T_{alpha}	Reference temperature for the heat convection coefficient
T_σ	Reference temperature for the radiation coefficient
T_o	Scaling temperature
V	Characteristic velocity
X, Y, Z	Axes

Lower Case Greek Characters

alpha	Heat convection coefficient
α	Material coefficient
β	Coefficient of thermal expansion
δ_i	Vector in the unit direction i
ϕ	Shape function
$\dot{\gamma}$	Local shear rate
$\dot{\gamma}_{yz}$	Cross channel local shear rate
$\eta(\dot{\gamma},T)$	Viscosity as a function of shear rate and temperature
η_o	Characteristic viscosity
φ	Screw flight angle
λ	Mixing efficiency
λ_t	Relaxation time

μ	Newtonian viscosity
θ	Screw tip angle (defined in Equation 6-1)
ρ	Density
ρ_c	Centreline ratio
ρ_T	Density at temperature T
ρ_o	Density at scalar temperature T_o
σ	Radiation coefficient
σ_s	Surface tension coefficient
ψ	Angle (in relation to screw geometry and defined in Equation 6-2)
ξ	Dimensionless screw height

Upper Case Greek Characters

K	Permeability tensor
K	Consistency factor
Ω_r	Angular rotational screw speed

Other Symbols

∇	Vector differential operator